MODERATE SPECTRAL ATMOSPHERIC RADIANCE AND TRANSMITTANCE CODE (MOSART).

Volume III: Technical Reference Manual

William M. Cornette
Prabhat Acharya
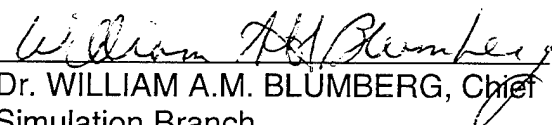David Robertson
Gail P. Anderson

19960212 145

7 November 1995

PHILLIPS LABORATORY
Directorate of Geophysics
AIR FORCE MATERIEL COMMAND
HANSCOM AFB, MA 01731-3010

"This technical report has been reviewed and is approved for publication"

William A.M. Blumberg
Dr. WILLIAM A.M. BLUMBERG, Chief
Simulation Branch
Optical Environment Division

Roger Van Tassel
Dr. ROGER A. VAN TASSEL, Director
Optical Environment Division

REPORT DOCUMENTATION PAGE

Form Approved
OMB No. 0704-0188

1. AGENCY USE ONLY *(Leave blank)*	2. REPORT DATE 7 November 1995	3. REPORT TYPE AND DATES COVERED Scientific Interim

4. TITLE AND SUBTITLE
Moderate Spectral Atmospheric Radiance and Transmittance Code (MOSART). Volume III: Technical Reference Manual

5. FUNDING NUMBERS
PR 3054
TA GD
WU 01

6. AUTHOR(S)
William M. Cornette*   Gail P. Anderson
Prabhat Acharya**
David Robertson**

7. PERFORMING ORGANIZATION NAME(S) AND ADDRESS(ES)
Phillips Laboratory/GPOS
29 Randolph Road
Hanscom AFB, MA 01731-3010

8. PERFORMING ORGANIZATION REPORT NUMBER
PL-TR-94-2244(III)
ERP, No. 1182

9. SPONSORING/MONITORING AGENCY NAME(S) AND ADDRESS(ES)

10. SPONSORING/MONITORING AGENCY REPORT NUMBER

11. SUPPLEMENTARY NOTES * Photon Research Associates, 10350 North Torrey Pines Road, Suite 300, La Jolla, CA 92037-1020; ** Spectral Sciences, Inc., 99 South Bedford St, Burlington, MA 01803-5169

12a. DISTRIBUTION/AVAILABILITY STATEMENT

Approved for public release; distribution unlimited

12b. DISTRIBUTION CODE

13. ABSTRACT *(Maximum 200 words)*

The Moderate Spectral Atmospheric Radiance and Transfer (MOSART) computer program calculates atmospheric transmission and radiation in the ultraviolet region through the microwave spectral regions (0.2 μm to infinity or 0 - 50,000 cm^{-1}. The spectral resolution is variable from a value of 2 cm^{-1} upward in increments of 1 cm^{-1}. It contains features which have been extracted from the MODTRAN code developed by the Geophysics Division (PL/GPOS) of the Air Force Phillips Laboratory and the APART code developed by Photon Research Associates (PRA). Because of the requirement that MOSART be compatible with various codes used in the SSGM (Strategic Scene Generation Model), the overall structure of this version of MOSART closely follows that of APART. However, MOSART contains all the MODTRAN atmospheric features and is easily used for that code's usual point-to-point calculations.
   This volume provides the user with information describing the installation of MOSART. The other volumes describe running the code (Vol. II), technical discussion (Vol. III), and the structure of MOSART (Vol. IV). To provide users with on-line assistance, this volume is available in a series of "html" files that can be viewed using the MOSART Input Builder or the MOSAIC Software.

14. SUBJECT TERMS
Atmospheric Propagation
Radiance
Transmittance
Backgrounds
Modelling

15. NUMBER OF PAGES
354

16. PRICE CODE

17. SECURITY CLASSIFICATION OF REPORT Unclassified	18. SECURITY CLASSIFICATION OF THIS PAGE Unclassified	19. SECURITY CLASSIFICATION OF ABSTRACT Unclassified	20. LIMITATION OF ABSTRACT SAR

NSN 7540-01-280-5500

Standard Form 298 (Rev. 2-89)
Prescribed by ANSI Std. Z39-18
298-102

TABLE OF CONTENTS

TABLE OF CONTENTS (continued)

v

LIST OF FIGURES

LIST OF FIGURES (continued)

LIST OF FIGURES (continued)

LIST OF FIGURES (continued)

LIST OF FIGURES (continued)

LIST OF FIGURES (continued)

LIST OF FIGURES (continued)

LIST OF FIGURES (continued)

LIST OF FIGURES (continued)

LIST OF TABLES

LIST OF TABLES (continued)

LIST OF TABLES (continued)

LIST OF TABLES (continued)

1.0 INTRODUCTION

The MOSART computer program calculates atmospheric transmission and radiation in the ultraviolet through the microwave spectral regions (0.2 μm to infinity or 0 - 50,000 cm⁻¹). It contains features which have been extracted from the MODTRAN code developed by the Geophysics Division (PL/GPOS) of the Air Force Phillips Laboratory and the APART code developed by Photon Research Associates (PRA). MODTRAN is widely used in many different atmospheric calculations for infrared (IR) signature studies of both targets and backgrounds, it has many features that are desirable for large simulation models. Because of the requirement that MOSART be compatible with various codes used in the SSGM (Strategic Scene Generation Model), the overall structure of this version of MOSART closely follows that of APART. However, MOSART contains all the MODTRAN atmospheric features and is easily used for that code's usual point-to-point calculations.

This volume of the Users manual provides a technical discussion of the various model elements used in MOSART. It describes the underlying physical assumptions and the equations actually used in the code to calculate the various quantities. References to previous work which led to the development of the various algorithms are also given. The other volumes in the Users Manual describe installation of MOSART (Vol. I), running the code (Vol. II), and the structure of MOSART (Vol. IV).

MOSART and its utility programs are written in ANSI X3.9-1978 FORTRAN (FORTRAN 77) and are very portable programs. The source codes delivered with MOSART include:

FPTEST:	Test machine dependent operations.
INSTDB:	Installs direct access binary data bases.
MOSART:	Is the main MOSART program.
PLTGEN:	Makes graphs of the results.
ASCBIN:	Converts binary files to ASCII and vice-versa.
CRFILE:	Assists in preparing the MOSART input file.
FACET:	Calculates the emitted and reflected radiance from a surface.
MRFLTR:	Degrades the spectral output using a filter function.
BBTEMP:	Converts radiance to equivalent blackbody temperatures.
VISUAL:	Converts visible radiances to luminances and determines color.

2.0 ENVIRONMENTAL CHARACTERIZATION

Prior to any calculation of the path geometry and the radiative transfer, the environmental conditions must be fully characterized with respect to:

- Atmospheric conditions

- Aerosols

- Hydrometeors

- Background materials

- Atmospheric turbulence

- Global data bases

The software in MOSART is driven by data bases that describe each of these atmospheric elements. In addition, there are supplemental data in the global data bases which provide mean values of those elements at any terrestrial location. This chapter discusses those data bases in detail, and provides graphs that show qualitatively the type of information in each data base. Since these graphs are typically in log-log or semilog format, it is not recommended that any quantitative information be obtained from the graphs. Instead this information should be obtained by printing the data base desired, following the instructions given below and in the Software Reference Manual.

2.1 Atmospheric Conditions

MOSART contains 23 model atmospheres (see Table 1) (plus the option for a user-defined atmosphere) in the following altitude grid:

- From 0 to 25 km in 1 km increments

- From 25 to 50 km in 2.5 km increments

- From 50 to 120 km in 5 km increments

- Above 120 km at 130, 150, 200, 250, 500 and 1000 kilometers

Table 1. Northern Hemisphere Model Atmospheres.

TYPE	LATITUDE	SEASONS
Equatorial	0	Summer Winter
Tropical	15	Winter Summer Annual*
Subtropical	30	Summer Winter
Midlatitude	45	Summer* Winter* Spring/Fall
Subarctic	60	Summer* Winter* Winter Model A (Warm) Winter Model B (Warm) Winter Model C (Warm) Winter Model D (Cold)
Arctic	75	Summer Winter
Polar	90	Summer Winter
U.S. Standard	-	*
Israeli Standard	-	Day/Night

* MODTRAN Atmospheres

Below 120 kilometers, the model atmospheres vary with latitude and season, while above 120 km, they depend upon the exospheric temperature and season.

The six standard LOWTRAN atmospheres are included along with seventeen other atmospheres. These additional model atmospheres include seasonal variations (e.g., summer, winter, spring/fall), local variations (e.g., normal, warm, and cold arctic winters), and latitudinal variations (i.e., equatorial to polar in 15 degree increments). These additional atmospheres are based on the AFGL tabulations (Kantor and Cole 1975, 1976, 1977a, 1977b) plus the Israeli standard day and night atmospheres. The dry stratosphere model is also provided as an option.

The U.S. Standard (1976) Atmosphere between 120 and 1000 km is included, along with the exospheric temperature and seasonal variations (U.S. Standard Atmosphere 1976; U.S. Standard Atmosphere Supplements 1966). An exospheric temperature can be either specified or calculated from the solar flux, sunspot activity, and geomagnetic planetary activity. The calculation of nonlocal thermal equilibrium (NLTE) radiative transfer through this portion of the atmosphere is currently in development, and can be addressed with the Strategic High Altitude Radiance Code (SHARC) (Sharma et al., 1993).

The complete set of MODTRAN boundary layer aerosols (i.e., rural, urban, maritime, oceanic, tropospheric, advection fog, and radiation fog) and stratospheric aerosols (i.e., background, aged volcanic, fresh volcanic, and meteoric dust) are incorporated. This includes absorption and scattering coefficients, plus all aerosol and molecular scattering phase functions (Shettle and Fenn, 1979). Following MODTRAN, the relative humidity dependence of the first five boundary layer aerosols is included. Also, the capability of handling light fogs (i.e., 99% relative humidity) is an additional run-time option. The separation between the tropospheric and stratospheric aerosol types and profiles is determined by the location of the tropopause, which is calculated using the temperature profile and the World Meteorological Organization (WMO) definition of the tropopause. The haze profiles from MODTRAN have been modified to coincide with the model atmosphere and the background altitude, and the extreme upper stratosphere haze is an additional run-time option.

All aerosol features from LOWTRAN 7 (Kneizys et al., 1988) have been incorporated into MOSART. These include the rain model, the cirrus cloud model and the Army vertical structure algorithm for the first few hundred meters of the boundary layer. The rain model has been modified to require a cloud model, which has been developed using the fog aerosol models from LOWTRAN. In addition, the rain model has been expanded to include the Marshall-Palmer distribution, the Joss

and Waldvogel models for drizzle, widespread rain, and a thunderstorm, and the Sekhon and Srivastava thunderstorm model.

Each of these topics is discussed in greater detail below:

2.1.1 Pressure, Temperature, and Density Profiles

Each model atmosphere contains altitude profiles of pressure, temperature, and molecular concentrations. The actual values can be found in BLOCK DATA ATMSBD for altitudes below 120 km and in BLOCK DATA UPPRBD for altitudes above 120 km. The model pressure profiles for all 23 model atmospheres are presented in Figure 1.

The six LOWTRAN model atmospheres were obtained from MODTRAN 2. The other atmospheric profiles were obtained from a variety of references. For those cases where the atmospheric profile was not defined up to 120 km, a normalized LOWTRAN model atmosphere was used to complete the profile. For example, the Equatorial profiles between 90 and 120 km were completed using a normalized Tropical Annual profile, while the Subtropical profile for the same altitude region were completed using a normalized average of the Tropical Annual and Midlatitude Summer or Winter profile.
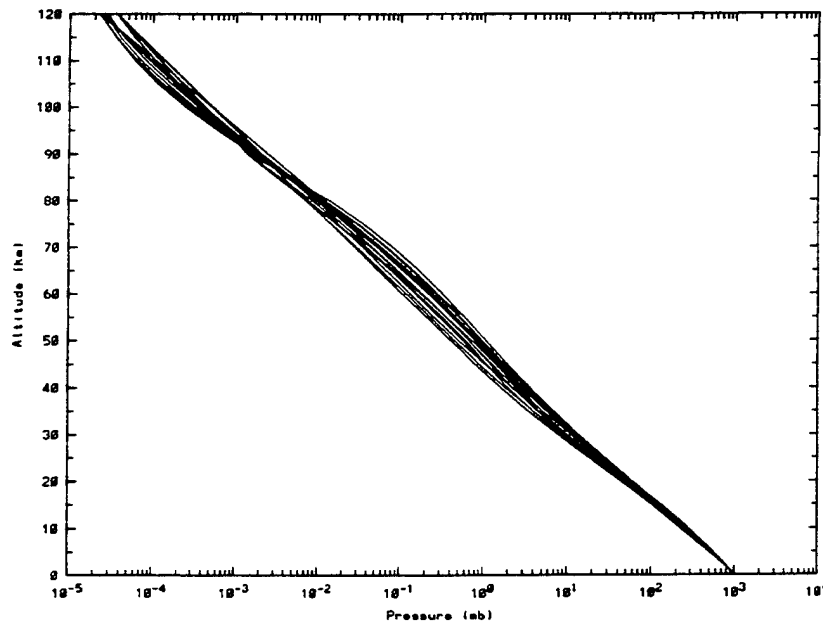
Figure 1. Model Pressure Profiles.

The summer and winter temperature profiles for the seven latitudes (i.e., 0°, 15°, 30°, 45°, 60°, 75°, and 90° N. Latitude) are presented in Figures 2 and 3, respectively. The temperature profiles for the Tropical (15° N. Latitude) model

5
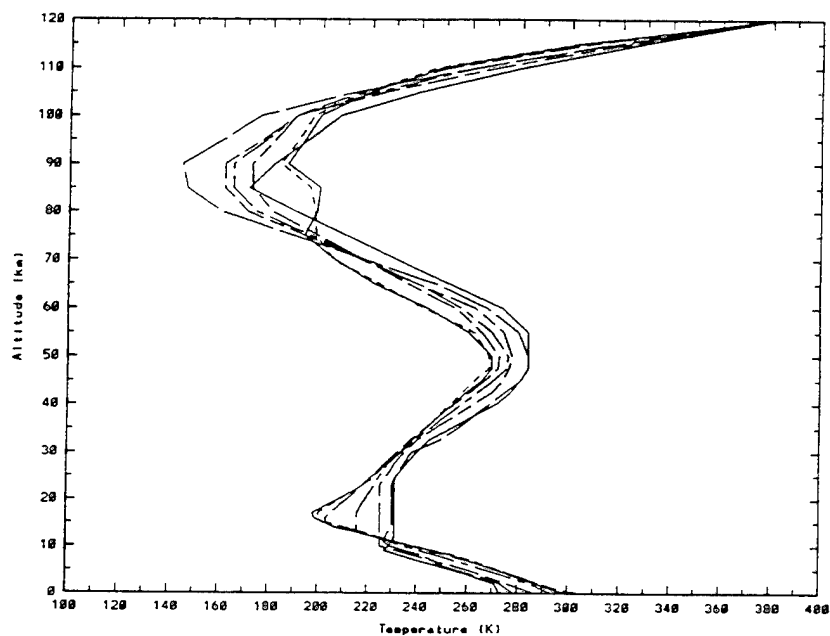
Figure 2. Model Summer Temperature Profiles.
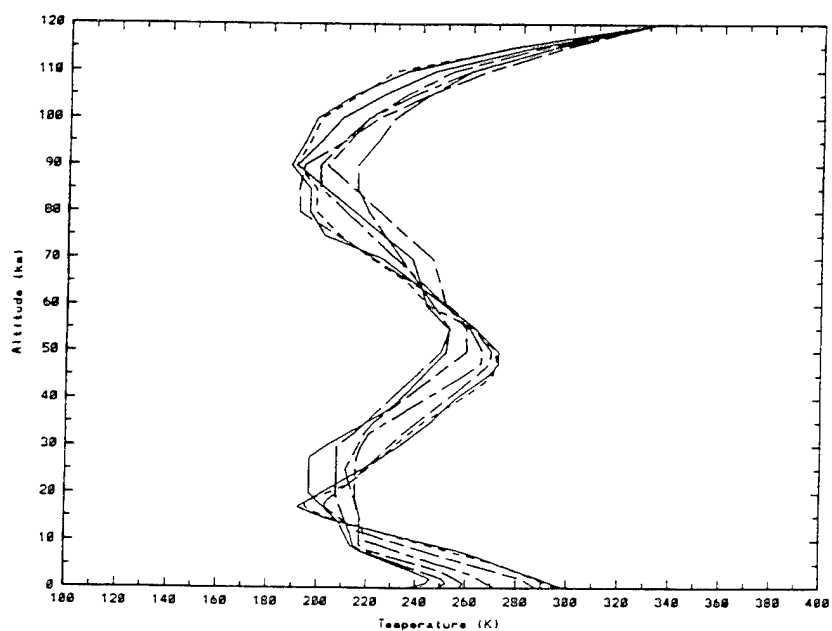
Figure 3. Model Winter Temperature Profiles.

atmospheres for summer, winter, and annual (from MODTRAN) are shown in Figure 4, while the Midlatitude Summer, Winter, and Spring/Fall temperature profiles are shown in Figure 5. It should be noted that the Midlatitude Spring/Fall is also recommended for latitudes between 30° and 60° North during the spring and fall.
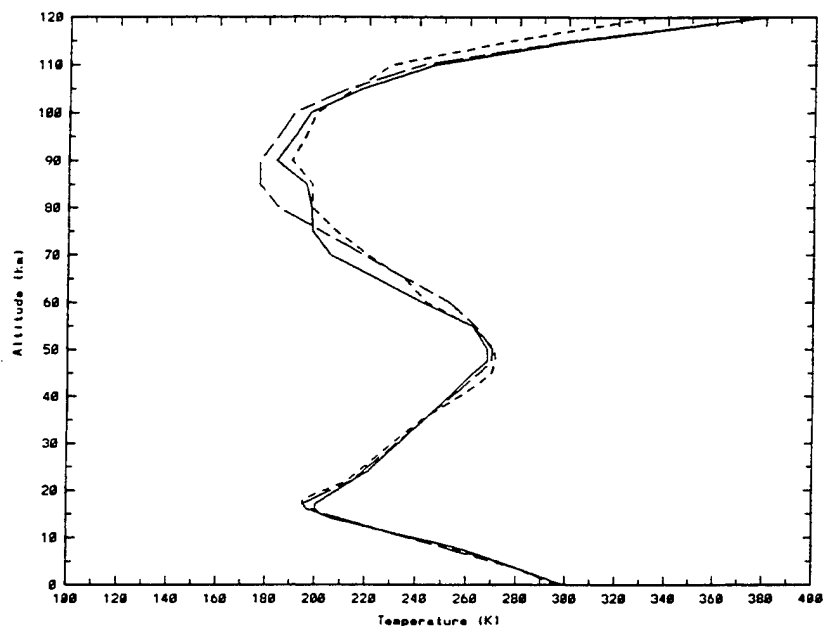
Figure 4. Tropical Temperature Profiles.
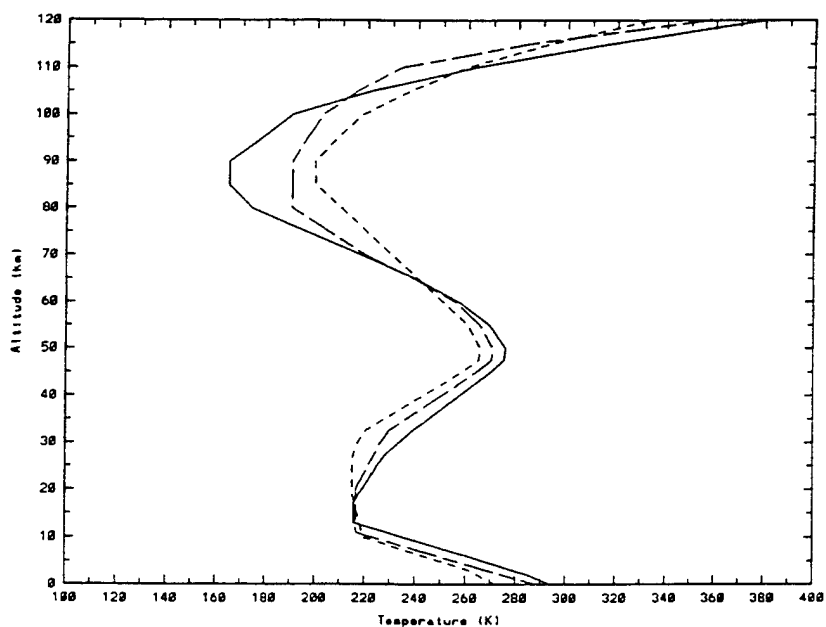
Figure 5. Midlatitude Temperature Profiles.

For the Subarctic Winter, there are five models (i.e., nominal, Model A (warm), Model B (warm), Model C (warm), Model D (cold)). The temperature profiles for the five model atmospheres are presented in Figure 6. The temperature profiles for the U.S. Standard atmosphere is shown in Figure 7, and that for the Israeli Standard atmospheres are shown in Figure 8. The temperature and pressure profiles of the six LOWTRAN model atmospheres are shown in Figure 9 and 10, respectively.
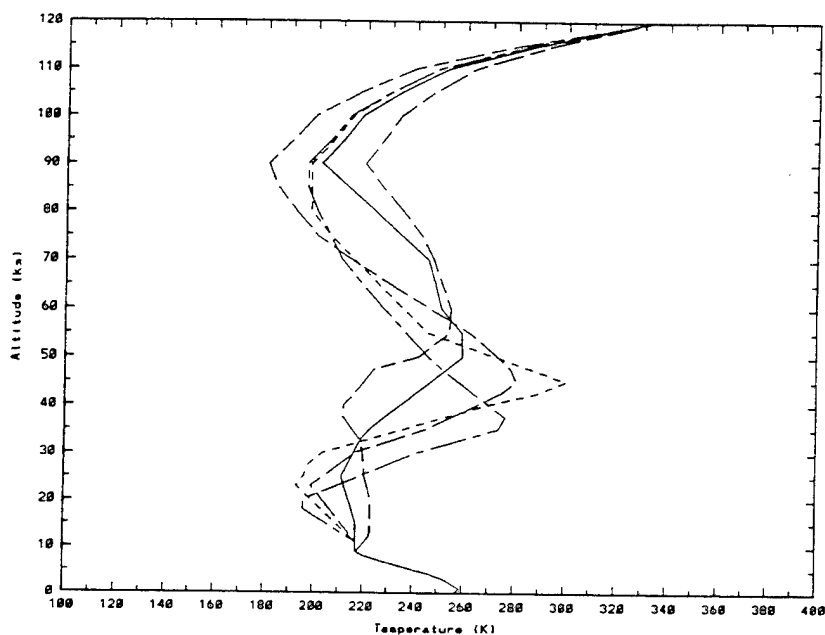
Figure 6. Subarctic Winter Temperature Profiles.
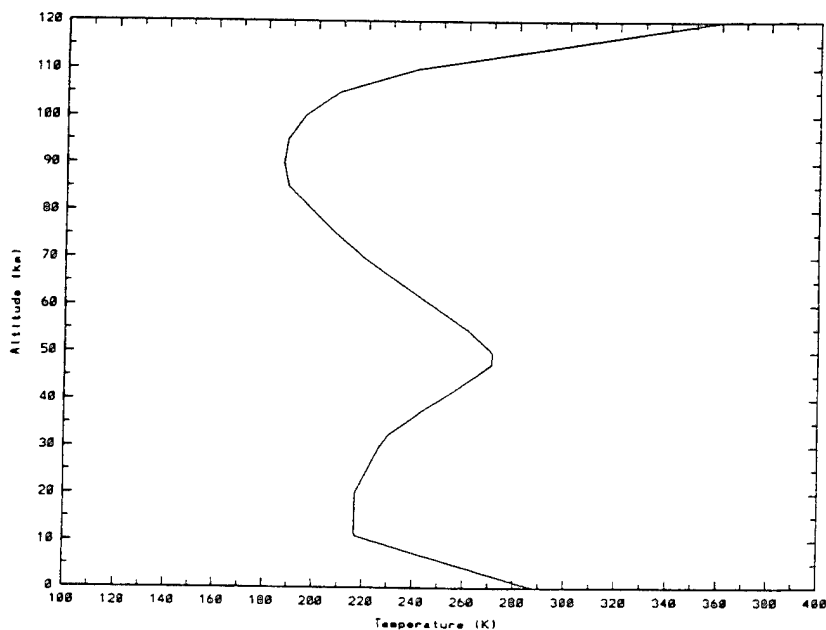
Figure 7. U.S. Standard Temperature Profile.

8
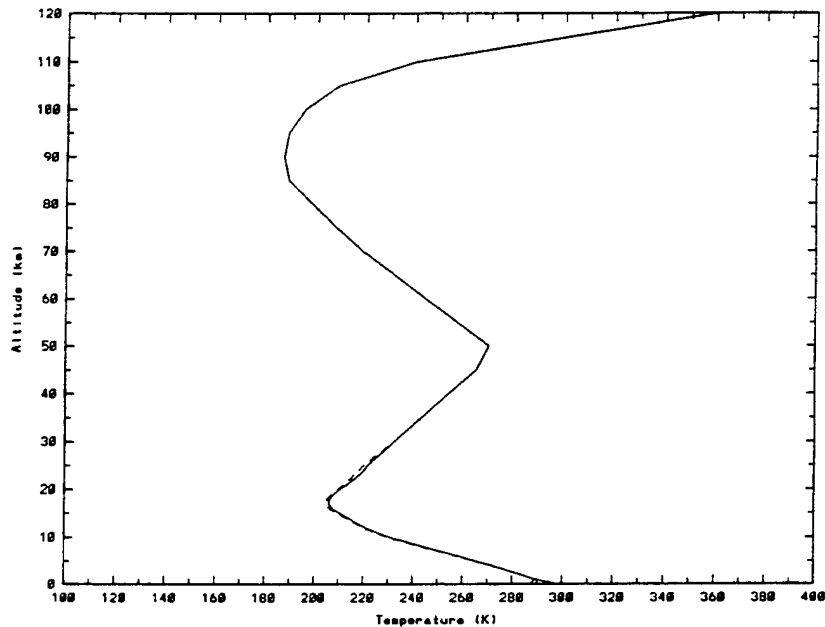
Figure 8. Israeli Standard Temperature (Day/Night) Profile.

2.1.2 Molecular Concentrations

Molecular concentrations are stored in MOSART as altitude-dependent profiles expressed in parts per million by volume (ppmv). The twenty-eight molecular species listed to the HITRAN Line Atlas (Rothman, et al., 1992) are represented. Like MODTRAN, only thirteen are presently used for radiative transfer calculations.
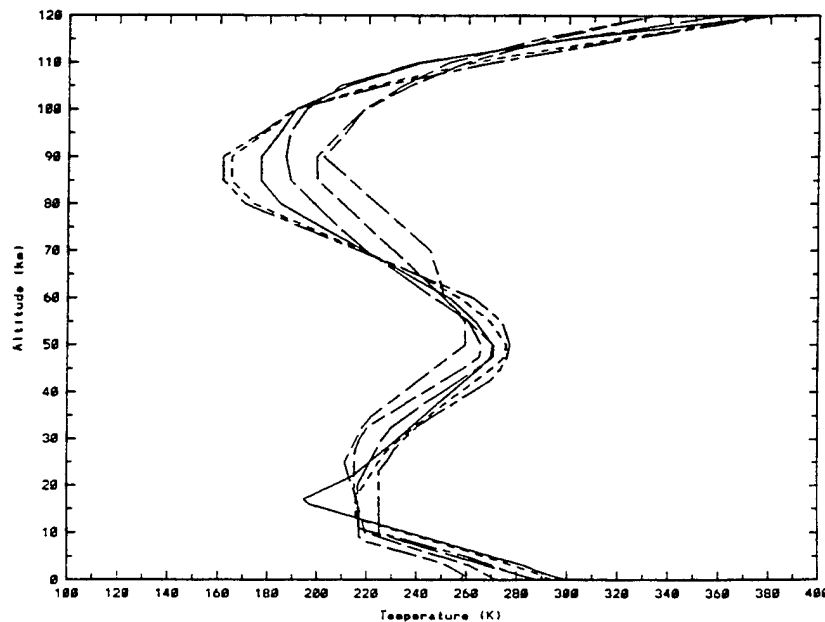
Figure 9. Temperature Profiles for the LOWTRAN Model Atmospheres.
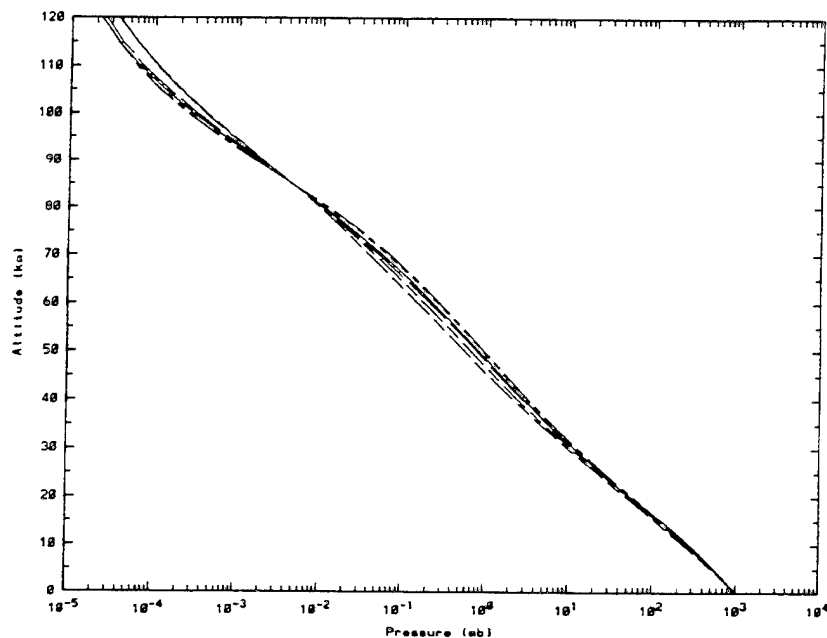
Figure 10. Pressure Profiles for the LOWTRAN Model Atmospheres.

Seven of the molecules in MOSART have molecular concentrations profiles that vary with latitude and season, namely,

- H_2O (water vapor)

- CO_2 (carbon dioxide)

- O_3 (ozone)

- N_2O (nitrogen oxide)

- CO (carbon monoxide)

- CH_4 (methane)

- O_2 (oxygen)

The molecular profiles for the six MODTRAN model atmospheres are shown in Figures 11 through 17. The profiles for the other model atmospheres were derived from these profiles.
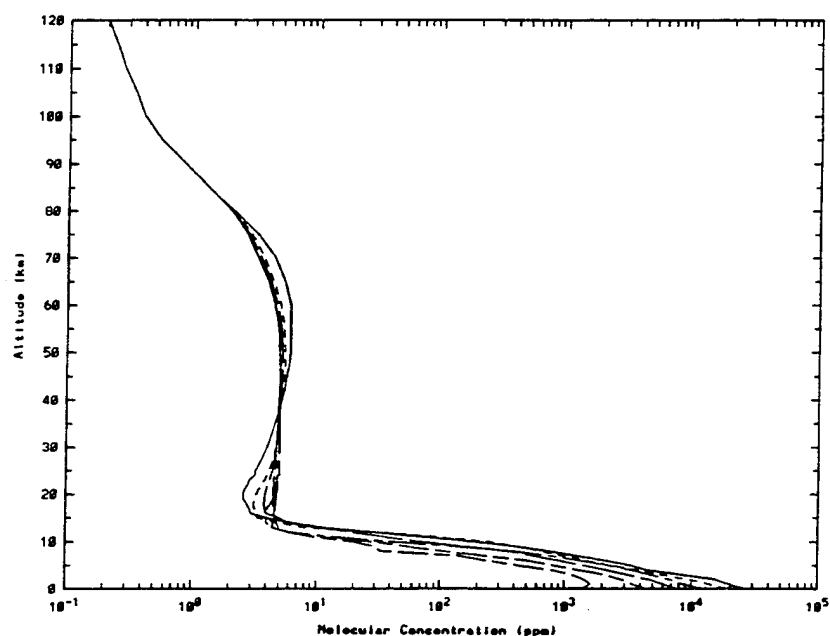
Figure 11. Water Vapor Profiles for the LOWTRAN Model Atmospheres.
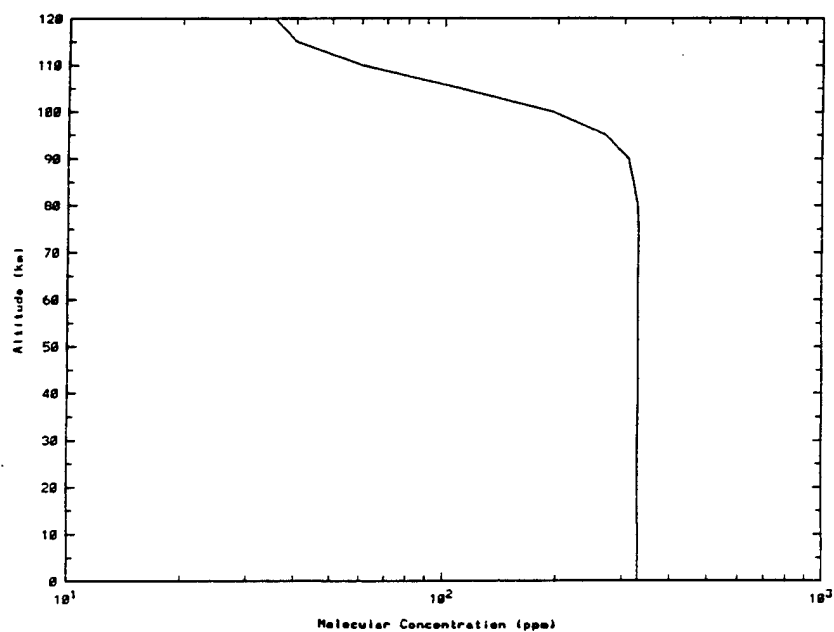
Figure 12. Carbon Dioxide.
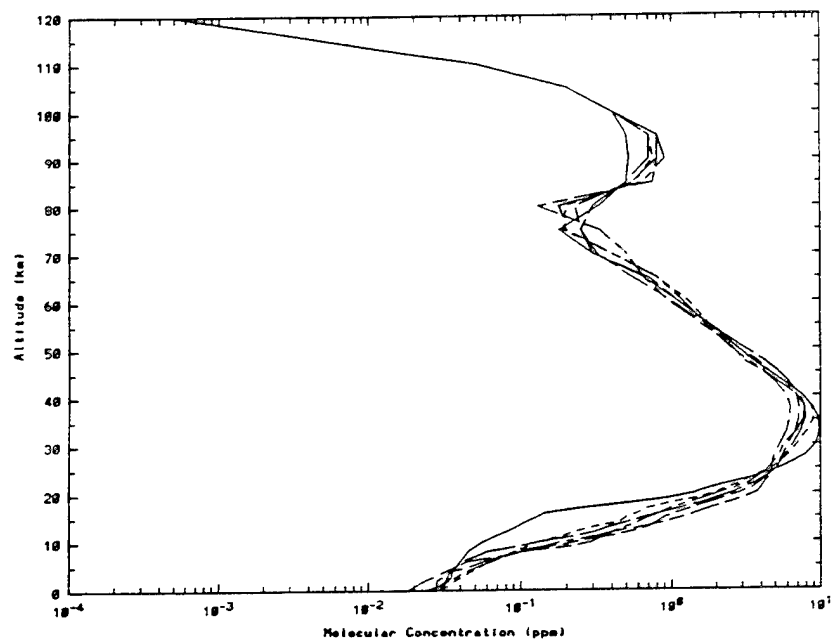
Figure 13. Ozone Profiles.
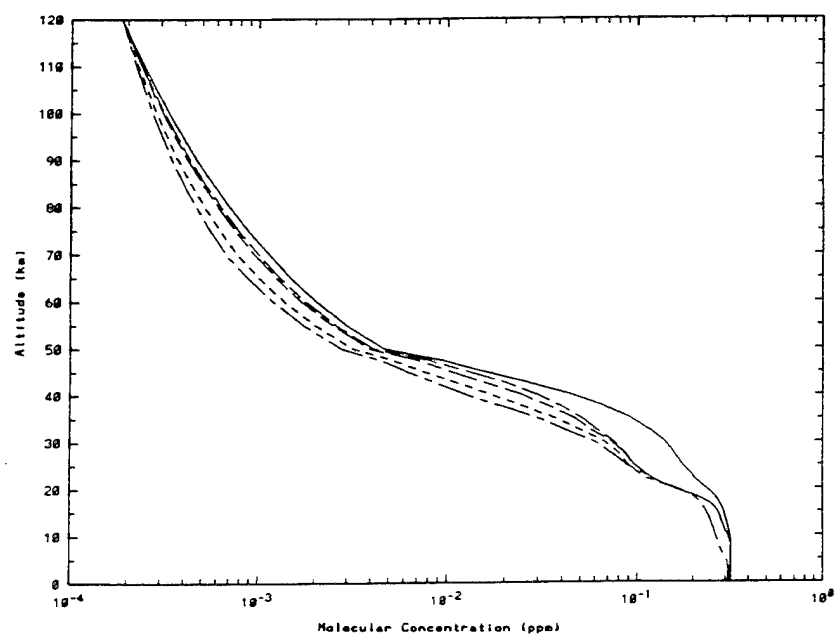
Figure 14. Nitrogen Oxide Profiles.

12
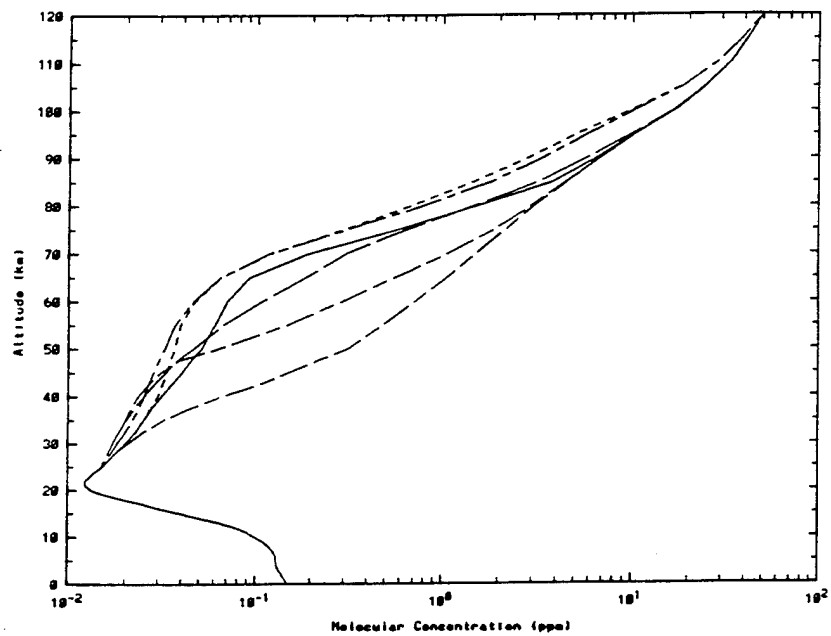
Figure 15. Carbon Monoxide Profiles.
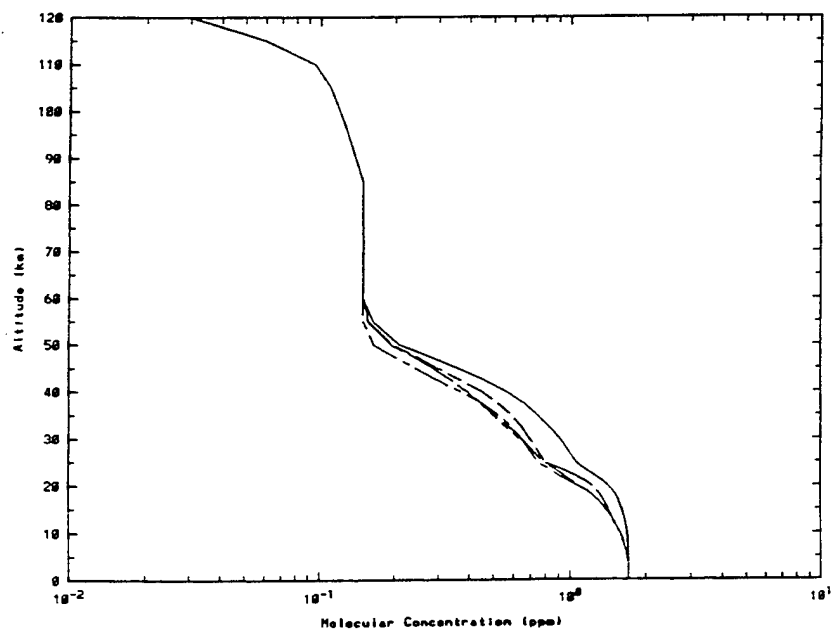
Figure 16. Methane Profiles.
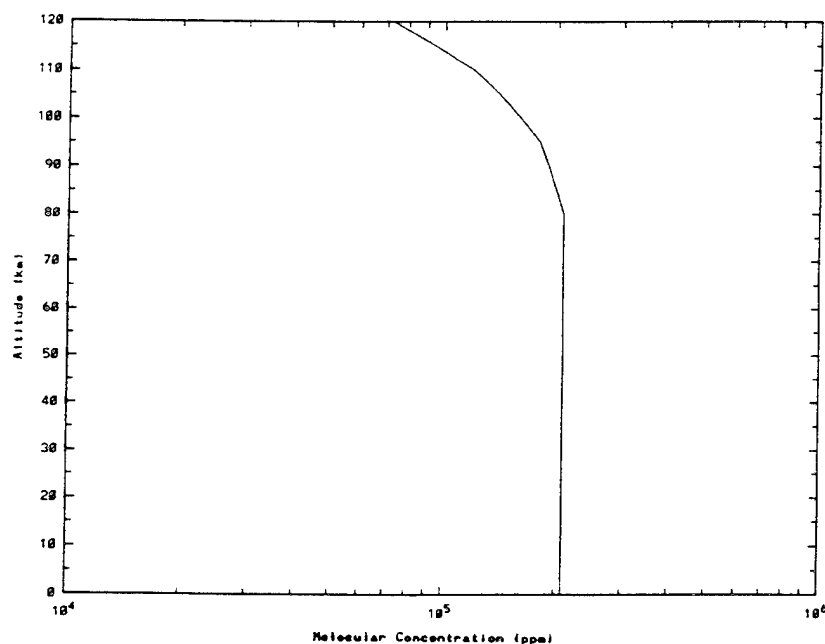
Figure 17. Oxygen Profiles.

The remaining molecular profiles are assumed to be latitude and season independent. These molecules are:

- NO (nitric oxide)
- NO_2 (nitrogen dioxide)
- HNO_3 (nitric acid)
- HF (hydrogen fluoride)
- HBr (hydrogen bromide)
- ClO (chlorine monoxide)
- H_2CO (formaldehyde)
- N_2 (nitrogen)
- CH_3Cl (methyl chloride)
- C_2H_2 (acetylene)
- PH_3 (phosphine)

- SO_2 (sulfur dioxide)
- NH_3 (ammonia)
- OH (hydroxyl radical)
- HCl (hydrogen chloride)
- HI (hydrogen iodide)
- OCS (carbonyl sulfide)
- HOCl (hypochlorous acid)
- HCN (hydrogen cyanide)
- H_2O_2 (hydrogen peroxide)
- C_2H_6 (ethane)

14

The molecular concentration profiles for each of these molecules are shown in Figures 18 through 36, with the exception of hydrogen iodide and phosphine which have been assigned constant volume mixing ratios of 3.0×10^{-6} and 1.0×10^{-14} ppmv, respectively. At the present time, only nitric acid, sulfur dioxide, nitrogen dioxide, ammonia, nitric acid, and nitrogen normally are used by MOSART.
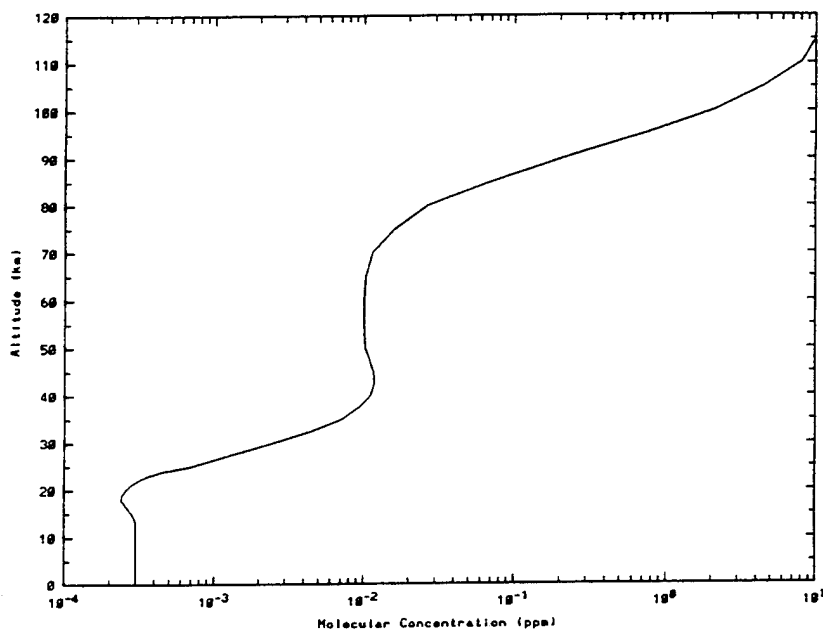
Figure 18. Nitric Oxide Profile.
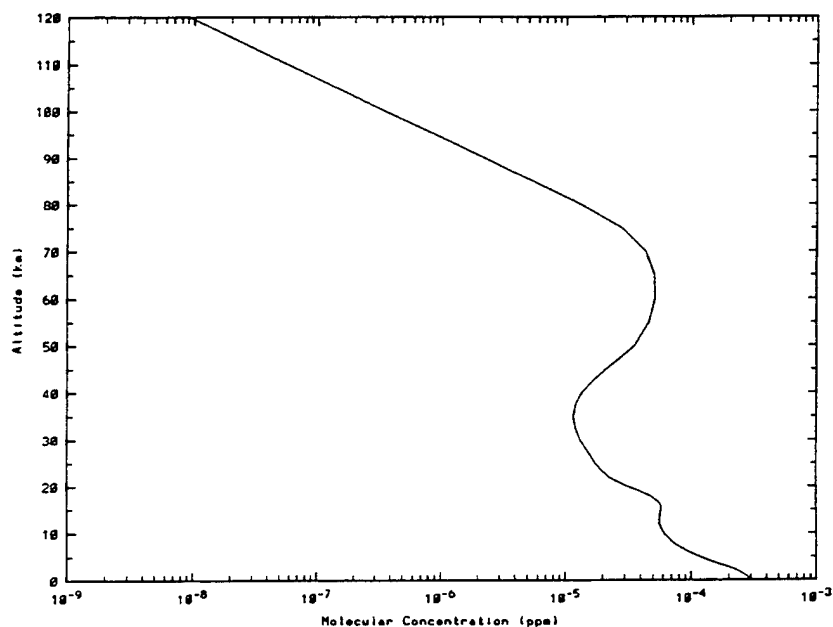
Figure 19. Sulfur Dioxide Profile.

15
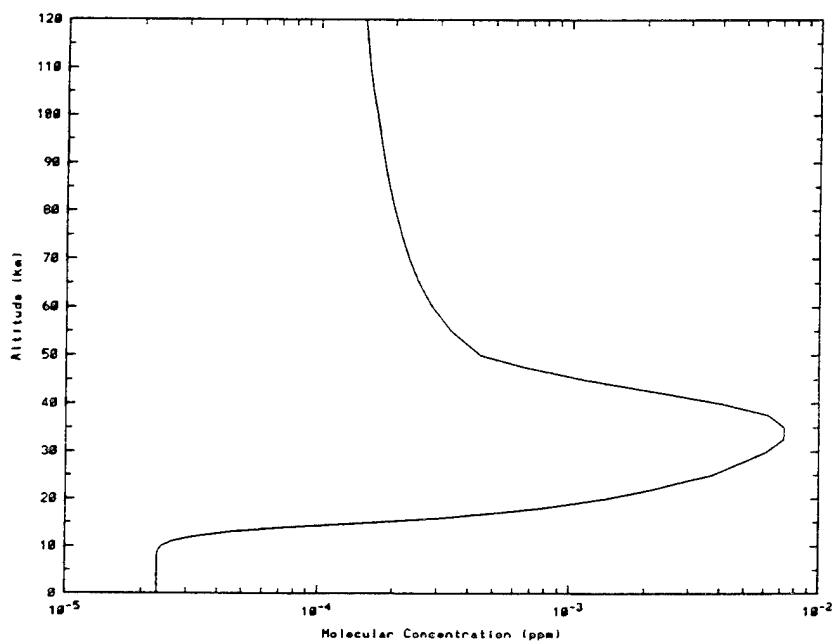
Figure 20. Nitrogen Dioxide Profile.
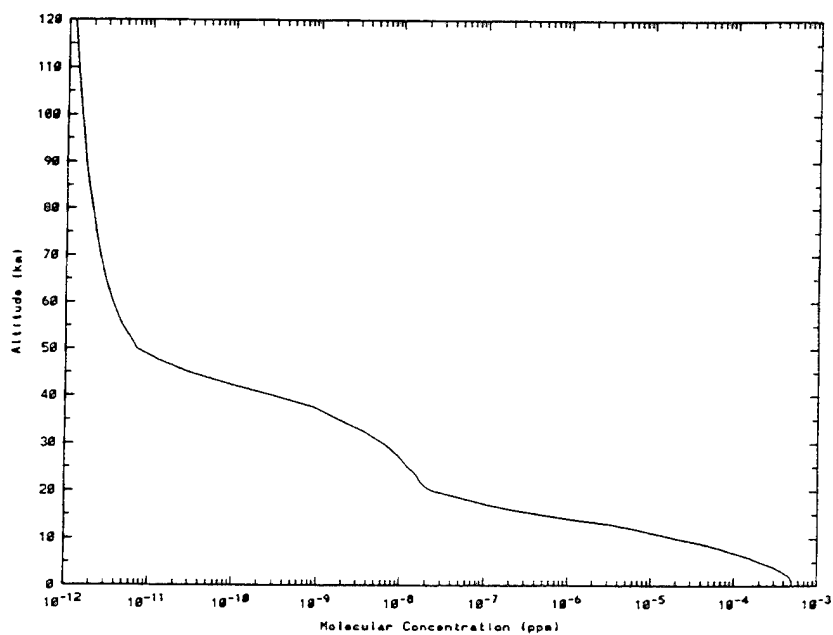
Figure 21. Ammonia Profile.

16
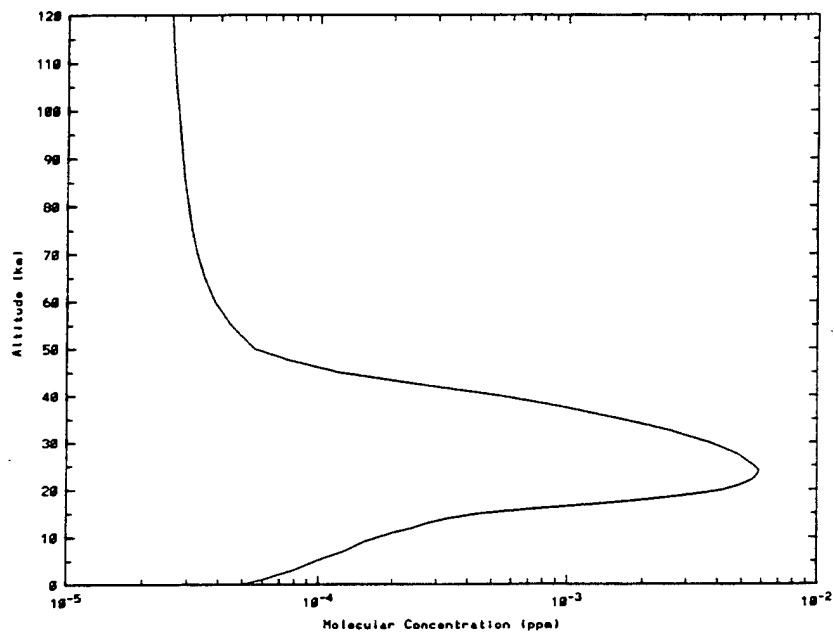
Figure 22. Nitric Acid Profile.
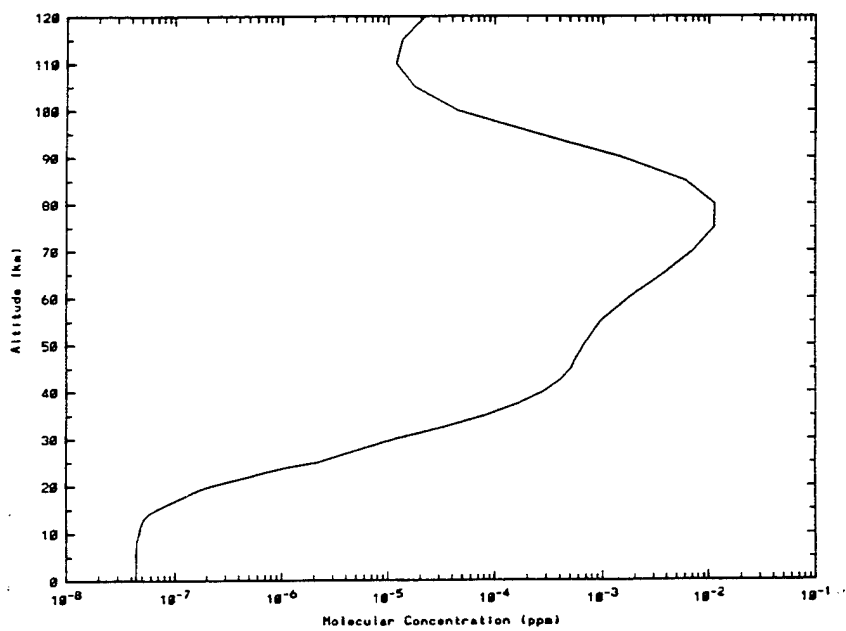
Figure 23. Hydroxyl Radical Profile.

17
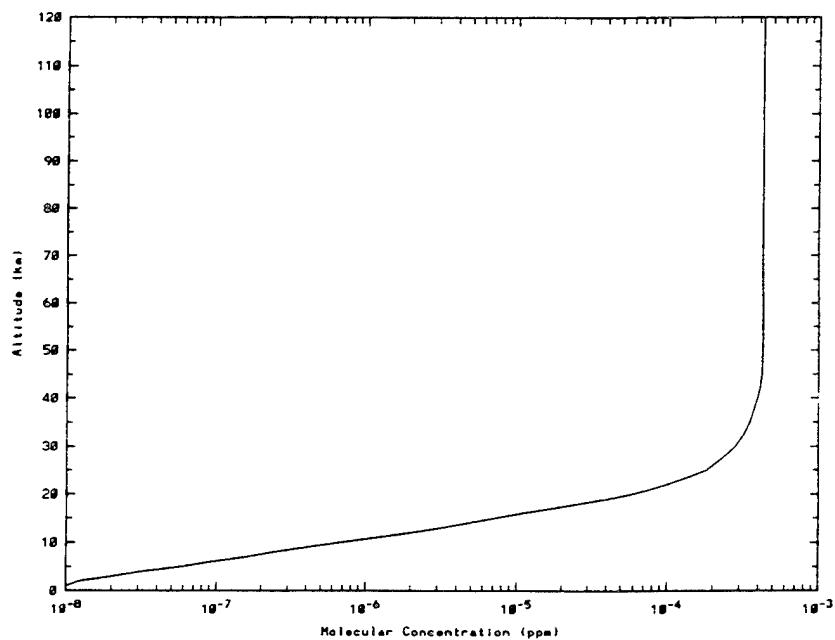
Figure 24. Hydrogen Fluoride Profile.
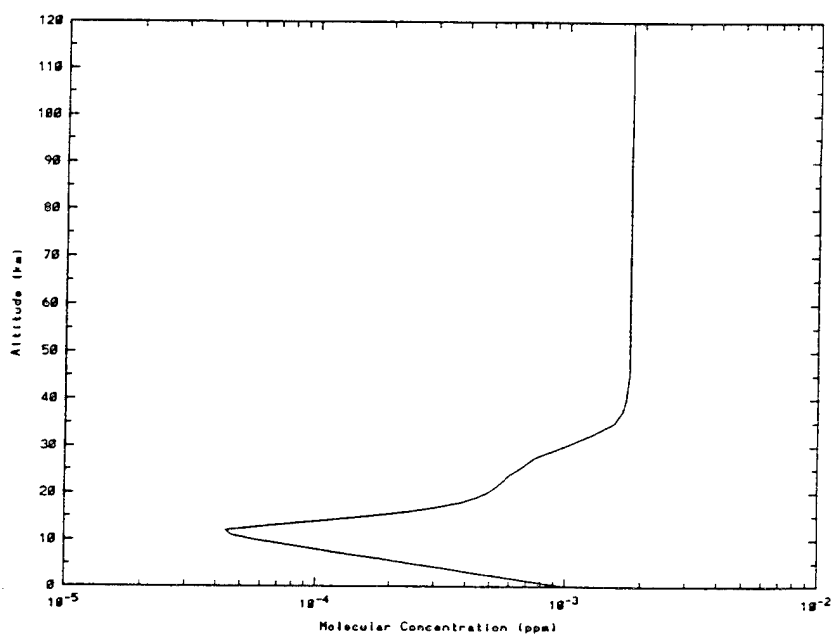
Figure 25. Hydrogen Chloride Profile.

18
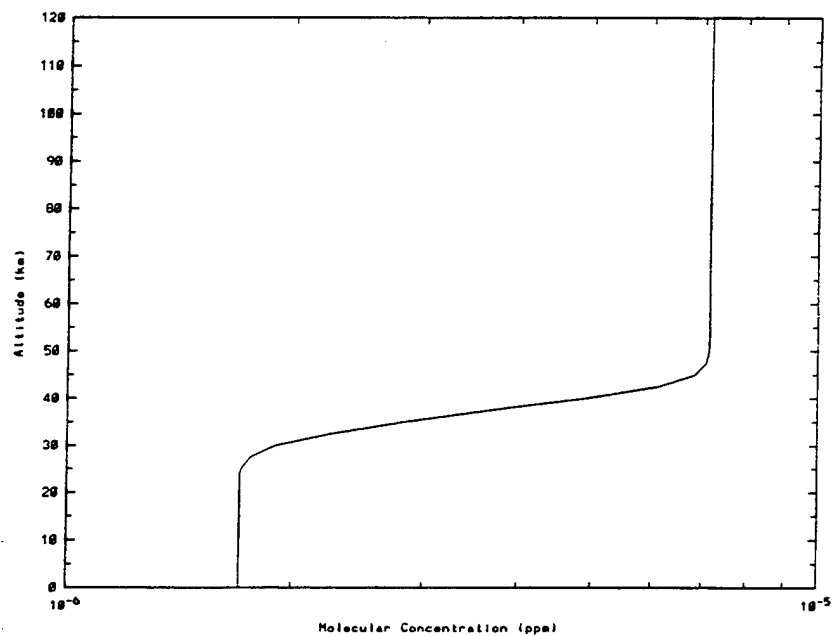
Figure 26. Hydrogen Iodide Profile.
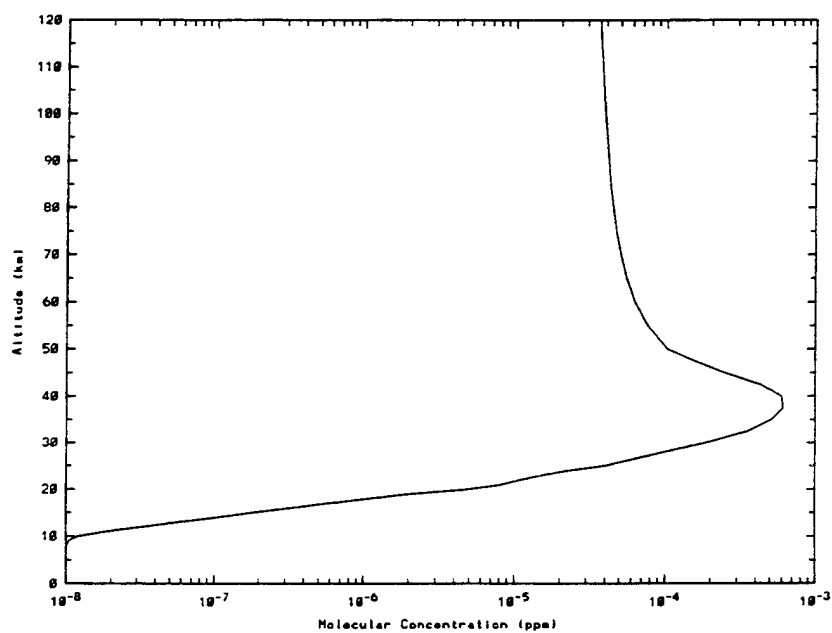
Figure 27. Chlorine Monoxide Profile.

19
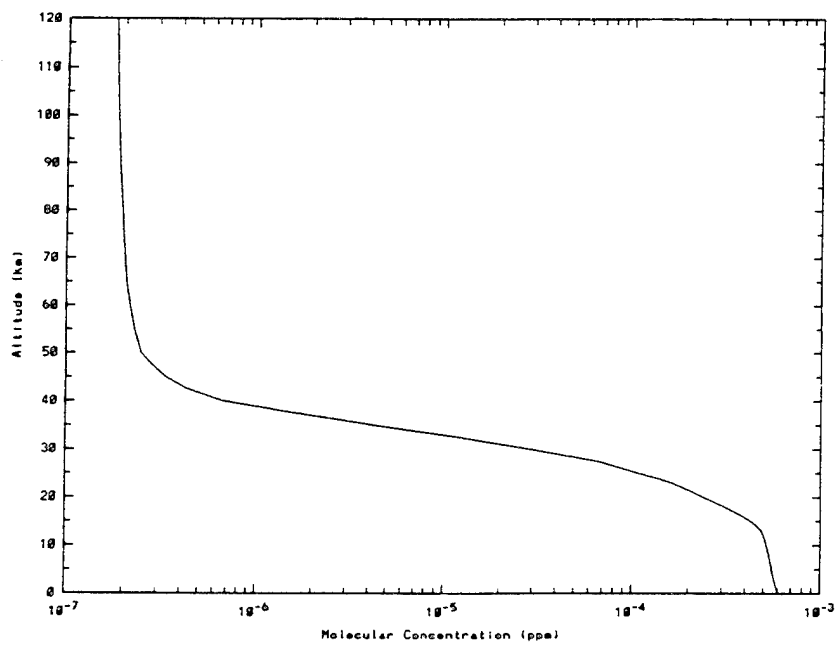
Figure 28. Carbonyl Sulfide Profile.
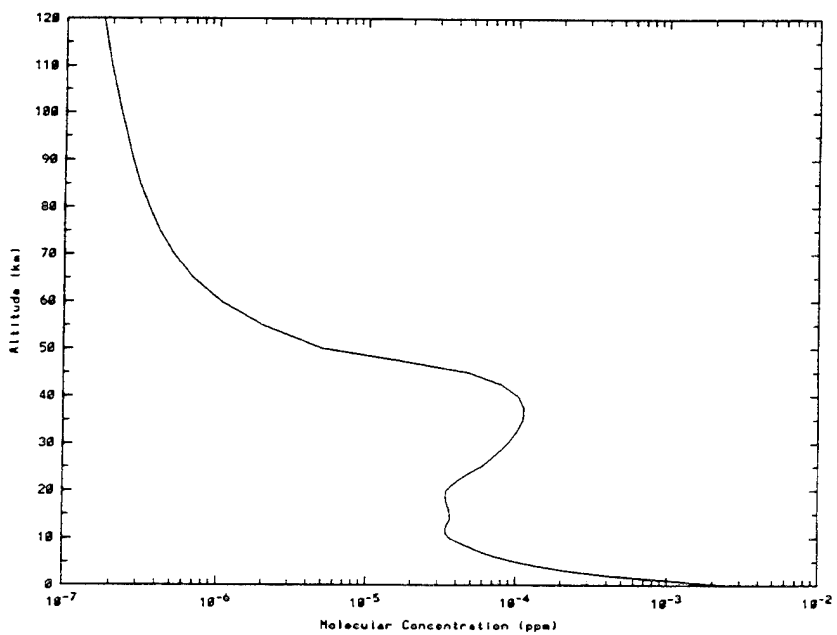
Figure 29. Formaldehyde Profile.

20
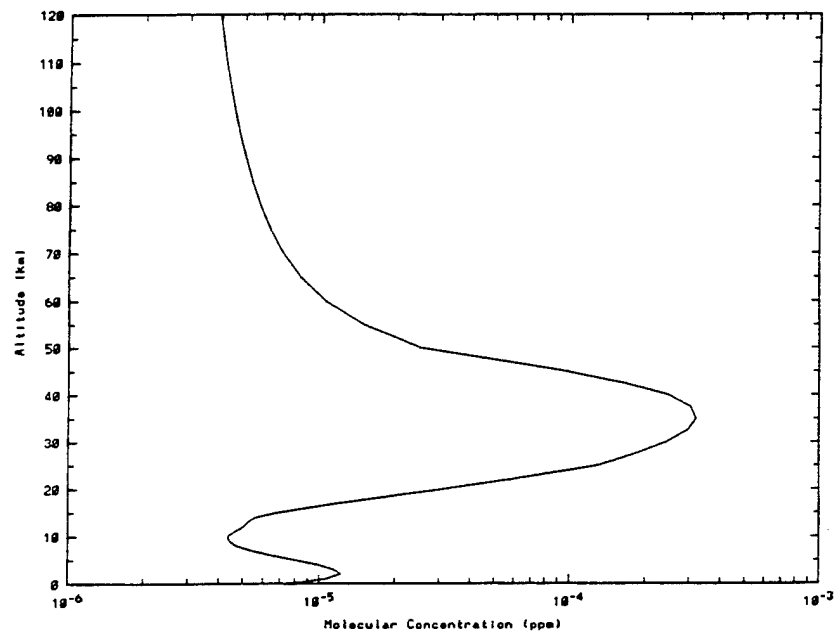
Figure 30. Hypochlorous Acid Profile.
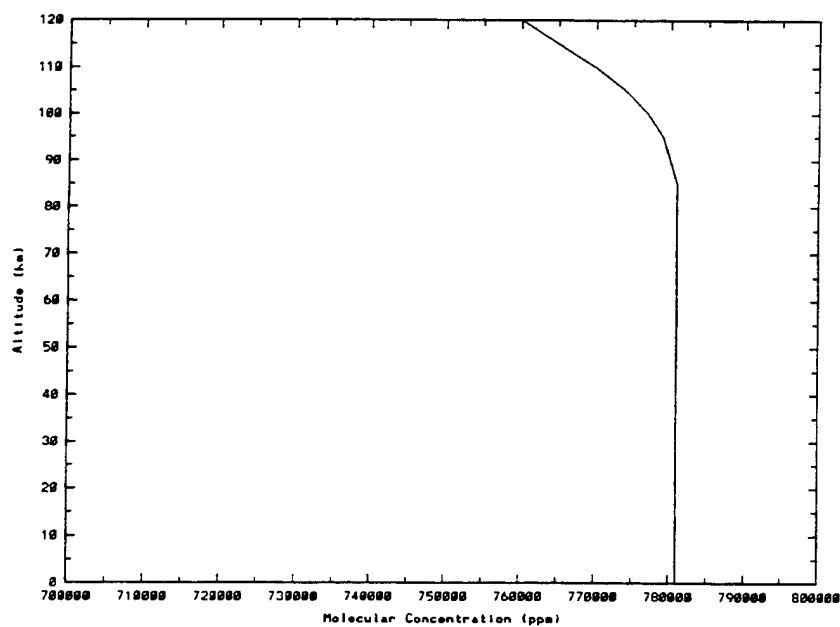
Figure 31. Nitrogen Profile.

21
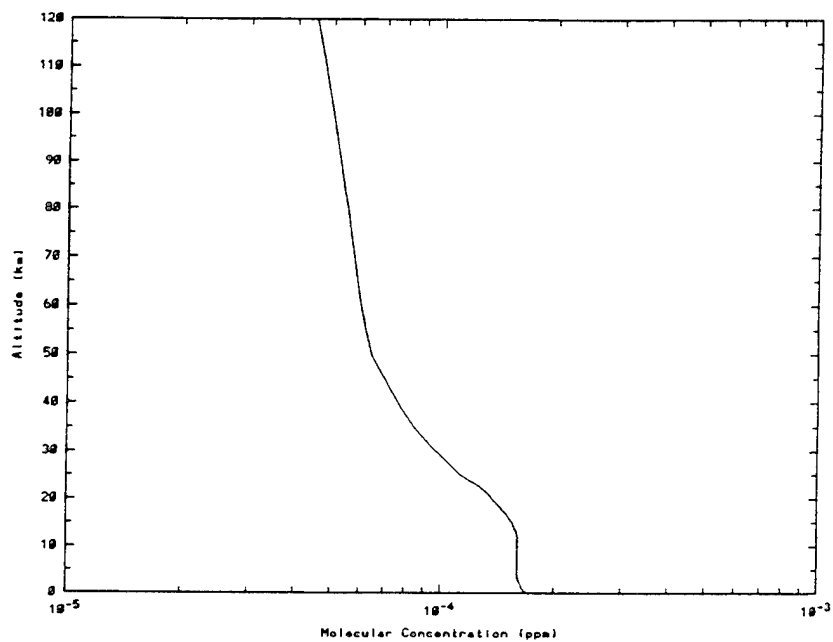
Figure 32. Hydrogen Cyanide Profile.
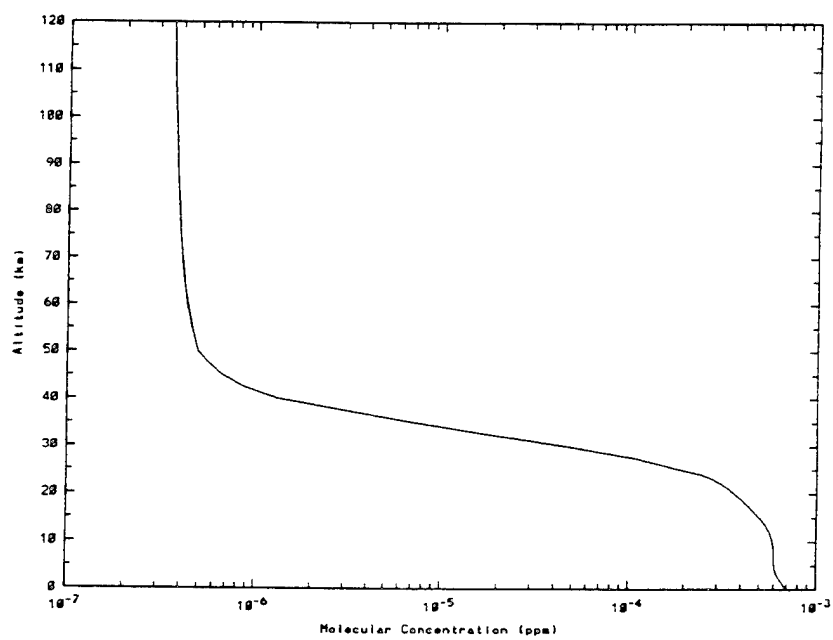
Figure 33. Methyl Chloride Profile.
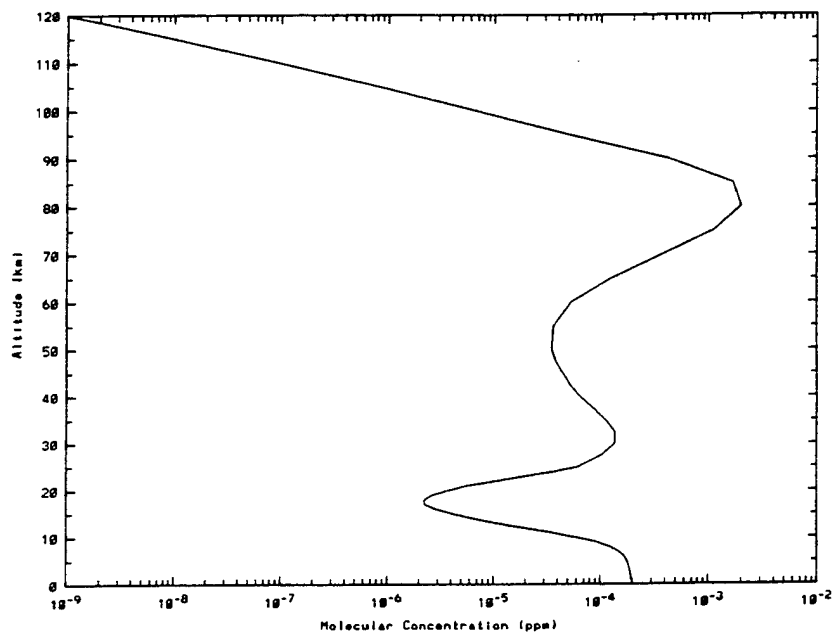
Figure 34. Hydrogen Peroxide Profile.
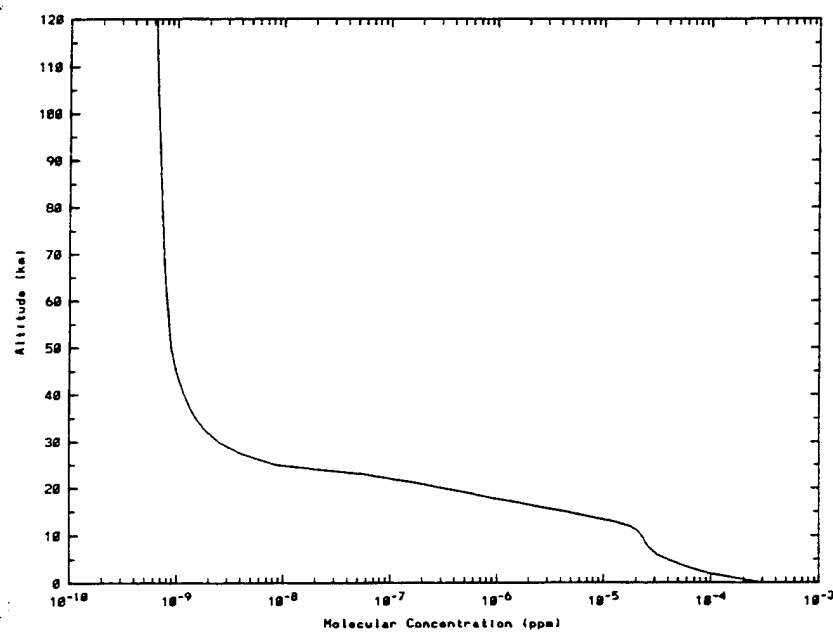
Figure 35. Acetylene Profile.

23
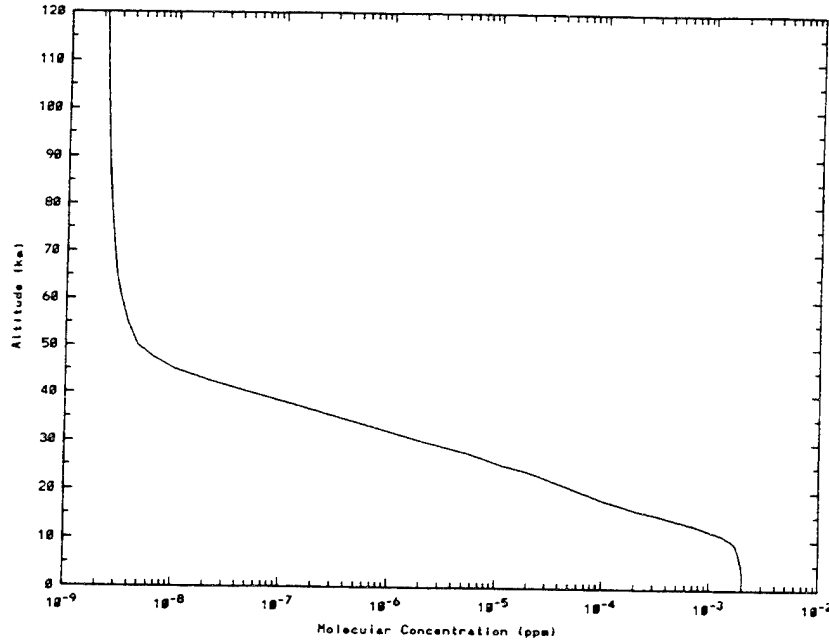
Figure 36. Ethane Profile.

2.1.3 Upper Atmosphere

The standard value for the exospheric temperature is 1000 K. The user has the option in MOSART either to enter another value for the exospheric temperature or to have it calculated from geomagnetic parameters. In the latter case, the temperature is calculated by

$$T_1 = 362.0 + 3.60\bar{F} + A(F - \bar{F}) + 28.0\ K_p + 0.03\ e^{K_p}$$

$$+ \left(0.37 + 0.14\ \sin\left[\frac{2\pi\ (DAY - 151)}{365}\right]\right)$$

$$\times\ \sin\left[4\pi\ \frac{DAY - 59}{365}\right]\bar{F}$$

$$T_{exo} = T_1\ [1 + 0.28\ \sin^{1.5}(\theta/2)]\ x\ [1 + 0.28\ \alpha\ \cos^{2.5}\ (\tau)]$$

where   F is the instantaneous 10.7-cm solar flux (10^{22} W/m²/Hz)

$\bar{F}$ is the average of F over three 27-day solar rotations

K_p is the 3-hour geomagnetic planetary index with a time lag of 7.2 ± 0.2 hours for latitudes below 55 degrees and 5.8 ± 0.5 hours for latitudes above 55 degrees

24

DAY is the day of year

A is a sunspot activity factor
     A = 1.5 minimum activity
     A = 1.8 average activity
     A = 2.4 maximum activity

θ = latitude

$$\alpha = \frac{\cos(\theta/2) - \sin(\theta/2)}{1 + 0.28 \sin(\theta/2)}$$

$$\tau = H^* - 45° + 12° \sin(H^* + 45°)$$

H^* is the hour angle of the sun

The seasonal standard temperature and pressure values above 120 km, together with the seasonal values as a function of exospheric temperature, are shown in Figures 37 and 38.

2.2 Aerosols

The aerosol models in MOSART have been taken directly from MODTRAN. They are modeled using the same technique (e.g., the number density is expressed in terms of the extinction coefficient at 0.55 μm, and each model describes variations in the aerosol size distributions and compositions relative to this value.)

2.2.1 Haze Profiles

The haze profile is defined separately in the following regions:

- Boundary Layer

- Troposphere

- Stratosphere

- Upper Atmosphere

25
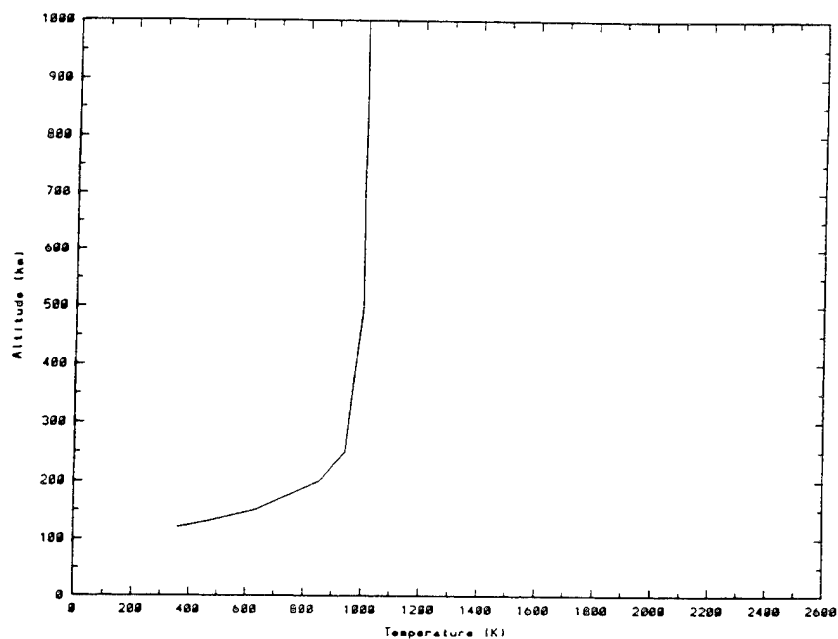
a) Standard Upper Atmosphere Temperature
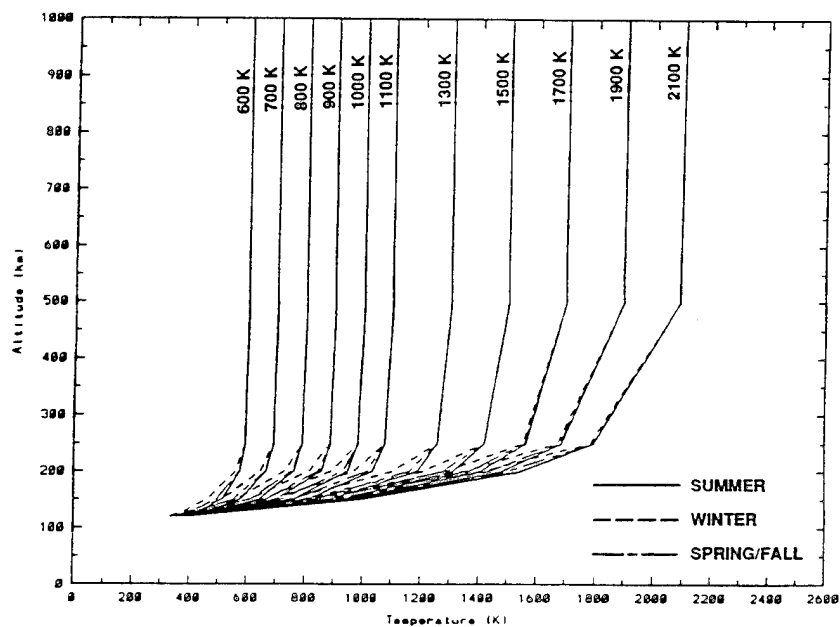
b) Seasonal/Solar Activity Dependent Upper Atmosphere Temperatures

Figure 37. Upper Atmosphere Temperature.

26
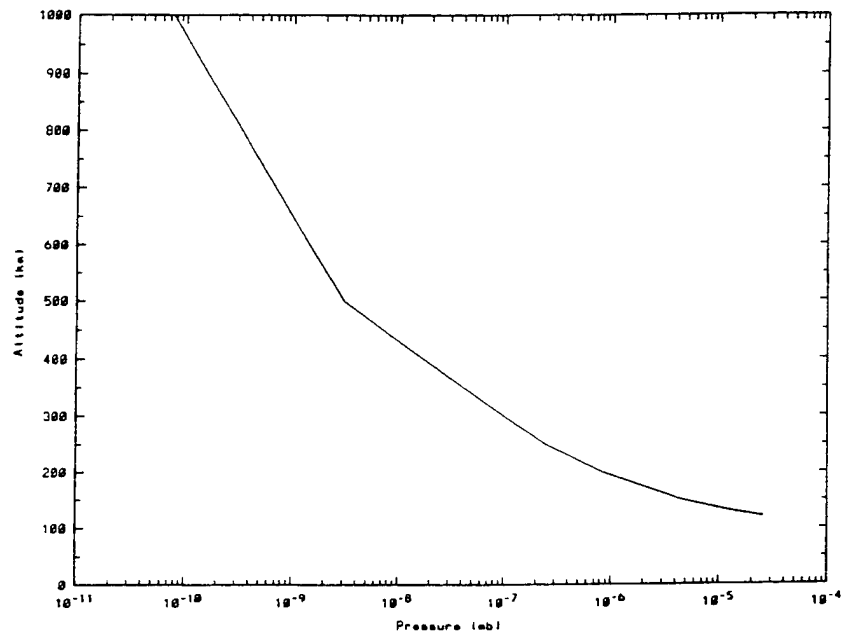
a) Standard Upper Atmosphere Pressure
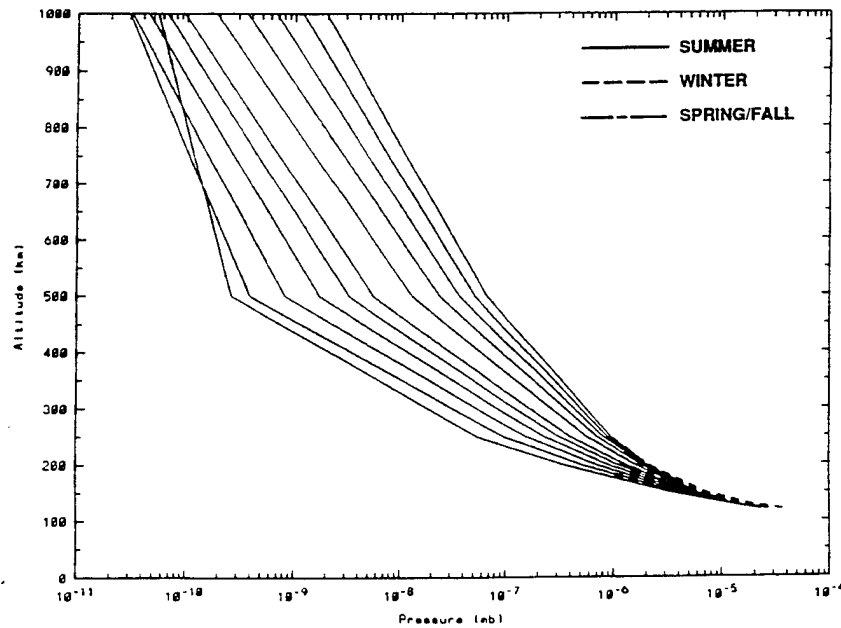
b) Seasonal/Solar Activity Dependent Upper Atmosphere Pressures

Figure 38. Upper Atmosphere Pressures.

27

The haze profile in the boundary layer is defined by the visible range. The stratospheric portion of the profile is defined in terms of recent volcanic activity, while the tropospheric portion is a transition between the boundary layer and the stratosphere. The upper atmosphere is defined in terms of a normal profile and an extreme profile. These profiles are shown in Figures 39 and 40.
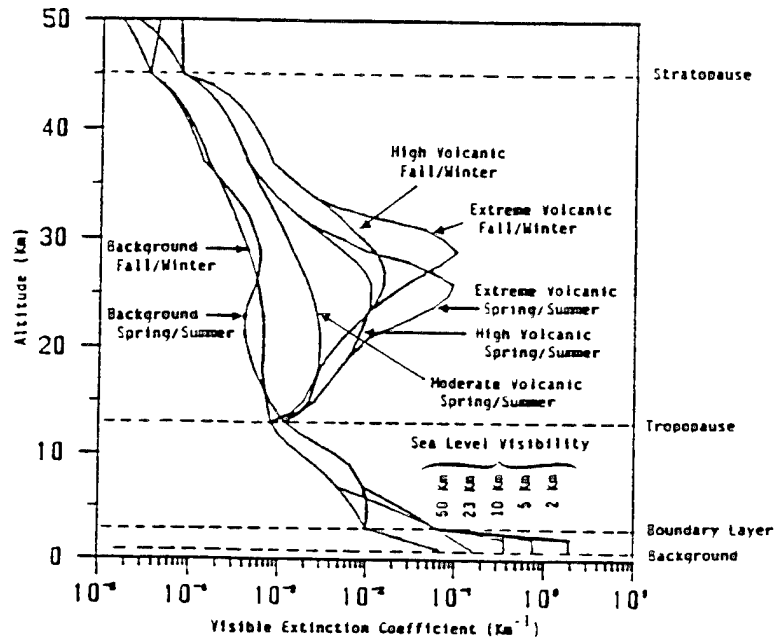
Figure 39. Haze Profiles.
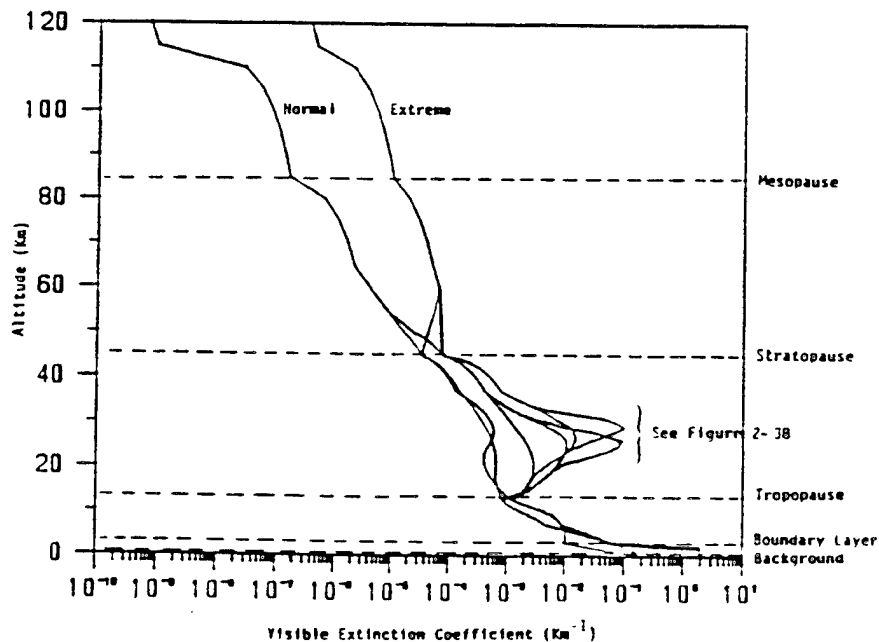
Figure 40. Haze Profiles.

28

The profiles have been extracted from MODTRAN. However, in MODTRAN the boundaries between each region are fixed. MOSART either expands or contracts each region to be consistent with the model atmosphere, so that the boundaries of aerosol models match the surface boundary layer, tropopause, and stratopause. This is shown in Table 2.

Table 2. Haze Profiles.

HAZE MODEL	MODTRAN ALTITUDE REGION (km)	MOSART ALTITUDE REGION
Boundary Layer	Background altitude to boundary layer altitude	Background altitude to boundary layer altitude
Troposphere	2 - 10	Boundary layer altitude to tropopause
Stratosphere	10 - 30	Tropopause to stratopause
Upper Atmosphere	Above 30	Above stratopause

2.2.2 Aerosols

The aerosol types, which have been extracted from MODTRAN (Kneizys et al., 1988; Shettle and Fenn, 1979), are shown in Table 3. The spectral extinction coefficients (normalized to unity at 0.55 μm) and the scattering albedo for each of these aerosols are shown in Figures 41 through 48. The oceanic, or Navy aerosol model, is not shown as the extinction coefficient and scattering albedo are functions of relative humidity, wind speed (current and 24-hour average), and aerosol history. This model is identical to that in LOWTRAN, so reference should be made to the LOWTRAN manual for further details. Also, the background stratospheric aerosol model has been modified to include the temperature dependence of the index of refraction of sulfuric acid.

The aerosol models differ from MODTRAN in two ways. First, MODTRAN uses a selected subset of the phase functions which are approximated to the correct values by a key in the code. In MOSART, the complete set of 702 phase functions are used. Secondly, in MODTRAN, the altitude distribution is based on a fixed grid.

29

Table 3. Aerosol Types.

Boundary Layer/Troposphere

    Rural (0, 70, 80, 99% humidity)

    Urban (0, 70, 80, 99% humidity)

    Maritime (0, 70, 80, 99% humidity)

    Oceanic (Navy)

    Tropospheric (0, 70, 80, 99% humidity)

Stratosphere

    Background (Temperature Dependent)

    Aged Volcanic

    Fresh Volcanic

Upper Atmosphere

    Meteoric Dust
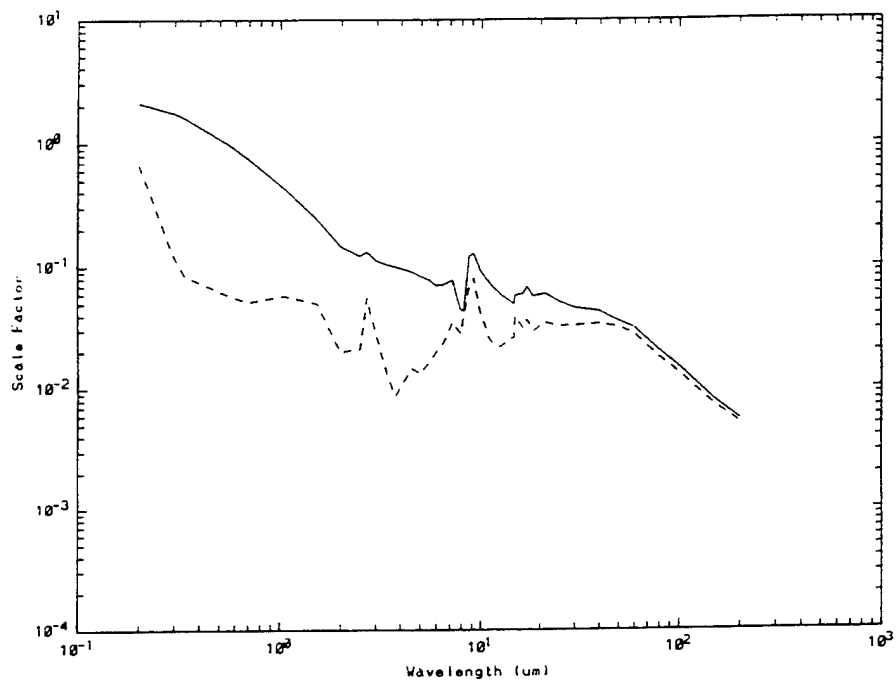
a) Spectral Extinction Coefficient
(Normalized to Unity of 0.55 μm)
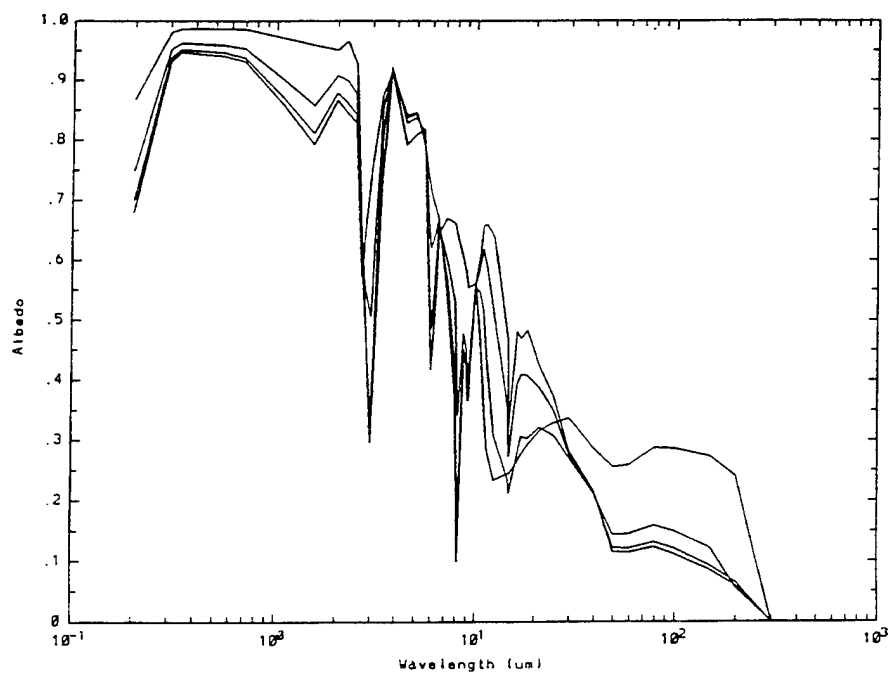
b) Spectral Scattering Albedo

Figure 41. Rural Aerosol Model.
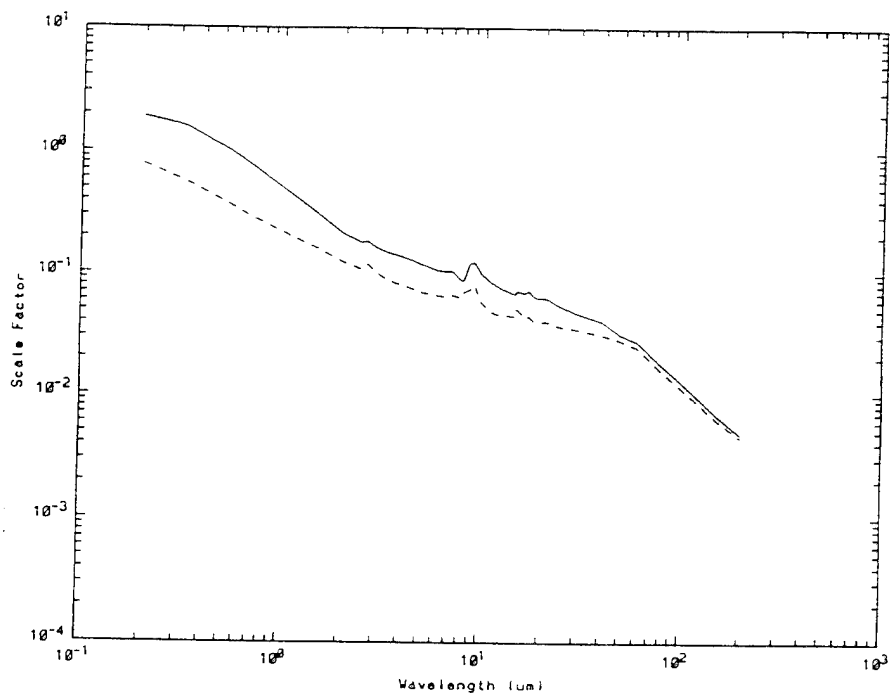
31

a) Spectral Extinction Coefficient
(Normalized to Unity of 0.55 μm)
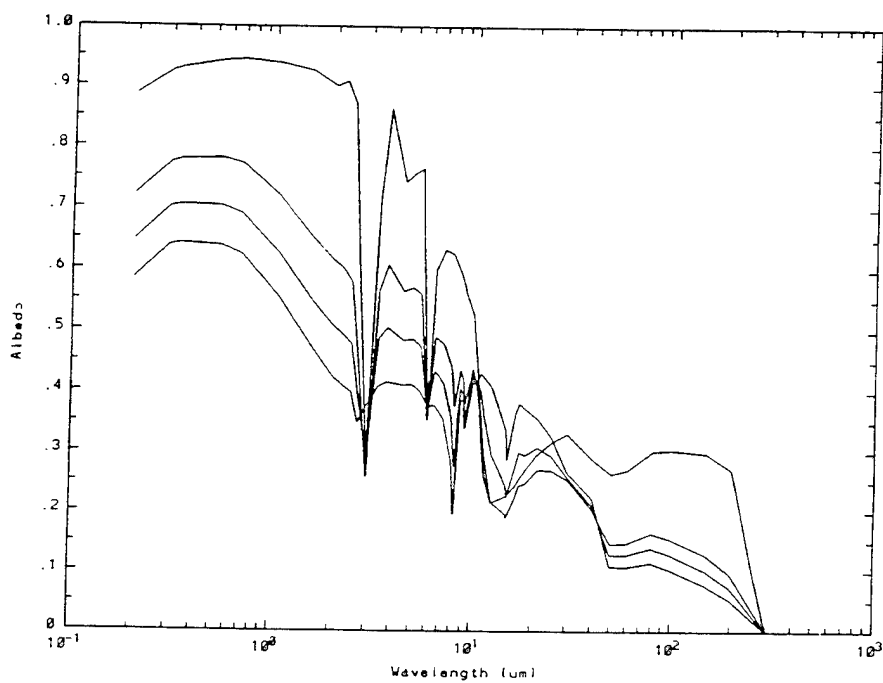
b) Spectral Scattering Albedo

Figure 42. Urban Aerosol Model.
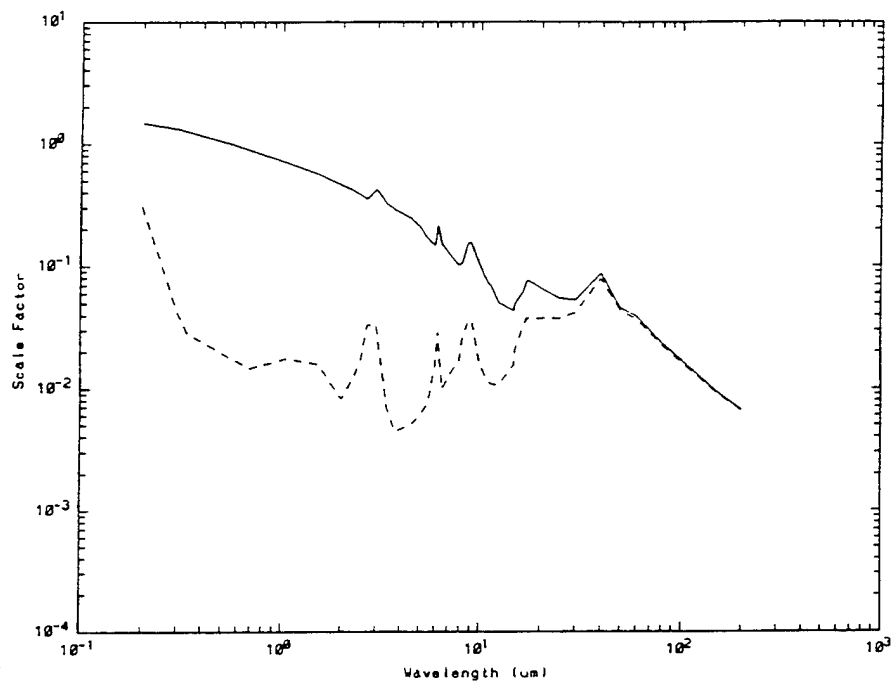
32

a) Spectral Extinction Coefficient
(Normalized to Unity of 0.55 μm)
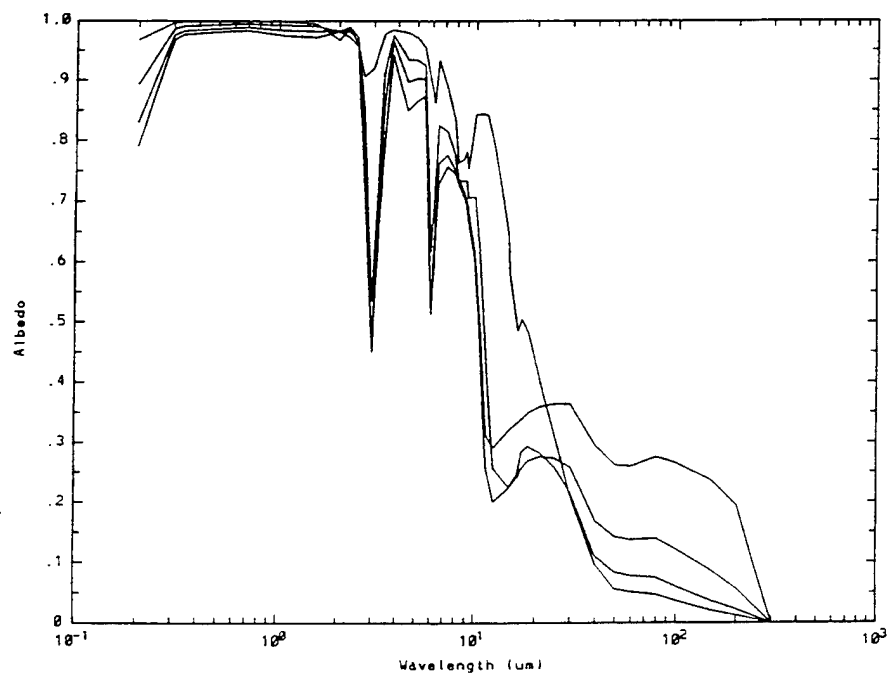
b) Spectral Scattering Albedo

Figure 43. Maritime Aerosol Model.
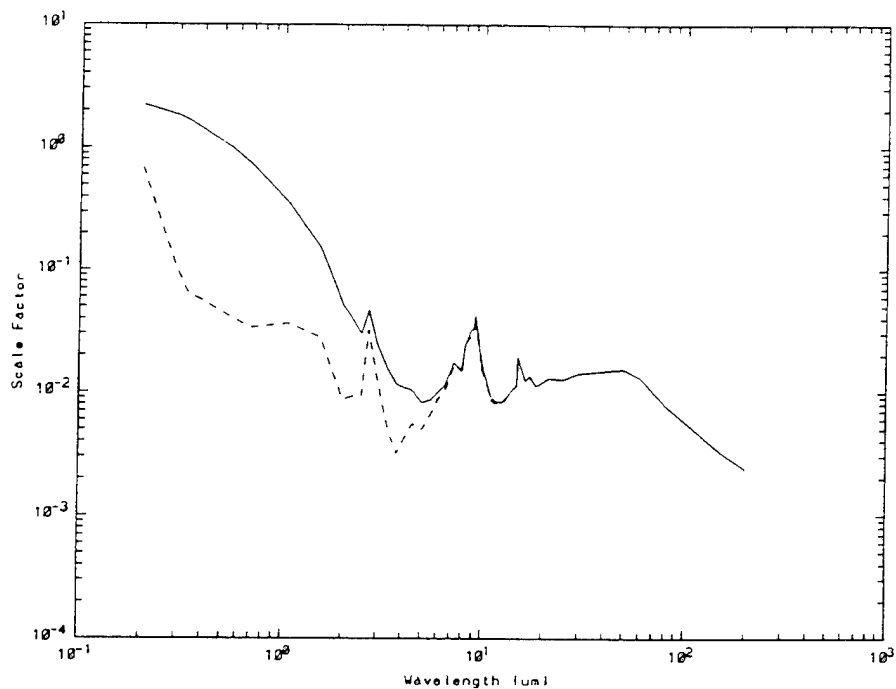
33

a) Spectral Extinction Coefficient
(Normalized to Unity of 0.55 μm)
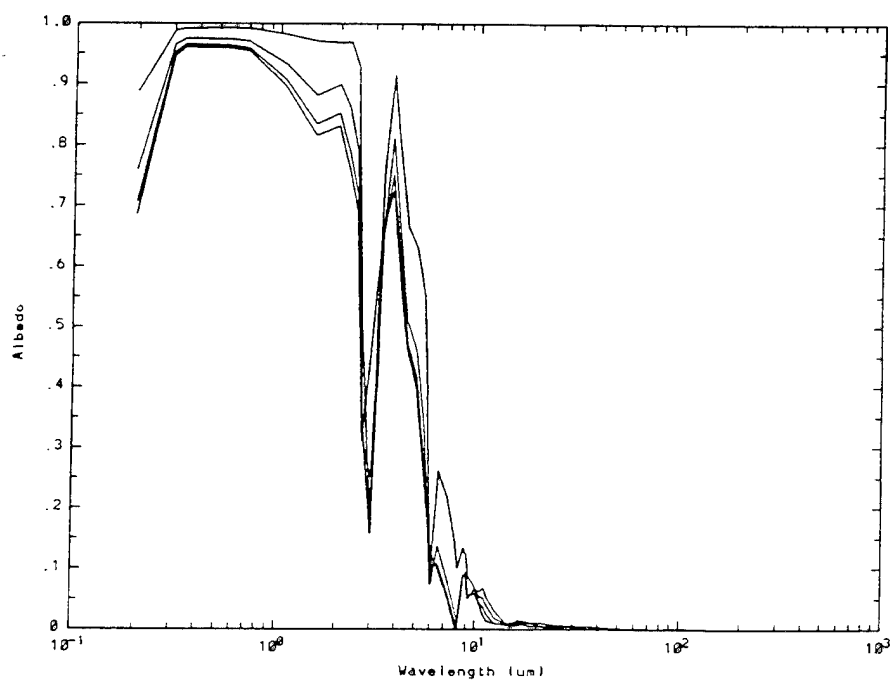
b) Spectral Scattering Albedo

Figure 44. Tropospheric Aerosol Model.
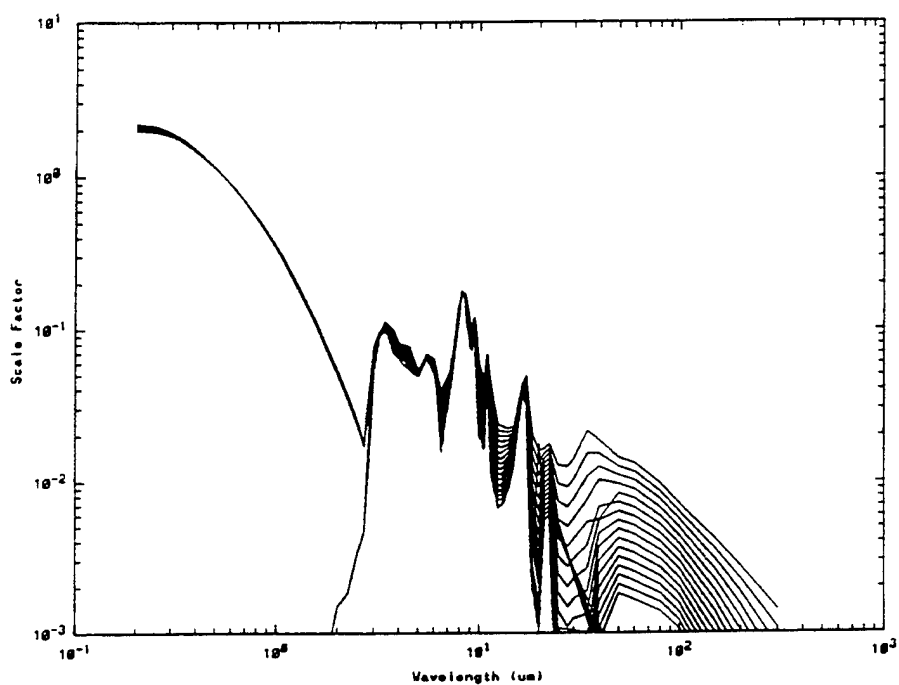
a) Spectral Extinction Coefficient
(Normalized to Unity of 0.55 μm)
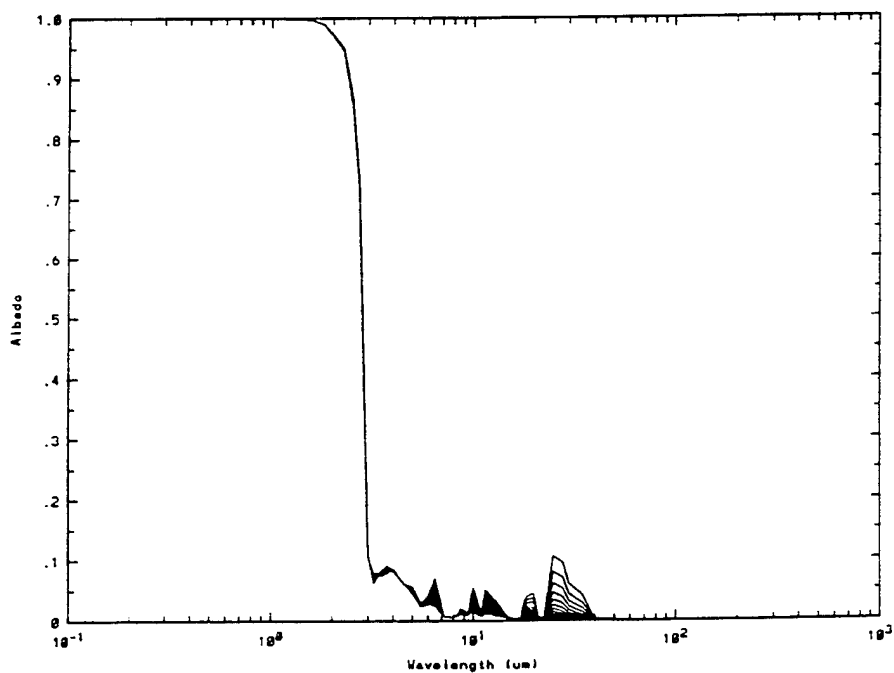
b) Spectral Scattering Albedo

(Temperatures 150 - 300 K in 10 K increments)

Figure 45. Background Stratospheric Aerosol Model.
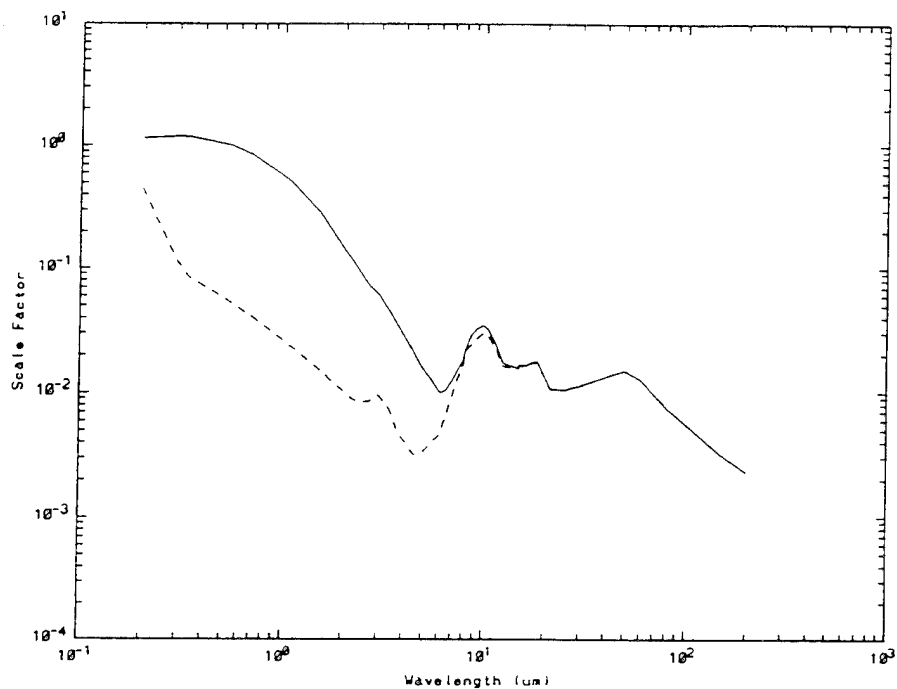
35

a) Spectral Extinction Coefficient
(Normalized to Unity of 0.55 μm)
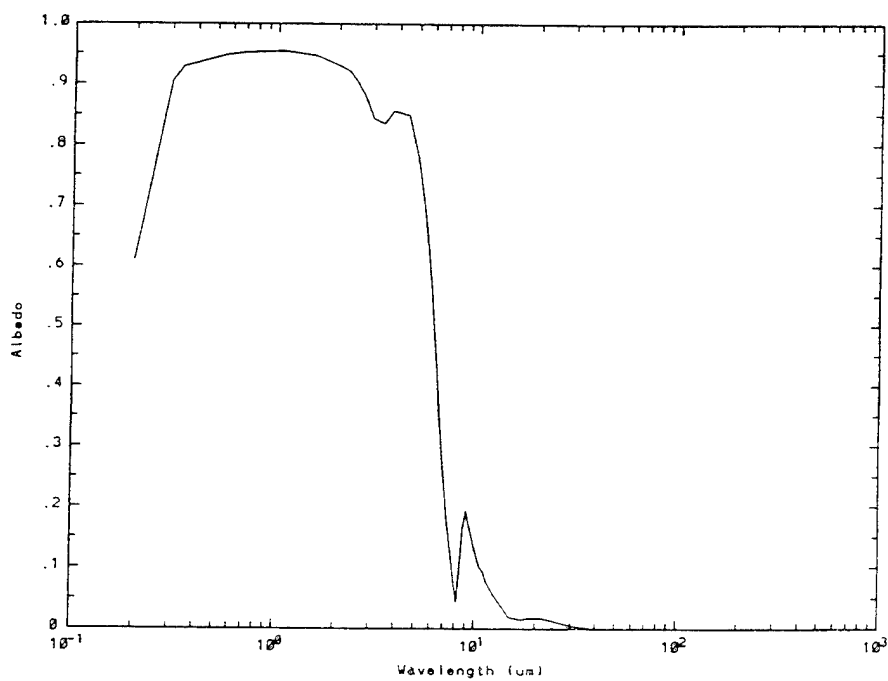
b) Spectral Scattering Albedo

Figure 46. Aged Volcanic Stratospheric Aerosol Model.
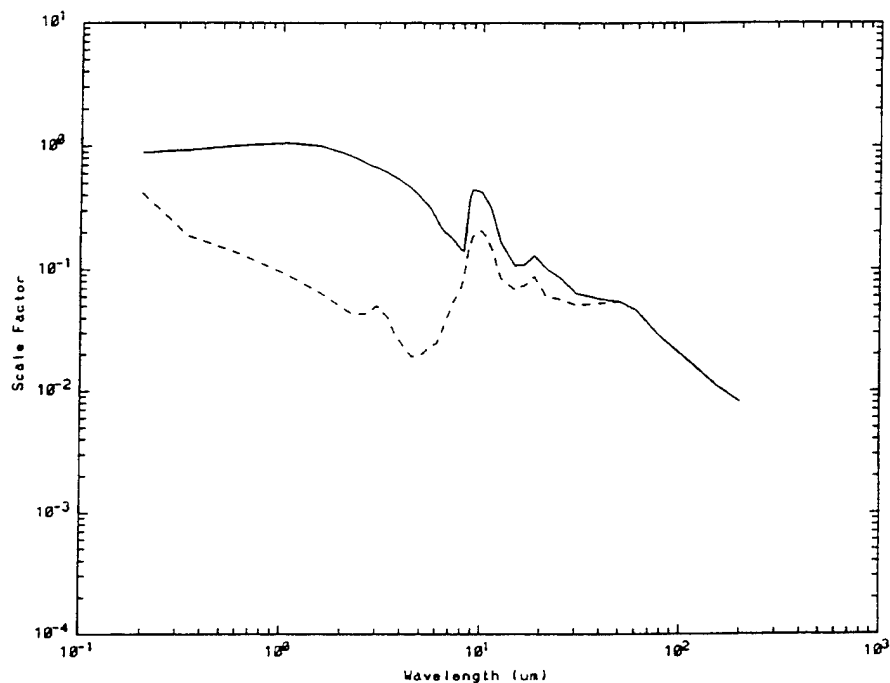
a) Spectral Extinction Coefficient
(Normalized to Unity of 0.55 μm)
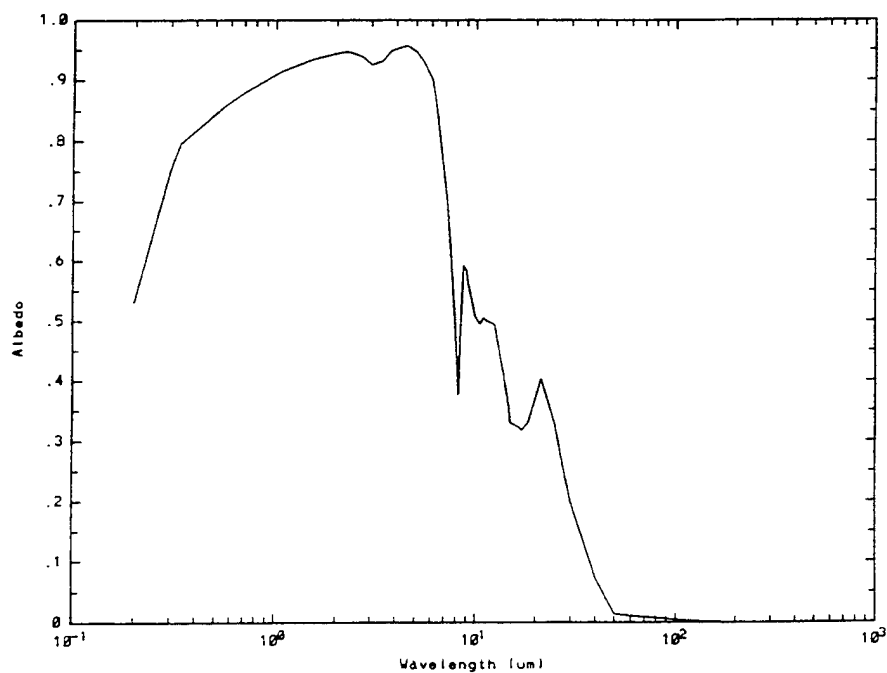
b) Spectral Scattering Albedo

Figure 47. Fresh Volcanic Stratospheric Aerosol Model.
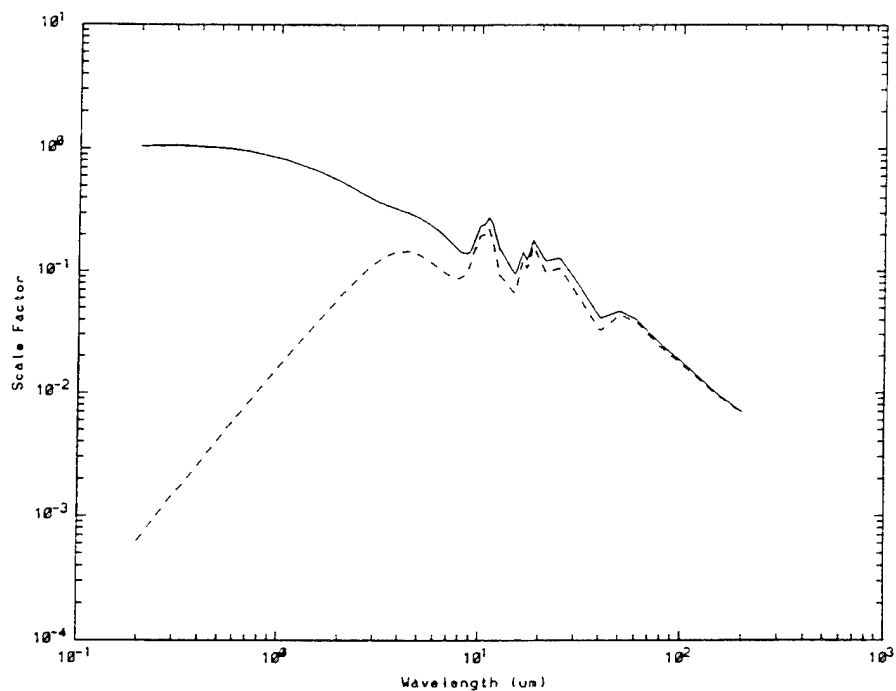
37

a) Spectral Extinction Coefficient
(Normalized to Unity of 0.55 μm)
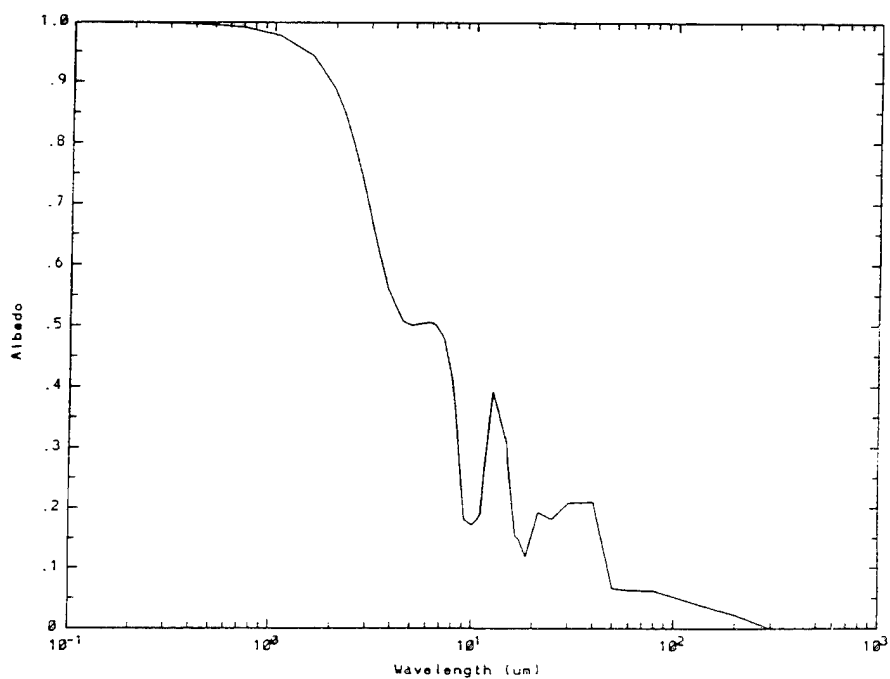
b) Spectral Scattering Albedo

Figure 48. Meteoric Dust Aerosol Model.

38

In MOSART, the altitude distribution is compatible with the haze profile and is shown in Table 4. This altitude distribution is based upon the following assumptions:

- The altitude of the top boundary layer should roughly follow the terrain altitude. This model is intended to treat the so-called "Denver problem".

- The divisions between aerosol models above the boundary layer occur at points of stability, or minimal vertical mixing, namely the tropopause and stratopause. Therefore, these models in MOSART vary with the model atmosphere.

Table 4. MOSART Aerosol Altitude Distribution.

ALTITUDE	AEROSOL TYPE
Background altitude to boundary layer altitude	Boundary Layer/Tropospheric Aerosol Model
Boundary layer altitude to Tropopause	Tropospheric Aerosol Model
Tropopause to Stratopause	Stratospheric Aerosol Model
Above Stratopause	Meteoric Dust Aerosol Model

2.3 Hydrometeors

MOSART models condensed atmospheric water with the following:

- Clouds (water/ice/both)

- Cirrus clouds

- Fogs

- Rain

- Snow

These models contain all the MODTRAN models except for the NOAA statistical Cirrus Cloud Model.

2.3.1 Water Cloud Models

The low-altitude MOSART cloud models are listed in Table 5. Their extinction coefficients and albedos are presented in Figures 49 through 58. The scattering asymmetry parameters are presented in Figure 59. The liquid water content profiles are shown in Figures 60 through 70. The equivalent MODTRAN models are also indicated, although the cloud thickness may be slightly different.

For temperatures below 273.15 K, ice particles are assumed to exist in the cloud (or fog). For temperatures below 253.15 K, the cloud (or fog) is assumed to be all ice. MOSART automatically combines the water and ice coefficients for the transition temperatures (i.e., 253.15 to 273.15 K).

2.3.2 Cirrus Cloud Models

The Standard and Subvisual Cirrus cloud models from LOWTRAN 7 are included in MOSART. The extinction coefficients and albedos are presented in Figures 71 and 72 for the standard and subvisual models, respectively. The phase function asymmetry factors for both models are contained in Figure 73.

2.3.2.1 Fog Models

Two MOSART fog models, the Advection Fog and Radiation Fog, have been extracted from MODTRAN. The extinction coefficients and scattering albedo for these fog models are shown in Figures 74 and 75. The scattering asymmetry parameters are presented in Figure 59.

In addition, MOSART has four other fog models with altitude structure as shown in Table 6. The extinction coefficients and scattering albedos are shown in Figures 76 through 79. The liquid water content profiles are presented in Figures 80 through 83. See Section 2.3.1 for comments on ice fog.

2.3.3 Rain Models

As shown in Table 7, the rain rate profiles (see Figure 84) are associated with certain clouds. These rain rates are truncated above the cloud in accordance with AFGL recommendation (L.W. Abreu, private communication, 1988). Each rain profile model can have a different raindrop size distribution as shown in Table 8. However, at present, the raindrop size distributions are defined in the rain data base and are not a run-time option.

Table 5. Cloud Models: Dropsize Distributions.

| $n(r) = a\,r^{\alpha}\exp[-br]$ | | | | | Index | |
Cloud Type	α	b	$N_o(cm^{-3})$	a	MOSART	MODTRAN
Advection Fog 1	3	0.3	20	0.027	1	
Advection Fog 2	3	0.375	20	0.06592	2	
Radiation Fog 1	6	1.5	100	2.37305	3	
Radiation Fog 2	6	3.0	200	607.5	4	
Cumulus	3	0.5	250	2.604	5	1
Altostratus	5	1.11	400	6.268	6	2
Stratocumulus I	5	0.8	200	0.4369	7	
Nimbostratus I	1	0.333	100	11.089	8	
Stratus I	3	0.667	250	8.247	9	
Stratus II	2	0.6	250	27.00	10	3
Stratus-Stratocumulus	2	0.75	250	52.734	11	4
Stratocumulus II	2	0.5	150	9.375	12	
Nimbostratus II	2	0.425	200	7.676	13	5
Cumulus-Cumulus Congestus	2	0.328	80	1.4115	14,15	
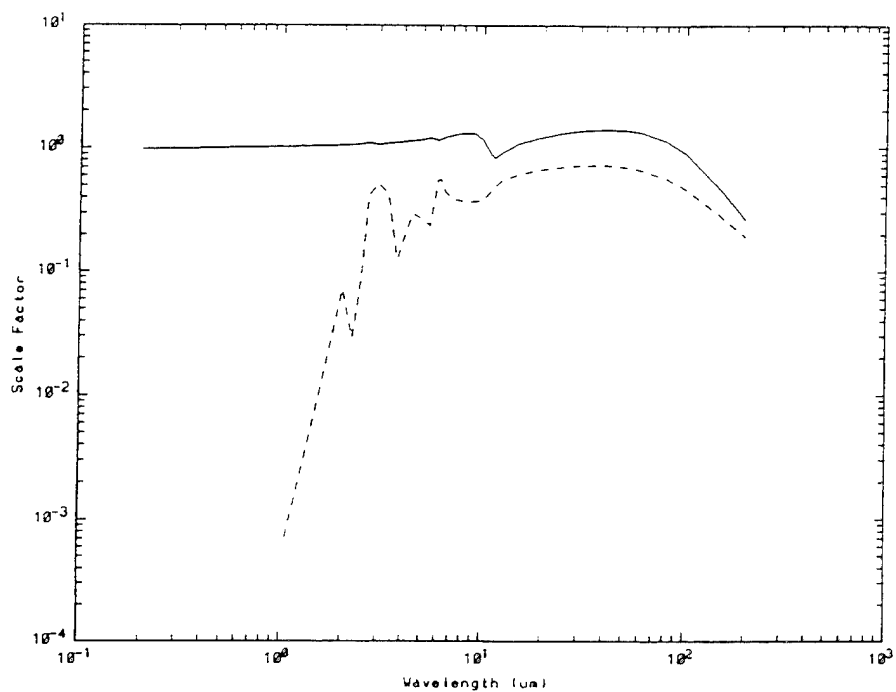
a) Spectral Extinction Coefficient
(Normalized to Unity of 0.55 μm)
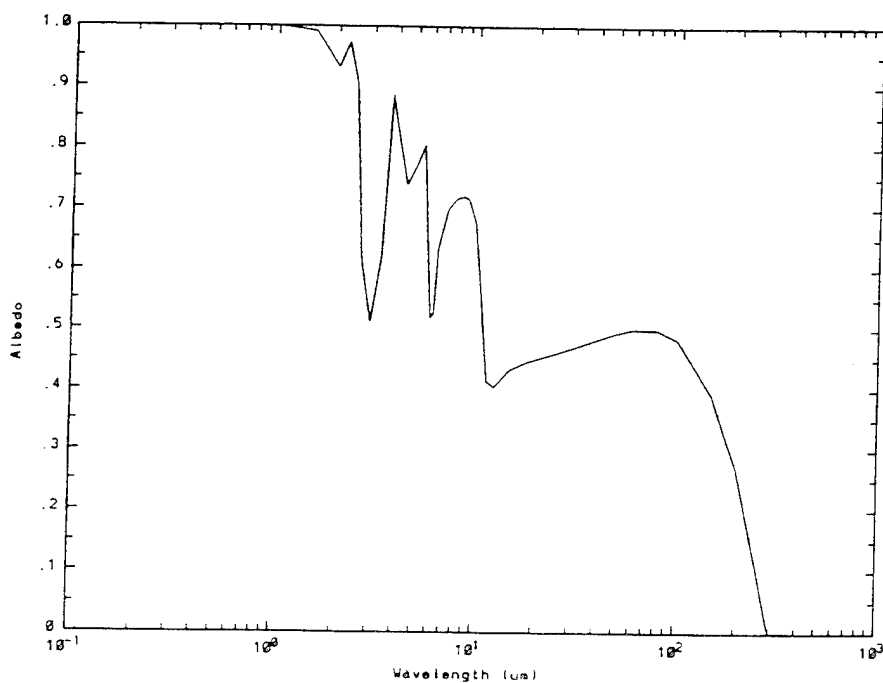
b) Spectral Scattering Albedo

Figure 49. Cumulus.
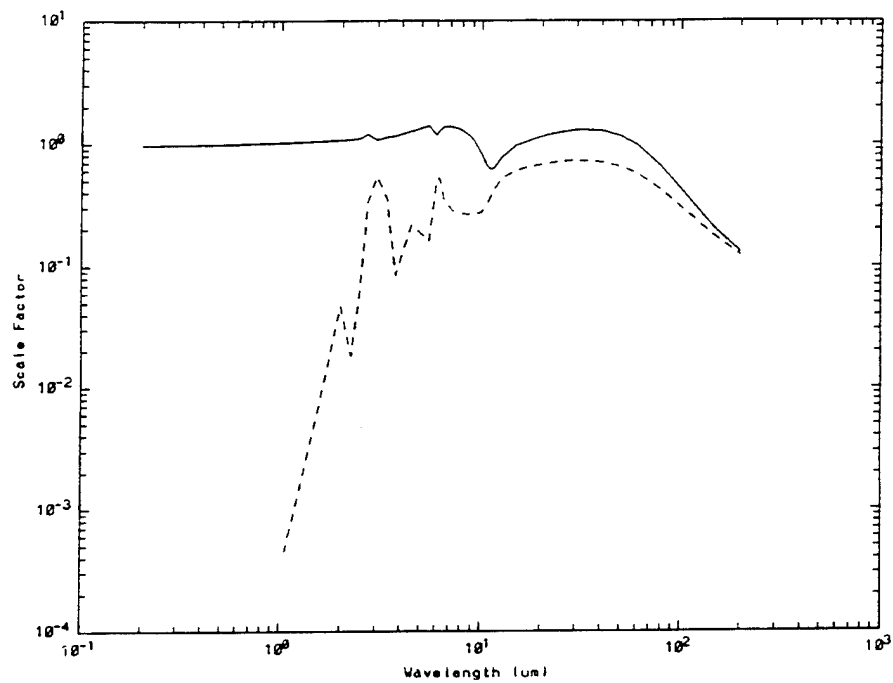
42

a) Spectral Extinction Coefficient
(Normalized to Unity of 0.55 μm)
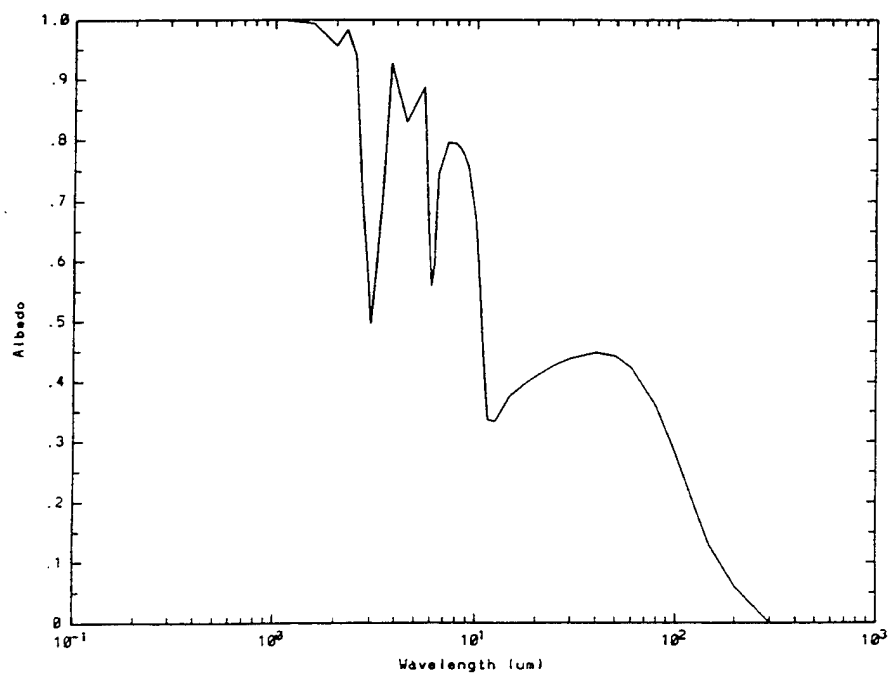
b) Spectral Scattering Albedo

Figure 50. Altostratus.
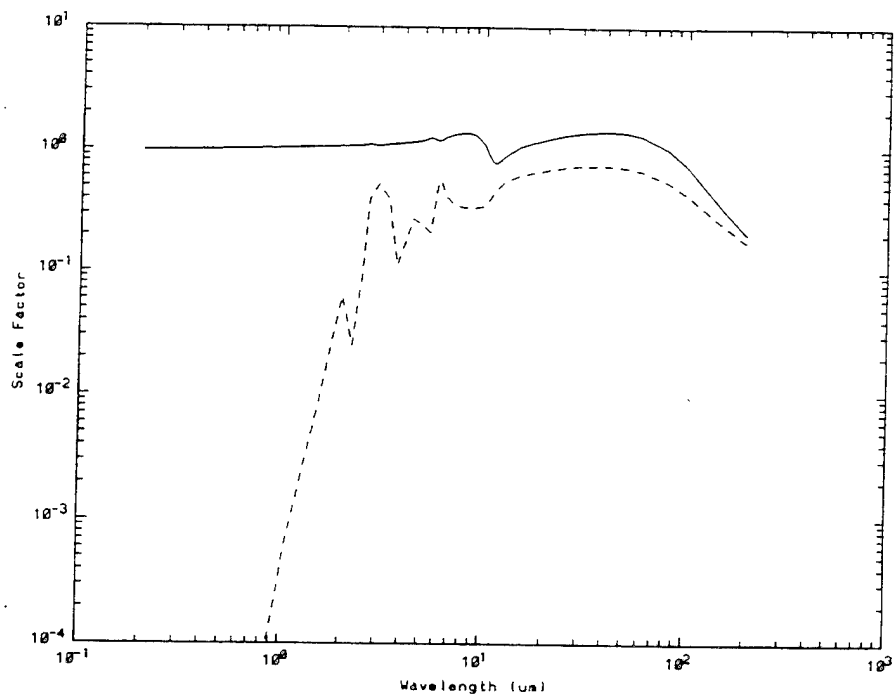
43

a) Spectral Extinction Coefficient
(Normalized to Unity of 0.55 μm)
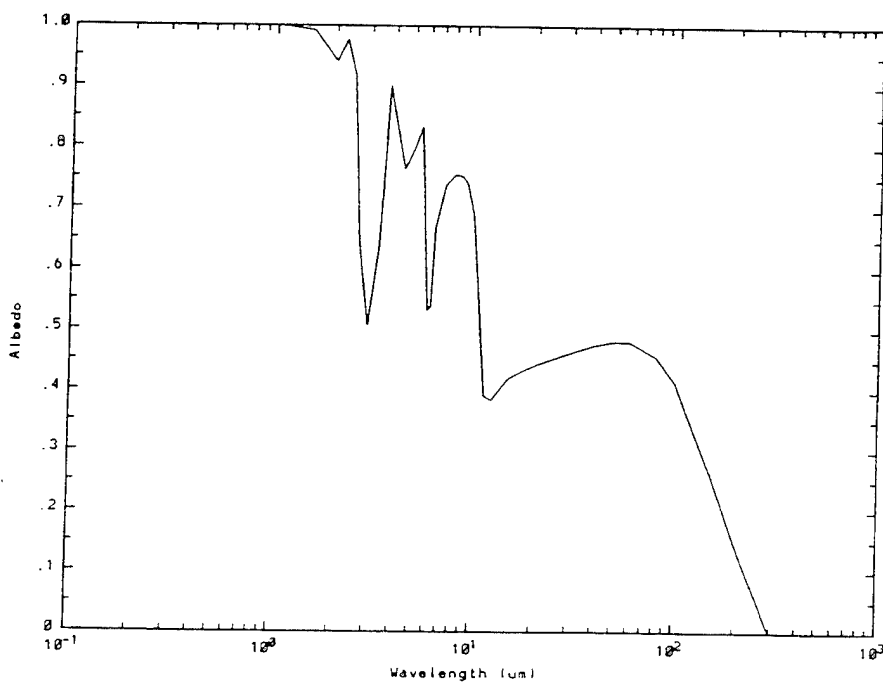
b) Spectral Scattering Albedo

Figure 51. Stratocumulus I.
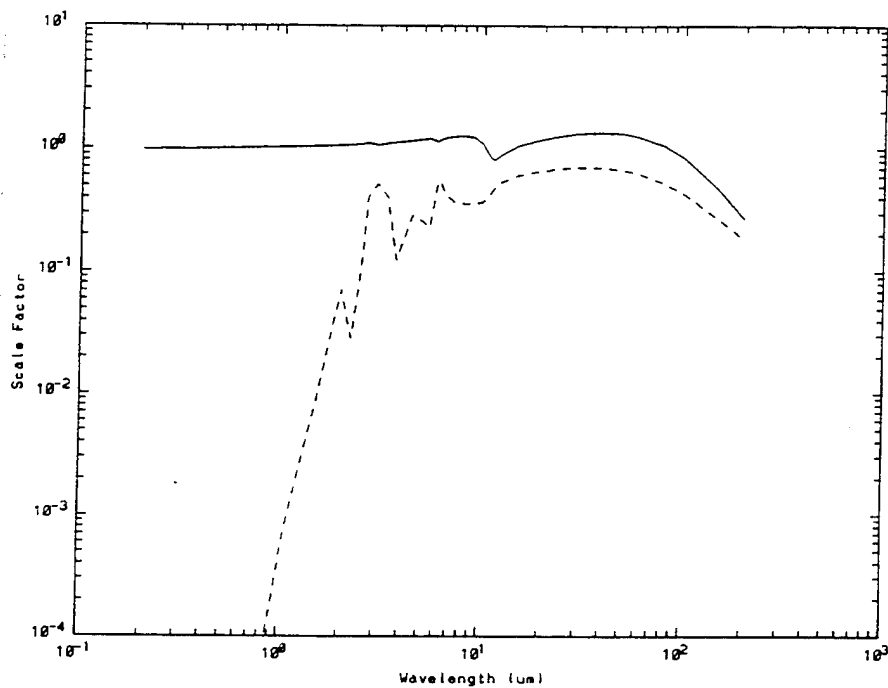
44

a) Spectral Extinction Coefficient
(Normalized to Unity of 0.55 μm)

b) Spectral Scattering Albedo

Figure 52. Nimbostratus I.
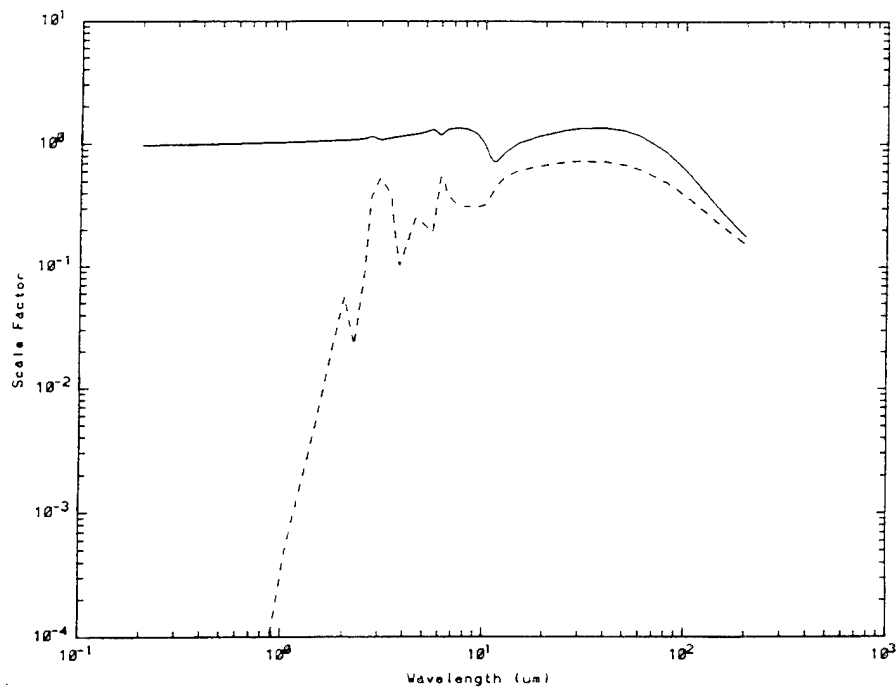
45

a) Spectral Extinction Coefficient
(Normalized to Unity of 0.55 μm)
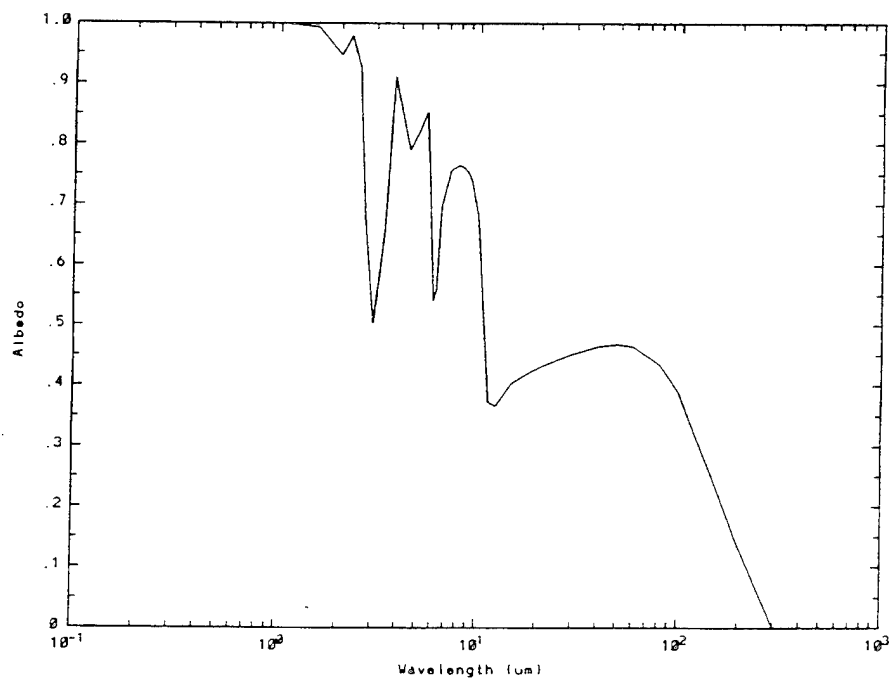
b) Spectral Scattering Albedo

Figure 53. Stratus I.
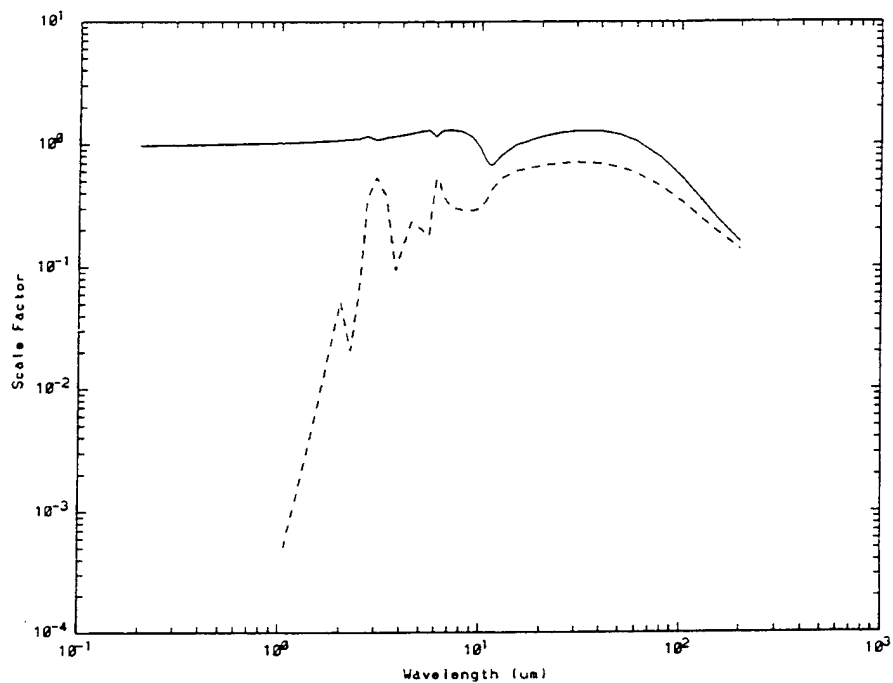
46

a) Spectral Extinction Coefficient
(Normalized to Unity of 0.55 μm)
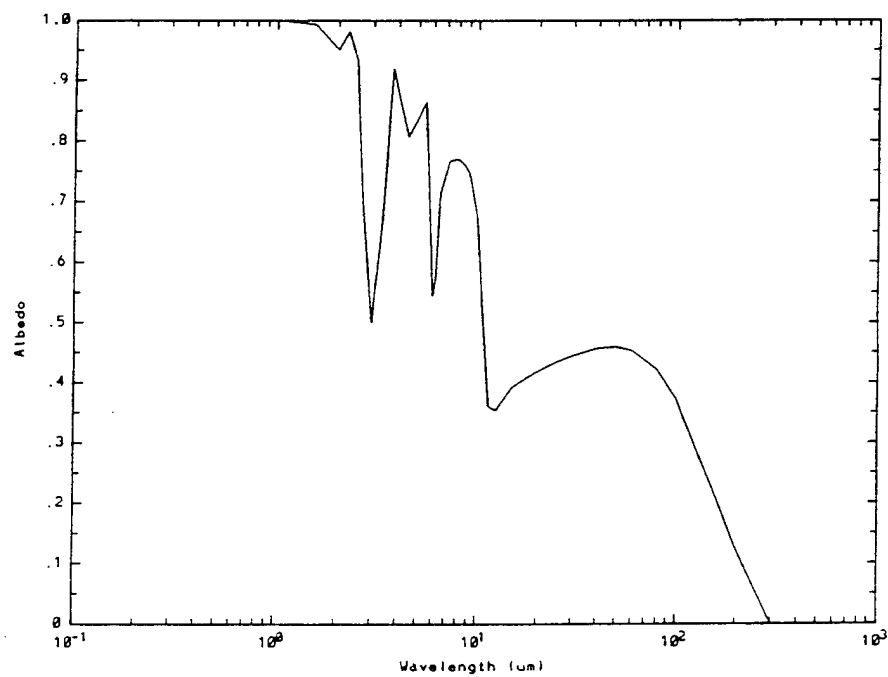
b) Spectral Scattering Albedo

Figure 54. Stratus II.
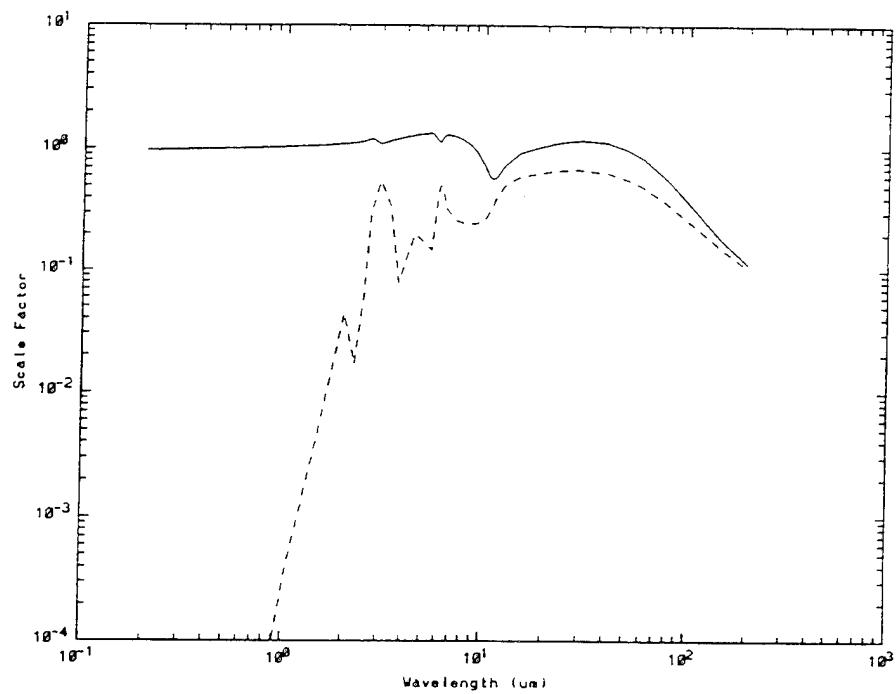
47

a) Spectral Extinction Coefficient
(Normalized to Unity of 0.55 µm)

b) Spectral Scattering Albedo

Figure 55.   Stratus-Stratocumulus.
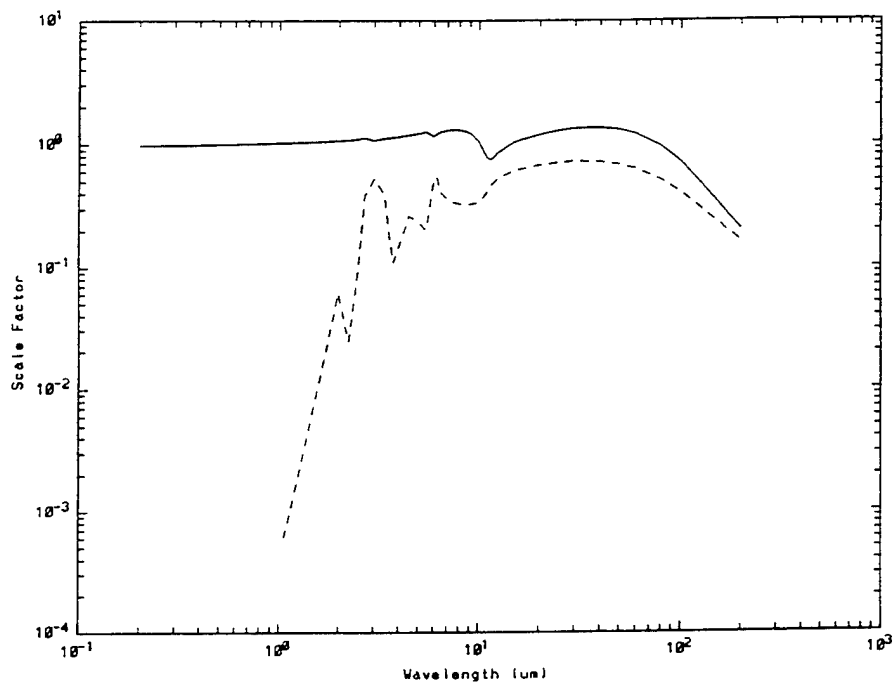
a) Spectral Extinction Coefficient
(Normalized to Unity of 0.55 μm)
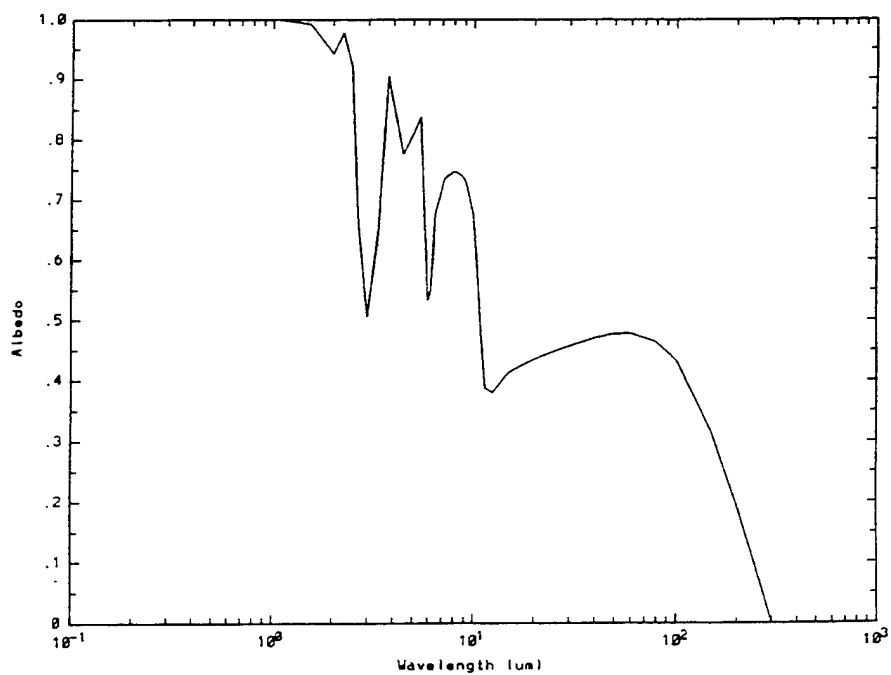
b) Spectral Scattering Albedo

Figure 56. Stratocumulus II.
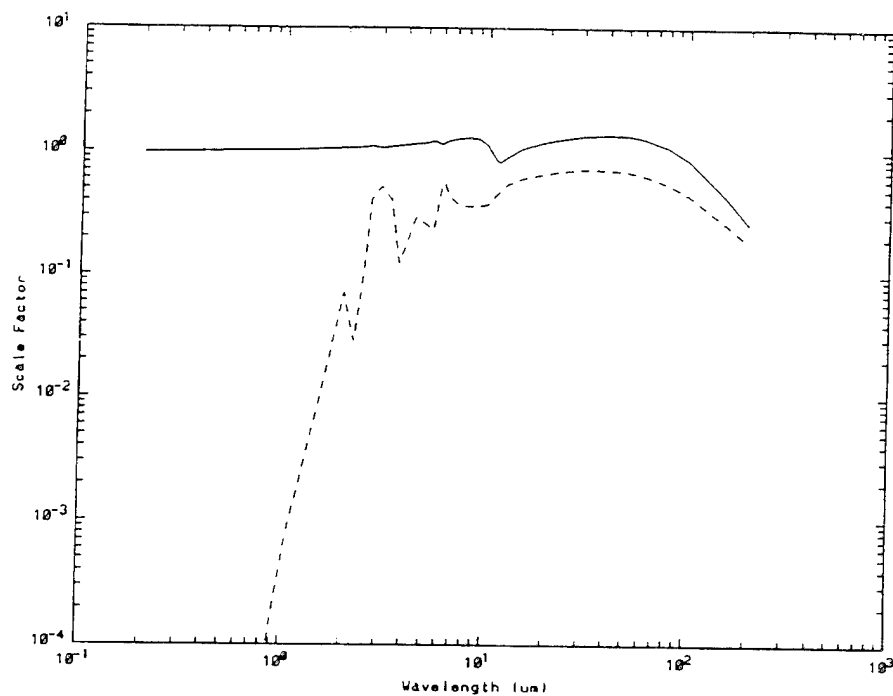
49

a) Spectral Extinction Coefficient
(Normalized to Unity of 0.55 μm)
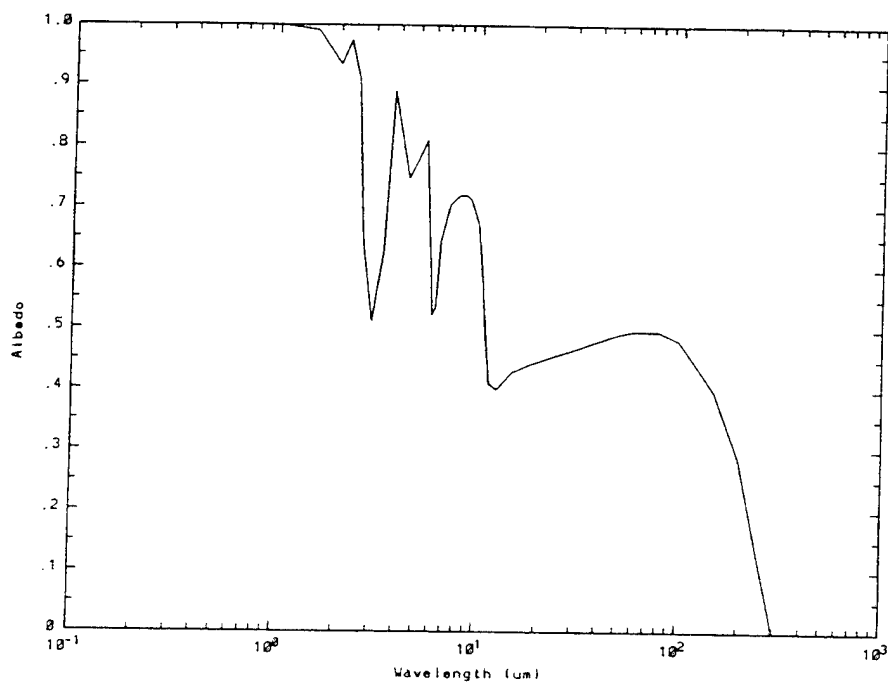
b) Spectral Scattering Albedo

Figure 57. Nimbostratus II.
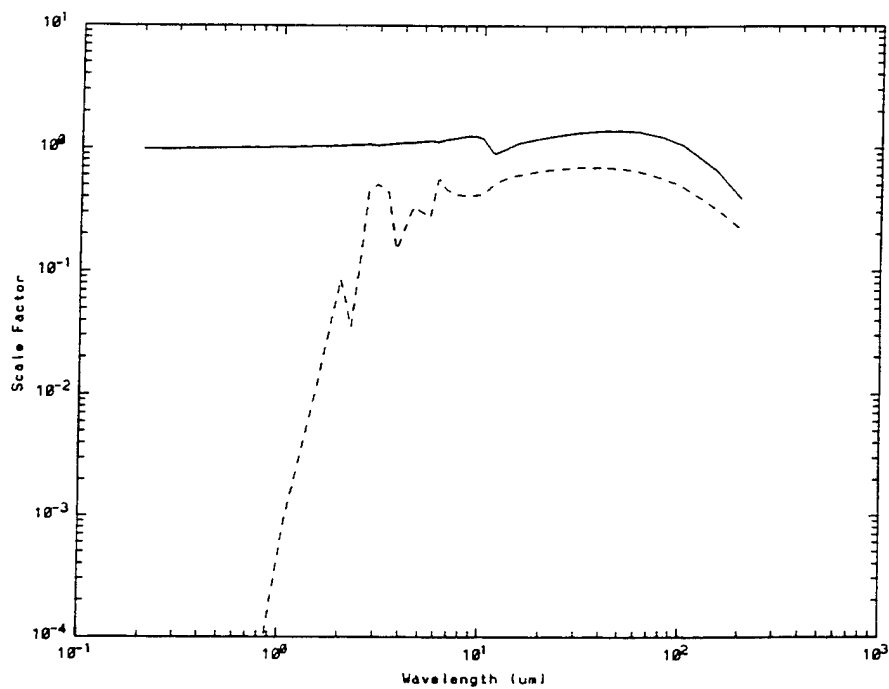
a) Spectral Extinction Coefficient
(Normalized to Unity of 0.55 μm)
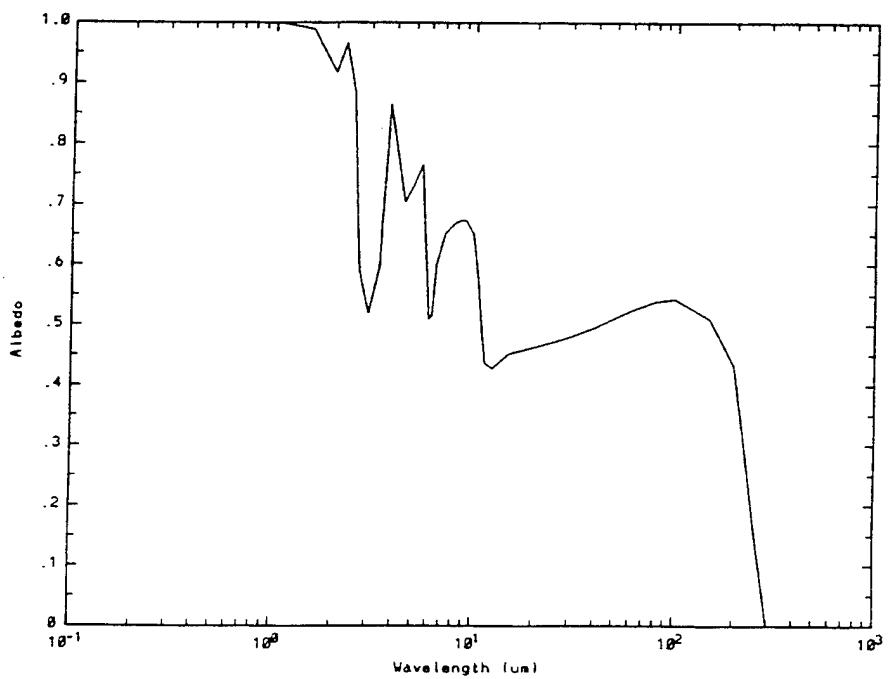
b) Spectral Scattering Albedo

Figure 58. Cumulus/Cumulus Congestus.
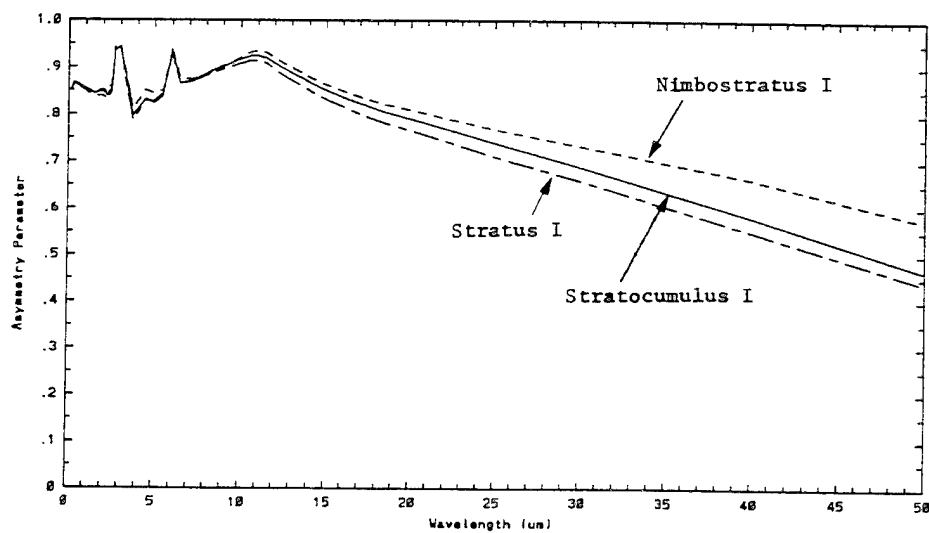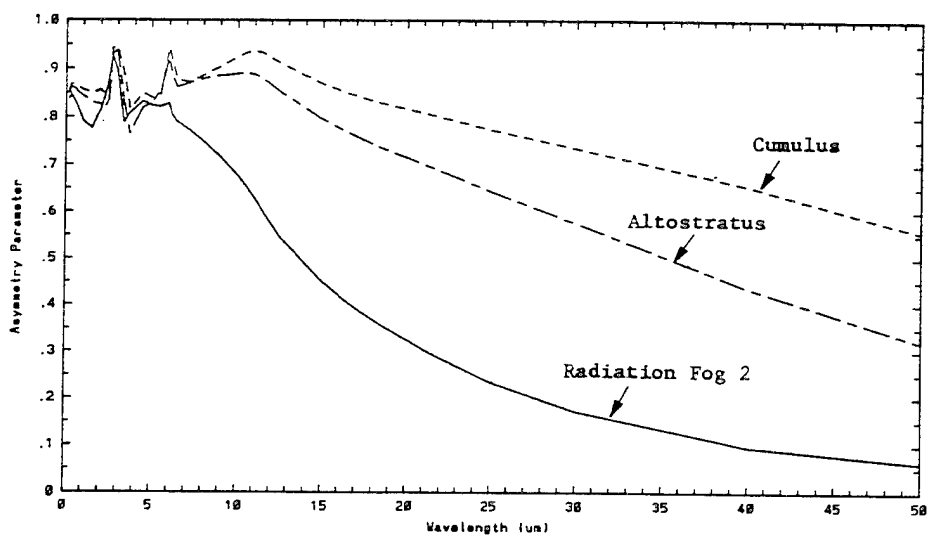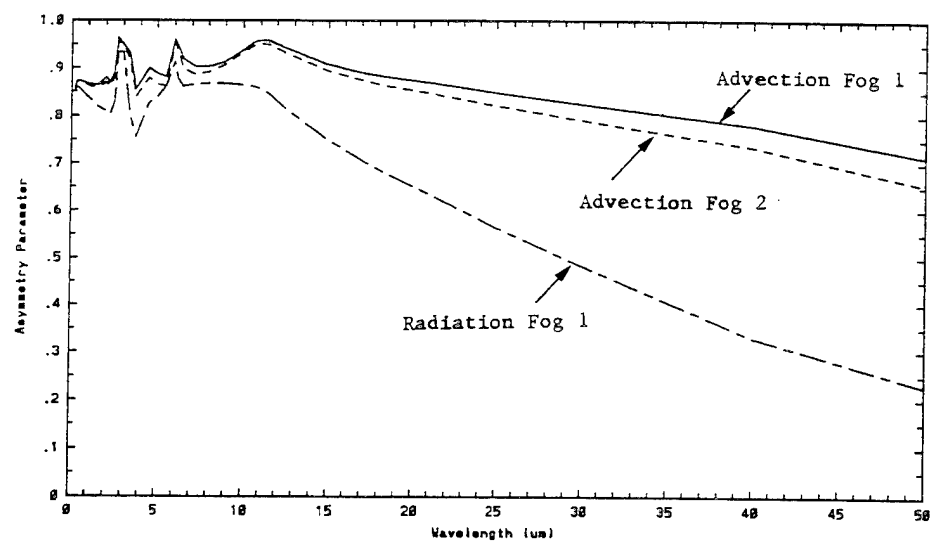
Figure 59. Cloud/Fog Scattering Asymmetry Parameters.
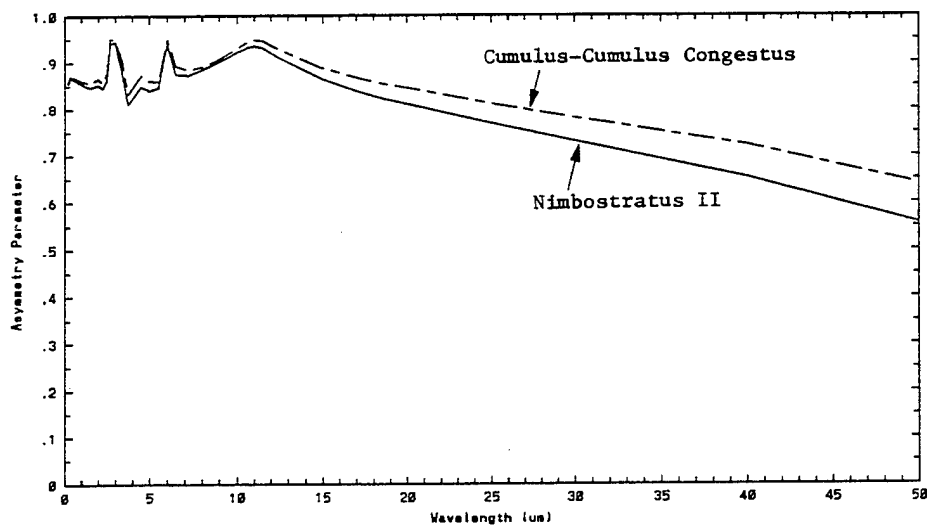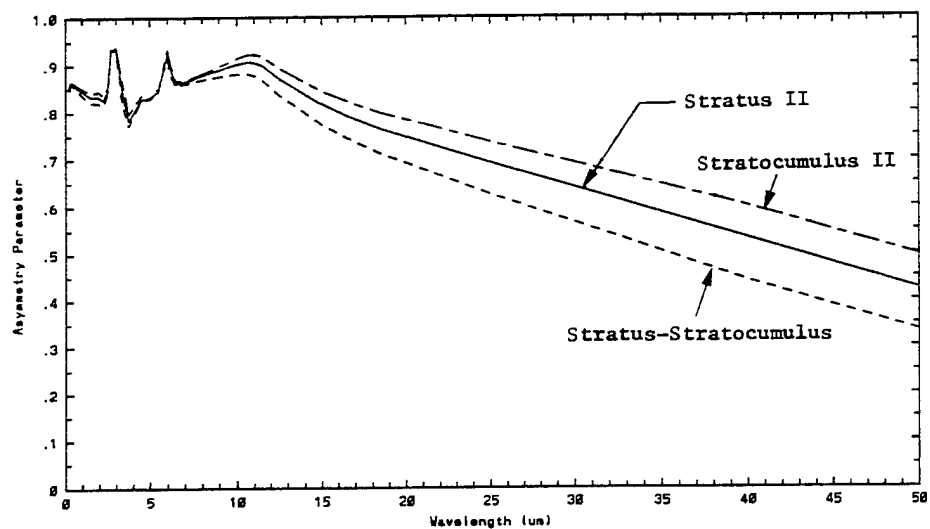
Figure 59. Cloud/Fog Scattering Asymmetry Parameters (continued).
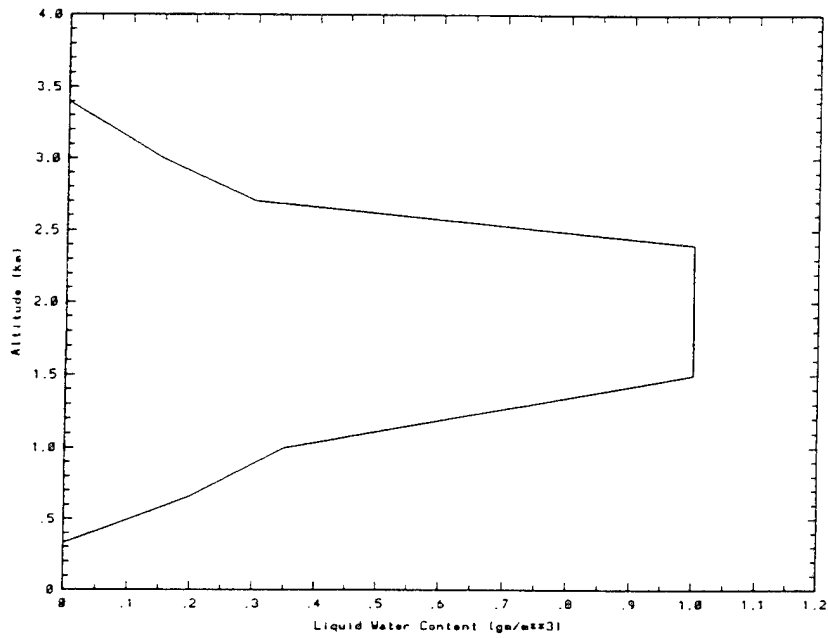
Figure 60. Cumulus Cloud.
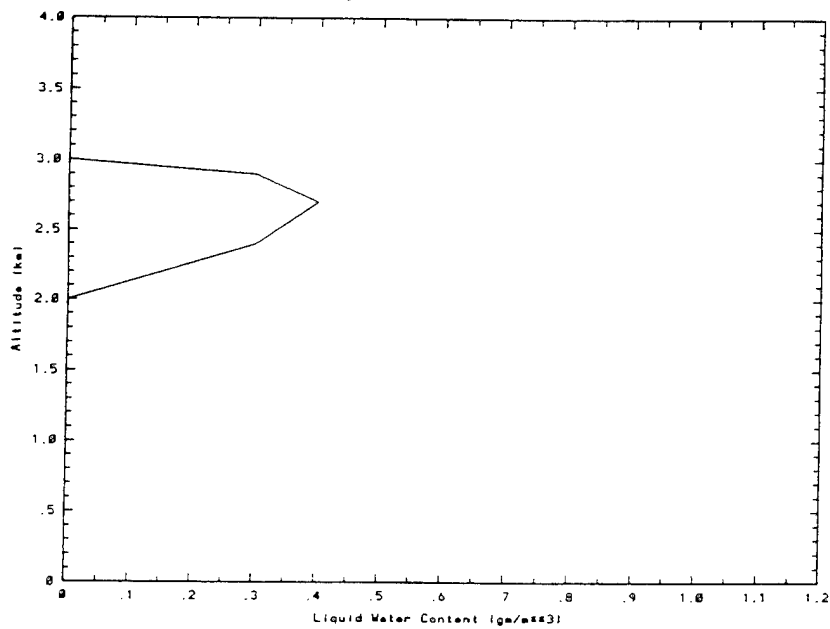
Figure 61. Altostratus Cloud.

54
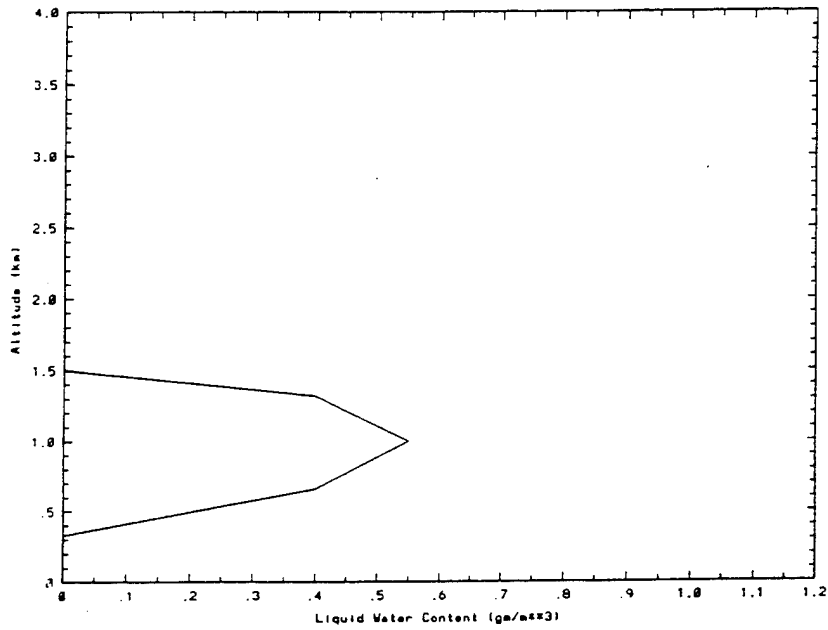
Figure 62. Stratocumulus I Cloud.
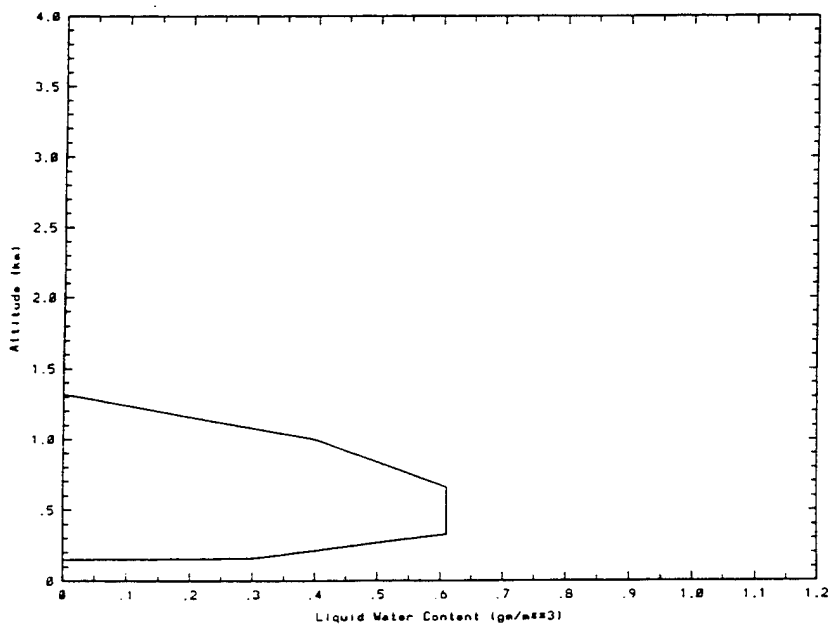
Figure 63. Nimbostratus I Cloud.

55
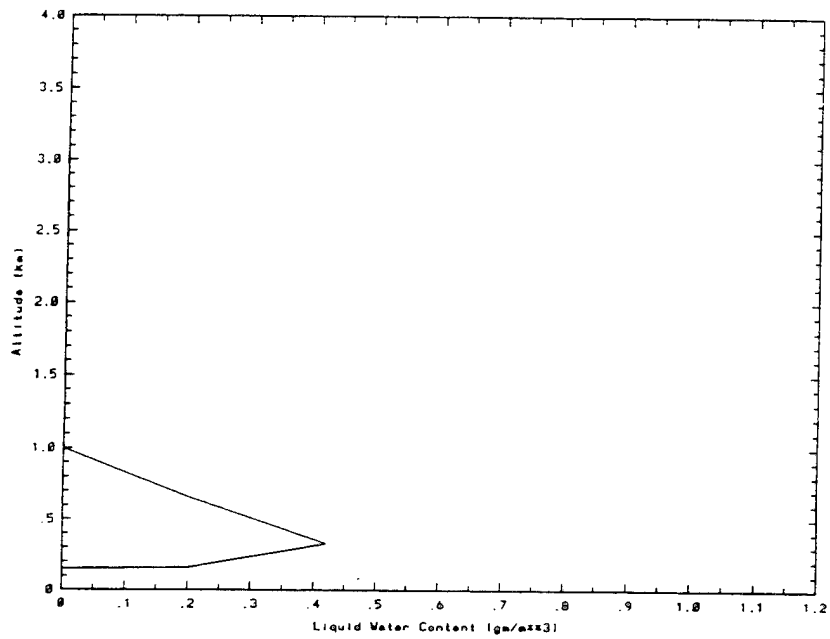
Figure 64. Stratus I Cloud.
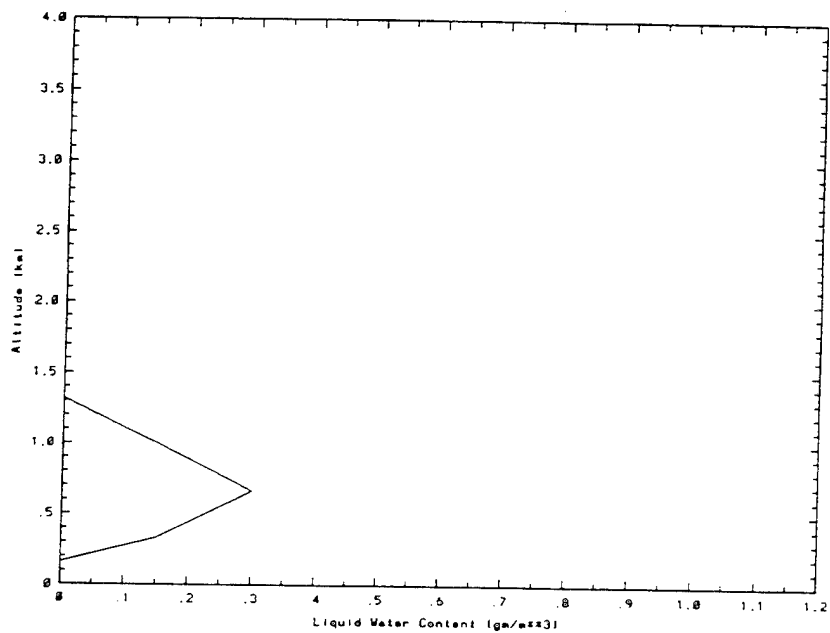
Figure 65. Stratus II Cloud.

56
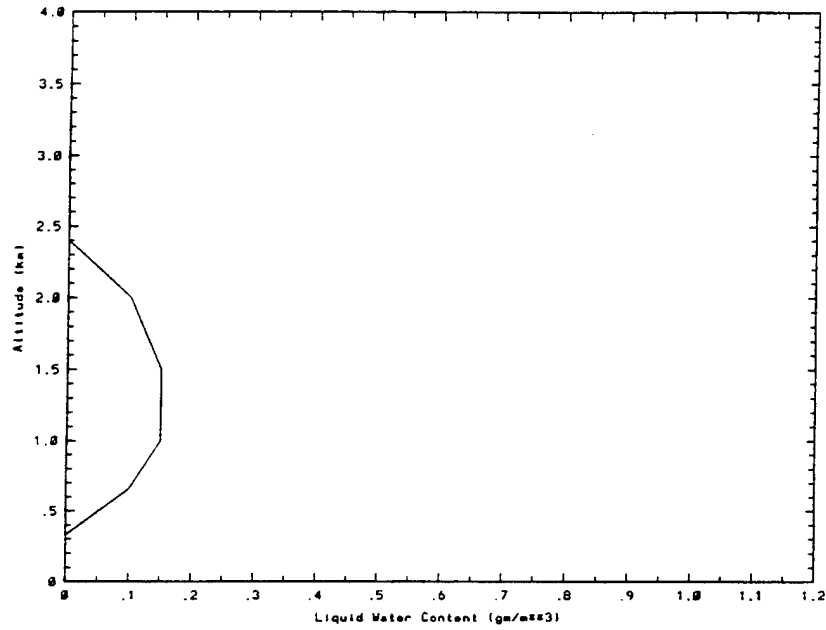
Figure 66. Stratus-Stratocumulus Cloud.
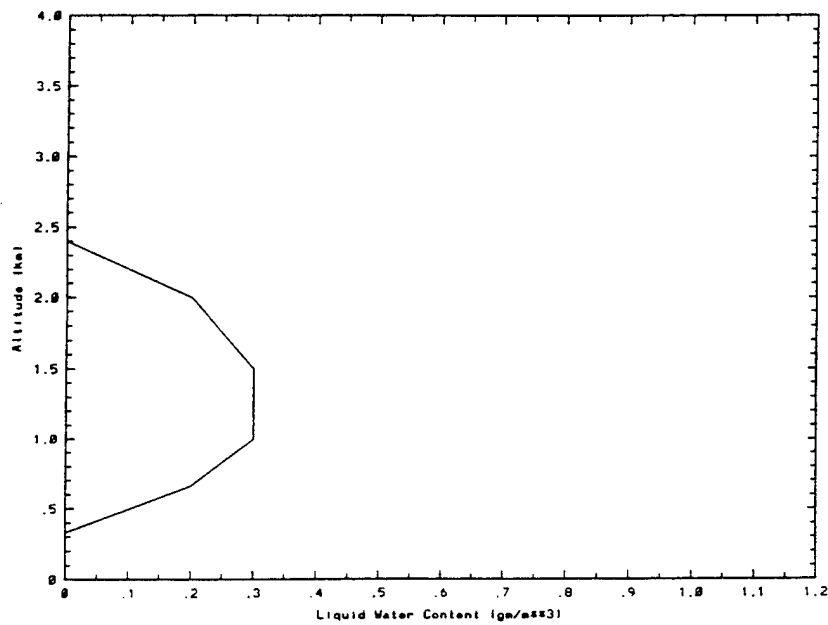
Figure 67. Stratocumulus II Cloud.

57
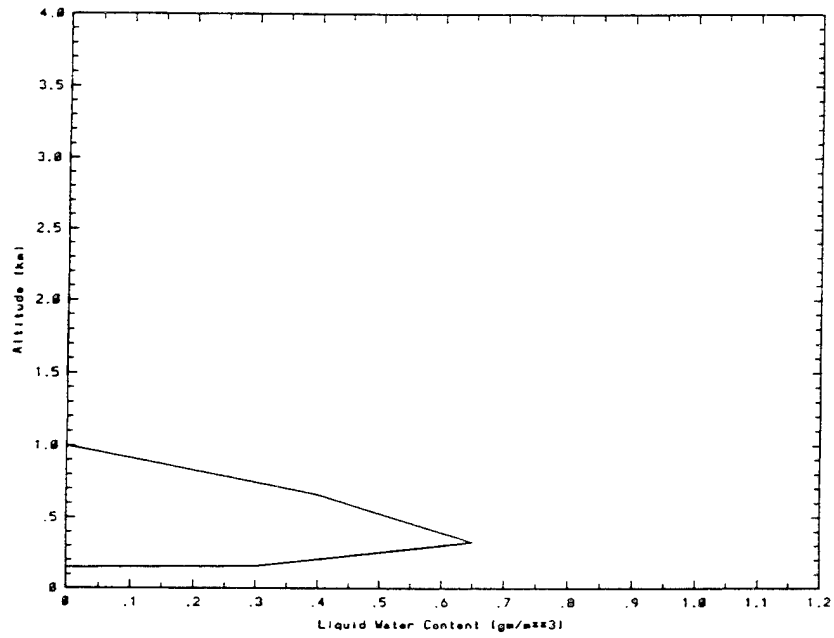
Figure 68. Nimbostratus II Cloud.
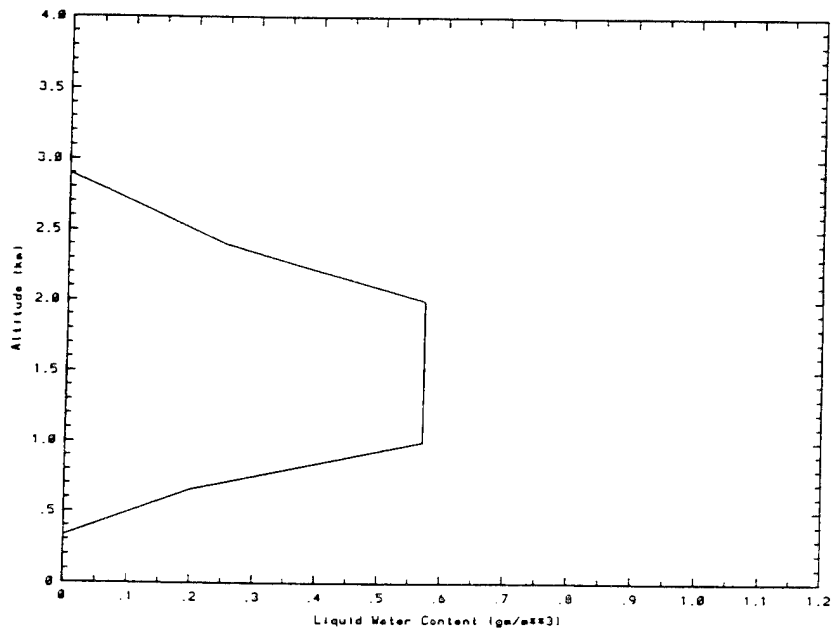
Figure 69. Cumulus-Cumulus Congestus I Cloud.

58
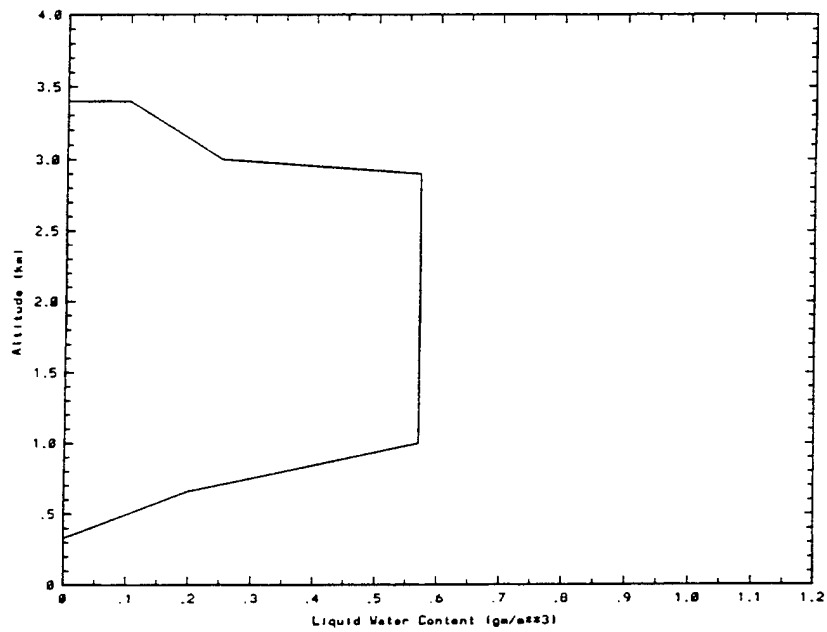
Figure 70. Cumulus-Cumulus Congestus II Cloud.
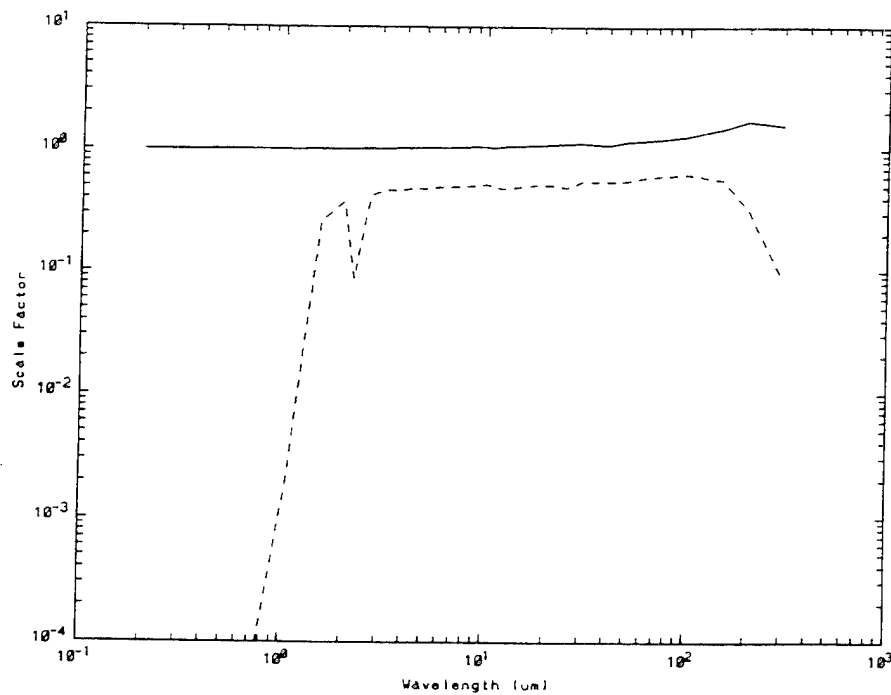
a) Spectral Extinction Coefficient
(Normalized to Unity of 0.55 μm)
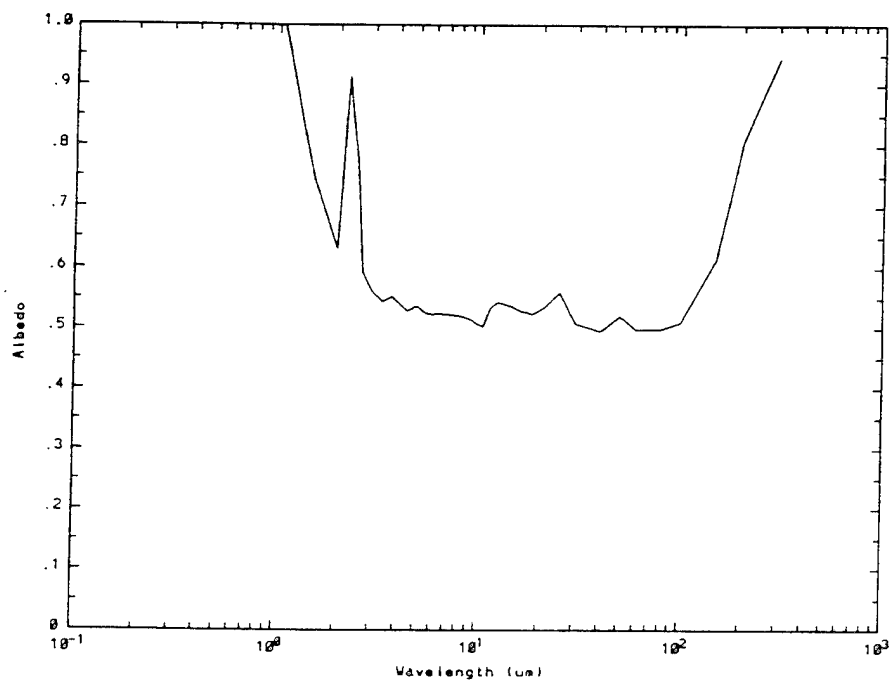
b) Spectral Scattering Albedo

Figure 71. Standard Cirrus.
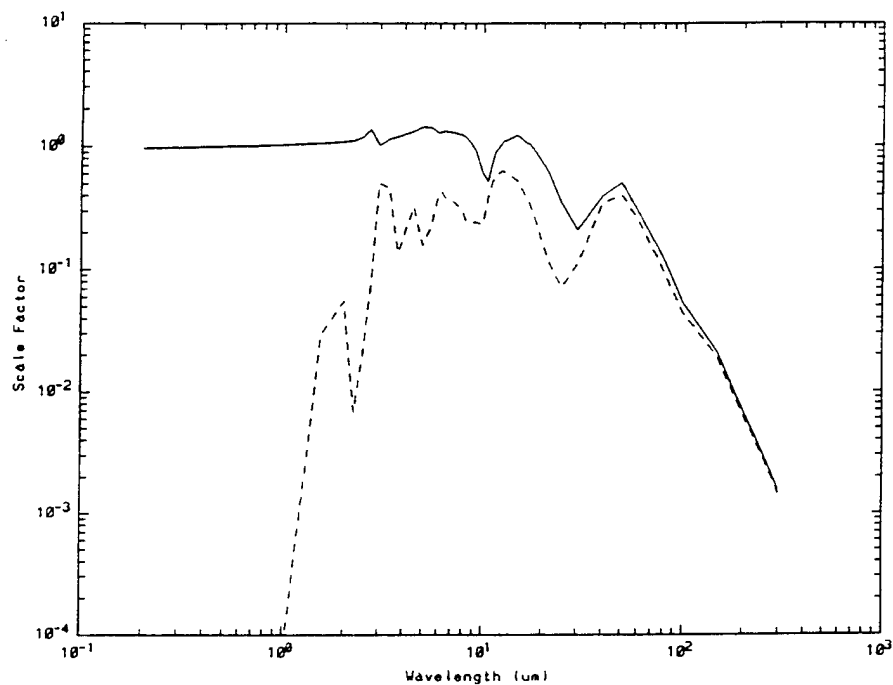
a) Spectral Extinction Coefficient
(Normalized to Unity of 0.55 µm)
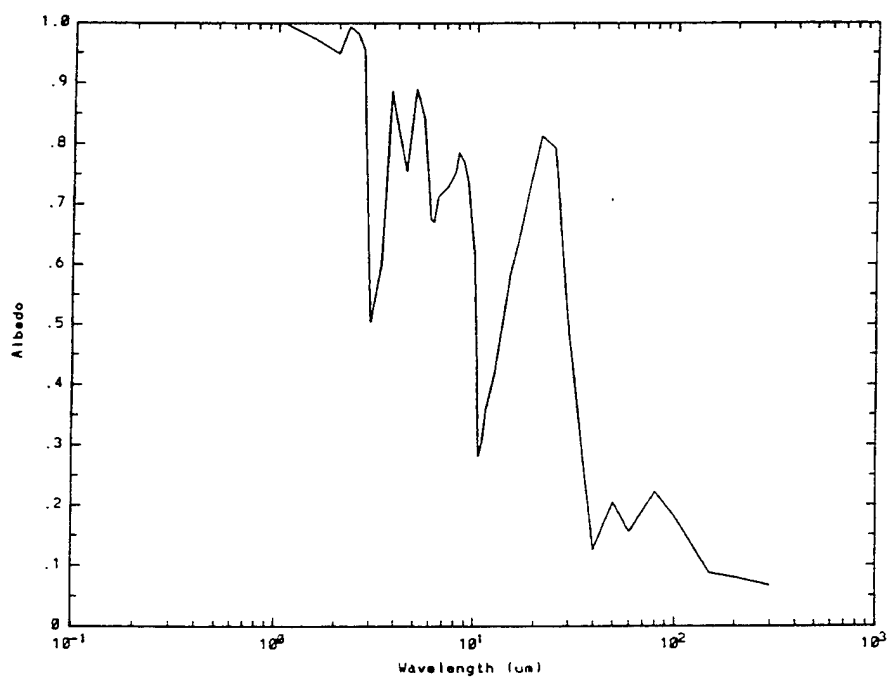
b) Spectral Scattering Albedo

Figure 72. Subvisual Cirrus.

61
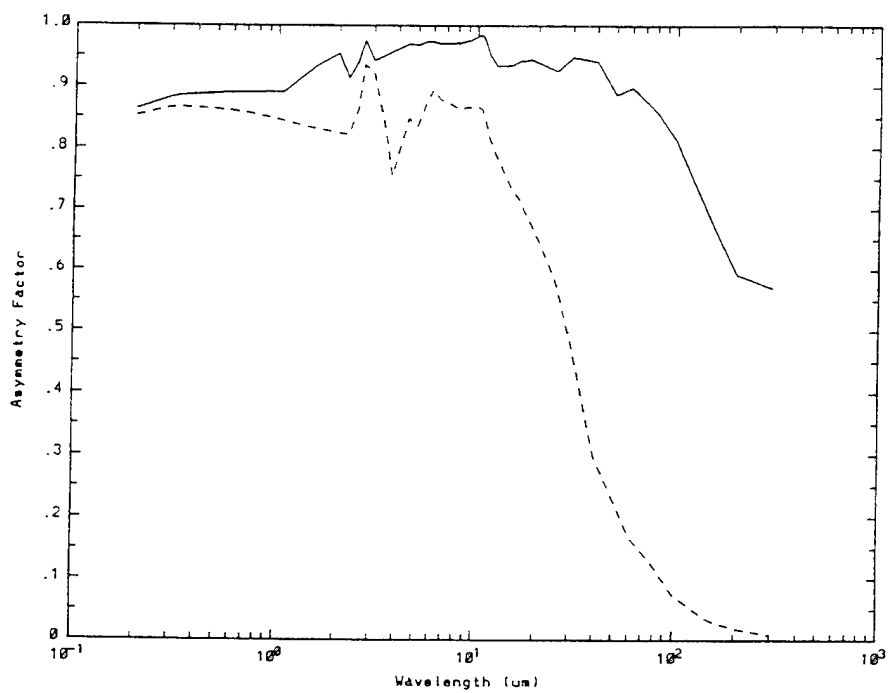
Figure 73. Asymmetry Parameter for Standard and Subvisual Cirrus.
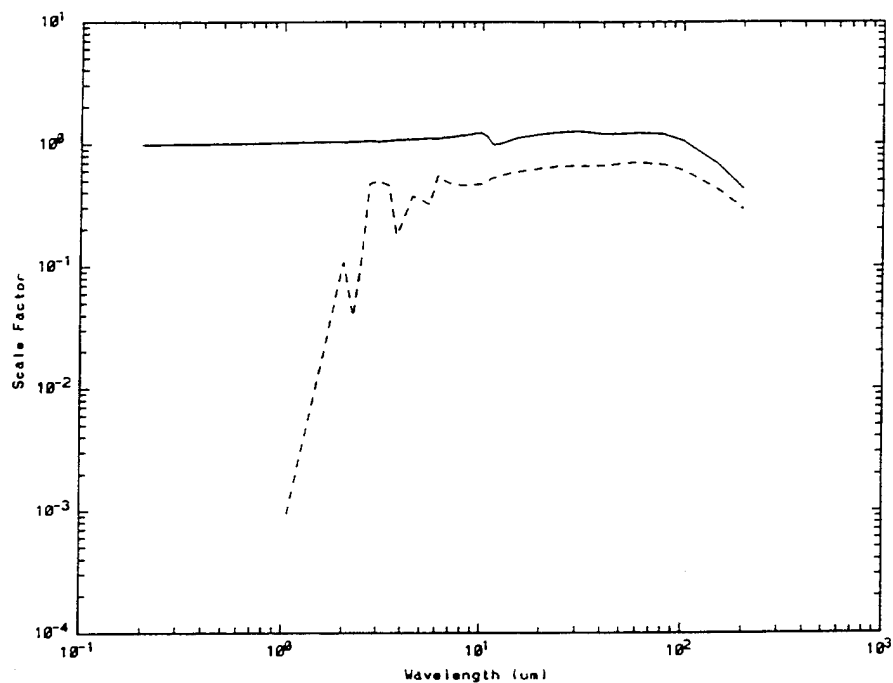
a) Spectral Extinction Coefficient
(Normalized to Unity of 0.55 μm)
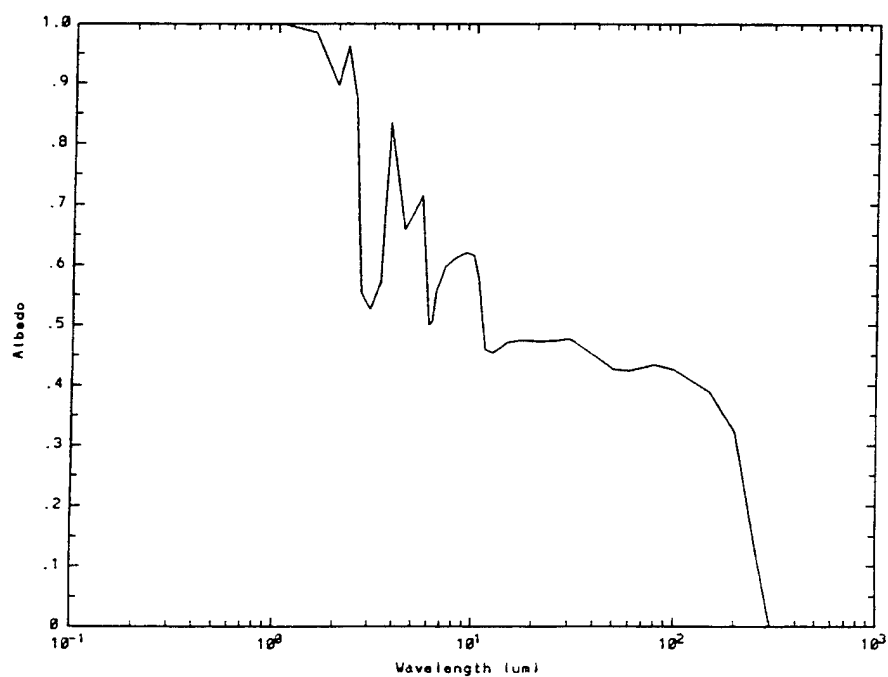
b) Spectral Scattering Albedo

Figure 74. Advection Fog Model.
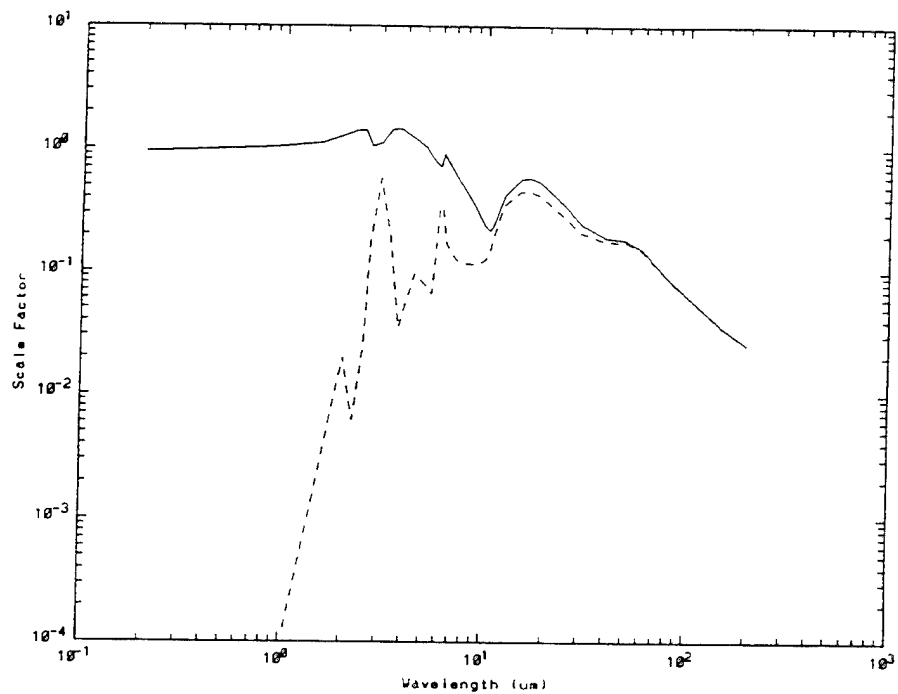
63

a) Spectral Extinction Coefficient
(Normalized to Unity of 0.55 μm)
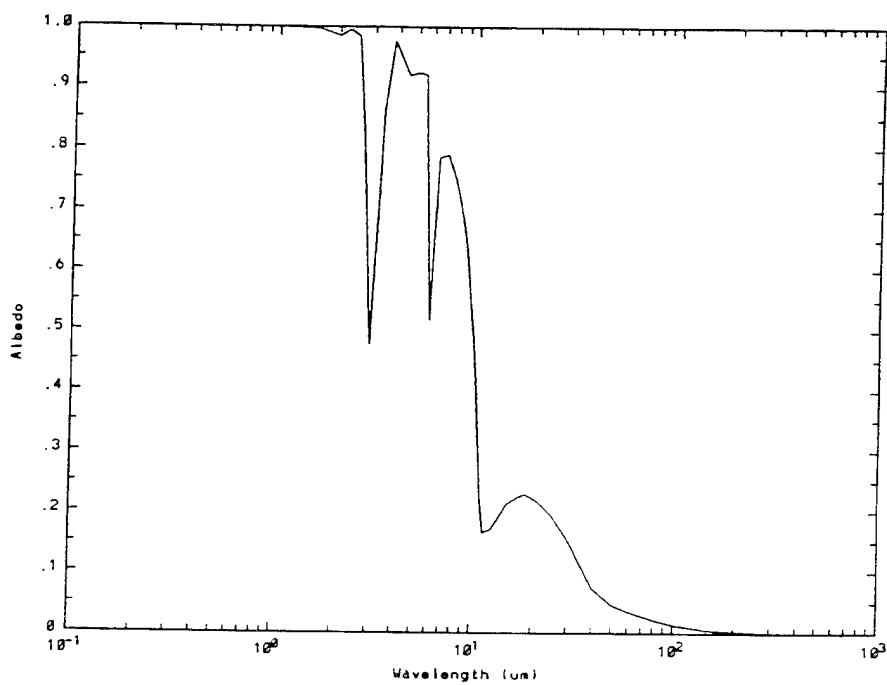
b) Spectral Scattering Albedo

Figure 75. Radiation Fog Model.

64

Table 6. Altitude Structured Fog Models.

Radiation Fog No. 1 (0 - 75 meters)
Radiation Fog No. 2 (0 - 75 meters)
Advection Fog No. 1 (0 - 150 meters)
Advection Fog No. 2 (0 - 150 meters)

Table 7. Rain/Cloud Models.

Cloud Type	Altitudes (km)	Rain	Surface Rate
Stratus II	0.33 - 1.00	Drizzle	2.0 mm/hr
Nimbostratus II	0.16 - 0.66	Light	5.0 mm/hr
Nimbostratus II	0.16 - 0.66	Medium	12.5 mm/hr
Cumulus	0.66 - 2.70	Heavy	25.0 mm/hr
Cumulus	0.66 - 2.70	Extreme	50.0 mm/hr

Table 8. Rain Size Distributions.

Distribution	N	a	b
Marshall-Palmer General Rain	8.0	4.1	0.21
Joss and Waldvogel Drizzle	30.0	5.7	0.21
Joss and Waldvogel Widespread Rain	7.0	4.1	0.21
Joss and Waldvogel Thunderstorm	1.4	3.0	0.21
Sekhon and Srivastava Thunderstorm	$7.0*RR^{0.37}$	3.8	0.14
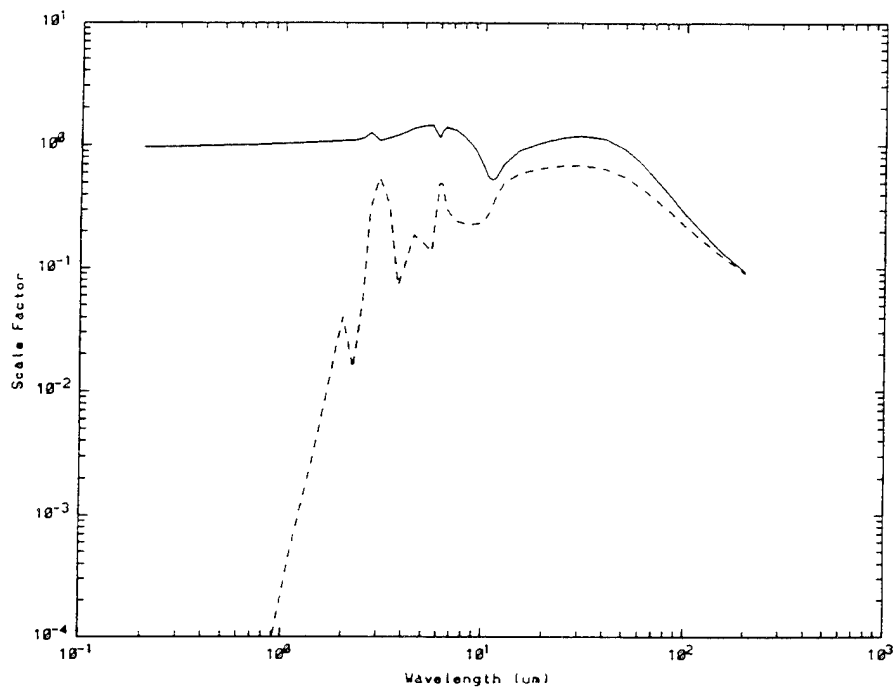
a) Spectral Extinction Coefficient
(Normalized to Unity of 0.55 μm)
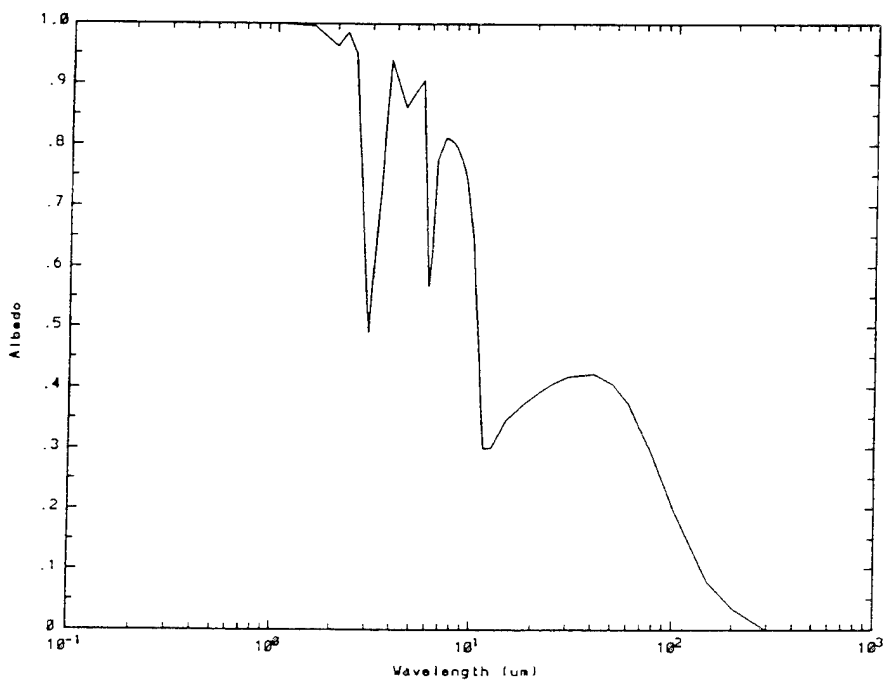
b) Spectral Scattering Albedo

Figure 76. Radiation Fog #1.
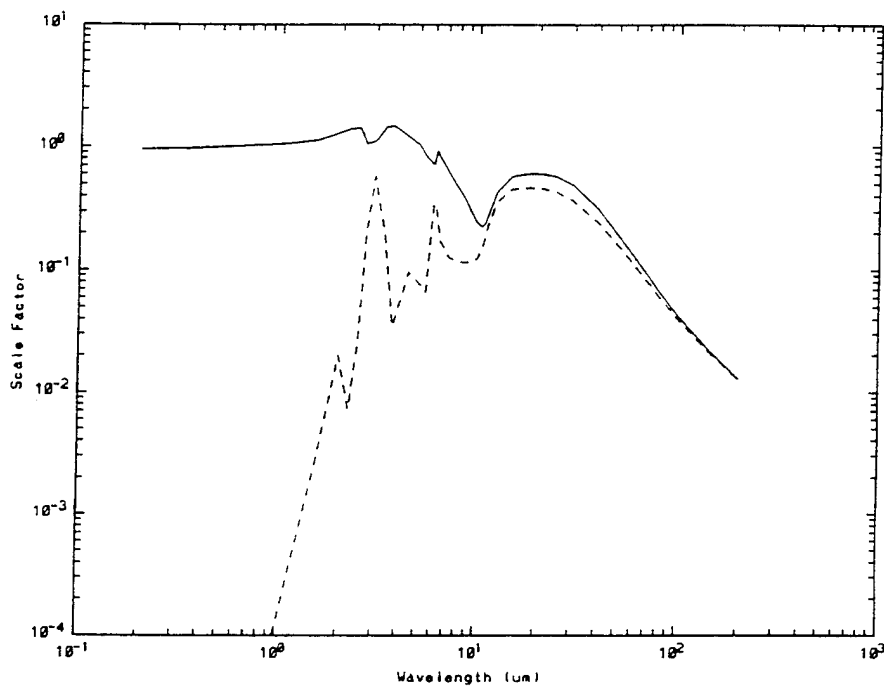
66

a) Spectral Extinction Coefficient
(Normalized to Unity of 0.55 μm)
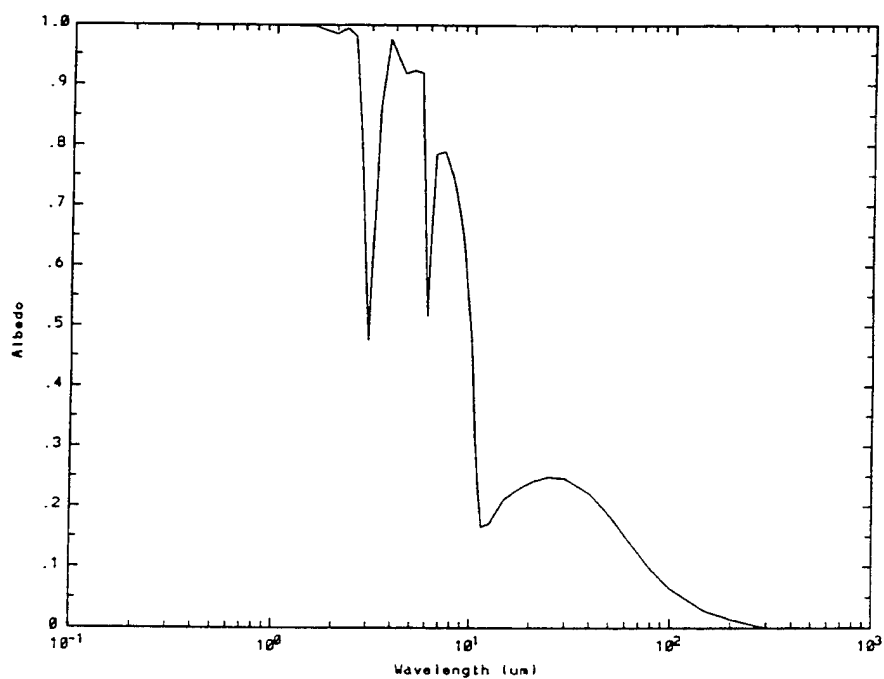
b) Spectral Scattering Albedo

Figure 77. Radiation Fog #2.
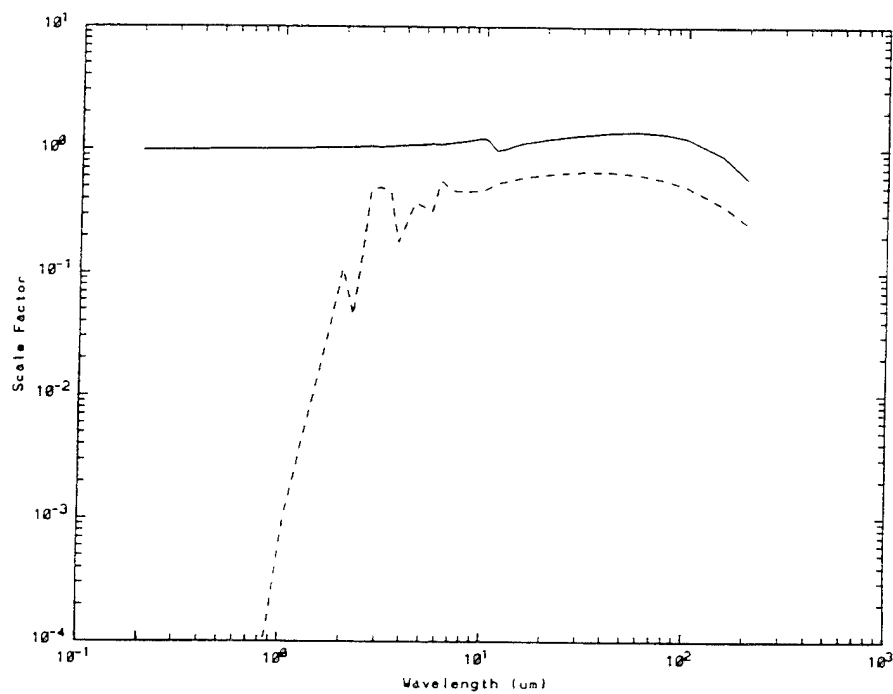
a) Spectral Extinction Coefficient
(Normalized to Unity of 0.55 μm)
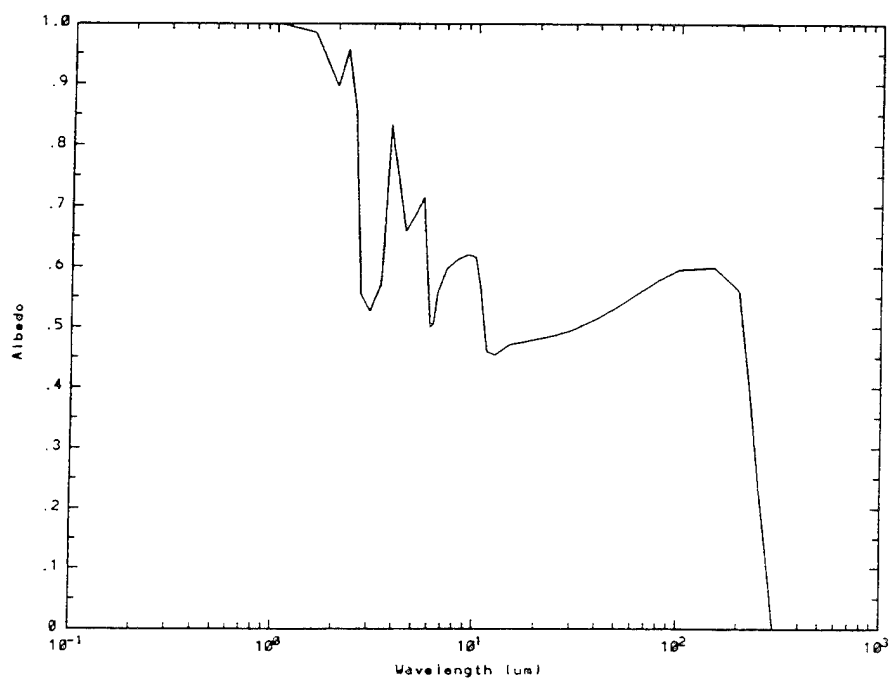
b) Spectral Scattering Albedo

Figure 78. Advection Fog #1.
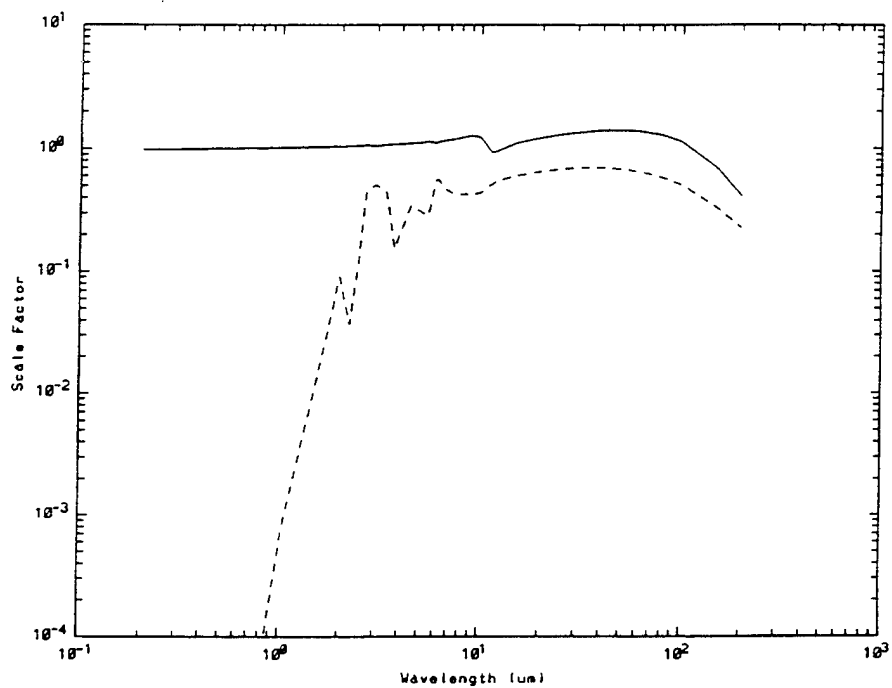
68

a) Spectral Extinction Coefficient
(Normalized to Unity of 0.55 μm)
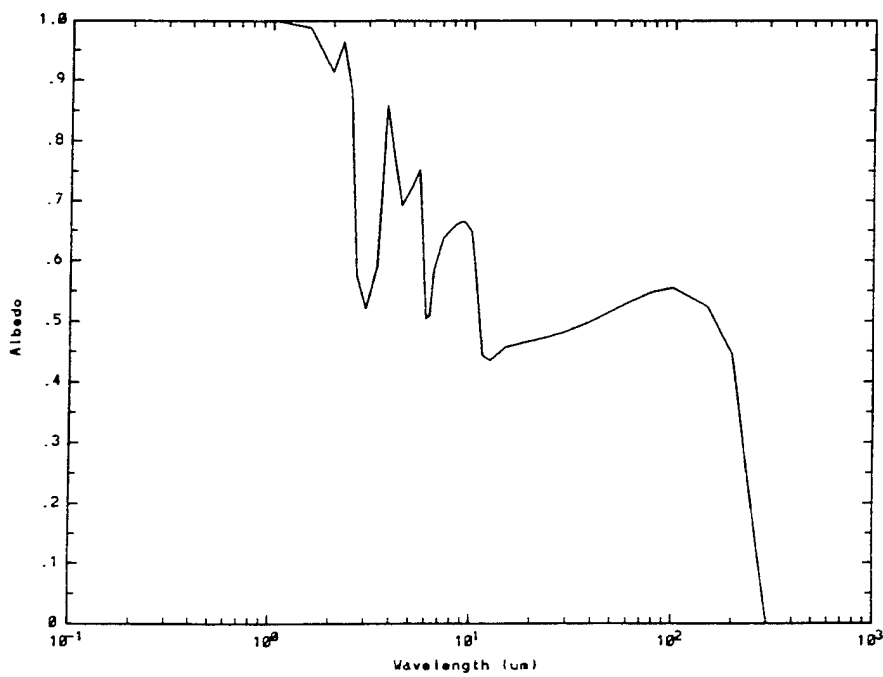
b) Spectral Scattering Albedo

Figure 79. Advection Fog #2.

69
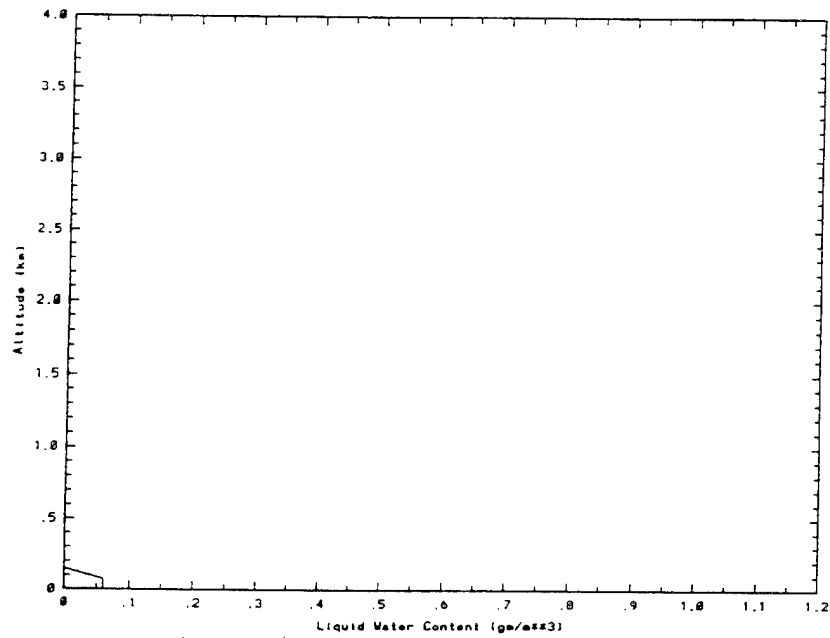
Figure 80. Radiation Fog #1.
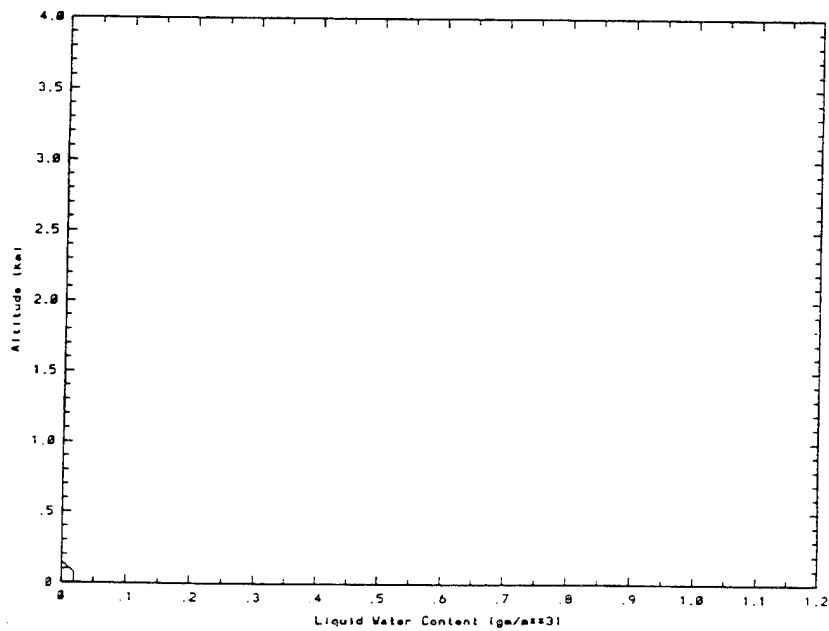
Figure 81. Radiation Fog #2.
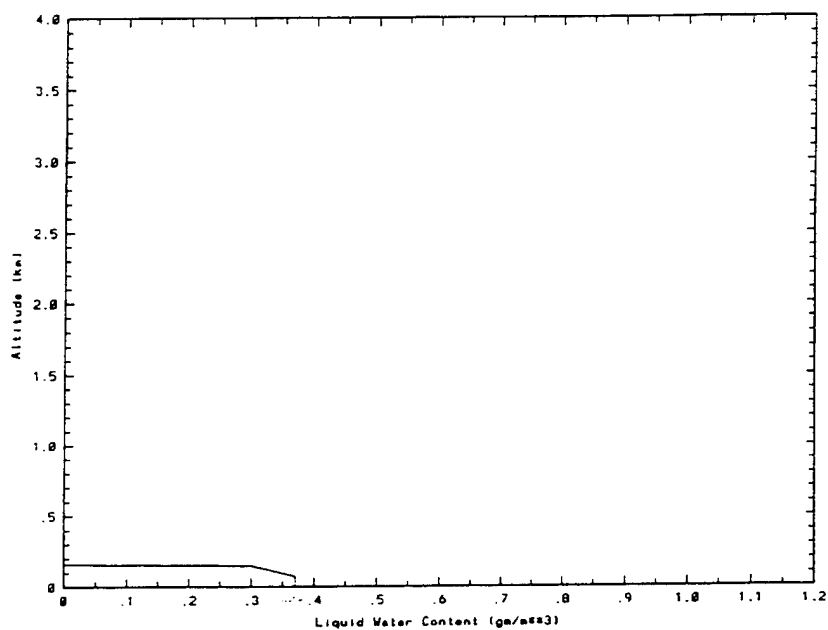
Figure 82. Advection Fog #1.
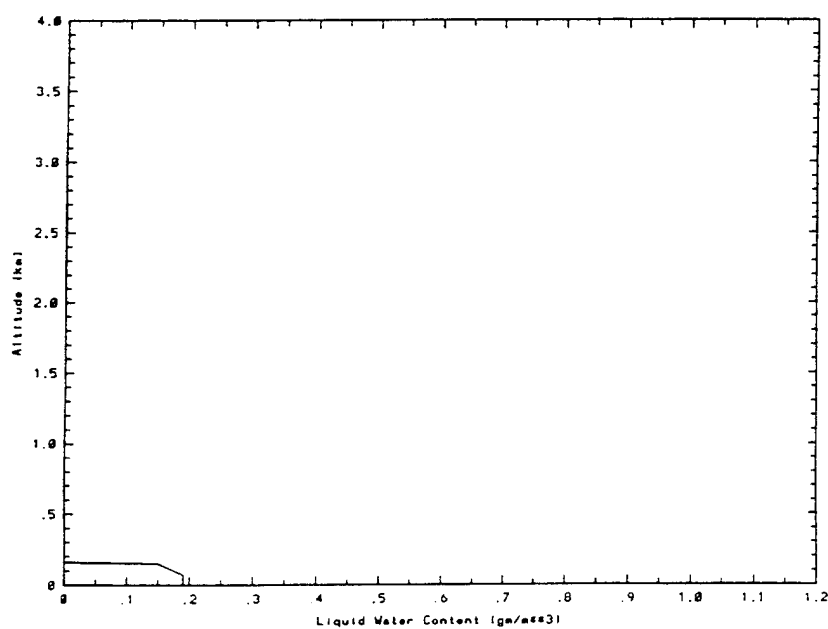
Figure 83. Advection Fog #2.

71
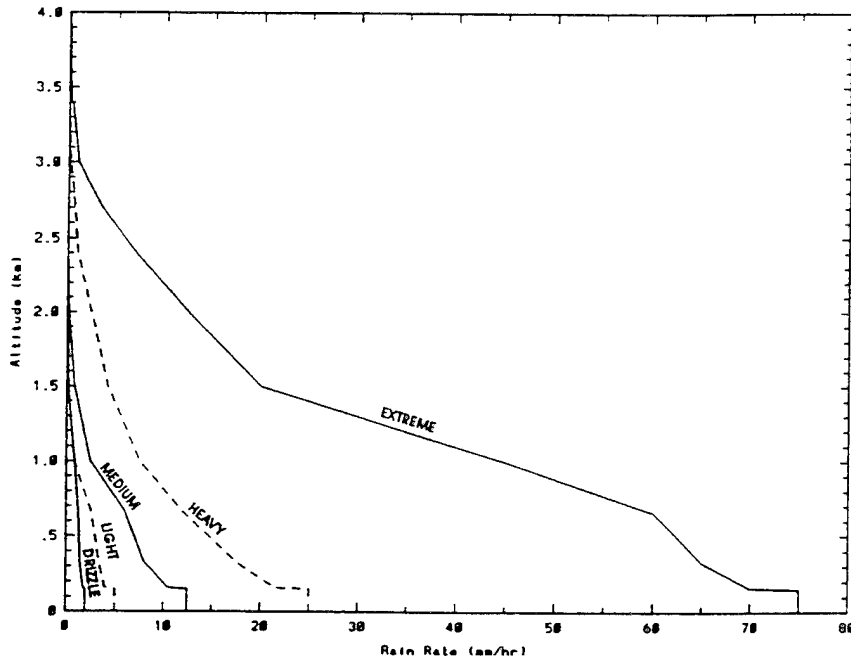
Figure 84. Model Rain Rate Profiles.

The extinction coefficient at 0.55 μm for rain is defined by

$$\sigma_{RAIN} = \pi \ N \ RR^b/a$$

where RR is the rain rate in mm/hr, and the constants N, b, and a are defined in Table 8. The normalized spectral extinction coefficients, absorption coefficients, and asymmetry parameters are shown in Figure 85.

2.3.4 Snow Models

The ambient temperature is used to determine whether the precipitation is rain or snow. If a rain model is selected and the temperature is below 267.15 K, it is assumed to be snow; between 275.15 and 267.15 it is assumed to be a mixture of rain and snow. The snow can consist of any of several crystal shapes as shown in Table 9.

The extinction coefficient at 0.55 μm for snow is defined by

$$\sigma_{snow} = \frac{\rho_{water}}{\rho_{ice}} * SR * \frac{\int P(r) \ 4\pi r^2 \ Q_{ext} dr}{\int P(r) \ \frac{4\pi}{3} r^3 \ v \ dr}$$
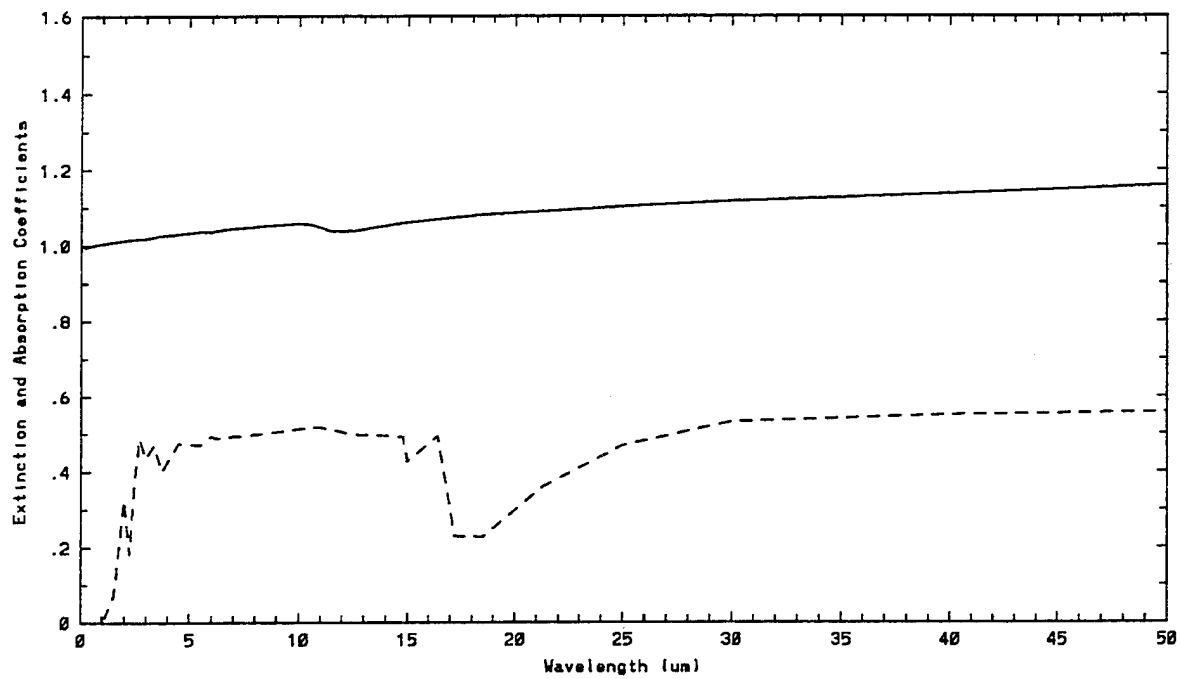
72

a) Normalized Spectral Extinction Coefficient and Absorption Coefficient
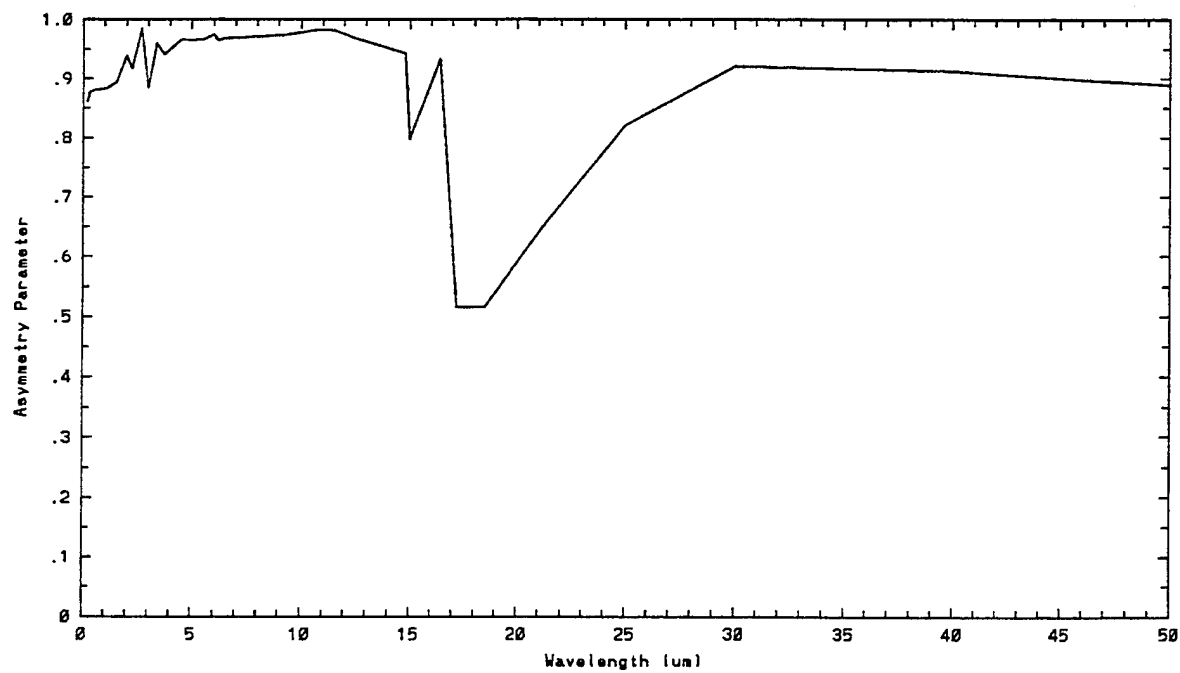
b) Asymmetry Parameter

Figure 85. Rain Optical Properties.

Table 9. Snow Models.

	Falling Velocity (*)			Crystal Size (**)	
	a_0	a_1	a_2	b_0	b_1
Needle	-14.14	86.16	-22.95	0.0254	-0.0026
Plain Dendritic	31.16	-0.26	0	0.0277	0
Spatial Dendritic	58.78	-0.55	0	0.0495	0
Powder Snow	50.78	-0.55	0	0.0495	0
Crystal with Droplet	86.08	6.15	0	0.086	0
Graupel	-29.06	108.69	-20.06	0.177	-0.004

(*)   Falling velocity (cm/sec) $= a_0 + a_1 d + a_2 d^2$, where d is crystal size

(**)

$$d = \begin{cases} R_{eff}^{3/2}/b_0 & \text{if } b_1 = 0 \\ b_0^2 + 4b_1 R_{eff}^{3/2} & \text{otherwise} \end{cases}$$

where R_{eff} is the spherical volume equivalent radius

where ρ_{water} is the density of water;

ρ_{ice} is the density of ice;

SR is the snow rate in terms of water content (mm/hr);

P(r) is the distribution of effective crystal radii, given by

$$1.7 \, r^{1.5} \, e^{-\frac{3}{5}\left(\frac{r}{1.7}\right)^{2.5}} \quad ;$$

r is the effective crystal radius;

v is the falling velocity; and

Q_{EXT} is the extinction efficiency, which is assumed to be 2.0 in MOSART.

74

The normalized spectral extinction coefficient, absorption coefficient, and asymmetry parameter for snow are shown in Figure 86.
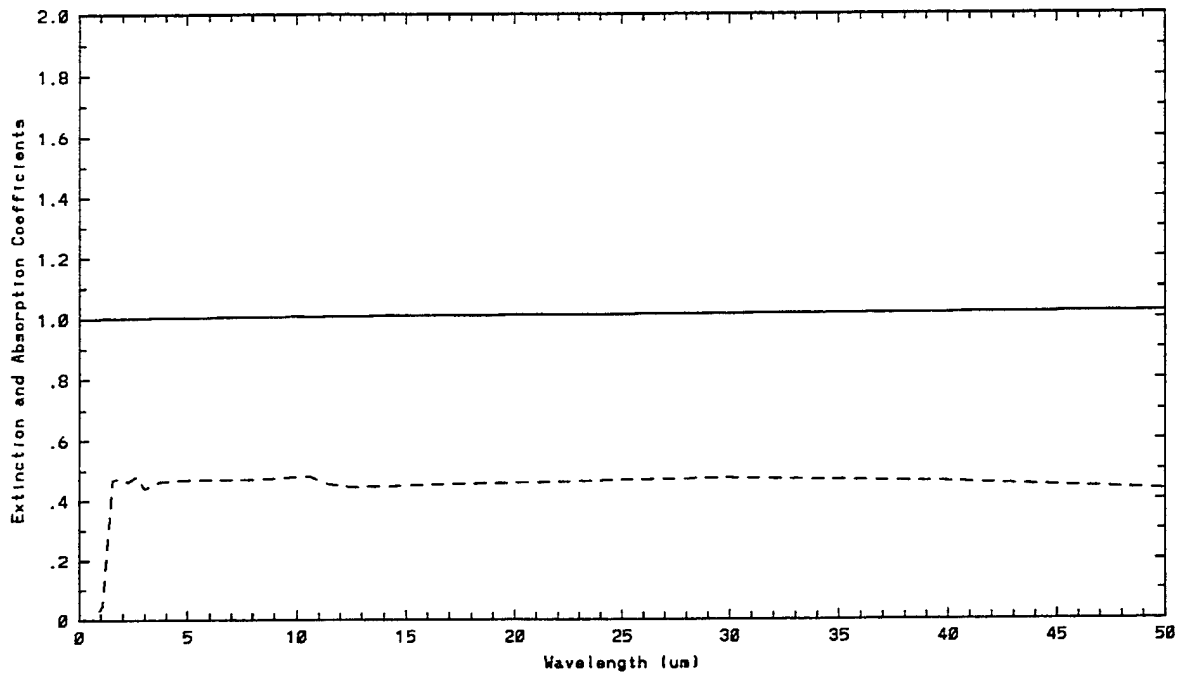
a) Normalized Spectral Extinction Coefficient and Absorption Coefficient
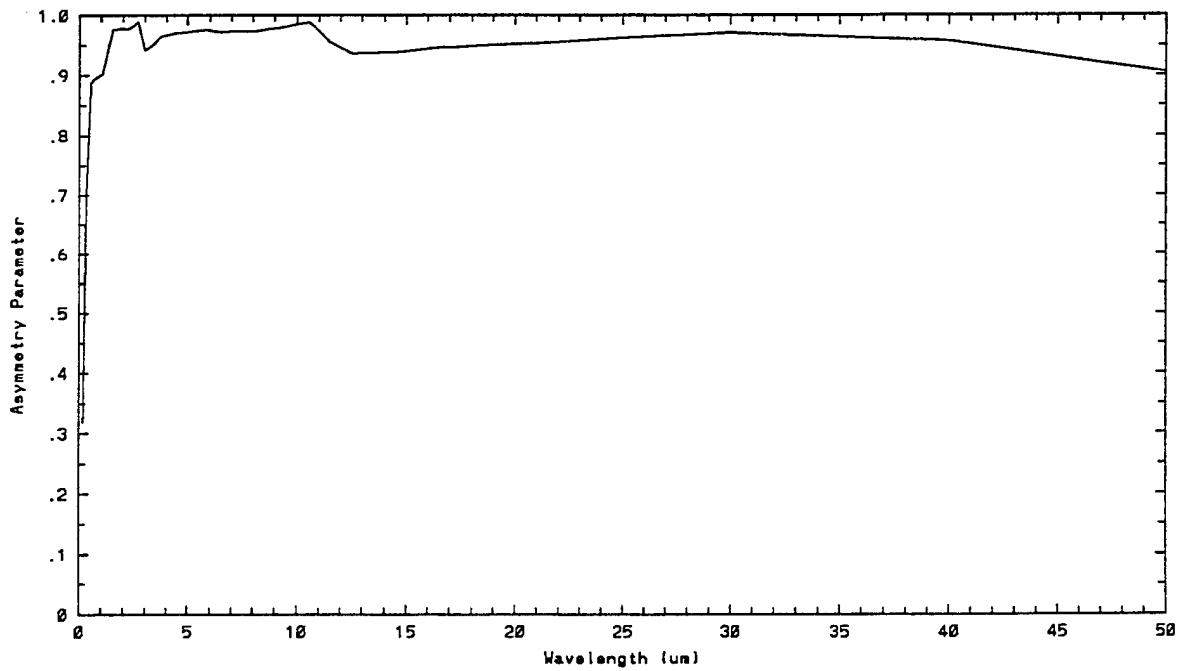
b) Asymmetry Parameter

Figure 86. Snow Optical Properties.

75

2.4 Terrain Backgrounds

MOSART contains a library of terrain backgrounds based on the GENESSIS Reference Scenes and materials (Acquista and Anding, 1986). It should be noted, however, that the representation of these scenes and materials are only statistical in nature; if a two-dimensional deterministic background is required, the GENESSIS code should be used.

2.4.1 Materials

The MOSART terrain background data base contains 20 representative materials. The materials are shown in Table 10. For each material, there is a spectral reflectivity data base and a thermal heat transfer data base.

Table 10. Terrain Background Materials.

Fresh Water	Scrub
Sea Water	Pine Trees
First Year Ice	Broadleaf Trees (Summer)
Multi-Year Ice	Broadleaf Trees (Winter)
Dry Snow	Packed Soil
Wet Snow	Sand
Blackbody	Rock
Whitebody	Asphalt
Grass/Meadow	Concrete
Irrigated Vegetation	Metal Building Roof

The spectral reflectivity data bases are essentially derived from GENESSIS between 0.4 and 15 µm. These data bases have been extended spectrally for 0.20 - 50.0 µm. These extensions are based upon available data, but have not been extensively validated.

The MOSART code calculates the material temperatures as a function of the time of day. To illustrate these calculations, the difference between the material temperature and the ambient air temperature as a function of the time of day is also presented. The values presented were calculated at the equator on the summer solstice for maximum solar loading. These curves are presented only to illustrate the type of diurnal variability that can be expected when using this MOSART option.

The spectral reflectivities and temporal temperature differences are shown in Figures 87 through 101. The blackbody and whitebody materials are at ambient air temperature with a reflectivity of 0.00 and 1.00, respectively. A description of the other properties of each material is presented in Tables 11 through 26.
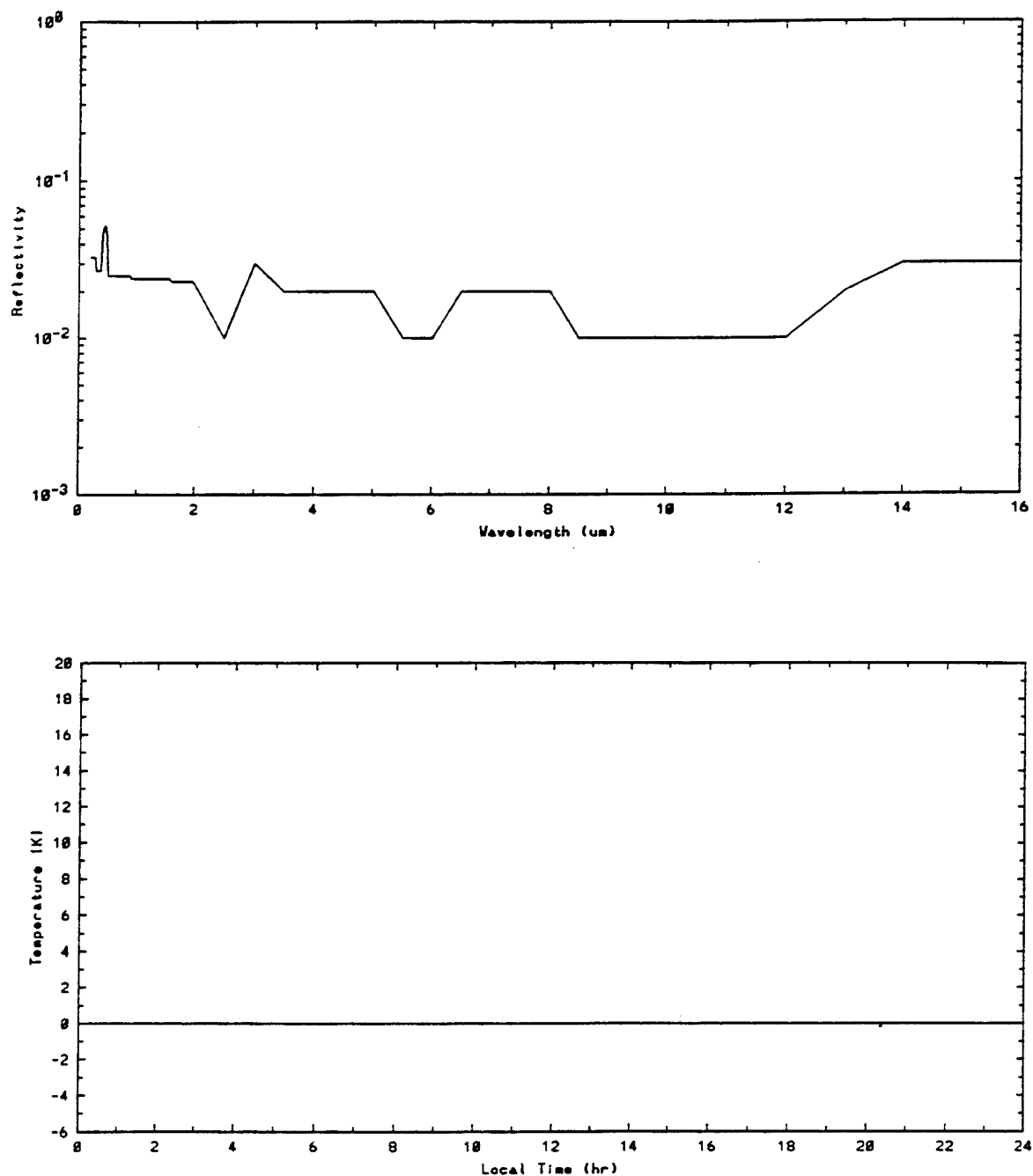
Figure 87. Spectral Reflectivity and Temporal Temperature Difference for Water.

77
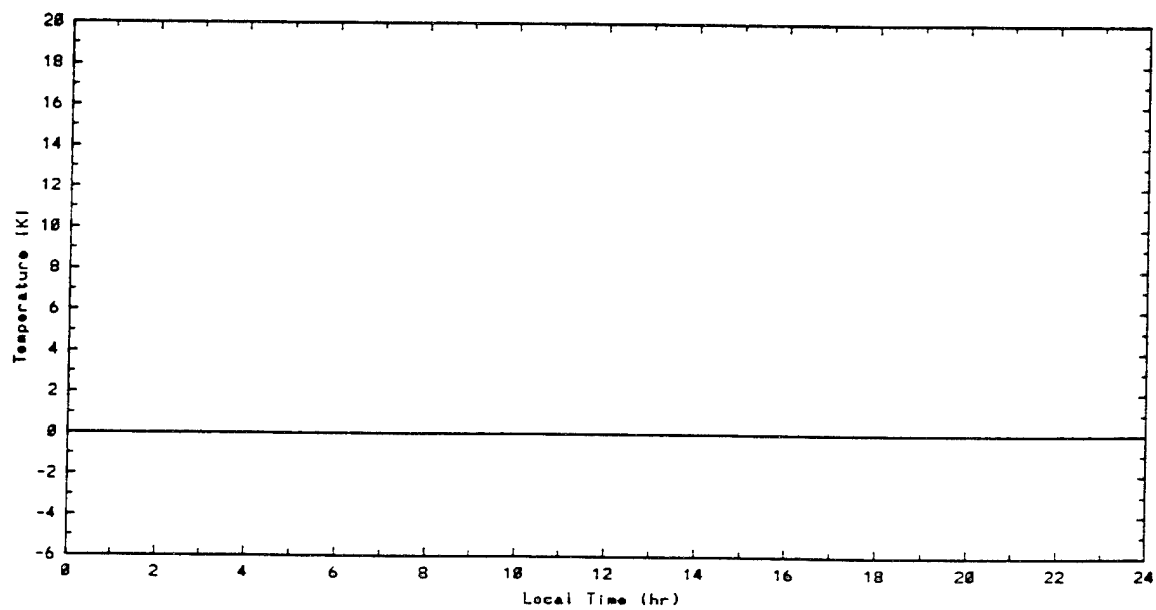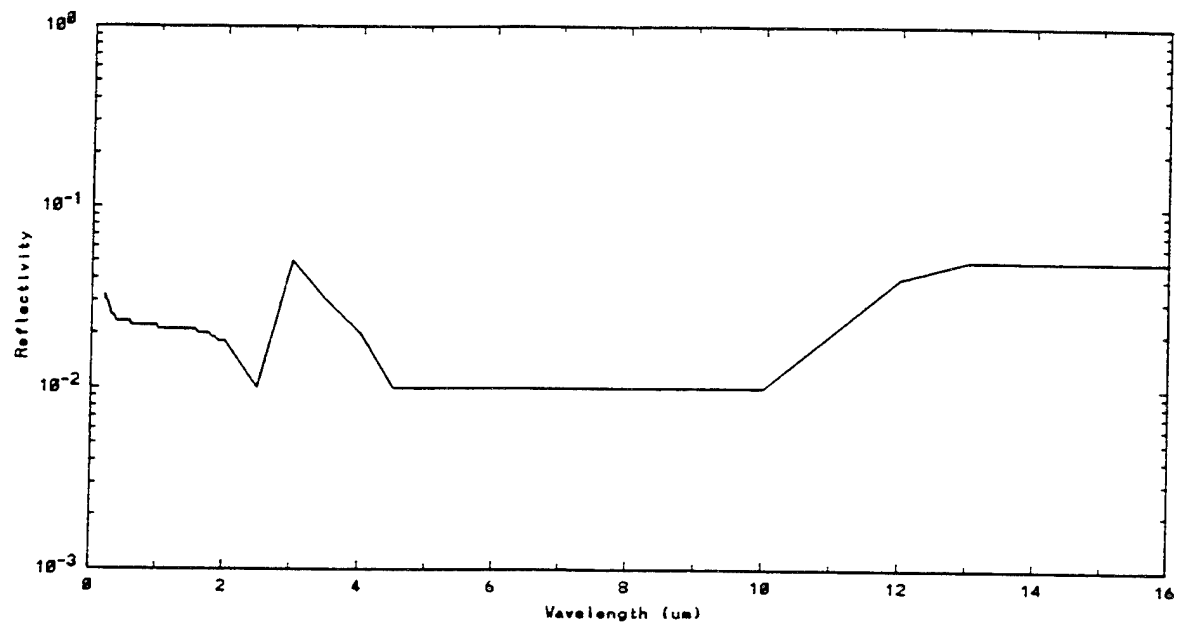
Figure 88. Spectral Reflectivity and Temporal Temperature Difference for Ice.
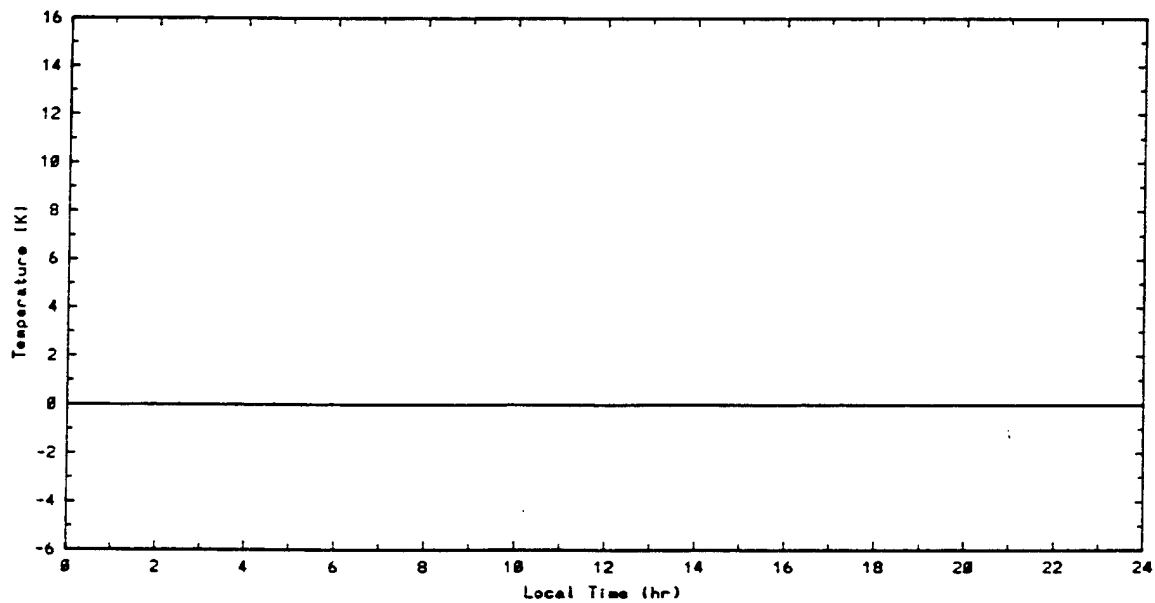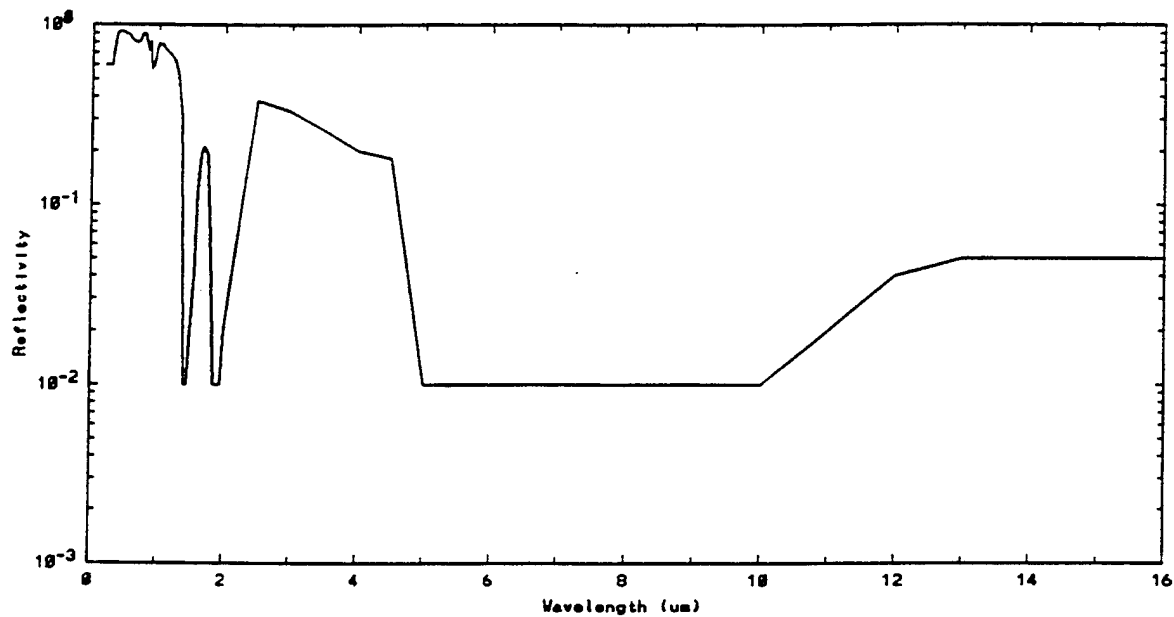
Figure 89. Spectral Reflectivity and Temporal Temperature Difference for Snow.
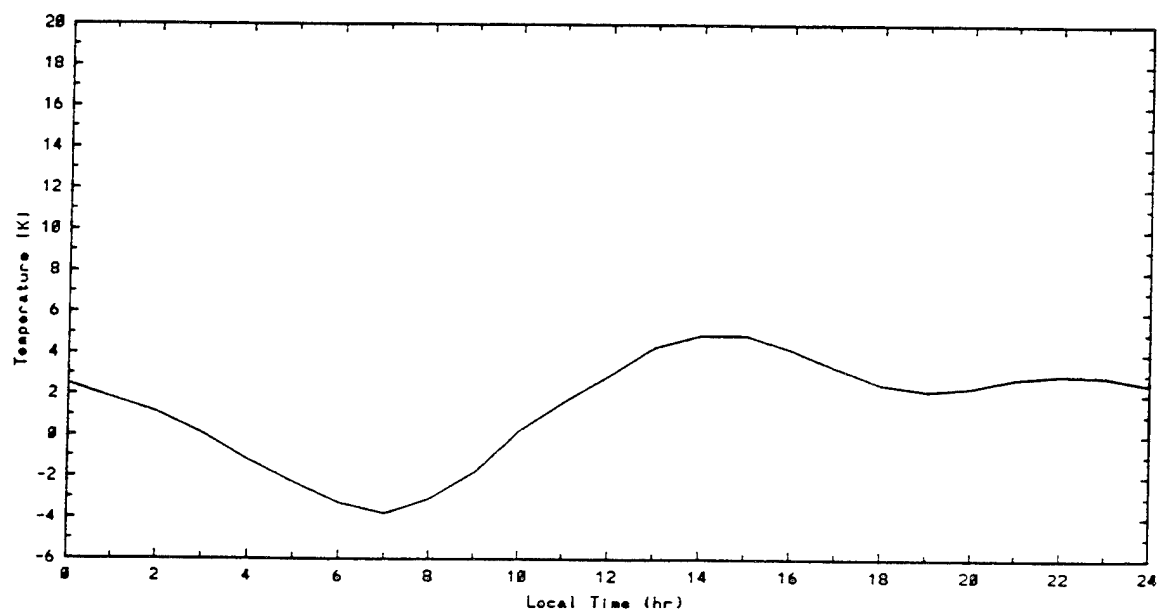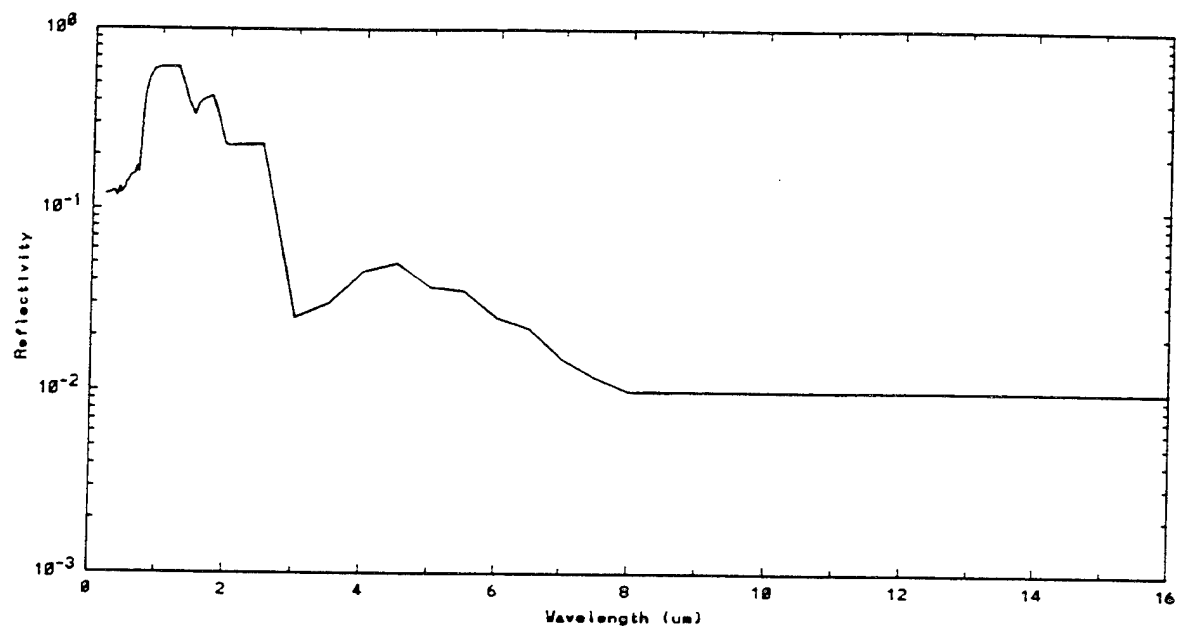
Figure 90. Spectral Reflectivity and Temporal Temperature Difference for Pine Trees.
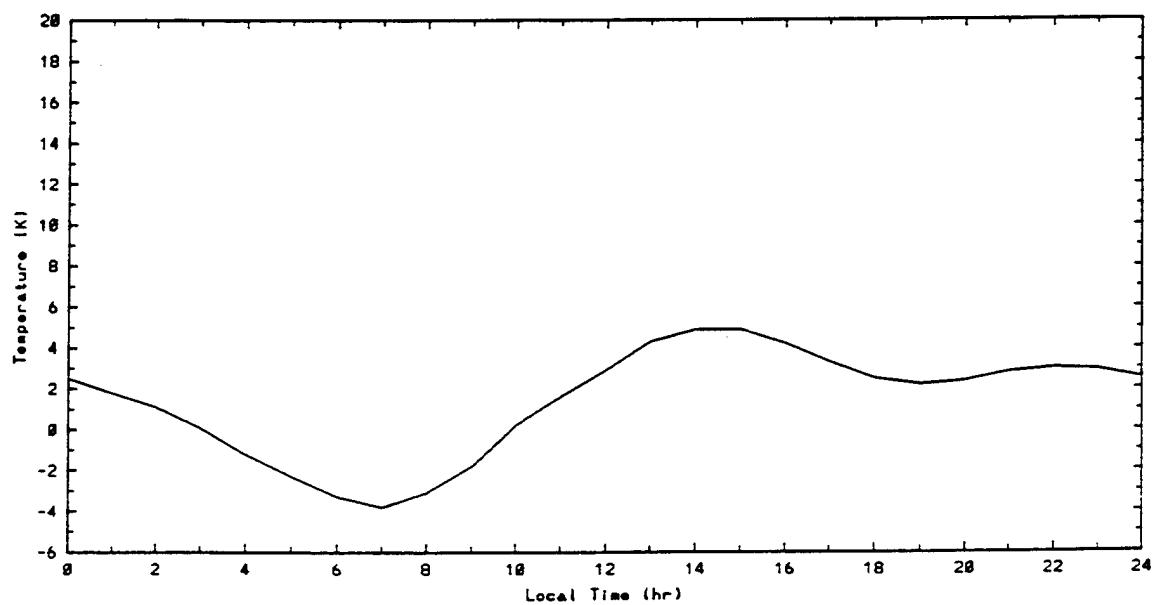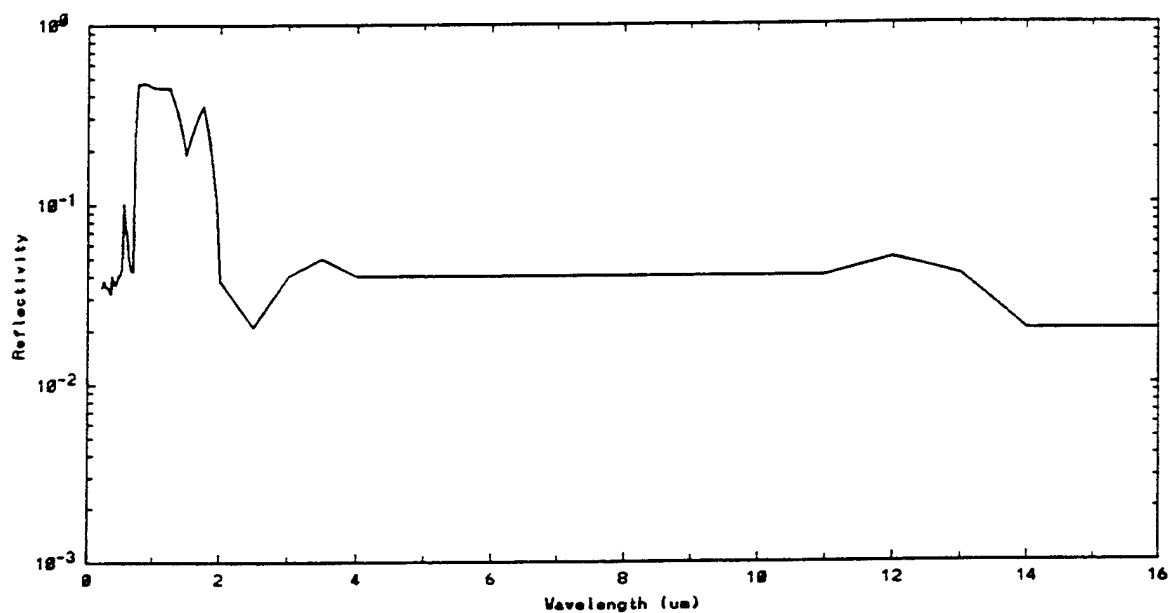
Figure 91. Spectral Reflectivity and Temporal Temperature Difference for Broadleaf Trees (Summer).
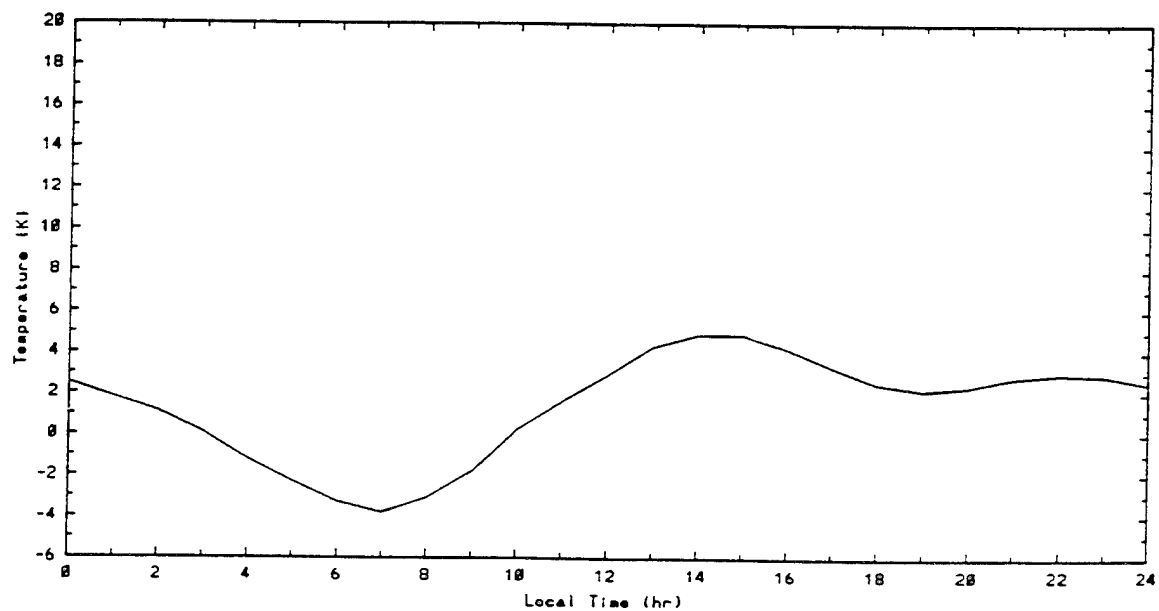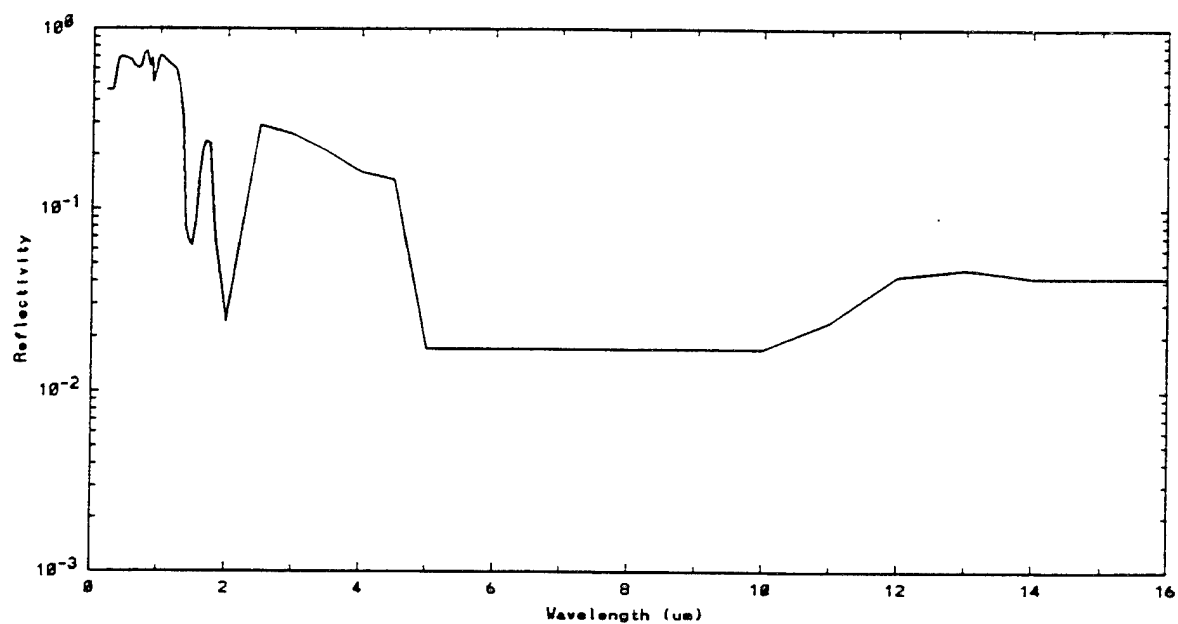
Figure 92. Spectral Reflectivity and Temporal Temperature Difference for
Broadleaf Trees (Winter).

82
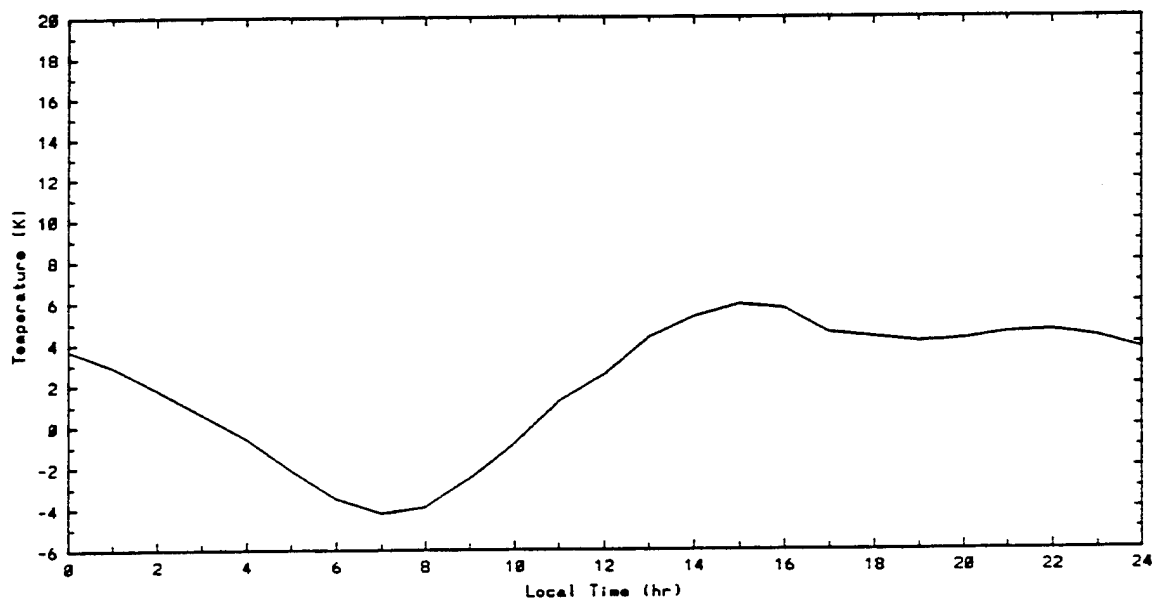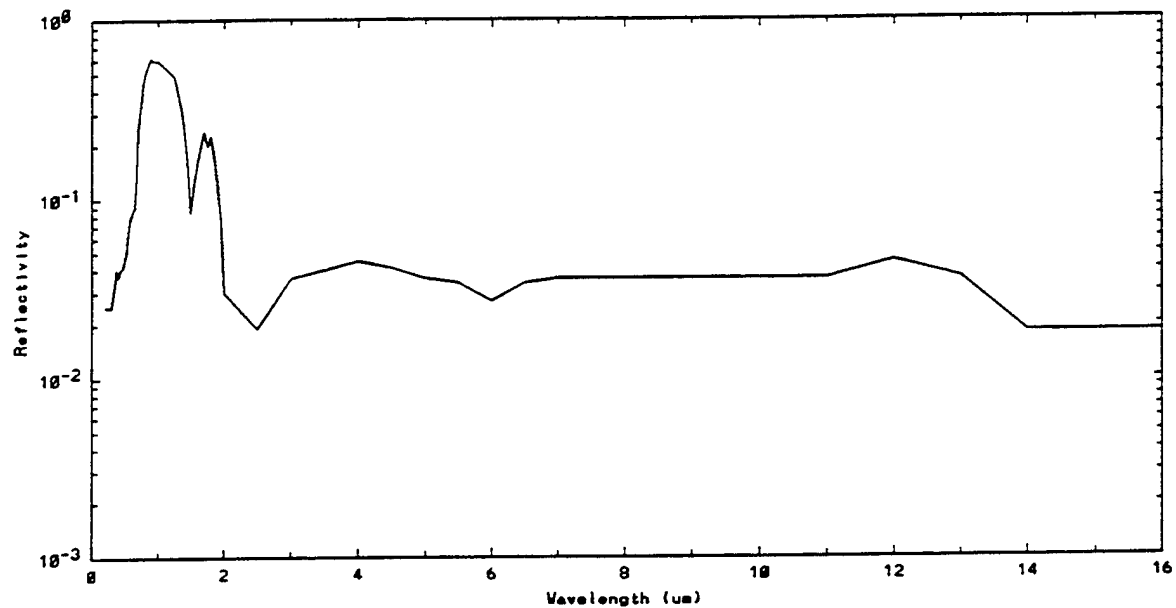
Figure 93. Spectral Reflectivity and Temporal Temperature Difference for Irrigated Low Vegetation.
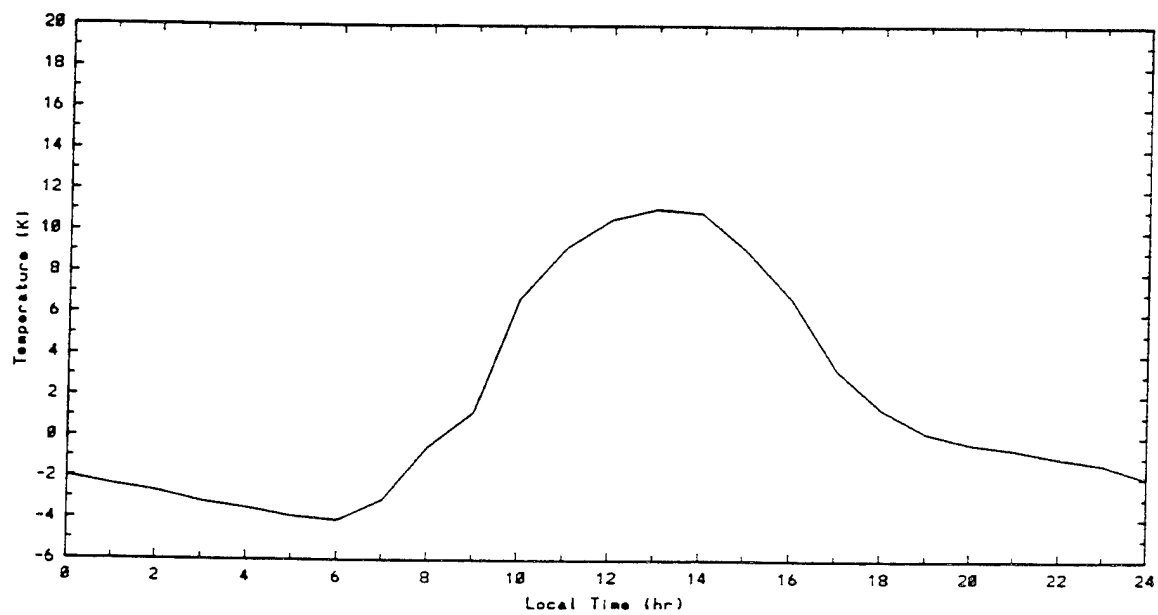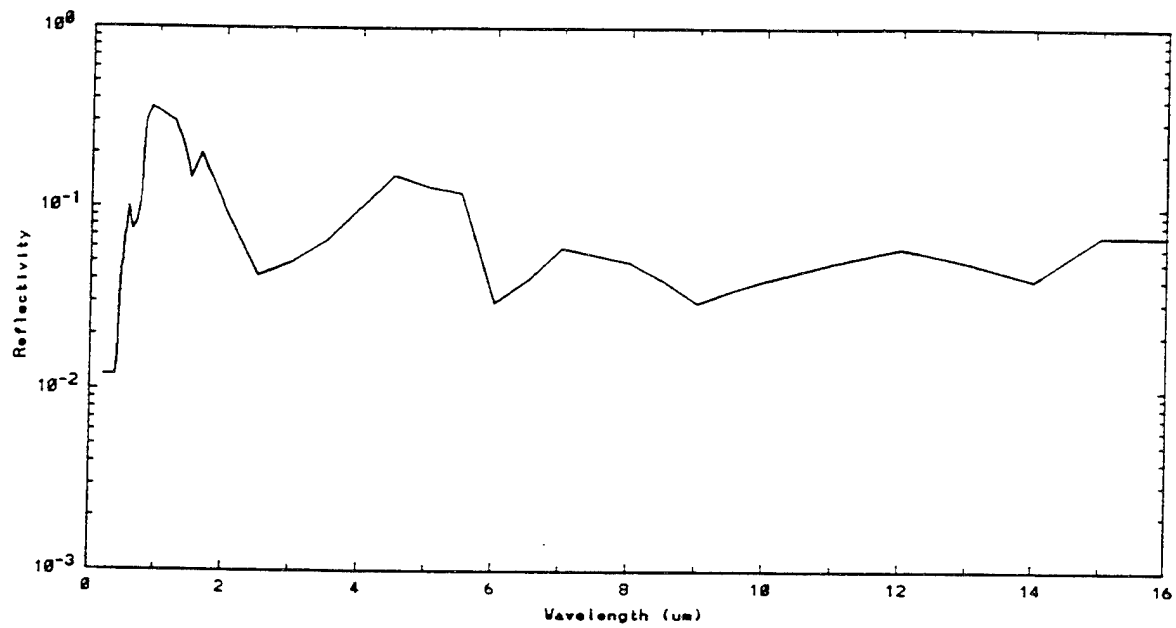
Figure 94. Spectral Reflectivity and Temporal Temperature Difference for Scrub.

84
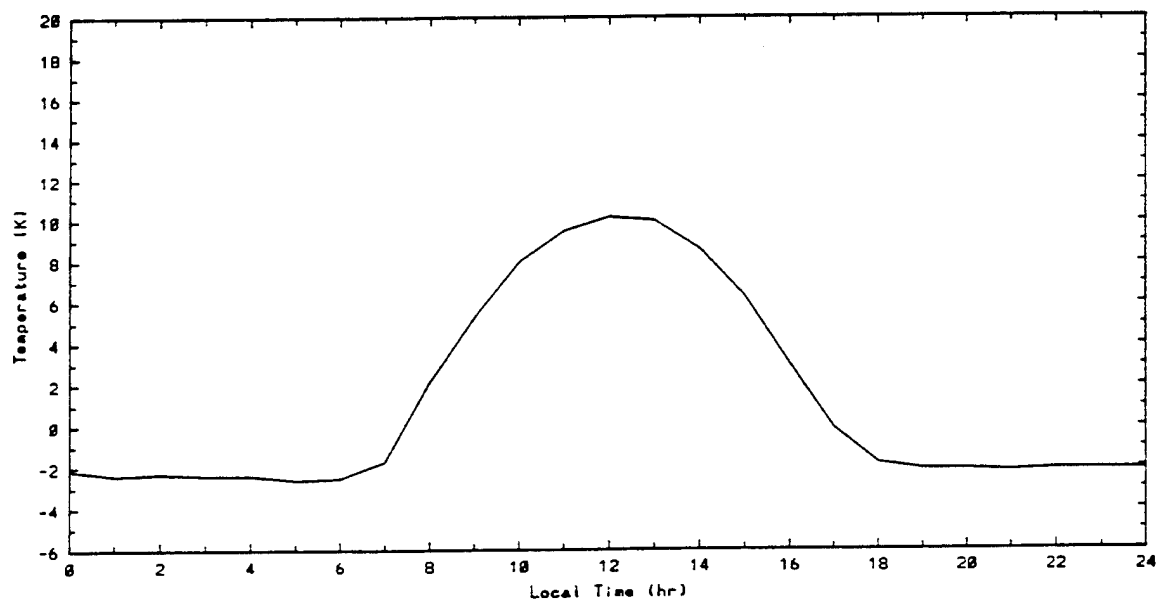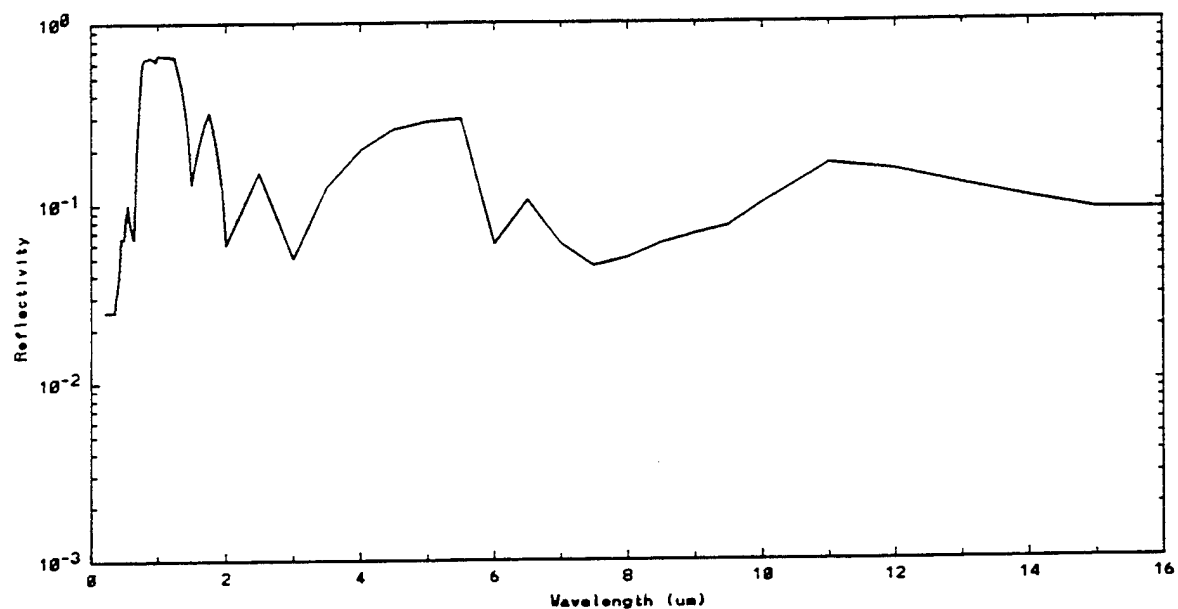
Figure 95. Spectral Reflectivity and Temporal Temperature Difference for Meadow/Grass.
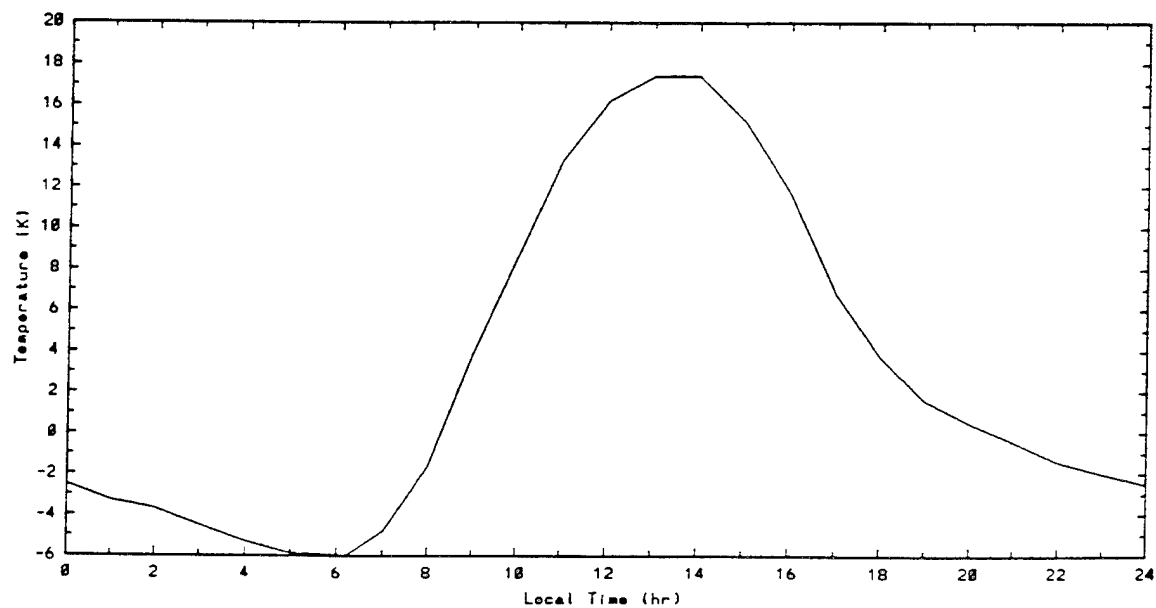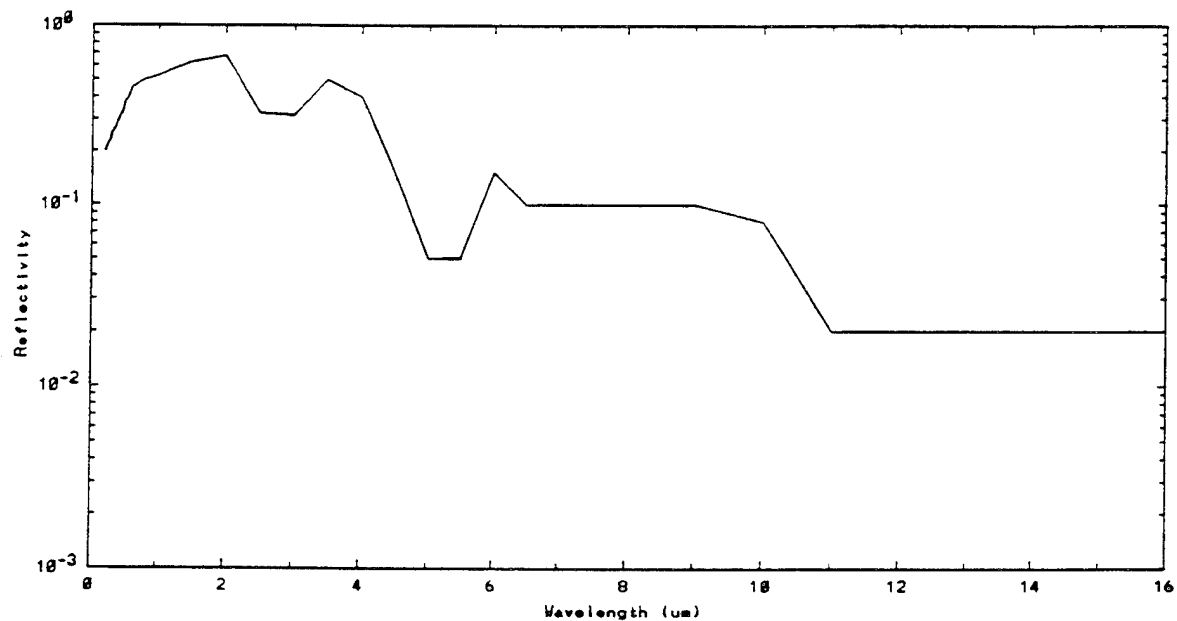
Figure 96. Spectral Reflectivity and Temporal Temperature Difference for Sand.
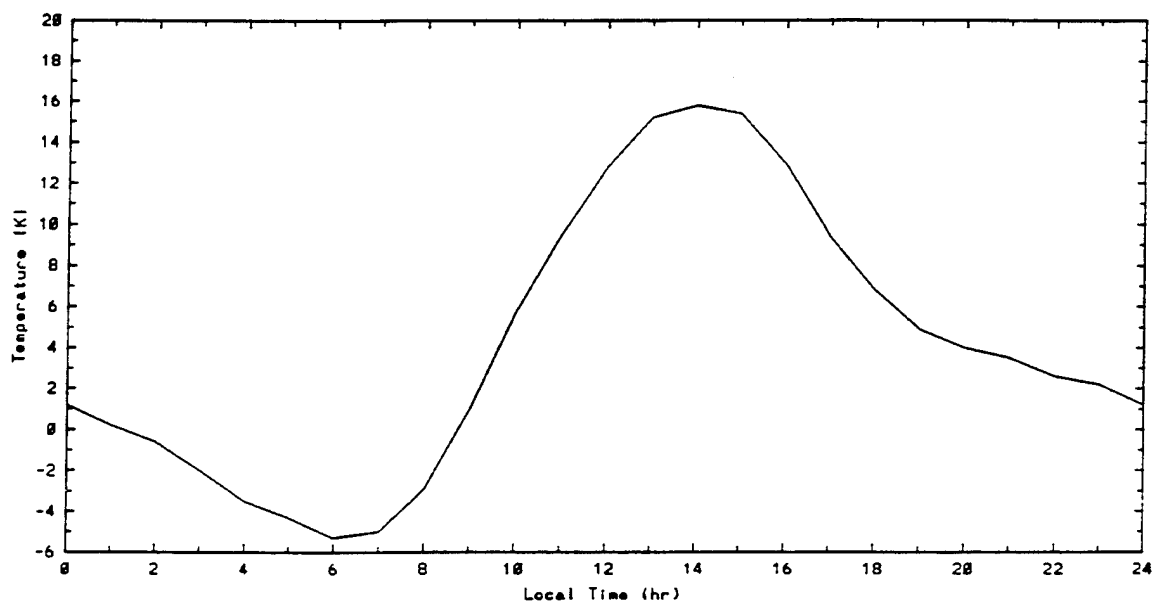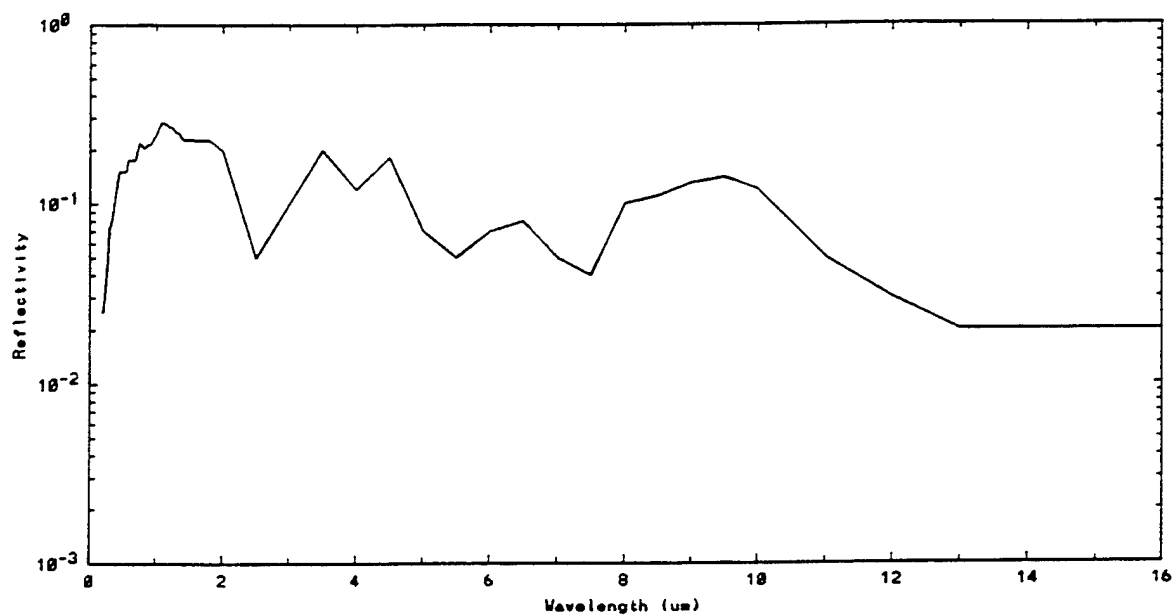
Figure 97. Spectral Reflectivity and Temporal Temperature Difference for Rock.
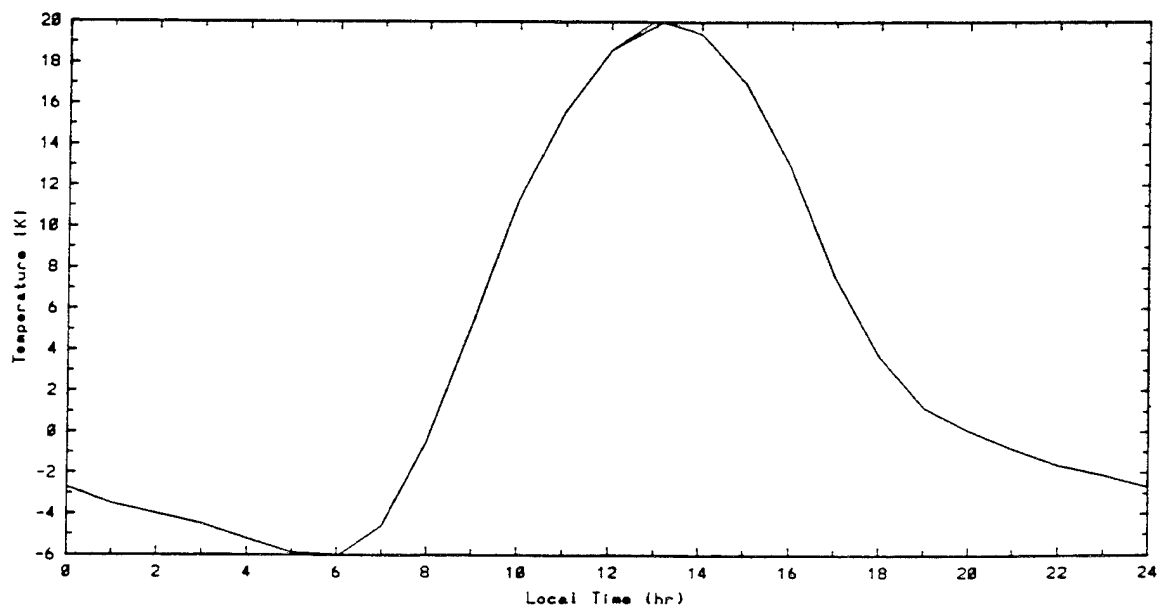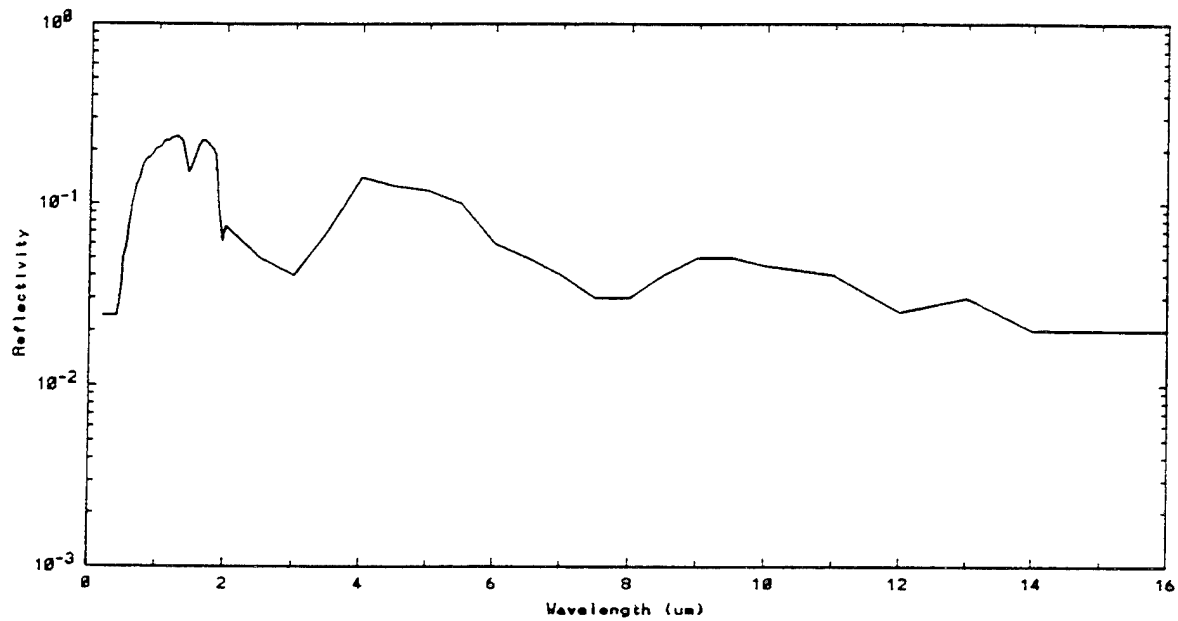
Figure 98.   Spectral Reflectivity and Temporal Temperature Difference for
Packed Dirt.
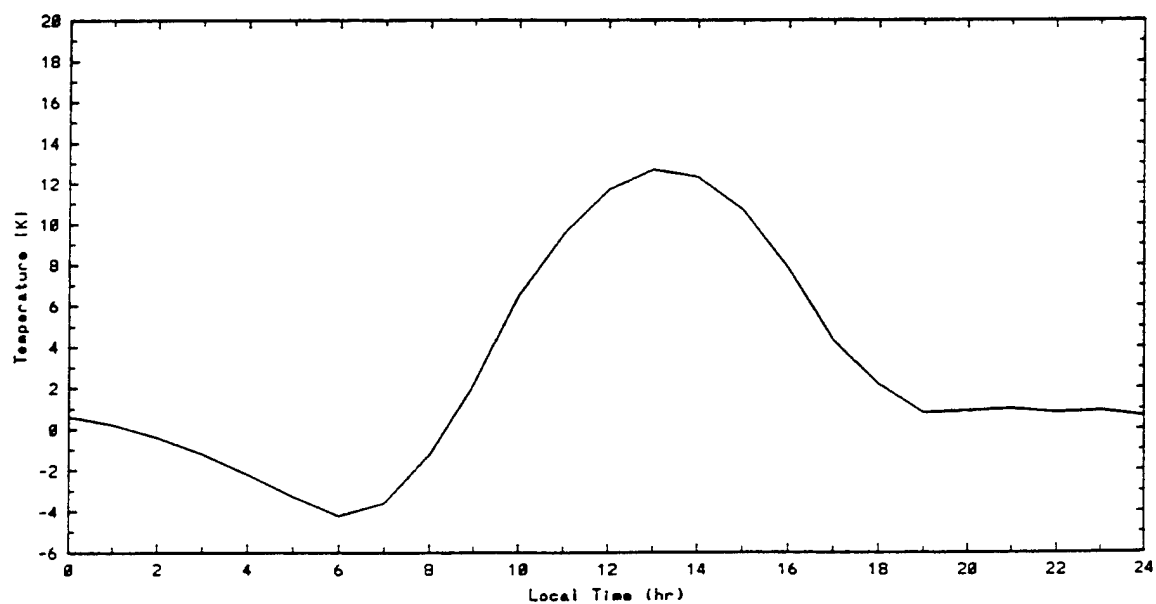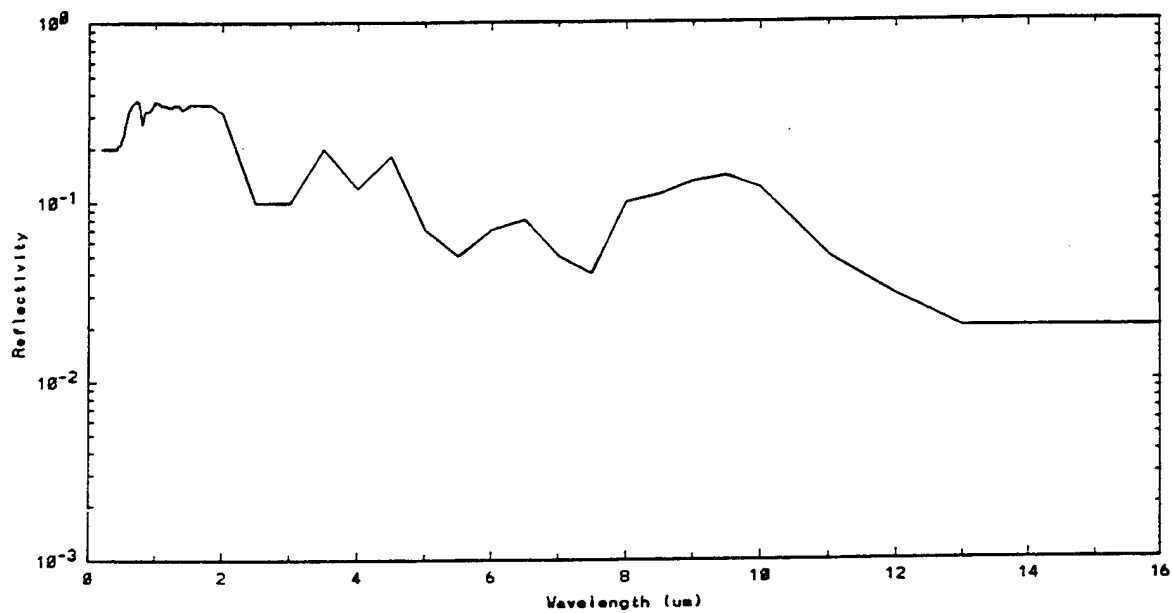
Figure 99. Spectral Reflectivity and Temporal Temperature Difference for Concrete.
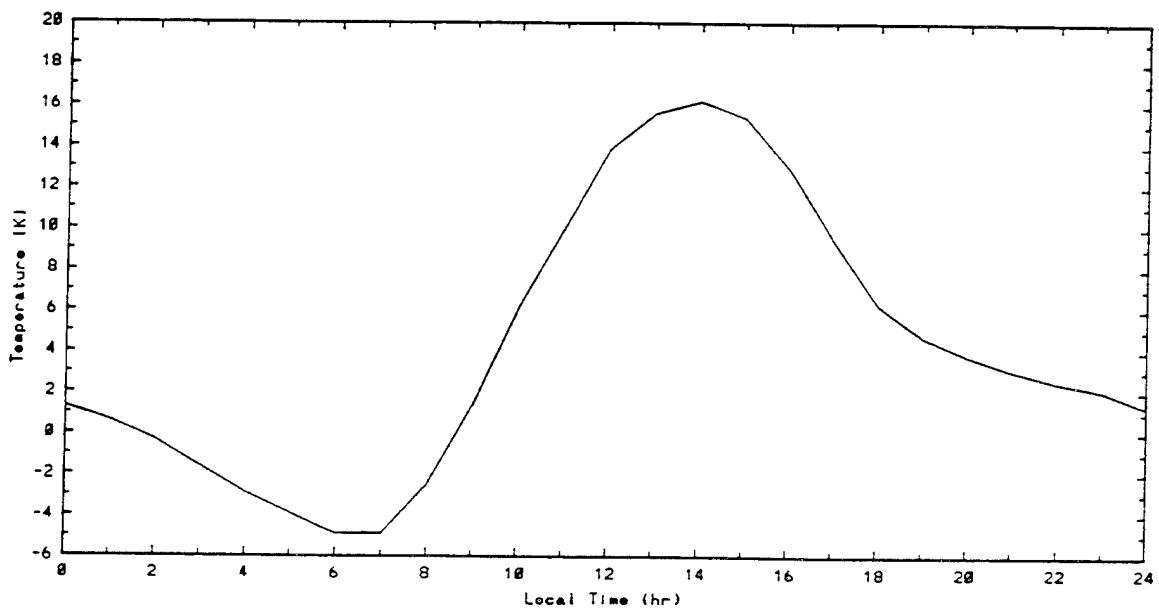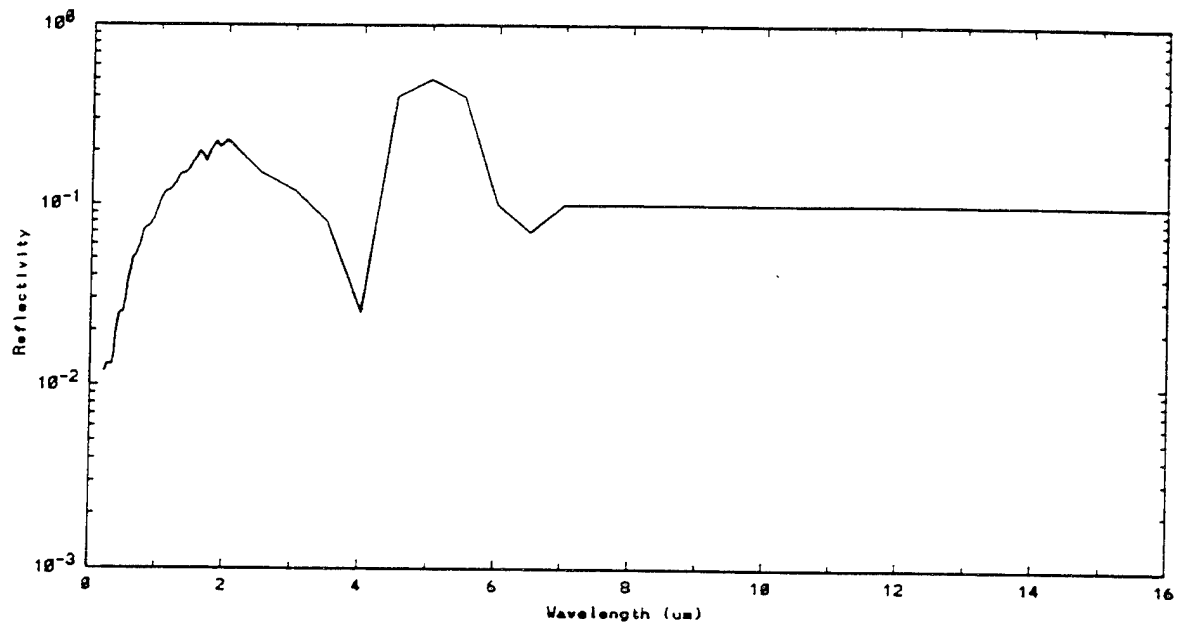
Figure 100. Spectral Reflectivity and Temporal Temperature Difference for Asphalt.
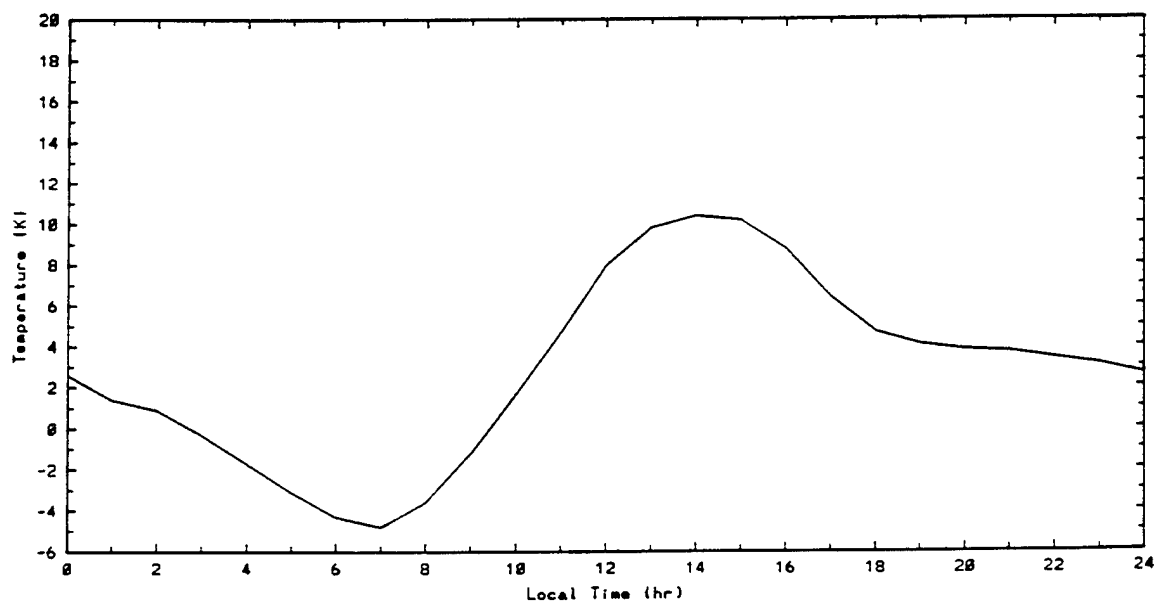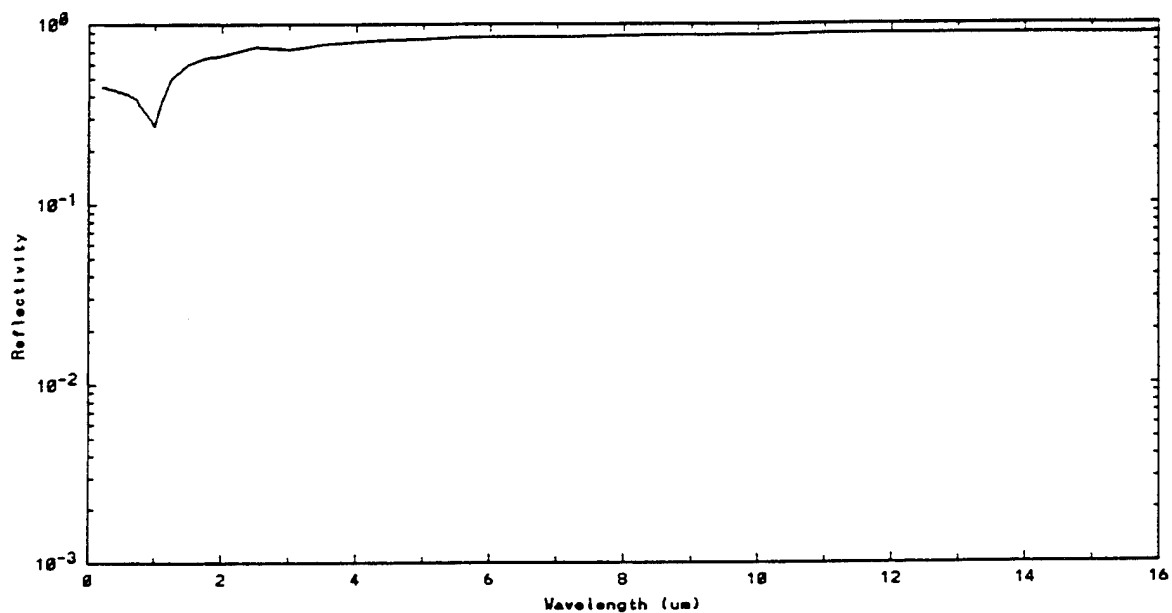
Figure 101. Spectral Reflectivity and Temporal Temperature Difference for Building Roof.

Table 11. Fresh/Sea Water.

Bidirectional reflectance (10% diffuse)
Directional Emittance
  Roughness standard deviation = 0.010
  Correlation length = 0.150
  Gaussian correlation
Fresh: Temperature calculated by heat balance; not less than 273.15 K
Sea: Temperature set by data base
Solar absorptivity = 0.977853
Thermal emissivity = 0.972462
Thermal conductivity = 0.58 W/m/K (nominal value; see THCWTR)
Specific heat = 4.91 W-sec/gm/K (nominal value; see SPHWTR)
Density = 1.00E+06 gm/m^3 (nominal value; see DENWTR)

Table 12. First Year/Multi-Year Ice.

Bidirectional reflectance (10% diffuse)
Directional Emittance
  Roughness standard deviation = 0.200
  Correlation length = 2.000
  Exponential correlation
Temperature calculated by heat balance; does not exceed 273.15 K
Solar absorptivity = 0.977577
Thermal emissivity = 0.953630
Amount of air = 0.10
Thermal conductivity = 2.24 W/m/K (nominal value; see THCICE)
Specific heat = 2.10 W-sec/gm/K (nominal value; see SPHICE)
Density = 9.17E+05 gm/m^3

Table 13. Dry/Wet Snow.

Bidirectional reflectance (10% diffuse)
Directional Emittance
Roughness standard deviation = 0.010
Correlation length = 0.050
Exponential correlation
Temperature calculated by heat balance; does not exceed 273.15 K
Solar absorptivity = 0.676897
Thermal emissivity = 0.953536
Amount of air/water = 0.30/0.00 (dry); 0.05/0.25 (wet)
Thermal conductivity = 0.08/0.16 W/m/K
Specific heat = 2.09 W-sec/gm/K
Density = 1.00E+05/2.00E+05 gm/m^3

Table 14. Broadleaf Trees (Summer/Winter).

Temperature calculated using heat balance
Diffuse reflectivity
Solar absorptivity = 0.835475/0.719875
Thermal emissivity = 0.976762/0.959826
Thermal conductivity = 0.17 W/m/K
Specific heat = 2.38 W-sec/gm/K
Density = 5.45E+05/4.15E+05 gm/m^3

Table 15. Pine Trees.

Temperature calculated using heat balance
Solar absorptivity = 0.756114
Thermal emissivity = 0.989832
Thermal conductivity = 0.12 W/m/K
Specific heat = 2.80 W/m/K
Density = 5.37E+05 gm/m^3

Table 16. Irrigated Low Vegetation.

Temperature calculated using heat balance
Directional reflectivity (90% diffuse)
Solar absorptivity = 0.830624
Thermal emissivity = 0.979109
Thermal conductivity = 0.14 W/m/K
Specific heat = 2.64 W-sec/gm/K
Density = 5.45E+05 gm/m^3

Table 17. Scrub.

Diffuse reflectivity
Temperature calculated using heat balance
Solar absorptivity = 0.861496
Thermal emissivity = 0.933998
Thermal conductivity = 0.14 W/m/K
Specific heat = 2.64 W-sec/gm/K
Density = 5.45E+05 gm/m^3

Table 18. Meadow Grass.

Directional reflectivity (90% diffuse)
Temperature calculated using heat balance
Solar absorptivity = 0.747616
Thermal emissivity = 0.905468
Thermal conductivity = 0.14 W/m/K
Specific heat = 2.64 W-sec/gm/K
Density = 5.45E+05 gm/m^3

Table 19. Packed Dirt (Compacted Soil).

```
Directional reflectivity (50% diffuse)
Temperature calculated using heat balance
Solar absorptivity = 0.883092
Thermal emissivity = 0.977359
Thermal conductivity = 0.90 W/m/K
Specific heat = 1.36 W-sec/gm/K
Density = 1.75E+06 gm/m³
```

Table 20. Sand.

```
Directional reflectivity (50% diffuse)
Temperature calculated using heat balance
Solar absorptivity = 0.598904
Thermal emissivity = 0.975139
Thermal conductivity = 0.40 W/m/K
Specific heat = 0.92 W-sec/gm/K
Density = 1.70E+06 gm/m³
```

Table 21. Rock.

```
Directional reflectivity (90% diffuse)
Temperature calculated using heat balance
Solar absorptivity = 0.841122
Thermal emissivity = 0.973385
Thermal conductivity = 2.19 W/m/K
Specific heat = 0.81 W-sec/gm/K
Density = 2.65E+06 gm/m³
```

Table 22. Asphalt.

Directional reflectivity (50% diffuse)
Temperature calculated using heat balance
Solar absorptivity = 0.857932
Thermal emissivity = 0.899323
Thermal conductivity = 0.43 W/m/K
Specific heat = 1.67 W-sec/gm/K
Density = 1.10E+06 gm/m^3

Table 23. Concrete.

Directional reflectivity (80% diffuse)
Temperature calculated using heat balance
Solar absorptivity = 0.776133
Thermal emissivity = 0.973385
Thermal conductivity = 1.73 W/m/K
Specific heat = 0.88 W-sec/gm/K
Density = 2.40E+06 gm/m^3

Table 24. Metal Building Roof (Galvanized Iron).

Directional reflectivity (50% diffuse)
Temperature calculated using heat balance
Solar absorptivity = 0.360901
Thermal emissivity = 0.120954
Thermal conductivity = 65.00 W/m/K
Specific heat = 0.46 W-sec/gm/K
Density = 7.86E+06 gm/m^3

Table 25. Blackbody.

Diffuse reflectivity
Temperature set to air temperature
Solar absorptivity = 1.000000
Thermal emissivity = 1.000000

Table 26. Whitebody.

Diffuse reflectivity Temperature set to air temperature Solar absorptivity = 0.000000 Thermal emissivity = 0.000000

2.4.2 Scenes

The DARPA Standard Reference Scenes (Acquista and Anding, 1986; Reeves, et al., 1988) are represented in MOSART in a statistical manner. The MOSART representations are composed of percentages of the materials used in the corresponding reference scene. Also, other scenes have been constructed to provide a global coverage of representative scenes. These scenes are listed in Table 27, and the composition of each scene is presented in Tables 28 through 59. In addition to these scenes, a scene can be composed of a single material.

2.5 Space Backgrounds

If a ray terminates in space, as opposed to a terrain background altitude, an emitted component, consisting of:

- Mean stellar radiance

- Zodiacal radiance

- Galactic radiance

- Extra-galactic radiance

is added to the terminator radiance, and the reflected component is assumed to be identically zero. This model provides a simplified representation of the space background. If this background radiance is significant to the user's calculation, Celestial Background Scene Descriptor should be considered (Price and Kennealy, 1989). Each of these components is discussed below.

2.5.1 Mean Stellar Radiance

The mean stellar radiance is the galactic infrared emission due to infrared stars. The model used in MOSART for the mean stellar radiance was developed by C.B. Ludwig (1985), which uses an 800 K blackbody to match the spectral characteristics, and an exponential function of galactic azimuth and elevation to match the spectral characteristics, as defined in the Infrared Handbook (Wolf and Zissis, 1978).

Table 27. Background Scenes.

Scene	Description	Location
City/Harbor	City and Harbor	San Diego, CA
Arctic Tundra	Arctic Tundra/Land-Sea Interface with Melt Lakes	Pt. Barrow, AK
Forest/Lake	Forested Low Relief Terrain with Lakes and Rivers	Wa Wa, Ontario, Canada
Subarctic	Subarctic Rocky Land-Sea Interface	Trondheim, Norway
Forest/Agriculture	Forested Low Relief Terrain with Agricultural Farms	Fulda, Germany
Agriculture	Flat Agricultural Terrain	Alberta Farms, Alberta, Canada
Desert/Dunes	Desert Pavement with Dunes	Imperial Valley, CA
Desert/Water	Desert/Land-Sea Interface	Salton Sea, CA
Forest/Mountains	Low Relief Forested Mountains with Cultural Features	Santa Cruz, CA
Sea Ice	Multi-Year Sea Ice with Cracks	Beaufort Sea
Mountains/Scrub	Arctic Mountains with Scrub Cover	Brooks Range, AK
Arctic Tundra with Melt Lakes	Unvegetated Arctic Tundra with Patterned Summer Melt Lakes	--
Open Ocean/Lake	Open Ocean	--
Mixed Farmland/Orchards	Mixture of Farmland, Orchards, Low Mountains, and Cultural Features (30 m Resolution)	Camarillo, California

Table 27. Background Scenes (continued).

Scene	Description	Location
Southern California	Land-Sea Interface with Cultural Features, Desert and Mountains (400 m Resolution)	Southern California
Tundra (Type No. 1)	--	--
Pine Forest	--	--
Mixed Forest/Farmland	--	--
Grassland/Savannah	--	--
Scrub/Chaparral	--	--
Scrub Desert	--	--
Urban	--	--
Rural Land/Sea Interface	--	--
Tropical Forest	--	--
Tropical Savannah	--	--
Tropical Desert	--	--
Tropical Land/Sea Interface	--	--
Continental Ice	Glaciers	Greenland Antarctica
Urban/Commercial	City Environment	--
Urban/Residential	Suburban Environment	--
Tilled Soil/Farmland	--	--
Tundra (Type No. 2)	--	--

Table 28. City/Harbor Land/Sea Interface.

```
   City and Harbor (San Diego, California)
      In winter, 0.90 of dirt and irrigated vegetation, 0.85 of
      urban commercial, 0.75 of scrub, and 0.70 of broadleaf
      trees converted to snow.  The correlation length and
      other parameters is estimated.
      Latitude:  32 deg 40 min N
      Longitude: 117 deg 12 min W
      Altitude (mean):      0.0645 km
               (std. dev):  0.0665 km
               (minimum):   0.000 km
               (maximum):   0.461 km
```

	Roughness		
	Cor.Len. (m)	St.Dev. (m)	Power Law
City/Harbor Land/Sea Interface (San Diego, CA)	1000.	4000.	2.4

	Composition		Cor.Len.	PSD Slope	Std. Dev.
	Summer	Winter			
Sea Water	0.2666	0.2666	4000.0	1.65	-2.80
Irrigated Vegetation	0.0968	0.0118	110.0	1.20	-1.60
Scrub	0.1451	0.0363	90.0	1.20	-1.40
Broadleaf Trees (Summer)	0.0598	0.0000	110.0	1.20	-1.60
Packed Soil	0.0948	0.0116	120.0	1.20	-1.60
Sand	0.0056	0.0056	80.0	1.20	-2.00
Asphalt	0.2868	0.0429	470.0	1.20	-1.80
Concrete	0.0441	0.0094	80.0	1.20	-1.60
Building Roof (Galvanized Iron)	0.0004	0.0004	100.0	1.20	-3.50

Table 29. Arctic Tundra Land/Sea Interface.

```
Arctic Tundra/Land-Sea Interface with Melt Lakes
   (Pt. Barrow, Alaska)
   In winter, the water is converted to ice and 0.90 of the
   tundra is converted to snow. The correlation length and other
   parameters are assumed to be the same as the tundra.
   Latitude:   71 deg 12 min N
   Longitude: 156 deg 30 min W
   Altitude (mean):        0.0046 km
            (std. dev.):   0.0046 km
            (minimum):     0.0000 km
            (maximum):     0.020 km
```

	Roughness Cor.Len. (m)	St.Dev. (m)	Power Law
Arctic Tundra Land/Sea Interface (Pt. Barrow, AK)	2500.	22500.	2.8

	Composition Summer	Winter	Cor.Len.	PSD Slope	Std. Dev.
Fresh Water	0.2925	0.0000	5000.0	1.80	-3.30
Sea Water	0.0256	0.0256	5000.0	1.80	-3.30
First Year Ice	0.3122	0.3122	720.0	1.80	-0.70
Grass/Meadow	0.1139	0.0259	720.0	1.80	-0.70
Scrub	0.0284	0.0065	720.0	1.80	-0.70
Pine Trees	0.0284	0.0065	450.0	1.80	-1.60
Packed Soil	0.0853	0.0195	720.0	1.80	-0.70
Rock	0.1137	0.0259	5000.0	1.80	-1.40

Table 30. Forested Low Relief Terrain.

```
    Forested Low Relief Terrain with Lakes and Rivers
       (Wa Wa, Ontario, Canada)
       (Broadleaf Forest)
    In winter, 0.90 of soil and irrigated vegetation and 0.70 of
    broadleaf trees is converted to snow.  The correlation length
    and other parameters for the scrub and sand are estimated.
    Latitude:    47 deg 48 min N
    Longitude:   84 deg 30 min W
    Altitude (mean):        0.392 km
             (std. dev.):   0.0547 km
             (minimum):     0.211 km
             (maximum):     0.548 km
```

	Roughness Cor.Len. (m)	St.Dev. (m)	Power Law
Forested Low Relief Terrain (Wa Wa, Ontario, Canada)	1600.	3000.	2.6

	Composition Summer	Winter	Cor.Len.	PSD Slope	Std. Dev.
Fresh Water	0.0710	0.0711	400.0	1.80	-2.40
Irrigated Vegetation	0.2866	0.0287	250.0	1.80	-1.60
Scrub	0.1847	0.0000	250.0	1.80	-1.40
Broadleaf Trees (Summer)	0.4310	0.0000	220.0	1.80	-1.75
Packed Soil	0.0265	0.0027	220.0	1.80	-1.40
Sand	0.0002	0.0000	250.0	1.80	-1.40

Table 31. Subarctic Rocky Land/Sea Interface.

```
Subarctic Rocky Land-Sea Interface (Trondheim, Norway)
   In winter, 0.90 of tilled soil and rock and 0.75 of pine trees
   converted to snow.  The correlation length and other parameters
   for the broadleaf trees, scrub, soil, grass, and snow are
   estimated.
   Latitude:    63 deg 35 min N
   Longitude:   10 deg 36 min E
   Altitude (mean):        0.152 km
            (std. dev.):   0.155 km
            (minimum):     0.0000 km
            (maximum):     0.600 km
```

	Roughness		
	Cor.Len. (m)	St.Dev. (m)	Power Law
Subarctic Rocky Land/Sea Interface (Trondheim, Norway)	2000.	150.	2.8

	Composition			PSD	Std.
	Summer	Winter	Cor.Len.	Slope	Dev.
Sea Water	0.5467	0.5467	5000.0	1.80	-3.30
Grass/Meadow	0.0420	0.0042	250.0	1.80	-1.40
Irrigated Vegetation	0.0497	0.0050	140.0	1.80	-1.40
Scrub	0.0387	0.0039	250.0	1.80	-1.40
Pine Trees	0.0105	0.0230	450.0	1.80	-1.60
Broadleaf Trees (Summer)	0.0659	0.0000	250.0	1.80	-1.40
Packed Soil	0.0645	0.0064	250.0	1.80	-1.40
Rock	0.1820	0.0182	5000.0	1.80	-1.40

Table 32. Forested Terrain/Agricultural Terrain.

```
Forested Low Relief Terrain with Agricultural Farms
   (Fulda, Germany)
   In winter, the water is converted to ice, 0.90 of dirt
   and irrigated vegetation and 0.80 of broadleaf trees
   converted to snow.  The correlation length and other parameters
   for snow are estimated.
   Latitude:   50 deg 15 min N
   Longitude:  10 deg 30 min E
   Altitude (mean):        0.335 km
            (std. dev.):   0.040 km
            (minimum):     0.249 km
            (maximum):     0.499 km
```

	Roughness Cor.Len. (m)	St.Dev. (m)	Power Law
Forested Terrain/Agricultural Terrain (Fulda, Germany)	2000.	40.	2.8

	Composition Summer	Winter	Cor.Len.	PSD Slope	Std. Dev.
Fresh Water	0.0008	0.0000	160.0	1.65	-1.80
Irrigated Vegetation	0.0159	0.0016	90.0	1.65	-1.70
Broadleaf Trees (Summer)	0.2929	0.0000	830.0	1.65	-1.90
Packed Soil	0.6867	0.0687	830.0	1.65	-1.80
Sand	0.0037	0.0037	90.0	1.65	-1.70

Table 33. Flat Agricultural Terrain.

```
Flat Agricultural Terrain (Alberta Farms, Alberta, Canada)
   (farmland)
   In winter, water is converted to ice and 0.85 of soil, tilled
   soil, and irrigated vegetation converted to snow.
   Latitude:   54 deg  9 min N
   Longitude: 113 deg 45 min W
   Altitude (mean):        0.600 km
            (std. dev.):   0.0000 km
            (minimum):     0.600 km
            (maximum):     0.600 km
```

	Roughness Cor.Len. (m)	St.Dev. (m)	Power Law
Flat Agricultural Terrain (Alberta, Canada)	1000.	0.	2.5

	Composition Summer	Winter	Cor.Len.	PSD Slope	Std. Dev.
Fresh Water	0.0162	0.0000	500.0	1.30	-3.40
Irrigated Vegetation	0.3950	0.0578	280.0	1.50	-3.30
Packed Soil	0.5888	0.0892	220.0	1.50	-3.50

Table 34. Desert Pavement with Dunes Terrain.

```
Desert Pavement with Dunes (Imperial Valley, California)
   (Barren Desert)
   Winter same as summer.
   Latitude:   32 deg 54 min N
   Longitude: 115 deg  6 min W
   Altitude (mean):        0.052 km
            (std. dev.):   0.035 km
            (minimum):     0.005 km
            (maximum):     0.162 km
```

	Roughness		
	Cor.Len. (m)	St.Dev. (m)	Power Law
Desert Pavement with Dunes Terrain (Imperial Valley, CA)	500.	1200.	2.7

	Composition		Cor.Len.	PSD Slope	Std. Dev.
	Summer	Winter			
Packed Soil	0.1184	0.1184	1000.0	1.20	-2.50
Sand	0.4468	0.4468	4000.0	1.80	-2.50
Rock	0.4348	0.4348	2000.0	1.20	-2.50

Table 35. Desert Land/Sea Interface.

```
Desert Land-Sea Interface (Salton Sea, California)
   Winter is same as summer.
   Latitude:   33 deg 12 min N
   Longitude: 115 deg 54 min W
   Altitude (mean):        0.0054 km
            (std. dev.):   0.0097 km
            (minimum):     0.001 km
            (maximum):     0.097 km
```

	Roughness		
	Cor.Len. (m)	St.Dev. (m)	Power Law
Desert Land/Sea Interface (Salton Sea, CA)	2400.	100.	2.6

	Composition		Cor.Len.	PSD Slope	Std. Dev.
	Summer	Winter			
Sea Water	0.5167	0.5167	10000.0	1.80	-3.50
Irrigated Vegetation	0.0346	0.0346	1700.0	1.80	-3.10
Packed Soil	0.1631	0.1631	10000.0	1.80	-2.70
Sand	0.2519	0.2519	10000.0	1.80	-2.70
Rock	0.0337	0.0337	300.0	1.80	-2.70

Table 36. Forested Mountains/Cultural Terrain.

```
Low Relief Forested Mountains with Cultural Features
   (Santa Cruz, California)
   In winter 0.90 of irrigated vegetation and grass, 0.80 of
   urban commercial, and 0.70 of broadleaf trees converted to
   snow.  The correlation length and other parameters for scrub
   and snow are estimated.
   Latitude:   37 deg 15 min N
   Longitude: 122 deg 15 min W
   Altitude (mean):       0.315 km
            (std. dev.):  0.200 km
            (minimum):    0.0000 km
            (maximum):    0.976 km
```

	Roughness Cor.Len. (m)	St.Dev. (m)	Power Law
Forested Mountains/Cultural Terrain (Santa Cruz, CA)	2100.	200.	2.5

	Composition Summer	Winter	Cor.Len.	PSD Slope	Std. Dev.
Sea Water	0.0671	0.0671	5000.0	1.80	-2.70
Grass/Meadow	0.0856	0.0086	380.0	1.80	-1.40
Irrigated Vegetation	0.0305	0.0038	200.0	1.80	-1.50
Scrub	0.0002	0.0002	250.0	1.80	-1.50
Broadleaf Trees (Summer)	0.7465	0.0000	1000.0	1.80	-1.40
Packed Soil	0.0076	0.0008	380.0	1.80	-1.50
Sand	0.0014	0.0024	160.0	1.80	-1.20
Asphalt	0.0535	0.0107	380.0	1.80	-1.50
Concrete	0.0076	0.0015	380.0	1.80	-1.50

Table 37. Multi-Year Sea Ice.

```
Multi-Year Sea Ice with Cracks (Beaufort Sea)
   In winter, the amount of water is reduced, and most of ice is
   covered with snow.
   Latitude:    Unspecified
   Longitude:   Unspecified
   Altitude (mean):        Unknown
            (std. dev.):   Unknown
            (minimum):     Unknown
            (maximum):     Unknown
```

	Roughness		
	Cor.Len. (m)	St.Dev. (m)	Power Law
Multi-Year Sea Ice (Beaufort Sea)	1000.	0.	2.5

	Composition		Cor.Len.	PSD Slope	Std. Dev.
	Summer	Winter			
Sea Water	0.1500	0.0110	50.0	3.00	-2.00
First Year Ice	0.4500	0.0030	50.0	3.00	-2.00
Dry Snow	0.4000	0.9860	400.0	2.50	-1.90

Table 38. Arctic Mountains with Scrub Terrain.

```
Arctic Mountains with Scrub Cover (Brooks Range, Alaska)
   (Mountainous Terrain)
   In winter, 0.70 of rock and 0.80 of the scrub, dirt, grass, and pine
   trees (i.e., tundra) is converted to snow, and the water is converted
   to ice.  The correlation length and other parameters for scrub, dirt,
   grass, and pine trees are assumed to be the same as the tundra.  The
   correlation length and other parameters for water and snow are
   estimated.
   Latitude:    67 deg 45 min N
   Longitude: 149 deg 30 min W
   Altitude (mean):        1.022 km
            (std. dev.):   0.289 km
            (minimum):     0.365 km
            (maximum):     1.995 km
```

	Roughness		
	Cor.Len. (m)	St.Dev. (m)	Power Law
Arctic Mountains with Scrub Terrain (Brooks Range, AK)	1300.	84000.	3.0

	Composition		Cor.Len.	PSD Slope	Std. Dev.
	Summer	Winter			
Fresh Water	0.2022	0.0000	250.0	1.80	-0.70
Grass/Meadow	0.1155	0.0231	720.0	1.80	-0.70
Scrub	0.0289	0.0058	720.0	1.80	-0.70
Pine Trees	0.0289	0.0058	720.0	1.80	-0.70
Packed Soil	0.0866	0.0173	720.0	1.80	-0.70
Rock	0.5379	0.1614	720.0	1.80	-0.70

Table 39. Arctic Tundra with Melt Lakes Terrain.

```
   Unvegetated Arctic Tundra with Patterned Summer Melt Lakes
      In winter, the water is converted to ice, and 0.90 of
      other materials is converted to snow.  The correlation length
      and other parameters are estimated.
   Latitude:    Unspecified
   Longitude:   Unspecified
   Altitude (mean):       Unknown
            (std. dev.):  Unknown
            (minimum):    Unknown
            (maximum):    Unknown

                                                     Roughness
                                          Cor.Len.  St.Dev.  Power
                                            (m)       (m)     Law

Arctic Tundra with Melt Lakes Terrain     1000.      0.      2.5

                          Composition                  PSD    Std.
                       Summer    Winter   Cor.Len.    Slope   Dev.

Fresh Water            0.6425    0.0000     500.0     1.80   -0.70
Grass/Meadow           0.1100    0.0110     250.0     1.80   -0.70
Scrub                  0.0275    0.0028     250.0     1.80   -0.70
Pine Trees             0.0275    0.0028     250.0     1.80   -0.70
Packed Soil            0.0825    0.0083     250.0     1.80   -0.70
Rock                   0.1100    0.0110     250.0     1.80   -0.70
```

Table 40. Open Ocean/Lake.

```
   Open Ocean - Winter is same as summer.
      Latitude:    Unspecified
      Longitude:   Unspecified
      Altitude (mean):       0.0000 km
               (std. dev.):  0.0000 km
               (minimum):    0.0000 km
               (maximum):    0.0000 km

                                                     Roughness
                                          Cor.Len.  St.Dev.  Power
                                            (m)       (m)     Law

Open Ocean/Lake                            1000.      0.      2.5

                          Composition                  PSD    Std.
                       Summer    Winter   Cor.Len.    Slope   Dev.

Sea Water              1.0000    1.0000       1.0     2.40   -3.30
```

Table 41. Mixed Farmland/Orchards Terrain.

```
   Mixed Farmland/Orchard (Camarillo, California)
      In winter, 0.50 of the irrigated vegetation is converted to
      tilled soil.  The correlation length and other parameters are
      estimated.
      Latitude:   34 deg 12 min N
      Longitude: 119 deg  2 min W
      Altitude (mean):        0.0493 km
               (std. dev.):   0.0602 km
               (minimum):     0.001 km
               (maximum):     0.416 km
```

	Roughness		
	Cor.Len. (m)	St.Dev. (m)	Power Law
Mixed Farmland/Orchards Terrain (Camarillo, CA)	1000.	4000.	2.4

	Composition		Cor.Len.	PSD Slope	Std. Dev.
	Summer	Winter			
Fresh Water	0.0100	0.0100	100.0	1.80	-1.50
Irrigated Vegetation	0.4460	0.3820	200.0	1.80	-1.50
Scrub	0.1100	0.1100	200.0	1.80	-1.50
Broadleaf Trees (Summer)	0.1200	0.0000	200.0	1.80	-1.50
Packed Soil	0.2940	0.3580	200.0	1.80	-1.50
Asphalt	0.0100	0.0100	200.0	1.80	-1.50
Concrete	0.0100	0.0100	200.0	1.80	-1.50

Table 42. Southern California Land/Sea Interface.

```
Southern California Land/Sea Interface
  (409.6 x 409.6 km from Mexican border north and from
Santa Cruz Island east)
In winter, 0.50 of rock and 0.20 of scrub is converted to
snow.  The correlation length and other parameters are
estimated.
Latitude:   32 deg 35 min N to  36 deg 30 min N
Longitude: 115 deg         W to 121 deg         W
Altitude (mean):        0.623 km
          (std. dev.):  0.578 km
          (minimum):    0.0000 km
          (maximum):    3.048 km
```

	Roughness Cor.Len. (m)	St.Dev. (m)	Power Law
Southern California Land/Sea Interface (Southern California)	1000.	4000.	2.4

	Composition Summer	Winter	Cor.Len.	PSD Slope	Std. Dev.
Sea Water	0.1869	0.1869	1000.0	1.80	-1.50
Irrigated Vegetation	0.0676	0.0676	250.0	1.80	-1.50
Scrub	0.1647	0.1318	250.0	1.80	-1.50
Pine Trees	0.0348	0.0348	250.0	1.80	-1.50
Broadleaf Trees (Summer)	0.0348	0.0000	250.0	1.80	-1.50
Packed Soil	0.2105	0.2105	250.0	1.80	-1.50
Sand	0.0452	0.0452	250.0	1.80	-1.50
Rock	0.2448	0.1224	250.0	1.80	-1.50
Asphalt	0.0090	0.0089	250.0	1.80	-1.50
Concrete	0.0017	0.0017	250.0	1.80	-1.50

Table 43. Tundra (Type No. 1) Background.

Tundra (Type No. 1) (modified Pt. Barrow, Alaska scene, where ice is
converted half to water and half to tundra.) In winter, the
water is converted to ice and 0.90 of tundra converted to snow.

			Roughness Cor.Len. (m)	St.Dev. (m)	Power Law
Tundra (Type No. 1) Background			3000.	25.	2.1

	Composition			PSD	Std.
	Summer	Winter	Cor.Len.	Slope	Dev.
Fresh Water	0.5281	0.0000	750.0	1.80	-2.80
Grass/Meadow	0.1452	0.1305	1000.0	1.80	-2.60
Scrub	0.0363	0.0327	1000.0	1.80	-2.60
Pine Trees	0.0363	0.0326	1000.0	1.80	-2.60
Packed Soil	0.1089	0.0980	1000.0	1.80	-2.60
Rock	0.1452	0.1306	1000.0	1.80	-2.60

Table 44. Pine Forest Background.

Pine Forest (modified Santa Cruz, California scene, where
water is converted to grass and broadleaf trees converted to
to pine trees.) In winter, 0.90 of irrigated vegetation and
grass and 0.70 of pine trees and urban residential converted
to snow.

			Roughness Cor.Len. (m)	St.Dev. (m)	Power Law
Pine Forest Background			2100.	4000.	2.5

	Composition			PSD	Std.
	Summer	Winter	Cor.Len.	Slope	Dev.
Grass/Meadow	0.1130	0.0110	380.0	1.80	-1.40
Irrigated Vegetation	0.0510	0.0105	290.0	1.80	-1.50
Pine Trees	0.8060	0.2420	1000.0	1.80	-1.00
Packed Soil	0.0028	0.0009	380.0	1.80	-1.40
Sand	0.0020	0.0020	160.0	1.80	-1.20
Asphalt	0.0196	0.0060	380.0	1.80	-1.40
Concrete	0.0056	0.0016	380.0	1.80	-1.40

112

Table 45. Mixed Forest/Farmland Background.

Mixed Forest-Farmland (modified Fulda, Germany scene, where irrigated vegetation and soil swapped.) In winter, water is converted to ice, and 0.90 of soil, tilled soil, and irrigated vegetation and 0.80 of broadleaf trees converted to snow.

		Roughness		
		Cor.Len. (m)	St.Dev. (m)	Power Law
Mixed Forest/Farmland Background		2000.	1600.	2.8

	Composition			PSD	Std.
	Summer	Winter	Cor.Len.	Slope	Dev.
Fresh Water	0.0010	0.0000	160.0	1.65	-2.80
Irrigated Vegetation	0.5580	0.0558	830.0	1.65	-1.70
Broadleaf Trees (Summer)	0.2910	0.0000	830.0	1.65	-1.90
Packed Soil	0.1480	0.0152	90.0	1.65	-1.80
Sand	0.0020	0.0020	90.0	1.65	-1.70

Table 46. Grassland/Savannah Background.

Grassland-Savannah (modified Alberta Farms, Alberta, Canada scene, where 1.00 of irrigated vegetation, 0.85 of tilled soil, and 0.50 of soil converted to grass.) In winter, the water is converted to ice, 0.90 of grass and 0.70 of soil and tilled soil converted to snow. The correlation length and other parameters for soil are estimated from the Alberta Farms parameters.

		Roughness		
		Cor.Len. (m)	St.Dev. (m)	Power Law
Grassland/Savannah Background		1000.	0.	2.5

	Composition			PSD	Std.
	Summer	Winter	Cor.Len.	Slope	Dev.
Fresh Water	0.0160	0.0000	520.0	1.30	-3.40
Grass/Meadow	0.7030	0.0700	400.0	1.50	-3.30
Irrigated Vegetation	0.0288	0.0084	42.0	1.50	-3.50
Packed Soil	0.2522	0.0756	110.0	1.50	-3.50

Table 47. Scrub/Chaparral Background.

```
 Scrub-Chaparral (modified Santa Cruz, California scene, where
   scrub and broadleaf trees swapped and water fraction added
   to broadleaf trees.)  Winter same as summer.

                                            Roughness
                                    Cor.Len.  St.Dev.  Power
                                      (m)       (m)     Law

Scrub/Chaparral Background            2100.    4000.    2.5

                          Composition             PSD   Std.
                       Summer    Winter   Cor.Len.  Slope  Dev.

Grass/Meadow           0.0740    0.0740      380.0  1.80  -1.40
Irrigated Vegetation   0.0510    0.0510      290.0  1.80  -1.50
Scrub                  0.8060    0.8060     1000.0  1.80  -1.40
Broadleaf Trees (Summer) 0.0390  0.0390      100.0  1.80  -1.40
Packed Soil            0.0028    0.0028      380.0  1.80  -1.50
Sand                   0.0020    0.0020      360.0  1.80  -1.20
Asphalt                0.0196    0.0196      380.0  1.80  -1.50
Concrete               0.0056    0.0056      380.0  1.80  -1.50
```

Table 48. Scrub Desert Background.

```
 Scrub Desert (modified Wa Wa, Ontario, Canada scene, where
   water converted to sand, irrigated vegetation converted to
   soil, and broadleaf trees converted to scrub.)  In winter,
   0.90 of soil and sand, and 0.70 of scrub converted to
   snow.

                                            Roughness
                                    Cor.Len.  St.Dev.  Power
                                      (m)       (m)     Law

Scrub Desert Background               1600.    3000.    2.6

                          Composition             PSD   Std.
                       Summer    Winter   Cor.Len.  Slope  Dev.

Scrub                  0.6160    0.1850      220.0  1.80  -1.75
Packed Soil            0.3140    0.0310      250.0  1.80  -1.60
Sand                   0.0700    0.0070      400.0  1.80  -2.40
```

Table 49. Urban Background.

Urban (modified San Diego, California scene, where water is
   reduced to 0.048, and other materials are renormalized.)
   In winter, 0.90 of soil and irrigated vegetation, 0.85 of
   urban commercial, 0.75 of scrub, and 0.70 of broadleaf
   trees converted to snow.

| | | | Roughness | | |
			Cor.Len. (m)	St.Dev. (m)	Power Law
Urban Background			1000.	4000.	2.4

| | Composition | | | PSD | Std. |
	Summer	Winter	Cor.Len.	Slope	Dev.
Fresh Water	0.0480	0.0480	4000.0	1.65	-2.80
Irrigated Vegetation	0.3420	0.0150	470.0	1.20	-1.60
Scrub	0.1530	0.0380	90.0	1.20	-1.40
Broadleaf Trees (Summer)	0.1080	0.0000	110.0	1.20	-1.60
Packed Soil	0.0958	0.0150	300.0	1.20	-1.60
Sand	0.0080	0.0080	80.0	1.20	-2.00
Asphalt	0.1876	0.0560	470.0	1.20	-1.80
Concrete	0.0576	0.0120	470.0	1.20	-1.60

Table 50. Rural Land/Sea Interface Background.

Rural Land-Sea Interface (modified Santa Cruz, California
   scene, where water fraction is set to 0.125 and other
   materials are renormalized.) In winter, 0.90 of
   irrigated vegetation and grass, 0.80 of urban residential,
   and 0.70 of broadleaf trees is converted to snow.

| | | | Roughness | | |
			Cor.Len. (m)	St.Dev. (m)	Power Law
Rural Land/Sea Interface Background			2100.	4000.	2.5

| | Composition | | | PSD | Std. |
	Summer	Winter	Cor.Len.	Slope	Dev.
Sea Water	0.1250	0.1250	5000.0	1.80	-2.70
Grass/Meadow	0.0670	0.0070	380.0	1.80	-1.40
Irrigated Vegetation	0.0465	0.0070	290.0	1.80	-1.50
Broadleaf Trees (Summer)	0.7340	0.0000	1000.0	1.80	-1.40
Packed Soil	0.0026	0.0005	380.0	1.80	-1.50
Sand	0.0020	0.0020	160.0	1.80	-1.20
Asphalt	0.0179	0.0035	380.0	1.80	-1.50
Concrete	0.0050	0.0010	380.0	1.80	-1.50

Table 51. Tropical Forest Background.

```
     Tropical Forest - The summer scene is identical to Wa Wa,
        Ontario, Canada.  The winter scene is identical to the summer.
        The correlation length and other parameters for scrub and sand
        are estimated from the Wa Wa scene.

                                              Roughness
                                         Cor.Len. St.Dev. Power
                                            (m)      (m)   Law

     Tropical Forest Background              1600.    3000.   2.6

                              Composition              PSD   Std.
                           Summer    Winter   Cor.Len. Slope  Dev.

     Fresh Water           0.0710    0.0710     400.0  1.80  -2.40
     Irrigated Vegetation  0.2866    0.2866     250.0  1.80  -1.60
     Scrub                 0.1847    0.1847     250.0  1.80  -1.40
     Broadleaf Trees (Summer) 0.4310 0.4310     220.0  1.80  -1.75
     Packed Soil           0.0265    0.0265    1000.0  1.20  -2.50
     Sand                  0.0002    0.0002     250.0  1.80  -1.40
```

Table 52. Tropical Savannah Background.

```
     Tropical Savannah - modified Grassland-Savannah.  The winter
        scene is the same as the summer scene.

                                              Roughness
                                         Cor.Len. St.Dev. Power
                                            (m)      (m)   Law

     Tropical Savannah Background            1000.      0.    2.5

                              Composition              PSD   Std.
                           Summer    Winter   Cor.Len. Slope  Dev.

     Fresh Water           0.0160    0.0160     520.0  1.30  -3.40
     Grass/Meadow          0.7030    0.7030     400.0  1.50  -3.30
     Irrigated Vegetation  0.0288    0.0288      42.0  1.50  -3.50
     Packed Soil           0.2522    0.2522     110.0  1.50  -3.50
```

Table 53. Tropical Desert Background.

Tropical Desert - modified Scrub Desert. The winter
scene is the same as the summer scene.

			Roughness		
			Cor.Len. (m)	St.Dev. (m)	Power Law
Tropical Desert Background			1600.	3000.	2.6

	Composition			PSD	Std.
	Summer	Winter	Cor.Len.	Slope	Dev.
Scrub	0.6160	0.6160	220.0	1.80	-1.75
Packed Soil	0.3140	0.3140	250.0	1.80	-1.60
Sand	0.0700	0.0700	400.0	1.80	-2.40

Table 54. Tropical Land/Sea Interface Background.

Tropical Land-Sea Interface - modified Rural Land-Sea
Interface. The winter scene is the same as the summer
scene.

			Roughness		
			Cor.Len. (m)	St.Dev. (m)	Power Law
Tropical Land/Sea Interface Background			2100.	4000.	2.5

	Composition			PSD	Std.
	Summer	Winter	Cor.Len.	Slope	Dev.
Sea Water	0.1250	0.1250	5000.0	1.80	-2.70
Grass/Meadow	0.0670	0.0670	380.0	1.80	-1.40
Irrigated Vegetation	0.0465	0.0465	290.0	1.80	-1.50
Broadleaf Trees (Summer)	0.7340	0.7340	1000.0	1.80	-1.40
Packed Soil	0.0026	0.0026	380.0	1.80	-1.50
Sand	0.0020	0.0020	160.0	1.80	-1.20
Asphalt	0.0179	0.0179	380.0	1.80	-1.50
Concrete	0.0050	0.0050	380.0	1.80	-1.50

117

Table 55. Continental Ice Background.

```
    Continental Ice (Antarctica and Greenland, primarily)
       Same as the sea ice scene, but with no water.
       Latitude:    Unspecified
       Longitude:   Unspecified
       Altitude (mean):       Unknown
                (std. dev.):  Unknown
                (minimum):    Unknown
                (maximum):    Unknown
```

	Roughness Cor.Len. (m)	St.Dev. (m)	Power Law
Continental Ice Background	1000.	0.	2.5

	Composition Summer	Winter	Cor.Len.	PSD Slope	Std. Dev.
First Year Ice	0.5000	0.0140	50.0	3.00	-2.00
Dry Snow	0.5000	0.9860	400.0	2.50	-1.90

Table 56. Urban/Commercial Background.

```
    Urban/Commercial
       Originally, a GENESSIS background material, but it was constructed as
       a composite, so it is included here
       Latitude:    Unspecified
       Longitude:   Unspecified
       Altitude (mean):       Unknown
                (std. dev.):  Unknown
                (minimum):    Unknown
                (maximum):    Unknown
```

	Roughness Cor.Len. (m)	St.Dev. (m)	Power Law
Urban/Commercial	1000.	0.	2.5

	Composition Summer	Winter	Cor.Len.	PSD Slope	Std. Dev.
Irrigated Vegetation	0.1000	0.1000	470.0	1.20	-1.80
Broadleaf Trees (Winter)	0.7000	0.7000	470.0	1.20	-1.80
Packed Soil	0.1000	0.1000	470.0	1.20	-1.80
Concrete	0.1000	0.1000	470.0	1.20	-1.80

Table 57. Urban/Residential Background.

```
    Urban/Residential
      Originally, a GENESSIS background material, but it was constructed as
      a composite, so it is included here
      Latitude:    Unspecified
      Longitude:   Unspecified
      Altitude (mean):       Unknown
               (std. dev.):  Unknown
               (minimum):    Unknown
               (maximum):    Unknown

                                                  Roughness
                                         Cor.Len.  St.Dev.  Power
                                           (m)       (m)     Law

Urban/Residential                        1000.       0.      2.5

                             Composition                PSD     Std.
                          Summer    Winter   Cor.Len.  Slope    Dev.

Irrigated Vegetation      0.5000    0.5000     380.0    1.80   -1.50
Broadleaf Trees (Winter)  0.3500    0.3500     380.0    1.80   -1.50
Packed Soil               0.0500    0.0500     380.0    1.80   -1.50
Concrete                  0.1000    0.1000     380.0    1.80   -1.50
```

Table 58. Tilled Soil/Farmland Background.

```
    Tilled Soil/Farmland
      Originally, a GENESSIS background material, but it was constructed as
      a composite, so it is included here
      Latitude:    Unspecified
      Longitude:   Unspecified
      Altitude (mean):       Unknown
               (std. dev.):  Unknown
               (minimum):    Unknown
               (maximum):    Unknown

                                                  Roughness
                                         Cor.Len.  St.Dev.  Power
                                           (m)       (m)     Law

Tilled Soil/Farmland                     1000.       0.      2.5

                             Composition                PSD     Std.
                          Summer    Winter   Cor.Len.  Slope    Dev.

Irrigated Vegetation      0.6000    0.6000     280.0    1.65   -2.40
Packed Soil               0.4000    0.4000     280.0    1.65   -2.40
```

119

Table 59. Tundra (Type No. 2) Background.

```
Tundra (Type No. 2)
    Originally, a GENESSIS background material, but it was constructed as
    a composite, so it is included here
    Latitude:    Unspecified
    Longitude:   Unspecified
    Altitude (mean):        Unknown
             (std. dev.):   Unknown
             (minimum):     Unknown
             (maximum):     Unknown

                                                  Roughness
                                         Cor.Len.  St.Dev.  Power
                                           (m)       (m)     Law

Tundra (Type No. 2) Background           1000.      0.      2.5

                             Composition                  PSD    Std.
                         Summer    Winter   Cor.Len.   Slope   Dev.

Fresh Water              0.3500    0.0000    1000.0     1.80   -2.60
Grass/Meadow             0.2000    0.1000    1000.0     1.80   -2.60
Scrub                    0.0500    0.0250    1000.0     1.80   -2.60
Pine Trees               0.0500    0.0250    1000.0     1.80   -2.60
Packed Soil              0.1500    0.0750    1000.0     1.80   -2.60
Rock                     0.2000    0.1000    1000.0     1.80   -2.60
```

2.5.2 Zodiacal Radiance

The zodiacal light model was developed for consistency with the Strategic Scene Generation Model (Cornette, 1992b).

2.5.3 Galactic Radiance

The contribution to the space background by non-stellar galactic radiance has been estimated by C.B. Ludwig (1978), using data from IRAS (Hauser et al., 1984; Low et al., 1984; Pottasch et al., 1984). The model used in MOSART for the non-stellar galactic radiance uses a 550 K blackbody to match the spectral characteristics, and an exponential function of galactic azimuth and an inverse function of galactic elevation to match the spatial characteristics.

2.5.4 Extra-Galactic Radiance

The model in MOSART for the contribution of all emissions outside of the galaxy assumes a spatially homogeneous source. The spectral characteristics between 3 and 30 μm have been obtained from The Infrared Handbook (Wolfe and Zissis, 1978). At the present time, extra-galactic radiance below 2 μm is assumed to be identically zero.

2.6 Structure Constant

The structure constant, C_n^2, is used to calculate the scintillation and atmospheric emission variations (see Section 4.7). The values of C_n^2 are based upon the Hufnagel model (Wolfe and Zissis, 1978), modified by G.C. Valley (1980) and by Peter Ulrich (1988). The structure constant is defined as a function of altitude by:

$$C_n^2 = A_{Valley} \times (2.2 \times 10^{-3} \, V_{V_o} \left(\frac{Z}{100}\right)^{10} * e^{-Z} + 1.0 \times 10^{-16} \, e^{-Z/1.5}$$
$$+ \left(C_{n_o}^2 - 1.0 \times 10^{-16}\right) e^{-Z/0.1})$$

where $A_{Valley} = 1.03$

$V_{V_o} = 1.8 \times U/27$.

$C_{n_o}^2$ is the surface level value; the default value is 1.7×10^{-14}

U is the mean wind speed, which is recommended to have a mean value of 27 m/sec, with a standard deviation of 9 m/sec.

Z is the altitude for a surface of 0.0 km, and a tropopause of 10 km. For other conditions, the region between the surface and the tropopause is mapped linearly into the 0-10 km region, while the region between the tropopause and 100 km is mapped linearly into the 10-100 km region.

2.7 Global Data Bases

The MOSART code contains several global data bases that characterize elements of the earth's environment. The MOSART data bases provide the user with an average set of values for characterizing the environment at any location on the globe. It should be emphasized that these data bases only characterize the mean properties and do not pretend to provide a full description of the range of local variations. These data bases include:

- Surface Elevation

- Terrain Scene Classification

- Cloud Cover and Altitude

- Surface Temperature

- Miscellaneous Data (Snow Cover, Cirrus Cover, Land Cover)

121

These data bases were initially developed for APART (Cornette, 1989) and have been carried over to MOSART. Each of these is discussed briefly below.

2.7.1 Elevation

The National Geophysical Data Center (NGDC), a division of NOAA, has a variety of topography and terrain data sets available for use in geoscience applications. The data were obtained from U.S. Government agencies, academic institutions, and private industries. The data coverage is regional to worldwide; data collection methods encompass map digitization to satellite remote sensing.

MOSART utilizes NGDC elevation data based on a 10-minute geographic grid that has full global coverage (see Figure 102). These data, which include 2.3 million global observations, were originally compiled by the U.S. Navy from navigational and aeronautical charts. Error checks and refinements have been made by the National Center for Atmospheric Research and NGDC.

The data set includes modal, minimum, and maximum elevations; number and orientation of ridges; terrain characteristics; and percentages of water surfaces and urban development for each 10-minute area. MOSART contains only the modal data.

A pictorial representation of the altitude map is shown in Figure 103.

871-B07-001   871-B07-002   871-B07-003

R-023-91.105 BC/Mac
R-077-90..2-105 BC/Mac
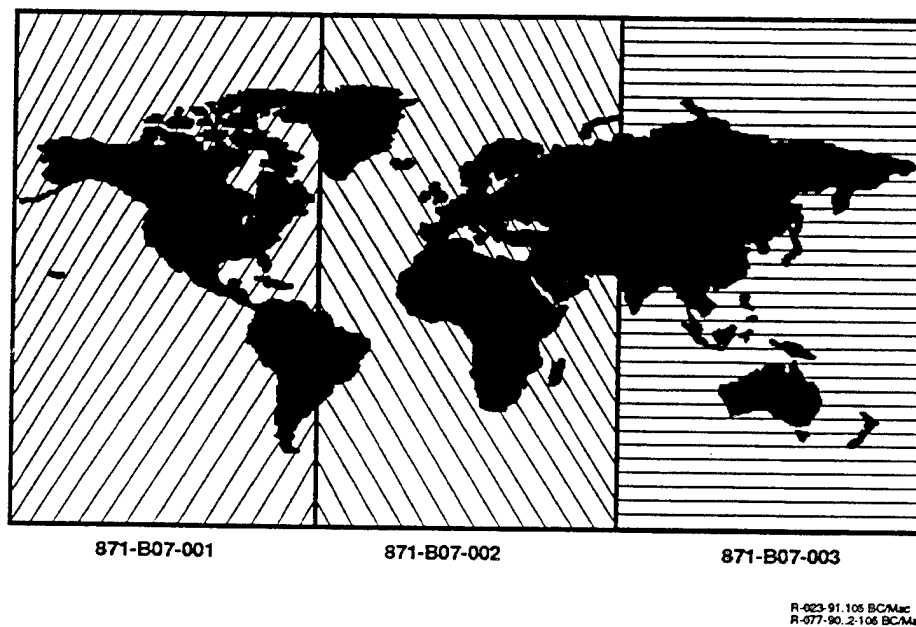
Figure 102.   Index Map Showing 10-Minute Data Divisions by Longitude. These data are also available by geographical regions (continents).
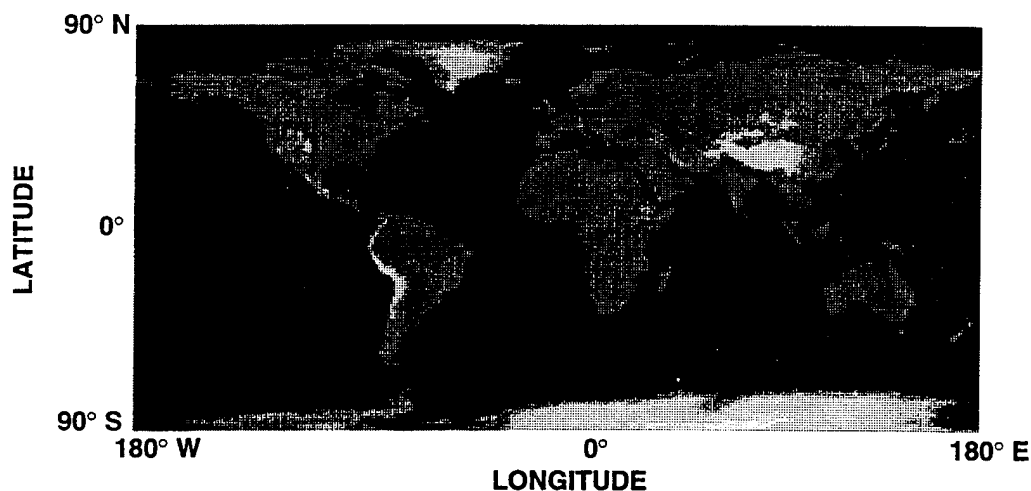
Figure 103. Pictorial Representation of the Altitude Map.

2.7.2 Terrain Scene Classification

During execution of the MOSART code, the user is given the opportunity to select a representative terrain background model from the Scene Data Base (see Section 2.4.2). This selection is based upon the simulation date and location and type of background desired by the user. If the user does not select a background model, MOSART will select a default based upon the latitude, longitude, and date (season).

The MOSART data base contains terrain and surface cover characteristics for the entire earth's surface. Each 1° x 1° rectangular area of the earth's surface has been assigned a scene type. This scene data base was constructed from a digitized version of the World Vegetation Map from the Times of London Atlas of the World. The digitized World Vegetation Map provided surface vegetation data for land areas of the world. The final data base was constructed in several stages. These are described below. CIA maps of the polar areas were used to determine seasonal variability in the sea ice (CIA, 1978).

The global assignments for the terrain scenes are presented in Figures 104 through 133.

123
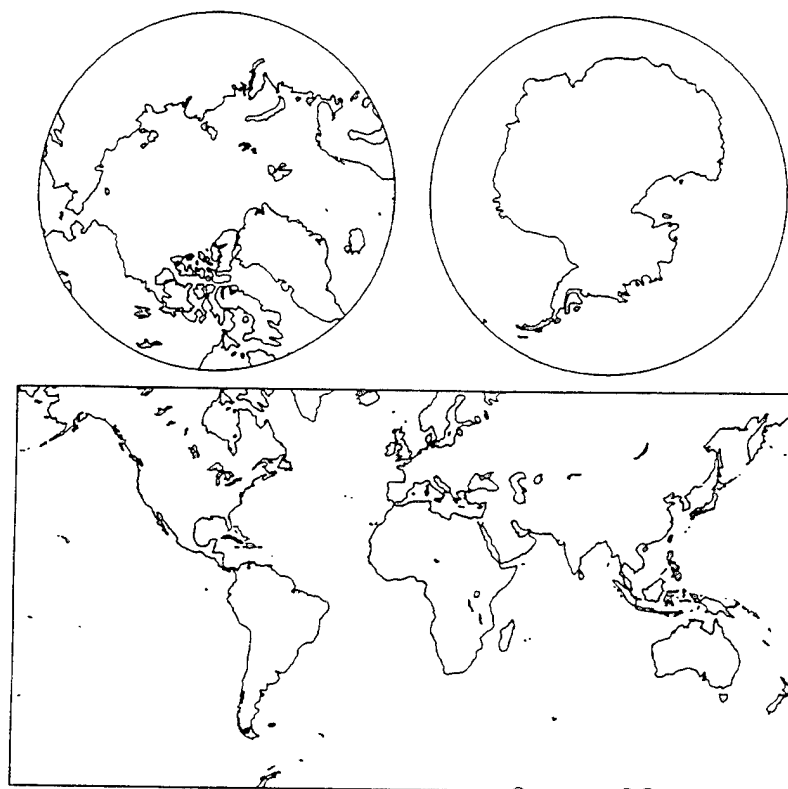
Figure 104. City/Harbor Land/Sea Interface (San Diego, California).
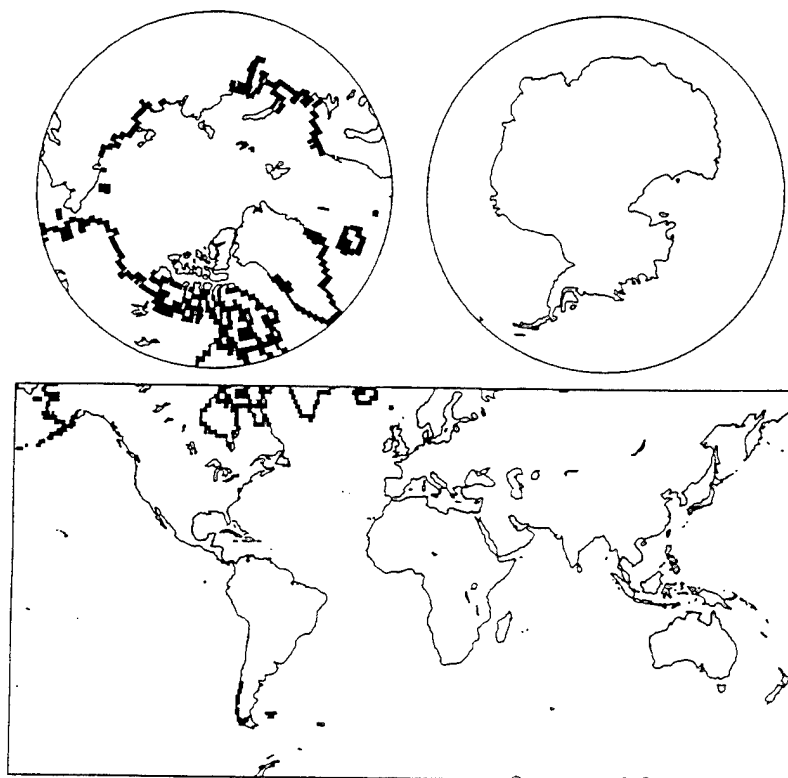
Figure 105. Arctic/Tundra Land/Sea Interface (Pt. Barrow, Alaska).

124
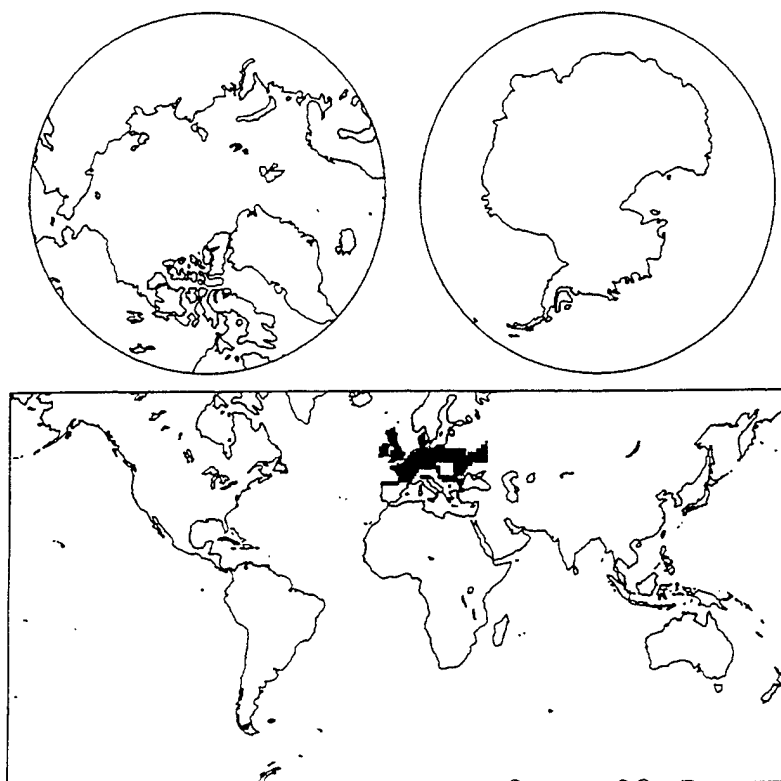
Figure 106. Forested Low Relief Terrain (Wa Wa, Ontario, Canada).
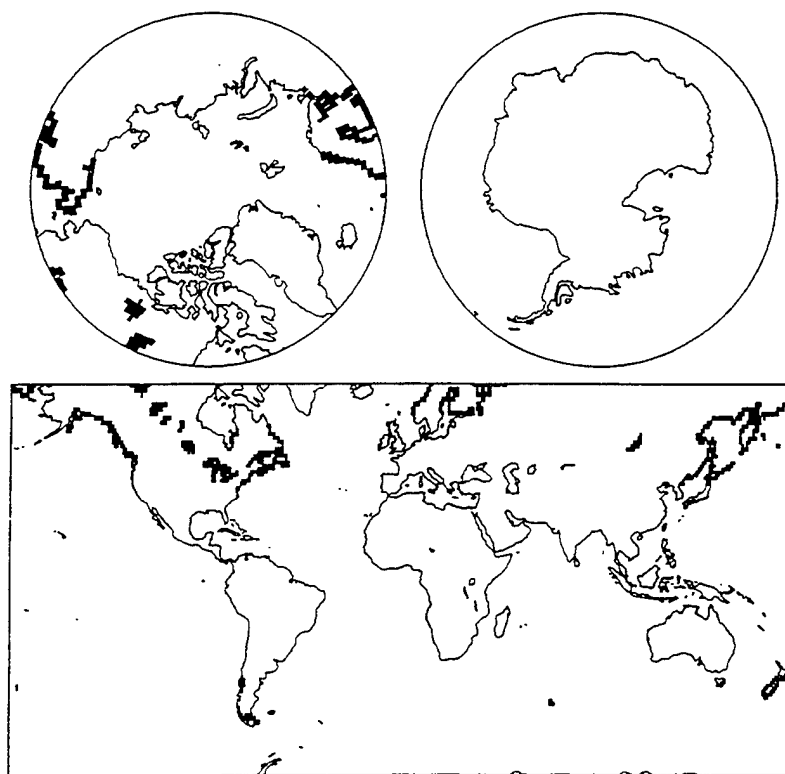
Figure 107. Subarctic Rocky Land/Sea Interface (Trondheim, Norway).

125
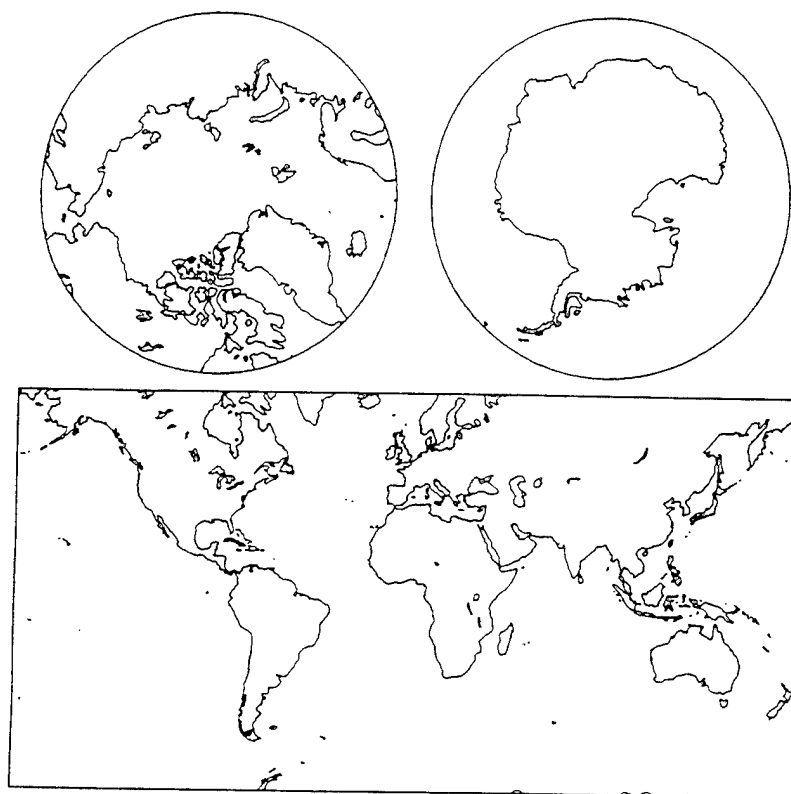
Figure 108. Forested Terrain/Agricultural Terrain (Fulda, Germany).
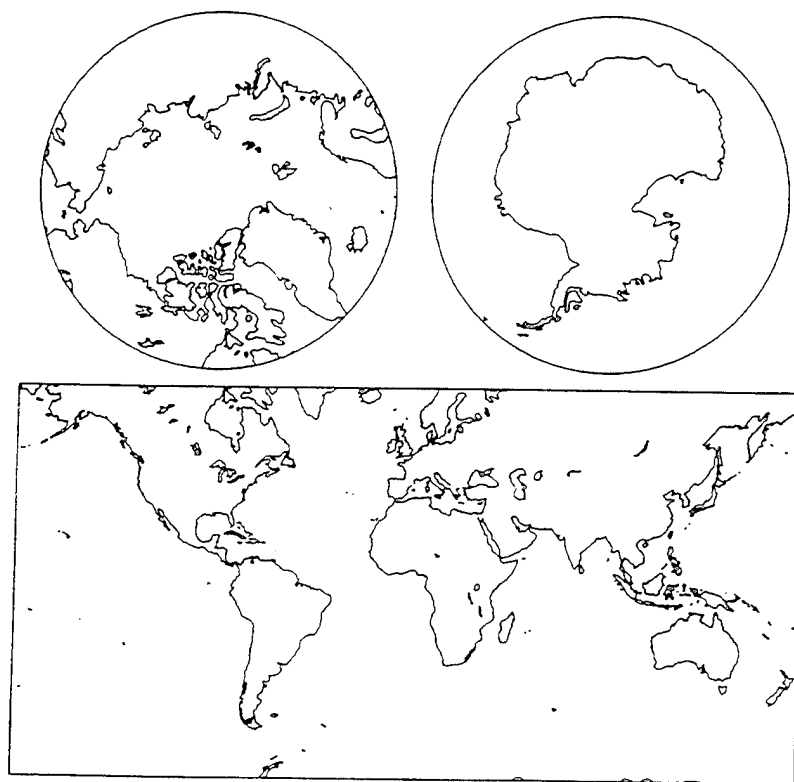
Figure 109. Flat Agricultural Terrain (Alberta, Canada).

126
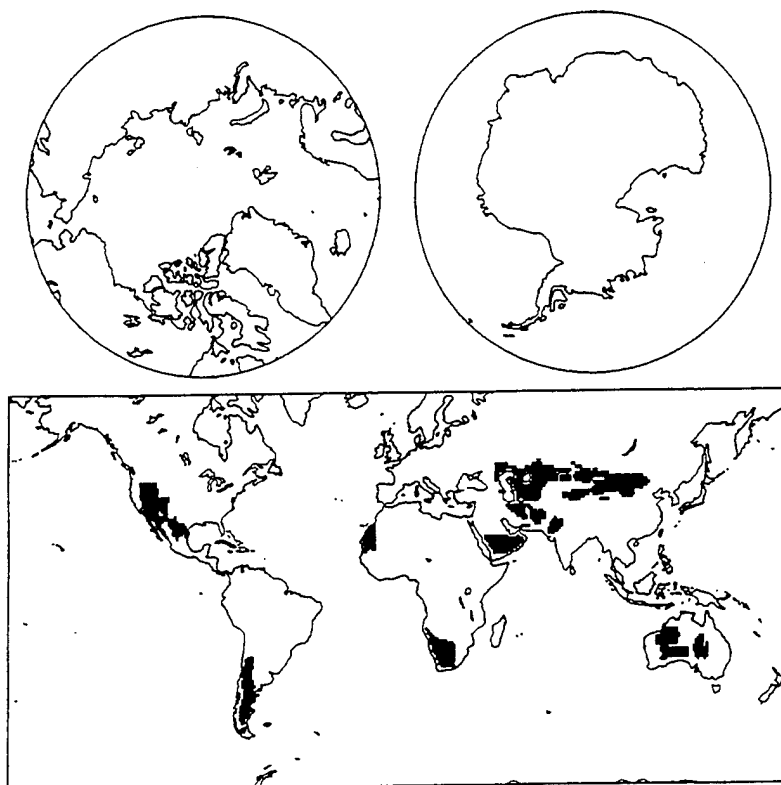
Figure 110. Desert Pavement with Dunes Terrain (Imperial Valley, California).
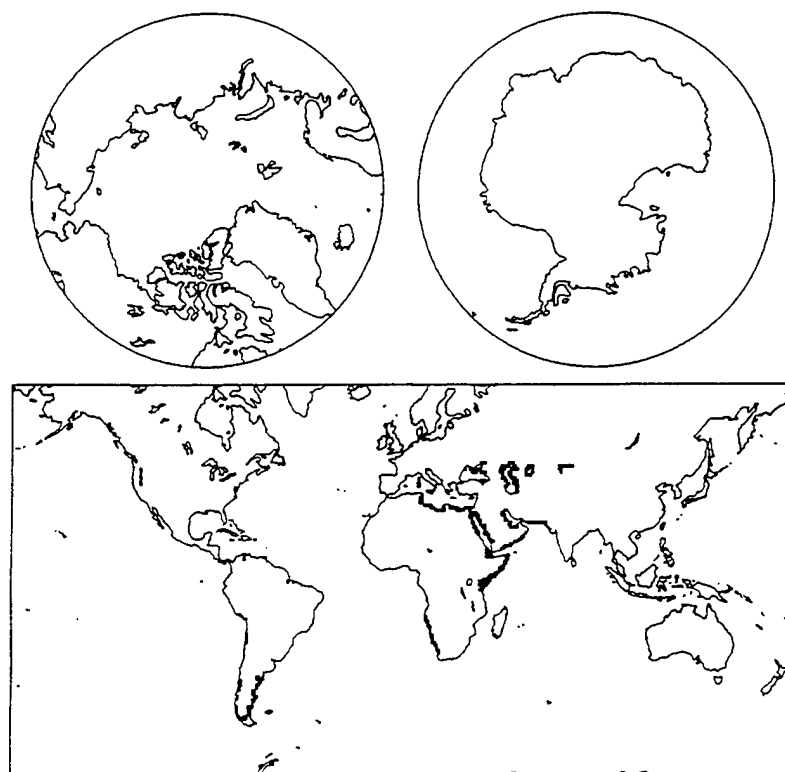
Figure 111. Desert Land/Sea Interface (Salton Sea, California).
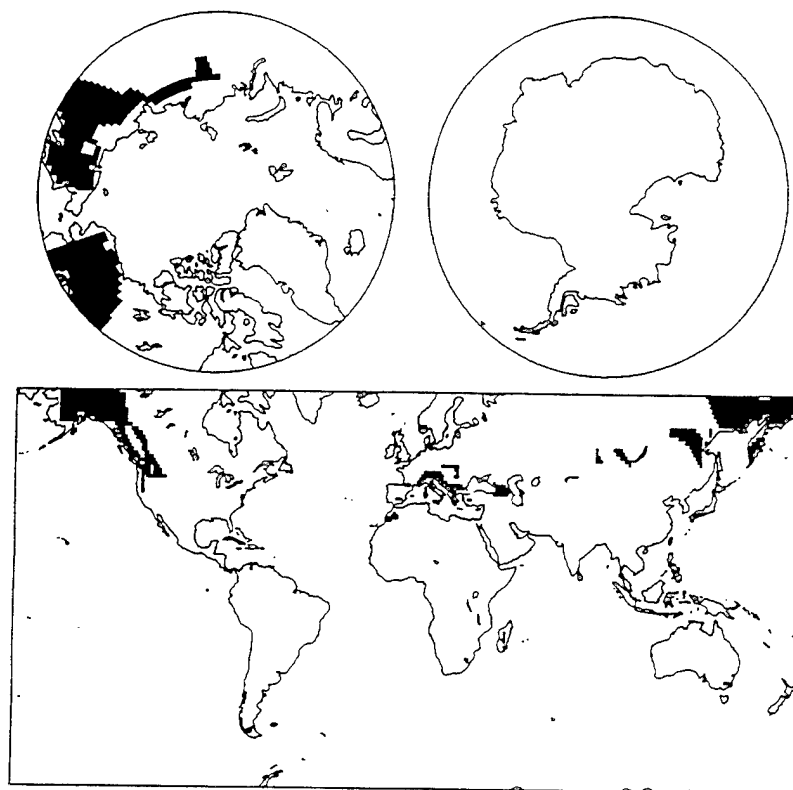
Figure 112. Forested Mountains/Cultural Terrain (Santa Cruz, California).
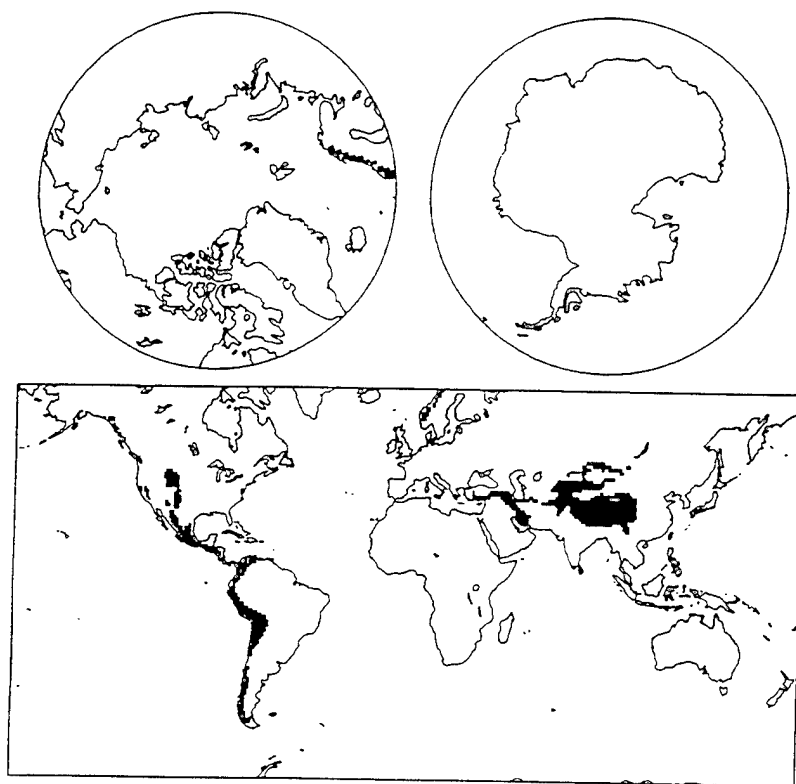
Figure 113. Arctic Mountains with Scrub Terrain (Brooks Range, Alaska).
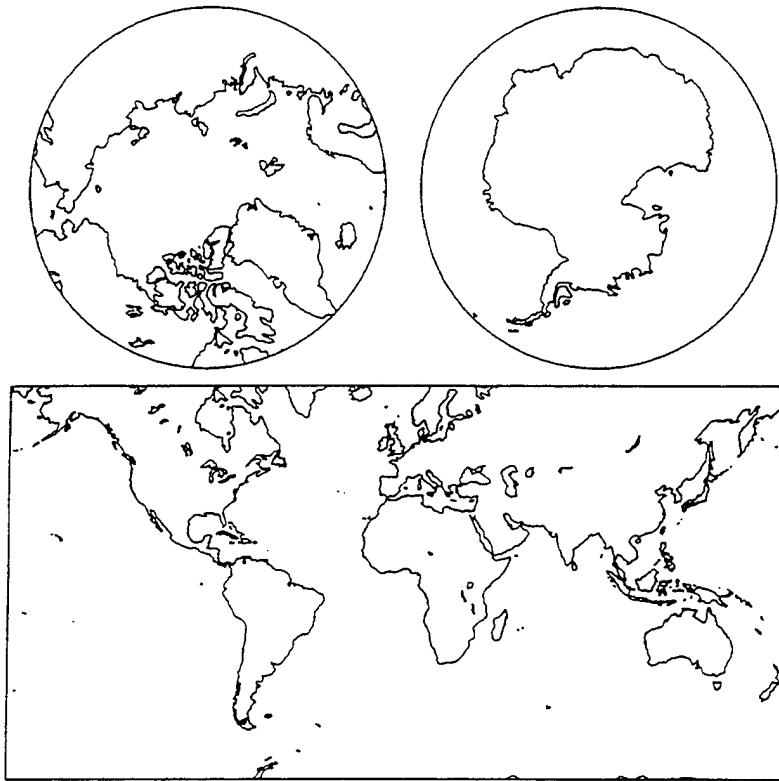
Figure 114. Arctic Tundra with Melt Lakes Terrain.
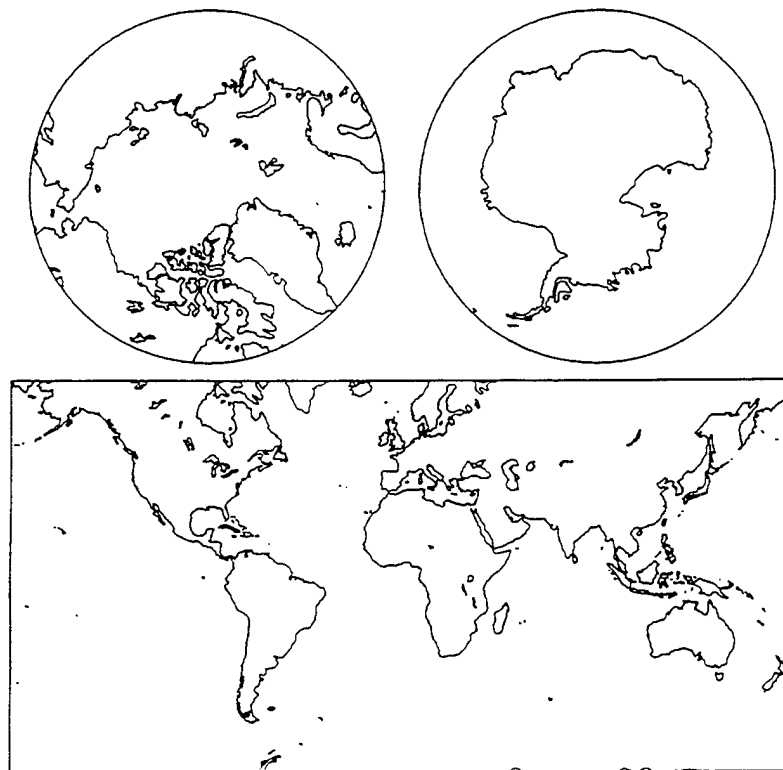
Figure 115. Mixed Farmland/Orchards Terrain (Camarillo, California).

129
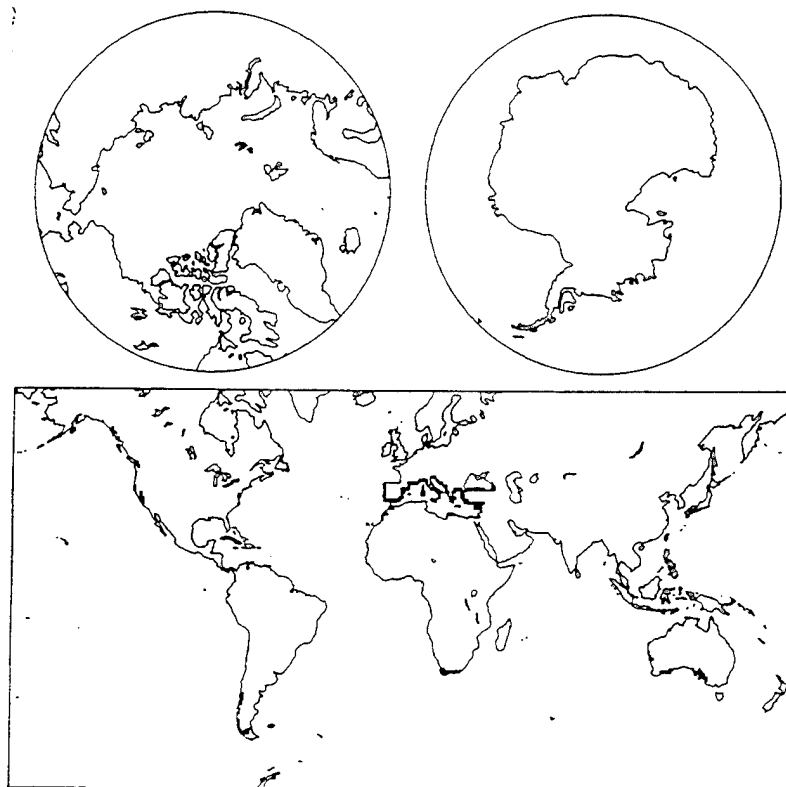
Figure 116. Southern California Land/Sea Interface (Southern California).
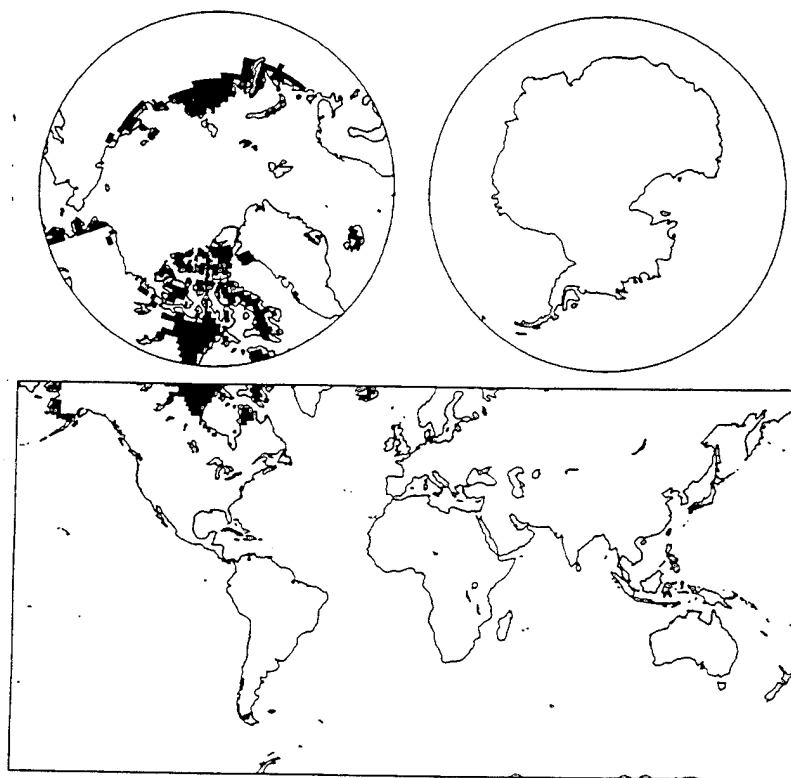
Figure 117. Tundra Background.
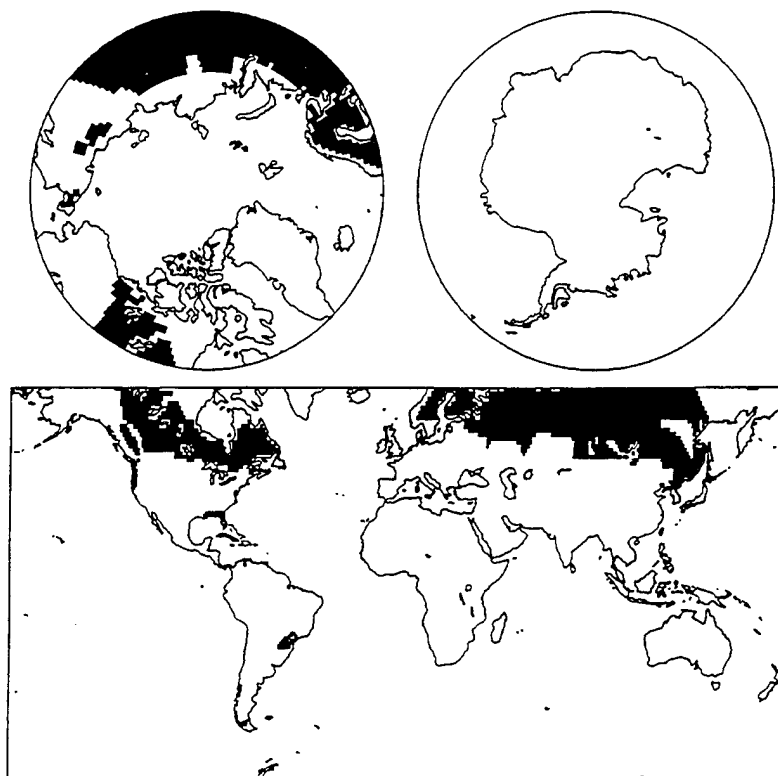
Figure 118. Pine Forest Background.
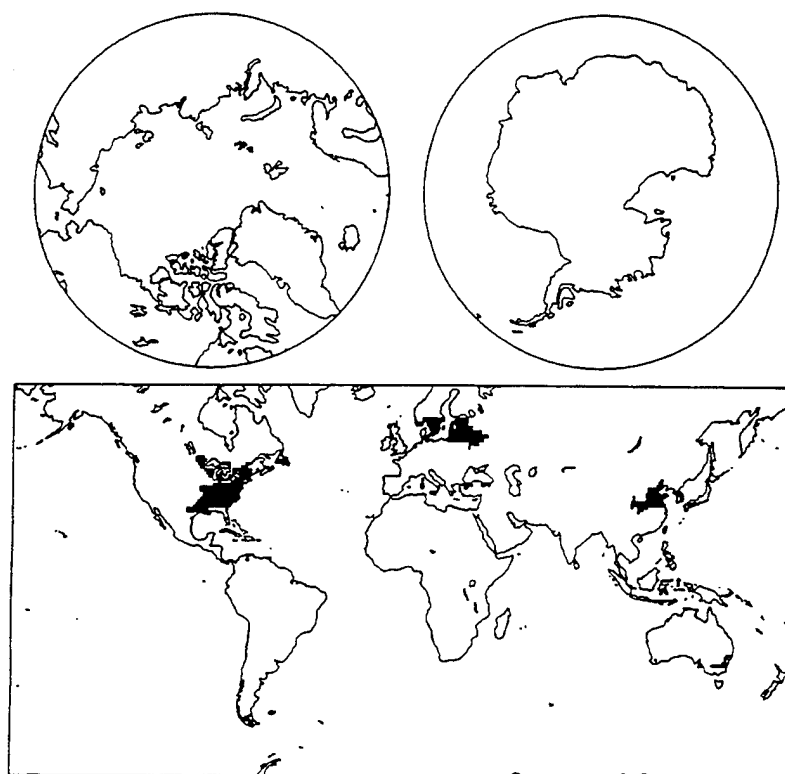
Figure 119. Mixed Forest/Farmland Background.

131
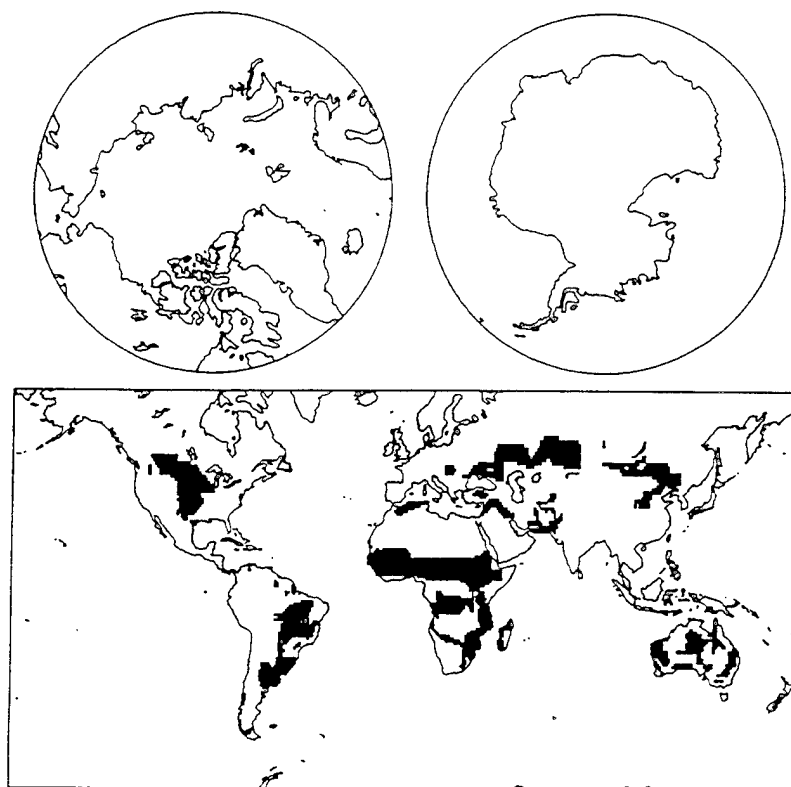
Figure 120. Grassland/Savannah Background.
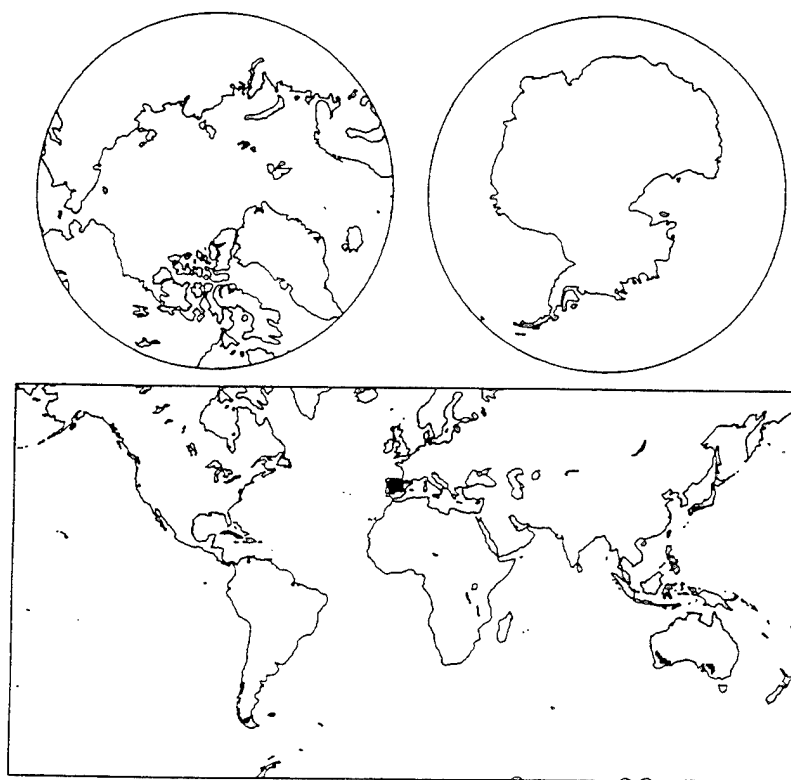
Figure 121. Scrub/Chaparral Background.
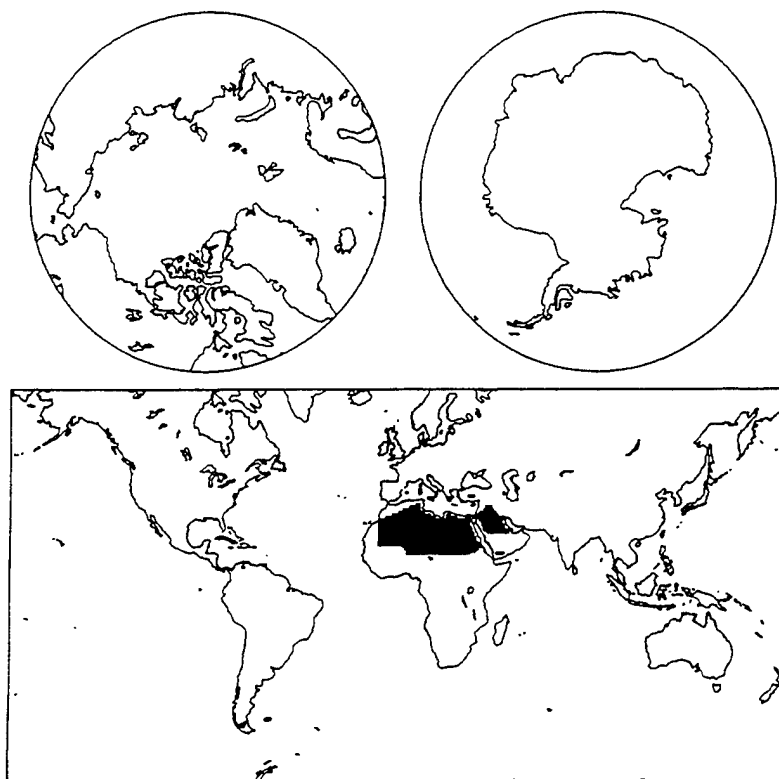
Figure 122. Scrub Desert Background.
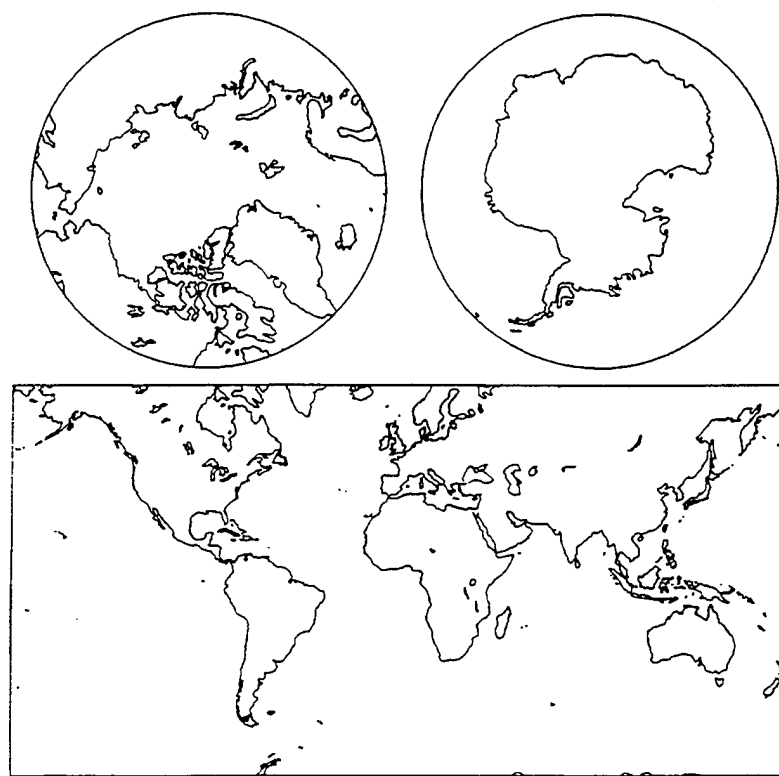
Figure 123. Urban Background.

133
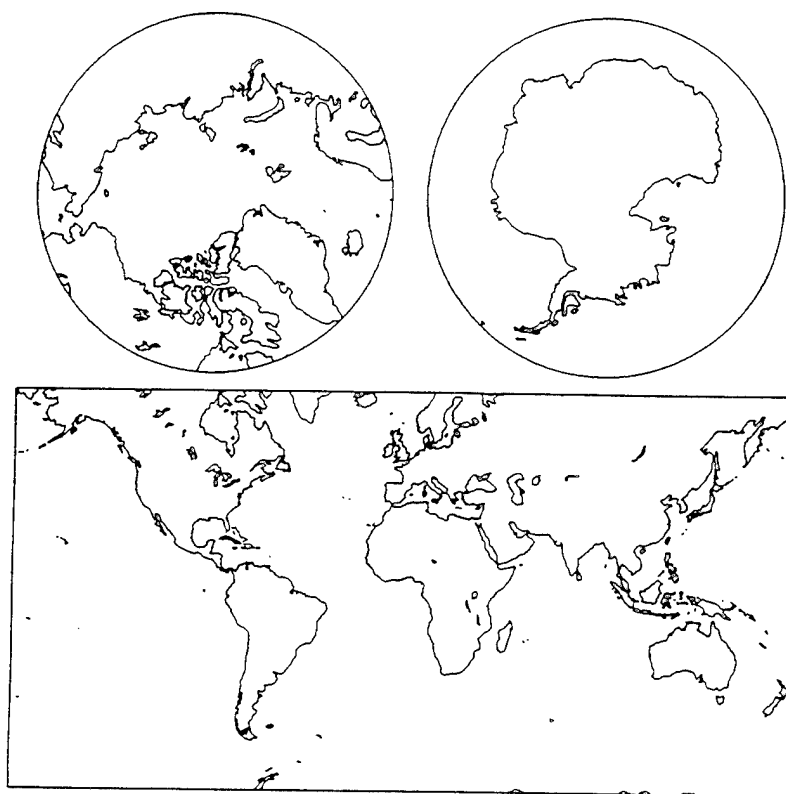
Figure 124. Rural Land/Sea Interface Background.
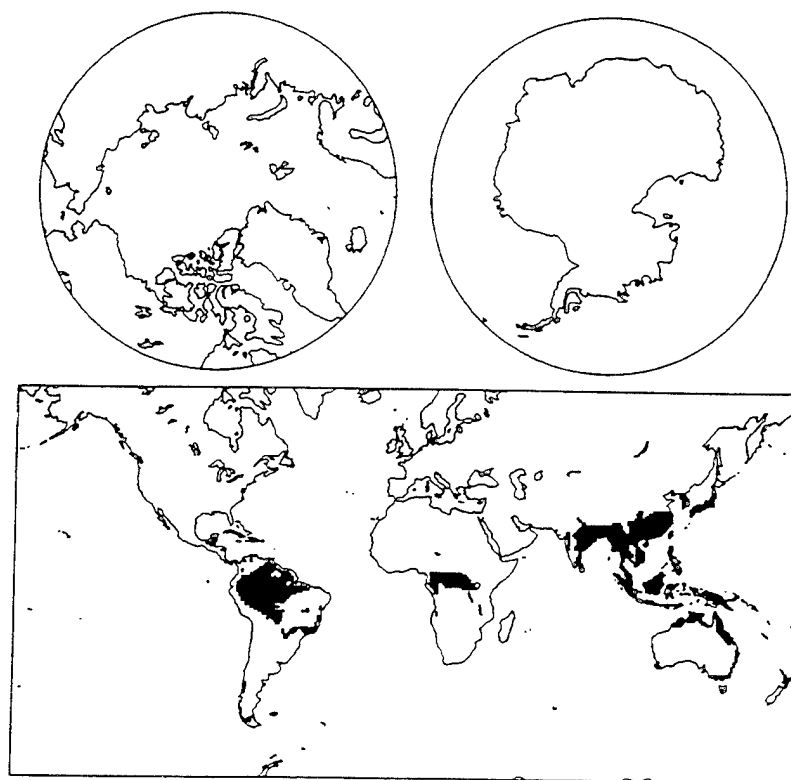
Figure 125. Tropical Forest Background.
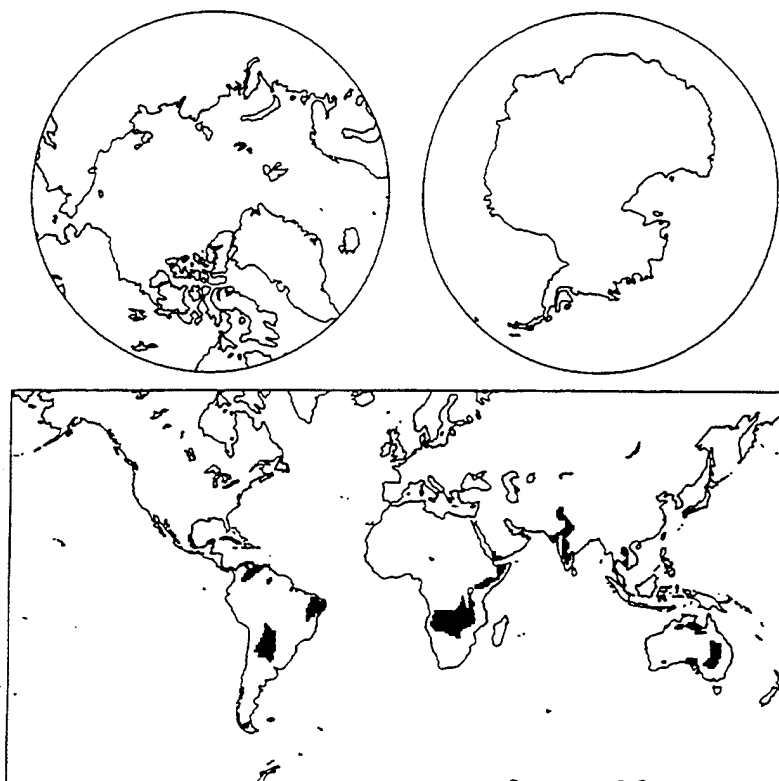
Figure 126. Tropical Savannah Background.
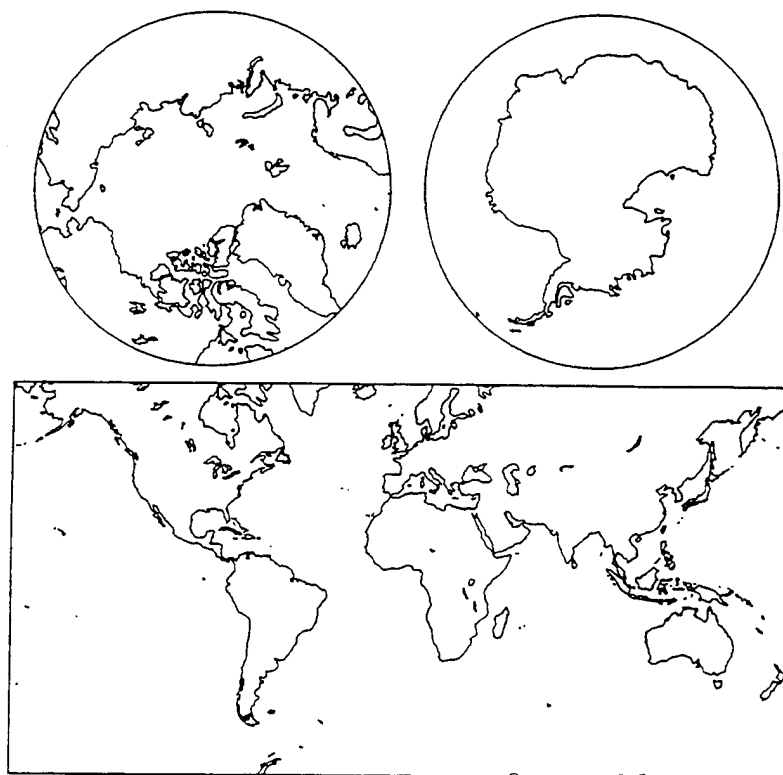
Figure 127. Tropical Desert Background.

135
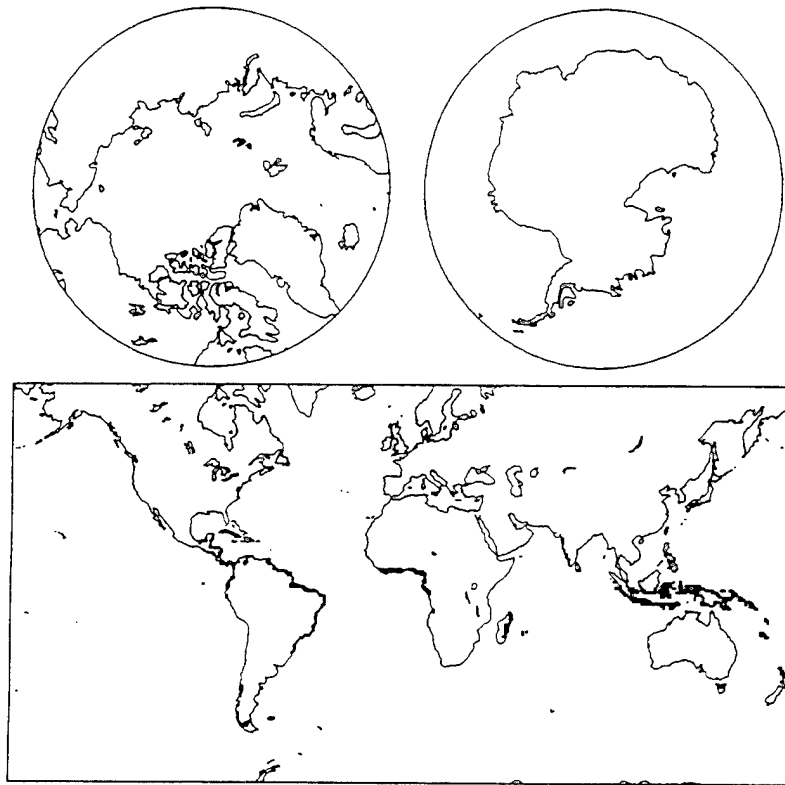
Figure 128. Tropical Land/Sea Interface Background.
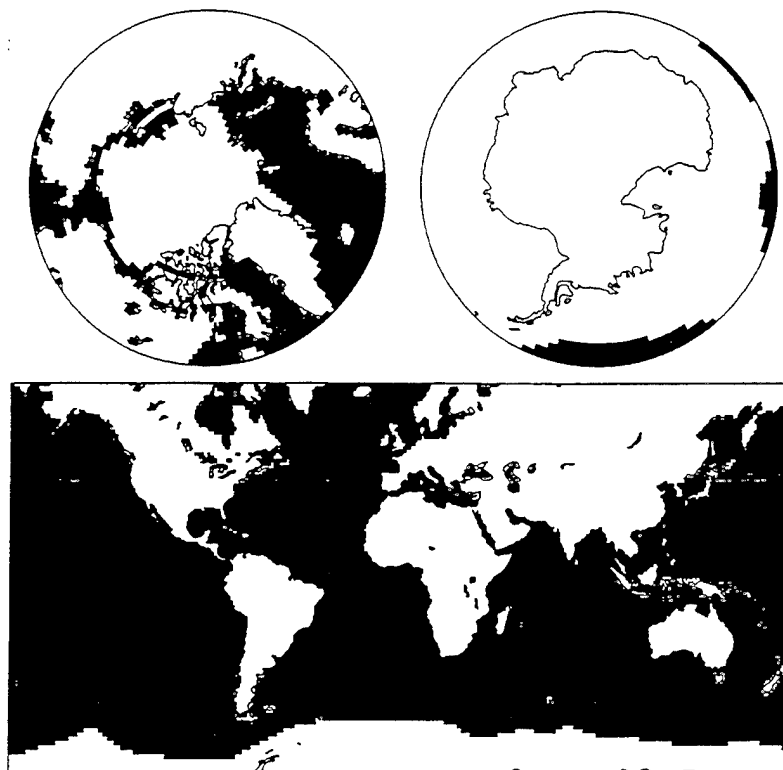
Figure 129. Open Ocean/Lake Background (April-October).

136
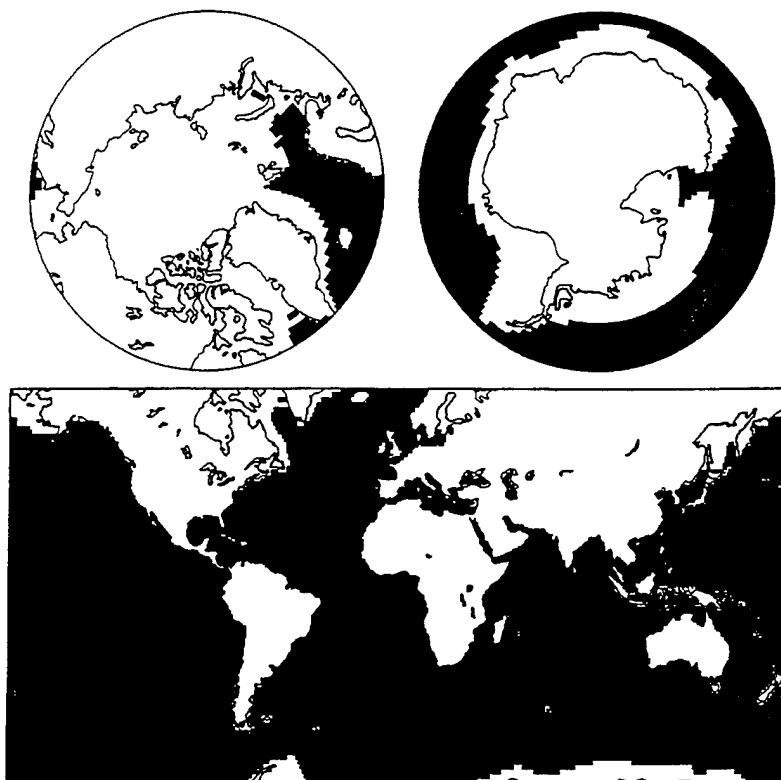
Figure 130. Open Ocean/Lake Background (October-April).
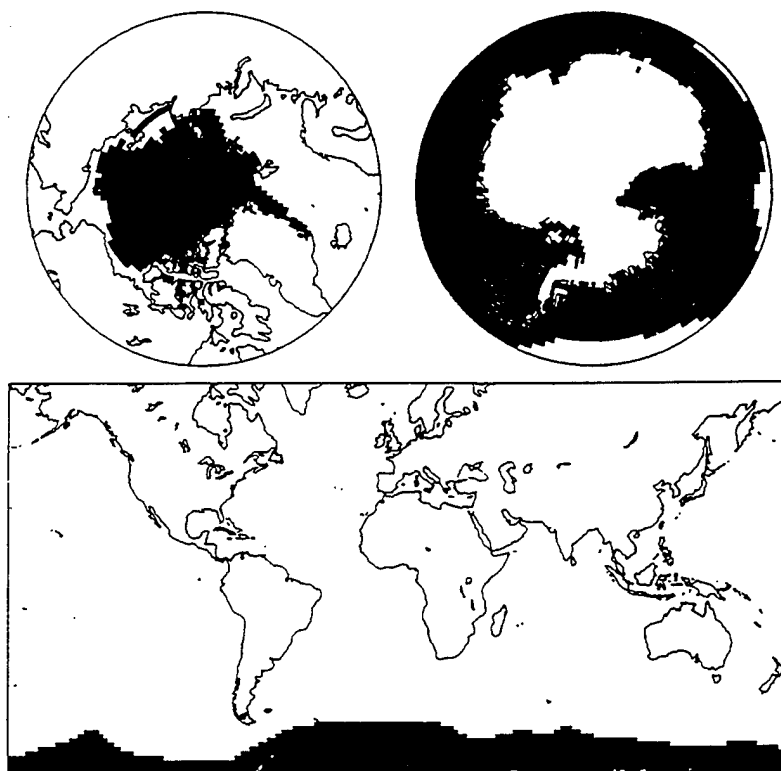
Figure 131. Multi-Year Sea Ice (Beaufort Sea) (April-October).

137
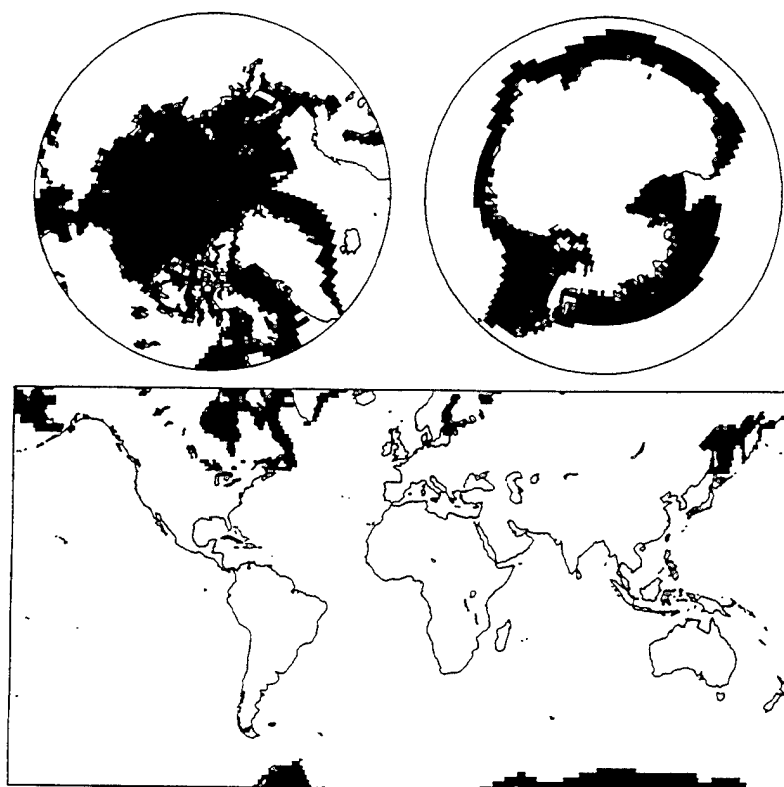
Figure 132. Multi-Year Sea Ice (Beaufort Sea) (October-April).
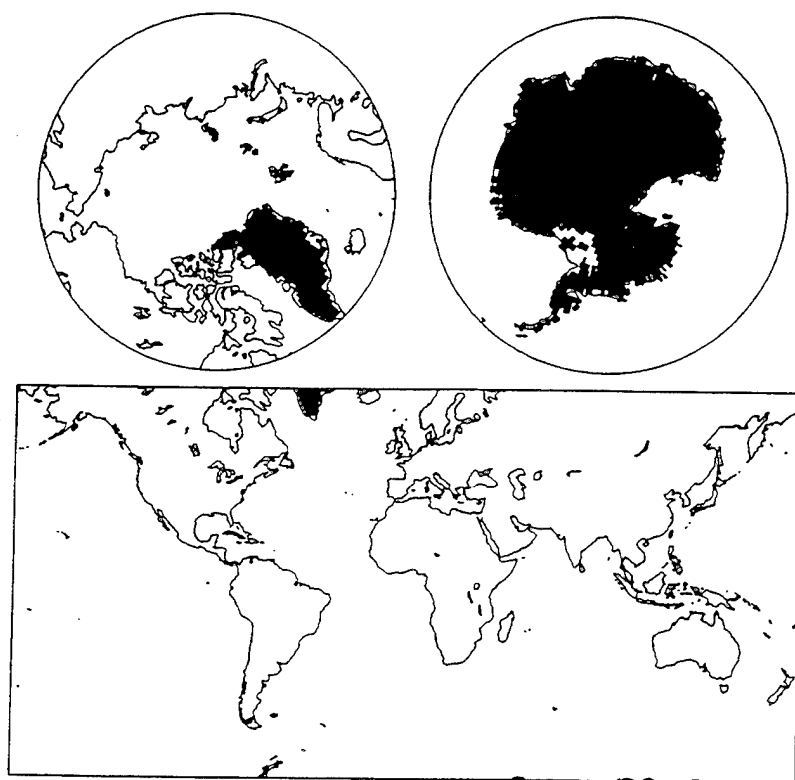
Figure 133. Continental Ice.

138

2.7.3 Cloud Cover and Altitude

In the absence of specific user-supplied inputs for cloud cover percentage, cloud thickness, and cloud top altitude, the MOSART code obtains default estimates of these values from the Cloud Cover Data Base. The Cloud Cover Data Base is derived from the NOAA NIMBUS-7 C-MATRIX cloud cover data base, a collection of worldwide cloud cover observations made using the NIMBUS-7 satellite.

The Cloud Cover Data Base is only used by MOSART to estimate cloud conditions for background temperature calculations; it is not used in the line-of-sight radiation transport calculations at this time. It contains cloud cover and cloud radiance data for grid cells covering the entire earth's surface. The data base contains the following monthly average measurements, collected for both daytime (noon) and nighttime (midnight). The radiance values are tabulated in units of 0.125 $W/cm^2/sr$.

- % High Cloud Cover
- High Cloud Radiance

- % Mid-level Cloud Cover
- Mid-level Cloud Radiance

- % Low Cloud Cover
- Low Cloud Radiance

The MOSART Cloud Cover Data Base is derived from a larger data base, the NIMBUS-7 C-MATRIX data base compiled by NOAA. The C-MATRIX data base contains daily and monthly estimates for 116 different cloud cover and cloud radiance parameters, compiled for the 5-year period 1979 through 1983. These estimates are based upon analysis of imagery acquired by two instruments aboard the NIMBUS-7 satellite: The Temperature Humidity Infrared Radiometer (THIR), and the Total Ozone Mapping Spectrometer (TOMS). Data from the 11 μm THIR channel and the .38 μm TOMS channel were used to classify global cloud cover into high, medium and low categories and to estimate the radiance for each category. The data are organized into 2070 "Target Data Areas," each covering an area of 500 square kilometers. Each Target Data Area spans 4.5 degrees of latitude and from 4.5 degrees (at the equator) to 120 degrees (at the poles) of longitude.

Sample data are presented in Figure 134.

2.7.4 Surface Temperature

The surface temperature data base in MOSART is based upon the Air Force Surface Temperature Analysis Archive. It is tabulated at the same spatial resolution as the cloud cover data (see Section 2.7.3). Sample data are presented in Figure 135.

LOW

MID

HIGH

July/Noon

0%   89%
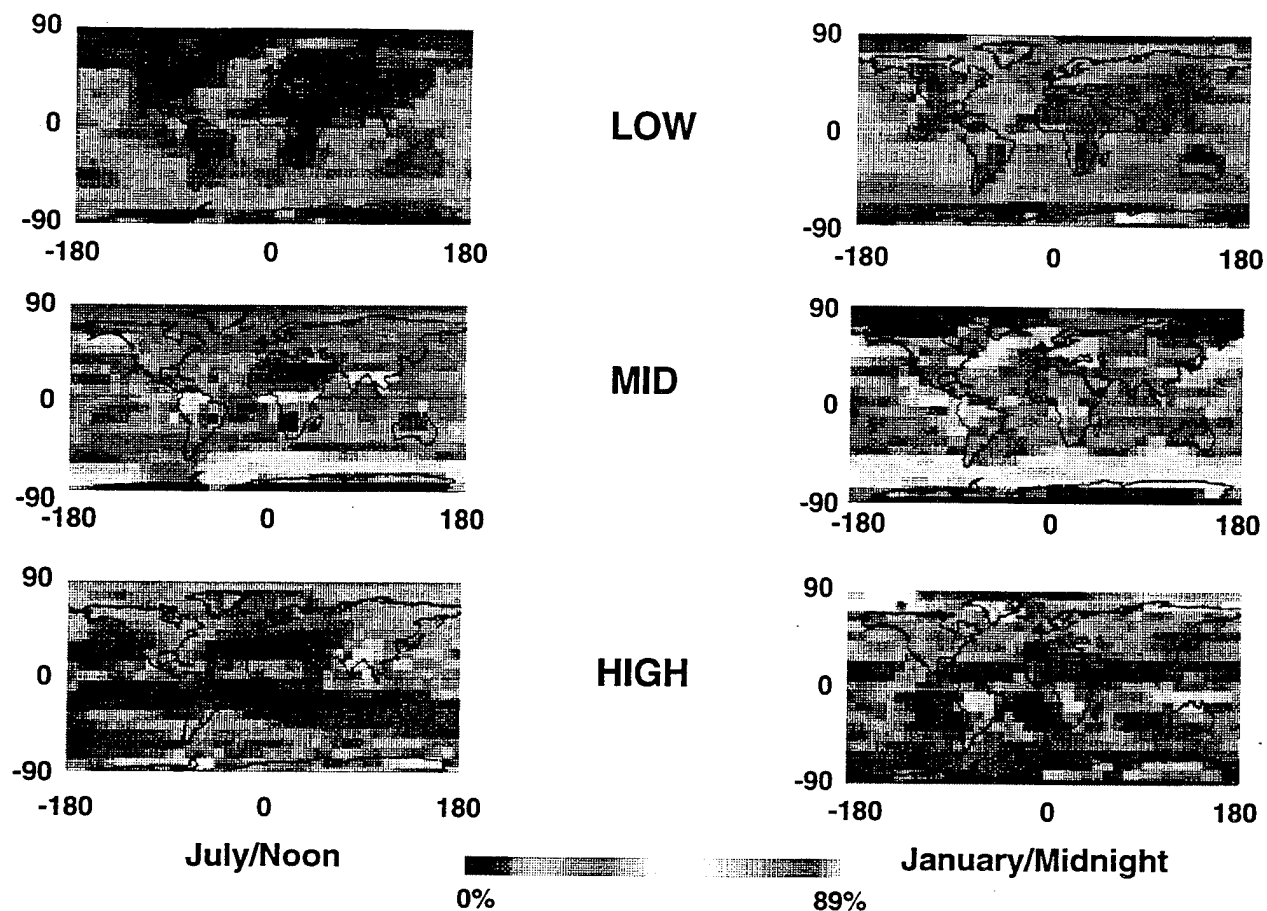
January/Midnight

R-077-90.3-137 BC/Mac

Figure 134.   Sample Cloud Cover Data.

- **July/Noon**
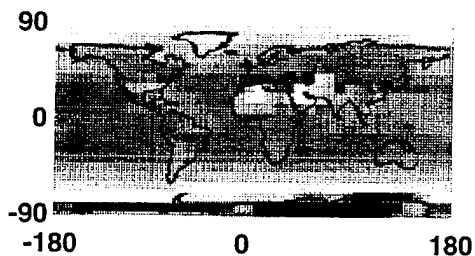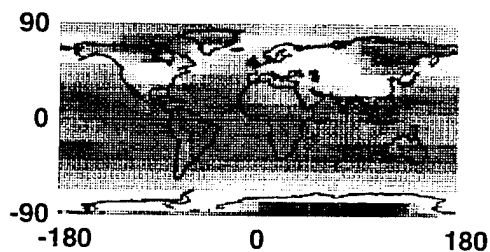
- **NOAA Nimbus-7 C-Matrix Data Base**

- **Air Force Surface Temperature Analysis Archive Data Base**

- **January/Midnight**

209k   310K

R-077-90.2-138 BC/Mac

Figure 135.   Sample Surface Temperature Data.

140

2.7.5 Miscellaneous Data

Other data included in the global data base are:

- % Snow Cover (used to modify scene composition)

- % Land Area (not used at this time)

- % Cirrus Clouds (not used at this time)

These have been compiled for MOSART from readily available sources such as NGDC and NOAA.

3.0 GEOMETRY

Atmospheric refraction significantly changes long line-of-sight paths, particularly for near horizontal angles. The determination of the geometry for each scenario involves ray tracing through a spherically symmetric atmosphere. Both of MOSART's predecessor codes (i.e., APART and MODTRAN) have refractive modules. Although MODTRAN's numerical stability problems have been solved in MODTRAN 2, MOSART uses the APART algorithm because it also incorporates the effects of subrefraction, superrefraction, and trapping (or ducting). This model has been extensively used in modelling interference effects (e.g., multipath) at radar wavelengths, and is numerically very stable (Cornette, 1978). The ray tracing techniques used by MOSART, together with a brief description of the refractivity model, specific geometries, and azimuths, together with the solar and lunar ephemeris models and the radius of the earth, are presented below.

3.1 Ray Tracing

From Fermat's principle of least action, electromagnetic radiation (i.e., photons) always propagate along a geodesic in free space or through any homogeneous medium. However, if the radiation is propagating through an inhomogeneous medium (e.g., the earth's atmosphere), gradients in the speed of light in the medium cause the path of the photons, or ray, to deviate from a geodesic, or straight line. If the speed of light in the medium is discontinuous, the ray path will not be differentiable (e.g., at reflection points); however, for the earth's atmosphere it is reasonable to assume that the speed of light is a differentiable function of location. Then, the rays are twice differentiable curves through the atmosphere, and hence a curvature can be defined along the ray path.

The curvature of ray paths due to inhomogeneities in the atmosphere causes considerable difficulties in attempting to solve various geometric problems. Although ray tracing is used in MOSART, an initial estimate is required under some conditions. A transformation that maps the curved rays into straight lines and preserves various geometric parameters with sufficient accuracy can be used to solve certain problems (see Figure 136). The most common method used to compensate for the ray curvature in the earth's atmosphere is to use an effective earth's radius, which is usually larger than the true earth's radius, that supposedly conformally transforms the curved rays into straight lines. The treatment of ray curvature and the effective earth's radius in the standards of the literature has not been sufficiently rigorous due to either unnecessary or tacit assumptions. This incompleteness leads to incorrect results due to improper use of the effective earth's
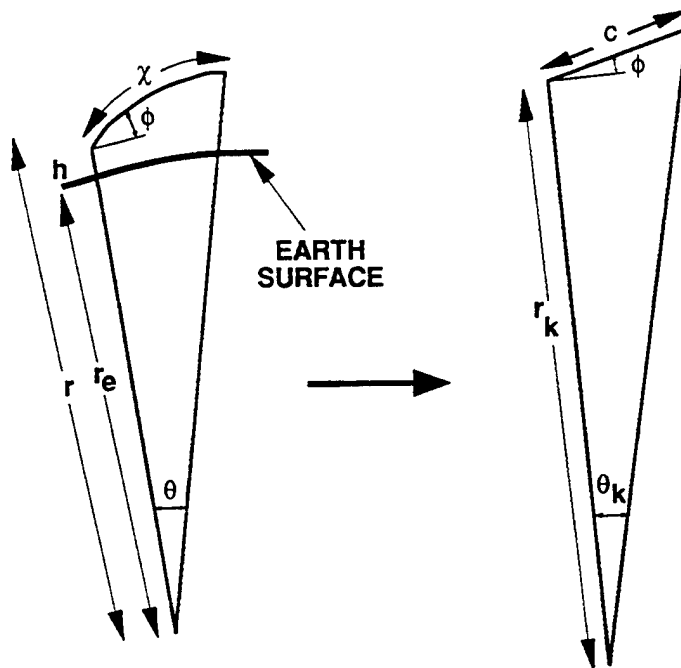
Figure 136. Geometry.

radius. In addition, the effective earth's radius is not a conformal transformation, and it does not transform the curved rays into straight lines. Instead, the curved rays are transformed into rays with a greater radius of curvature.

In this section, after a brief discussion of geometric optics, the effective earth's radius is derived and some of the associated errors are discussed. Finally, a transformation that properly compensates for the ray curvature is derived and compared with the effective earth's radius.

3.1.1 Geometric Optics

Since the concepts of geometric optics are used in developing the geometrics in MOSART, it is useful to evaluate when geometric optics, or ray tracing, is valid and to give the expressions for ray tracing in the earth's atmosphere. For a more detailed treatment of the subject, the reader is referred to Stavroudis (1972), an excellent mathematical treatment of ray theory. Ray tracing is a valid approximation to the propagation of electromagnetic waves through a medium if the phase index of refraction does not change significantly within a distance comparable to the wavelength of the signal (i.e., $|\nabla n| \ll 2\pi n^2 \lambda$) and if the relative change in the effective spacing, L, between neighboring rays does not change significantly with

143

respect to the wavelength of the signal (i.e., $|\nabla L| \ll 2\pi nL/\lambda$). Both of these assumptions are valid for non-trapping atmospheric conditions. If trapping occurs, special care must be taken to avoid caustics and various diffraction phenomena.

The assumption is made for the remainder of this section that the phase index of refraction is a differentiable function that depends on altitude only. The assumption that n depends upon r only (i.e., the atmosphere is spherically stratified, or horizontally homogeneous) is a fairly conventional one; although this assumption is not necessary for the development of ray tracing, it simplifies the mathematics somewhat. The assumption that n is a differentiable function is not too stringent a condition; at worst, it may simply require some smoothing of experimental data.

Propagating light rays obey Snell's Law, namely,

$$nr \cos \phi = \text{constant} .$$

Using this relationship and some simple differential geometry, the above assumptions quickly give rise to the following relations for a ray propagating through a horizontally homogeneous atmosphere:

$$\frac{dr}{d\phi} = \frac{r \tan \phi}{1 + \Gamma}$$

$$\frac{d\theta}{d\phi} = \frac{1}{1 + \Gamma}$$

$$\frac{dr}{d\phi} = r \tan \phi$$

$$\frac{dx}{dr} = \frac{n}{\sin \phi}$$

$$C = \frac{1}{\rho} = \frac{-\Gamma \cos \phi}{r}$$

where r is the distance from the earth's center, ϕ is the angle between the ray and the surface of constant refractivity, θ is the earth-center angle, x is the distance along the ray between the ray's end points, C is the ray curvature, ρ is the radius of curvature of the ray, and Γ is the ray factor.

It should be noted that the actual value of the earth's radius is not of great importance. This discussion is concerned only with rays propagating between two points in the earth's atmosphere and the interaction of the electromagnetic wave with the earth's surface is not considered. Therefore, all of the analysis herein is valid for an atmosphere whose surfaces of constant refractivity are concentric spheres and whose radii may have nothing whatsoever to do with the radius of the earth. However, Section 3.6 contains a brief discussion of the radius of the earth.

144

3.1.2 Effective Earth's Radius

In order to perform some of the preliminary calculations (e.g., estimating elevation angle given the slant range), some method of compensating for the ray's curvature is required. The classical approach to compensate for the curvature of ray paths due to atmospheric refraction is to assume that the earth's radius is somewhat larger than it actually is. This method was advanced by Schelling, Burrows and Ferrell (1933) and has been used by many authors since then. The concept is to absorb the curvature of the ray into the curvature of the effective earth so that the relative curvature remains the same. If r is the distance from a point on the ray to the center of the earth and ρ is the radius of curvature of the ray at that point, the effective radius r_k is defined to be

$$r_k = [r^{-1} - \rho^{-1}]^{-1}$$

Since any twice differentiable curve has a radius of curvature associated with each point on the curve, this technique applies to any realistic ray path (i.e., if n is differentiable). The negative sign results from the convention that a downward curving ray has positive curvature and an upward curving ray has negative curvature. This results in an effective radius of

$$r_k = \frac{r}{1 + \Gamma \cos\phi} \quad .$$

This equation is applicable for any atmospheric condition in which ray tracing is valid. However, both Γ and ϕ are functions of the position of the point along the ray path; therefore, $\Gamma \cos\phi$ varies along the ray path. For this reason, the effective radius is useful if and only if the variation in $\Gamma \cos\phi$ along the ray path is small and can be ignored. However, it should be pointed out that at low altitudes for exponential and linear atmospheres, r_k decreases with increasing altitude.

Many authors have treated the effective earth's radius using assumptions that are not always explicitly stated. The effective earth's radius, $r_k(o)$, is defined as the effective radius evaluated at the earth's surface with $\phi = 0$, so

$$r_k(o) = \frac{r_e}{1 + \Gamma}$$

where r_e is the radius of the earth. It is then claimed that the effective radius that should be used is

$$r_k(h) = r_k(o) + h \quad ,$$

since $r = r_e + h$. It should be noted that there is significant difference between r_k and $r_k(h)$. For normal microwave propagation, $\Gamma \approx -1/4$, so $r_k(o) = 4/3r_e$, the so-called 4/3-earth model; for optical frequencies $\Gamma \approx -1/5$, so a 6/5-earth model is obtained. If normal propagation is assumed for small look angles ($\phi \approx 0$), differences of 33% exist between the altitude difference of the ray's end points calculated using the effective earth's radius and that using the effective radius; for near zenith paths ($\phi \approx \pi/2$), the difference is approximately zero. Also, due to the high chances of subrefraction, superrefraction, and trapping propagation conditions in certain areas of the world, other values of Γ may be necessary. Depending upon the atmospheric conditions, the actual differences might be less or greater than those above.

It is often assumed that the effective earth's model is applicable only when the linear atmosphere is valid. However, the only requirement for applicability is that Γ be relatively uniform over the ray path between the transmitter and the receiver, and the details of the atmospheric refractivity model are immaterial.

Using the effective earth's radius, it is assumed that all transformed rays can be represented as straight lines over the surface of the effective earth and that the transformation is conformal (i.e., angles are preserved). However, if one examines the transformed rays, it becomes readily apparent that they are <u>not</u> straight lines, and the transformation is <u>not</u> conformal. For example, since the effective earth's radius transformation does not alter the earth's center angle between the transmitter and the receiver, it is impossible to draw a triangle that also preserves the angles, ϕ_1 and ϕ_2, between the ray and the surfaces of constant refractivity at the transmitter and receiver, respectively; therefore, if the transformed rays were straight, the transformation would not be conformal. Also, a detailed study of the transformed rays show that although their curvature has decreased, it is not zero (i.e., it is not a straight line). In the following section, a transformation that maps the curved rays into straight lines is derived, and the differences between that transformation and both the effective earth's radius and the effective radius transformations are demonstrated.

3.1.3 Refraction Compensation Transformation (Cornette, 1977c)

The curvature of a twice differentiable curve in spherical coordinates is defined to be

$$C = \frac{r^2 + 2\dot{r}^2 - r\ddot{r}}{(r^2 - \dot{r}^2)^{3/2}}$$

146

where r implies differentiation with respect to θ. Requiring that the angle ϕ be preserved all along the ray, and using differential geometry, the condition that the transformed ray is a straight line (i.e., the curvature is zero) is satisfied by

$$r^2 + 2\dot{r}^2 = r\,\ddot{r}$$

which is satisfied if and only if

$$\frac{dr_s}{dr} = \frac{r_s}{r}(1 + \Gamma)$$

$$\left(\frac{d\theta_s}{d\phi}\right)^2 = 1$$

Solving these equations and using simple geometry, the refraction compensation transformation is defined as follows:

$$r_s = \alpha n r$$
$$\theta_s = \phi - \phi_1$$

where (r_s, θ_s) is the transformed polar coordinate representation of the point (r, θ), ϕ is the look angle at the point (r, θ), ϕ_1 is the look angle at the point $(r_1, 0)$ and α is some arbitrary constant. The value of the constant α depends upon the application of the transformation. For example, if it is desired that the transformed ray length is equal to the true ray length, then

$$\alpha = \left[1 + \frac{\int \Gamma\,dx}{\int dx}\right]^{-1}$$

where the line integrals are evaluated along the ray. Therefore, the parameter α is dependent upon the ray direction, or look angle, ϕ. To analyze the validity of certain approximations to α for all rays, two atmospheric regions for exponential atmospheres were studied - namely, the region between the surface and 1 kilometer, which can be considered as fairly linear in nature, and the region between the surface and 10 kilometers, where the exponential nature of refractivity becomes more apparent.

Recognizing that

$$\frac{d}{dr}(nr) = n(1 + \Gamma)$$

147

it is possible to approximate α for rays propagating between altitudes of r_1 and r_2 by

$$\alpha_1 \approx \frac{r_2 - r_1}{n_2 r_2 - n_1 r_1}$$

Another approximation for α is given by

$$\alpha_2 \approx \left[1 + \frac{\Gamma_1 + \Gamma_2}{2} \right]^{-1}$$

where Γ_1 and Γ_2 are the ray factors at r_1 and r_2, respectively.

The equations for α_1 and α_2 have comparable errors for elevation angles less than 1°, but α_2 is a better approximation for angles above 1°, especially for the surface to 10 kilometer region. A comparison between the two approximations is given in Table 60. It should be noted that the errors given in Table 60 are for unstratified atmospheres, such that $-0.5 \leq \Gamma \leq 0.0$ (i.e., normal propagation), where the refractivity can be approximated either by a linear or by an exponential fit. Larger errors generally occur for more negative values of Γ; this implies that extreme care should be taken when using these approximations in superrefracting atmospheres unless the elevation angle is adequately large (i.e., greater than 10°).

Table 60. Approximations to α.

Elevation Angle	Error			
	α_1		α_2	
	0 - 1 km	0 - 10 km	0 - 1 km	0 - 10 km
0°	1.0 - 3.2	4.2 - 9%	1.0 - 3.5%	< 2%
0.5°	< 1%	4.0 - 5.5%	< 1.8%	< 3%
1°	< 1%	4 - 5 %	< 1.5%	< 4.5%
>10°	< 0.04%	< 0.18%	< 0.9%	2 - 9%

Several remarks are in order concerning the refraction compensation transformation:

a. The factor of n in the radial component of the transformation is crucial. Although n is very close to unity, the gradient of n is comparable with r^{-1} so that this factor is important and should not be deleted.

b. The earth-center angle, θ, does not appear directly in the transformed coordinates. Therefore, extreme care should be taken in the use of the transformed earth-center angle, θ_s. This difference between θ and θ_s is not considered in the effective radius or effective earth's radius transformations.

c. The radius of the earth does not enter directly into the calculations of the transformed coordinates. The parameter r equals r_e + h and for a spherically stratified atmosphere is the radius of curvature of the surface of constant refractivity. This is the most serious defect in the effective earth's radius model. The same relative errors in altitude exist between the effective earth's radius and the refraction compensation transformations as between the effective earth's radius and the effective radius transformations [i.e., approximately $\Gamma/(1+\Gamma)$].

d. Although the evaluation of the parameter α does depend slightly upon angle ϕ, the dependence is nowhere near as great as indicated by the effective radius transformation, which is inaccurate except for low angles.

The effective earth's radius model, although in use for many years, is essentially in error. The techniques used to derive it do not produce a transformation that maps rays into straight lines. As a result, it is possible to obtain significant errors under certain applications. The refraction compensation transformation does produce transformed rays which have zero curvature. Also, the effects of the transformation on the earth-center angle, which are ignored in the effective earth's radius model, can be significant. In general, the author feels that the use of an effective earth's radius contains enough errors to justify its removal from use in the literature. The refraction compensation transformation presented here is used in MOSART; also it should be used to replace the effective earth's radius transformation whenever possible.

3.2 Refractivity

After defining the geometric aspects of refraction in MOSART, the model for the strength of the refraction is discussed. The index of refraction of a medium is defined to be

$$m = \sqrt{\varepsilon\mu} = n - ik\lambda/2\pi$$

where ε is the dielectric constant and μ is the magnetic permeability of the medium. The real part of the index of refraction, n, called the phase index, is the ratio of the speed of light in a vacuum to that in the medium, while the imaginary part of the index of refraction is the absorption index, k. For the earth's atmosphere, the real index does not normally exceed unity by more than 450×10^{-6}, so a parameter called refractivity is defined by

$$N = (n - 1) \times 10^6 \ .$$

3.2.1 Microwave Refractivity

For microwave frequencies below 30 GHz, the refractivity is given by Debye theory for polar and non-polar molecules as:

$$N = K_1 \, P_d/T + K_2 \, e/T + K_3 \, e/T^2 + K_4 \, P_c/T$$

where P_d is the atmospheric pressure of dry air, P_c is the partial pressure of carbon dioxide, e is the partial pressure of water vapor, and T is the atmospheric temperature. However, since in the troposphere (i.e., for altitudes less than 10 kilometers) the concentration of carbon dioxide by molecular weight is approximately 0.03 percent and since $K_4/K_1 \approx 5/3$, it is customary to combine the pressure of dry air, P_d, with the partial pressure of carbon dioxide, P_c, resulting in

$$N = K_1' \, P_t/T + K_2 \, e/T + K_3 \, e/T^2$$

where P_t is the total atmospheric pressure. Experimental data results in the following values for the constants.

$$K_1' \quad = 77.607 \pm 0.13 \qquad \text{K/mb}$$

$$K_2 \quad = 71.6 \pm 8.5 \qquad \text{K/mb}$$

$$K_3 \quad = (3.747 \pm 0.031) \times 10^5 \quad \text{K}^2/\text{mb}$$

3.2.2 Optical Refractivity

There exist several models of refractivity in the optical region (e.g., Edlen (1953), Edlen (1966), Owens (1967)). MOSART uses the Owens (1967) model defined by the dispersion relation

$$\frac{n^2 - 1}{n^2 + 2} = \sum_{i=1}^{3} R_i \, \rho_i$$

where the indices are:

1 - dry, CO_2-free air
2 - water vapor
3 - carbon dioxide

and

$$R_i = \frac{(n_o)_{i2} - 1}{(n_o)_{i2} + 2} \frac{1}{(\rho_o)_i}$$

The formulae for these values are given in Table 61.

It should be noted that the Owens (1967) formulae have been validated over the spectral region 0.36 - 0.64 µm, although parts of the formula are valid up to 2.0 µm.

MODTRAN uses the Edlen (1966) refractivity model, defined by

$$N = (n - 1) \times 10^6$$
$$= K_A \left(\frac{P}{P_o} \right) \left(\frac{T_o + 15}{T} \right) - K_B \frac{E}{P_o}$$

where

$$K_A = 83.42 + \frac{24052997}{129.96 + \sigma^2} + \frac{160.034}{38.938 + \sigma^2}$$

and $K_B = 43.49 - 0.346 \, \sigma^2$.

The similarity for the dry, CO_2-free Sellmeier formula (Table 61) and the K_A term indicates that the two models give essentially identical results. However, due to the improved dispersion and the inclusion of a CO_2-dependence in the Owens (1967) model, it was selected for use in MOSART.

Table 61. Refractivity Model.

	Range of Validity	Density ρi	Sellmeier Formula ($\sigma = 1/\lambda$)
Dry, CO_2-free Air	0.23 - 2.06 μm 240 K < T < 330K 0 < P < 4 atm	348.328 P_1/T {1 + P_1 x [57.90x10^{-8} - 9.4581x10^{-4}/T + 0.25844/T^2]}	$83.4078 + \dfrac{24056.40}{130 - \sigma^2}$ $+ \dfrac{159.94}{38.9 - \sigma^2}$
Water Vapor	0.36 - 0.64 μm 250 K < T < 320K 0 < P < 100 mb	216.582 P_2/T {1 + P_2 x [1 + 0.00037P_2] x [-2.37321x10^{-3} + 2.23366/T - 710.792/T_2 + 7.75141x10^4/T^3]	2.95325 + 0.026422σ^2 - 0.00032380σ^4 + 0.00004028σ^6
Carbon Dioxide	0.24 - 0.69 μm 240 K < T < 330K 0 < P < 17 mb	529.37 P_3/T	$228.221 + 1.178\sigma^2$ $+ \dfrac{24060.30}{130 - \sigma^2}$ $+ \dfrac{159.97}{38.9 - \sigma^2}$

3.2.3 Non-Standard Atmospheres

The use of mean and standard atmospheres has created much erroneous data and misconceptions concerning the propagation of radiation in the earth's atmosphere, since many operational personnel have treated these atmospheres as the most likely ones. Non-standard atmospheres which involve various anomalous effects are quite common in various parts of the world and have a significant effect

upon the propagation of electromagnetic waves. A study of these non-standard atmospheres is beyond the scope of this manual; however, certain propagation conditions can be classified:

Subrefraction:	$0.0 < \Gamma$
Normal refraction:	$-0.5 < \Gamma < 0.0$
Superrefraction:	$-1.0 < \Gamma < -0.5$
Trapping (ducting):	$\Gamma < -1.0$

where Γ is the ray factor defined by:

$$\Gamma = \frac{r}{n} \frac{dn}{dr}$$

where n is the phase index of refraction, which is assumed to be a differentiable function of r, and r is the radius of curvature of the surface of constant refractivity. It should be noted that this classification distinguishes between superrefraction and trapping. This distinction is not always made in the literature; however, due to the significant differences in propagation characteristics, it is felt that the distinction should always be made.

3.3 Line-of-Sight Geometries

Several line-of-sight geometries are calculated in MOSART. The primary geometry is the observer-source path which is defined in terms of the following parameters:

- Source altitude

- Observer altitude

- Slant range

- Ground range

- Source elevation angle

- Observer elevation angle

In general, the observer altitude and two other parameters are required to define the geometry uniquely.

For some of the angle specifications, an ambiguity exists between long and short paths, so the desired path must be specified. It should be noted that co-altitude paths are, by definition, long paths and must be so specified. If the slant or ground range is specified, the ray tracing solution does not exist in closed form. An initial estimate of the elevation angles is made using the refraction compensation transformation, and then a modified Newton-Raphson iterative technique is used to solve for the proper angles. The iterative technique is quite stable, with the logic built in to switch from short to long paths when required. In general, the iteration will solve for the elevation angles to produce a range (either slant or ground) within one meter of the requested value within 4 to 5 iterations; however, for extremely long grazing paths, word size on 32-bit machines may not permit accuracies much better than a few tenths of a percent of the total range.

All other geometries (e.g., observer-background, direct solar, scattered solar, reflected solar, earthshine, skyshine) are all defined internally within the code, using switches that are user defined.

3.4 Azimuths

There are two types of azimuths used in MOSART, namely those with a geographical reference (i.e., north is 0 degrees) and those with a solar/lunar (relative) reference (i.e., the solar direction is 0 degrees). All angles are measured in a clockwise direction from the reference direction when viewed from above, so east is 90 degrees and west is 270 degrees for the geographical reference. A user input variable selects whether a true or relative reference frame is desired.

Another user-selected reference is whether a source-centered or observer-centered reference is chosen. This selects which position (i.e., source or observer) is at the latitude and longitude given and whether the azimuths are measured relative to the source or the observer (see below).

The solar and lunar azimuths in MOSART always use the geographical reference. Their values can either be calculated by MOSART's ephemeris code or be input by the user.

For a relative reference, all other azimuths are defined using the sun as a reference, or if no solar direction is specified, the moon is used as a reference. If neither solar nor lunar directions are specified, the calculations are independent of azimuth, and a value of 0 degrees is arbitrarily chosen.

If a true reference is chosen all azimuths are relative to north.

154

One area of possible confusion in the definition of relative arises in distinguishing observer- and source-centered coordinate systems. The source-centered observer azimuth is defined in terms of the location of the observer relative to the source (and vice-versa for an observer reference). Thus an observer azimuth of 0 degrees refers to an observer positioned between the source and the sun and looking away from the sun; and an observer azimuth of 180 degrees refers to an observer looking toward the sun. However, for the earth/skyshine azimuths, 0 degrees is toward the sun, while 180 degrees is away from the sun. (Earth/skyshine calculations can only be requested for a source-centered reference and are not defined for an observer-centered reference.) In the observer-centered system, source and solar relative azimuths of 0 degrees means that the observer is looking toward the sun.

The one exception to the relative azimuths is the evaluation of the space background. The galactic and ecliptic coordinates are always obtained from the azimuth relative to the sun. However, since relative azimuth can be somewhat ambiguous with respect to the global reference frame, the determination of the space background can only be considered representative when relative azimuths are used.

3.5 Ephemeris Calculations

The solar and lunar ephemeris calculations implemented in MOSART are described below.

3.5.1 Celestial Coordinate Systems

In a description of the celestial mechanics of the solar system, usually four types of origins are considered.

a. Heliocentric systems: the origin is the center of the sun

b. Geocentric systems: the origin is the center of the earth

c. Topocentric system: the origin is the local observer

d. Barycentric system: the origin is the center of mass of the solar system

In the following, reference will be made to five types of coordinate systems. These are the horizon, hour angle, right ascension, orbital, and ecliptic systems. All of these systems have their origin at the observer. Due to the small radius of the

earth compared to its distance to the sun, unless otherwise stated, for solar calculations the origin of the observer is also assumed to be the center of the earth. For lunar calculations, this is not assumed. Each system is based on two reference planes perpendicular to each other. Table 62 gives these planes and the primary parameters defining a point in each system. Figures 137 to 141 also show these parameters.

Table 62. Coordinate System.

System	Reference Planes		Parameters	
horizon	horizon	meridian	zenith angle Z	azimuth A
hour angle or local equatorial	celestial equator	hour circle of observer's zenith	declination δ_s	hour angle h
right ascension or celestial equatorial	celestial equator	hour circle of equinox	declination δ_s	right ascension α
ecliptic	ecliptic	ecliptic meridian of the equinox	latitude β	longitude λ
orbital	ecliptic	orbital plane	orbital latitude β_o	orbital longitude λ_o

For reference, the celestial equator is the plane perpendicular to the direction of the North Celestial Pole. The meridian is a plane perpendicular to the equator and passing through the North Pole and the local zenith. The hour circle is a plane perpendicular to the celestial equator passing through the North Pole. The ecliptic is the lane in which the sun moves, while the equinoxes are the points on the celestial equator where the ecliptic plane crosses. The equinox at which the sun passes the celestial equator going from south to north is called the vernal equinox and occurs around March 21st. The equinoctial colure is the hour circle passing through the equinoxes.

O is the origin of the observer and S an arbitrary point on the celestial sphere.

3.5.1.1 Horizon System

Zenith Angle, Z, is the angle between the direction OS and the observer's zenith. The azimuth, A, is the angle between the vertical plane of S and the meridian measured from the North Pole to the east.

156
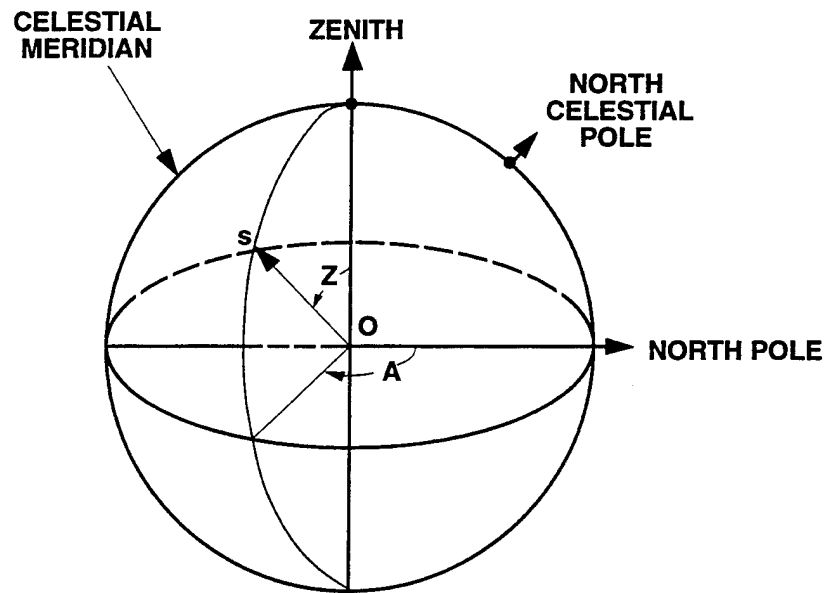
R-077-90.3-2 BC/Mac

Figure 137. Horizon System.
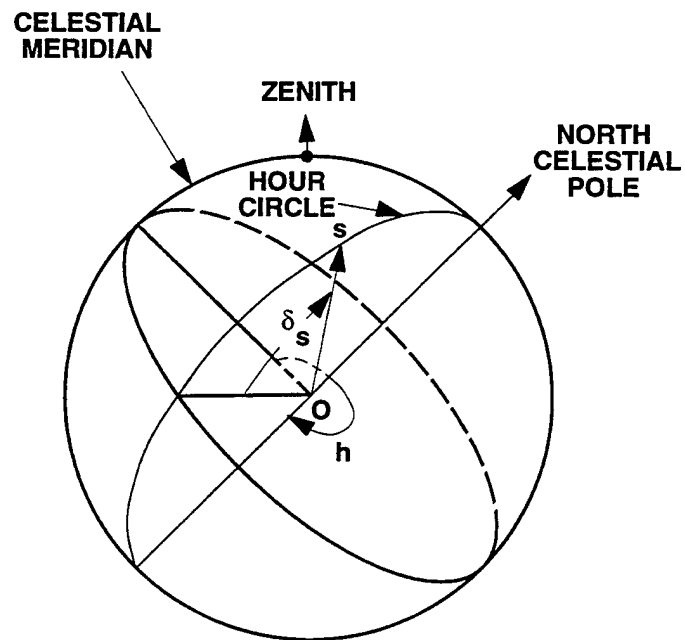
R-077-90.3-3 BC/Mac

Figure 138. Hour Angle System.

157

CELESTIAL
MERIDIAN

ZENITH

NORTH
CELESTIAL
POLE

EQUINOCTIAL
COLOR

HOUR
CIRCLE

VERNAL
EQUINOX

O

s

α

δs

ε

CELESTIAL
EQUATOR

ECLIPTIC

R-077-90.3-4 BC/Mac

Figure 139. Right Ascension.

NORTH
ECLIPTICAL
POLE

NORTH
CELESTIAL
POLE

s

ECLIPTIC
MERIDIAN

O
β

λ

ε

ECLIPTIC

VERNAL
EQUINOX

CELESTIAL
EQUATOR

R-077-90.3-5 BC/Mac

Figure 140. Ecliptic System.

158
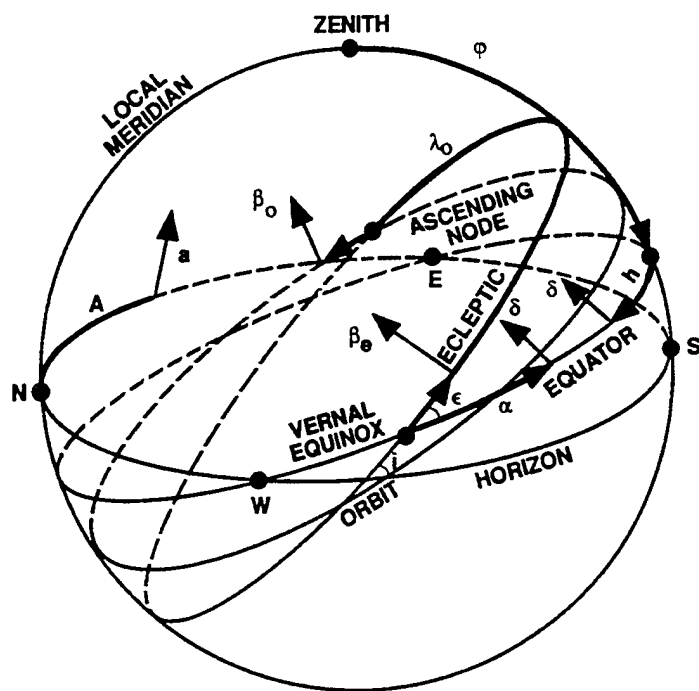
λ   = ecliptic longitude   δ = declination

$β_e$ = ecliptic latitude   h = local hour angle

ε   = obliquity of the ecliptic   A = azimuth

$λ_o$ = orbital longitude   a = altitude

$β_o$ = orbital latitude   ℓ = geographic latitude

i   = inclination of the orbit   (angles ε and i are not drawn on scale)

α   = right ascension

Figure 141. Coordinate System.

159

3.5.1.2 Hour Angle System

Declination, δ_s, is the angle between the direction OS and the celestial equator. It is positive if toward the North Pole and negative if away from it. The hour angle, h, is the angle between the hour circle of S and the hour circle of the observer (the celestial meridian). It is measured to the west (i.e., in the direction of S's apparent daily motion).

3.5.1.3 Right Ascension System

Right Ascension, α, is the angle between the hour circle of S and the hour circle of the vernal equinox (equinoctial colure). It is measured from the vernal equinox to the east in the plane of the celestial equator. The declination, δ_s, is the same as defined in the hour angle system.

3.5.1.4 Orbital System

This system is used for the moon.

Orbital longitude, λ_o, is measured in the orbital plane. The orbital longitude of the moon is measured from the vernal equinox along the ecliptic eastwards to the ascending node, and then along the orbit. The node is the point of intersection of the orbit and the plane of the ecliptic; the ascending node is passed by the moon from south to north. Orbital latitude, β_o, is measured perpendicular to the orbital plane (e.g., of the moon), positive is to the north. The inclination, i, of the orbit is defined as the angle between the orbital plane and the ecliptic.

3.5.1.5 Ecliptic System

The (ecliptic) latitude, β, is the angle between the direction OS and the ecliptic measured in the ecliptic meridian of S. It is positive if north of the ecliptic and negative if south. The (ecliptic) longitude, λ, is the angle between the ecliptic meridian of S and that of the equinox meridian (vernal equinox) measured to the east.

The vernal equinox is the point where the orbit of the sun intersects the equatorial plane of the earth from south to north; sometimes it is called the First Point of Aries.

The angle between the celestial equator and the ecliptic is referred to as the obliquity of the ecliptic, ε.

One coordinate, the distance of an object, is the same for all these geocentric coordinate systems. Instead of the distance between the earth and a celestial body, sometimes the equatorial horizontal parallax is used, that is, the ratio of the equatorial radius of the earth and the distance. The average value of the parallax is called the mean parallax.

3.5.1.6 Coordinate System Conversion

The base equations are in terms of the longitude, λ, and latitude, β, (ecliptic system) of the sun.

The declination, δ_s, and right ascension, α, may be obtained from λ and β by

$$\sin\delta_s = \cos\beta\sin\lambda\sin\alpha + \sin\beta\cos\varepsilon$$

$$\cos\delta_s\cos\alpha = \cos\beta\cos\lambda$$

$$\cos\delta_s\sin\alpha = \cos\beta\sin\lambda\cos\varepsilon - \sin\beta\sin\varepsilon$$

In general, β is on the order of 1" ($0°.0028$), so that

$$\sin\delta_s \approx \sin\lambda\sin\varepsilon$$

$$\tan\alpha \approx \tan\lambda\cos\varepsilon$$

Referring to Figure 142, where ST, the Local Sidereal Time, is defined as the hour angle of the vernal equinox, then,

$$h = ST - \alpha$$

To convert the horizon system,

$$\cos Z = \sin\delta_s\sin\phi + \cos\delta_s\cos\phi\cos h$$

and

$$\cos A = \frac{\sin\delta_s\cos\phi - \cos\delta_s\sin\phi\cos h}{\sin Z}$$

where ϕ is the astronomic latitude of the observer defined in the hour angle system (i.e., using the celestial equator and the North Pole as references).

NORTH CELESTIAL POLE

CELESTIAL MERIDIAN

EQUINOCTIAL COLOR

VERNAL EQUINOX

h

α

ST

HOUR CIRCLE
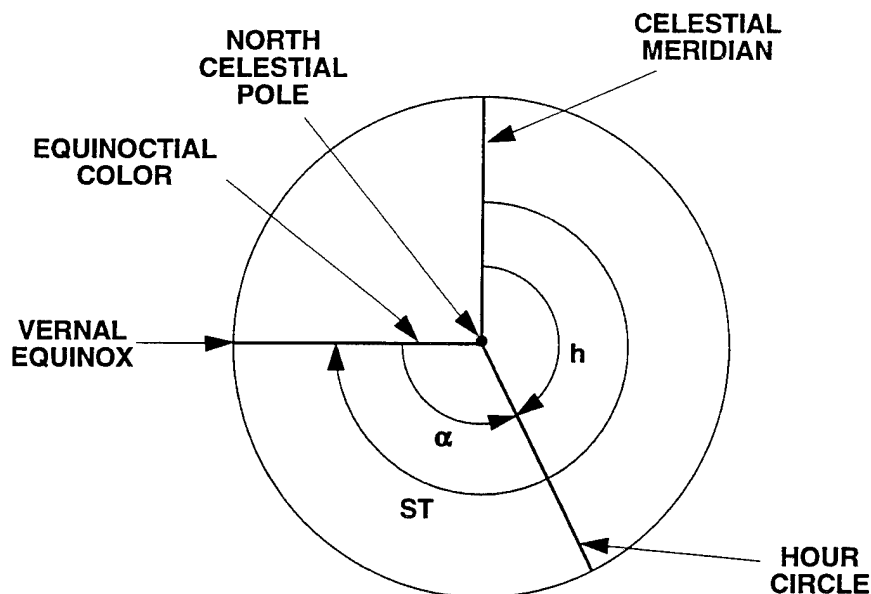
R-077-90.3-7 BC/Mac

Figure 142. View of the Plane of the Celestial Equator Viewed from the North Celestial Pole.

A relation between the ecliptic longitude λ_e, ecliptic latitude β_e, and inclination of the orbit i, and the ecliptic longitude of the ascending node Ω, is derived from spherical trigonometry, namely, $\tan \beta_e = \tan i \sin (\lambda_e - \Omega)$.

3.5.2 Systems of Time Measurement

There are two fundamentally different measurements of time, Ephemeris and Universal. When Newcomb (1895) first constructed his tables, these two were thought to be identical. However, more precise measurements of the earth's years and daily rotation have shown that the two systems are different and that this difference is constantly changing. At the beginning of 1979 their difference was on the order of 50 sec.

3.5.2.1 Ephemeris Time

Ephemeris Time, ET, is theoretically uniform, depending for its determination on the laws of dynamics. It is the independent variable in the theory of motion of

162

the sun, moon, and planets and is the basis used in the construction of the tables in the Nautical Almanac (1974).

Ephemeris time is measured from an epoch which is designated 1900 January 0^d 12^h ET. This instant is defined to be that time when the mean longitude of the sun, referred to as the mean equinox of date, was 279° 41' 48".04.

The primary unit of ephemeris time is defined as the interval during which the sun's mean longitude, referred to the mean equinox of date, increases by 360°. The measure of this unit is determined by the coefficient, T, measured in centuries of 36,525 ephemeris days.

3.5.2.2 Universal Time

Universal Time, UT, is the precise measure of time used as the basis of all civil time keeping: it conforms very closely to the mean diurnal motion of the sun. It is changed at periodic intervals (1 to 2 times per year) in order to stay in synchrony with the changing diurnal rotation of the earth. Universal time may be identified with Greenwich Mean Time, GMT.

The difference, ΔT, between Ephemeris and Universal time is constantly changing and is tabulated yearly in the Nautical Almanac (1974). The difference is defined as:

$$\Delta T = ET - UT \ .$$

A plot of ΔT between 1940 and 1980 is given in Figure 143.

The following points should be understood:

First, the ephemeris algorithms technically must use ephemeris time, ET, in computing the solar longitude and latitude in order to duplicate the answers in the Nautical Almanac (1974).

Second, given the correct apparent longitude and latitude or right ascension and declination, Universal Time, UT, must be used in computing the correct hour angle (which is based on the earth's reaction).

In the algorithm it is assumed that ΔT has little effect on the computed solar longitude and latitude to the degree of accuracy normally required. Sample calculations have shown that a difference of ΔT of 40 seconds leads to errors in the computed apparent solar longitude on the order of 2". This error propagated in the
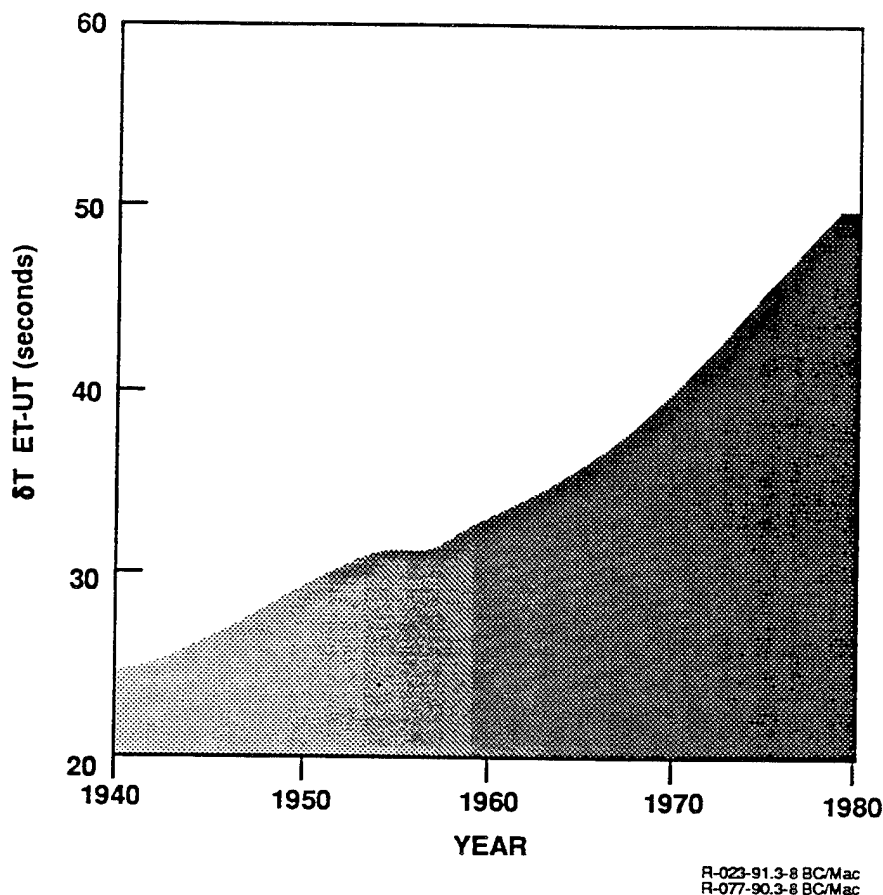
Figure 143. Change in Variation Between Ephemeris Time and Universal Time.

computation of the two quantities, declination and equation of time, yields errors on the order of 0".1 and 0".005, respectively.

3.5.2.3 Date and Time Conventions

As mentioned in the last section, the algorithm uses the quantity T as an argument in computing the ephemeris. T is the ephemeris time since 1900 January 0^d 12^h ET. In order to facilitate keeping track of dates, Julian Day Numbers are used in computing T. This number is defined to be 0 for the day starting at Greenwich mean noon on January 1, 4713 B.C.

For 1900 January 0^d 12^h ET the Julian Date is 2415020.00. There are a number of algorithms available to compute the Julian Date. The algorithm used by MOSART has been checked for the years 1750 to 2100. Further extension should be checked by the individual user.

Universal Time, UT, (or Greenwich Mean Time) is defined as

$$UT = h_m{}^G + 12^h$$

where $h_m{}^G$ is the hour angle of the mean sun referred to the Greenwich meridian. Also,

$$GTT = h_s{}^G + 12^h$$

is the Greenwich apparent (true) solar time where $h_s{}^G$ is the hour angle of the apparent (true) sun referred to the Greenwich meridian. Notice should be made of the earlier defined quantity ST. ST, the apparent (true) sidereal time, is equal to h_s. The quantity Eq.T, sometimes called the equation of time, is the difference between the true and mean solar times. Thus,

$$Eq.T = GTT - UT = h_s{}^G - h_m{}^G \quad .$$

For any other meridian located at longitude Λ, referenced to the Greenwich meridian, Local Mean Time, LMT, is defined as

$$LMT = UT - \Lambda = h_m{}^G + 12^h - \Lambda \quad .$$

Note also that the local mean angle of the mean sun, h_m, referred to the meridian at Λ, is

$$h_m = h_m{}^G - \Lambda \quad .$$

Thus,

$$LMT = h_m + 12^h \quad .$$

To facilitate civil timekeeping, local mean time is usually referred to standard meridians 15° apart in longitude. Thus, Local Standard Mean Time, LSMT, is defined as

$$LSMT = UT + \Delta Z * i$$

where $\Delta Z = 15° = 1^h$, and
        $i = 1, 2, ..., 12$ if meridian to the east of Greenwich
        $i = -1, ..., -12$ if meridian to the west of Greenwich

165

To convert the local mean time, LMT, from local standard mean time, LSMT, the equation

$$LMT = LSMT + 15° * sign(\Lambda) * int \left(\frac{7.5° + |\Lambda|}{15°} \right) - \Lambda$$

is used.

The function sign(x) extracts the algebraic sign of x. The function int(x) extracts the integral part of x.

Care should be taken that the proper units are used. Thus, LMT and LSMT are usually expressed in terms of fractions of days, or in hours, minutes, and secs, while the second term as written is usually in degrees. All three variables must have the same units.

This equation assumes that the standard time zones are 15° apart. In some parts of the world (e.g., the continental United States), standard time zones do not follow these 15° intervals. The algorithm as now written assumes the 15° intervals. Thus care should be taken in entering standard correct time.

In computing local zenith and azimuth angles, it is necessary to know the apparent (true) local hour angle, h_s. One can compute h_s given the observer's meridian Λ, the local standard time LSMT and the Eq.T. Thus,

$$h_s = Eq.T + LSMT + 15° * sign(\Lambda) * int \left(\frac{7.5° + |\Lambda|}{15°} \right) - \Lambda - 12^h$$

The relation between Greenwich mean sidereal time GMST, and UT is not exactly linear because of the variable rotation of the earth, but within good accuracy a linear approximation can be made from the reference date 1977 Jan 1 0h00 UT (noted as 1977.0):

$$h_{ARIES,G} = n_A(t - t_{1977.0})$$

where $h_{ARIES,G}$ = Greenwich hour angle (GHA) of the mean vernal equinox = GMST (expressed in radians), t is reckoned in mean solar days. When y_t is the number of mean solar days in a tropical year, it is easy to see that the number of sidereal days

166

during this tropical year is $y_t + 1$, so the daily rate of motion of the GHA of the mean equinox is:

$$n_A = 2\pi \frac{y_t + 1}{y_t} \qquad \text{radians/mean solar day}$$

The value of y_t is given by the Astronomical Ephemeris

$$y_t = 365^d \ 05^h \ 48^m \ 46^s.0 - 0^s.530 \ T \ ,$$

where $T = d/36,525$ is the number of Julian centuries from 1899 Dec. 31 at 12 noon ET, and d is the number of ephemeris days since this date. The expression for y_t is one of a set of formulae, derived by Newcomb in 1895, which are still used by the Astronomical Ephemeris for the calculation of relevant solar data. Similar formulae have been derived for lunar data. In all these formulas T and d are expressed in ephemeris time; there is, however, one exception, namely Newcomb's formula for the Greenwich hour angle of the mean vernal equinox (GMST) at 0 h UT

$$h_{ARIES,G,0h \ UT} = 6^h 38^m 45^s.836 + 8640184^s.542 \ T_U + 0^s.0929 \ T_U^2 \ ,$$

where $T_U = d_u/36,525$; d_u is expressed in universal days and differs from d by ΔT (expressed in days) as defined earlier.

3.5.3 Solar Ephemeris

This section has been extracted from Wilson (1980).

The motion of the earth around the sun may be described by an ellipse using Kepler's equations. In Figure 144, the ellipse APB in which a planetary body moves is plotted with its auxiliary circle AXB. C is the center of the circle while S is one of the foci of ellipse APB.

Because the body is moving in an ellipse, its motion about C is not uniform (i.e., it speeds up or slows down depending on its orbital position). The angle M is defined as the angle which would have been described by the radius vector if it had moved uniformly with the average rate. It is referred to as the mean anomaly, M, and is the angle ASX. The angle ACX is defined as the eccentric anomaly, E, while the actual angle (position of the body at P) is ASP and is called the true anomaly, V. Notice should be made that the anomalies M, E, and V are measured with respect to the perihelion of the orbit.

167
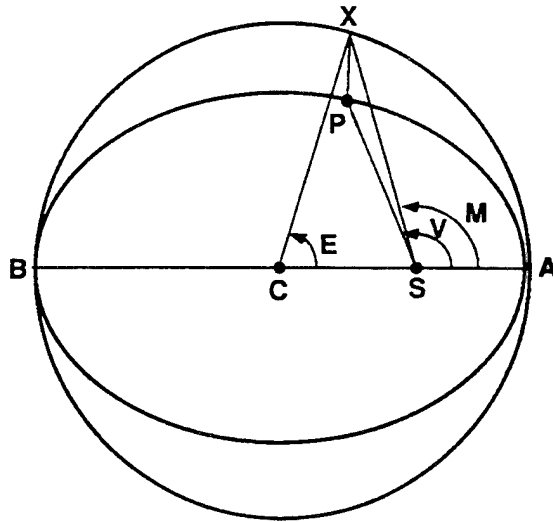
R-023-91.3-9 BC/Mac
R-077-90.3-9 BC/Mac

Figure 144. Kepler's Equations for Planetary Motion.

Standard orbital theory yields the relation

$$M = E - e*\sin E.$$

where e is the eccentricity of the electrical orbit. The equation is referred to as Kepler's equation. It can further be shown that

$$V = 2*\tan^{-1} \frac{\sqrt{1+e}}{\sqrt{1-e}} * \tan \frac{E}{2}$$

where again V is the true anomaly.

The quantity V - M is referred to as the equation of centers. Before computers allowed the quick and easy solution of Kepler's equation, much effort was devoted to developing methods of computing the quantity V - M.

The position of the sun in the ecliptic with respect to the vernal equinox is the sum of the mean longitude, L (i.e., the position of a uniformly moving sun), and the equation of centers, V - M. Thus,

$$\Lambda = L + (V - M) \ .$$

168

If the earth and the sun were strictly a two-body system, this equation would accurately describe the longitude of the sun. However, due to the gravitational effects of other celestial bodies such as the moon and planets, the celestial equator and ecliptic are continuously in motion.

The motion of the equator contains two components due to the solar and lunar gravitational effects on the earth. The first is a smooth long-period motion of the mean pole of the equator about the pole of the ecliptic with a period of about 26,000 years. This is referred to as general precession, P. The other component is the motion of the true pole around the mean pole. This is referred to as nutation. Besides these two, there are other second order perturbations due to the planets and moon.

Since the solar position is referenced to the intersection of the ecliptic with the celestial equator (the vernal equinox), the motion of the equinox due to precession will not affect the computation of solar position for a particular date. However, if the solar position needs to be referenced to an earlier or later date when the equinox was at a different location in space, then correction of the solar longitude and latitude for precession needs to be made. This is the reason that the entries in the Nautical Almanac and the computations described below all refer to "mean equinox of date". This means that the quantities are referred to the equator and equinox for the particular date specified.

Typically one finds that celestial positions are referred to either the beginning of the year (i.e., mean equinox of 1979.0), or to the standard equinox of 1950.0. The rate of precession, ψ, is approximately 50'/year. The algorithm used in MOSART gives solar position referred to the equinox of date and also computes the precession in longitude from the beginning of the year to date.

Nutation is mainly due to the orbital characteristics of the moon. It affects longitude, and the resultant quantity is referred to as nutation in longitude $\Delta\psi$. Its effect is on the order of 17". The lunar motion also affects the obliquity of the ecliptic and is referred to as nutation in obliquity, $\Delta\varepsilon$. It is on the order of 9". The numerical series for $\Delta\psi$ and $\Delta\varepsilon$ consist of 69 and 40 terms respectively. The principle term for longitude has an amplitude of 17".2327 and obliquity 9".21, the period being 6798 days (18.02 years). The amplitude 9".21 is known as the constant of nutation. The degree of accuracy required will dictate the number of terms used in the series. The moon also has an effect on the solar position due to its mass. This effect has the label $\Delta\lambda_m$ for longitude and is on the order of 6". The similar perturbation for solar latitude is $\Delta\beta$ and is on the order of 1".

All of the planets have an effect on solar position, mainly on longitude. The perturbations have the form

$$S \cos(K - jg' - ig) \ ,$$

where S and K are constants and g and g' are the mean anomalies of the sun and particular planet. They are typically on the order of 1 - 10". Due to their planetary masses, the planets also produce what are termed inequalities of long period in the mean longitude. These are referred to by the symbol δL and are on the order of 7".

Because the velocity of light is finite, it takes approximately 8.3 minutes for the light from the sun to reach earth. This corresponds to a change in solar longitude of approximately 20".47. This constant is defined as the constant of aberration and the aberration correction is defined as

$$\Delta\lambda_A = -20".47/R$$

where R is the radius vector which has a value of 1 at the mean solar-earth distance.

Due to the fact that Earth has a finite radius, the apparent position of the sun viewed from the earth's surface will be displaced from the computed position, which assumes an observing point at the earth's center. This shift, referred to as parallax, ΔZ_p, is, for all practical purposes, a small first order correction to the computed zenith angle. It may be computed by the equation

$$\sin\Delta Z_p = \sin\pi{}^*\sin Z \ ,$$

where Z is the apparent solar zenith angle and π the horizontal parallax. For the sun,

$$\pi = 8".794/R$$

where R is the radius vector, so ΔZ_p can thus be approximated by

$$\Delta Z_p = \pi{}^*\sin Z \ .$$

As is evident, parallax is a very minor correction amounting to at most about an 8".9 (0°.0025) shift in zenith angle, and thus can almost always be ignored.

The accuracy of the solar ephemeris algorithm depends ultimately on the number of terms used for the perturbation effects. In order to give some insight into

the degree of accuracy achievable, this section will explore the effect of the various component parts on the final result.

The value of major concern is the apparent zenith angle Z. This value is a function of declination δ_s, observer latitude ϕ and solar hour angle h_s. Thus,

$$\cos Z = \sin\delta_s \sin\phi + \cos\delta\cos\phi\cos h_s \quad .$$

We also know

$$h_s = h_m + Eq.T = h_m + \alpha_m - \alpha$$

or, combining known quantities

$$h_s = LMT - \alpha - \Lambda + C \quad .$$

Thus taking derivatives and assuming the maximum possible error for each component, one obtains

$$\Delta Z \approx \Delta\delta_s + \Delta\alpha + \Delta LMT + \Delta\Lambda + \Delta\phi \quad .$$

Note that the maximum possible error will not occur simultaneously for each of the components. The maximum error $\Delta\Lambda$ will occur when $\phi = 0$; the maximum error $\Delta\delta_s$ will occur when $\phi = 0$ and $\delta_s = 0$, but $h_s = 0°$ or $90°$. Performing the analysis in this manner, however, illustrates the relative importance of each component.

The present requirements for the algorithm have been to compute ΔZ to within $0°.1$ or $6'$. If this error is then divided proportionally among the five components, each must have maximum errors of $0°.02$ or $72''$.

Since $0°.02$ of latitude is 1.2 nautical miles, the required latitude determination is fixed. A longitude increment of $0°.02$, in terms of surface distance, is given by

$$0°.02/\cos\phi \quad .$$

However, the maximum error $\Delta\Lambda$ is proportional to $\cos\phi$, so that again a determination of Λ to within 1.2 nautical miles will give the requisite accuracy.

A change in arc degrees of $0°.02$ in zenith angle is equivalent to 4.8 seconds of time. Again, this is proportional to $\cos\phi$, so that at higher latitudes this requirement is relaxed.

From declination one obtains

$$\sin\delta_s = \sin\lambda * \sin\varepsilon \ ,$$

and therefore

$$\Delta\delta_s = \frac{\sin\lambda\cos\varepsilon}{\cos\delta_s}\Delta\varepsilon + \frac{\cos\lambda\sin\varepsilon}{\cos\delta_s}\Delta\lambda$$

Since ε, the obliquity, is on the order of $23°.5$, the maximum error for $\Delta\varepsilon + \Delta\lambda$ is on the order of

$$\Delta\delta_s = \Delta\varepsilon + 0.4\text{x}\Delta\lambda \ .$$

For $\Delta\delta_s = 0°.02$, and dividing maximum error proportionally,

$$\Delta\varepsilon = 36"$$

and

$$\Delta\lambda = 90' = 1'30" \quad .$$

Right ascension α is computed as

$$\tan\alpha = \tan\lambda\cos\varepsilon$$

or

$$\Delta\alpha = \frac{\sec^2\lambda\cos\varepsilon}{\sec^2\alpha} * \Delta\lambda + \frac{\tan\lambda\sin\varepsilon}{\sec^2a} * \Delta\varepsilon$$

Putting in values for maximum error, the relationship

$$\Delta\alpha = \Delta\lambda + 0.7*\Delta\varepsilon$$

is obtained.

For $\Delta\alpha = 0°.02$ and dividing the maximum error proportionally,

$$\Delta\varepsilon = 90" = 1'30"$$

and

$$\Delta\lambda = 36"$$

The analysis of errors due to declination and right ascension shows that, in general, for $\Delta Z = 0°.1$, the error in obliquity $\Delta\varepsilon$ should be less than 36". This is also true for the error in solar longitude $\Delta\lambda$.

The major source of error in obliquity is the inclusion of the nutation of obliquity $\Delta\varepsilon$. Addition of all of the coefficients for nutation of obliquity gives the sum of 10".04. If the four highest terms are summed, the value of 9".94 is obtained. Thus the maximum possible error is not 36" but on the order of 10". If the four largest terms for nutation of obliquity are used this reduces the maximum error to 0".1. Therefore the maximum error for longitude $\Delta\lambda$ may be increased to 62" or 72".

The errors in the computation of longitude are listed in Table 63 along with the corrections used in the present algorithm.

Table 63. Solar Longitude Errors.

	All Corrections	Algorithm Corrections	# of Terms
Nutation of Long $\Delta\psi$	19".36	19".03	5
Moon perturbation of long $\Delta\lambda_m$	7".34	7".34	7
Inequalities of Long Period δL	9".84	9".84	5
Perturbations of Planets			
VENUS	17".57	16".11	6
MARS	7".02	5".60	6
JUPITER	15".65	14".71	5
SATURN	1".04	0".74	2
TOTAL	77".82	73".37	

It can be seen that the maximum error $\Delta\lambda$ is about 78". This is just 16" higher than the maximum allowable error of 62" from $\Delta Z = 0°.01$. Since this is the maximum allowable error, the computation of λ without any nutation and perturbation corrections should allow Z to be computed to within $0°.1$ under most conditions. The addition of the nutation terms in the obliquity and longitude calculations using only

173

those 9 terms used in the present algorithm will reduce the maximum allowable error in longitude to 49" which is well within the requirement.

The use of all the terms for nutation and perturbations in the present algorithm reduces the error in longitude computation on the order of 4".5. This degree of accuracy is far greater than is needed for most applications. Their inclusion merely illustrates the technique required for a highly accurate solar ephemeris.

Figures 145 through 147 show solar elevation, azimuth, and normalized distance observed from 30° N Latitude, 0° Longitude during the month of June 1974.
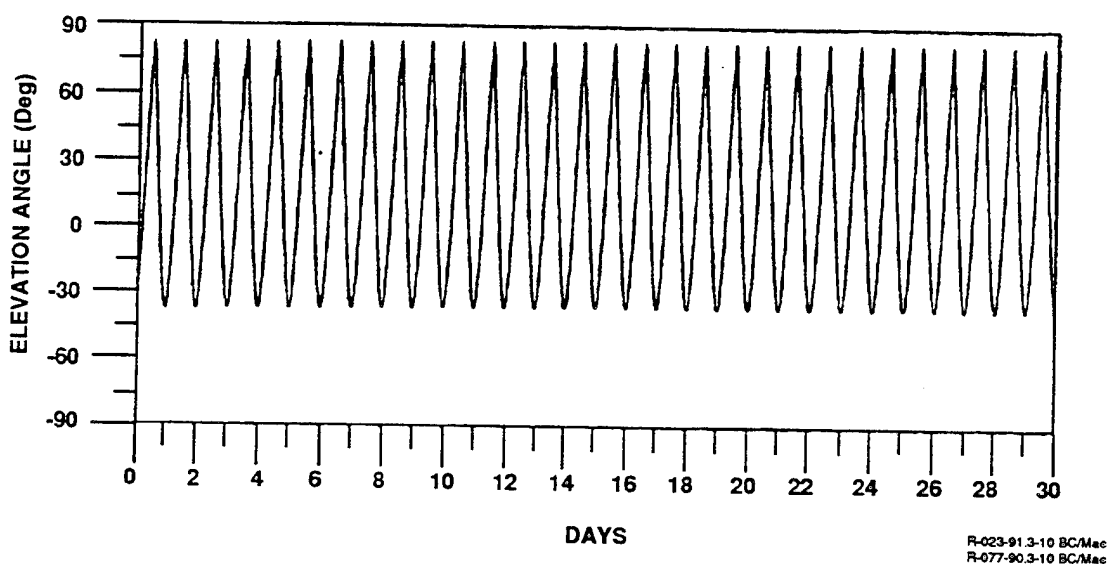
Figure 145. Solar Elevation. 30° N. Latitude, 0° Longitude. June 1974.
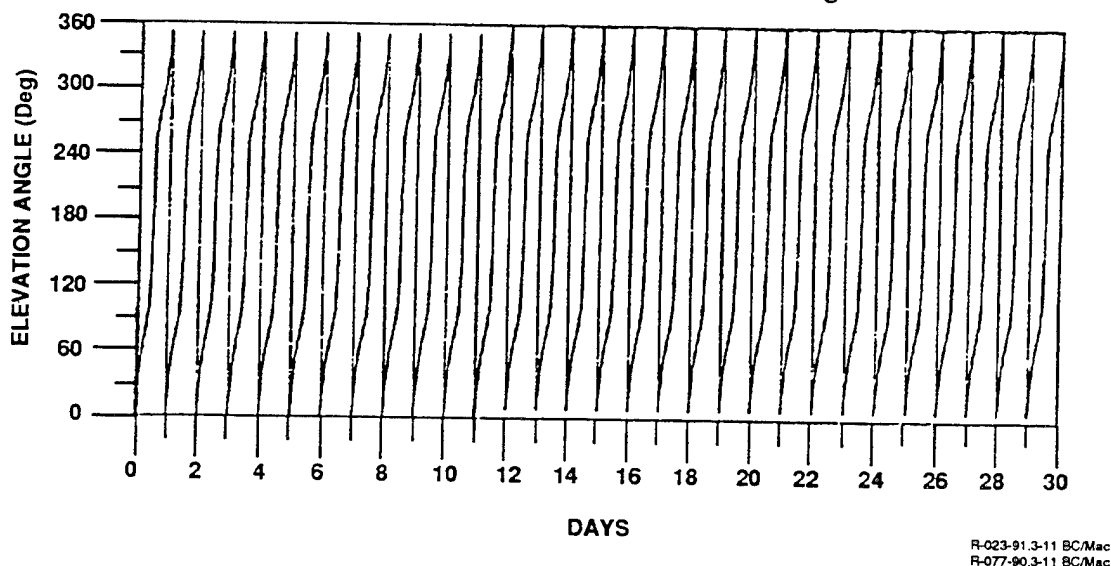
Figure 146. Solar Azimuth. 30° N. Latitude, 0° Longitude. June 1974. (Note: Sampling is every 30 minutes, resulting in poor definition near 0° and 360°.)

174
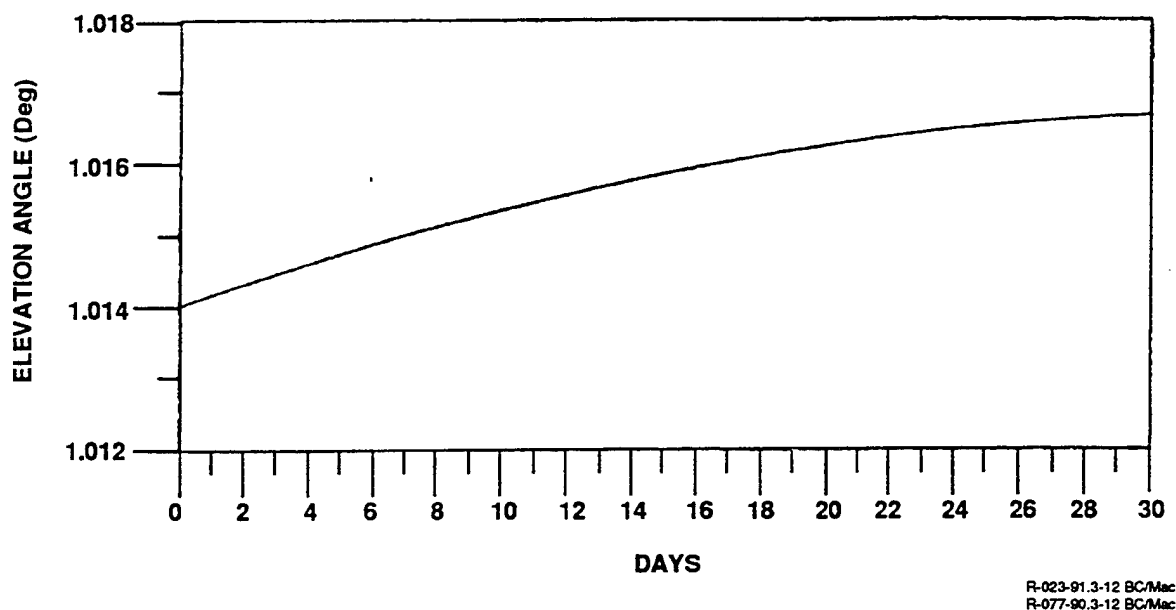
Figure 147. Normalized Solar Distance 30° N. Latitude, 0° Longitude.
June 1974.

3.5.4 Lunar Ephemeris

The orbit of the moon, relative to the earth, can also be approximated by a plane ellipse. The orbital plane makes a small angle with the ecliptic; this angle is called the inclination of the moon's orbit. The nodes of the moon defined as the points of intersection of the orbit and the plane of the ecliptic, the ascending node is passed from south to north, and the descending node from north to south. The points of minimum and maximum distance from the earth are called the perigee and the apogee of the orbit of the moon. The mean elements of the moon, defined analogous to those of the sun, can be calculated from a set of extrapolation formulas:

(i)   Mean orbital longitude (relative to mean equinox)

$$\lambda_{o,m} = 270°.434358 + 13°.17639\ 6528d - 0°.001133T^2 + 0.°.00000\ 19T^3$$

(ii)   Mean orbital longitude of the perigee (relative to mean equinox):

$$\Gamma_m = 334°.329653 + 0°.11140\ 40803d - 0°.010325T^2 - 0°.000012T^3$$

175

(iii)　　Mean ecliptic longitude of the ascending node (relative to mean equinox):

$$\Omega_m = 259° \ 183275 - 0°.05295 \ 39222d + 0°.002078T^2 + 0°.000002T^3$$

(iv)　　Eccentricity:

$$e_m = 0.05490 \ 0489$$

(v)　　Inclination:

$$1/2 \sin i_m = 0.04488 \ 6967$$

(vi)　　Mean parallax:

$$P_{m,mean} = 57'02''.608$$

T and d are defined in the same way as in Section 3.2.

　　　Comparison of the order of magnitude of the motion of the lunar perigee, β_m, and of the lunar node, γm, (periods resp. about 9 and 18 years) with that of the solar perigee, β_s, (period about 20,000 years) shows that the variations included in the mean elements of the moon are much faster than those of the sun. This is caused by the strong influence of the sun on the orbit of the moon. For the same reason the periodic perturbations in the orbit of the moon, caused by the sun, are too large to be neglected. E.W. Brown (1919) has made an extensive calculation on this subject, resulting in his "Tables of the Motion of the Moon". These tables contain a number of periodic correction terms for the longitude, latitude, and parallax of the moon, to be added to the mean elements.

　　　To find a selection criterium for the 391 correction terms for the longitude it was required (more or less arbitrary) that the sum of the amplitudes of the excluded terms should be less than 1' (the average error is then much less than 1', because the terms partially neutralize each other). This leads to a reasonable number of 40 terms for the longitude, when the terms less than 3" are neglected. Of the 185 correction terms for the parallax, the terms less than 0.6" were neglected, which resulted in 13 remaining terms. The sum of the unused terms for the parallax is then 5", which is 0.15% of the total parallax. E.W. Brown also calculated a number of terms of planetary perturbations, which have been neglected. The sum of the amplitudes of the planetary terms in longitude, for example, is about 0.75'.

For the application of Brown's correction terms it is necessary to define l_m, l_s, F and D with the equations:

$$l_m = \lambda_{o,m} - \Gamma_m$$

$$l_s = \lambda_{e,s} - \Gamma_s$$

$$F = \lambda_{o,m} - \Omega_m$$

$$D = \lambda_{o,m} - \lambda_{e,s}$$

Then the correction for the longitude can be written in the form:

$$\sum_i a_i \sin(k_{i1}l_m + k_{i2}l_s + k_{i3}F + k_{i4}D)$$

The latitude correction has the same form; for the correction of the equatorial horizontal parallax we write:

$$\sum_i a_i \cos(k_{i1}l_m + k_{i2}l_s + k_{i3}F + k_{i4}D)$$

The amplitudes a_i and the integers k_{i1}, k_{i2}, k_{i3}, k_{i4} are listed in Brown's tables, for each correction term in longitude, latitude and parallax.

The correction terms for the longitude include the eccentricity of the orbit and reduction to the ecliptic, so addition of these terms to the mean orbital longitude λ_m directly gives the corrected ecliptical longitude of the moon.

There are two possibilities for calculating the corrected latitude. The method chosen (for reasons of efficiency) starts with computing the corrected ecliptic longitude, then calculating the latitude by applying a transformation formula followed by the addition of the latitude correction terms. The other method also uses these latitude correction terms, but combined with another set of correction terms, also produced by Brown, which makes it possible to calculate the corrected latitude directly from the mean orbital longitude.

The correction terms for the parallax also includes the eccentricity of the orbit. The corrected parallax is constructed by adding the correction terms to the mean parallax.

The corrected ecliptical coordinates of the moon can be transformed to the altitude and azimuth. Since the azimuth, altitude and distance is desired as seen by the local observer, the geocentric coordinates must be converted into topocentric coordinates, to bring a local parallax effect into account. The effect does not change the azimuth. The corrected altitude and equatorial parallax (ratio of the equatorial radius of the earth and the distance from the local observer to the center of the moon) are calculated using

$$p' = \frac{p}{1 - p \sin q}$$

$$a' = a - p' \cos a$$

Where a, p and a', p' are respectively the uncorrected and the corrected altitude and parallax. The corrected distance, relative to the mean distance, then follows as:

$$r_m = p_{mean}/p_{corr}$$

For the calculations of lunar illumination and eclipse prediction it is useful to define three quantities which give information about the spatial configuration of sun, moon, and earth (Figures 148 through 151).
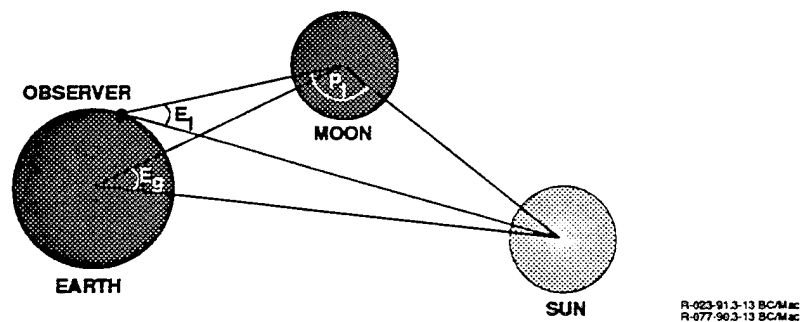
Figure 148. Definition of Elongations and Phase.
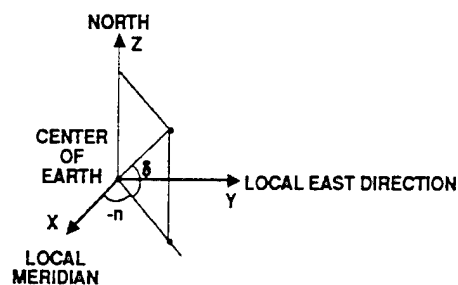
Figure 149. Calculation of the Geocentric Elongation.
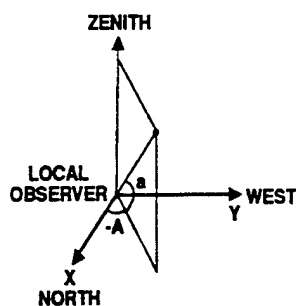
Figure 150. Calculation of the Local Elongation.
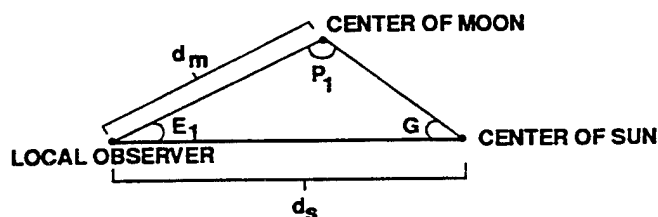
Figure 151. Calculation of the Local Phase.

a. The geocentric elongation (E_g) is the angle between the directions of the centers of sun and moon, as seen from the center of the earth. The geocentric elongation is approximately zero at new moon, then increases to approximately 180 degrees at full moon and then decreases to approximately zero at new moon. The times of new and full moon are defined as the times when the difference between the apparent geocentric longitudes of sun and moon is resp. 0° and 180°. The geocentric elongation is important for the description of a lunar eclipse.

b. The local elongation (E_1) is defined in the same way as the geocentric elongation, but as seen from the place of the observer. The local elongation is used in a description of a solar eclipse.

c. The local phase P_1 of the moon is the angle between the directions of the center of the sun and the place of the observer on earth as seen from the center of the moon. The sign of the phase is taken so that it is approximately 0 degrees at new moon, grows to approximately 180 degrees at full moon, then grows to

179

approximately 360 degrees at the next new moon. The phase is used as a measure of the illuminated part of the moon's disc, and is therefore important for the calculation of the illumination on the earth by moonlight.

For the calculation of the geocentric elongation, a rectangular coordinate system is defined with the origin in the center of the earth, the z-axis along the rotation axis of the earth, and the x-axis pointing to the local meridian. The rectangular geocentric coordinates of the sun and the moon are:

$$x_s = \cos h_s \cos \delta_s \qquad x_m = \cos h_m \cos \delta_m$$

$$y_s = -\sin h_s \cos \delta_s \qquad y_m = -\sin h_m \cos \delta_m$$

$$z_s = \sin \delta_s \qquad z_m = \sin \delta_m$$

where h_s, h_m, δ_s, and δ_m are respectively the local hour angles and declinations of sun and moon. Since the vectors $\bar{x}_s = (X_s, Y_s, Z_s)$ and $\bar{x}_m = (X_m, Y_m, Z_m)$ both are unit vectors, their scalar product is equal to the cosine of the angle between the vectors:

$$\cos E_g = X_s X_m + Y_s Y_m + Z_s Z_m$$

In a similar way we compute the local elongation. In this case a rectangular coordinate system is chosen with its origin at the observer's position, the z-axis to the zenith and the x-axis to the north. The coordinates of the unit vectors pointing to the centers of sun and moon are:

$$X_s = \cos A_s \cos a_s \qquad X_m = \cos A_m \cos a_m$$

$$Y_s = -\sin A_s \cos a_s \qquad Y_m = -\sin A_m \cos a_m$$

$$Z_s = \sin a_s \qquad Z_m = \sin a_m$$

A_s, A_m, a_s, and a_m are the azimuth and altitude of the sun and moon, including the correction for local parallax. Then the local elongation follows from:

$$\cos E_1 = X_s X_m + Y_s Y_m + Z_s Z_m$$

The local phase P_1 can be calculated from the local elongation by means of planar trigonometry:

$$P_1 = \pi - E_1 - \theta \ .$$

3.5.5 Eclipses

For a description of solar and lunar eclipses, the following parameters (see Figures 152 and 153) are defined:
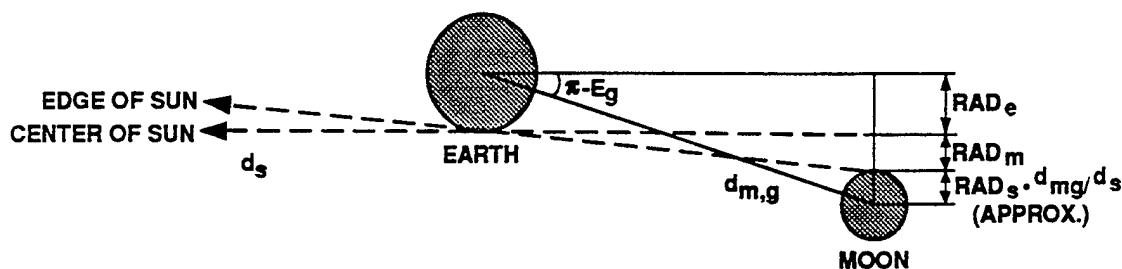
Figure 152. Lunar Eclipse.
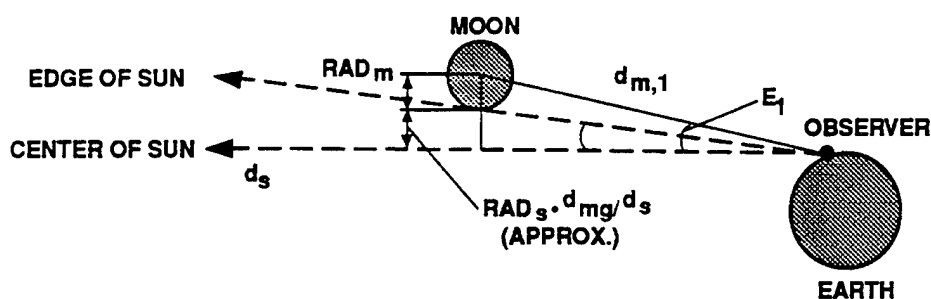
Figure 153. Solar Eclipse.

RAD_s, RAD_m, RAD_e	:	Radius of sun, moon, and earth
d_s	:	distance between the centers of earth and sun
$d_{m,g}$	:	distance between the centers of earth and moon
$d_{m,l}$	:	distance between the observer and the center of the moon
E_g	:	geocentric elongation of sun and moon
E_l	:	local elongation of sun and moon
Δ_{max}	:	maximal expectable error in the calculated elongation
E_{cr}	:	critical elongation (see below)

181

According to Figure 152, a lunar eclipse will probably occur if:

$$\pi - E_g < E_{cr,m}$$

with

$$E_{cr,m} = RAD_s/d_s + RAD_m/d_{m,g} + RAD_e/d_{m,g} + \Delta_{max}$$

where $RAD_e/d_{m,g}$ is equal to the equatorial horizontal parallax of the moon.

Figure 153 shows that a solar eclipse will probably occur if

$$E_1 < E_{cr,s}$$

with

$$E_{cr,s} = RAD_s/d_s + RAD_m/d_{m,l} + \Delta_{max}$$

within this approximation $d_{m,l}$ may be taken equal to $d_{m,g}$ which has been done in MOSART.

Figures 154 through 157 show lunar elevation, azimuth, normalized distance, and phase as observed from 30° latitude, 0° longitude during the month of June 1974.

R-023-91.3-19 BC/Mac
R-077-90.3-19 BC/Mac
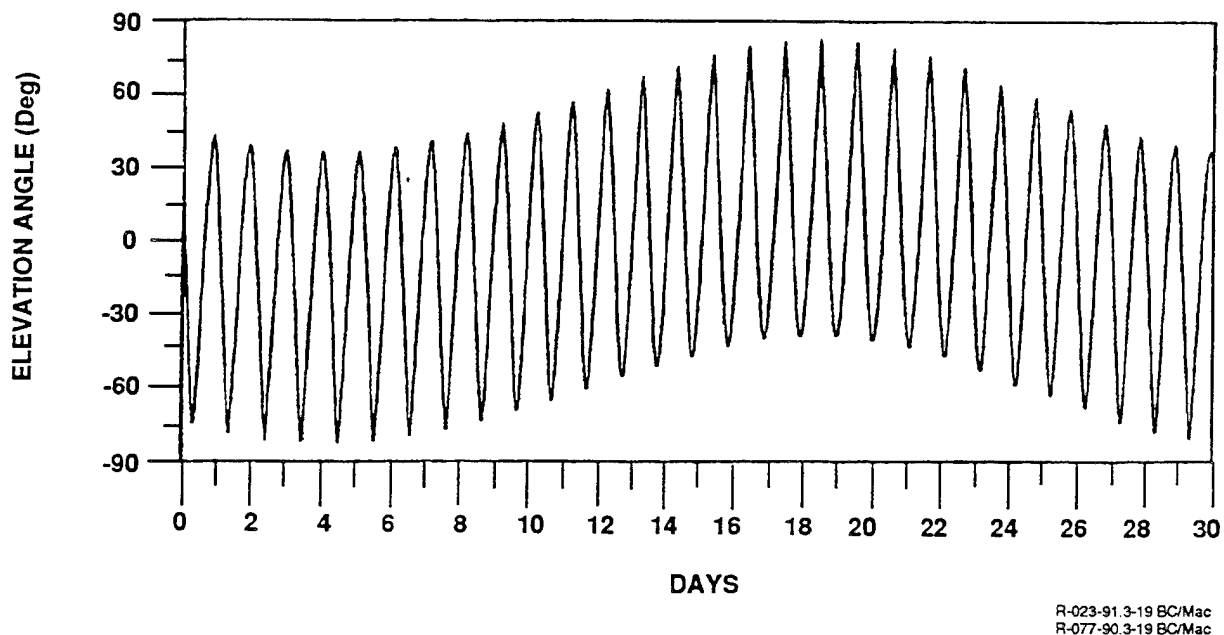
Figure 154.   Lunar Elevation.   30° N. Latitude, 0° Longitude.   June 1974.

182
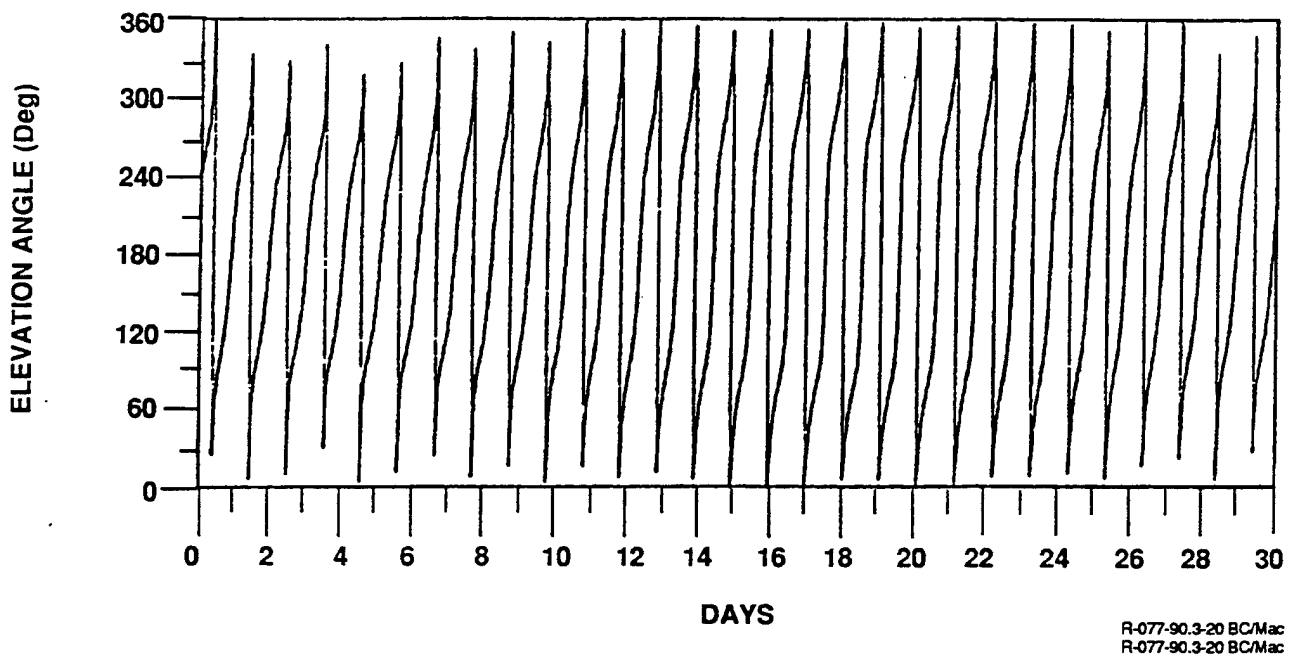
Figure 155. Lunar Azimuth. 30° N. Latitude, 0° Longitude. June 1974.
(Note: Sampling is every 30 minutes, resulting in poor
definition near 0° and 360°.)
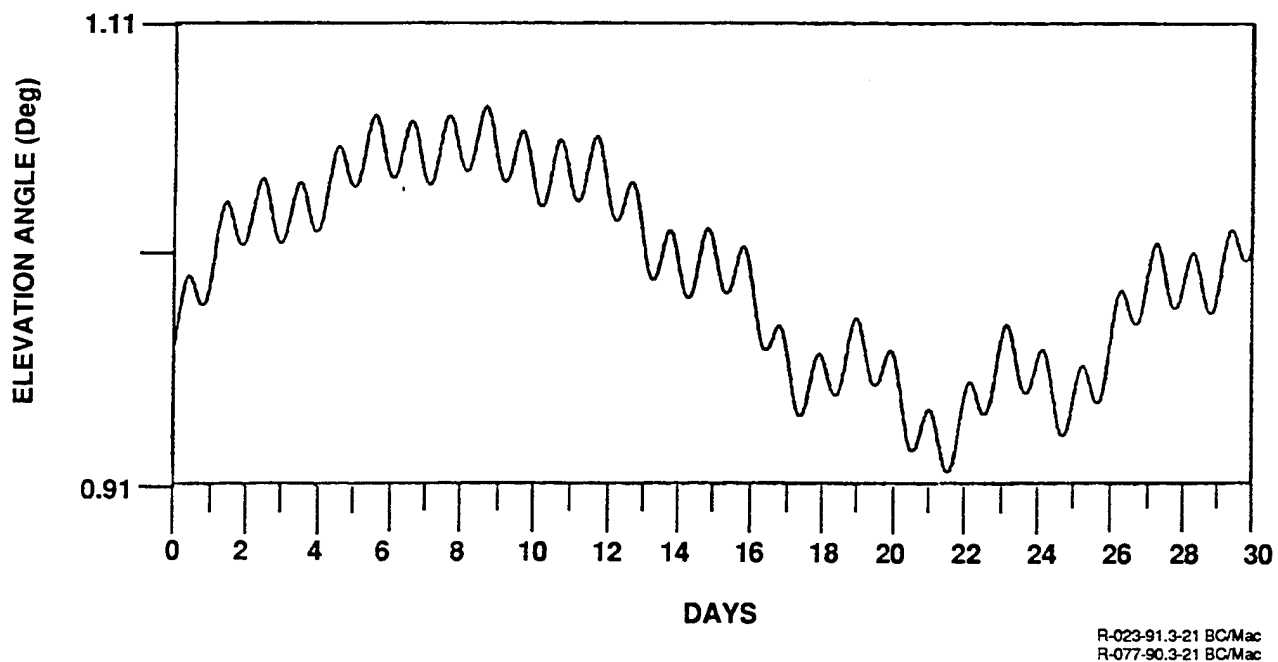
Figure 156. Normalized Lunar Distance. 30° N. Latitude, 0° Longitude.
June 1974. (Note: Diurnal variations are due to the observer's
location on the surface of the earth.)

183
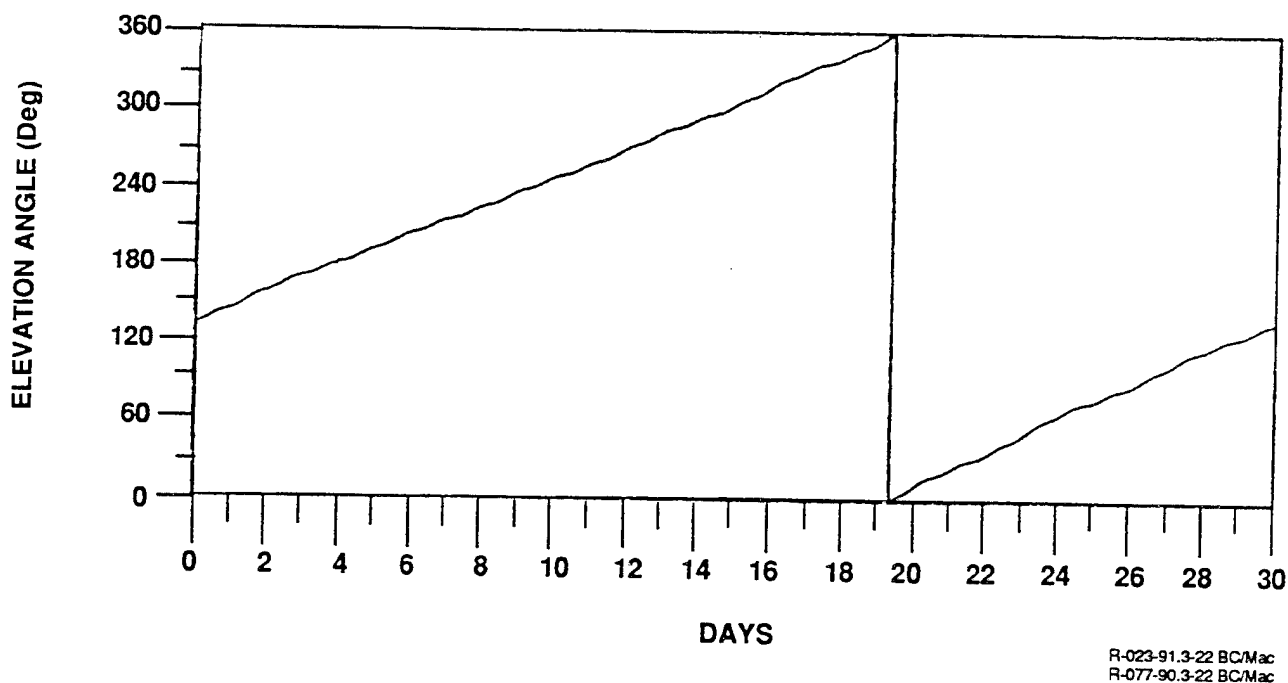
Figure 157. Lunar Phase. 30° N. Latitude, 0° Longitude. June 1974.
(Note: Diurnal variations due to parallax of observer.
Minor irregularity at 180° (full moon) is due to numerical
inaccuracies of algorithm.)

3.5.6 Refraction Corrections

In computing the zenith angle of the sun in the horizon system, it is often necessary to correct for atmospheric refraction. The effect is such that at the horizon (Z = 90°) a celestial object approximately 34' below the geometric horizon is still visible. The refractive effect of the earth's atmosphere is that extraterrestrial objects appear higher in the sky than if there was no atmosphere.

Since atmospheric refraction depends on atmospheric thickness and composition, an accurate correction is difficult to make, especially for large zenith angles. Table 64 shows representative refractive corrections which need to be added to the observed zenith angle in order to obtain the true or apparent zenith angle. The MOSART code uses the ray tracing techniques described above to determine the refractive conditions for the actual atmospheric conditions.

The correction should be subtracted from the zenith angle, Z, computed from the solar ephemeris algorithm to obtain the observed zenith angle. Thus,

$$\Delta Z_R = P/T \left[3.430289\{Z - \sin^{-1}[0.9986047 \sin(0.9967614)]\} - 0.011115929Z \right]$$

184

Table 64. Sea-Level Refraction Corrections for Zenith Angles of Astronomical
Lines of Sight.[*]

Observed (deg)	Zenith (min)	Refraction Correction (min)	Observed Zenith (deg)	Refraction Correction (min)
90	00	34.5	79	4.9
89	45	31.4	78	4.5
89	30	28.7	77	4.1
89	15	26.4	76	3.8
89	00	24.3	75	3.6
88	45	22.5	74	3.3
88	30	20.9	73	3.1
88	15	19.5	72	2.9
88	00	18.3	71	2.8
87	45	17.2	70	2.6
87	30	16.1	65	2.1
87	15	15.2	60	1.7
87	00	14.4	55	1.4
85	30	10.7	40	0.8
85	00	9.9	35	0.7
84	00	8.5	30	0.6
83	00	7.4	25	0.5
82	00	6.6	20	0.4
81	00	5.9	10	0.2
80	00	5.3	0	0.2

where P is the atmospheric pressure in millibars and T the temperature in Kelvin at the observation point.

3.6 Radius of the Earth

Generally, the earth can be considered as an oblate spheroid (i.e., a sphere flattened at the poles). Due to a non-uniform mass-distribution, the direction of the gravity vector is tilted away from the center of the earth; the shape of the earth whose surface is normal to the direction of gravity is called a geoid. Over land the radius of the spheroid is generally less than the radius of the geoid, while over the sea the opposite is generally true. Due to slight irregularities in the shape of the earth, several different models exist for the effective earth radius. The four values usually given are:

185

(a) Equatorial radius, r_a;

(b) Polar radius, r_b;

(c) Mean radius, $(2r_a + r_b)/3$

(d) Ellipticity or flattening, $e = (r_a - r_b)/r_a$

The more commonly occurring values for the above values are given in Table 65. The various models are:

(i) Clarke Spheroid of 1866. Computed by the English geodesist, A.R. Clarke, this model is used for charts of North America. Since Clarke did not clearly define his units, the U.S. Coast and Geodetic Survey adjusted Clarke's values in 1880 by adding approximately 85 feet to obtain the standard values given in Table 65, which are used for all charts and maps of North America.

Table 65. Earth Radii.

	Equatorial Radius (m)	Polar Radius (m)	Mean Radius (m)	Ellipticity
Clarke Spheroid of 1866	6378206.4	6356583.8	6370998.9	$(294.98)^{-1}$
Clarke Spheroid of 1880	6378249.145	6356514.870	6371004.387	$(293.465)^{-1}$
International Spheroid	6378388.000	6356911.946	6371299.315	$(297)^{-1}$
Jeffreys (3rd Edition)	6378099.	6356641.	6370943.	$(297)^{-1}$
Jeffreys (5th Edition)	6378269 $(1+u')^*$	--	--	$0.00336700+e'^*$

* u' and e' are small corrections; good estimates are $u' = e' = 0$

(ii) Clarke Spheroid of 1880. These values are new estimates made by Clarke in 1880; however, they have not been adopted by the United States.

186

(iii) International Spheroid. In 1909-10, Hayford conducted measurements such that the error in the equatorial radius is ±18 meters and the error in e^{-1} is ±0.5. These values are considered to be a slight improvement over either of Clarke's models. However, Helmut increased three errors to ±53 meters and ±1.2, respectively. This model is currently used by MOSART.

(iv) Sir Harold Jeffreys (1952 and 1970). Jeffreys is a standard reference for parameters concerning the earth; however, the values given therein are not referenced to any experiment.

For most applications, the mean radius of the International Spheroid used by MOSART is usually adequate. If a more accurate value is required, assume an elliptical earth, and use

$$r_e = \left[\sqrt{r_a^{-2}\cos^{-2}\theta + r_b^{-2}\sin^{-2}\theta}\right]^{-1} \quad .$$

where θ is the latitude.

4.0 PROPAGATION AND RADIATION TRANSFER

The actual radiative transfer calculations are the most computer intensive portion of the code. The band model, band parameter integration formulation, and turbulence models are presented below.

4.1 Band Model

The band model is used for molecular absorption in the 0 - 20,000 cm^{-1} spectral region for water vapor, carbon dioxide, ozone, nitrous oxide, carbon monoxide, methane, oxygen, nitric oxide, sulfur dioxide, nitrogen dioxide, ammonia, nitric acid, and nitrogen.

If desired, the hydroxyl radical, hydrogen fluoride, hydrogen chloride, hydrogen bromide, hydrogen iodide, chlorine monoxide, carbonyl sulfide, formaldehyde, hypochlorous acid, hydrogen cyanide, methyl chloride, hydrogen peroxide, acetylene, ethane, phosphine, and other molecules of interest can be included, once the data bases have been generated from the HITRAN data base (Rothman et al., 1992).

4.1.1 Voight Statistical Model

The molecular transmittance calculation is based upon a combination of a statistical model of Plass (1958) for the line centers and a deterministic model for the line wings. The statistical line center model applies to a finite number of lines in a finite spectral interval, and uses an average of the single line equivalent width over the line strength distribution in the spectral interval, W. The molecular transmittance, τ, is defined for the line center by the power law equation:

$$\tau = \left(1 - \frac{W}{\Delta v}\right)^{\Delta v/d}$$

where Δv is the spectral interval, or resolution, and d is the mean line spacing.

The effective number of lines, $n = \Delta v/d$, is usually fairly low (i.e., less than 10) at atmospheric temperatures and at 5 cm^{-1} resolution; however, for large n, the power law equation reduces to the exponential form:

$$\lim_{n \to \infty} \tau = \exp(-W/d)$$

The use of an equivalent line width has been used extensively in the past for Doppler and Lorentz (collision) broadening, with both weak and strong line assumptions.

The exact value for the equivalent width of a single line with a Voight line shape is calculated from the expression:

$$W = \left(2\gamma_D/(\ln 2)^{1/2}\right) \int_0^{x_m} \left\{1 - \exp\left[-(su/\gamma_D)(\ln 2/\pi)^{1/2} F(x,y)\right]\right\} dx$$

$$F(x,y) = \frac{y}{\pi} \int_{-\infty}^{\infty} \frac{\exp(-t^2)}{y^2 + (x-t)^2} dt$$

$$x = (\ln 2)^{1/2} (v - v_0)/\gamma_D$$

$$y = (\ln 2)^{1/2} \gamma_c/\gamma_D$$

where γ_D is the Doppler linewidth, γ_c is the collision broadened linewidth, S is line strength, u is optical path length, v is frequency, x is dimensionless frequency, y is dimensionless linewidth, and F(x,y) is the Voight lineshape function. Numerical integration of the integral from 0 to x_m is extremely time-consuming; however, it is not necessary to numerically integrate over the entire interval. There is always a value of x, say x_ℓ, beyond which the asymptotic expression for F(x,y) is quite accurate and is given by

$$\lim_{x\to\infty} f(x,y) = \frac{y}{\sqrt{\pi x^2}}$$

Therefore, the integral can be numerically integrated up to x_ℓ, and from x_ℓ to x_m the integration is given directly by

$$\int_{x_\ell}^{x_m} \exp(-\beta^2/x^2) dx = \beta\left\{\frac{e^{-z_m^2}}{z_m} - \frac{e^{-z_\ell^2}}{z_\ell} + \sqrt{\pi}\left[\text{erf}(z_m) - \text{erf}(z_\ell)\right]\right\}$$

where

$$\beta = \sqrt{(Su/\gamma_D)(\ln 2/\pi)^{1/2}(y/\sqrt{\pi})}$$

$$z = \beta/x$$

where the error function, erf(z), is evaluated by a rational approximation.

For the calculation of Voight lineshape, F, an algorithm developed by Humlicek (1978) is utilized.

189

At lower altitudes, where collision broadening predominates, x_ℓ is of the order of 100; at higher altitudes, where Doppler and collision broadening are comparable, an x_ℓ of 3 or less is usually sufficient. For a resolution of 5 cm^{-1}, a typical value of x_m is of the order of 1000. At altitudes where Doppler broadening predominates $(y < 0.001)$, the equivalent width integral is approximated as the sum of a pure Doppler $(y = 0)$ equivalent width and the asymptotic contribution with $x \approx 3$, where the Doppler equivalent width is given by (Ludwig, Malkmus, Reardon, and Thomson, 1973):

$$\lim_{y \to 0} W_D \approx (2 \ln 2)^{1/2} \gamma_D \sqrt{\ln[1 + (\ln 2/2)(Su/\gamma_D)^2]}$$

The statistical line center model described above only considers the absorption by that part of the line shape that is within ± 2.5 cm^{-1} (half of the resolution) of the line center. The contribution of that portion of the line shape outside of the spectral interval (i.e., the line wings) to the molecular absorption is provided for by

$$\tau = \exp (-cu)$$

where C is the molecular line wing absorption coefficient (sometimes referred to as the continuum) and u is the optical path length.

Presently, the line wing absorption coefficient for the kth spectral interval is defined by

$$C(T,P,vk) = \frac{P}{P_o} \frac{\sqrt{T_o}}{T} \frac{\Delta v}{\pi} \sum_{i \neq k} \frac{s/d(v_i,T) \gamma_i^\circ}{(v_i - v_k)^2} X(v_i - v_k)$$

where $X(v_i - v_k)$ is a form factor expressing deviation from Lorentzian behavior, and the sum is all over spectral intervals, i, excluding i = k. P and T are the pressure and temperature, respectively, while the zero subscript represents standard conditions. γ_i is the line width for the ith spectral interval. For the CO_2 bands the Burch (1969) form factor is used, while for the other molecules, 500 cm^{-1} Lorentz tails are assumed.

The accuracy of this statistical line center/deterministic line wings approach is illustrated in Figure 158. The data was obtained over a 17.5 m path at sea level with a Michelson interferometer operating at 4 cm^{-1} resolution. The 5 cm^{-1} resolution calculations reproduce the measured features quite accurately; in fact, although not shown, the difference between the 5 cm^{-1} calculations and the line-by-line calculations degraded to 5 cm^{-1} is minimal. In comparison, the 20 cm^{-1} resolution calculations do not agree as well as might be desirable.
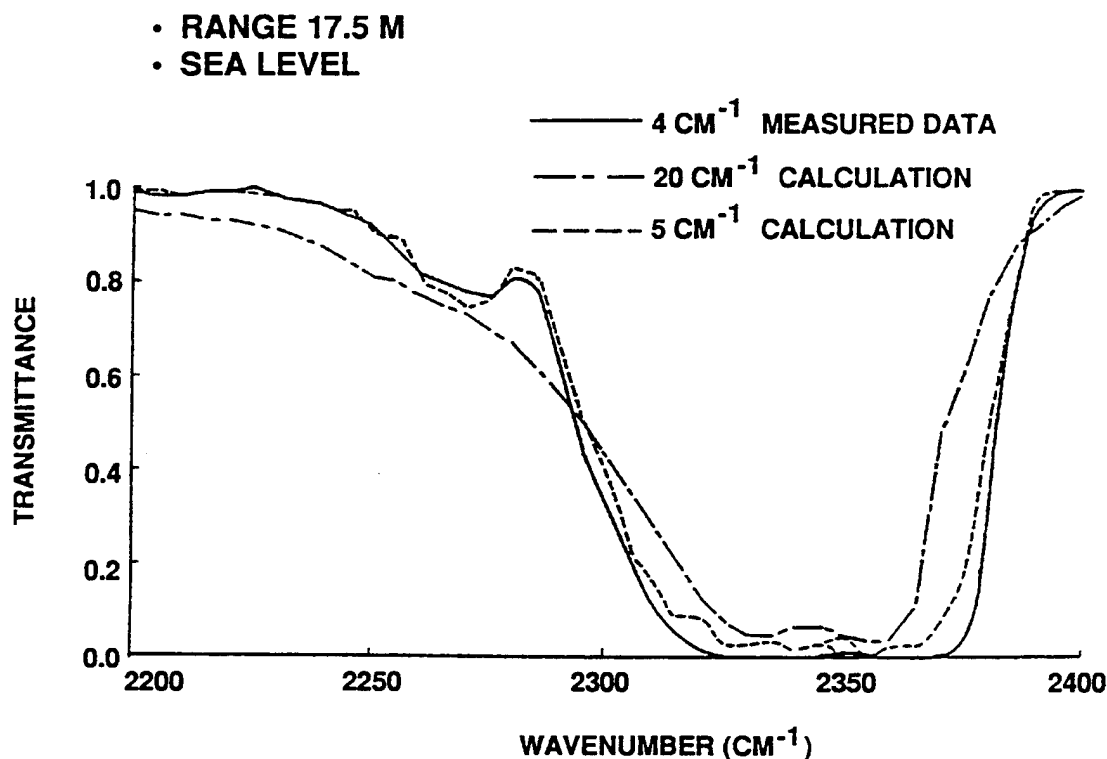
Figure 158. Comparison Between Measured Transmittance Data and Calculated Transmittance Values.

4.1.2 Collision Line Width Broadening

Broadening is determined by the forces between molecules. When two molecules approach each other sufficiently close that strong forces between them come into play, they are said to "collide". The collision process may be viewed as an interruption to the process of emission or absorption of radiation. The net effect of man such random interruptions is a spreading of frequencies associated with a particular transition. This spread of frequencies is defined by a line shape, which is determined by the nature of the forces between the molecules at the time of collision.

A linear dependence of the line width γ on pressure has been well established both experimentally and theoretically. However, it is necessary to ascribe different broadening powers to each component of a mixture.

191

The general expression for the half-width, γ, of a spectral line can be written as

$$\gamma = \sum_i \gamma_{0_i} P_i = \left(\sum_i \gamma_0 c_i \right) P$$

where P is the total pressure, P_i and c_i are the partial pressure and mole fraction, respectively, of component i of the gas mixture, and γ_0 is the line half-width resulting from a unit pressure of component i. The quantities $(\gamma_0)_i$ are usually determined by experiment, although it is possible to calculate them with some accuracy. Model values used by the SIRRM code for the collision line width parameters are shown in Table 66.

Table 66. Model Values for the Collision Line Width Parameters.

Molecule (i)	Broadener (j)	$(\gamma_{i,j})_{273}$ $cm^{-1}atm^{-1}$	$(\gamma_{i,i})_{273}$ $cm^{-1}atm^{-1}$
H_2O	H_2O	(0.09)	0.44
	N_2	0.09	
	O_2	0.04	
	CO_2	0.12	
	CO	(0.10)	
CO_2	CO_2	0.09	0.01
	H_2O	(0.07)	
	N_2	0.07	
	O_2	0.055	
	CO	(0.06)	
CO	CO	0.06	0.0
	H_2O	(0.06)	
	CO_2	(0.07)	
	N_2	0.06	
	O_2	0.05	

Values in parenthesis are estimated.

Quite apart from Doppler broadening, the ambient temperature T plays an important part in the collision process. Under simplest assumptions of kinetic theory, at least for foreign gas broadening, an inverse square root dependence on temperature is predicted. However, the calculations of Benedict and Kaplan (1964) indicate that a

somewhat improved representation for H_2O-N_2 collisions can be obtained with an exponent of 0.6 to 0.7 instead of 0.5. The 1986 AFGL Line Atlas includes the exponent for each transition, which is used in the model.

The situation for self-broadening is somewhat more complicated, at least for highly polar molecules, such as H_2O. The collisions between like molecules may be divided into two categories: resonant and nonresonant. Nonresonant collisions are analogous to inert-gas broadening and can be so treated. Resonant collisions, on the other hand, are more effective in broadening the spectral lines. The mechanism involved is more complex, and the temperature dependence is different. Generally, it is assumed that, for resonant collisions, the contribution to the self-broadened line width is given by the inverse power of temperature, for an exponent of approximately unity.

Therefore, the line width of the ith molecule can be evaluated by

$$\gamma_i = \left[\sum_j (\gamma_{i,j})_{273} p_j (273/T)^{0.5} \right] + (\gamma_{i,i})_{273} p_i (273/T)$$

It has been found that good agreement with experimental data at room temperature has been obtained by assuming the line width is proportional to $(\gamma_a p_a + \gamma_b p_b)$, where the subscripts a and b designate self broadening and foreign gas broadening.

4.1.3 Variable Resolution

One of the major complications involved with a higher spectral resolution capability in a computer code is the increase in computer time due to the greater number of spectral calculations required. The model compensates for this increase in computer time through the inclusion of three run-time options:

(i) The calculations can be performed at the resolution of the band parameters;

(ii) The calculations can be performed at an integral multiple of the resolution of the band parameters;

(iii) The calculations can be performed at a relatively constant wavelength (i.e., variable wavenumber) resolution.

The first option, which permits a 5 cm^{-1} resolution, is simply a direct implementation of the band model discussed in Section 4.1.2.

The second option, which is derived from an APART capability, permits resolutions of 10, 15, 20, 25 (or larger) cm^{-1}. This option is possible due to the design and implementation of the band model and the band parameters. Using the 5 cm^{-1} resolution band parameters, a resolution of an integral multiple of 5 cm^{-1} can be obtained by simply determining the arithmetic average of the S/d, line width, and line wing parameters. The value of 1/d is evaluated by the expression

$$\frac{1}{d} = \frac{1}{(S/d)} \left[\frac{1}{n} \sum_{i=1}^{n} \left[\left(\frac{1}{d}\right)_i \left(\frac{S}{d}\right)_i \right]^{1/2} \right]^2$$

where $(S/d)_i$ and $(1/d)_i$ are the band parameters for the ith 5 cm^{-1} resolution set, n is the integral multiple of 5 cm^{-1} selected, and S/d is the arithmetic mean of the $(S/d)_i$.

Figure 159 shows the transmittance for a 1 km path at 1 km altitude. The curve for 5 cm^{-1} resolution is shown, along with the 5 cm^{-1} resolution curve degraded to 25 cm^{-1} resolution, and the transmittance calculated at 25 cm^{-1}. The comparison between the degraded and the calculated 25 cm^{-1} resolution curves is quite good. The two curves agree to within less than 1% for over 65% of the spectral range shown, and they agree to within less than 4% over the whole range, except for the wing of the water vapor band near 2000 cm^{-1}, where 6-8% variations occur.

The third option, which utilizes the algorithms discussed above, permits the wavenumber resolution to change spectrally so that the calculations are performed at approximately a constant wavelength resolution according to the formula

$$\Delta\lambda = \lambda/\nu \; \Delta\nu$$

The band model parameters are degraded to a value of $\Delta\lambda$ which most closely corresponds to the constant $\Delta\lambda$ while using the wavenumber resolution of the band parameters (i.e., 1 cm^{-1} for MOSART). For example, consider a calculation over the 3 - 5 μm (2000 - 3335 cm^{-1}) spectral interval at constant $\Delta\lambda$. If the calculations start at 5 cm^{-1} resolution at 2000 cm^{-1}, which corresponds to a 0.0125 μm resolution at 5 μm, at 3335 cm^{-1} (3 μm), the spectral resolution will be 14 cm^{-1}, or 0.01259 μm.

The use of this third option is particularly useful in avoiding excessive computer run-time when calculating below 2 μm.
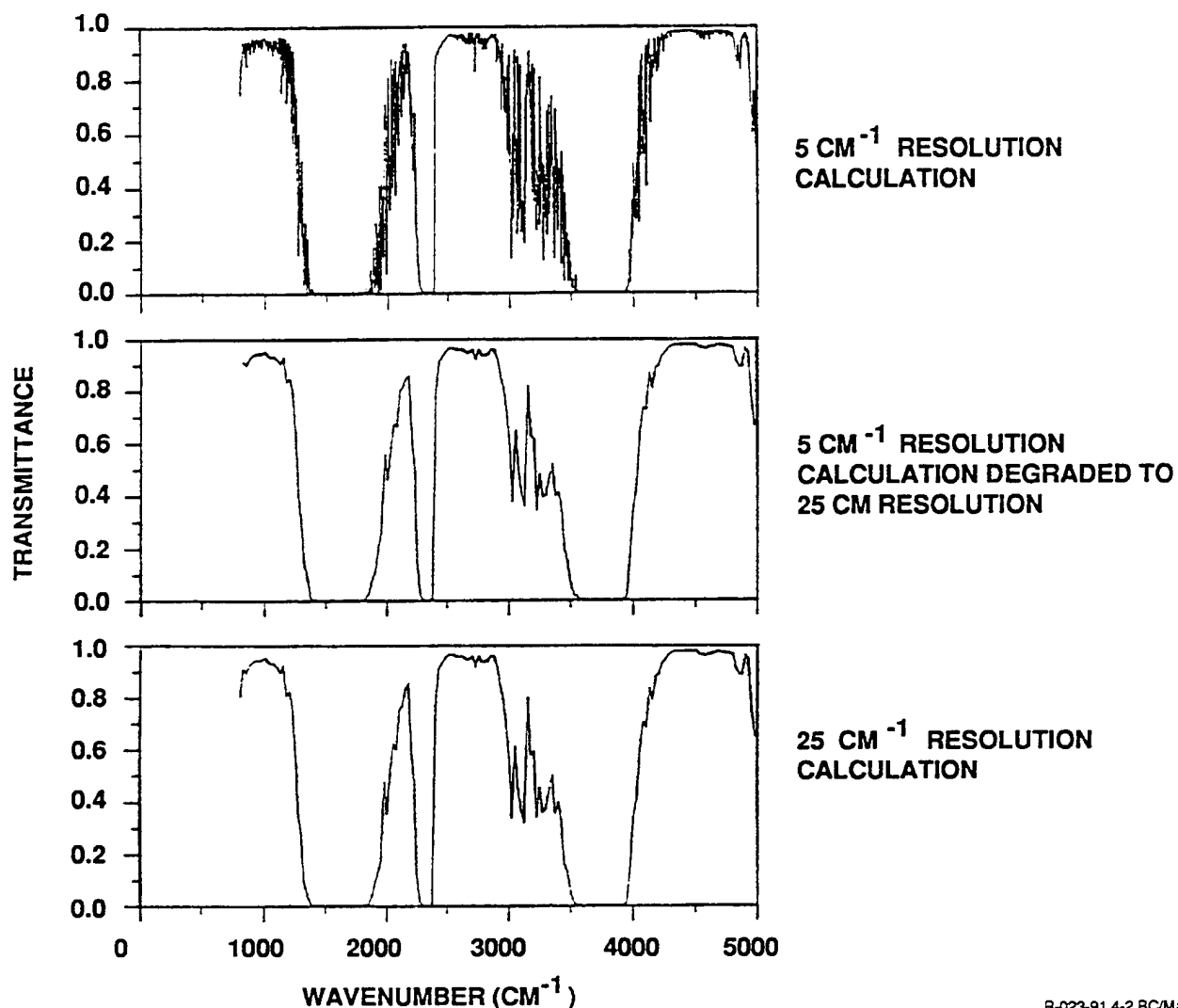
Figure 159. Accuracy of Variable Resolution Calculations.

A fourth option is under consideration. For this option, the code would use some built-in criteria, so that in window regions, where low resolution calculations are appropriate, the calculations could be performed very quickly; however, in absorption regions, particularly in the wings, a higher resolution would be performed for improved accuracy. This option has not been implemented at the present time, but is under consideration.

4.1.4 Spectral Resolution

The spectral resolution required for a specific application will vary depending upon the application and the accuracy required. For a detailed analysis over a narrow spectral band, the use of a line-by-line technique (e.g., FASCODE) will be necessary. For wide band applications, the LOWTRAN resolution of 20 cm^{-1} may be appropriate. In general, the resolution required depends upon

(i)   the need to identify and/or distinguish certain special features; and

(ii)   the accuracy required for determining the transmission through inhomogeneous paths.

An example of the first is shown in Figure 160, where the radiance for a hot gas plume, as seen from space, is shown for the spectral region between 2380 and 2400 cm^{-1} (i.e., the CO$_2$ "blue spike"). This blue spike was calculated using a line-by-line approach, and therefore all of the spectral features, including line reabsorption, are shown. Figure 161 shows the same blue spike after having the resolution degraded using a triangular resolving window. For 0.25 cm^{-1} resolution, the basic line structure, as well as the band head, are still visible; for 1.00 cm^{-1} resolution, essentially all line structure has disappeared, although the band head is still somewhat apparent. The 4.00 cm^{-1} resolution blue spike no longer shows the band head. (Calculations were terminated at 2398 cm^{-1} so no information is shown past this point.) At 20 cm^{-1} resolution, the blue spike has been smeared significantly.
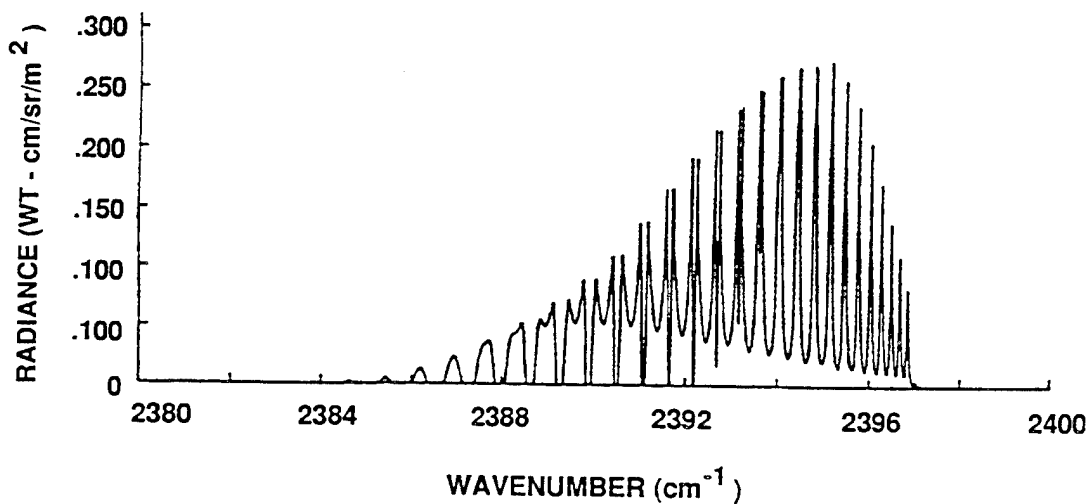
R-023-91.4-3 BC/Mac
R-077-90.4-3 BC/Mac

Figure 160. High Resolution in Blue Spike Radiance as Viewed from Space.
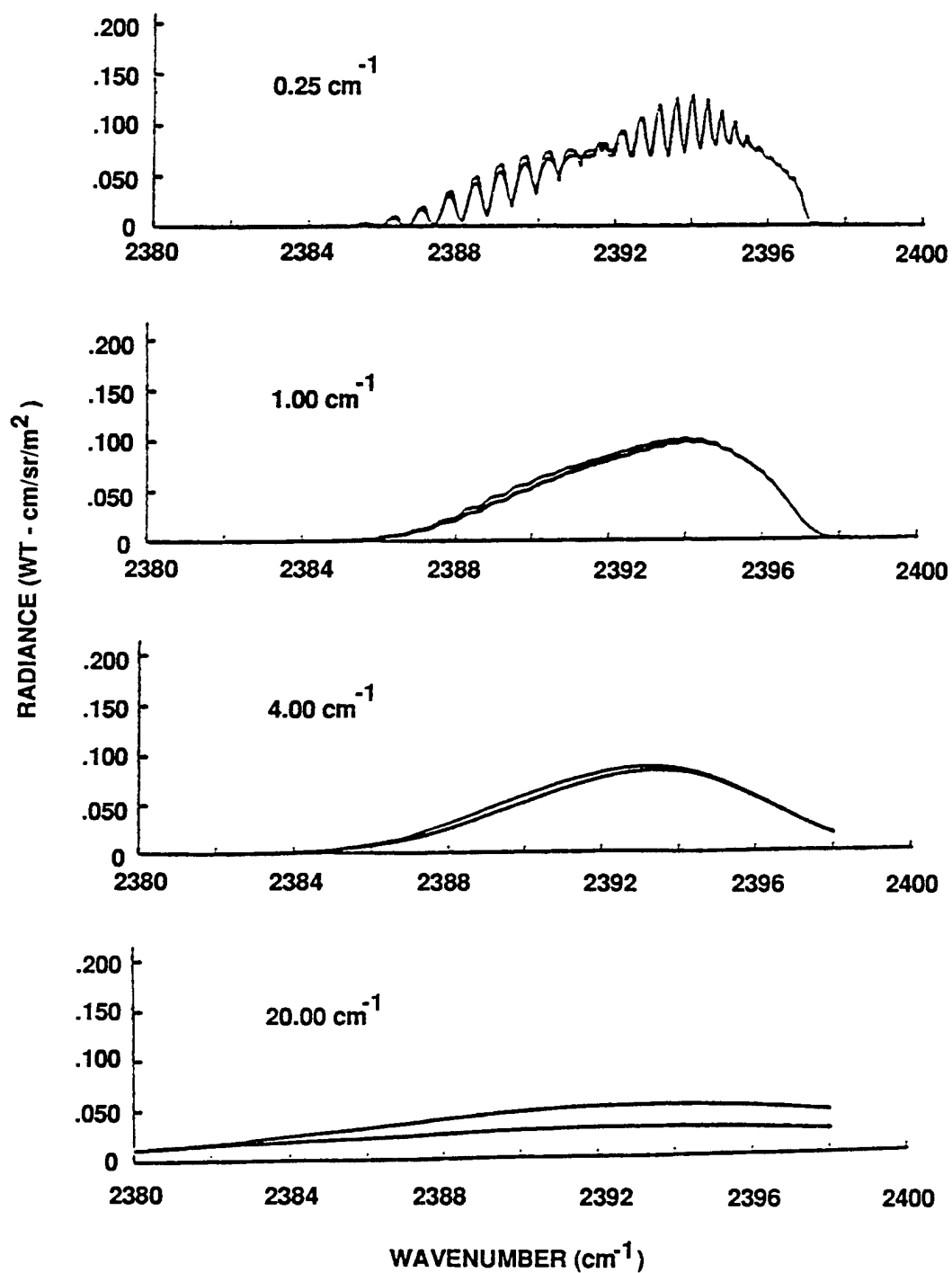
Figure 161. Impact of Resolution on Blue Spike Radiance. Triangular resolution window used. Upper curve in each graph assumes no correlation between the plume and the atmosphere. Lower curve assumes proper correlation.

The effect of resolution can also be analyzed by taking the absolute value of the Fourier transform (i.e., the power spectrum) of the blue spike, as shown in Figure 162. Since the horizontal scale of the graph can be considered as the inverse of the resolution, a comparison between resolution and information content can be made.
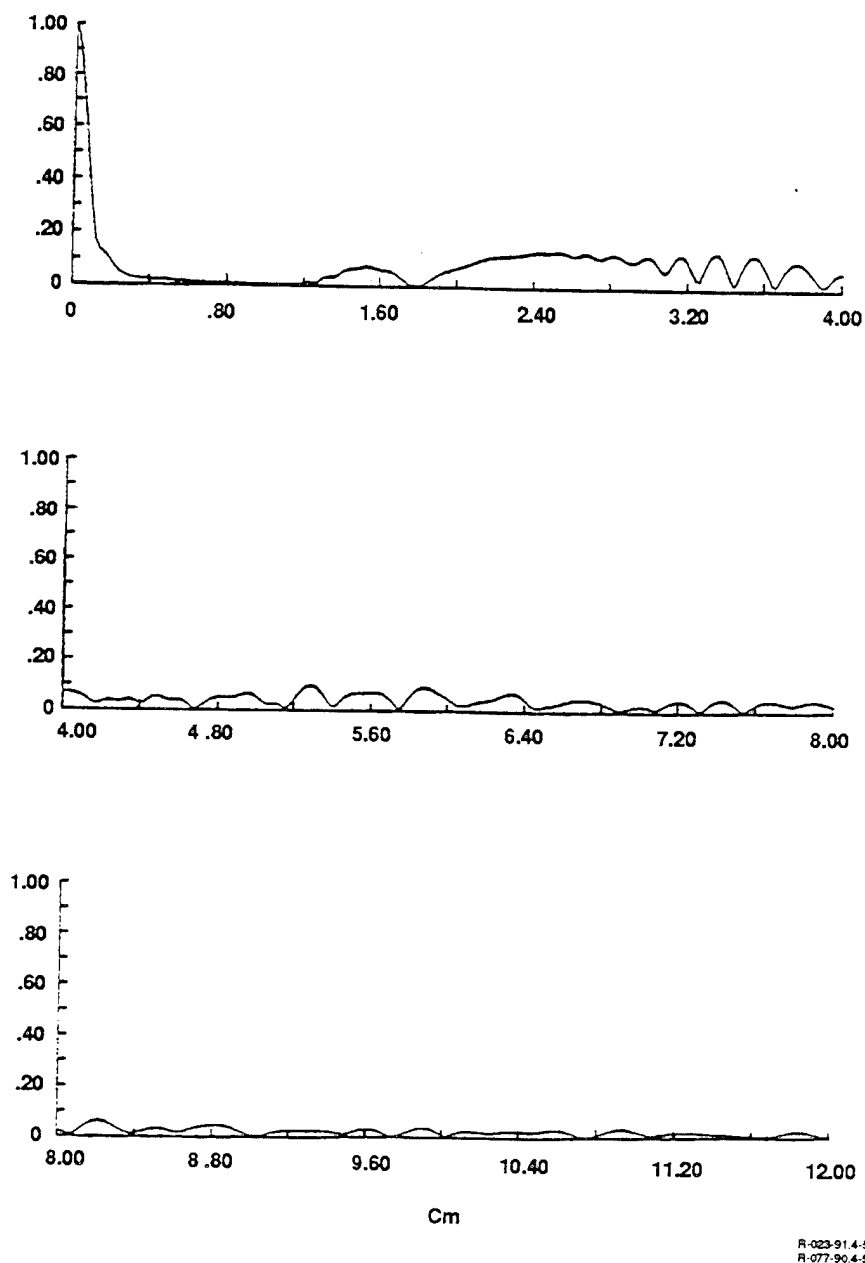
Figure 162. Normalized Absolute Value of the Fourier Transform of the Blue Spike in Figure 160.

Figure 163 shows the same power spectrum on different scale with the filters associated with 20 cm^{-1} and 4 cm^{-1} triangular resolving windows. The 20 cm^{-1} resolution window will filter out much of the information contained in the blue spike, while the 4 cm^{-1} window retains most of the low frequency information. However, the band head, which is represented by the information in the 0.12 - 0.20 cm region, is filtered out. Most of the line data and the sharpness of the band head are contained in the 1.20 - 4.00 cm region, which is contained within a 0.25 cm^{-1} resolution filter. Using this Fourier transform technique, the required resolution can be determined accurately. For example, based on Figure 162, 2 cm^{-1} resolution may provide just as much information as 1 cm^{-1} resolution.
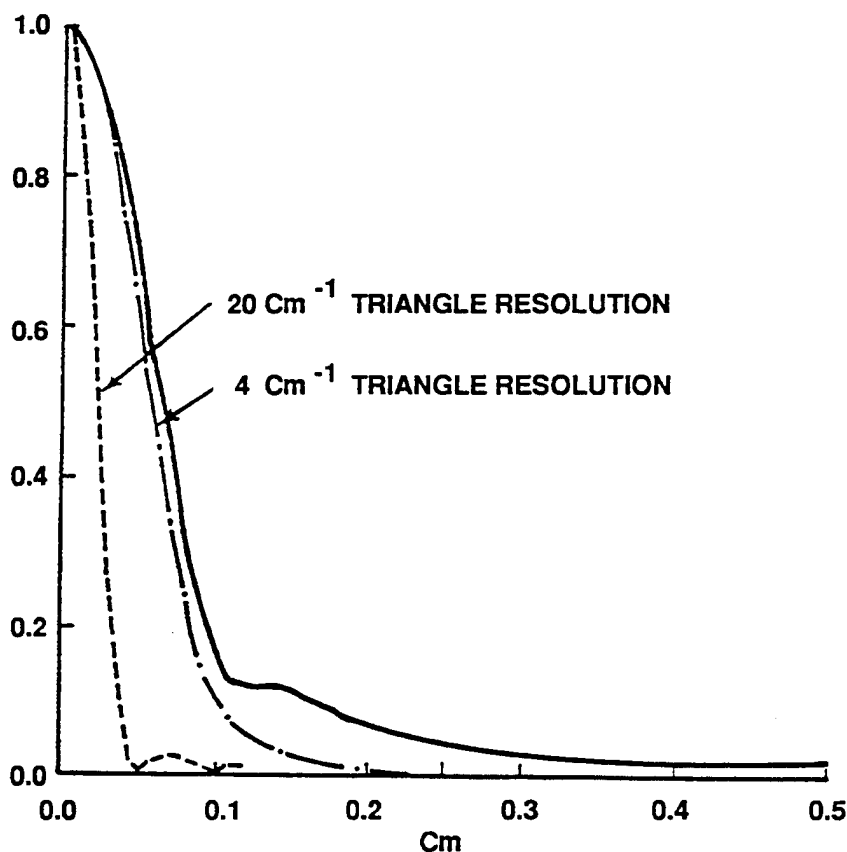
R-023-91.4-6 BC/Mac
R-077-90.4-6 BC/Mac

Figure 163. Normalized Absolute Value of the Fourier Transform of the Blue Spike. The dashed lines are the filters corresponding to 4 cm^{-1} and 20 cm^{-1} triangle resolving windows.

4.2 Band Parameters

The S/d, 1/d, line wing, and line width band model parameters are generated from the 1992 HITRAN Data Base (Rothman et al, 1992) for MODTRAN 2 (see Table 67 for molecules, isotopes, and relative abundances), using the equations

$$S/d(\nu,T) = \left[\sum_i S_i(T)\right]\bigg/ \Delta\nu$$

$$1/d(\nu,T) = \left[\sum_i \sqrt{S_i(T)}\right]^2 \bigg/ \left[\Delta\nu^2 S/d(\nu,T)\right]$$

where $S_i(T)$ is the integrated line strength of the ith transition at temperature, T, and $\Delta\nu$ is the spectral resolution (5 cm^{-1}). The sums are subject to the constraint that the line center, ν_i, of each transition must be within the spectral interval, $\nu - \Delta\nu/2 \leq \nu + \Delta\nu/2$. The line strength at an arbitrary temperature can be scaled from the line strength at the reference temperature T_o, of 296 K by

$$S_i(T) = \frac{Q_v(T_o)Q_r(T_o)}{Q_v(T)Q_r(T)} \exp\left[-E_i(T_o - T)/(kT_oT)\right]$$

$$\times \{[1 - \exp(-hc\nu_i/(kT))]/[1 - \exp(-hc\nu_i/(kT_o))]\} S_i(T_o)$$

where Q_v and Q_r are the vibrational and rotational partition functions, respectively, and E_i is the energy of the lower transition state.

The S/d, 1/d, and line wing parameters are computed at 1 cm^{-1} resolution from 0 to 20,000 cm^{-1} (0.5 - ∞ μm) and at 100, 200, 225, 250, 275, and 300 K. The band parameters for a temperature of 300 K are shown in Figures 164 through 175, with the line center contribution (i.e., s/d) shown as a solid line and the line wing contribution shown as a dashed line. Figure 164 shows the S/d and line wing parameters for water vapor at a temperature at 300 K. The contribution of both the line centers and the continuum to the total absorption exists at essentially all wave numbers, although the line wings are about two orders of magnitude less than the line center. The molecular absorptivity of carbon dioxide is much more concentrated in certain spectral regions, as shown in Figure 165. Since MOSART uses the MODTRAN 2 molecular data base, only the first twelve molecules in Table 67 (plus nitrogen) are used. Other molecules can be added, once the band parameters are generated.

In Figure 174, the absorption coefficients for ammonia between 3050 and 3600 cm^{-1} are not from the HITRAN data base, but were obtained from APART.

Table 67. Relative Natural Abundance of Molecular Species on Data Base.

Molecule	AFGL Isotope Code	Relative Natural Abundance	Molecule	AFGL Isotope Code	Relative Natural Abundance
H_2O	161	0.9973	HNO_3	146	0.9891
	181	0.0020			
	171	0.0004	OH	61	0.9975
	162	0.0003		81	0.0020
				62	0.00015
CO_2	626	0.9842			
	636	0.0110	HF	19	0.99985
	628	0.0039			
	627	0.0008	HCl	15	0.7576
	638	0.000044		17	0.2423
	637	0.000009			
	828	0.0000040	HBr	19	0.5068
	728	0.000002		11	0.4930
O_3	666	0.9928	HI	17	0.99985
	668	0.0040			
	686	0.0020	ClO	56	0.7559
				76	0.2417
N_2O	446	0.9904			
	456	0.0036	OCS	622	0.937
	546	0.0036		624	0.0416
	448	0.0020		632	0.0105
	447	0.0004		822	0.0019
CO	26	0.9865	H_2CO	126	0.9862
	36	0.011		136	0.0111
	28	0.0020		128	0.0020
	27	0.0004			
			HOCl	165	0.7558
CH_4	211	0.9883		167	0.2417
	311	0.0111			
	212	0.00059	N_2	44	0.9928
O_2	66	0.9952	HCN	124	0.9852
	68	0.0040		134	0.0111
	67	0.0008		125	0.0036
NO	46	0.9940	CH_3Cl	215	0.7490
	56	0.0036		217	0.2395
	48	0.0020			
			H_2O_2	1661	0.9949
SO_2	626	0.9454			
	646	0.0420	C_2H_2	1221	0.9776
				1231	0.0219
NO_2	646	0.9916			
			C_2H_6	1221	0.9776
NH_3	4111	0.9960			
	5111	0.0036	PH_3	1111	0.99955
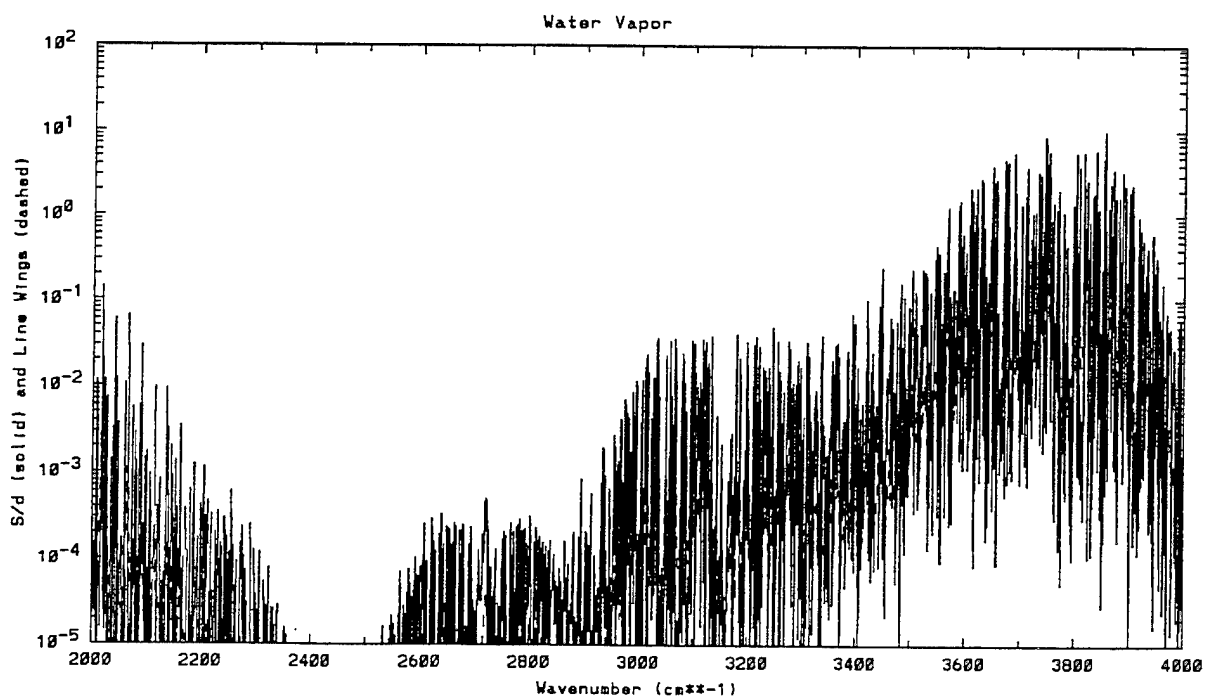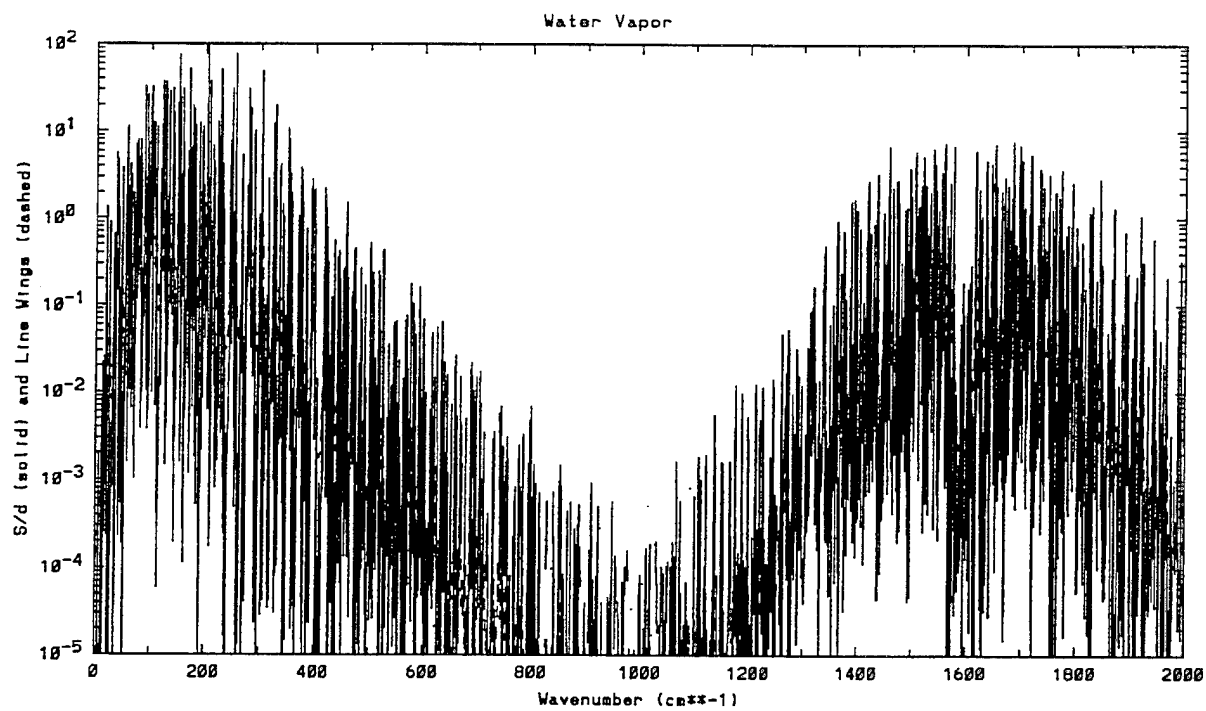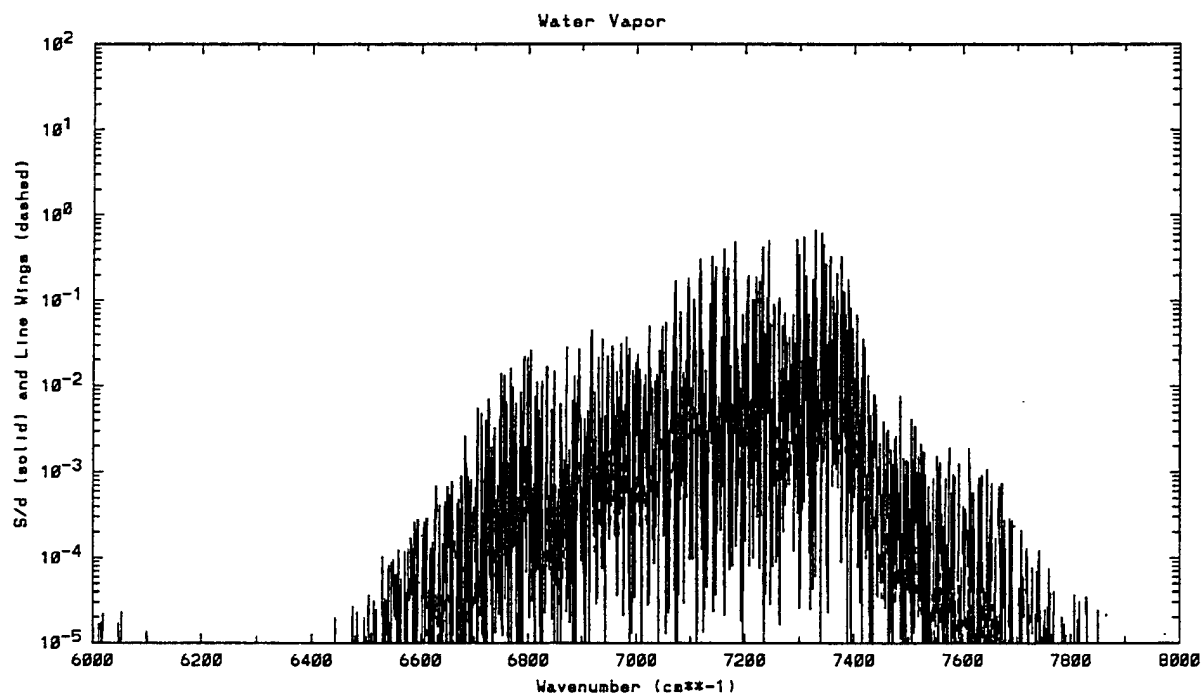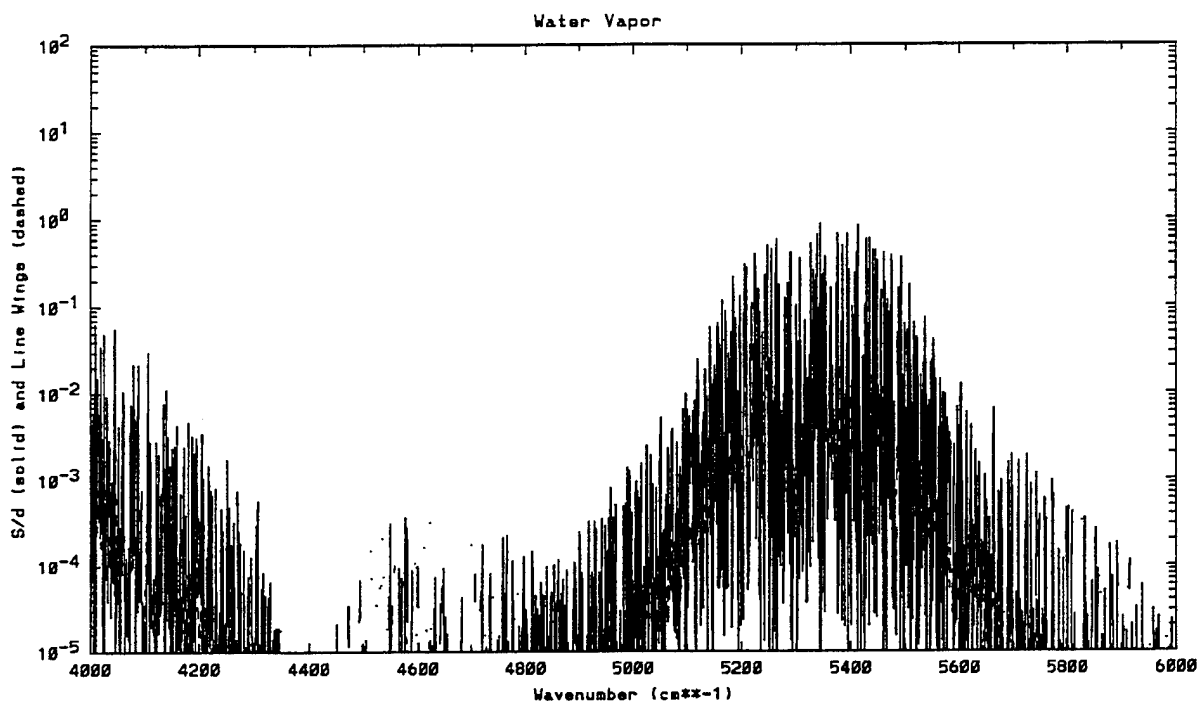
Figure 164. Absorption and Line Wing Coefficients for Water Vapor.

Figure 164. Absorption and Line Wing Coefficients for Water Vapor (continued).
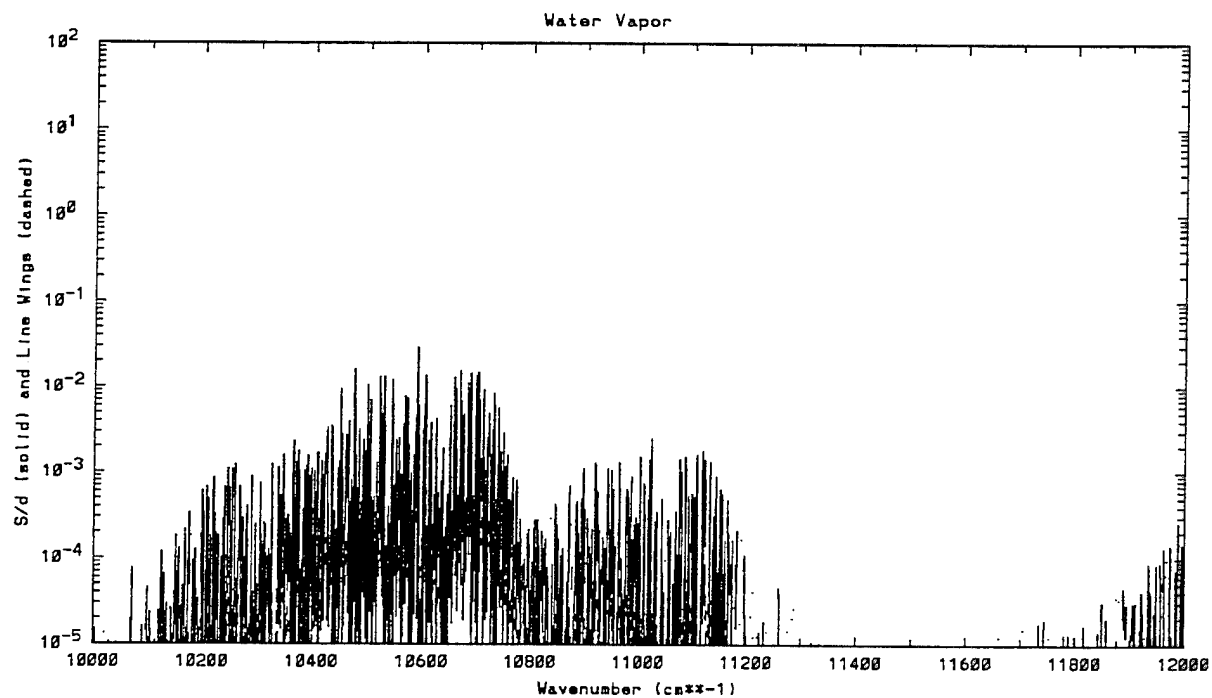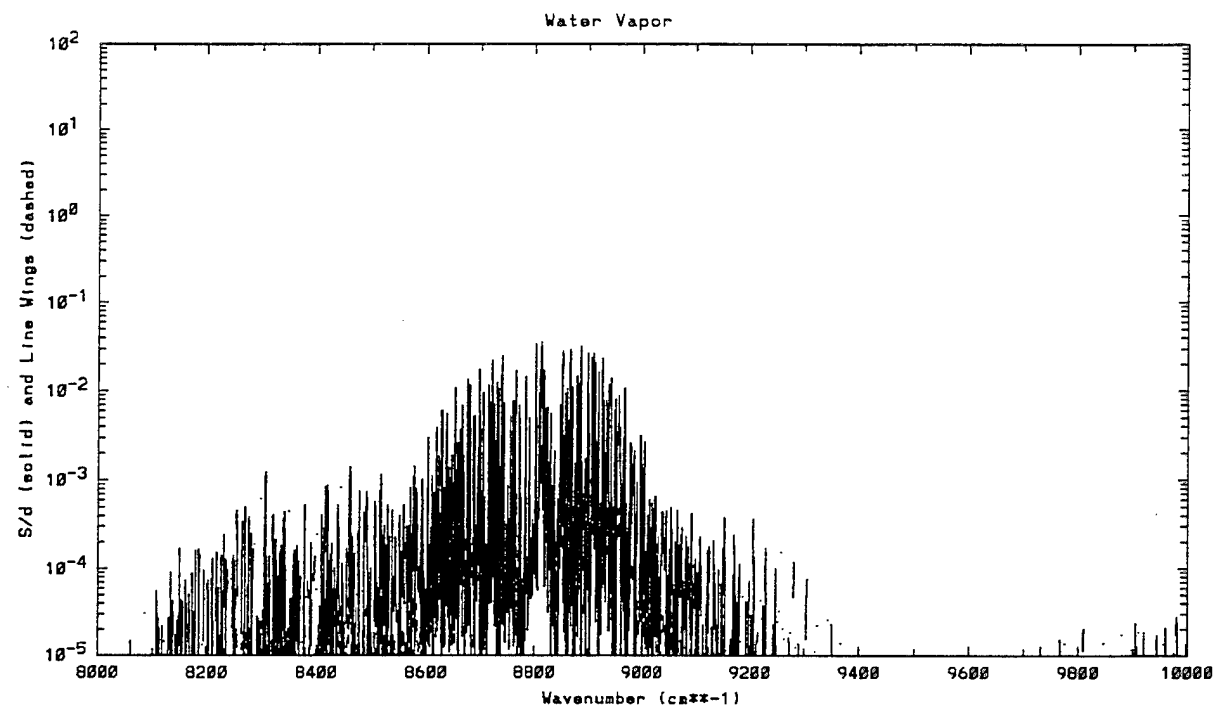
Figure 164. Absorption and Line Wing Coefficients for Water Vapor (continued).
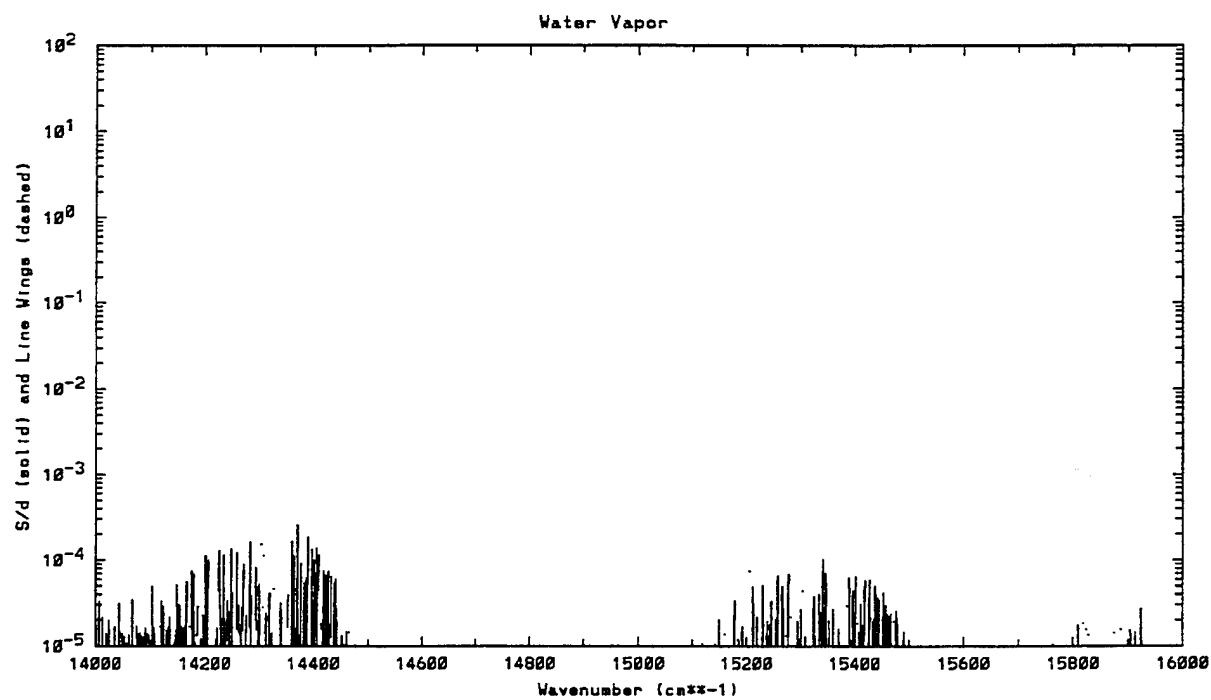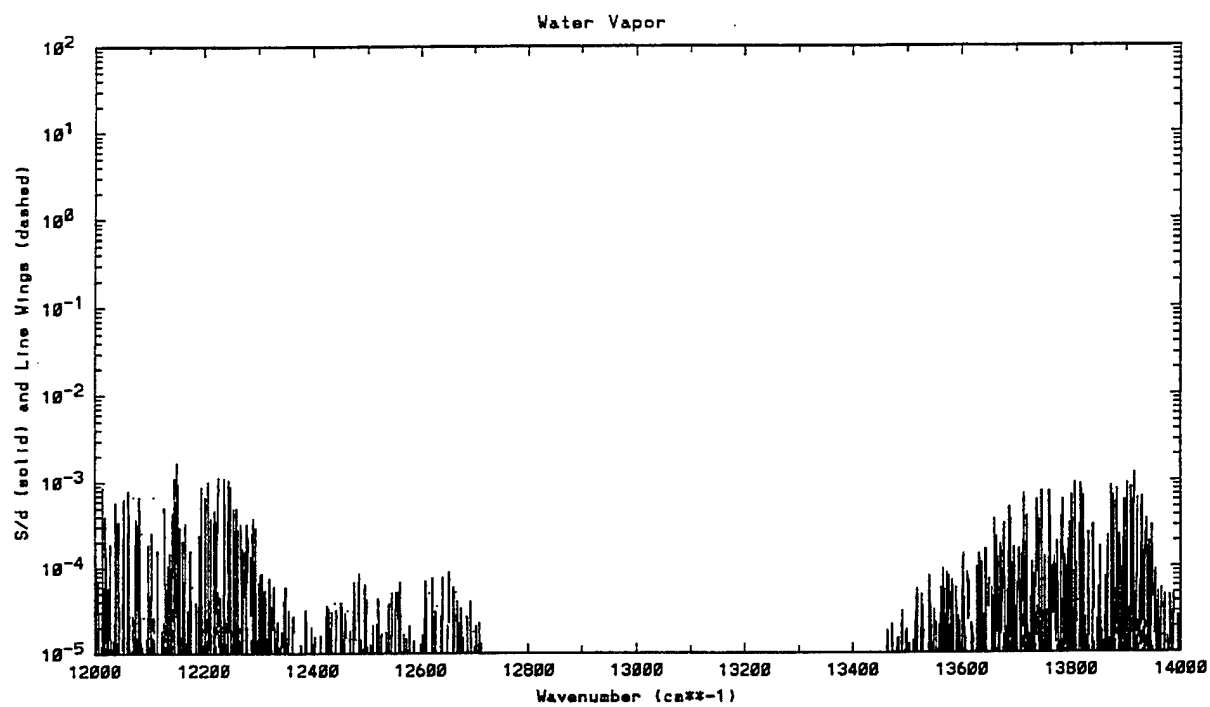
Figure 164. Absorption and Line Wing Coefficients for Water Vapor (continued).
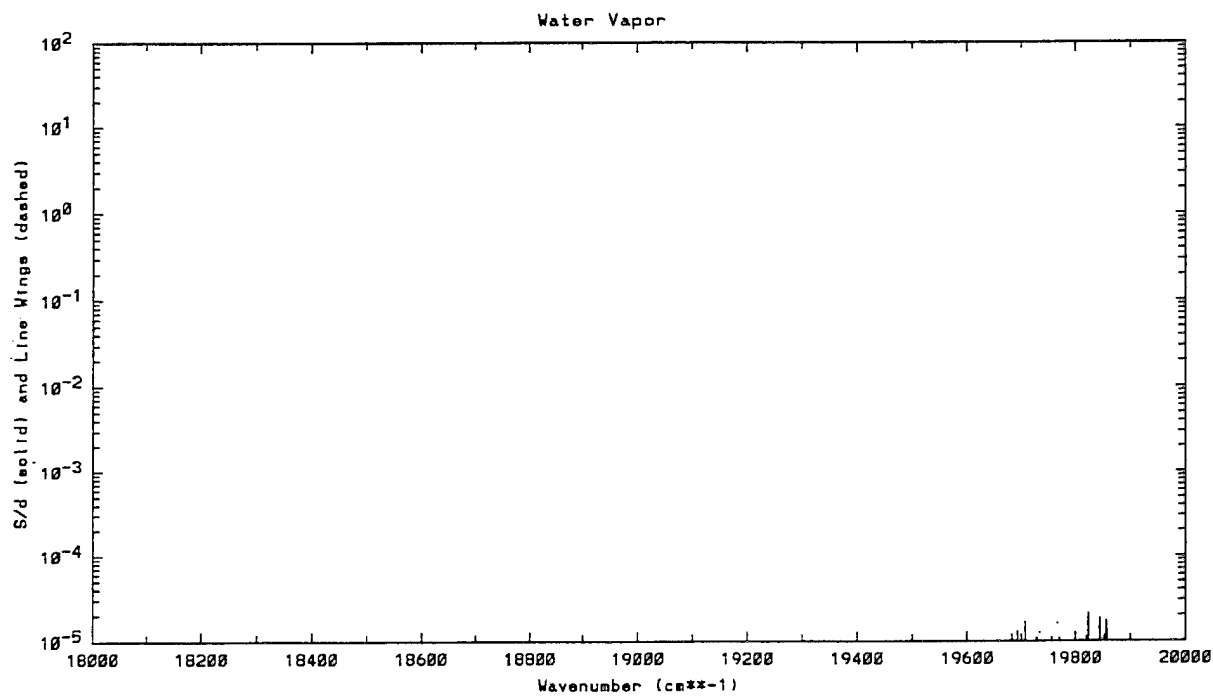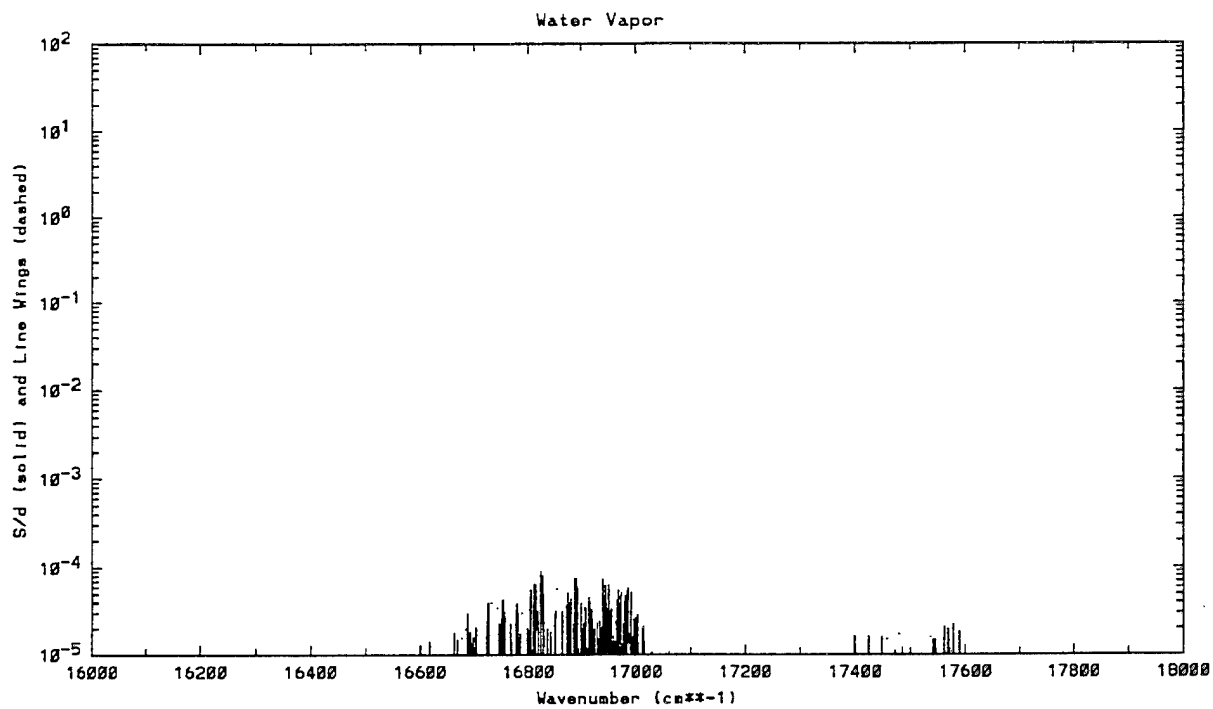
Figure 164. Absorption and Line Wing Coefficients for Water Vapor (continued).
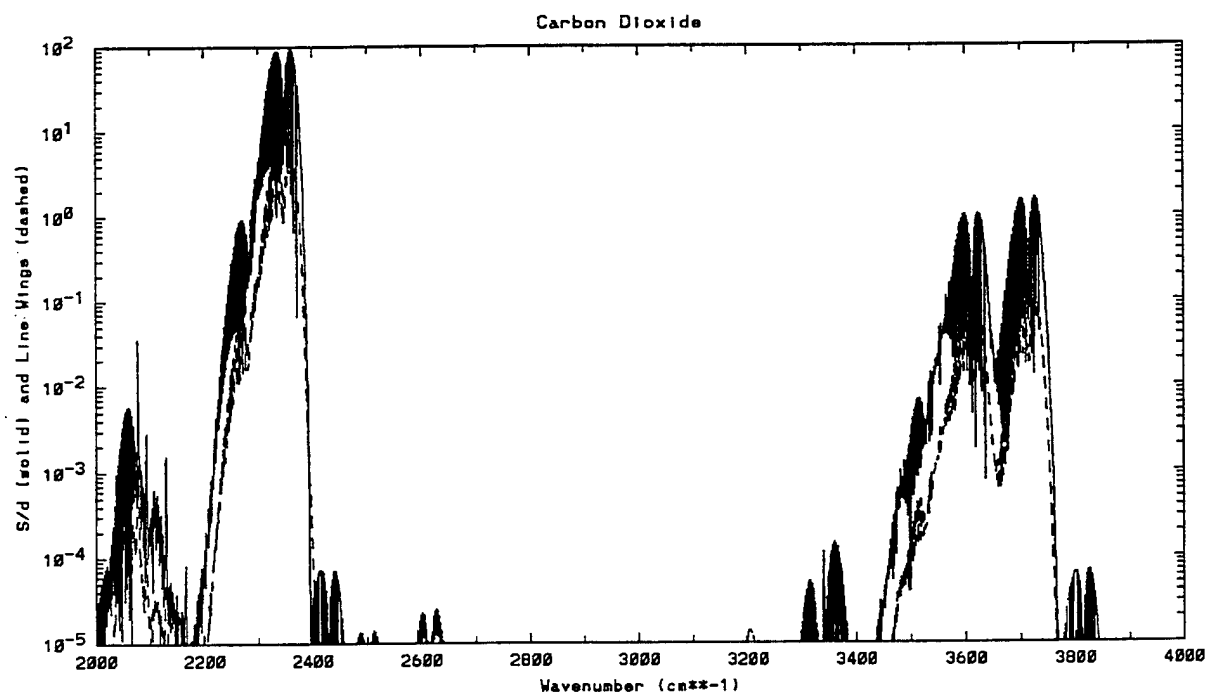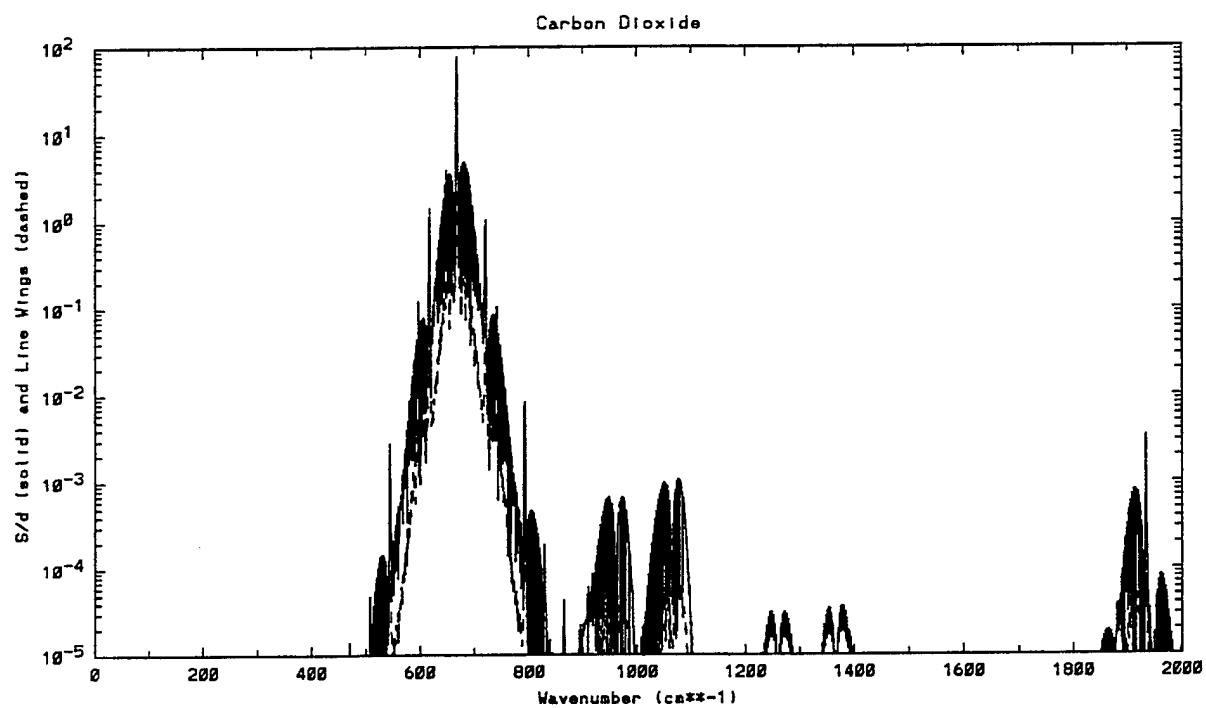
Figure 165. Absorption and Line Wing Coefficients for Carbon Dioxide.

Figure 165. Absorption and Line Wing Coefficients for Carbon Dioxide (continued).

208
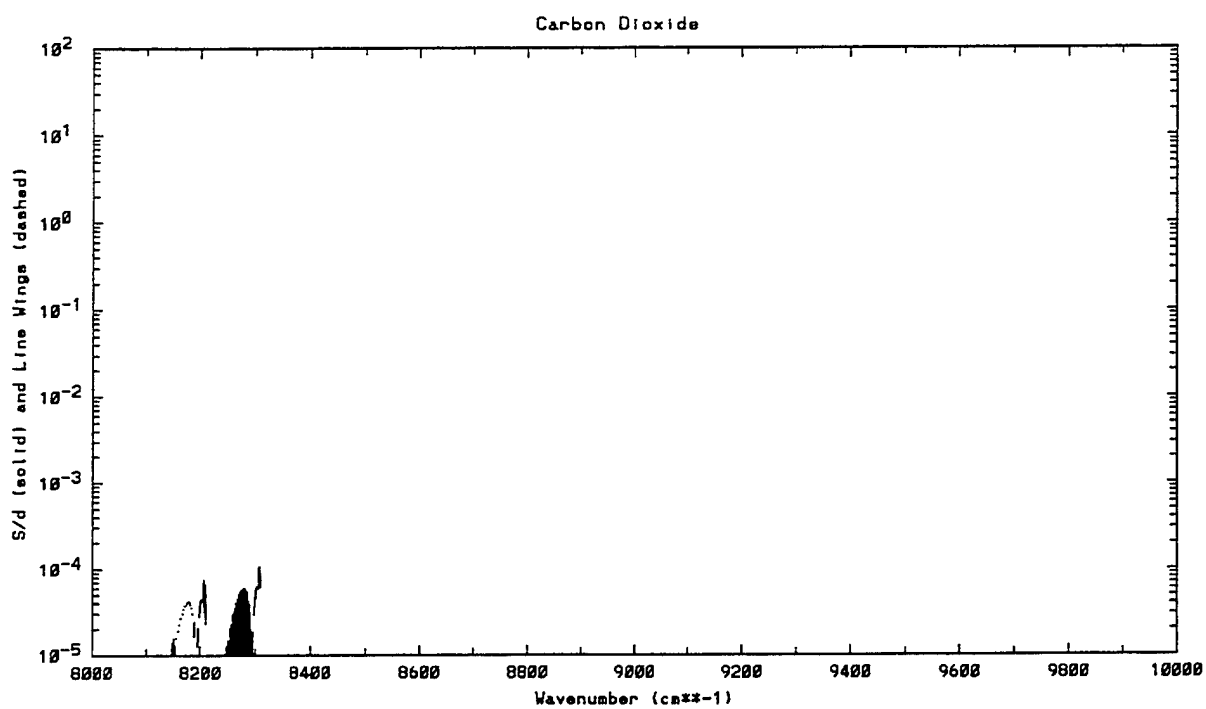
Figure 165. Absorption and Line Wing Coefficients for Carbon Dioxide (continued).
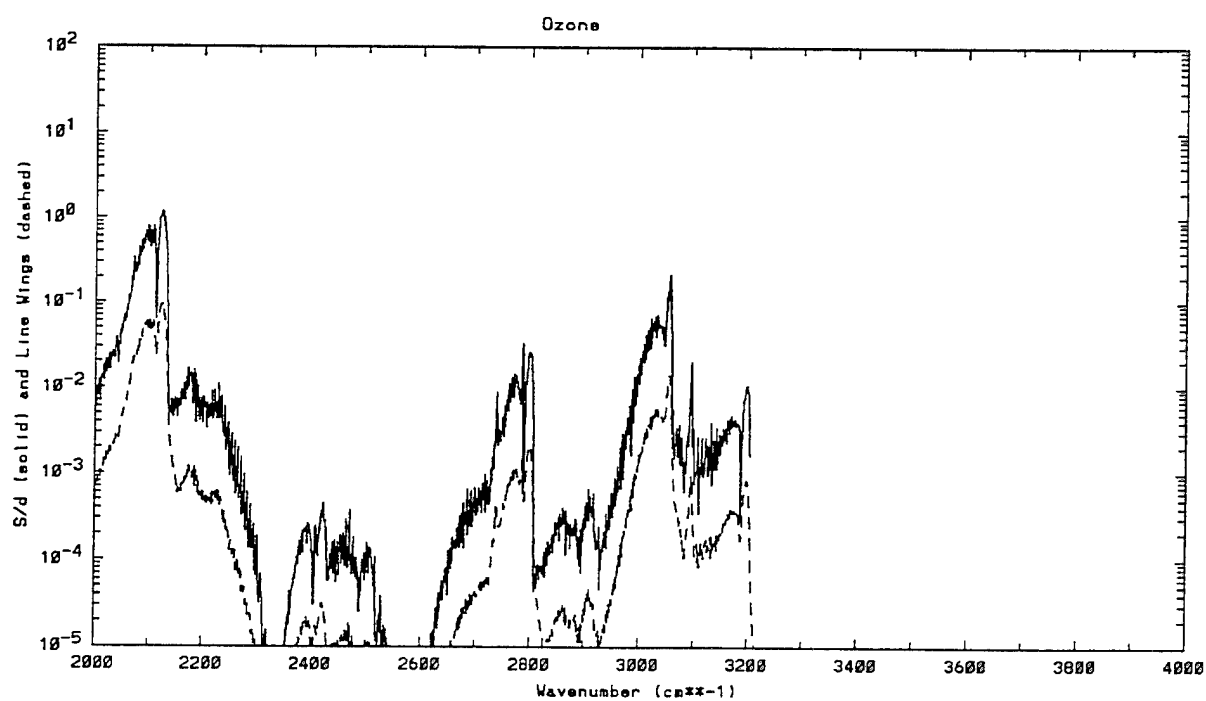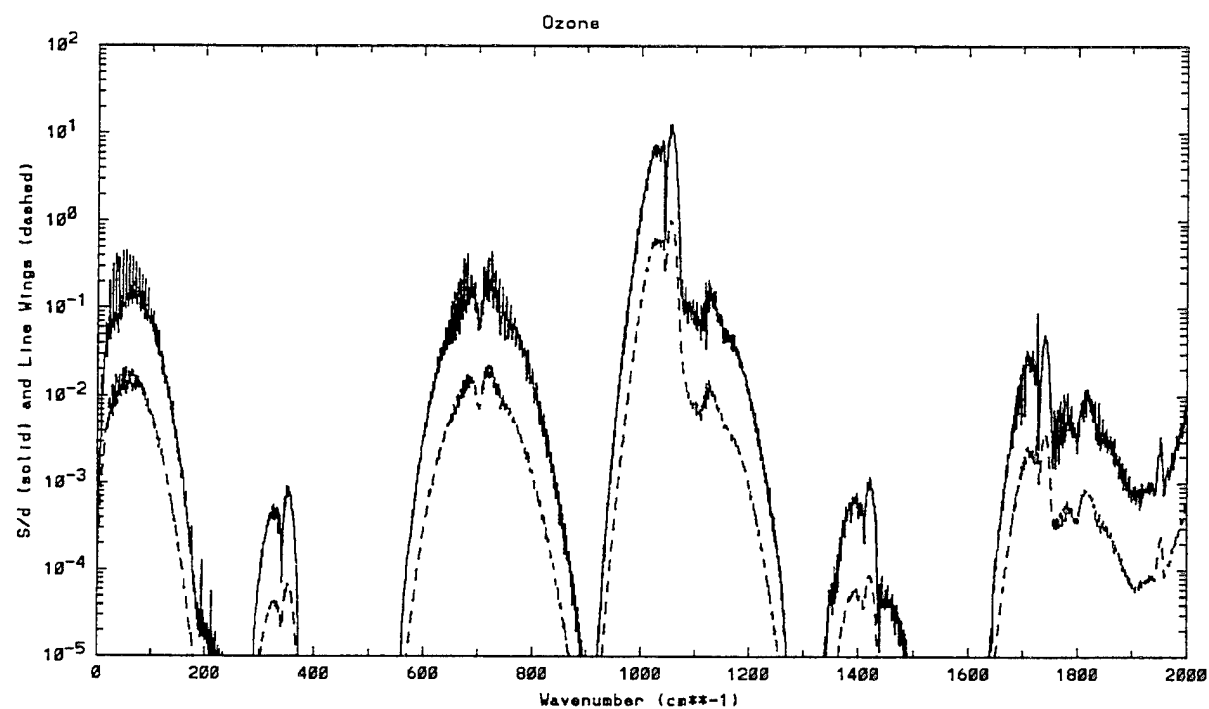
Figure 166. Absorption and Line Wing Coefficients for Ozone.
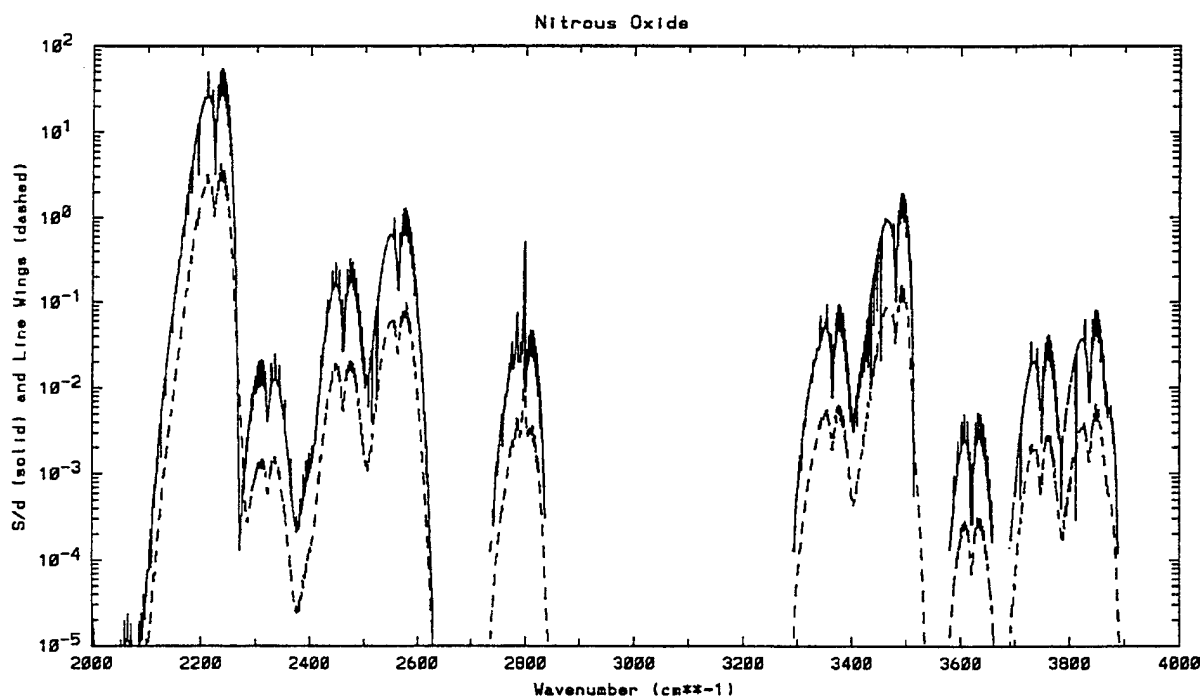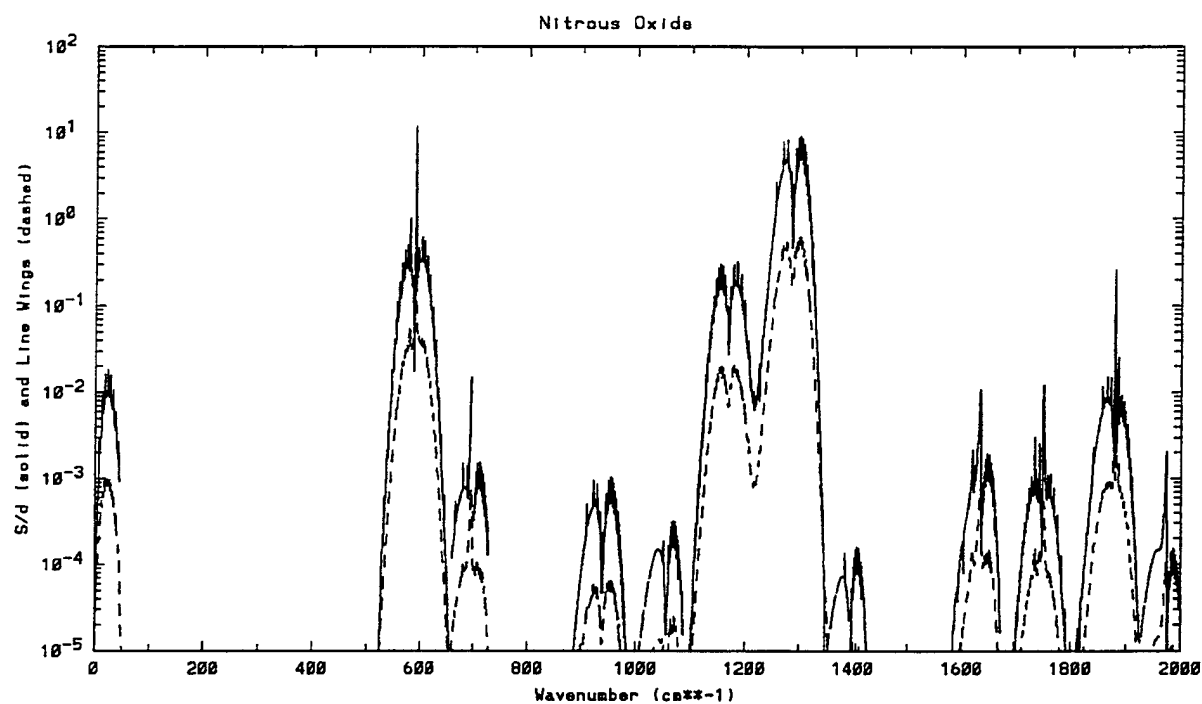
Figure 167. Absorption and Line Wing Coefficients for Nitrous Oxide.

211
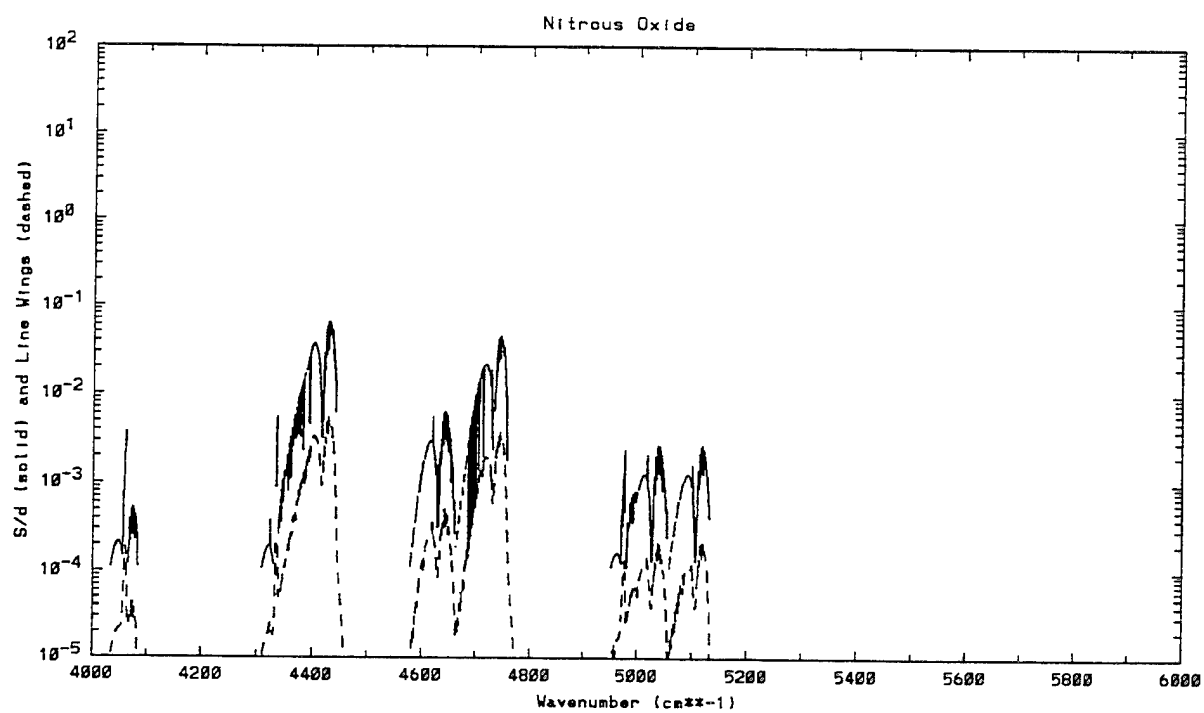
Figure 167. Absorption and Line Wing Coefficients for Nitrous Oxide (continued).
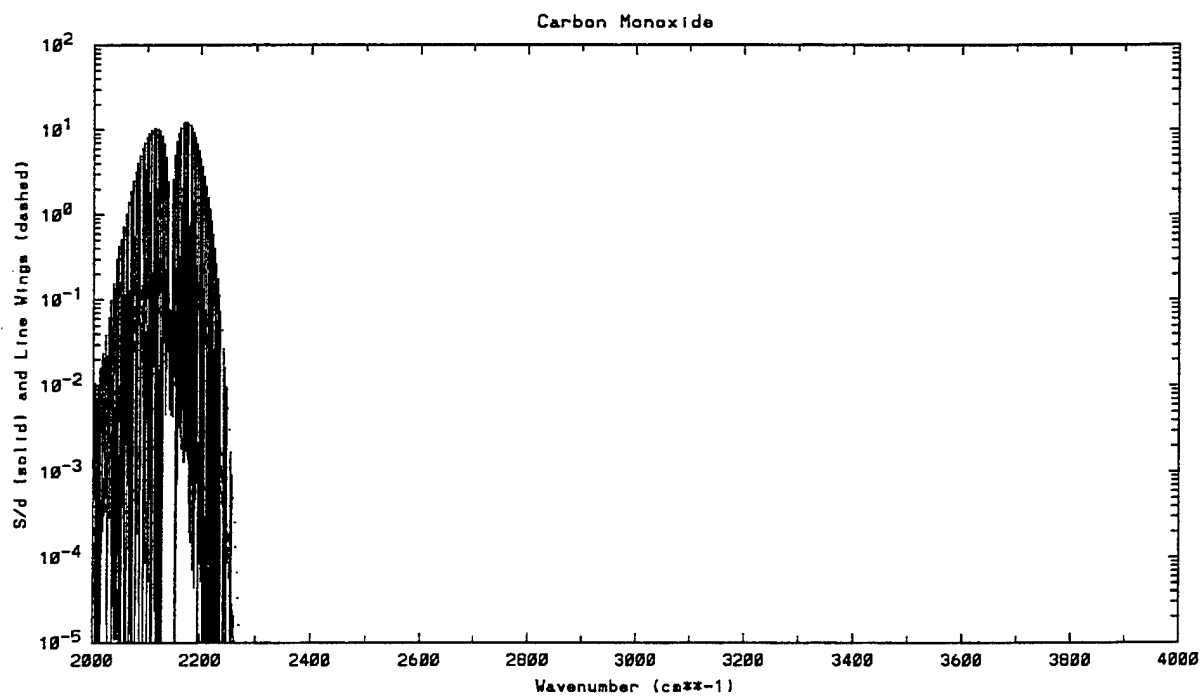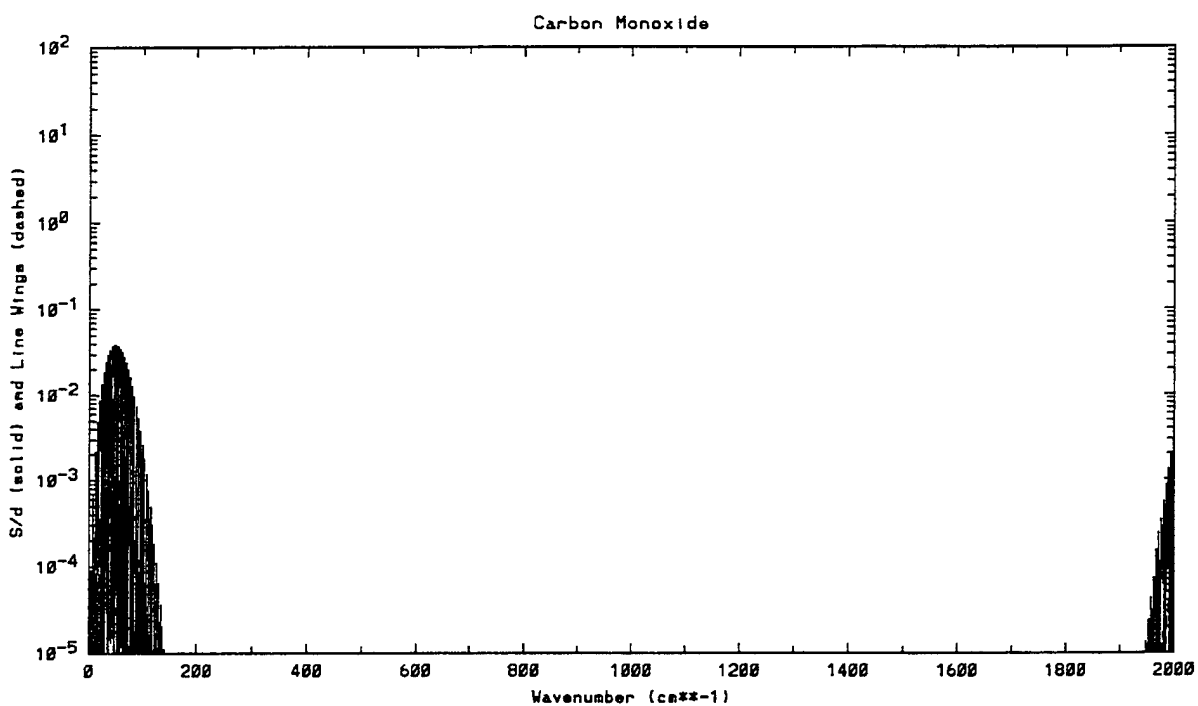
Figure 168. Absorption and Line Wing Coefficients for Carbon Monoxide.

213
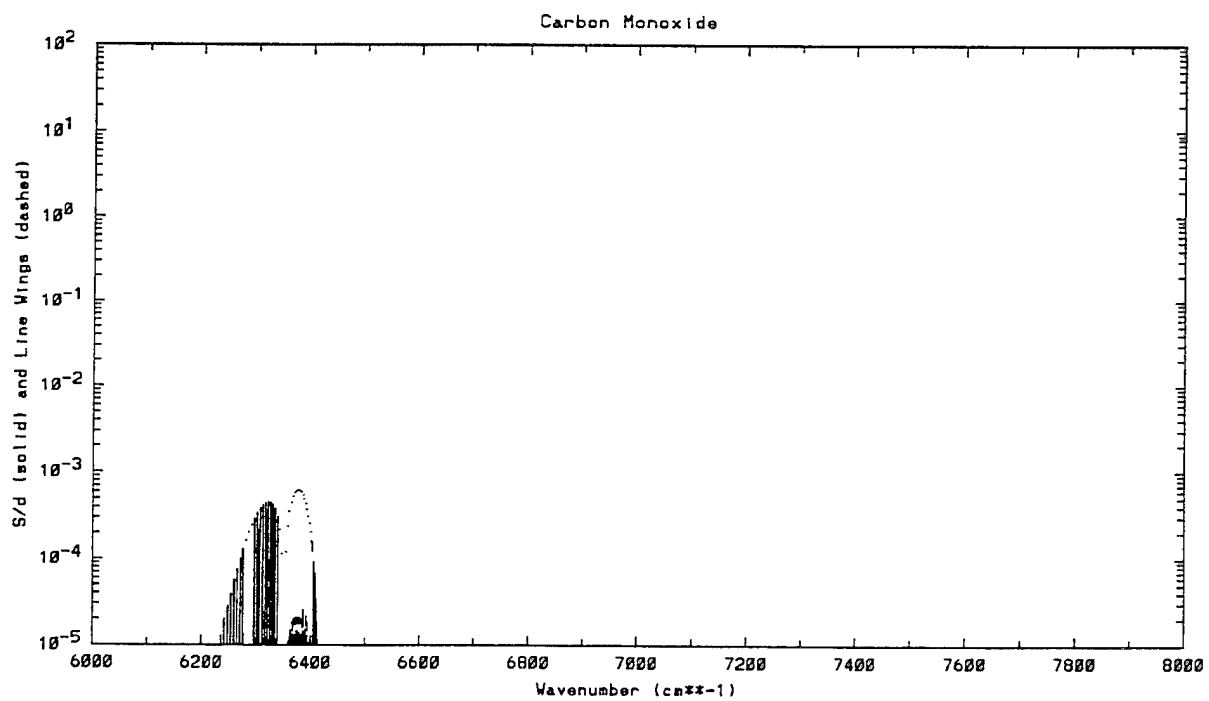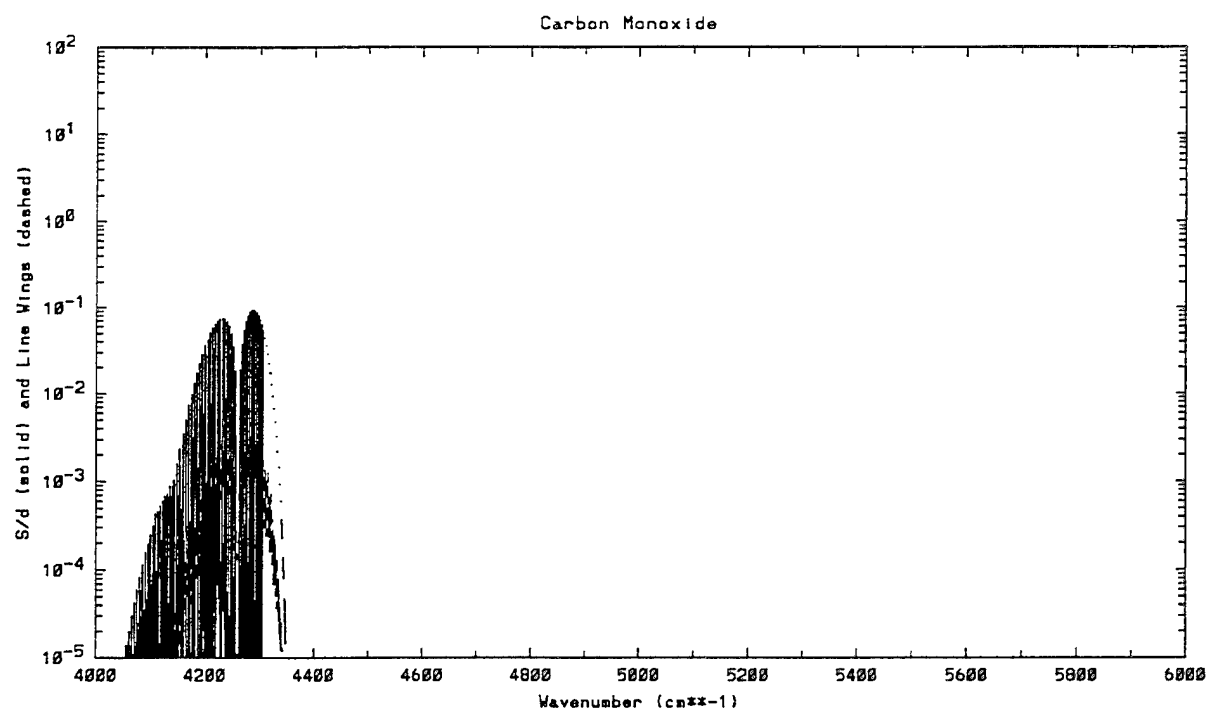
Figure 168. Absorption and Line Wing Coefficients for Carbon Monoxide (continued).
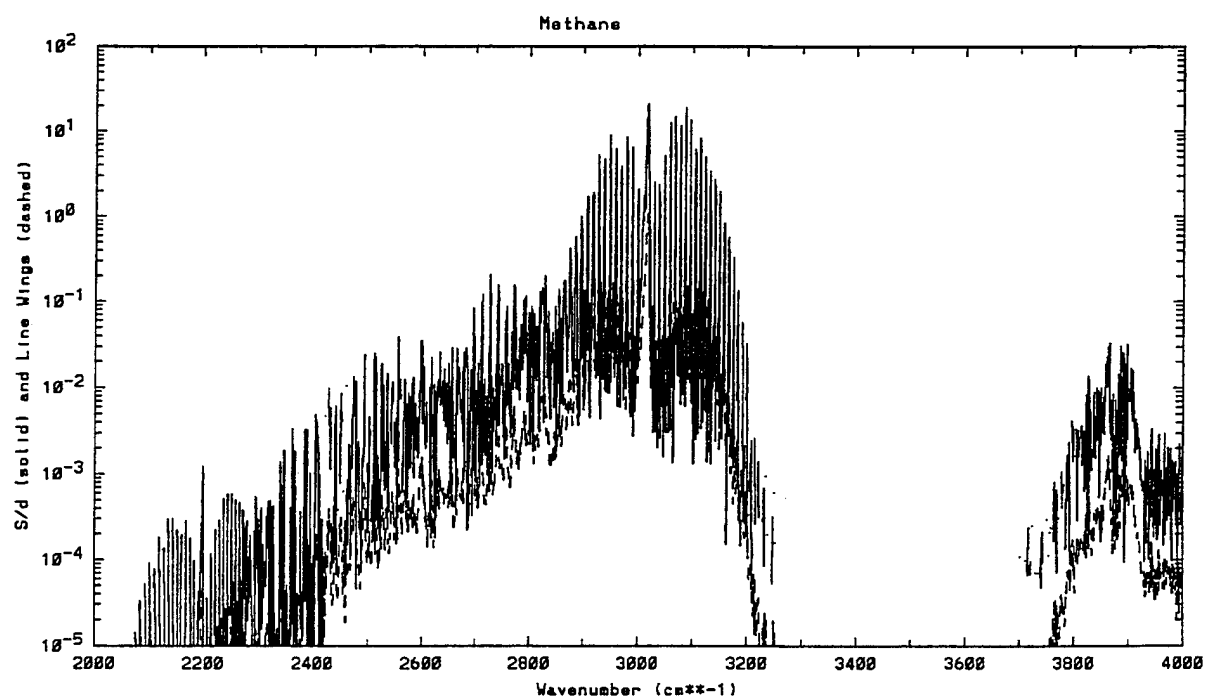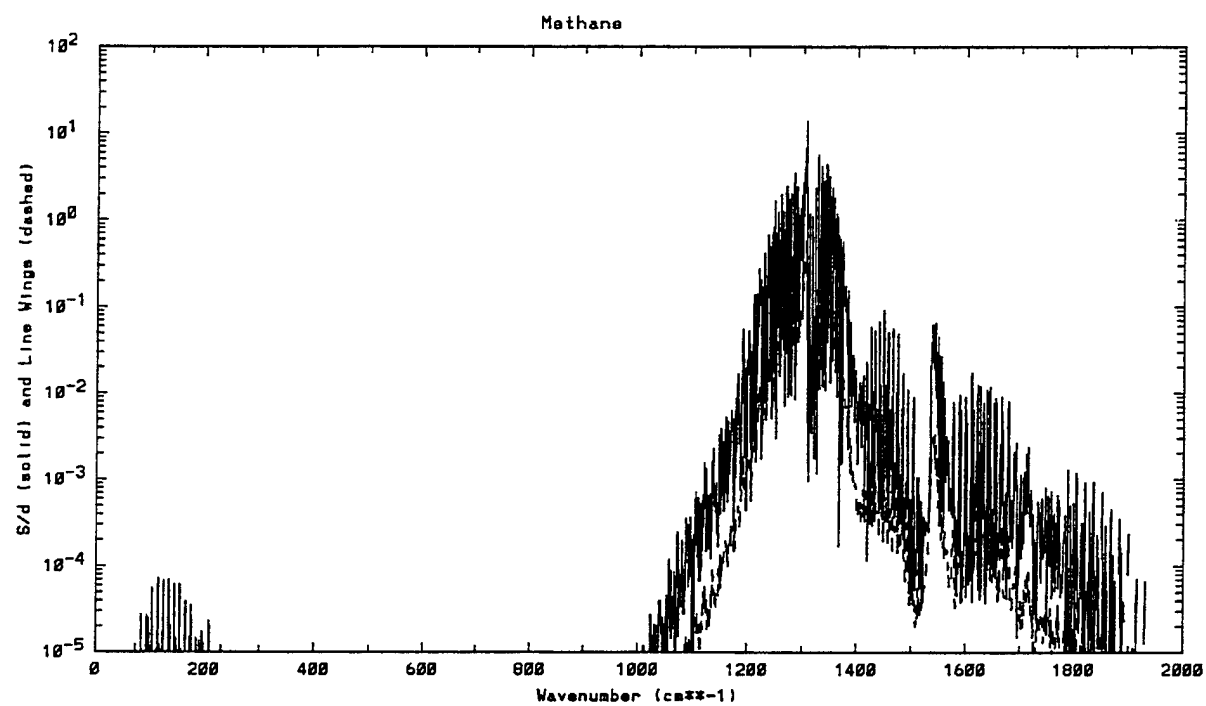
Figure 169. Absorption and Line Wing Coefficient for Methane.
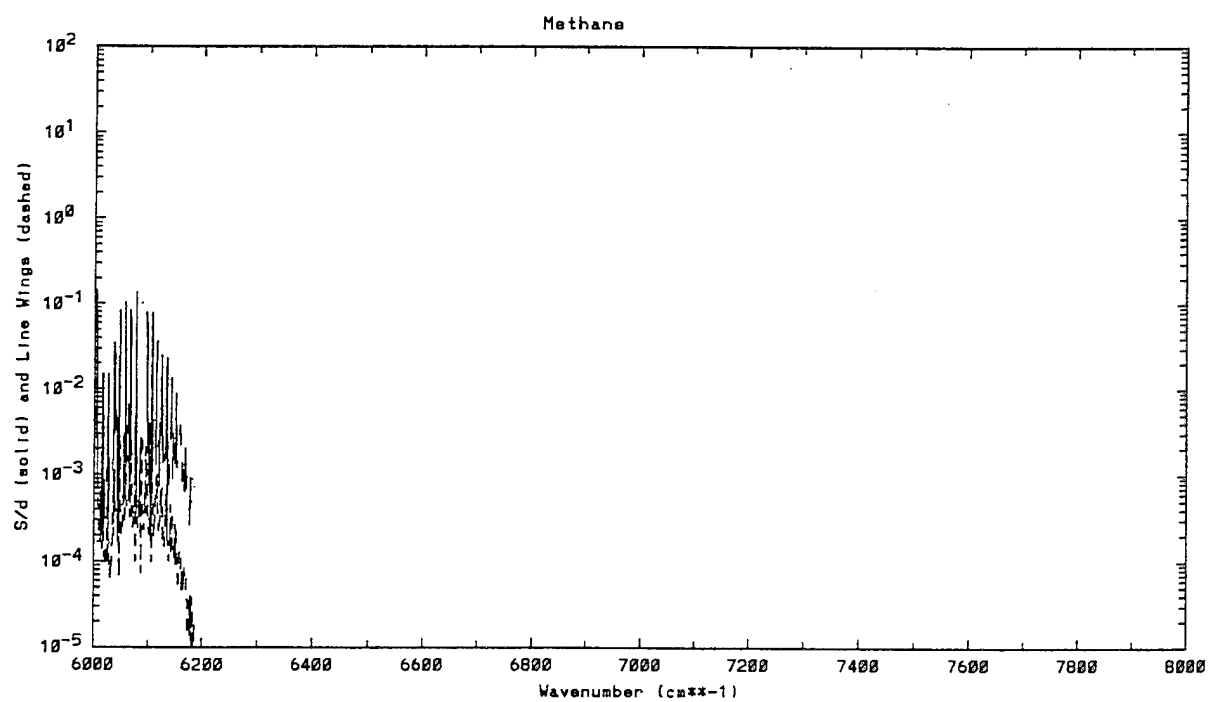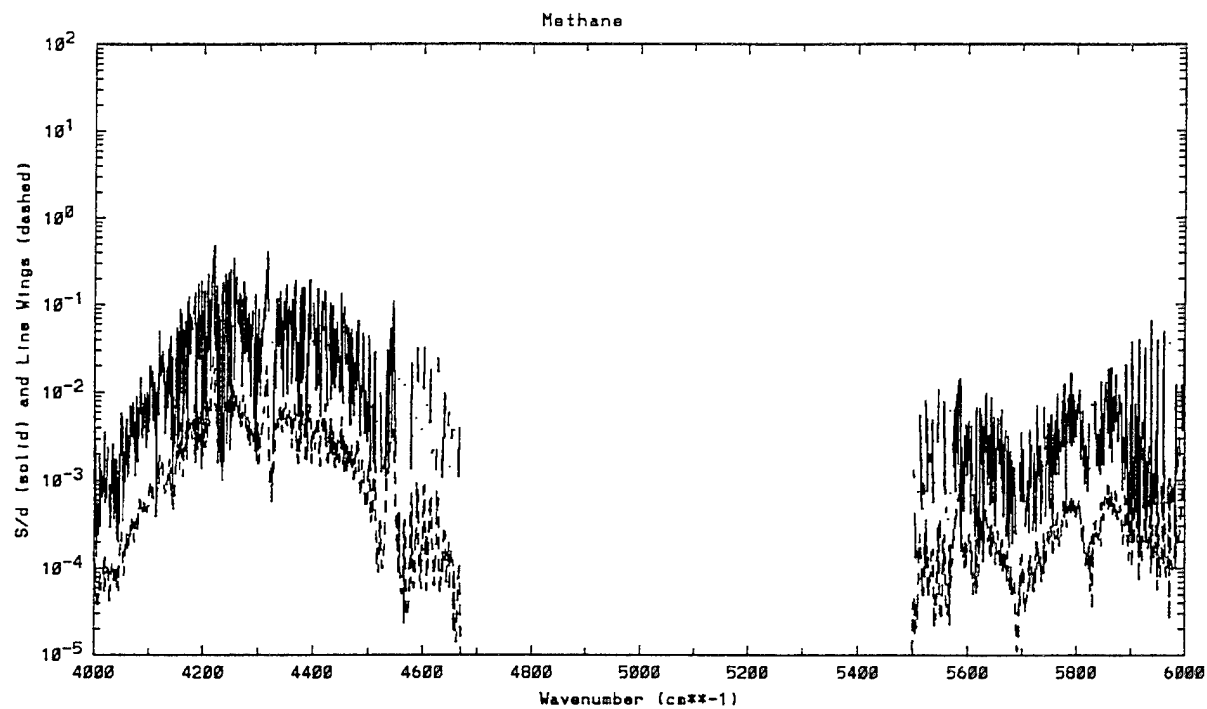
Figure 169. Absorption and Line Wing Coefficient for Methane (continued).
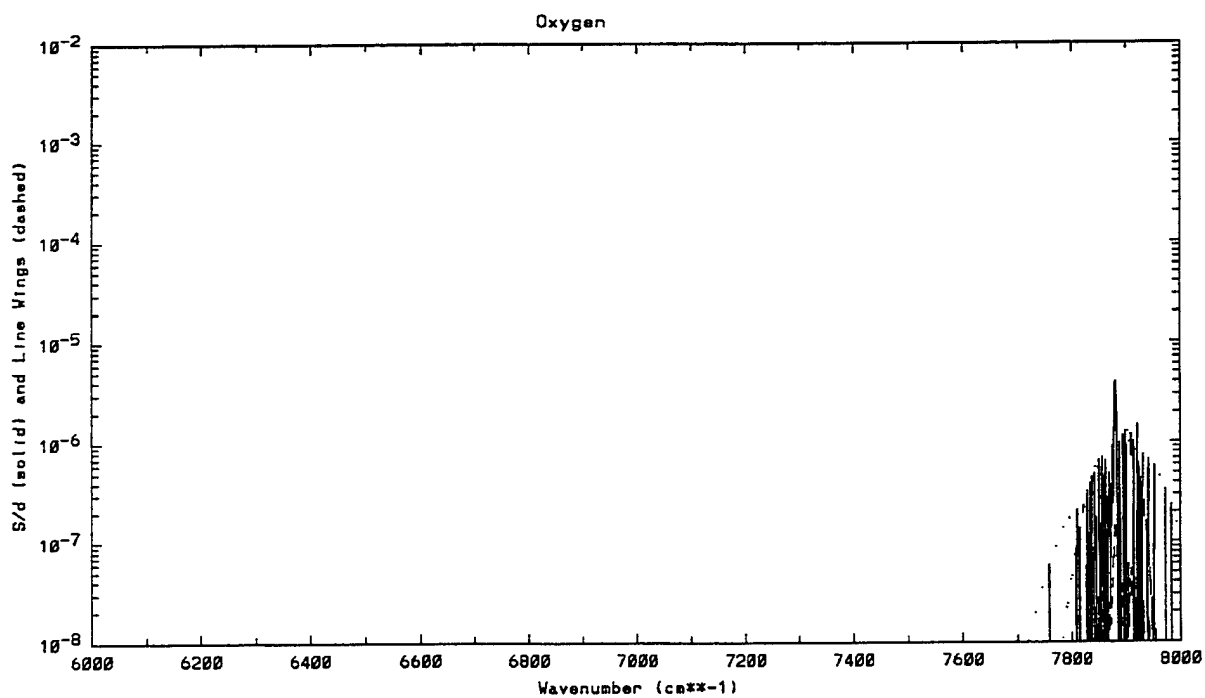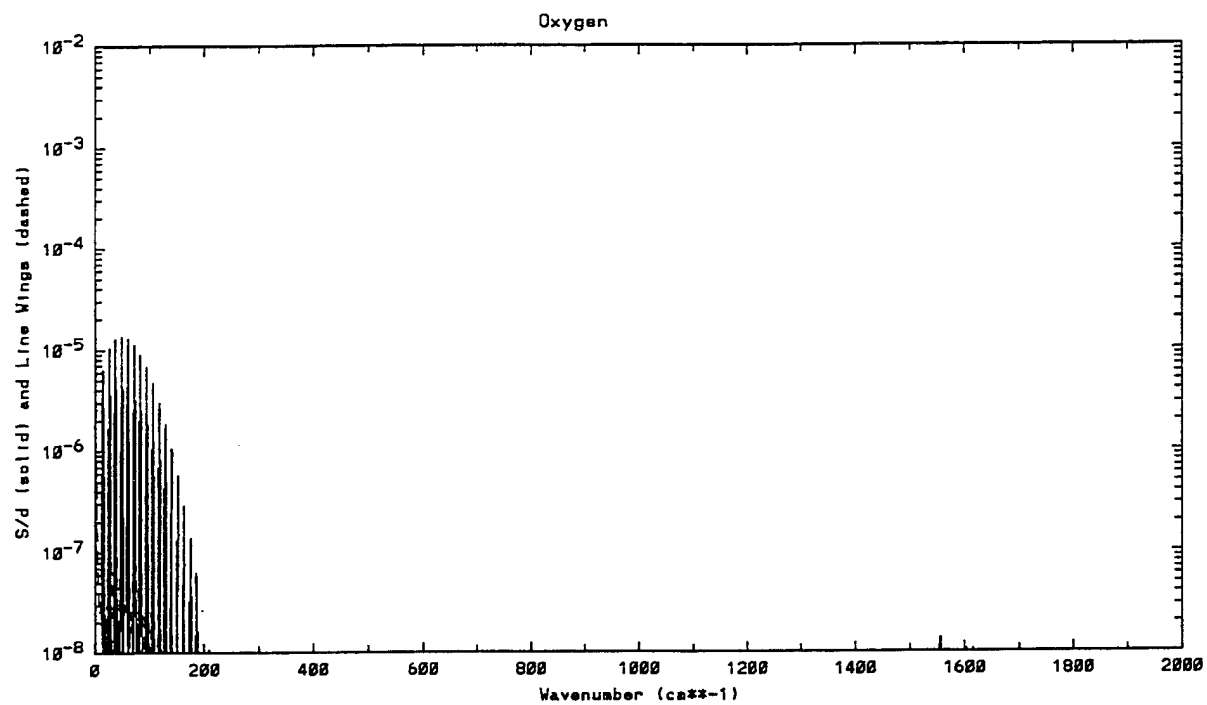
Figure 170. Absorption and Line Wing Coefficient for Oxygen.
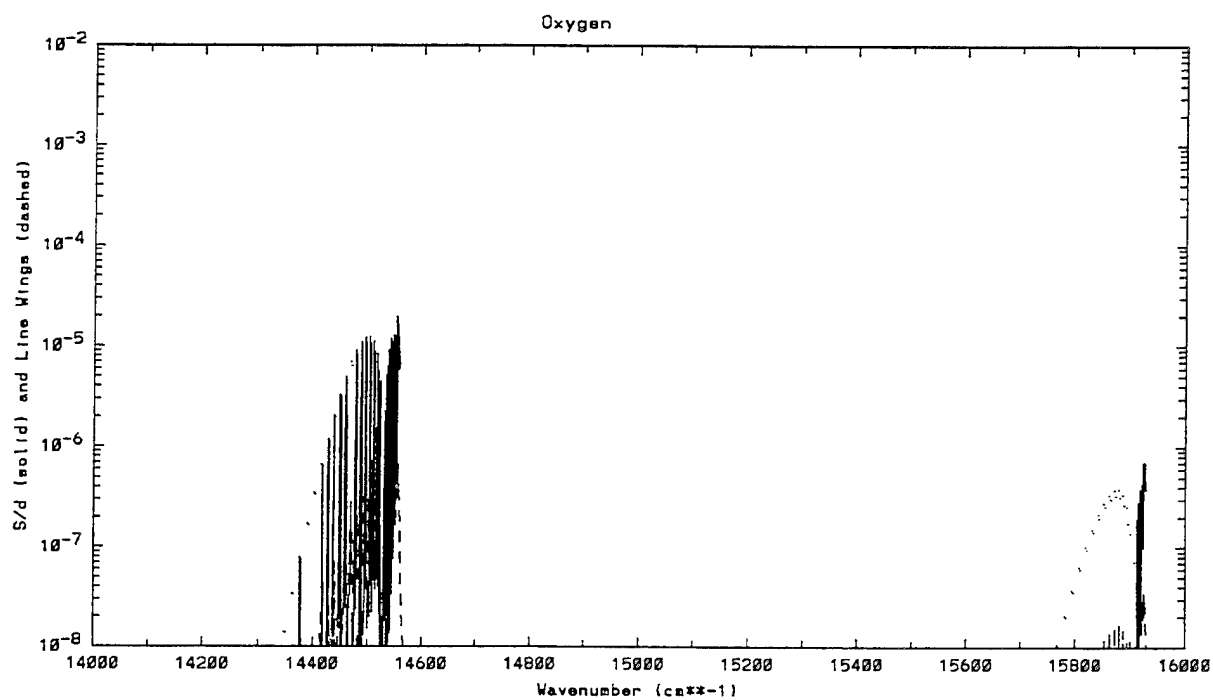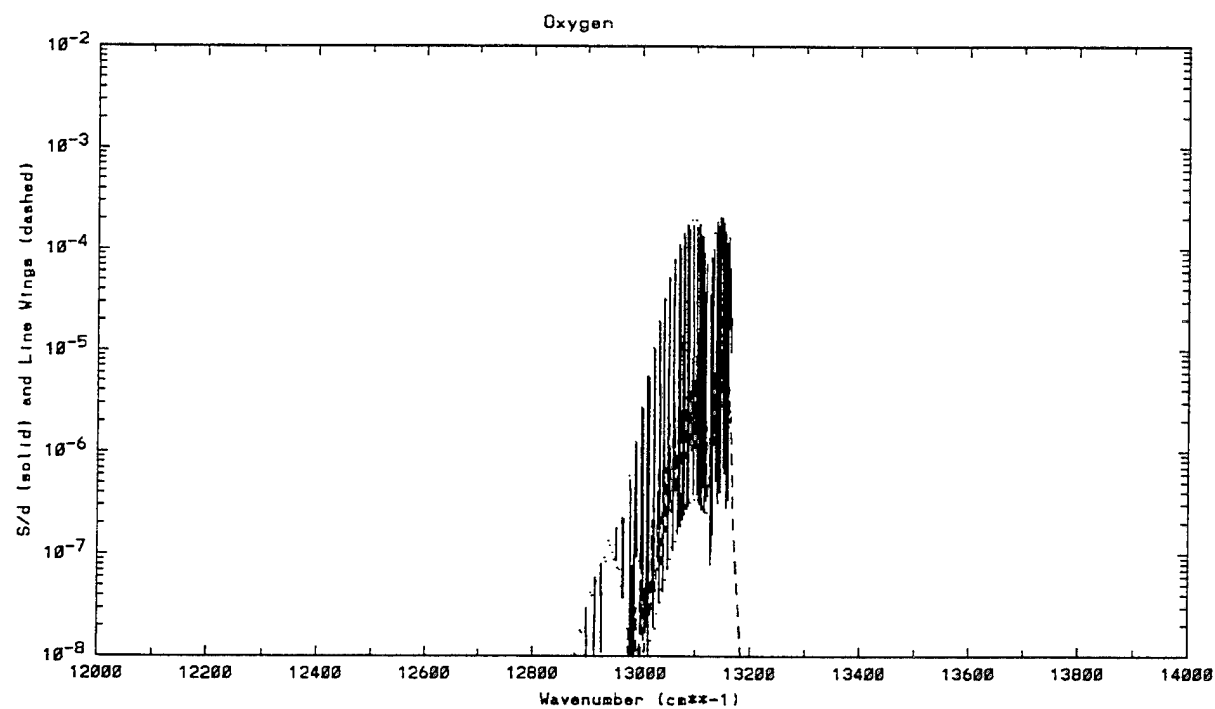
Figure 170. Absorption and Line Wing Coefficient for Oxygen (continued).
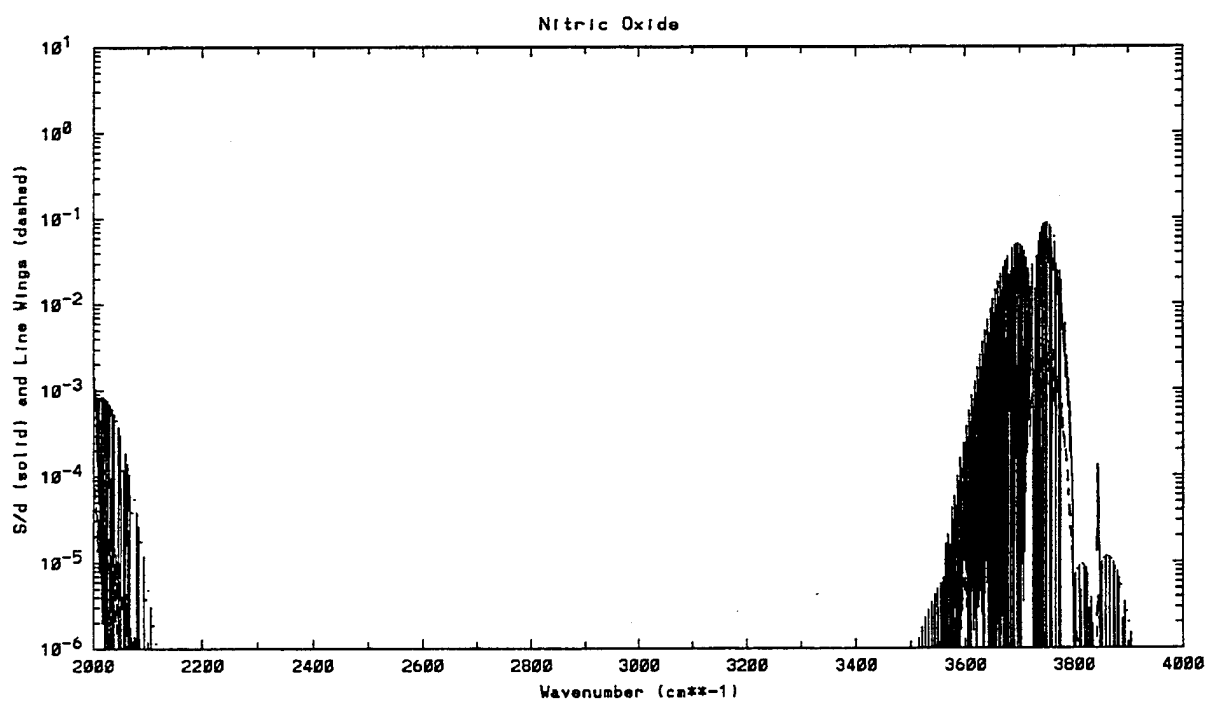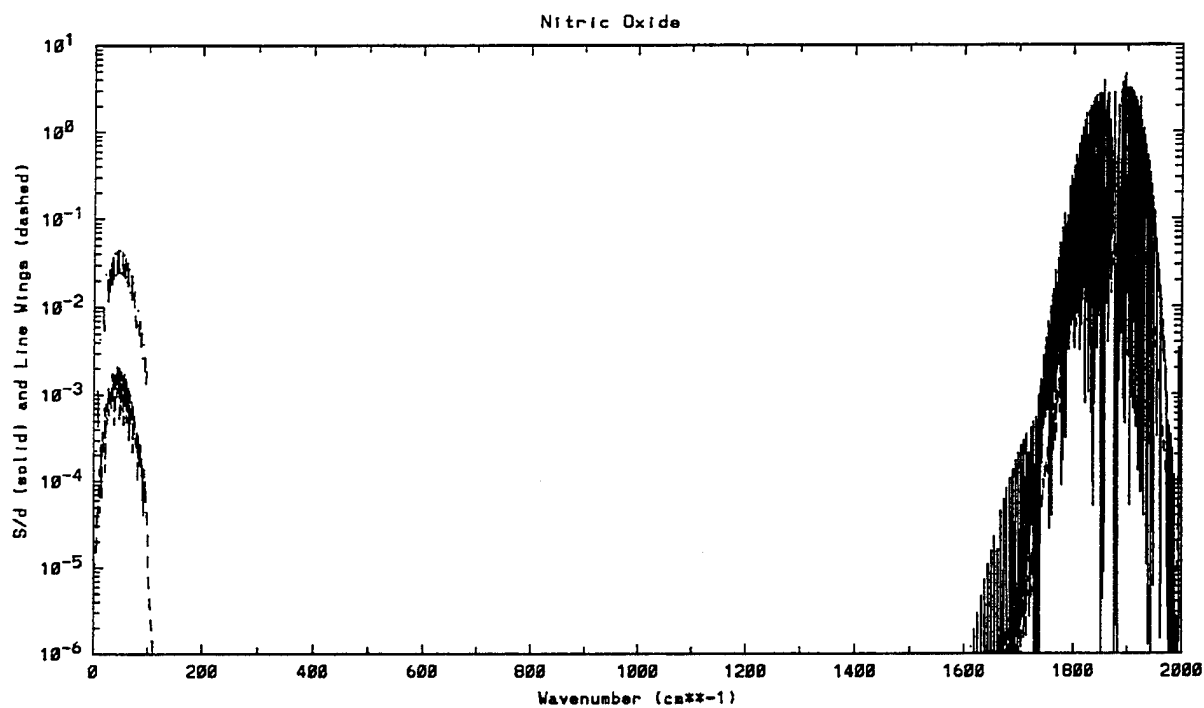
Figure 171. Absorption and Line Wing Coefficient for Nitric Oxide.
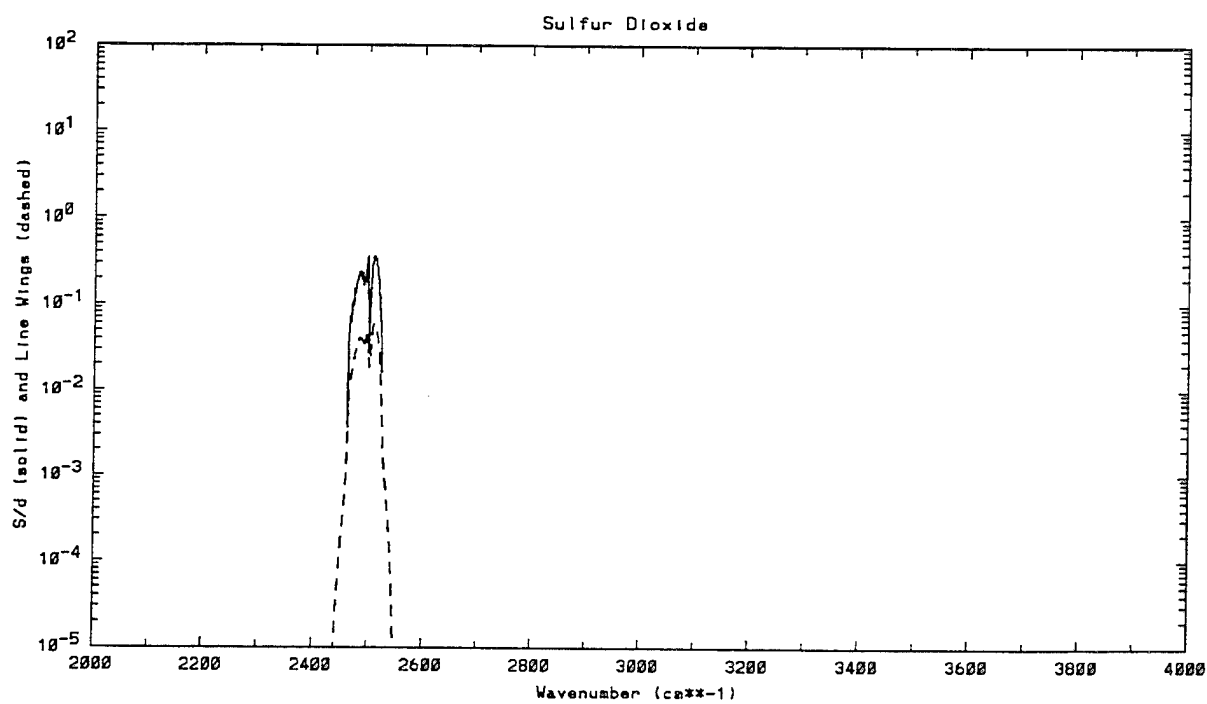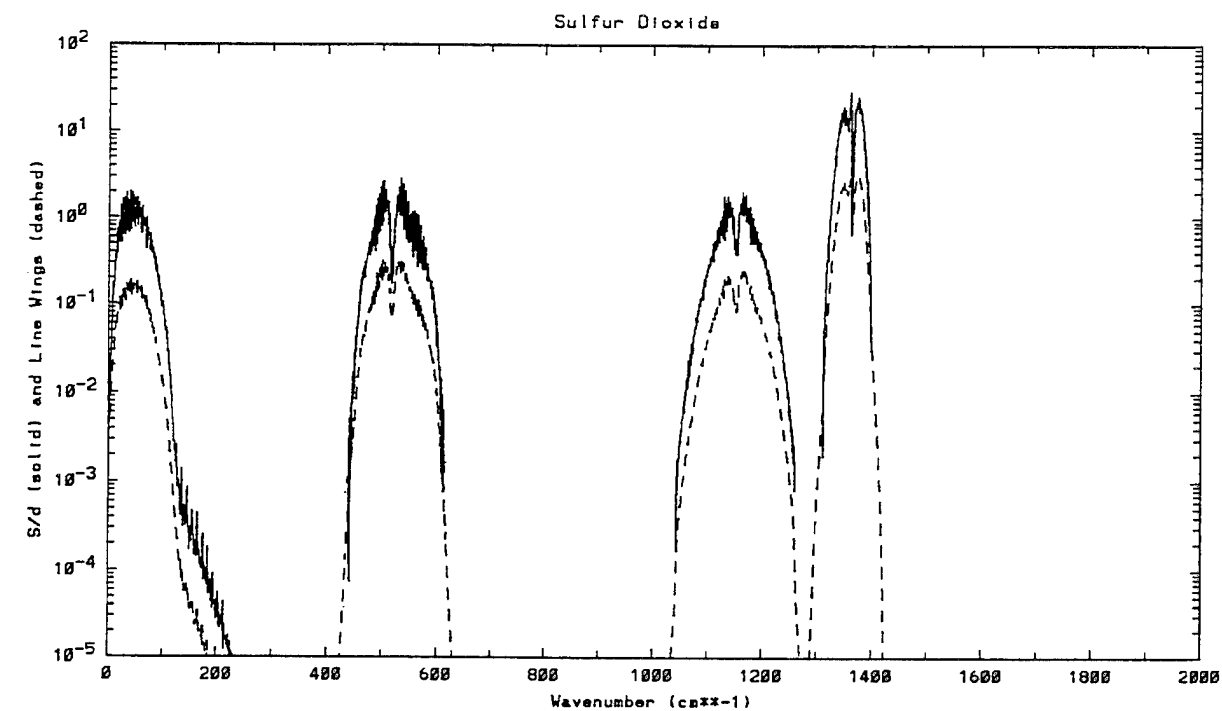
Figure 172. Absorption and Line Wing Coefficient for Sulfur Dioxide.

220
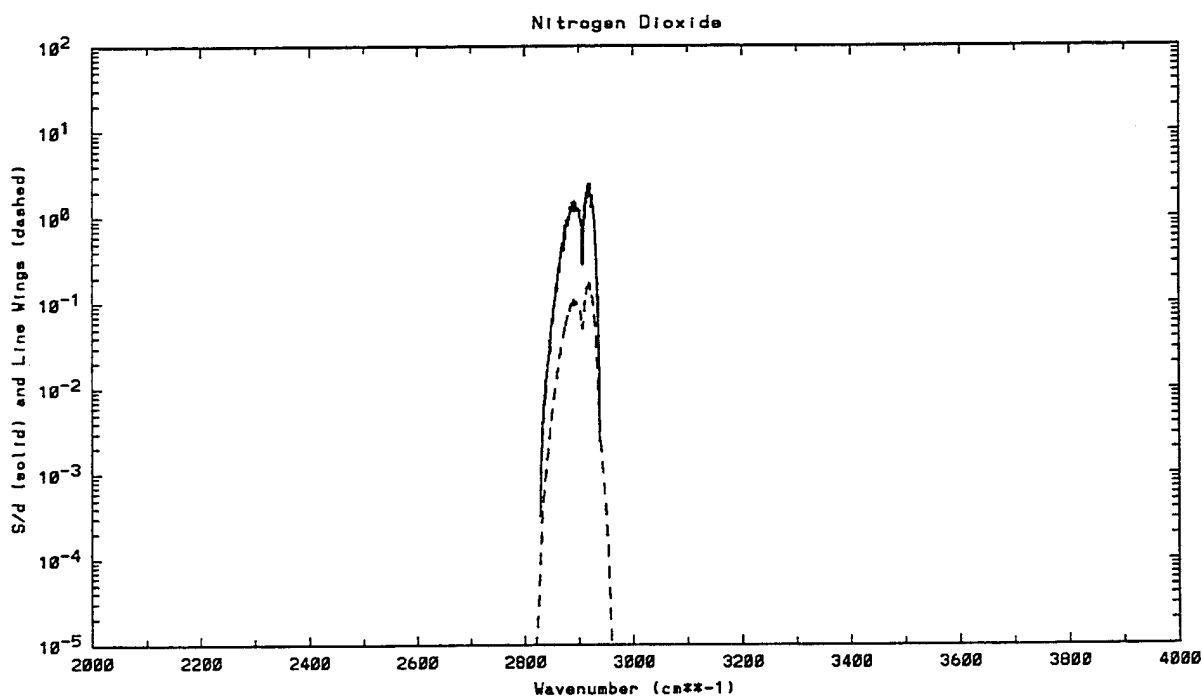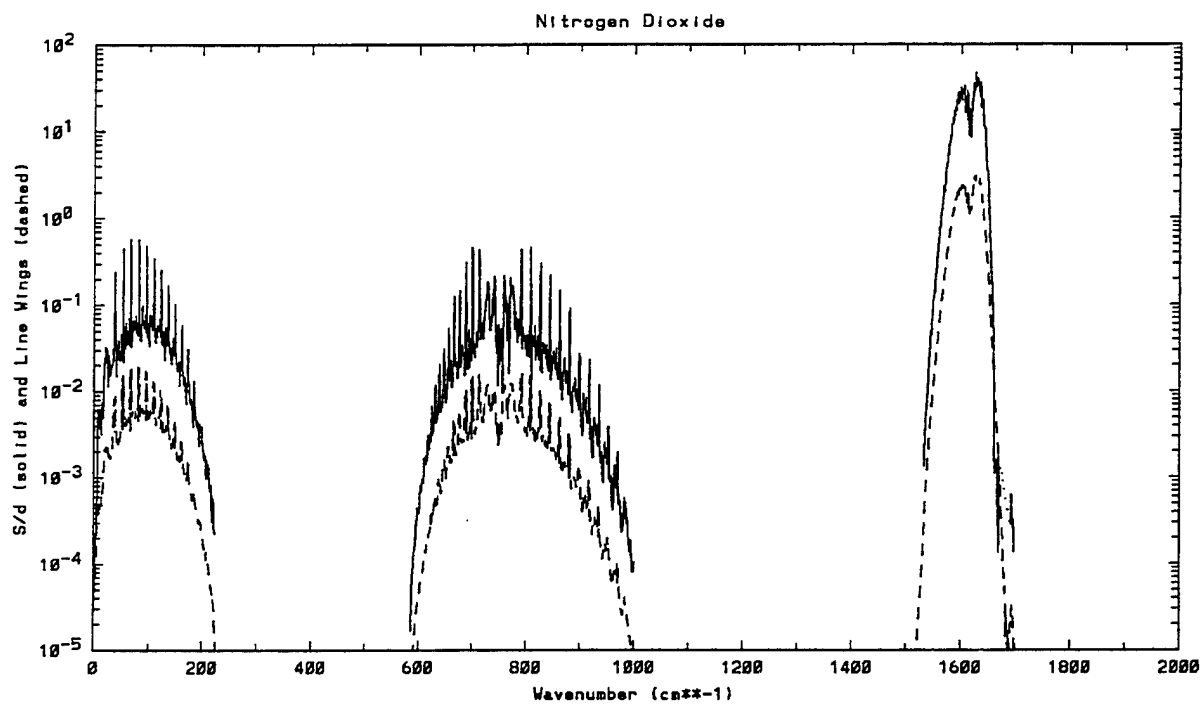
Figure 173. Absorption and Line Wing Coefficient for Nitrogen Dioxide.

221
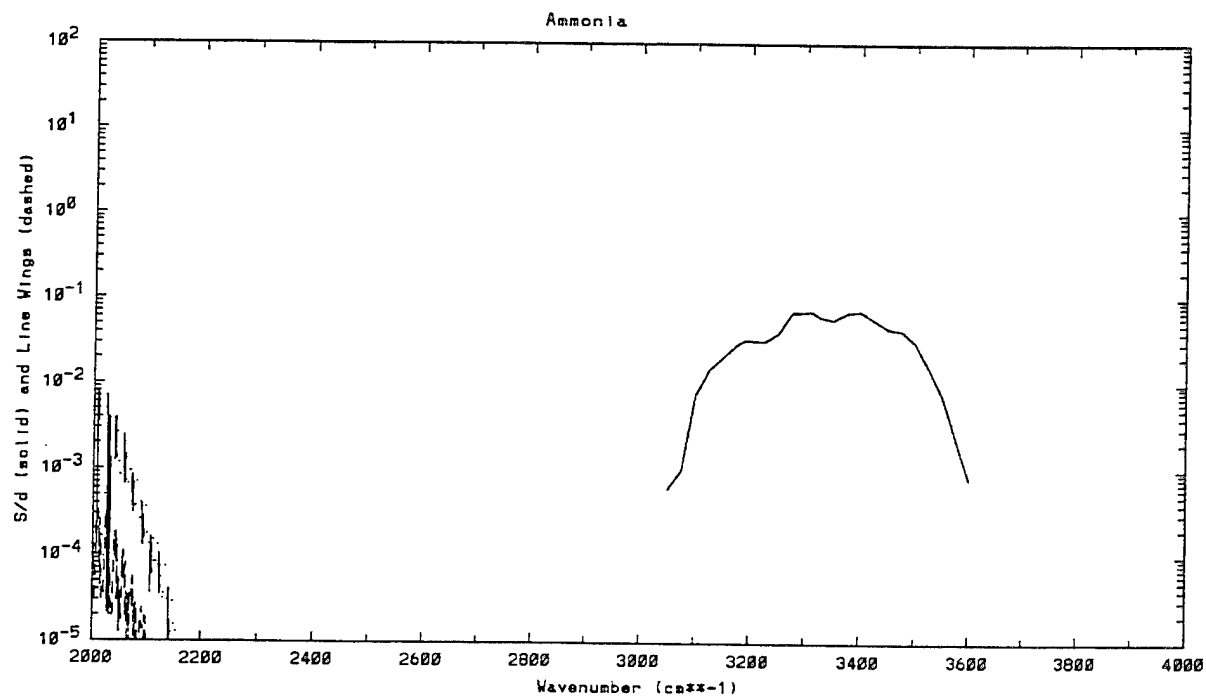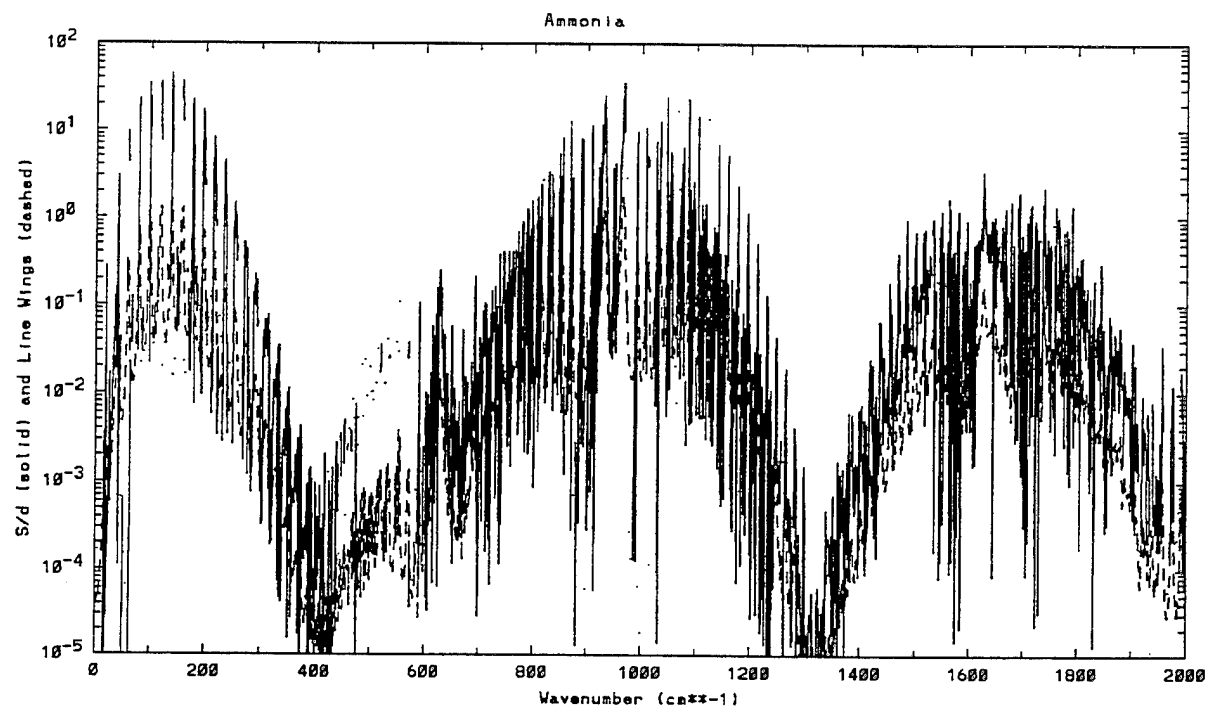
Figure 174. Absorption and Line Wing Coefficient for Ammonia.

222
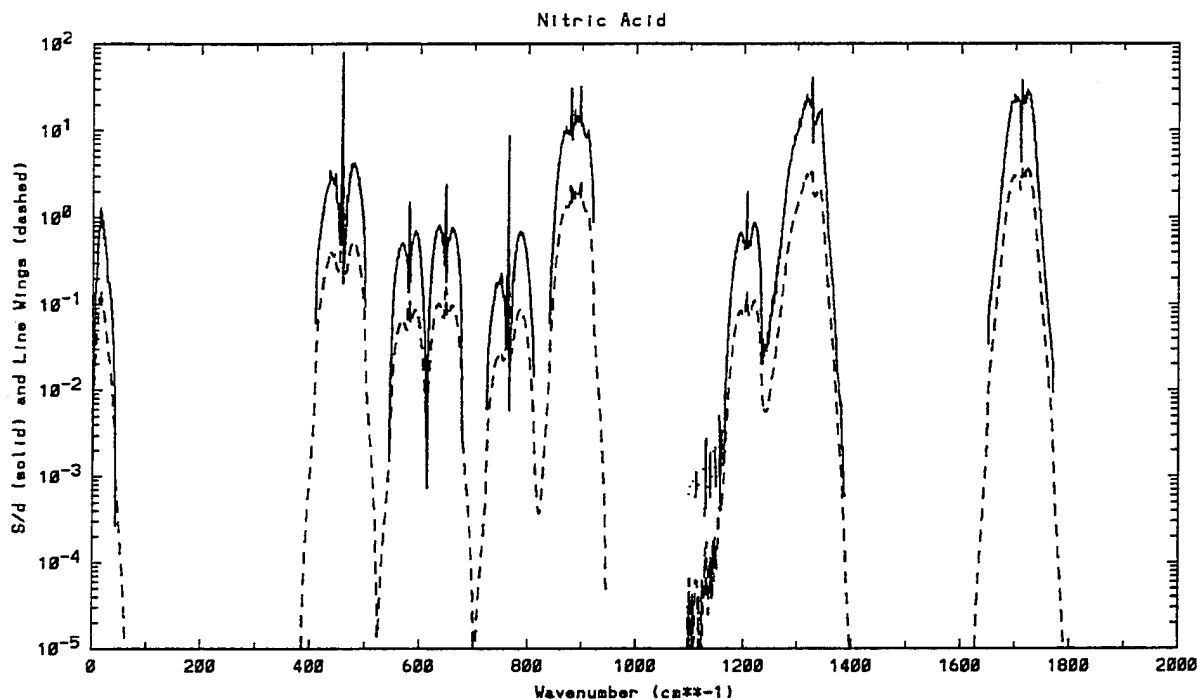
Figure 175. Absorption and Line Wing Coefficient for Nitric Acid.

4.3 Molecular Continua

In addition to the line wings presented in Section 4.2, the molecular continuum components for H_2O, N_2, and O_2 have been taken from MODTRAN.

Since the actual line shape of the water vapor molecule deviates significantly from the Lorentz shape, the line wings from Section 4.2 are replaced by the water vapor self- and foreign-broadened continua from LOWTRAN as shown in Figure 176. The new Jaycor "fudge" factor from MODTRAN (i.e., in SUBROUTINE FUDGE) is included in MOSART.

Although the line absorption of nitrogen is extremely weak, the nitrogen continuum does affect longer paths in the troposphere over the 3.8 - 4.8 μm spectral interval. The absorption coefficients were taken from LOWTRAN and are shown in Figure 177.

A weak oxygen continuum (in addition to the line structure in Section 4.2) is shown in Figure 178.

223
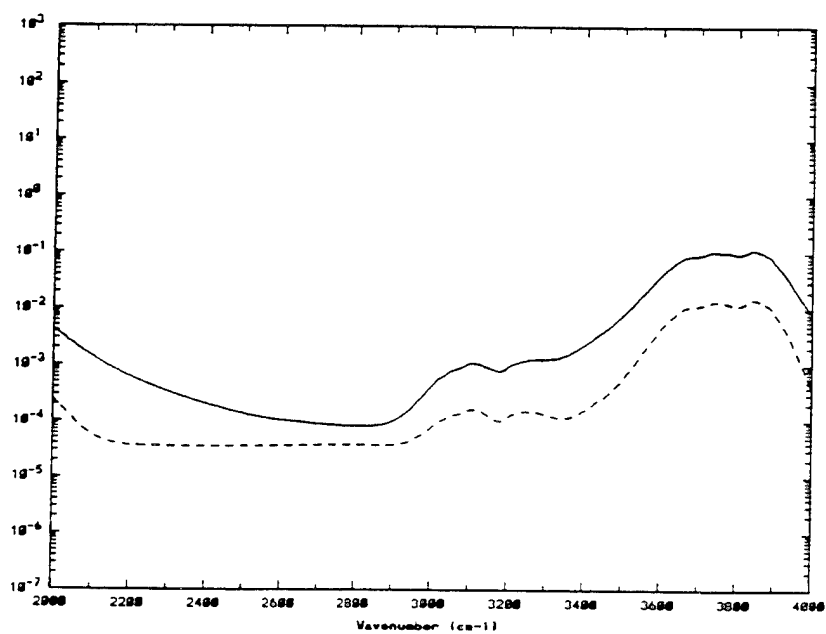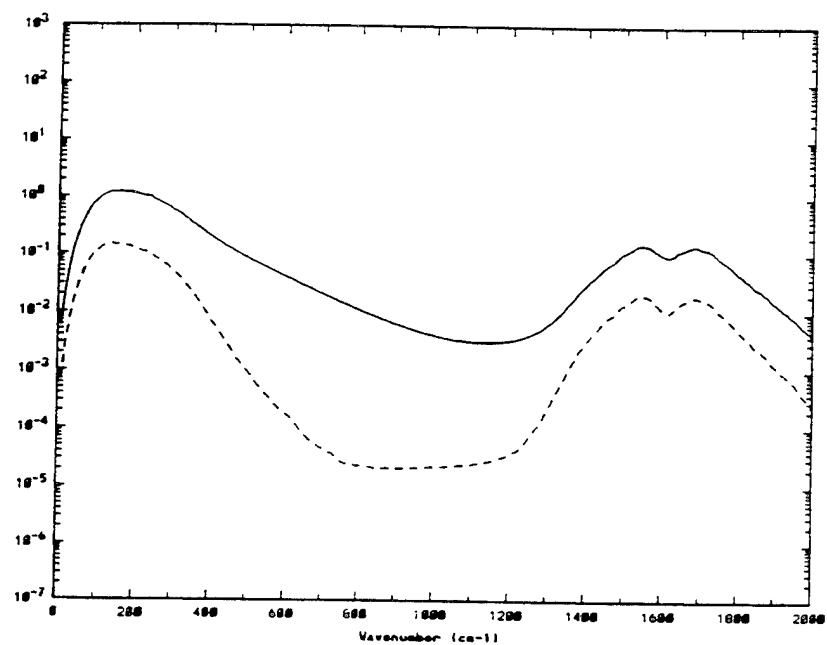
Figure 176. Water Vapor Continuum.
(Self-Broadened: Solid Line, Foreign-Broadened: Dashed Line)

Figure 176. Water Vapor Continuum (Continued).

225

Figure 176. Water Vapor Continuum (Continued).

226

Figure 176. Water Vapor Continuum (Continued).

227
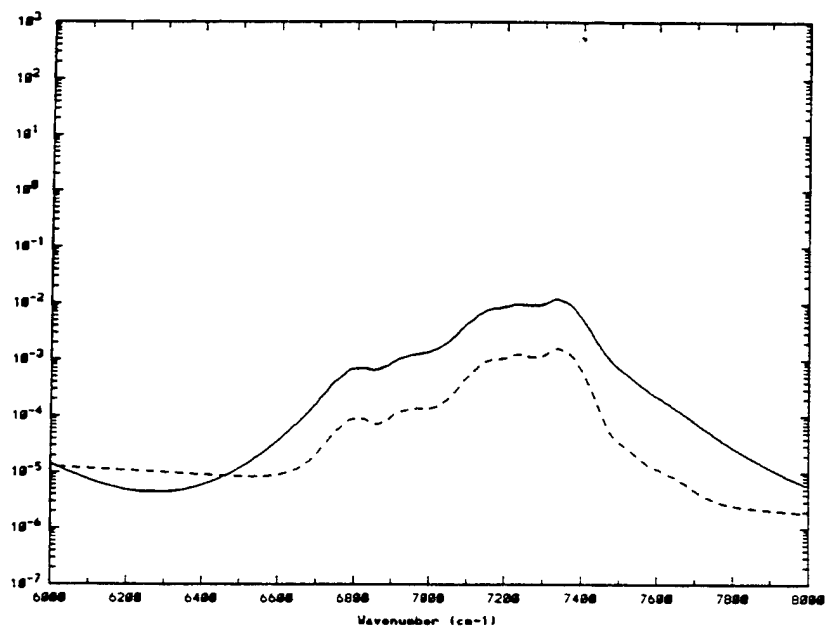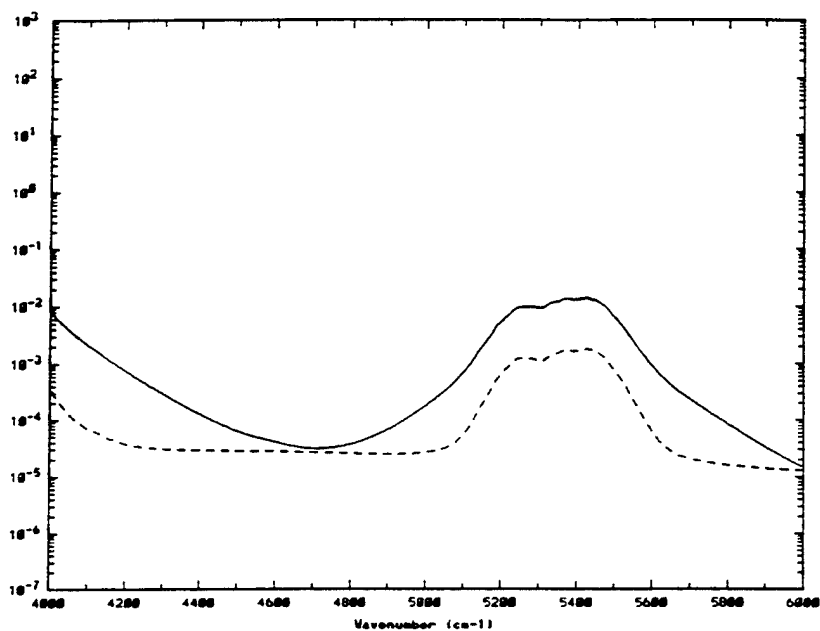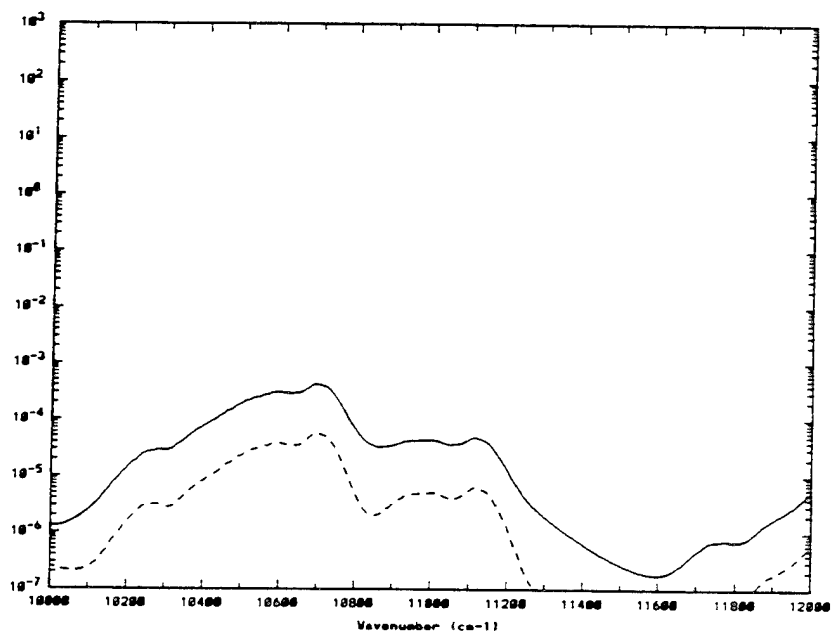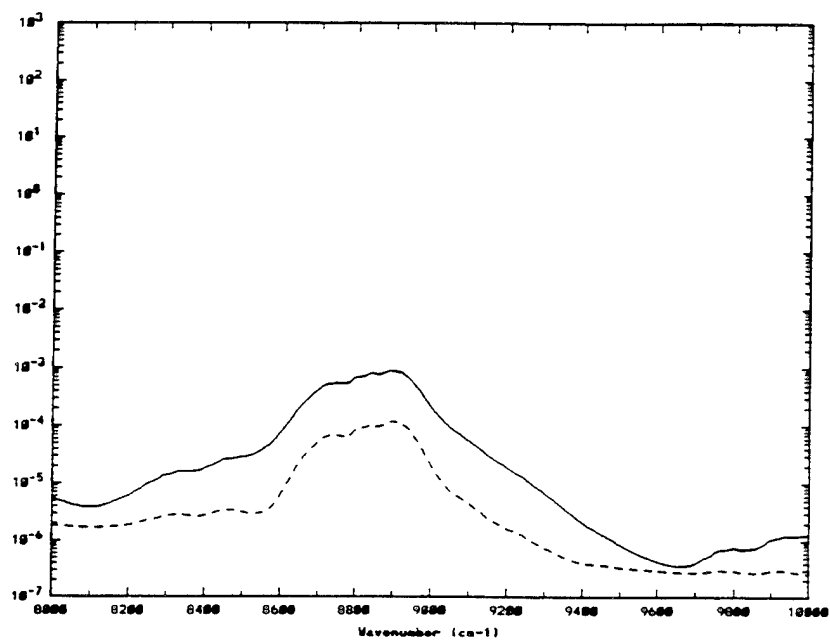
Figure 176. Water Vapor Continuum (Continued).
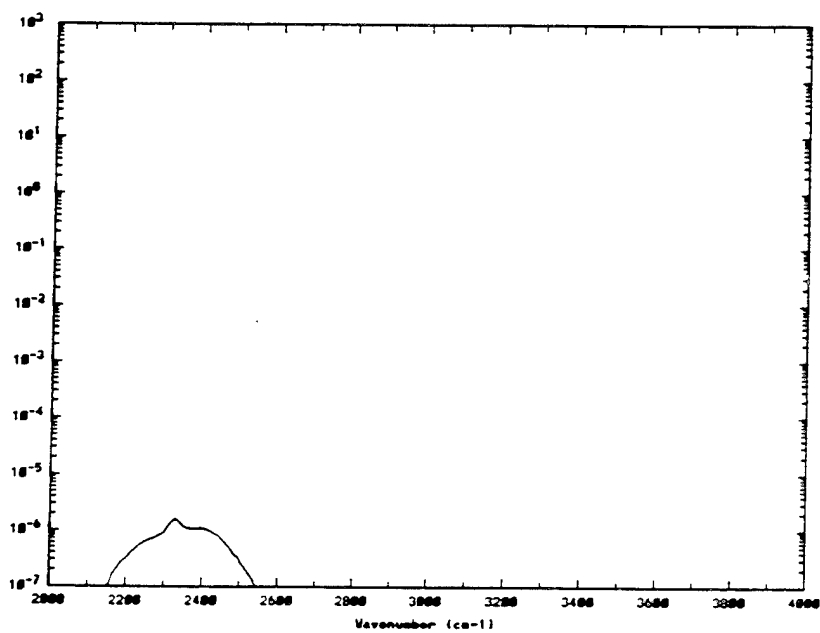
Figure 177. Nitrogen Continuum.

228
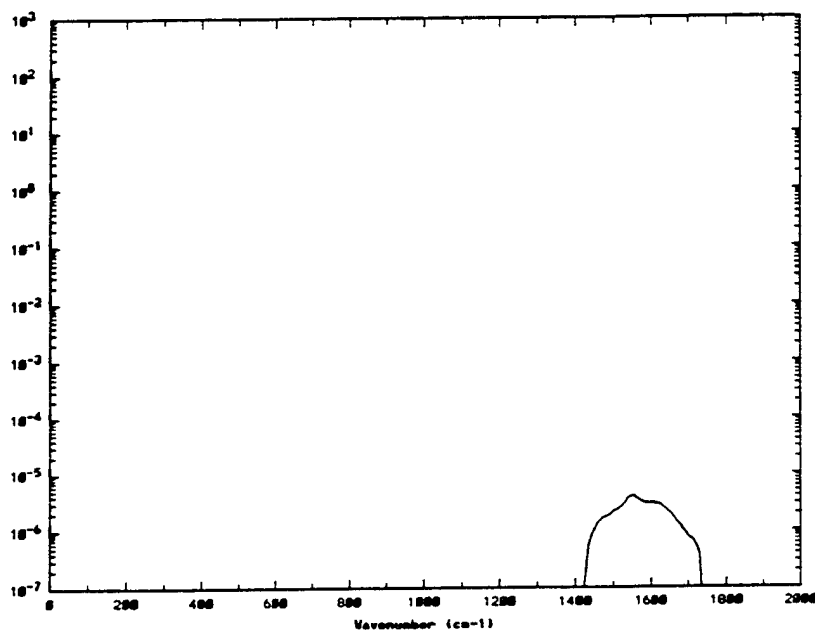
Figure 178. Oxygen Continuum.

4.4 Ultraviolet/Visible Molecular Absorption

Since the AFGL Line Atlas and hence the MOSART band parameters do not extend beyond approximately 18,800 cm^{-1}, the absorption by certain molecules in the ultraviolet and the visible is modeled separately.

4.4.1 Ozone

The molecular absorption due to ozone in the ultraviolet and visible, shown in Figure 179, has been taken from MODTRAN.

4.4.2 Oxygen

The absorption coefficients for molecular oxygen (O_2) (which were obtained from MODTRAN) have been extracted from two sources (Cheung, et al., 1986; Nicholls, Cann, and Shin, 1986). The work by Cheung et al. (1986) involved measurement of the absorption coefficient between 0.195 and 0.241 μm for pressures between 5 and 760 torr at temperatures between 296 and 300 K. A sample measured spectrum is shown in Figure 180. A significant pressure dependence was obtained so that the total absorption coefficient can be represented by

$$\tau_{TOT}(\lambda) = \tau_o(\lambda) + \alpha(\lambda)P$$

229

Figure 179. Ozone Absorption.

230
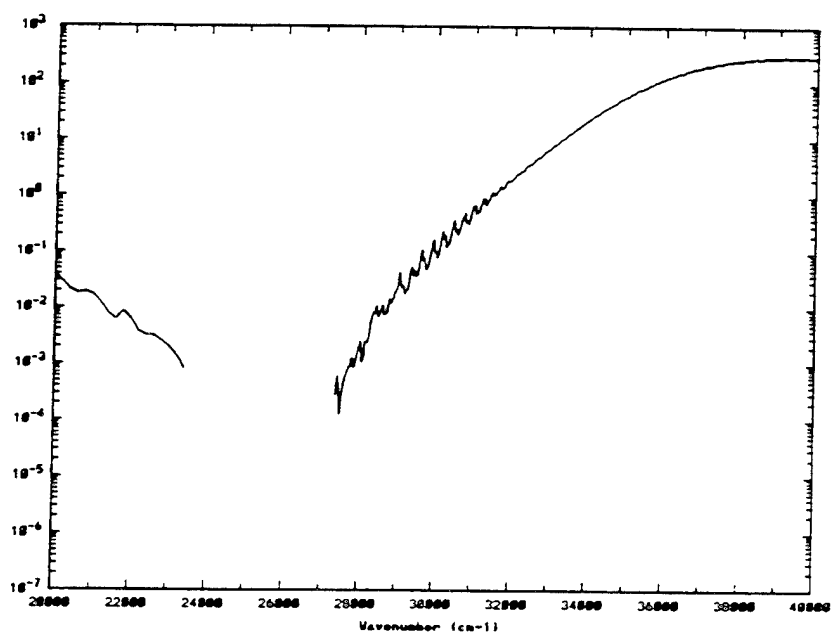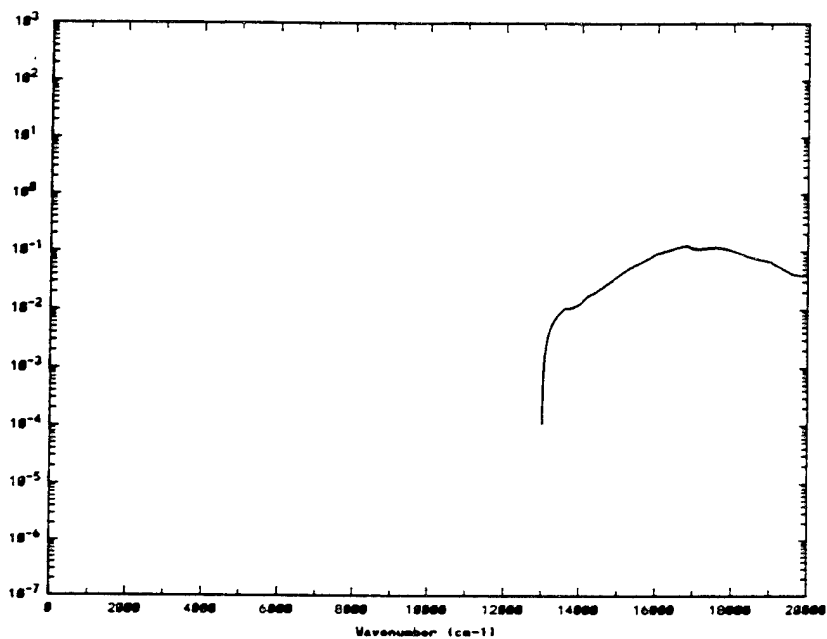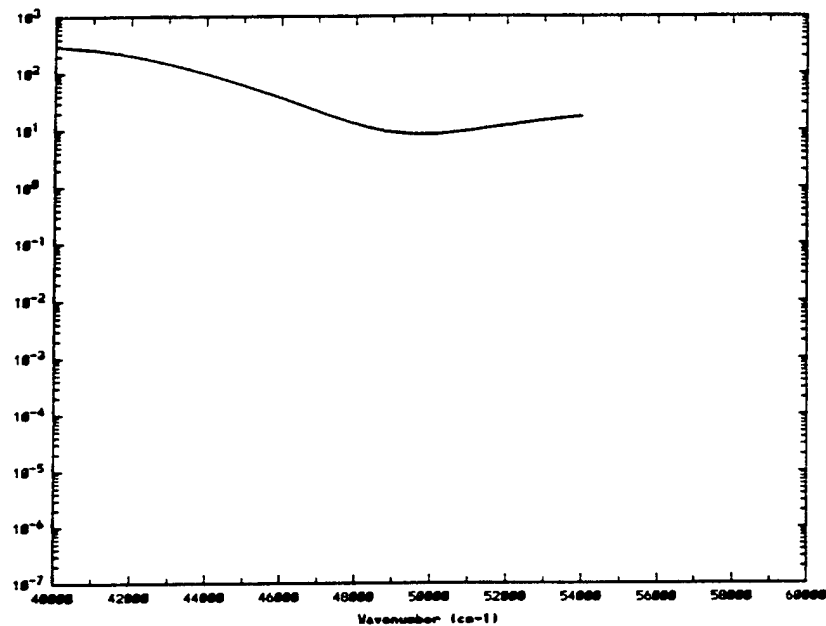
Figure 179. Ozone Absorption (continued).
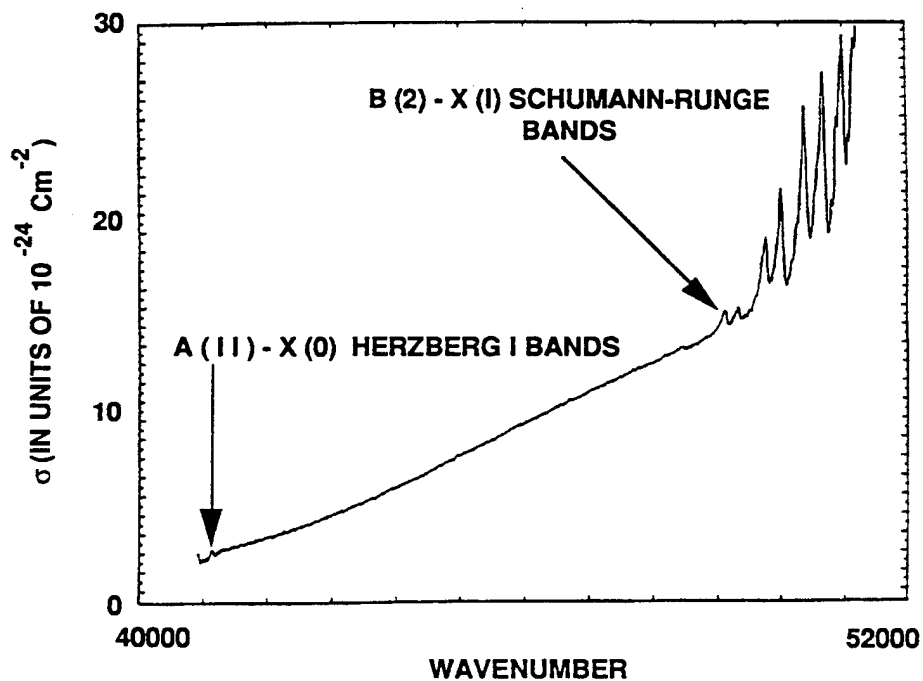
Figure 180. Measured UV Oxygen Spectrum at 357 Torr; Path Length: 133 m.

For P in torr, values in $\tau_o(\lambda)$ and $\alpha(\lambda)$ are shown in Table 68. Note that the Rayleigh scattering term is included in all of this data, but has been subtracted from the data used in the MOSART code. The Rayleigh scattering cross-section is 0.49×10^{-24} cm^2 at 0.195 µm and 0.15×10^{-24} cm^2 at 0.241 µm.

Table 68. Present Laboratory Values of the Continuum Cross-Section of Oxygen at 296-300 K and its Pressure Dependence in the Wavelength Region 193.5 - 241.0 nm of the Herzberg Continuum.[a]

λ	$\sigma_o(\lambda)$[b]	$\alpha(\lambda)$	λ	$\sigma_o(\lambda)$	$\alpha(\lambda)$
193.58	14.2±0.9	2.44±0.30	202.08	6.8±0.7	1.62±0.24
193.85	13.3±1.1	2.44±0.30	202.4[c]	7.55±0.31	1.54±0.10
194.40	11.8±0.8	2.43±0.29	203.4[c]	7.20±0.31	1.53±0.10
194.60	11.8±0.8	2.43±0.29	205.0	7.21±0.31	1.45±0.08
195.34	17.2±1.2	2.40±0.35	206.0	7.08	1.40
195.69	9.8±0.6	1.90±0.15	207.0	6.93	1.36
195.92	9.8±0.6	1.90±0.14	208.0	6.65	1.33
196.40	11.9±1.0	2.10±0.35	209.0	6.44	1.30
196.68	9.3±0.9	1.90±0.14	210.0	6.20±0.34	1.27±0.08
196.89	9.0±0.8	1.90±0.14	211.0	5.98	1.24
197.04	9.0±0.8	1.90±0.15	212.0	5.82	1.20
197.99	8.5±0.7	1.80±0.20	213.0	5.69	1.15
198.16	8.0±0.7	1.86±0.19	214.0	5.52	1.10
198.84	7.8±0.7	1.86±0.20	215.0	5.31±0.33	1.06±0.07
199.19	7.5±0.7	1.63±0.20	216.0	5.04	1.04
199.36	7.5±0.7	1.63±0.20	217.0	4.78	1.01
199.76	7.5±0.6	1.63±0.20	218.0	4.60	0.97
200.59	7.3±0.7	1.67±0.19	219.0	4.36	0.94
200.75	7.3±0.7	1.67±0.18	220.0	4.18±0.34	0.89±0.07
201.16	6.8±0.7	1.56±0.25	221.0	3.96	0.86
201.45	6.8±0.7	1.56±0.25	222.0	3.74	0.82
201.81	6.8±0.7	1.56±0.25	223.0	3.59	0.78
224.0	3.45	0.73	233.0	1.85	0.45
225.0	3.21±0.31	0.70±0.07	234.0	1.67	0.43
226.0	3.01	0.67	235.0	1.57±0.31	0.40±0.07
227.0	2.83	0.63	236.0	1.50	0.36
228.0	2.62	0.60	237.0	1.34	0.35
229.0	2.44	0.57	238.0	1.21	0.33
230.0	2.26±0.30	0.54±0.06	239.0	1.19	0.29
231.0	2.13	0.51	240.0	1.11±0.30	0.27±0.06
232.0	1.99	0.48	241.0	1.00	0.25

[a] The continuous cross-section is $\sigma_P(\lambda) = \sigma_o(\lambda) + \alpha(\lambda)P$, where P is the range 5 - 760 torr. The units for λ, $\sigma_o(\lambda)$ and $\alpha(\lambda)$ are nm, 10^{-24} cm^2 and 10^{-26} cm^2 torr^{-1}, respectively. In the region 205 - 241 nm, representative error estimates for $\sigma_o(\lambda)$ and $\alpha(\lambda)$ are given at 5 nm intervals.

[b] For λ = 202 nm, $\sigma_o(\lambda)$ obtained from high resolution measurements contains intrinsic line-wing contributions $\sigma_{SR}(\lambda)$ (Schumann-Runge).

[c] σ_o (202.4 nm) and σ_o (203.4 nm) obtained from low resolution measurements after removal of line-wing contributions due to limited resolution.

In order to provide a smooth transaction into the oxygen absorption region, the work of Nicholls, Cann, and Shin (1986) was used to extend the spectrum to 0.300 μm. Synthetic oxygen coefficient spectrum were generated, as shown in Figure 181. The Herzberg I ($X^3\Sigma$ - $A^3\Sigma$), the Herzberg II ($X^3\Sigma$ - $c'\Sigma$), and the Herzberg III ($X^3\Sigma$ - $A'\Delta$) systems, together with the bands and photo dissociation continua of the Schumann-Runge ($X^3\Sigma$ - $B^3\Sigma$) and continuum absorption of the $(O_2)_2$ dimer were considered. The primary region of interest to MOSART was the Herzberg I bands (0.250 - 0.300 μm). No pressure dependence was obtainable from this work so it was not included. The absorption coefficient is shown in Figure 182.

4.4.3 Other Molecules

The absorption coefficients for water vapor (Figure 183), nitrous oxide (Figure 184), nitrogen dioxide (Figure 185), and sulfur dioxide (Figure 186) are included in the code (Patterson and Gillespie, 1989).
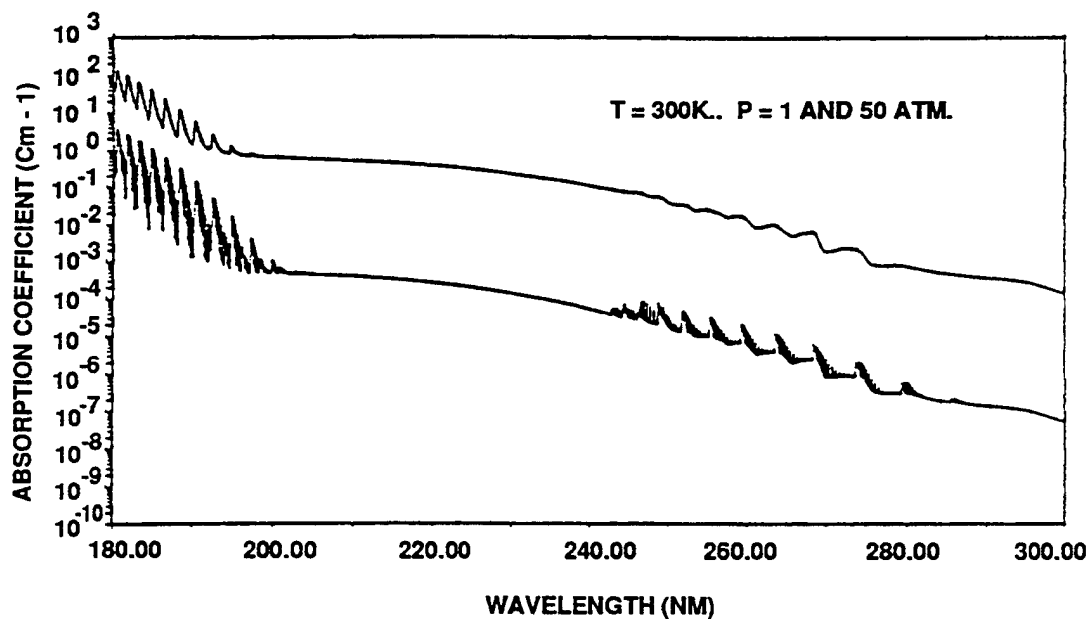
Figure 181. Synthesis of Degraded 300 K Oxygen Absorption Coefficient Spectrum. Upper curve 50 atm; lower curve 1 atm.

233
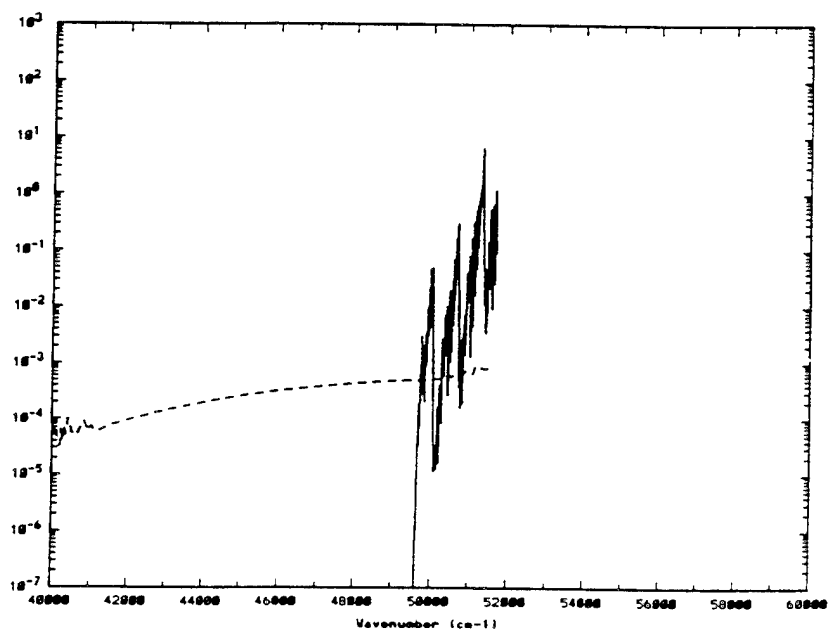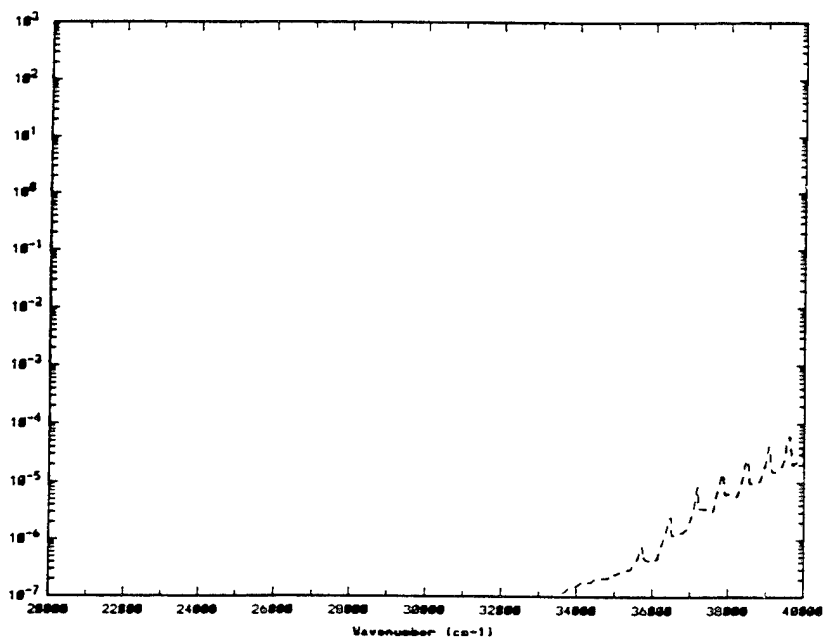
Figure 182. Oxygen Absorption. (Bands: solid line; continuum; dashed line.)

234
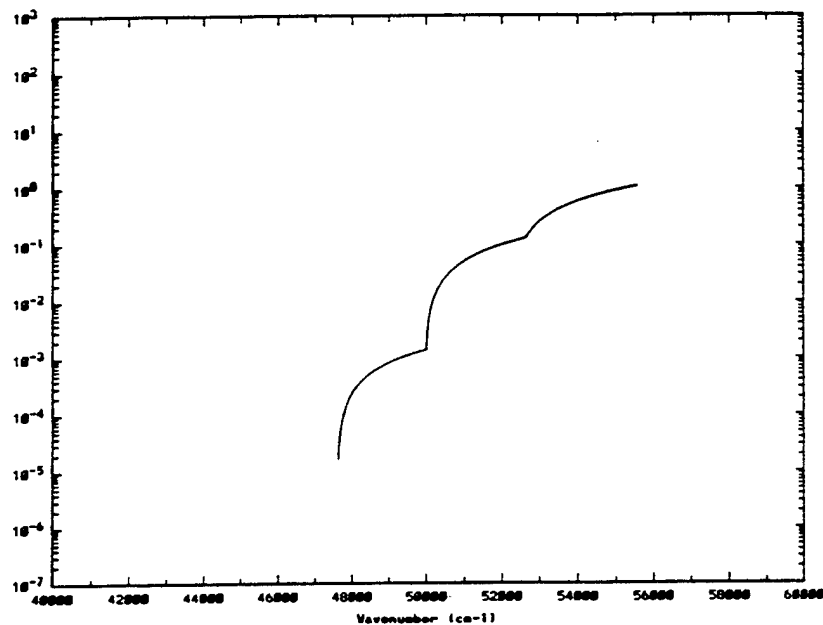
Figure 183. Water Vapor Absorption.
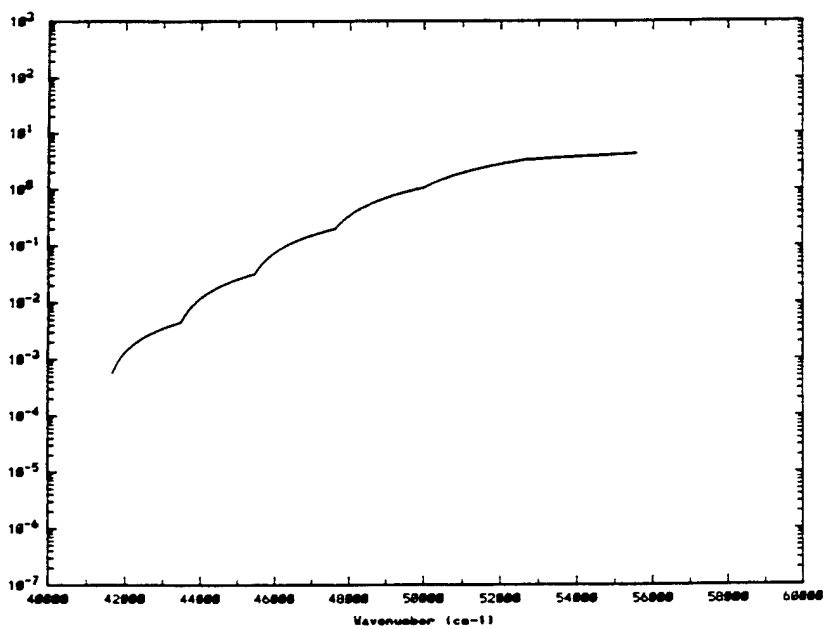
Figure 184. Nitrous Oxide Absorption.

235
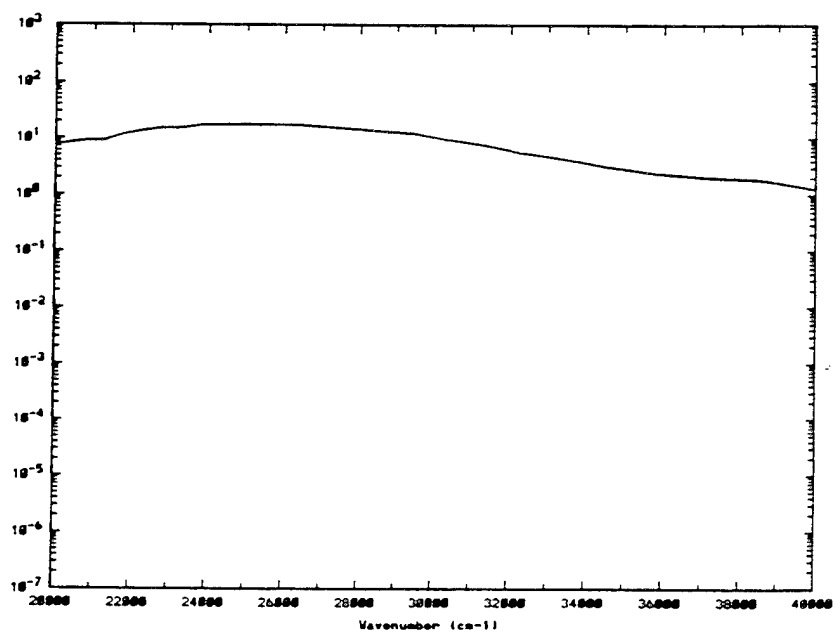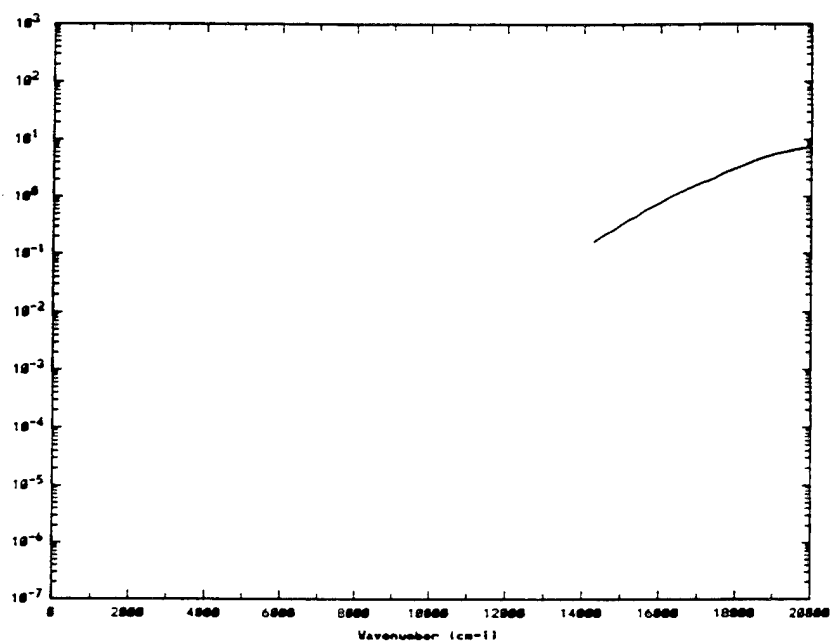
Figure 185. Nitrogen Dioxide Absorption.

236
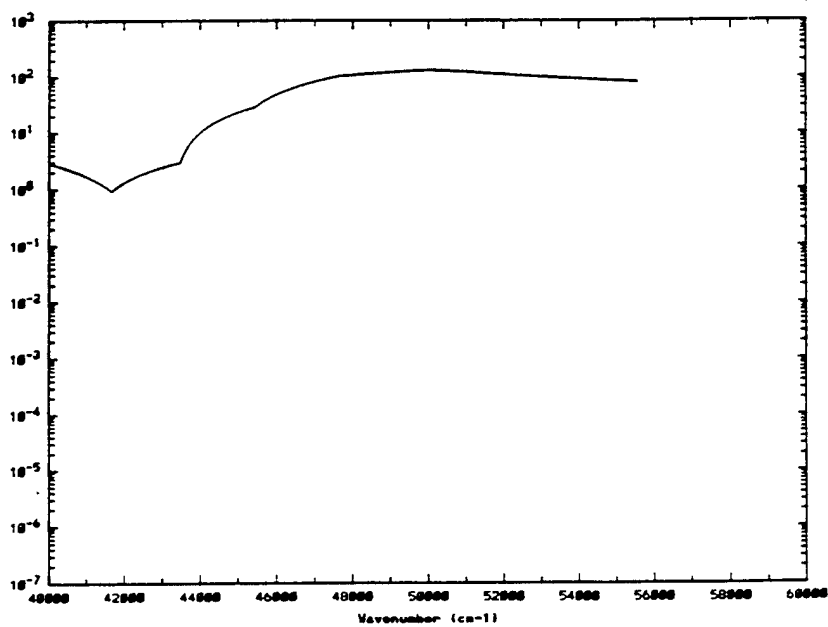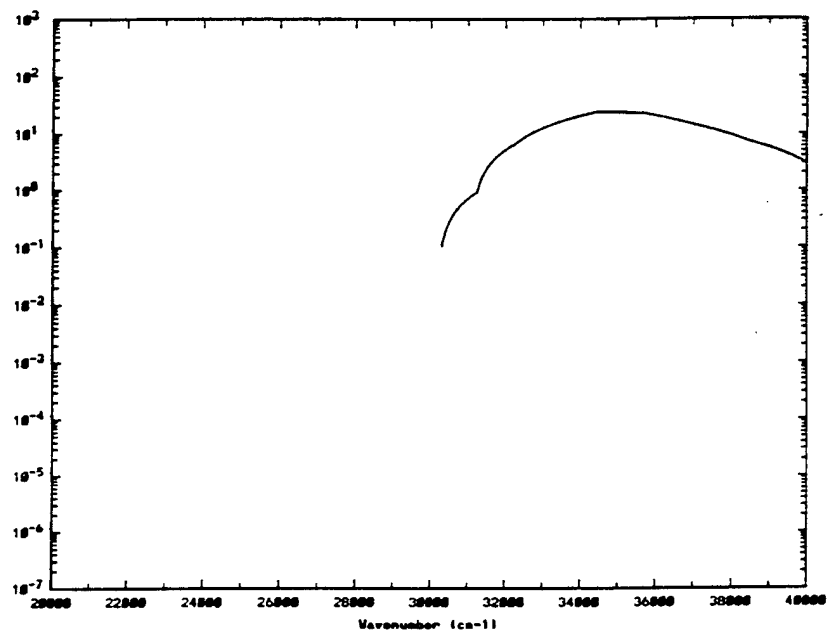
Figure 186. Sulfur Dioxide Absorption.

237

4.5 Line Correlation

Perhaps one of the major improvements that has been incorporated into the MOSART computer code when compared to other atmospheric transmission models is the calculation of fully correlated radiative environment. All band models assume certain statistical parameters regarding the line structure within the resolution of the band model. For any propagation path, the statistical correlation of this line structure will result in a transmission that is not simply the multiplicative transmission of segments of the path but is provided by a particular curve-of-growth. One of the most widely accepted techniques for accounting for this correlation over inhomogeneous paths is the Curtis-Godson approximation.

However, the reflected components of a vehicle or background signature (e.g., solar, skyshine, earthshine, diffuse solar) are not wide band sources, such as the thermal emissions. Although the sun and earth can be assumed to be wideband sources, their radiation must propagate through the atmosphere to the vehicle or background, so that the reflected energy will have significant line structure. Also the skyshine, since it is produced by the atmosphere, has line structure. To compensate properly for this structure of the reflected components, this radiation must be correlated with the structure in the target-vehicle path. If this correlation is not taken into account, the solar and earthshine components of the signature will generally be underpredicted, while the skyshine will be either over or underpredicted, depending upon the actual scenario.

The APART computer code was designed specifically to consider this correlation. The results of a comparison between the uncorrelated and correlated treatments were presented at the AFGL Conference on Atmospheric Transmission Models (Cornette, 1983). This capability is also included in MOSART.

Figure 187 presents the relative errors for a vehicle under two different viewing conditions. The first condition is for a high-altitude target as viewed from the ground; the second condition simply reverses the locations of the viewer and target.

The relative errors are highly dependent on both geometry and spectral region. In window regions and for relatively wide spectral bands, the errors in the reflected component of a target signature are relatively small (e.g., less than 10% in the 3-5 and 8-12 μm bands). However, near absorption bands errors of 100% or larger are very common, and errors of over 300% occur in the reflected signature component for selected spectral regions.
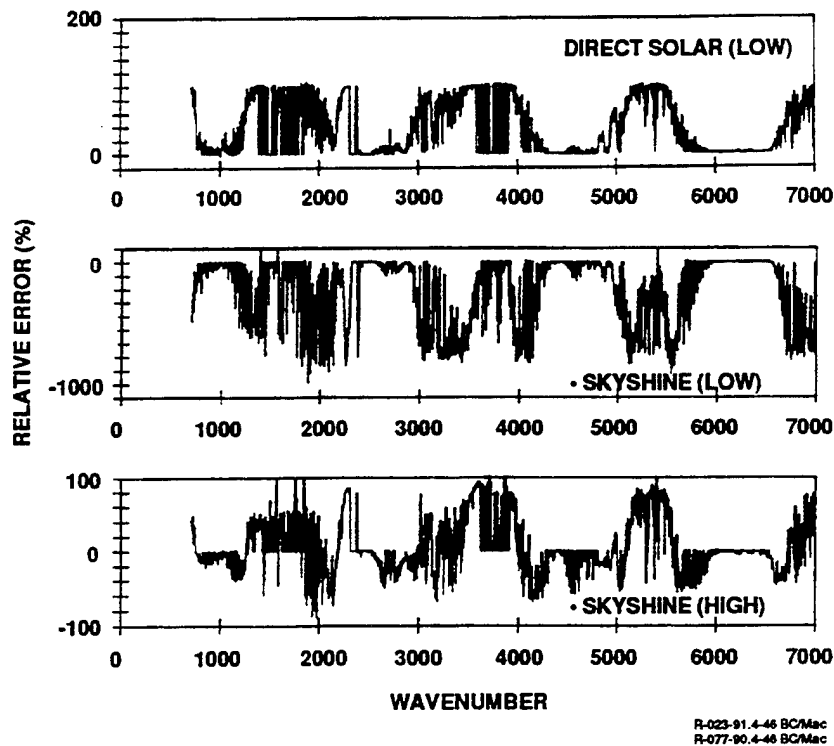
Figure 187. Errors Due to Lack of Atmospheric Correlation.

4.5.1 Curtis-Godson Single Line Group Approximation

With no scatterers present, the equation of radiative transfer reduces to

$$N\lambda = {}_sN_\lambda{}^o(T_s)d\tau_\lambda(s)$$

where N_p is the spectral (monochromatic) apparent radiance, $N_\lambda{}^o(T_s)$ is the spectral blackbody function with a temperature T_s existing at s and τ_λ is the spectral transmissivity along the line-of-sight segment ds. In the monochromatic case the transmission is given by

$$\tau_\lambda = e^{-\int_s n\sigma_\lambda{}^a ds'} = e^{-\int_s \kappa_\lambda(s')ds'}$$

where $k_\lambda(s')$ is the spectral absorption coefficient.

239

In the band-model approach, averages are taken over given spectral intervals, that is

$$\overline{N}_{\Delta\lambda} = \int_s \overline{N_{\Delta\lambda}{}^\circ}(T_s) \, d\overline{\tau}_{\Delta\lambda}(s)$$

where

$$\overline{N_{\Delta\lambda}}(s) = \exp\left\{-\int_s f\left[\overline{\kappa_{\Delta\lambda}}(T,s'), \overline{\alpha}_{\Delta\lambda}(T,s')\right] ds\right\}$$

The form of the function of f (curve-of-growth) depends on the arrangement of lines and their assumed intensity probable distribution. In the Goody model, which can be applied to all molecules within reasonable error limits, the function f has the form (for a homogeneous layer)

$$f = \sum_k \overline{\kappa}_k(\lambda,T)\overline{u}_k\left[1 + \kappa_k(\lambda,T)\,\overline{u}_k/4\overline{\alpha}_k(\lambda,T)\right]^{-1/2}$$

where $\overline{\kappa}_k(\lambda,T)$ is the absorption coefficient of species k at λ averaged over the interval $\Delta\lambda$ (i.e., from $\lambda - \Delta\lambda/2$ to $\lambda + \Delta\lambda/2$). u_k is the thickness of the homogeneous layer, and $\alpha_k(\lambda,T)$ is the averaged fine structure parameter.

The effect of line correlation is a problem in any statistical band model when applied to transmission through an inhomogeneous media. Paths through a real atmosphere usually pass through regions of changing pressure, temperature, and molecular concentration. The Curtis-Godson approximation replaces an inhomogeneous path with a homogeneous one by using average values for the equivalent width and transmittance parameters. The Curtis-Godson single line group approximation is very good for paths where the temperature or species gradient is not particularly steep. Where the gradients are steep, other techniques have been developed (Ludwig et al., 1973). The total optical depth is a sum over contributions from the individual layers and is given by

$$(S/d)u = \sum_i (S/d)_i \Delta u_i$$

where Δu_i is the incremental optical path and $(S/d)_i$ is the average molecular absorption coefficient for the ith layer. This quantity is used as the weighting function in calculating the mean value of γ/d, which is given by

$$\overline{(\gamma/d)} = \sum_i (\gamma/d)_i (S/d)_i \Delta u_i/(S/d)u$$

where γ stands for either γ_C or γ_D. The average values of the line density, $1/d$, and total number of lines, n, are analogously defined.

Figure 161 shows the impact of resolution on the correlation. Two curves are shown for each resolution. The upper curve calculates the hot gas radiance and atmospheric transmission separately and multiplies the two factors, thereby ignoring any line correlation, while the lower curves have assumed correlation. The errors due to ignoring correlation can be seen to increase with lower resolution, until at 20 cm^{-1}, the error is significant. The Curtis-Godson approximation will make corrections to compensate for these errors; however, for the higher resolution calculations, the required correction is less and the calculational results are more accurate.

4.5.2 Standard Infrared Radiation Model (SIRRM) Multiple Line Group Band Model

To extend the band model formalism to nonhomogeneous layers, the parameters κ and α are path-averaged [Curtis-Godson single line group (SLG) approximation] as discussed above in Section 4.5.1. This approximation works fairly well when the nonhomogeneities are not too large. But at the interface between a hot plume and the cold atmosphere the temperature gradient is appreciable, and the Curtis-Godson approximation becomes less accurate, especially for water vapor. The reason for this inaccuracy is that the "hot" lines within the plume are not correlated with the equivalent lines in the atmosphere. In order to account for the different temperature dependencies of spectral lines within a given spectral interval, they are divided into groups and the Curtis-Godson approximation is then applied to each line group in turn, and the net transmissivity is taken to be the product of the transmissivities calculated for each of the line groups [Curtis-Godson multiple line group (MLG) approximation]. This grouping is done on the basis of the value of the energy level of the lower state of the transition so that all the lines belonging to one group have the same temperature dependence. Thus, the function f for the layer i becomes

$$f_i = \sum_j \sum_k \overline{\kappa}_{ijk}(\nu)\overline{u}_{ik}\left[1 + \overline{\kappa}_{ijk}(\nu)\overline{u}_{ik}/4\overline{\alpha}_{ijk}(\nu)\right]^{-1/2}$$

241

where j is the number of particular group of lines having similar temperature dependence. The absorption coefficients κ, fine structure parameter α, and optical path u_{ik} are given by

$$\overline{\kappa}_{ijk}(\nu) = \sum_{i'=0}^{i} \kappa_{i'jk}(\nu) u_{i'k}/\overline{u}_{ik}$$

$$\overline{\alpha}_{ijk}(\nu) = \sum_{i'=0}^{i} \kappa_{i'jk}(\nu)\alpha^{*}_{i'k}(\nu) u_{i'k}/\kappa_{ijk}(\nu)\overline{u}_{ik}$$

and

$$\overline{u}_{ik} = \sum_{i'=1}^{i} u_{i'k} = \sum_{i'=1}^{i} c_{i'k} p_{i'} s_{i}$$

where $c_{i'k}$ is the concentration, $P_{i'}$ is the local pressure, and ℓ_i is the geometric length of the layer.

The values for $\kappa_{i'jk}$ for line group j are determined from the absorption coefficients κ at the temperature of layer i' by a relationship appropriate for the species, explicitly

$$\kappa_{i'jk}(\nu) = \kappa_{table}(\text{species } k, T_i, \nu) \exp(-j\theta/T)[1 - \exp(-\theta/T)]$$

where κ_{table} is the average absorption coefficient over the interval and where θ represents a characteristic temperature for the molecule (e.g., 2300 K for H_2O, 960 K for CO_2 and 3123 K for CO). Similarly, the fine structure parameter for the same line group is given by

$$a^{*}_{i'k}(\nu) = \gamma/d_{table}(\text{species } k, t_{i'}, \nu) \frac{1 - \exp(-\theta/2T)}{+ \exp(-\theta/2T)}$$

MOSART produces an atmospheric binary file that can interface to the SIRRM multiple line group band model.

4.6 Integration Formulation

The numerical integration of both the atmospheric emissions and scattered radiation along a line-of-sight requires special techniques to represent the phenomena involved accurately.

242

For example, the atmospheric emissions can be expressed by

$$\int_{\tau_1}^{\tau_2} N_p(T)\,d\tau$$

where $N_p(T)$ is the Planck blackbody function, τ is the transmission along the line-of-sight, and T is the temperature. To evaluate this integral numerically by using conventional trapezoidal or Simpson's integration would require different length increments along the line-of-sight for different spectral regions. For example, for a region with high transmissivity, the increments can be fairly coarse, while opaque regions require finer increments near the receiver. However, this method's numerical complexity does not make it very desirable. Instead, MOSART assumes that N_p and τ vary exponentially between increments along the line-of-sight, thereby correcting for the opaque atmosphere problem, and avoiding some of the problems involved with number of layers (Cornette, 1992a).

4.7 Turbulence

The present MOSART turbulence model has been taken from APART. It utilizes standard turbulence theory to predict statistical variations in transmission and temperature (and hence, radiance) for the line-of-sight of interest.

The impact of turbulence is two-fold. The first effect is the scintillation of the target signal which is easily observed in the twinkling of stars. For near grazing angles (i.e., for long-range viewing), this scintillation can have a significant impact on the ability of a sensor to detect a target. In general, scintillation will reduce the probability of detection by reducing the available signal-to-noise. Figure 188 shows the amount of scintillation observed when viewing infrared stars from the AMOS observatory in Maui (Ludwig, Klier, and Myer, 1982).

A much less obvious effect of turbulence is the impact on atmospheric radiance. Turbulence is usually expressed in terms of variations in the index of refraction (which can be related to variations in the air density). However, the major cause of refractive variations is temperature variations. For long slant paths, MOSART assumes either a constant or linear varying temperature profile for the total geographical region under consideration, although it is obvious that the temperature profile will vary over any sizeable region. Figure 189 shows a path radiance for a range of 300 km. The mean background radiance was calculated using a single temperature profile from a rawinsonde measurement. Using the turbulence capabilities in MOSART, the temperature along the LOS path is statistically varied in order to represent atmospheric inhomogeneities. The

243
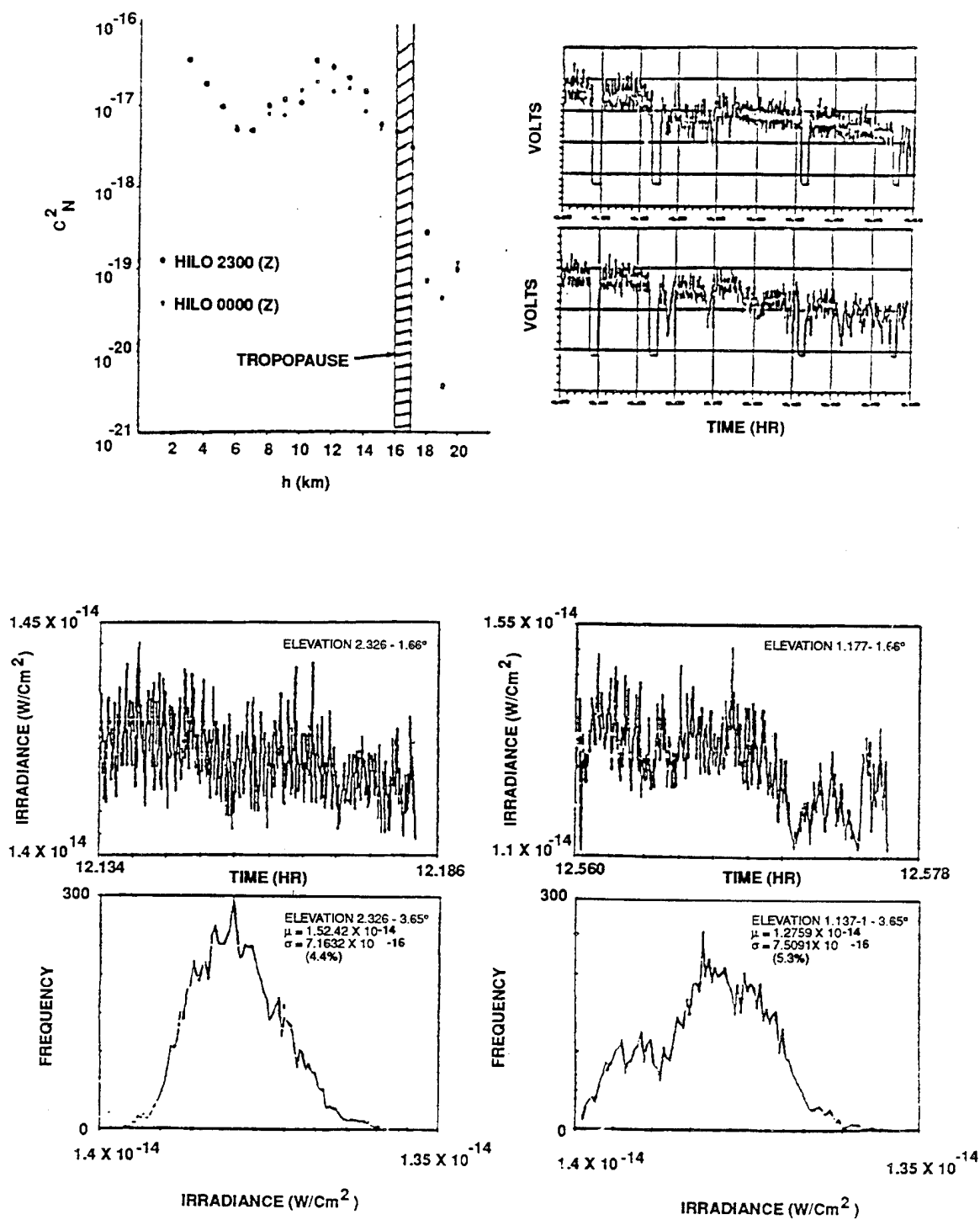
Figure 188. Atmospheric Scintillation (Ludwig, Klier, and Myer, 1982).

244

- Overcast Day

- Horizontal Path

- Receiver Altitude 4.7 km

- Cloud Range 300 km
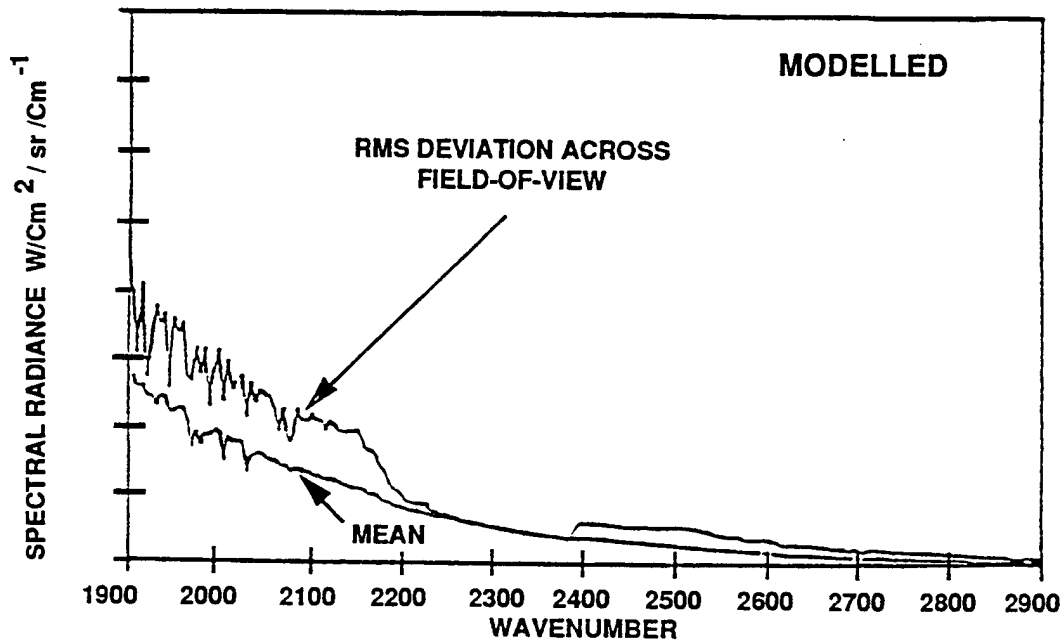
Figure 189. Sample Impact of Turbulence on Path Radiance.

modeled rms plus near radiance using this turbulence model demonstrates a significant difference from the mean radiance predicted solely from the rawinsonde profile.

Using some fairly reasonable assumptions, it is also possible to use turbulence to predict variations in the molecular and aerosol scattered component of the path radiance. This part of the turbulence calculations is still in development.

Illustrative sky noise spectra in the long wave spectral region are shown in Figure 190. Representation values are presented in Table 69.
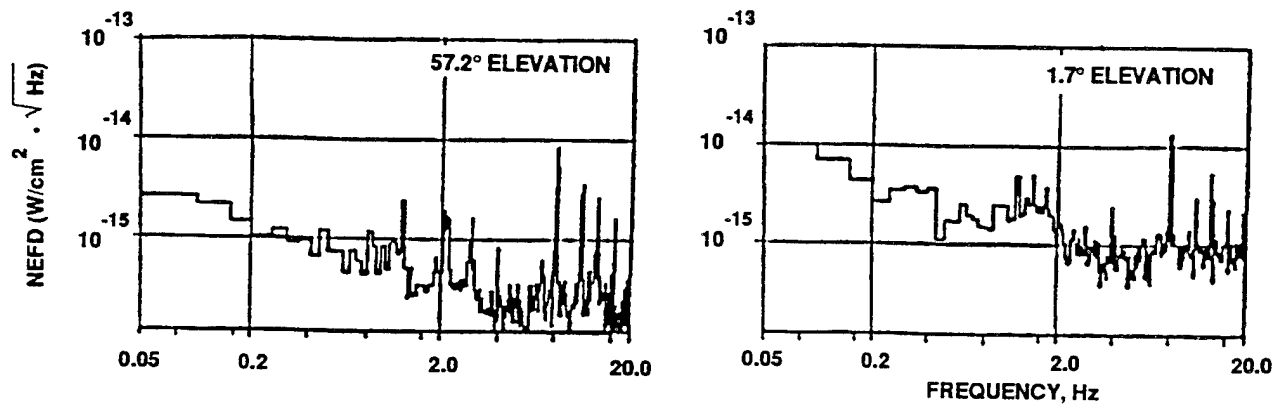
Figure 190. Sky Noise Spectrum.

4.8 Forward Scattering

Most transmission codes treat scattering as a loss mechanism. However, in van de Hulst (1980), it is stated that "scattering in the exact forward direction is no scattering at all" (page 480), and proposes a modification of the extinction coefficient by

$$\sigma \rightarrow \sigma(1 - \omega g)$$

where σ is the extinction coefficient
          ω is the single scattering albedo, and
          g is the phase function asymmetry factor

defined by

$$g = \frac{1}{4\pi} \int_{0}^{2\pi} d\phi \int_{-\pi/2}^{\pi/2} \cos\theta \sin\theta \, d\theta \, \Phi(\cos\theta)$$

where Φ is the single-scattering phase function, normalized to 4π.

246

Table 69. Sky Noise Spectrum.

Elevation (Degree)	Airmass	σ (W/cm^2·sr)	σ/μ (Normalized)
89.3	1	4.0E-4	1.00
57.2	1.2	4.3E-4	0.78
29.5	2.0	6.4E-4	0.68
15.8	3.7	9.9E-4	0.78
7.6	7.5	14.5E-4	0.58
1.7	28.0	25.3E-4	0.43

However, this modification does not consider the receiver instantaneous field-of-view (FOV) or the size of the collecting aperture, which in terms of scattering angle changes with range.

The basic equation of transfer is given by

$$\frac{dI}{dr} = -(a + k)I = -\sigma I$$

where   a is the absorption coefficient
k is the scattering coefficient
I is the intensity, and
r is the range

The amount of energy scattered into the forward cone with half-angle α is given by

$$P(\cos \alpha) \equiv \frac{1}{4\pi} \int_0^{2\pi} d\phi \int_0^{\alpha} \sin\theta \, d\theta \; \Phi(\cos\theta) = \frac{1}{2} \int_{\cos \alpha}^1 d\mu \; \Phi(\mu)$$

where

$$\mu = \cos\theta,$$

$$\alpha = \pi - \tan^{-1}\left[\frac{r_o - r}{r\tan(\psi/2) + a}\right] - \tan^{-1}\left[\frac{r}{r\tan(\psi/2) + 2a}\right]$$

r is the range to scattering event,
r_o is the range to target,
a is the aperture radius, and
ψ is the instantaneous FOV.

When the forward scattering is included, the equation of transfer is modified to

$$\frac{di}{dr} = -\sigma I + kP(\cos\alpha)I$$

which is equivalent to replacing the extinction coefficient by

$$\sigma \rightarrow \sigma(1 - \omega P(\cos\alpha))$$

Unfortunately, the modified extinction coefficient is now range dependent, even in a homogeneous medium. Therefore, the transmission, τ, is given by

$$-\ln\tau = \int_0^R dr\,\sigma(1 - \omega P(\cos\alpha))$$

where α is the angle defined above.

For a homogeneous medium (i.e., σ and ω are constant), so

$$= \frac{\ln\tau}{\sigma R} = \frac{\omega}{R}\int_0^R dR\int_{\cos\alpha}^1 d\mu\,\Phi(\mu)$$

For the Henyey-Greenstein phase function

$$\Phi(\cos\theta) = \frac{1 - g^2}{[1 + g^2 - 2g\cos\theta]^{3/2}}$$

248

so

$$P(\cos \alpha) = \frac{1 - g^2}{2g} \left\{ \frac{1}{1 - g} - \frac{1}{[1 + g^2 - 2g \cos \alpha]^{1/2}} \right\}$$

and

$$1 + \frac{\ln \tau}{\sigma R} = \frac{\omega(1 + g)}{2g} - \frac{\omega(1 - g^2)}{2g} \frac{a}{R} \int_0^{R/a} d\lambda [1 + g^2 - 2g\lambda/(1 + \lambda)^{1/2}]^{-1/2}$$

The evaluation of this term multiplied by R/a is provided in Table 70. For values of R/a ≳ 10 - 100, the factor appears to converge to the curve shown in Figure 191 for g < 0.9.

Table 70. Forward Scattering Correction Factor.

$$\frac{1}{\omega} \frac{R}{a} * \left(1 + \frac{\ln \tau}{\sigma R}\right)$$

g	R/a				
	1	10	100	1000	10,000
0.0	0.0	0.0	0.0	0.0	0.0
0.1	0.355	0.598	0.628	0.634	0.662
0.2	0.425	0.749	0.791	0.794	0.787
0.3	0.500	0.939	0.998	1.003	1.005
0.4	0.579	1.182	1.269	1.278	1.283
0.5	0.661	1.504	1.638	1.651	1.649
0.6	0.741	1.952	2.174	2.196	2.192
0.7	0.817	2.622	3.038	3.080	3.088
0.8	0.887	3.740	4.699	4.802	4.816
0.9	0.948	5.887	9.411	9.838	9.861
1.0	1.000	10.000	100.00	1000.00	10000.0

(Note: Integrals were evaluated with a 512-point Gauss-Legendre quadrature. This technique became unstable for R/a ≥ 100,000.)
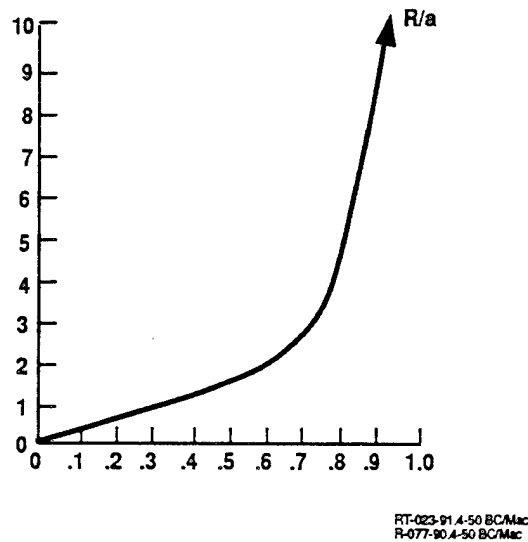
Figure 191. R/a Versus g.

4.9 Multiple Scattering

Because of time constraints and code structure requirements, the APART multiple scattering algorithm was adopted for this initial version of MOSART. A new MODTRAN multiple scattering model is under development (Stamnes, 1993). The best approach for MOSART will be determined at a later date.

The multiple scattering calculations involve:

(i)   correcting for the non-Beer's Law nature of the band model;
(ii)   developing the two- and three-stream models for thermal and solar/lunar components, respectively (see Figure 192);
(iii)   coupling of the atmospheric layers; and
(iv)   determining the amount of multiply scattered energy scattered into the line-of-sight.

Each of these elements is discussed below.

4.9.1 Exponential Sum Expansion

Multiple scattering models assume a monochromatic Beer's Law transmission, which cannot be applied directly to band models, which by definition average over some spectral interval. However, fitting the band model with exponential sums is "a widely used approximation for calculating spectrally integrated radiative fluxes in planetary atmospheres, especially when both line absorption and scattering are important." (Wiscombe and Evans, 1977). Unfortunately, exponential sum fitting is a classical ill-conditioned problem of numerical analysis. The technique used by MOSART is adopted

250

SOLAR FLUX

S_i

H_i^+

THERMAL EMISSION

$\}$ i - th LAYER

H_i^-
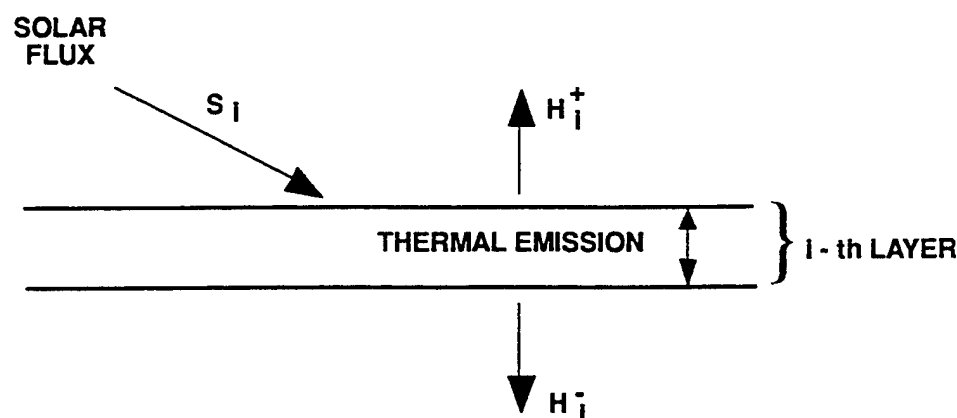
- Two and Three-Stream Scattering Model
  - Reflectance R_i
  - Transmittance T_i
  - Emittance $E_i = 1. - R_i - T_i$
  - Upward Scattered Flux $U_i\mu S_i$
  - Downward Scattered Flux $D_i\mu S_i$

Figure 192. Multiple Scattering.

from APART. Although not as accurate as the technique of Wiscombe and Evans, it is relatively fast and fairly accurate, and is preferred over the present MODTRAN algorithm, because the latter uses only a few terms in each wavenumber bin (only when using the 1 cm^{-1} band model).

The Malkmus band model is used (rather than the more detailed model used by MOSART for transmission calculations) since it has a closed form for the inverse Laplace transform.

The Malkmus random band model is defined by

$$\tau_M(u) = e^{\frac{\pi\alpha}{2d}(\sqrt{1-4u}-1)}$$

where α is the mean line halfwidth
         d is the mean line spacing

which has the following Laplace transformation:

$$f_M(k) = \frac{\beta e^\beta}{\sqrt{\pi}} \, k^{3/2} \, e^{\left(-\frac{k}{\tau} - \frac{\beta^2}{k}\right)}$$

where $k = \pi\alpha/2d$.

Using Gauss-Laguerre quadrature, it is possible to solve the equation

$$\tau_M(u) = \sum_{i=1}^{n} a_i e^{-k_i u}$$

MOSART presently uses a 15-point quadrature (i.e., $n = 15$ in the above equation). The resulting constants $\{a_i, k_i, i=1, n\}$ are then subject to the conditions:

1. If

$$\sum_{i=1}^{n} a_i > 1 \quad ,$$

redefine the $\{a_i\}$ so that equality occurs.

2. If

$$\sum_{i=1}^{n} a_i < 1 \quad ,$$

add an additional (a_{n+1}, k_{n+1}) to the expansion so that

$$\sum_{i=1}^{n} a_i = 1 \quad ,$$

and

$$\int_0^\infty \tau_m(u)\,du = \sum_{i=1}^{n+1} a_i/k_i$$

Figure 193 shows the maximum and root-mean-square (rms) errors over the $0 \le u \le 20$ range for:

    a)   the 15-term Gauss-Laguerre quadrature exponential sum expansion

    b)   the 15-term Gauss-Laguerre quadrature plus the above conditions.

As shown in Figure 193, 15 terms in the exponential sum fit is not sufficient using this technique to derive the coefficients $\{a_i, k_i\}$. However, the additional conditions reduce the maximum error to less than a few percent and the rms error to well under one percent.

It should be noted that the technique of Wiscombe and Evans typically results in 5-8 terms in the expansion with accuracies better than 10^{-3}. Future work in MOSART will consider this technique, the new MODTRAN algorithm under development (Stamnes, 1993), and the present method.

4.9.2 Two-Stream Thermal Flux

The two-stream flux, used for the thermal (i.e., terrain, atmosphere, and space emissions), is based on the Sagan and Pollack two-flux model. The outgoing upward and downward fluxes, U_0 and D_1, respectively (see Figure 192), are defined in terms of the incident upward and downward fluxes, D_0 and U_1, respectively, and the layer reflectance, R_1, and transmission, T (see Figure 194). The equations are:

$$U_0 = RD_0 + TU_1$$

$$D_1 = RU_1 + TD_0$$

$$R = \frac{(\alpha+1)\,(\alpha-1)\,(e^t - e^{-t})}{(\alpha+1)^2\,e^t - (\alpha-1)^2\,e^{-t}}$$

$$T = \frac{4\alpha}{(\alpha+1)^2\,e^t - (\alpha-1)\,e^{-t}}$$

253
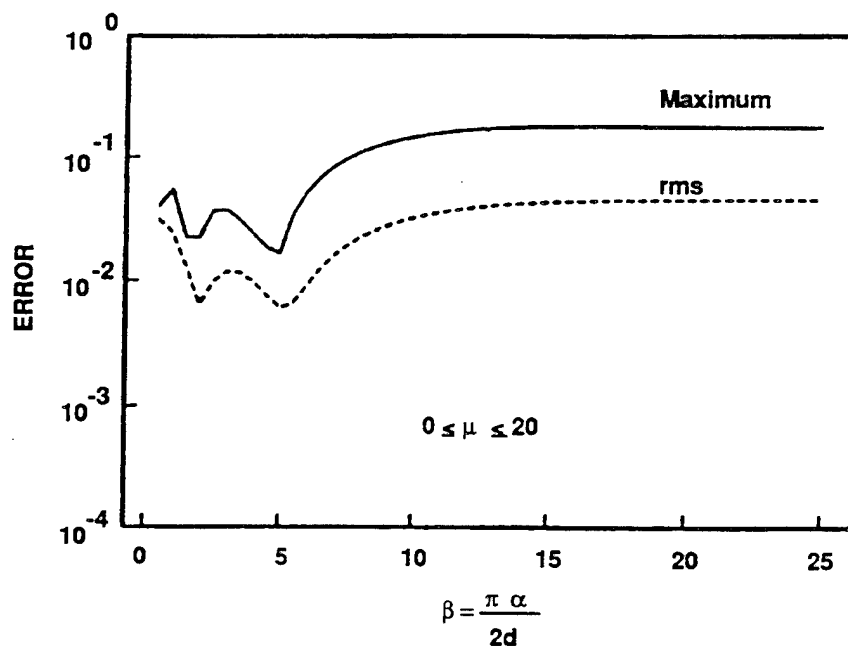
(a) Error Due to Gauss-Laguerre 15-Term Expansion
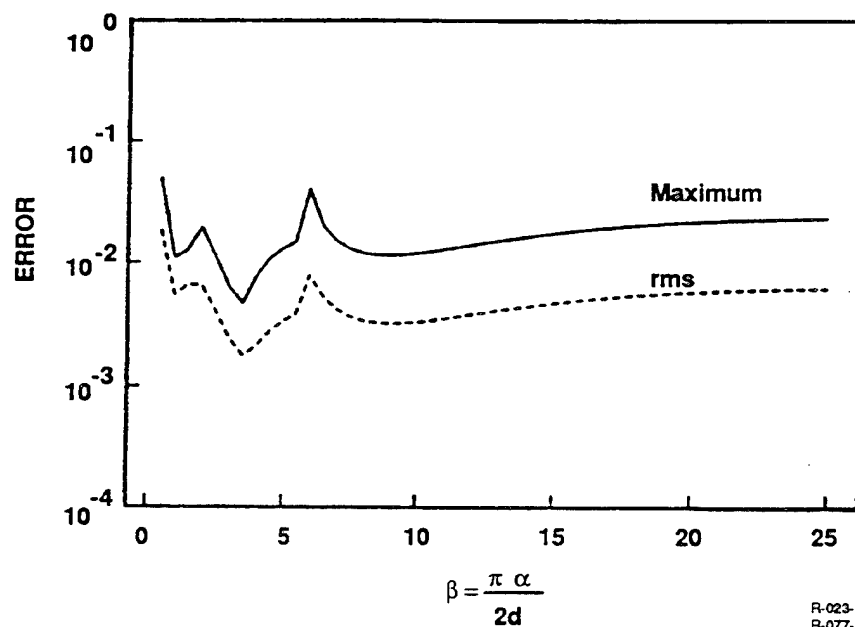
(b) Error Due to (a) Plus Correlations in Text

Figure 193. Errors Due to Exponential Sum Expansion.
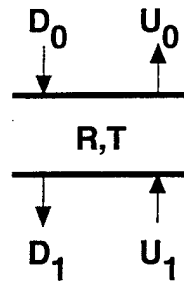
Figure 194. Two-Stream Thermal Flux.

where

$$\alpha^2 \equiv \frac{\omega_o + 2/3\,\omega_o}{1 - \omega_o}$$

$t = 2\alpha\,(1 - \omega_o)\,\tau$

β is the backscattered fraction,

ω_o is the single scattered albedo, and

τ is the optical depth.

4.9.3 Three-Stream Solar/Lunar Flux

The three-stream model, which is an extension of the two-stream model, adds a beam term, S_o, which produces outgoing upward and downward fluxes, U_s and D_s, respectively (see Figure 195), namely:

$$U_o = RD_o + TU_1 + U_s$$

$$D_1 = RU_1 + TD_o + D_s$$
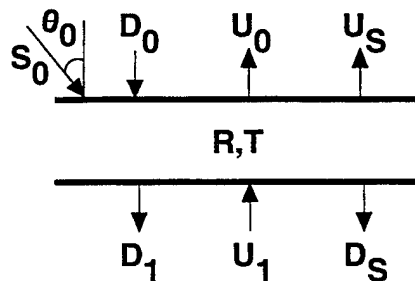
Figure 195. Three-Stream Flux Model.

255

The terms U_S and D_S are defined by

$$U_S = \left[\sigma\left(1 - Te^{-\tau/\mu_o}\right) + \delta R\right]\omega_o\mu_o S_o/\gamma$$

$$D_S = \left[\delta(T\ e^{-\tau/\mu_o}) + \sigma Re^{-\tau/\mu_o}\right]\omega_o\mu_o S_o/\gamma$$

where σ, δ, γ are functions of μ, $\beta(\mu)$, ω_o.

The backscattered fraction is defined in terms of the phase function, P, so

$$\beta(\mu,\phi) = \frac{1}{4\pi\omega_o} \int_0^{2\pi} \int_{-1}^{0} P(\mu,\phi;\mu',\phi')\,d\mu'\,d\phi'$$

$$\beta = \frac{1}{2\pi} \int_0^{2\pi} \int_{-1}^{0} \beta(\mu,\phi)\,d\mu\,d\phi$$

where
μ_o is the cos (θ_o)
ω_o is the single scattered albedo, and
τ is the optical depth.

The three-stream code can be used iteratively to account for solar and lunar beam terms.

4.9.4 Layer Coupling

The multiple scattering calculations must be iteratively coupled between layers, as shown in Figure 196. The equations for a composite layer, consisting of two different layers (i.e., layer "a" and layer "b"), are:

$$S = R_a * R_b[1-R_a{}^*R_b]^{-1} ,$$

$$D = T_a + S\ exp\ (-\tau_a/\mu_o) + ST_a ,$$

$$U = R_b\ exp\ (-\tau_a/\mu_o) + R_bD ,$$

$$R(\tau_a + \tau_b) = R_a + exp\ (-\tau_a/\mu)\ U + T_aU ,$$

$$T(\tau_a + \tau_b) = exp\ (\tau_b/\mu)\ D + T_b\ exp\ (-\tau_a/\mu_o) + T_bD$$

256
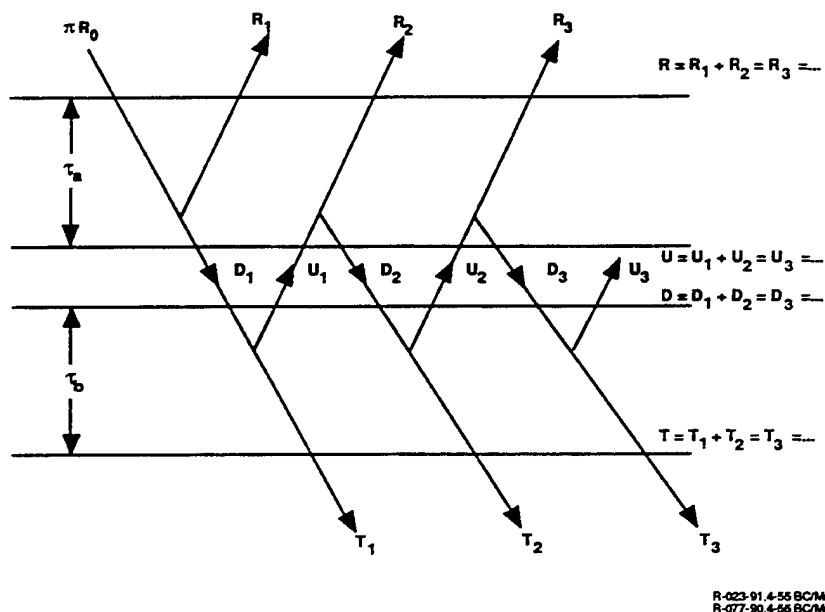
Figure 196. Layer Coupling.

where the subscripts refer to the layer ("a" or "b") and other terms have been previously defined.

The coupling is calculated iteratively, with the upward fluxes starting at the bottom (i.e., the earth) and the downward fluxes starting at the top (i.e., space). Usually, the iteration converges in three to six iterations.

4.9.5 Scattering Into the Line-of-Sight

Once the multiple scattered energy is properly coupled between atmospheric layers, the amount of multiple scattered flux that is scattered into a line-of-sight can be determined from the upward and downward fluxes. The three-flux algorithm discussed in Section 4.9.3 is inverted, and the component scattered into the line-of-sight is obtained from reciprocity.

4.10 Sample Results

An extensive verification and validation of MOSART is being performed, and the results will be reported later. However, a comparison of MODTRAN 2 and MOSART output in the visible and ultraviolet spectral regions (15,000 - 50,000 cm^{-1}, or 0.20 - 0.67 μm) is presented herein.

Some of the differences are due to data base and algorithm differences, including the following:

- MOSART uses full set of 702 aerosol phase functions, while MODTRAN uses a representative subset of 72 aerosol phase functions;
- MOSART uses a four-term exponential sum fit, while MODTRAN uses a single term;
- MOSART uses the Cornette-Shanks phase function (Cornette and Shanks, 1992a), while MODTRAN uses the Henyey-Greenstein phase function;
- MOSART includes additional molecular absorption terms in the ultraviolet (see Section 4.4);
- MOSART performs transmittance calculations using DOUBLE PRECISION to maintain accuracy even in absorption regions; and
- MOSART uses a three-stream multiple scattering algorithm, while MODTRAN uses a two-stream.

For the conditions shown in Table 71, transmittance and path radiance comparisons are made for two geometries:

(i)   An observer at 20 km with a line-of-sight having a tangent altitude of 10 km.
(ii)   The same observer with a zenith angle of 85.0 degrees.

The MOSART calculations were performed using the MODTRAN haze and aerosol profiles (e.g., transitions from troposphere to stratosphere at 10 km; see Section 2.2).

Figure 197 presents the transmittance for the first geometry, and Figure 198 presents the transmittance for the second geometry. The solid line (MODTRAN values) shows quantization effects since the values are printed with only four decimal places. The dashed line (MOSART values) agrees quite well for the first geometry. For the second geometry, a slight offset is apparent; this difference is being investigated. For both geometries, the differences between the conventional transmittance and the forward scattered transmittance (see Section 4.8) are considerable. This is due to several factors:

(i)   In the visible and ultraviolet, the aerosol phase function has a sharp, narrow peak in the forward direction; and
(ii)   The observer for this calculation has a large collecting aperture (1 m diameter) with a large field-of-view (1 mrad).

Figures 199 and 200 show the path radiance for the visible and near ultraviolet for the first and second geometries, respectively. Considering some of the code differences noted above, the agreement between MODTRAN and MOSART is quite good.

Table 71. Calculation Conditions.

```
MOSART Radiative Environment Summary (Ver. 1.10) Fri Oct 22 11:06:48 1993

Latitude   =     45.000 deg North
Longitude  =    100.000 deg West
Date       =  8 Jul 1993
Time       = 12:00:00.0 (GMT)

Model No.     1:  Midlatitude (45 N. Lat.) Summer Atmosphere
                     (Exospheric temperature = 1000.0 K)

Rural Boundary Layer Aerosol Model (Visibility = 23.0 km)
Background Stratospheric Aerosol Model (Type 2)
Shettle/Fenn Background Summer Aerosol Profile (L)
Normal Upper Atmosphere Aerosol Profile
Standard boundary layer vertical structure

Terrain type - Global Backgrounds
   Terrain altitude          =        0.609 km
   Air temperature           =      291.46 K (No. 1)
   Current wind speed        =        4.10 m/sec (No. 1)
   Surface turbulence, Cn2 = 1.000E-14 m**-2/3
   Av. hi alt. wind speed    =       27.00 m/sec

Observer-based coordinate reference frame

Fully correlated, complex geometry solar calculations
   Solar zenith     =       60.00 deg at Observer
   Solar azimuth    =      180.00 deg at Observer
   Solar latitude   =      -15.00 deg
   Solar longitude  =     -460.00 deg
   Solar distance   =      1.0000
   Solar constant   =     1373.18 w/m**2

No lunar calculations

Geometry Conditions (     2 positions)
```

No		Observer Altitude (km)	Src/Tang Altitude (km)	Slant Range (km)	Earth Center Angle (deg)	Obs. Look Angle (deg)	Src. Look Angle (deg)
1	Lz	20.00	10.00			93.13	
2	Lz	20.00	21.00			85.00	

```
Observer aperture       =      1.000 meters
Observer field of view =      1.000 mrad
Background material temperatures set to local air temperature
1 cm**-1 band parameters used
Multiple scattering calculations

Observer aperture       =      1.000 meters
Observer field of view =      1.000 mrad
Background material temperatures set to local air temperature
1 cm**-1 band parameters used
Multiple scattering calculations
```
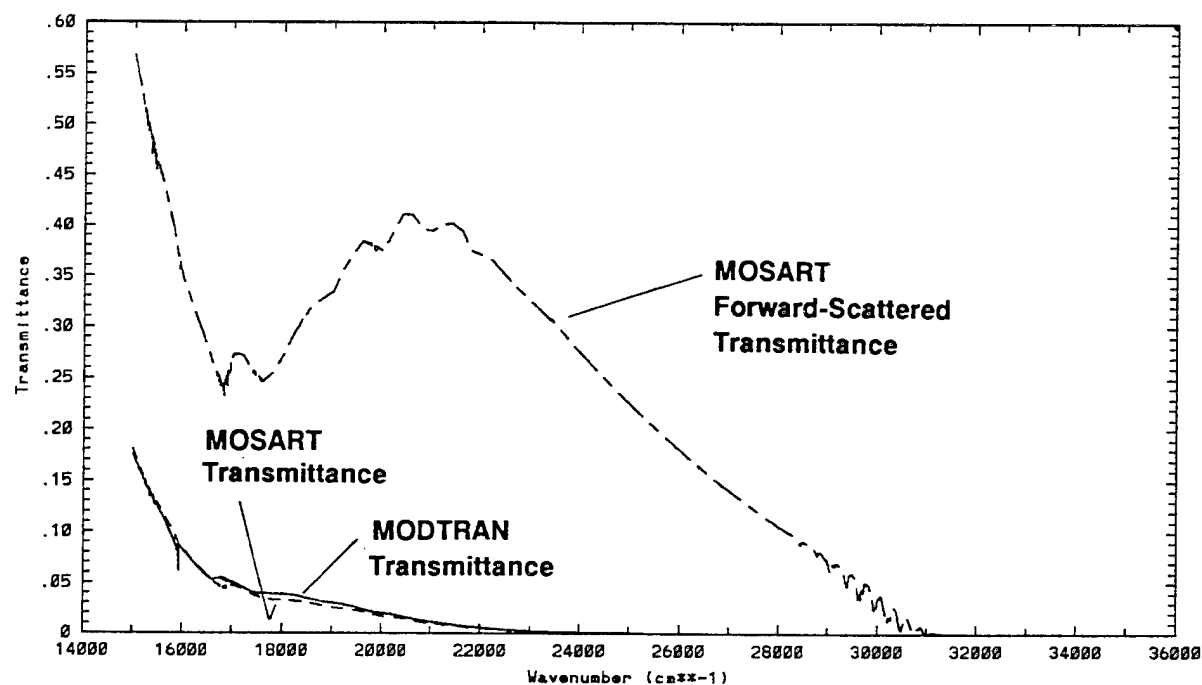
a) Linear Scale
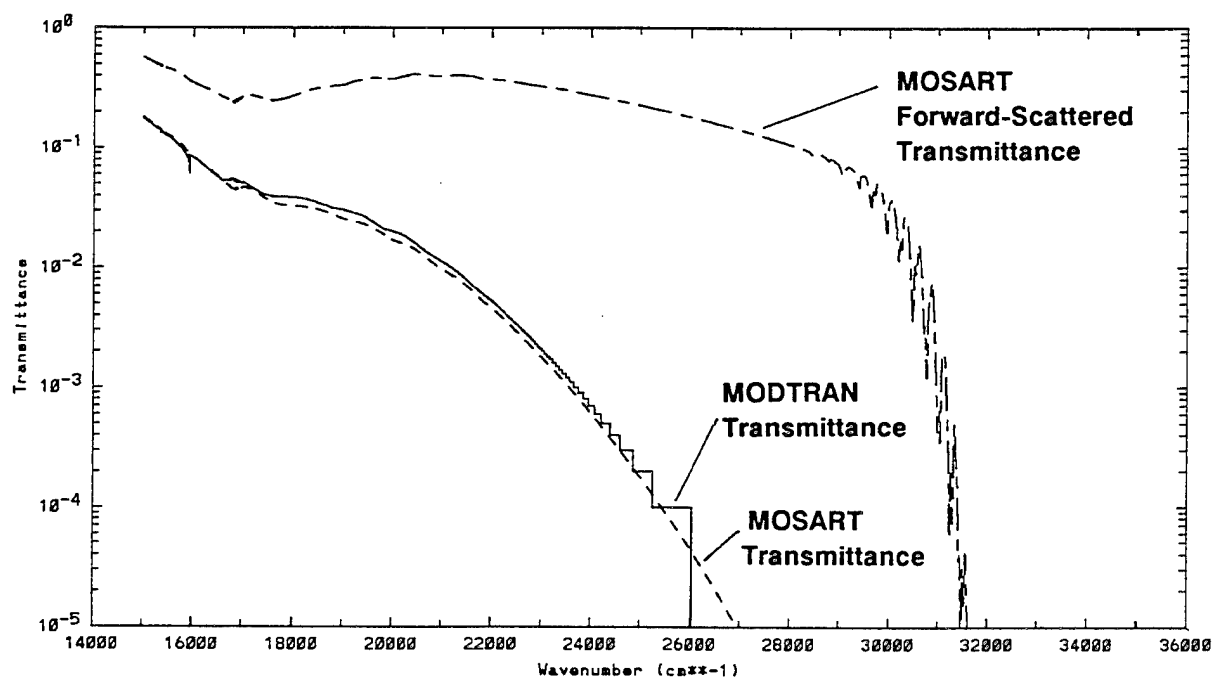
b) Logarithmic Scale

Figure 197. MODTRAN/MOSART Transmittance: First Geometry.
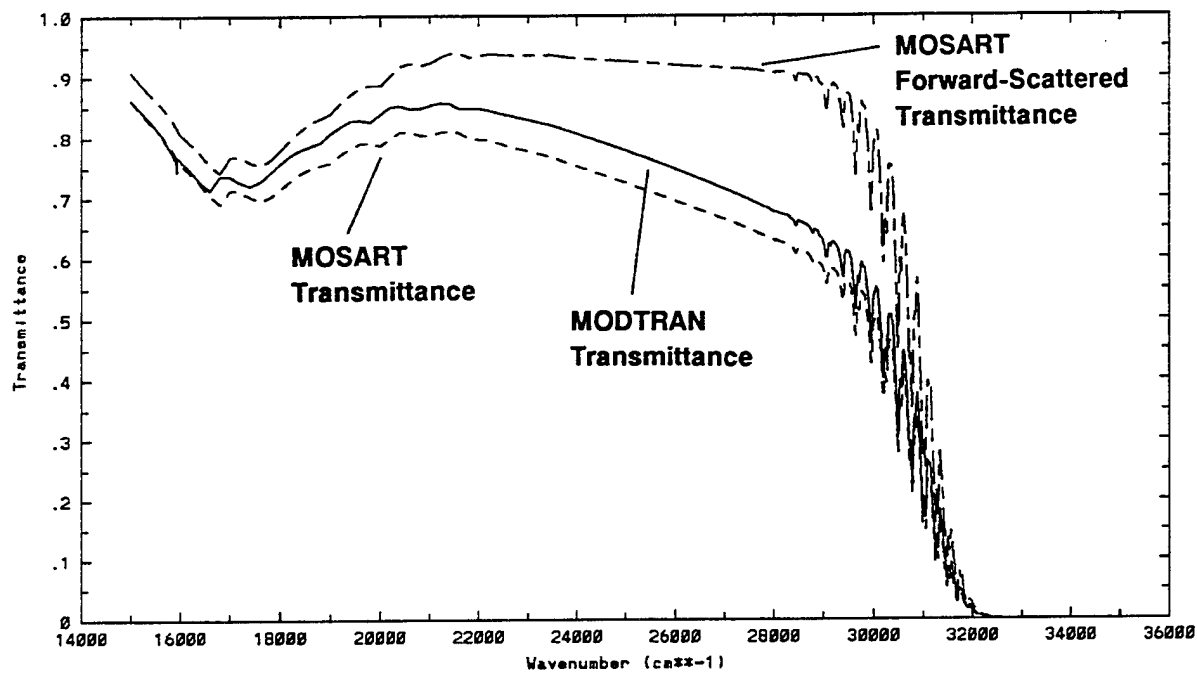
a) Linear Scale
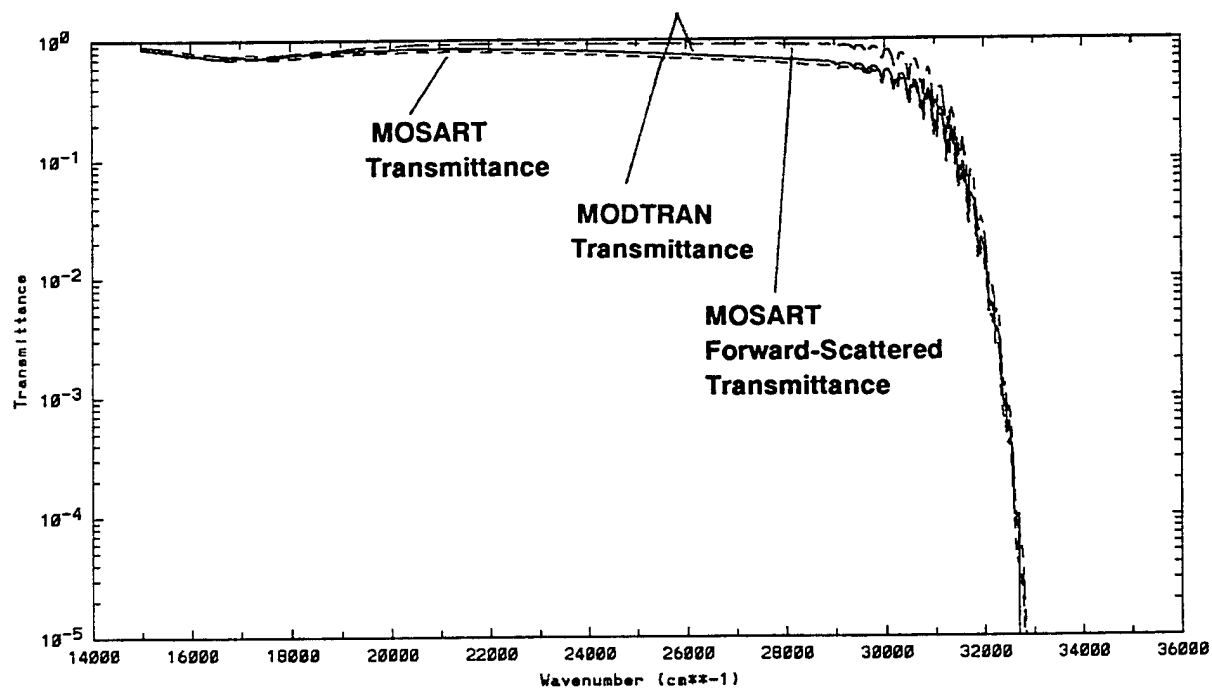
b) Logarithmic Scale

Figure 198. MODTRAN/MOSART Transmittance: Second Geometry.

261
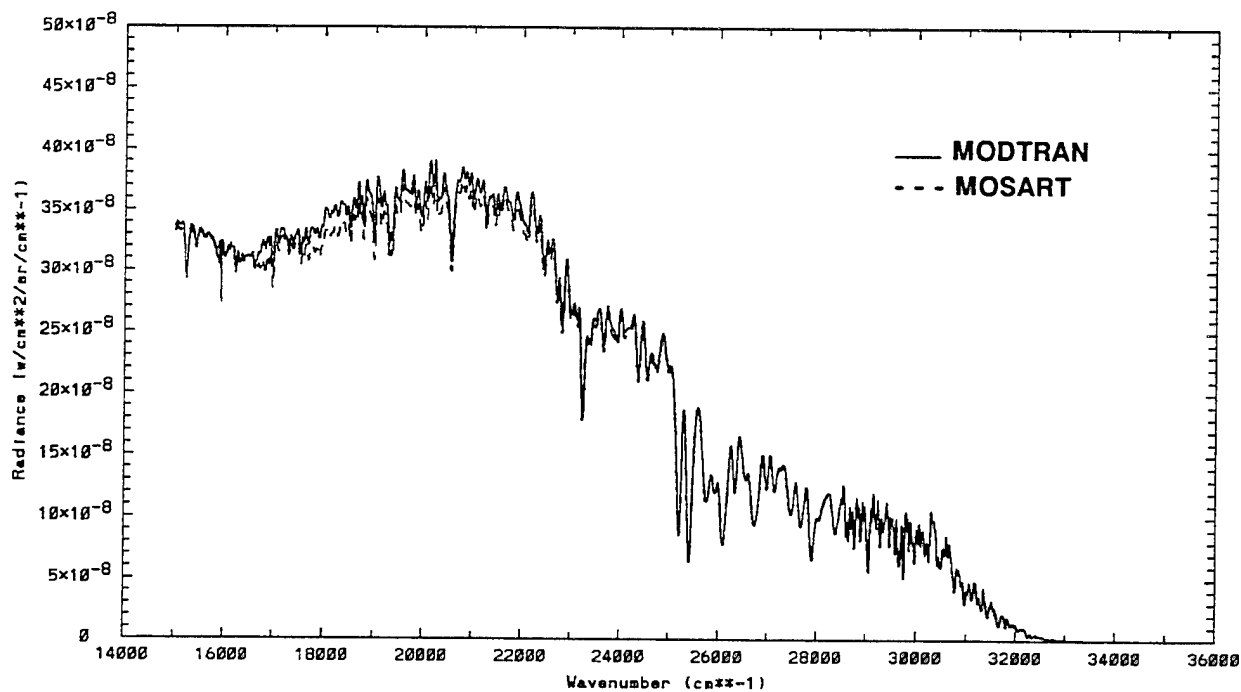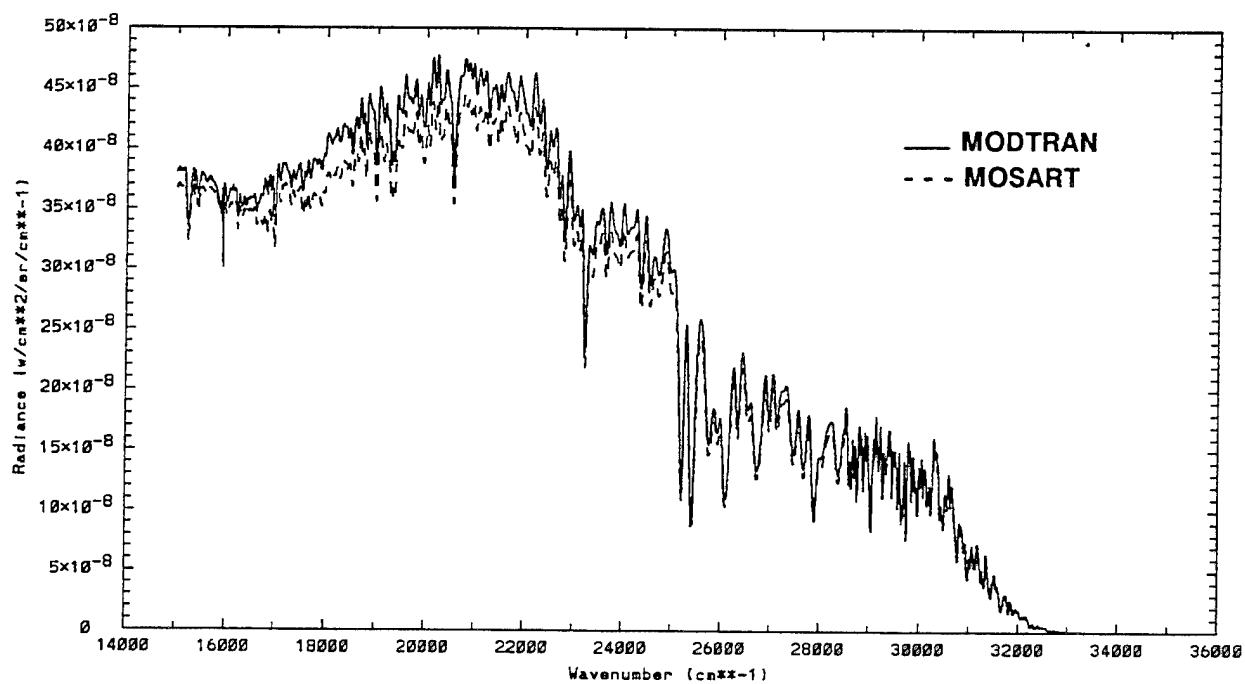
a) Single Scatter

b) Multiple Scatter

Figure 199. MODTRAN/MOSART Path Radiance: First Geometry.
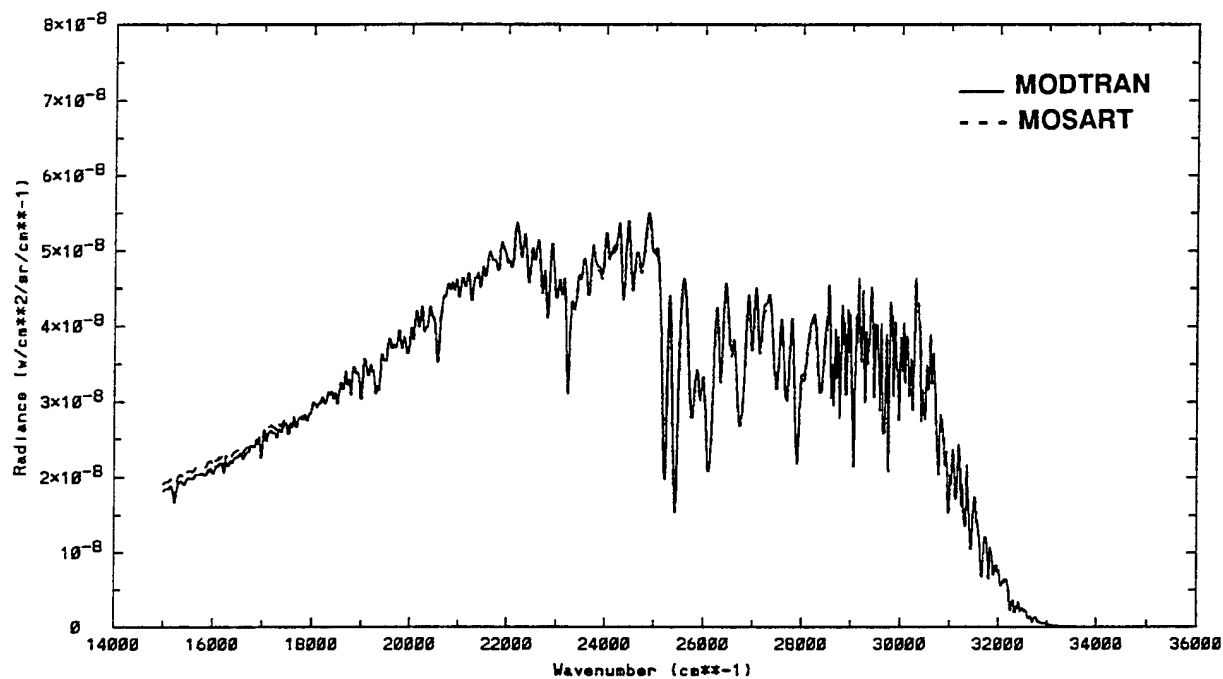
a) Single Scatter
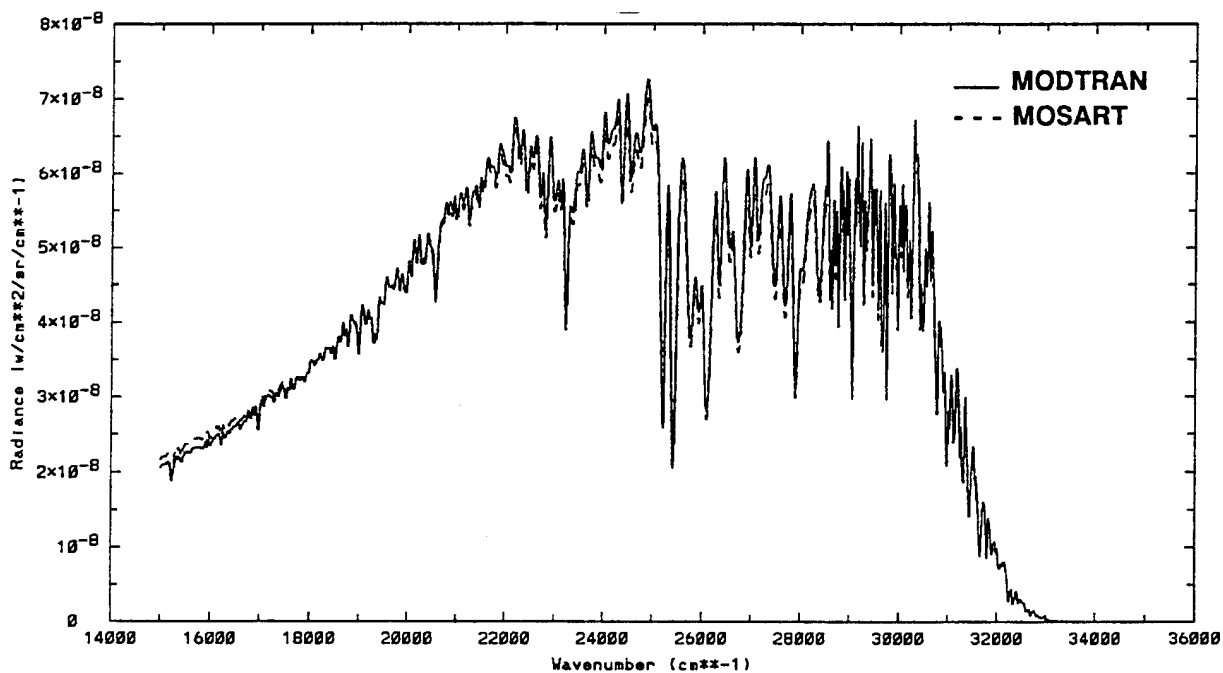
b) Multiple Scatter

Figure 200. MODTRAN/MOSART Path Radiance: Second Geometry.

263

(Note: as part of the verification and validation, an anomalous MODTRAN output has been obtained and is being investigated.)

Figures 201 and 202 show the path radiance for the far ultraviolet (i.e., 0.20 - 0.25 μm) for the first and second geometries, respectively. The significant differences between the predictions of the two codes are due primarily to the additional molecular absorption included in MOSART. Further validation is required in this spectral region.

To illustrate the sensitivity of the haze and aerosol profiles, Figures 203 and 204 present the same MODTRAN path radiances and the MOSART path radiances with the following changes:

(i)   The MODTRAN Stratospheric Background Aerosol Model is replaced by the temperature dependent model;

(ii)   The transition from Tropospheric to Stratospheric is changed from 10 km to 12 km (the tropopause);

(iii) The transition from Stratospheric to Meteoric Dust is changed from 30 km to 47.5 km (the stratopause); and

(iv)   The haze profile is modified to correspond to the tropopause and stratopause.

The most obvious change is the decrease in the path radiance for the downlooking (first) geometry and the increase for the uplooking (second) geometry between 15,000 and 25,000 cm^{-1}. This change is primarily due to the redistribution of aerosol particles by the haze profile. For wavenumbers above 25,000 cm^{-1}, the effects of molecular scattering and absorption dominate, so little difference is noted.
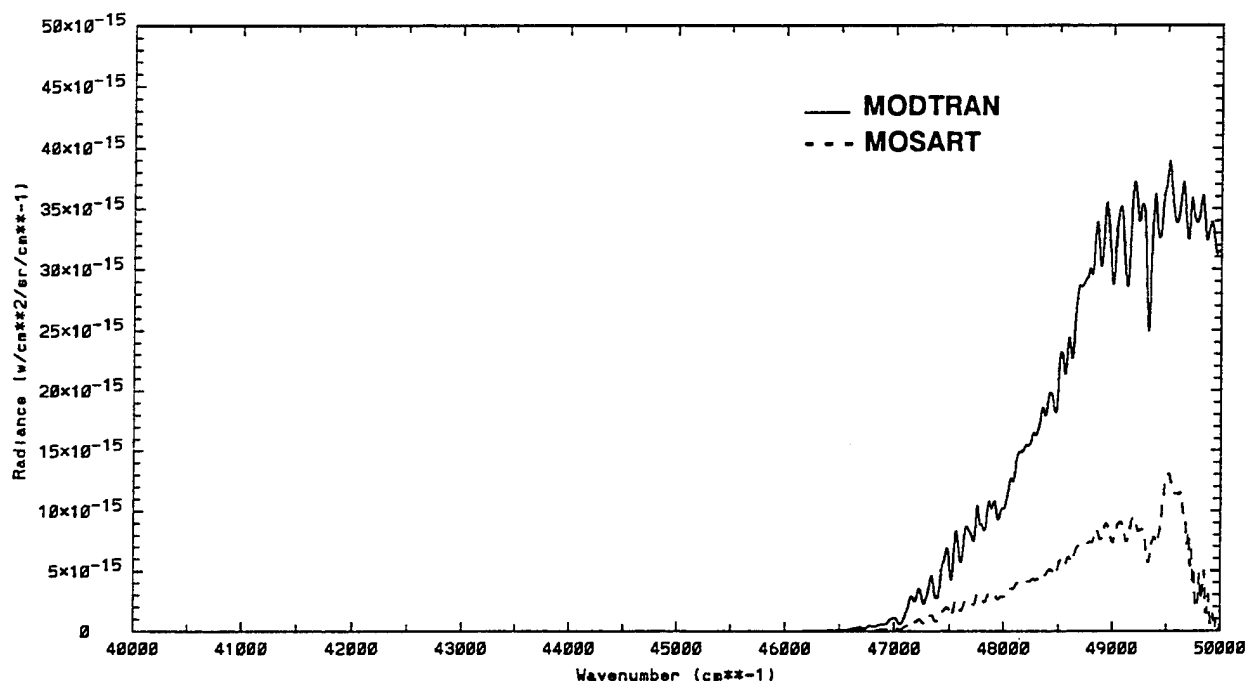
a) Single Scatter
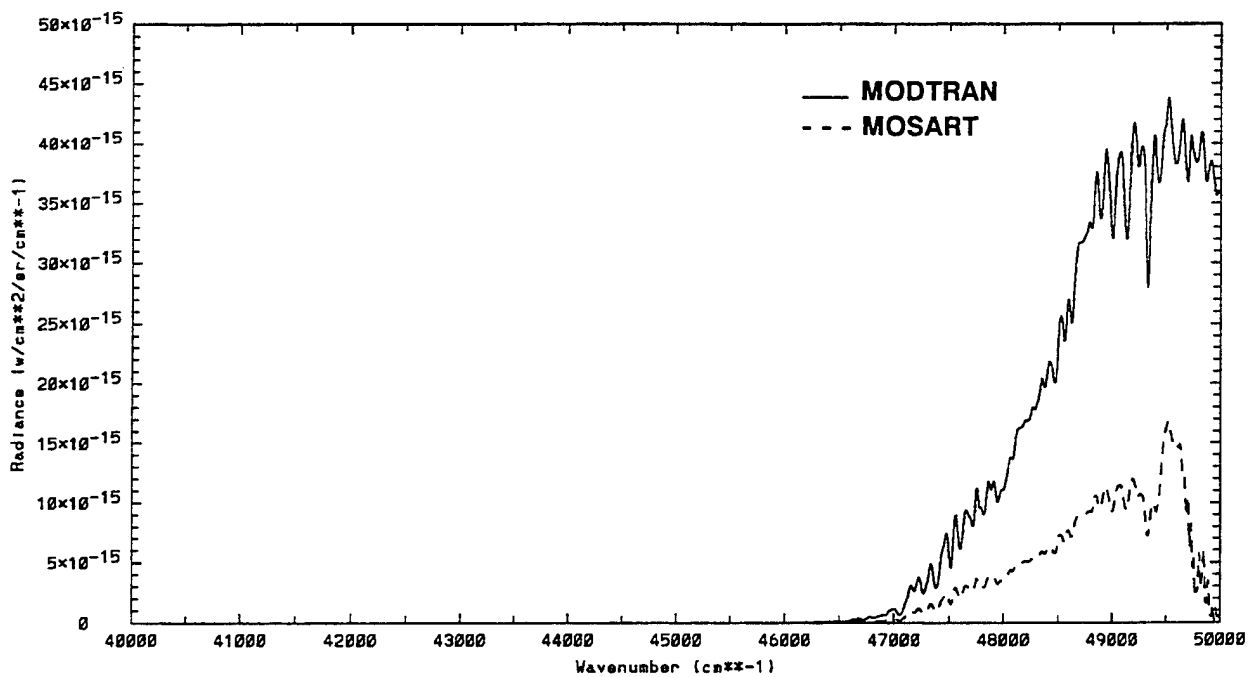
b) Multiple Scatter

Figure 201. MODTRAN/MOSART Path Radiance: First Geometry.
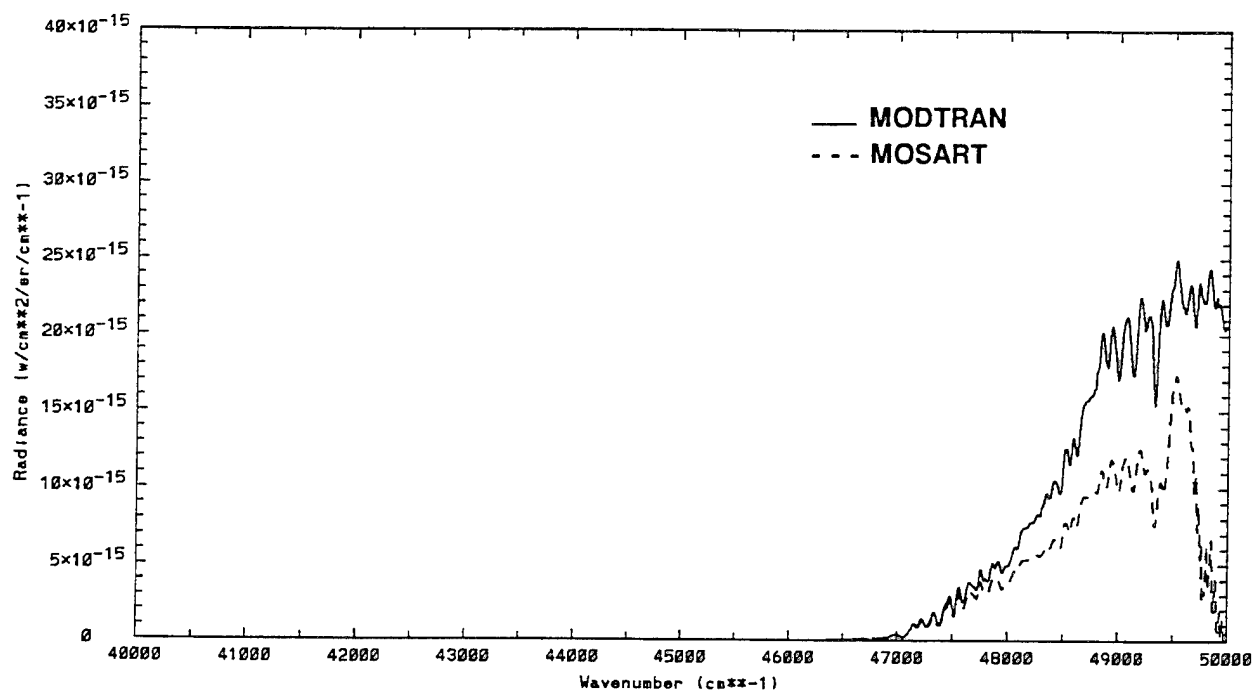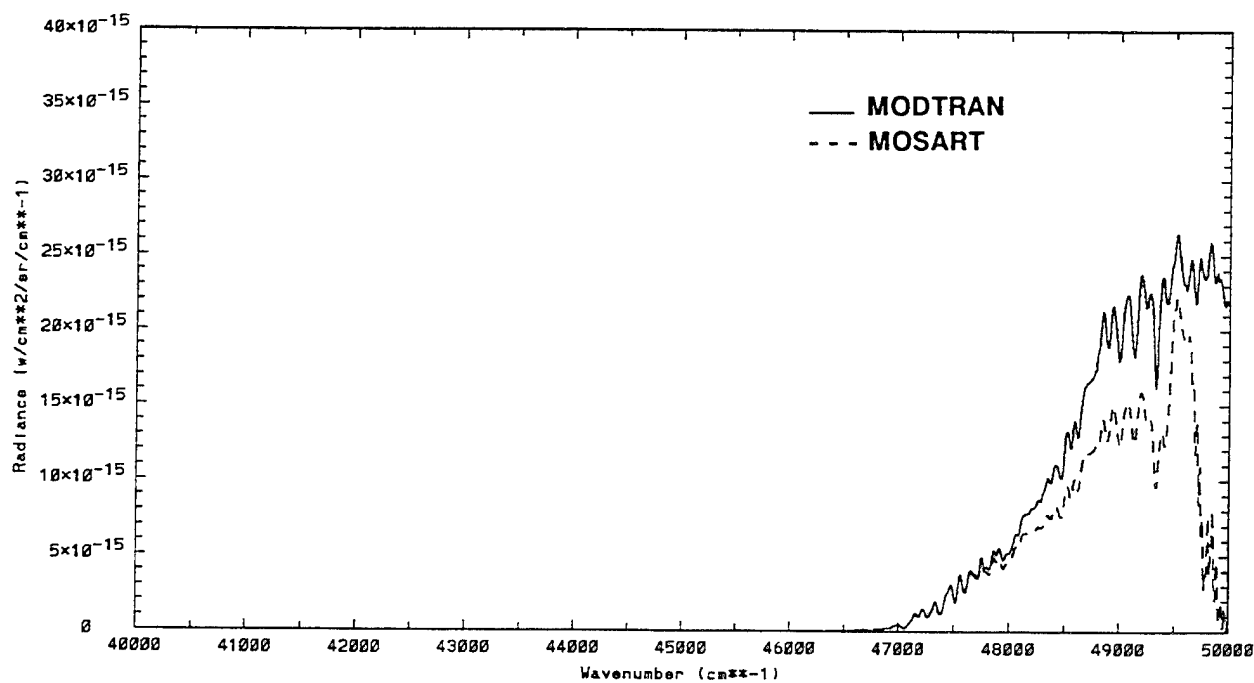
a) Single Scatter

b) Multiple Scatter

Figure 202. MODTRAN/MOSART Path Radiance: Second Geometry.
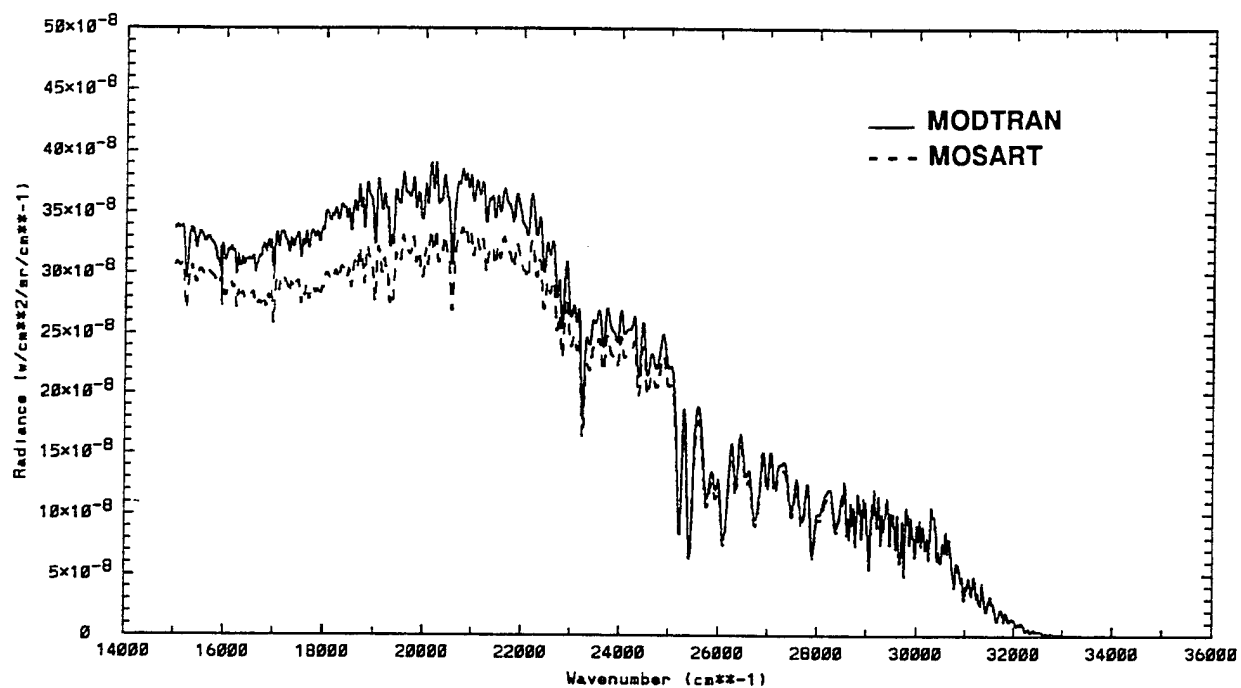
a) Single Scatter
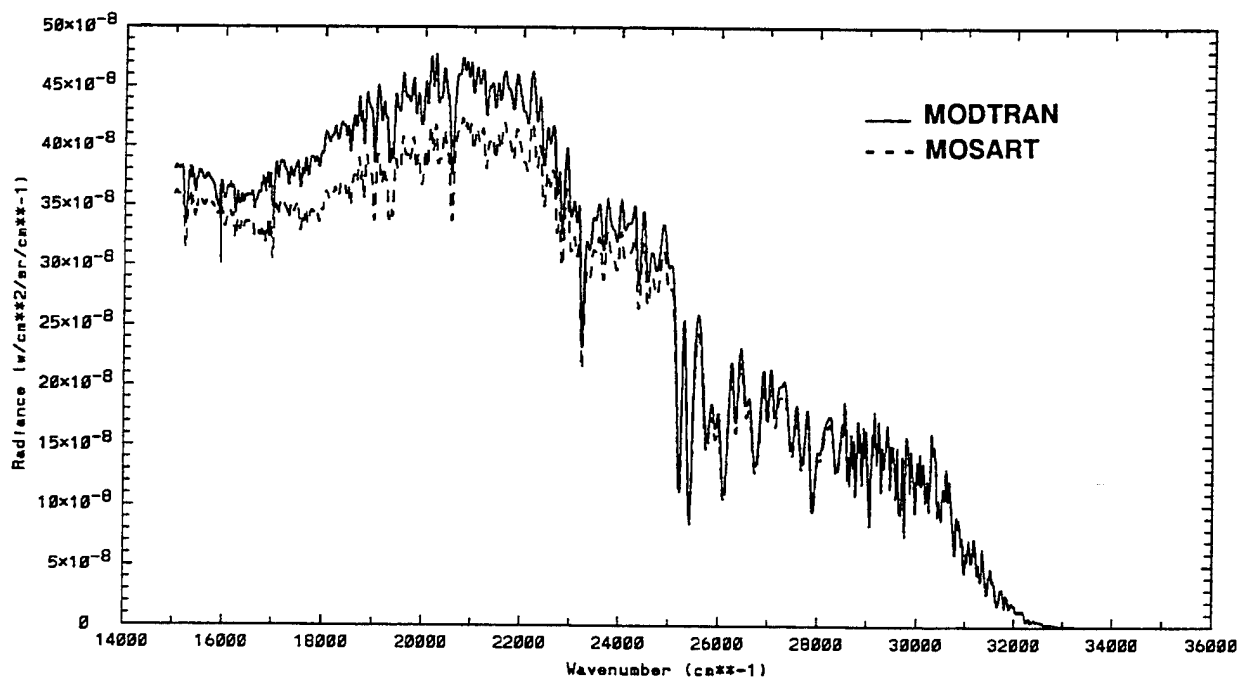
b) Multiple Scatter

Figure 203. MODTRAN/MOSART Path Radiance: First Geometry, Different Haze and Aerosol Profiles.

267
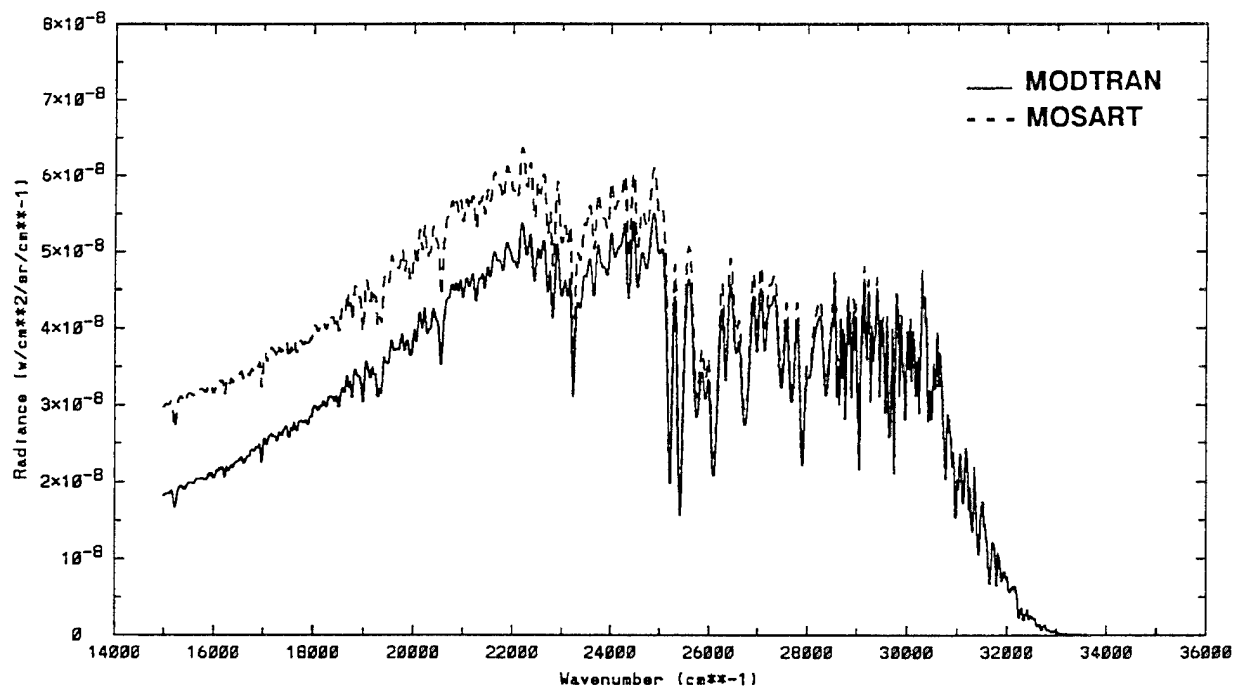
a) Single Scatter
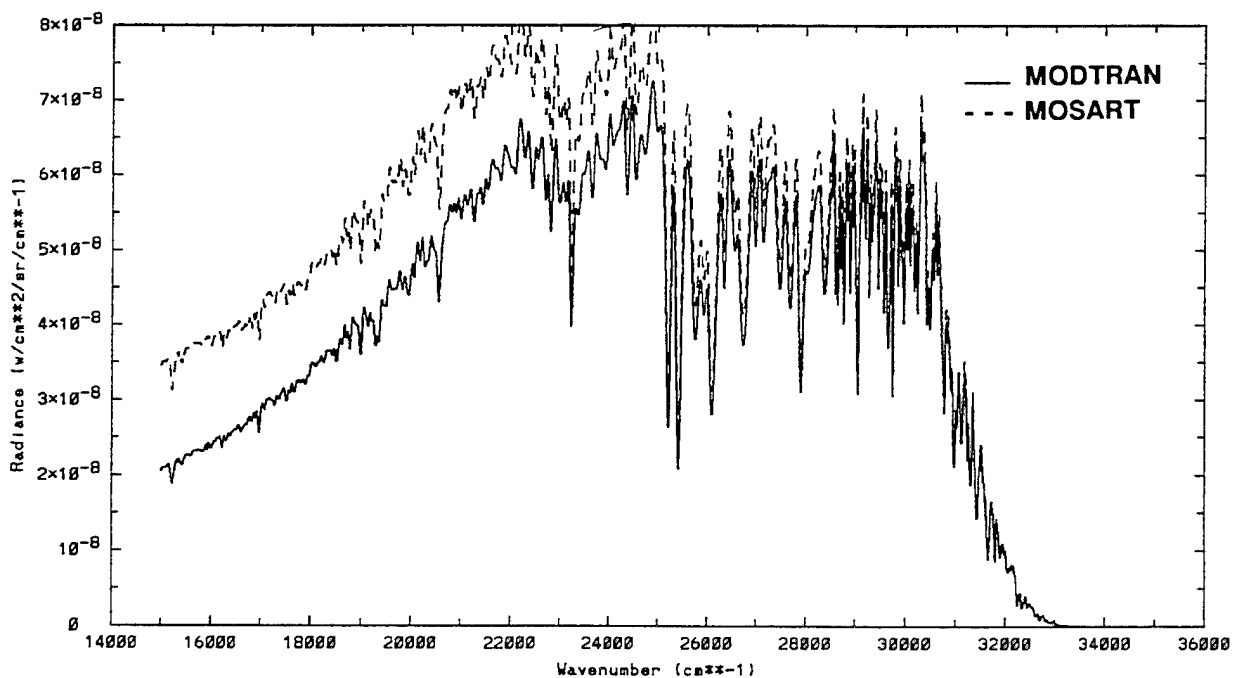
b) Multiple Scatter

Figure 204. MODTRAN/MOSART Path Radiance: Second Geometry, Different Haze and Aerosol Profiles.

5.0 HEAT TRANSFER

Since the temperature of the earth's surface is influenced by the radiative environment, the first step in computing this temperature is to compute the radiation environment. Surface temperatures are calculated by solving the radiative transfer problem in the earth's atmosphere. This amounts to balancing the total solar energy absorbed by the earth's surface against the thermal energy radiated by the surface. The steady state balance defines the temperature for each material in the scene. These calculations are accomplished by dividing all the incident and emitted radiation into two broad bands: a short-wave (solar) band from 0.4 to 4.0 μm, and a long-wave (thermal) band from 4 to 20 μm. While the approximations employed in this broad-band treatment are fairly crude, it is more than accurate enough for computing the net radiative fluxes used in the energy balance heat transfer calculation. The heat transfer module in MOSART has been taken from APART.

The model atmosphere used in the broad-band computations is illustrated in Figure 205. The atmosphere is divided into nine layers, which are specified by the relative positions of the low, middle, and high cloud layers. The atmospheric composition is obtained from the model atmosphere, and the air, subsurface, and first-guess surface temperatures are obtained from the internal data bases and/or user-supplied values.

The terrestrial band (longwave) calculations use a layer flux emissivity calculation to represent the radiative transfer through the nine-layer atmosphere. The longwave flux calculation proceeds as follows. Vertically integrated absorber amounts for each layer are computed for each of the major absorbers of longwave radiation (water vapor, carbon dioxide, and ozone), and are corrected for temperature and pressure effects with a multiplicative factor included to account for diffuse radiation. The vertical integration within each layer is high resolution (10 mb) and the vertical temperature structure is obtained from the model atmosphere. The layer flux transmissivities are then obtained from a two-dimensional interpolation from the Staley and Jurica (1970) flux emissivity tables. The upward and downward diffuse fluxes are then calculated by integrating the black body emission times the differential flux transmission between layers.

The transfer of solar band (shortwave) radiation through the atmosphere is accomplished using the two-stream approximation for each layer, and a three-layer addition scheme that is applied recursively to the nine-layer atmosphere. The two-stream approximation here employs a backscattering fraction defined in terms of a Legendre expansion. The solar beam is considered to be an internal source of diffuse radiation in each layer and is similar to the technique of Coakley and Chylek (1975).
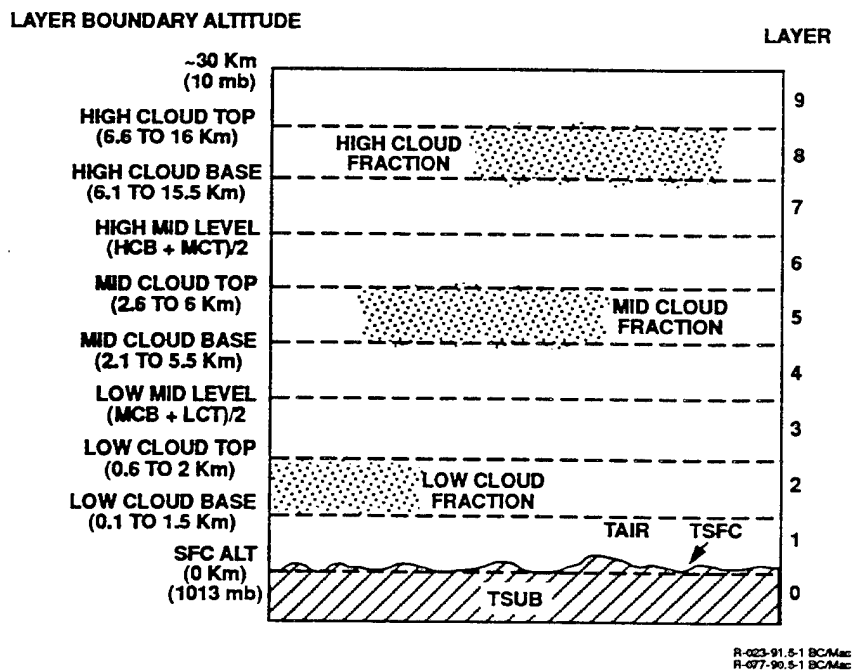
Figure 205. Atmospheric Layer Structure Defined in the Broad-Based Model.

The solution to the transfer equation in each layer (the layer reflectivities and transmissivities) are then added by a technique similar to that used by Lacis and Hansen (1974) (see also van de Hulst, 1980) to obtain the solution for a composite of different layers. For this application, instead of the top-down adding approach used by Lacis and Hansen, a recursive adding technique developed by Jafolla (1981) was used with a substantial increase in computational efficiency. In recursive adding, the total number of layers is a power of two or, in this case, three. A composite layer reflectivity and transmissivity is obtained explicitly for a three-layer composite and then is applied recursively to the individual layers, and then in turn to the composite layers to build up the atmosphere.

The solution to the transfer problem is then obtained by specifying the surface albedo and the individual layer shortwave parameters. The layer shortwave parameters that need to be defined are: the phase function asymmetry factor, the scattering optical path for cloud particles, the absorption (water vapor and ozone), and Rayleigh scattering optical paths.

270

5.1 Terrestrial Band Model

Starting from the equation of radiative transfer in a plane-parallel, azimuthally symmetric, homogeneous, non-scattering atmosphere in local thermodynamic equilibrium,

$$\frac{dI_\lambda(\tau,\theta)}{d\sigma_\lambda(\theta)} = I_\lambda^* - I_\lambda(\tau,\theta)$$

where $I_\lambda(\tau,\theta)$ is the longwave (4 to 40 μm) radiance (W/m^2/sr^1) in the direction θ (zenith angle), I_λ^* the diffuse black body emission at wavelength λ, and the optical path $d\sigma_\lambda(\theta)$ is given by

$$d\sigma_\lambda(\theta) = K_\lambda \sec\theta\, \rho(Z)dZ = \sec\theta\, d\tau$$

where K_λ is the wavelength dependent absorption coefficient, and $\rho(Z)dZ$ is the vertical absorber path length.

From Beer's law, the transmissivity between levels Z_1 and Z_2 is given by

$$T_\lambda = T_\lambda(Z_1,Z_2;\theta) = \exp\left[-\int_{Z_1}^{Z_2} d\sigma_\lambda(\theta)\right]$$

and the emissivity is given by

$$E_\lambda = 1 - T_\lambda$$

For a thin layer,

$$T_\lambda = \exp[-d\sigma_\lambda] \approx 1 - d\sigma_\lambda$$

and

$$E_\lambda \approx d\sigma_\lambda$$

So, the thin layer approximation to the transfer equation is given by

$$dI_\lambda = E_\lambda(I_\lambda^* - I_\lambda)$$

Multiplying by $\cos\theta$ and integrating over solid angle and wavelength gives the flux

$$dF = \int_0^\infty \int_{2\pi} dI_\lambda \cos\theta\, d\omega\, d\lambda = \int_0^\infty \int_{2\pi} E_\lambda (i_\lambda^* - I_\lambda)\, \cos\theta\, d\omega\, d\lambda \tag{5-1}$$

The flux transmissivity is defined by

$$T_f = \int_0^\infty \int_{2\pi} I_\lambda^* T_\lambda \cos\theta\, d\omega\, d\lambda \bigg/ \int_0^\infty \int_{2\pi} I_\lambda^* \cos\theta\, d\omega\, d\lambda$$

$$= \int_0^\infty \int_{2\pi} I_\lambda^* T_\lambda \cos\theta\, d\omega\, d\lambda \bigg/ \sigma^* T^4$$

and similarly, the flux emissivity is defined by

$$E_f = \int_0^\infty \int_{2\pi} I_\lambda^* E_\lambda \cos\theta\, d\omega\, d\lambda \bigg/ \int_0^\infty \int_{2\pi} I_\lambda^* \cos\theta\, d\omega\, d\lambda = 1 - T_f \tag{5-2}$$

Making the approximation

$$T_f \approx \int_0^\infty \int_{2\pi} I_\lambda T_\lambda \cos\theta\, d\omega\, d\lambda \bigg/ \int_0^\infty \int_{2\pi} I_\lambda \cos\theta\, d\omega\, d\lambda$$

and again using the thin layer approximation $T_f \approx 1 - d\sigma_f$, and $E_f \approx d\sigma_f$, Equation (5-1) can be rewritten as

$$dF = d\sigma_f (B^*(T) - F)$$

$$\frac{dF}{d\sigma_f} = B^*(T) - F \tag{5-3}$$

272

which is the flux form of the transfer equation, where $B^{*}(T)$ is the black body flux at temperature T. The solution to this differential equation is straightforward and is given by

$$Fe\downarrow(Z_r) = -\int_{Z}^{\infty} \exp[-\sigma_f(Z_r,Z')]B^{*}(T(Z'))\,d\sigma_f(Z') = \int_{Z_r}^{\infty} B*(T(Z'))\,dT_f(Z_r,Z')$$

for downward, clear sky radiation, where

$$T_f(Z_r,Z') = \exp\left[-\int_{Z}^{Z_r} d\sigma_f(Z)\right] .$$

Hence, for an n layer model,

$$Fe\downarrow(Z_r) = \sum_{j=r}^{n-1} B^{*}(T_j'[T_f(Z_r,Z_j) - T_f(Z_r,Z_{j+1})]$$
(5-4)

where T_j' is the average temperature of the layer between Z_j and Z_{j+1}. When an optically thick cloud is in layer c, Equation (5-4) becomes

$$Fe\downarrow(Z_r) = \sum_{j=r}^{c-1} B^{*}(T_j'[T_f(Z_r,Z_j) - T_f(Z_r,Z_{j+1})] + \varepsilon_c B^{*}(T(Z_c))\, T_f(Z_r,Z_c)$$

where ε_c is the emissivity of the cloud surface.

Similarly, for upward radiation, the solution to Equation (5-3) is

$$Fe\uparrow(Z_r) = \sum_{j=1}^{r-1} B^{*}[T_j'(Z_{j+1},Z_r) - T_f(Z_j,Z_r)] + \varepsilon_g B^{*}(T(Z=0))\, T_f(Z=0,Z_r)$$

$$Fe\uparrow(Z_r) = \sum_{j=c}^{r-1} B^{*}(T_j) [T_f(Z_{j+1},Z_r) - T_f(Z_j,Z_r)] + \varepsilon_c B^{*}(T(Z_c))\, T_f(Z_c,Z_r))$$

for the cloud-free case, and for a cloud in layer c respectively. Here, the ground emissivity is given by ε_g.

The flux transmissivities are calculated using Equation (5-2) and the flux emissivity tables of Staley and Jurica (1970). The flux emissivities are given as a function of absorber path length and temperature for absorption by water vapor in the 6.3 μm vibration band, the 9 to 12 μm window region and the rotation bands ($\lambda > 20$ μm); and absorption by carbon dioxide in the 15 μm, and ozone in the 9.6 μm bands.

Multiple absorbers are handled additively, assuming no overlap in the absorption bands. That is,

$$\sigma_f(Z_1,Z_2) = \int_0^\infty \int_{Z_1}^{Z_2} K_\lambda \ (1.66) \ \rho(Z) \, dz \, d\lambda$$

where K_λ is the absorption coefficient, $\rho(Z)$ is the absorber density, and the factor 1.66 comes from integrating over solid angle for diffuse radiation (see Elsasser and Culbertson, 1960). For non-overlapping absorption bands of water vapor, carbon dioxide, and ozone,

$$\sigma_f(Z_1,Z_2) = \sigma_f^u(Z_1,Z_2) + \sigma_f^v(Z_1,Z_2) + \sigma_f^w(Z_1,Z_2)$$

thus,

$$T_f(Z_1,Z_2) = T_f^u(Z_1,Z_2) + T_f^v(Z_1,Z_2) + T_f^w(Z_1,Z_2)$$

$$= (1 - E_f^u) \ (1 - E_f^v) \ (1 - E_f^w)$$

$$= 1 = E_f$$

where

$$E_f(Z_1,Z_2) = E_f^u + E_f^v + E_f^w - E_f^u E_f^v - E_f^u E_f^w - E_f^v E_f^w + E_f^u E_f^v E_f^w$$

Here u, v, and w represent the vertical column absorber amounts for water vapor, carbon dioxide, and ozone respectively, and E_f^u, E_f^v, and E_f^w are the corresponding flux emissivities obtained from the Staley and Jurica tables using a two-dimensional interpolation.

5.1.1 Calculation of Absorber Optical Paths

High resolution vertical profiles of altitude, temperature, and water vapor, carbon dioxide, and ozone densities are computed based upon the model atmospheric profiles. The profiles are specified versus pressure and vary from 10 mb (approximately 30 km) to 1010 mb (approximately 25 meters) at 10 mb resolution, giving 101 pressure levels.

The interpolation from the model atmospheric data is linear in altitude for temperature, and logarithmic for pressure and density. That is, the density at altitude Z, between levels Z_j and Z_{j+1}, is given by

$$\zeta(Z) = \zeta_j \exp[-(Z - Z_j) / H_\zeta]$$

where the density scale height H_ζ is

$$H_\zeta = Z_{j+1} - Z_j) / \ln(\zeta_j/\zeta_{j+1})$$

Then, the pressure index (1 to 101) is computed for each layer boundary. The layer boundaries between the low and middle cloud layers and the middle and high cloud layers are defined to be halfway between the lower cloud top and the upper cloud base.

The calculation of absorber path lengths is accomplished by a vertical integration in altitude. The absorber path lengths were reduced to standard pressure conditions $(P_o = 1013.25$ mb) according to the formula given by Elsasser

$$\Delta U = 1.66(P/P_o)\zeta'(Z) \Delta Z$$

where the factor 1.66 is included to account for the average path length for diffuse radiation, and ΔZ is in kilometers. The conversion factors are given by

$$\zeta'(Z) = \zeta_L (Z)/\left(\sqrt{273.15/T(Z)}\right)^{0.9} \quad [g/(cm^2/km)]$$

for water vapor, and

$$\zeta'(Z) = \zeta_L(Z) * 33/\left(\sqrt{273.15/T(Z)}\right)^{0.75} \quad [cm-atm/km]$$

275

for carbon dioxide (where the 33 comes from a volume mixing ratio of 330 ppm and units conversion), and

$$\zeta'(Z) = \zeta_L(Z)/\left(\sqrt{273.15/T(Z)}\,\right)^{0.4} \quad [cm-atm/km]$$

for ozone.

In addition, the water vapors paths in the cloud layers were corrected for 100% relative humidity by the equation

$$\Delta U_T = \Delta U(1 - C_f) + \Delta U_c C_f$$

$$\Delta U_c = 1.66(0.1\ f(T) - \zeta'(Z)P_o/P)(P/P_o)\ \Delta Z$$

where C_f is the cloud fraction and $f(T)$ is the saturated water vapor density as a function of temperature.

The vertical air mass in each layer is also computed here, to be used to compute Rayleigh scattering optical paths in the solar band model. The incremental air mass is given by

$$\Delta Y = \frac{q}{g\zeta_o}\ \Delta P \quad (cm)$$

where q is the "mixing ratio" of air (1000 g/Kg), g is the acceleration due to gravity (980 cm/s^2), ζ_o is the stp air density (1.2925x10^{-3} gm/cm^3), and ΔP is in millibars.

The vertical integration is performed from the top of the atmosphere to each layer boundary using the trapezoidal rule. The average temperature for each layer, weighted by the optical path, is computed as well. This is used in computing the temperature dependent flux emissivities.

5.1.2 Calculation of Flux Transmission

The flux emissivities for the major bands of water vapor, carbon dioxide, and ozone are calculated in order to compute the transfer of longwave radiation through the atmosphere. The computation involves a table look-up and two-dimensional interpolation over the data provided by Staley and Jurica (1970). The Staley and Jurica flux emissivities were evaluated from Elsasser's wavelength-dependent absorption coefficients and include all the major absorption bands: the vibrational (6.3 μm), rotational (>~20 μm),

and continuum (window region) bands for water vapor; 4.3 and 15 μm bands for CO_2; and the 9.6 μm band for ozone.

The flux emissivities (in percent) are tabulated versus temperature (K) and the base 10 log of pressure corrected optical depth (gm/cm^2 for water vapor, and cm-atm for carbon dioxide and ozone). A straightforward logarithmic interpolation is performed, and the contributions from the different gases are appropriately combined.

For a given layer boundary, the upward and downward diffuse fluxes of longwave radiation are now computed. Figure 206 shows a schematic representation of the implementation of this technique for the case of two cloud layers. The lettered arrows indicate the contribution of a combination of layers to a particular layer boundary; e.g.,

$$C = \sigma T_M{}^4(7,10) \ [T_f(1,7) - T_f(1,10)]$$

gives the contribution at the surface of the downward flux from the top three layers. σ is the Stefan-Boltzmann constant (5.67×10^{-8} W M^{-2} K^{-4}), $T_M(7,10)$ is the path-weighted average temperature for the top three layers, and $T_f(I,J)$ is the flux transmission between level I and J.
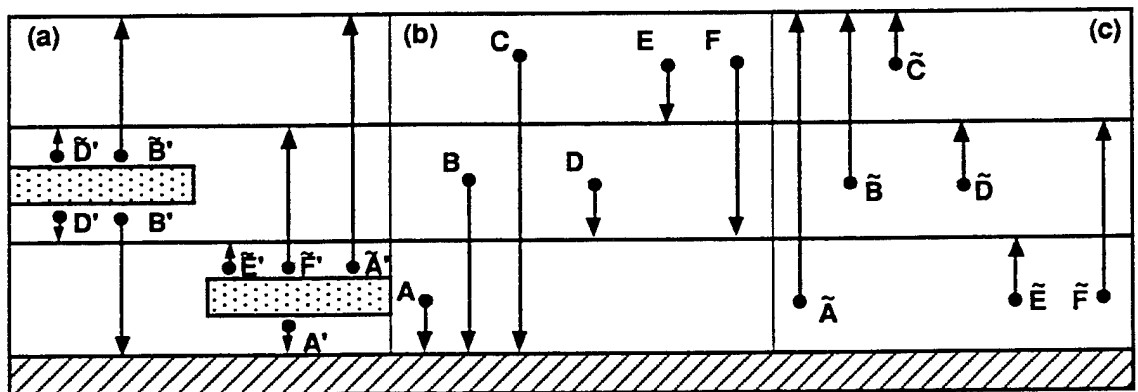
Figure 206. Schematic Representation of the Long Wave for Calculation for the Case of Two Cloud Layers. Each term represents the contribution of a particular major layer or sub-layer to the indicated level: (a) the upward and downward contributions from the sub-layers above and below the cloud layers; (b) the downward contributions from each major layer; and (c) the upward contribution from each major layer.

277

For this example, the total downward flux at the surface is given by

$$F_L\downarrow = (1\text{-}CC)(A+B+C) + C_M(1 - C_L)(\varepsilon_{MC}\sigma^4{}_{MCB} T_f(1,5) + B' + A)$$
$$+ C_L (\varepsilon_{LC}\sigma T^4{}_{LCB} T_f(1,2) + A')$$

where C_L and C_M are the low and middle-level cloud fractions and CC is the composite cloud fraction

$$CC = 1 - (1 - C_L) (1 - C_M)$$

and, ε_{LC}, ε_{MC} and T_{LCB} are the cloud emissivities and base temperatures, respectively. Equations of this type are included to compute the atmosphere, cloud, and surface contributions at each layer boundary.

5.2 Solar Band Model

The solar band calculations determine the upward and downward diffuse shortwave fluxes and the depleted solar beam at each layer boundary. The process is first to compute the shortwave optical properties for each atmospheric layer and the surface, and then to combine them radiatively to account for layer interactions.

Given the solar band input to the system (i.e., an exoatmospheric solar flux) and a solar zenith angle and earth-sun distance correction obtained from an ephemeris calculation, the layers are radiatively combined which accounts for multiple reflections between the atmospheric layers and the surface, and computes the net radiative flux at each layer boundary. The algorithms and techniques used to perform the calculations are described in the following sections.

5.2.1 Solution for Diffuse Radiation

The equation for radiative transfer for shortwave radiation (0.2 to 4 μm) through a plane parallel, scattering and absorbing atmosphere is given by Chandrasekhar (1960, page 22).

$$\frac{\mu dI(\tau,\mu,\phi)}{d\tau} = I(\tau,\mu,\phi) - \frac{1}{4\pi\omega_o} \int_o^{2\pi} \int_{-1}^{1} I(\tau,\mu',\phi')p(\mu,\phi;\mu',\phi')d\mu'd\phi$$

$$- S_o \exp(-\tau/\mu_o)p(\mu,\phi;\mu_o,\phi_o) \tag{5-5}$$

Here, $I(\tau,\mu,\phi)$ is the specific intensity of radiation at the optical depth τ; and $\mu = \cos\theta$, where θ is the zenith angle of the radiation stream with respect to the outward normal of the atmosphere. Also, $p(\mu,\phi;\mu',\phi')$ is the scattering phase function for the particular atmospheric constituent under consideration.

Following Coakley and Chylek (1975), (5-5) can be rewritten using the modified Schuster-Schwarzschild two-stream approximation

$$\frac{1}{2}\frac{dI_+}{d\tau} = I_+ - I_+\bar{\omega}_o(1 - \bar{\beta}) - I_-\bar{\omega}_o\bar{\beta} - \frac{S_o}{4}\exp(-\tau/\mu_o)\beta(\mu_o)$$

$$-\frac{1}{2}\frac{di_-}{d\tau} = I_- - I_-\bar{\omega}_o(1 - \bar{\beta}) - I_+\bar{\omega}_o\bar{\beta} - \frac{S_o}{4}\exp(-\tau/\mu_o)\beta(\mu_o) \qquad (5\text{-}6)$$

where I_+ and I_- are the average specific intensities in the upward and downward hemispheres, respectively, $\bar{\omega}_o$ is the single scattering albedo, and the factor 1/2 represents the average value of $\cos\theta$ over the hemisphere. The backscattered fraction is given by

$$\beta(\mu,\phi) = \frac{1}{4\pi\omega_o} \int_o^{2\pi} \int_{-1}^{1} p(\mu,\phi;\mu',\phi')\,d\mu'\,d\phi \qquad (5\text{-}7)$$

and

$$\bar{\beta} = \frac{1}{2\pi} \int_o^{2\pi} \int_{-1}^{1} \beta(\mu,\theta)\,d\mu\,d\phi \qquad (5\text{-}8)$$

From Acquista et al. (1981), Equations (5-7) and (5-8) can be written as a series expansion

$$\beta(\mu,\phi) = \beta(\mu) = \frac{1}{\omega_o}\sum_{\ell=1}^{\infty} \frac{h\,\bar{\omega}}{2\ell+1} P_\ell(|\mu|), \quad -1 < \mu < 1 \qquad (5\text{-}9)$$

279

where

$$h_o = 1/2,$$

$$h_{2\ell} = 0,$$

$$h_{2\ell+1} = (-1)^\ell (2\ell - 1/2) \frac{(2\ell-3)!!}{(2\ell)!!} \tag{5-10}$$

Also,

$$\overline{\beta} = \frac{1}{2} - \frac{1}{2\overline{\omega}_o} \sum_{\ell=1}^{\infty} \overline{\omega}_{2\ell+1} \left[\frac{(2\ell-3)!!}{(2\ell)!!} \right]^2 \tag{5-11}$$

where ω_ℓ are obtained by expanding the phase function in Legendre polynomials. These results in Equations 5-9 through 5-11 are similar to those obtained by Wiscombe and Grams (1976). The evaluation of $\beta(\mu)$ and $\overline{\beta}$ is discussed below.

The solution to the homogeneous part of Equation (5-6) for diffuse radiation, with the boundary conditions $I_-(0) = 1$ and $I_+(0) = 0$ (i.e., no surface reflection), is given by Sagan and Pollock (1967)

$$I_+(0) \equiv R = \frac{(\alpha+1)(\alpha-1)(e^t-e^{-t})}{(\alpha+1)^2 e^t - (\alpha-1)^2 e^{-t}}$$

$$I_-(\tau) \equiv T = \frac{4\alpha}{(\alpha+1)^2 e^t - (\alpha-1)^2 e^{-t}}$$

where

$$\alpha^2 = \frac{1 - \overline{\omega}_o + 2\beta\overline{\omega}_o}{1 - \omega_o}$$

$$t = 2\alpha(1 - \overline{\omega}_o)\tau$$

Energy conservation is expressed by

$$A = 1 - R - T$$

280

That is, the energy absorbed, A, in the layer is equal to the incident radiation, assumed to be 1, minus the part reflected by the layer, and transmitted through the layer.

For the arbitrary diffuse boundary conditions shown in Figure 207, D_0 is the diffuse flux illuminating the layer from above, and U_1 is the diffuse flux illuminating the layer from below. The solution is now given by

$$U_0 = RD_0 + TU_1$$

$$D_1 = RU_1 + TD_0$$

and the energy absorbed by the layer is given by

$$A = D_0 - D_1 + U_1 - U_0$$

or

$$A = (1-R-T)D_0 + (1-R-T)U_1$$
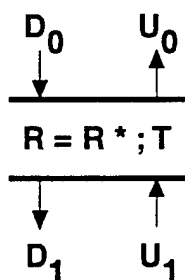
R-090-93.258

Figure 207. Arbitrary Layer Boundary Conditions for the Solution to the Homogeneous, Two-Stream Approximation to Equation (5-5). The diffusely reflected flux, πU_0, and transmitted flux, πD_1, in response to incident fluxes, πU_1 from below, and πD_0 from above. Here, R, R* are the diffuse reflectivities from above and below (equal to homogeneous layers), and T is the diffuse transmissivity, obtained from the solution for standard boundary conditions: $D_0 = 1$, and $U_1 = 0$.

281

This result is true for homogeneous layers, where the layer reflection and transmission functions for illumination from below (call them R* and T*) are equal to the reflection and transmission functions for illumination from above (R and T), as was discussed by Lacis and Hansen (1974).

5.2.2 Solar Beam Production of Diffuse Radiation

The particular solution to Equation (5-6) gives the addition to the diffuse streams by scattering from the solar beam. The complete solution to Equation (5-6) is

$$U_o = RD_o + TU_1 + U_s$$

$$D_a = RU_1 + TD_o + D_s$$

for the arbitrary boundary conditions D_o and U_1, with R and T defined as before. The upward and downward diffuse radiation scattered from the solar beam is given by

$$U_s = [\sigma(1 - T\exp(-\tau/\mu_o) + \delta R] \, \overline{\omega_o}\mu_o S_o/\gamma$$

$$D_s = [\sigma(T - \exp(-\tau/\mu_o) - \sigma R\exp(-\tau/\mu_o)] \, \overline{\omega_o}\mu_o S_o/\gamma \qquad (5\text{-}13)$$

where

$$\sigma = \beta(\mu_o) \, (1 - 2\mu_o) + 2 \, \mu_o\overline{\omega_o}(\beta(\mu_o) - \beta)$$

$$\delta = 1 - \beta(\mu_o) \, (1 + 2\mu_o) + 2\mu_o \, [(1-\overline{\omega_o}) + \overline{\omega_o}(\beta(\mu_o) - \beta)]$$

$$\gamma = 1 - 4\mu_o^2(1-\overline{\omega_o}) \, [(1-\overline{\omega_o}) + 2\overline{\omega_o}\beta)]$$

The energy absorbed in the layer is given by

$$A = \mu_o S_o(1 - \text{epx}(-\tau/\mu_o)) + D_o - D_1 + U_1 - D_o$$

or

$$A = \mu_o S_o(1 - \exp(-\tau/\mu_o)) - (U_s + D_s) + D_o \, (1-R-T) + U_1(1-R-T)$$

For conservative scattering, $\overline{\omega_o} = 1$, Coakley and Chylek (1975) have shown

$$R = 2\beta\overline{\tau}/(1+2\beta\overline{\tau})$$

$$T = 1/(1+2\beta\overline{\tau})$$

so that R + T = 1, and from Equation (5-13)

$$U_s + D_s = (1 - \exp(-\tau/\mu_o))\mu_o S_o$$

Thus, A = 0 and energy is conserved.

5.2.3 Multiple Layer Calculations

The next step in the solution of the radiative transfer Equation (5-5) is to specify a procedure for combining the reflection and transmission functions for a number of layers. The layer structure chosen for this model atmosphere suggests the definition of a three layer combination, as shown in Figure 208.
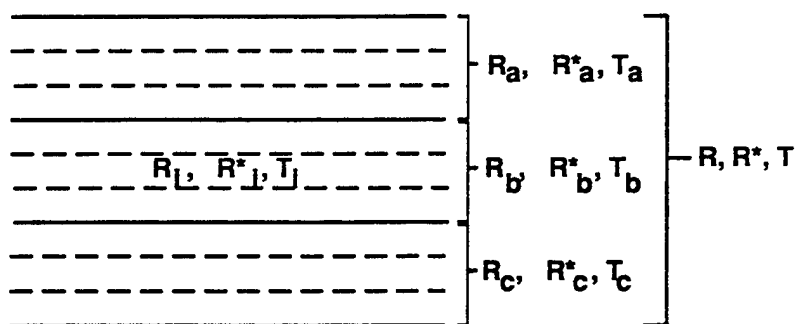
Figure 208. Layer Structure for the Recursive Adding Technique. The R's and T's for each sublayer are added to obtain the R's and T's for each major layer, which, in turn, are added to obtain the reflection and transmission of the atmosphere as a whole.

The solution to the two-stream model given by Equation (5-12) applied to each of the three layers in Figure 209 yields a set of six coupled algebraic equations

$$U_o = D_o R_1 + U_1 T_1 + U_{1s}$$

$$D_1 = D_o T_1 + U_1 R_1^* + D_{1s}$$

$$U_1 = D_1 R_2 + U_2 T_2 + U_{2s}$$

$$D_2 = D_1 T_2 + U_2 R_s^{\cdot} + D_{2s}$$

$$U_2 = D_2 R_3 + U_3 T_3 + U_{3s}$$

$$D_3 = D_2 T_3 + U_3 R_3^{\cdot} + D_{3s}$$

where U_{is} and D_{is} is the solar production of diffuse radiation in each layer from Equation (5-13). Here, $R_i^{\cdot}$ represents the diffuse reflectivity for illumination from below which is included for generality, but $R_i^{\cdot} = R_i$ for homogeneous layers.
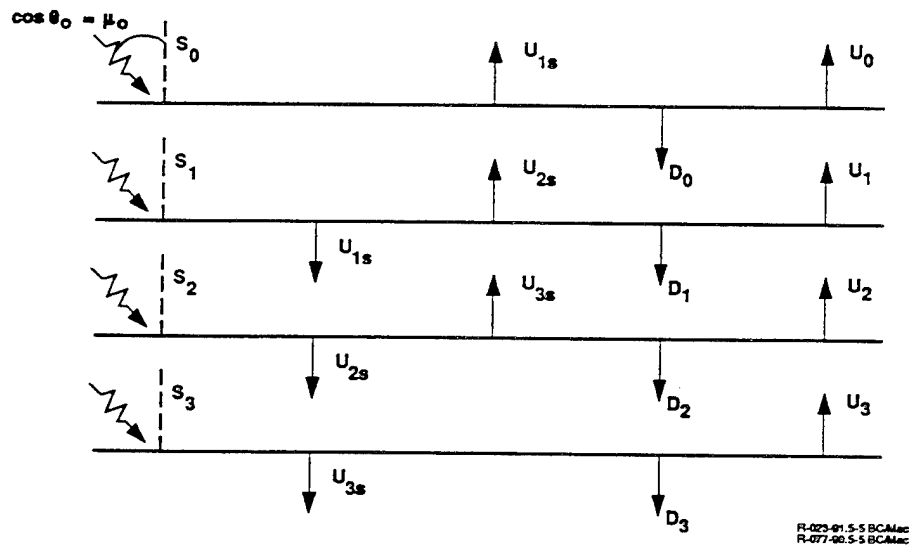
Figure 209. Specification of the Diffuse Streams and Solar Production of Diffuse Streams Used in the Three-Layer Addition Scheme.

The solution to Equation (5-14) is given by

$$U_o = D_o R_a + U_3 T_a + U_{as}$$

$$D_3 = D_o T_a + U_3 R_a + D_{as}$$

where

$$R_a = R_1(1-R_2^{\cdot}R_3)/\gamma_a + R_2(T_1^2-R_1^{\cdot}R_1)/\gamma_a + R_3(T_1^2-R_1^{\cdot}R_1)\ (T_2^2 R_2^{\cdot}R_2)/\gamma_a$$

$$R_a^{\cdot} = R_3(1-R_1^{\cdot}R_2)/\gamma_a + R_2(T_3^2-R_3^{\cdot}R_3)/\gamma_a + R_1(T_3^2-R_3^{\cdot}R_3)\ (T_2^2 R_2^{\cdot}R_2)/\gamma_a$$

$$T_a = T_1 T_2 T_3/\gamma_a$$

284

and

$$\gamma_a = (1 - R_1^* R_2)(1 - R_2^* R_3) - R_1^* R_3 T_2^2$$

It should be noted that the algebraic solution to Equation (5-14) implicitly includes the effects of multiple reflections between layers, and is represented by the term γ_a.

The diffuse radiation produced in the composite layer from the solar beam is given by

$$D_{as} = D_{1s} \frac{T_2 T_3}{\gamma_A} + U_{3s} \frac{T_3}{\gamma_A} (R_2^* + R_1^* (T_2^2 - R_2^* R_2))$$

$$+ D2s \frac{T_3}{\gamma_A} (1 R_1^* R_2) + U_{2s} R_1^* \frac{T_2 T_3}{\gamma_A} + D3s \tag{5-15}$$

and

$$U_{as} = D_{1s} \frac{T_1}{\gamma_A} (R_2 + R_3 (T_2^2 - R_2^* R_2)) + U_{3s} \frac{T_1 T_2}{\gamma_A}$$

$$+ D2s \frac{R_3 T_1 T_2}{\gamma_A} + U_{2s} T_1 \frac{(1 R_2^* R_3)}{\gamma_A} + U1s \tag{5-16}$$

This procedure is applied to each of the lower two composite layers, producing R_b, R_b^*, T_b, R_c, R_c^*, T_c, and then to the atmosphere as a whole giving

$$U_o = D_o R + U_9 T + U_{Ts}$$

$$D_9 = D_o T + U_9 R^* + D_{Ts}$$

where for the atmosphere as a whole, $D_o = 0$, and

$$U_9 = \alpha_g (D_9 + S_9)$$

285

Here, α_g represents the surface albedo, assumed to be Lambertian; and S_g is the depleted solar beam at the bottom of the atmosphere. Then,

$$D_g = \frac{R^*\alpha_g S_g + T_{Ts}}{1 - \alpha_g R^*}$$

(5-17)

and

$$U_o = \frac{T\alpha_g(D_{Ts} + S_g)}{1 - \alpha_g R^*} + U_{Ts}$$

The factor $(1-\alpha_g R^*)_{-1}$ represents the effect of multiple reflections between the surface and the atmosphere as a whole.

Solar radiation is handled as separate diffuse streams produced in each homogeneous layer, where D_{Ts} and U_{Ts} are obtained by applying Equation (5-15) and Equation (5-16) recursively to the composite layers and then to the homogeneous layers.

In order to evaluate the fluxes at each layer boundary, the net upward and downward diffuse fluxes within the composite layer must also be evaluated. These are given by

$$U_1 = \frac{[R_2 + R_3(T_2^2 - R_2^* R_2)]}{\gamma}(D_o T_1 + D_{1s})$$

$$+ \frac{T_2}{\gamma}(U_3 T_3 + U_{3s} + D_{3s} R_3) + U_{2s}\frac{(1 - F^* R_3)}{\gamma}$$

$$D_1 = \frac{(1 - R_2^* R_3)}{\gamma}(D_o T_1 + D_{1s} + U_{2s} + R_1^*) + \frac{R_1^* T_2}{\gamma}(U_3 T_3 + U_{3s} + R_3 D_{2s})$$

at the upper internal layer boundary, and

$$U_2 = \frac{R_3 T_2}{\gamma} (D_o T_1 + D_{1s} + U_{2s} + R_1^*) + \frac{(1 - R_1^* R_2)}{\gamma} (U_3 T_3 + U_{3s} + D_{2s} R_3)$$

$$D_2 = \frac{[R_2^* + R_1^* (T_2^{*2} - R_2^{*R_2})]}{\gamma} U_3 T_3 U_{3s} \frac{T_2}{\gamma} (D_o T_1 + D_{1s} + U_{2s} + R_1^*) + D_{2s} \frac{(1 - R_1^* R_2)}{\gamma}$$

at the lower internal layer boundary. Here, U_{is}, D_{is} represents the solar-produced diffuse at the ith layer boundary; R_i, R_i^*, and T_i are the layer two-stream diffuse reflection (from above and below) and transmission functions; γ is the factor that accounts for multiple reflections between layers; and D_o and U_3 are the downward and upward diffuse fluxes that are incident on the three-layer composite. These equations are also applied recursively to compute the fluxes at all layer boundaries.

The energy absorbed by the surface is obtained from Equation (5-17) by

$$A_{scf} = (1 - \alpha_g) \left[\frac{[\alpha_g R^* S_9 + D_{ts}]}{1 - \alpha_g R^*} + S_9 \right]$$

and the energy absorbed by the atmosphere as a whole is given by

$$A_T = S_o - S_9 + U_9 - U_o + D_o - D_9$$

Thus, the atmospheric absorption can be obtained for each composite and homogeneous layer by applying this equation, with the appropriate subscripts, for the radiation streams.

5.2.4 Specification of the Layer Parameters

The final step in the solution of the shortwave radiative transfer problem involves the specification of the parameters $\bar{\omega_o}$, $\bar{\beta}$, $\beta(\mu_o)$, and τ for each homogeneous layer. The optical depth, τ, for a layer is given by

$$\tau = \tau_r + \tau_c + \tau_a$$

where τ_r is the optical depth for Rayleigh scattering, τ_c is the optical depth for cloud and aerosol particle scattering, and τ_a is the optical depth for absorption. Then, the single scattering albedo is given by

$$\overline{\omega_o} = (\tau_r + \tau_c)/\tau$$

In this model, τ_o is assumed to be constant over the entire solar band (τ_c varies very little over wavelength (Twomey, 1976)), while τ_a and τ_r are wavelength dependent.

The solar band model divides the solar spectrum into three bands in the absorption regions of ozone, molecular oxygen, and water vapor with effective wavelengths of 0.5, 0.7, and 1.44 µm, respectively. The fraction of the total solar flux and the physical mechanisms assumed to be significant in each band are summarized by Table 72. Also shown in the table for comparison is the more detailed band model of Liou and Wittman (1979).

Rayleigh scattering is determined for the effective wavelength for each of the three bands shown in Table 72. The Rayleigh scattering coefficient for air is given by

$$s_\lambda = \frac{32\pi^3(n-1)^2\rho}{3_\lambda{}^4 N\rho_o}$$

where n_λ is the index of refraction at wavelength λ, N the number of molecules per cubic centimeter at STP, and ρ, ρ_o are the actual and STP densities of dry air. Johnson (1954, p. 48) gives sea level values for the constants

$$(n_\lambda-1)^2 = 293^2 \times 10^{-12}$$

$$N = 2.66 \times 10^{19} \text{ cm}^{-3}$$

The optical path for Rayleigh scattering is given by

$$d\tau(Z_1,Z_2) = \int_{Z_1}^{Z_2} S_\lambda dZ = \frac{32\pi^3(n_\lambda-1)^2}{3_\lambda{}^4 N\rho_o g} \int_{Z_1}^{Z_2} q(p)dp$$

where q(p) = 1000 is the "specific humidity" (g/kg) of air with respect to air. This path length is computed in the same routine that computes the absorber paths for the longwave model. The backscattering fraction for the Rayleigh phase function is simply

$$\beta(\mu) = \overline{\beta} = 0.5$$

Table 72. Three Band Model.

Band (μm)	Absorber	Fraction of Solar Flux	Fraction of Solar Flux	Effective Wavelength	Physical Mechanism
0.30	O_3	0.0872	0.3586	0.500	R,M,A
0.50	O_3	0.2696			
0.70	O_2	0.2034	0.2034	0.700	R,M
0.94	H_2O	0.1347			
1.10	H_2O	0.0892			
1.38	H_2O	0.1021	0.4397	1.437	R,M,A
1.87	H_2O	0.622			
2.70	H_2O	0.0300			
3.20	H_2O	0.0216			

R = Rayleigh scattering

M = Mie scattering (clouds and aerosols)

A = Absorption

The optical path for Mie scattering in the cloud layers is specified as a function of liquid water content (LWC) and cloud thickness. This function was parameterized by Stephens (1978b) based upon a set of calculations using data from a large number of "standard" cloud types. For conservative scattering, the optical depth is given by

$$\log_{10}(\tau) = 0.2633 + 1.7095 \log_e(\log_{10}(W))$$

where W is given by the product of the liquid water content and cloud thickness

$$W = LWC \times \Delta Z \ (g/m^2)$$

The phase function for cloud particles is approximated by the Heyney-Greenstein phase function. The use of the Heyney-Greenstein phase function for water droplets is well accepted and has been discussed by a number of authors (c.f., Wiscombe and Grams, 1975; Coakley and Chylek, 1975). The use of the Heyney-Greenstein phase function for non-spherical ice and aerosol particles is not as well justified, but is assumed for simplicity. Thus, in Equations (5-9) and (5-10), $\bar{\omega} = 2(2\ell+1)g^{\ell}$, and the backscattering fraction is specified by one parameter, g. The values of LWC and g for low, mid and high clouds (obtained from Stephens, 1978a) are shown in Table 73.

Table 73. Shortwave Parameters for Clouds.

Cloud Type	LWC (g/m^3)	g
Low Cloud	2.0	0.88
Mid Cloud	0.5	0.60
High Cloud	0.1	0.90

Absorption from the solar beam and diffuse streams is calculated for the water vapor bands using the exponential sum fitting technique described by Wiscombe and Evans (1977). The Solar Band Model used the fit obtained by Lacis and Hansen (1974) and is shown in Table 74. Then,

$$\tau_j(Z_1,Z_2) = k_j\Delta u(Z_1,Z_2) + \tau_s$$

where τ_s is the Rayleigh and Mie scattering optical path, and $\Delta u(Z_1,Z_2)$ is the water vapor path as computed in Section 5.1. Then,

$$\bar{\omega}_{oj} = \tau_s/\tau_j$$

is the single scattering albedo for the band k_j. The solution to the transfer equation for the water vapor bands is then obtained by summing the solutions associated with the fractional solar flux given by

$$S_j = S_o \times 0.4937 \times P(k_j)$$

Table 74. Exponential Fit for Water Vapor Absorption.

j	k_j	$P(k_j)$
1	4E-5	0.6470
2	0.002	0.0968
3	0.035	0.1443
4	0.377	0.0584
5	1.950	0.0335
6	9.800	0.0225
7	44.600	0.0158
8	190.000	0.0087

where $P(k_j)$ is the fraction of the band associated with the band parameter kj obtained from the exponential fitting technique.

Ozone absorption is approximated by depleting the solar beam in the stratospheric layers. The parameterization for ozone absorption is taken from Lacis and Hansen (1974), where

$$A_{oz}(x) = 0.02118x/(1 + 0.042x + 0.000323x^2) + 1.082/(1 + 138.6x)^{0.805}$$

$$+ 0.0658x/(1 + (103.6x)^3)$$

and, for the jth layer

$$x = (M/1.66)w(j-1,j)$$

Here, w(j-1,j) is the ozone amount for the jth layer as computed for the Terrestrial Band Model (see Section 5.1), and M is a magnification factor that accounts for slant path and refraction of the solar beam,

$$M = 35/(1224 \mu_o^2 + 1)^{0.5}$$

291

The divisor of 1.66 is used because the longwave paths were multiplied by that factor, accounting for the path length of diffuse radiation.

5.3 Surface Temperature Calculations

The primary purpose of the broad-based model is to compute the equilibrium surface temperature, by material type, for the materials that comprise the background scene. This calculation requires data from the Material Thermal Properties Data Base which is described in Section 2.4.

A heat balance computation is not required for all materials. The temperature of water is a user-specified input. Forest, tropical vegetation and trees assume ambient air temperature. Ice and snow assume the smaller of ambient air temperature and 273.15 K.

For all other materials, surface temperature is determined by the energy fluxes and thermal properties of the surface. The fluxes considered in the model are those resulting from solar irradiance, sky irradiance, convection to the air, self-emitted radiation, latent heat flux due to evaporation of surface moisture, and the distributed flux through the material to a substrate. The heat balance solution of the dynamic surface temperature employs two simplifying assumptions. These are that the lateral heat flux at the surface is zero, and that the distributed heat flux to the substrate can be calculated using n discrete layers, the lowest of which is adjacent to a diurnally constant subsurface. The resultant physical model and its equivalent electrical circuit are given in Figure 210.

The heat balance equation for the physical model is

$$\phi_{sun} + \phi_{sky} + \phi_{stored} = \phi_{conv} + \phi_{evap} + \phi_{emit} + \phi_{cond}$$

All fluxes are in units of W/m^2 and all vary with time. Each of these fluxes is expressed as follows.

The solar irradiance flux, ϕ_{sun}, is calculated by

$$\phi_{sun} = \alpha(s)E(sun,t)\cos\zeta(t)$$

where

$\alpha(s)$ is the effective solar absorptance,

$\zeta(t)$ is the time dependent angle between the vector to the sun and the surface normal vector, and

$E(sun,t)$ is the time dependent solar irradiance at the surface
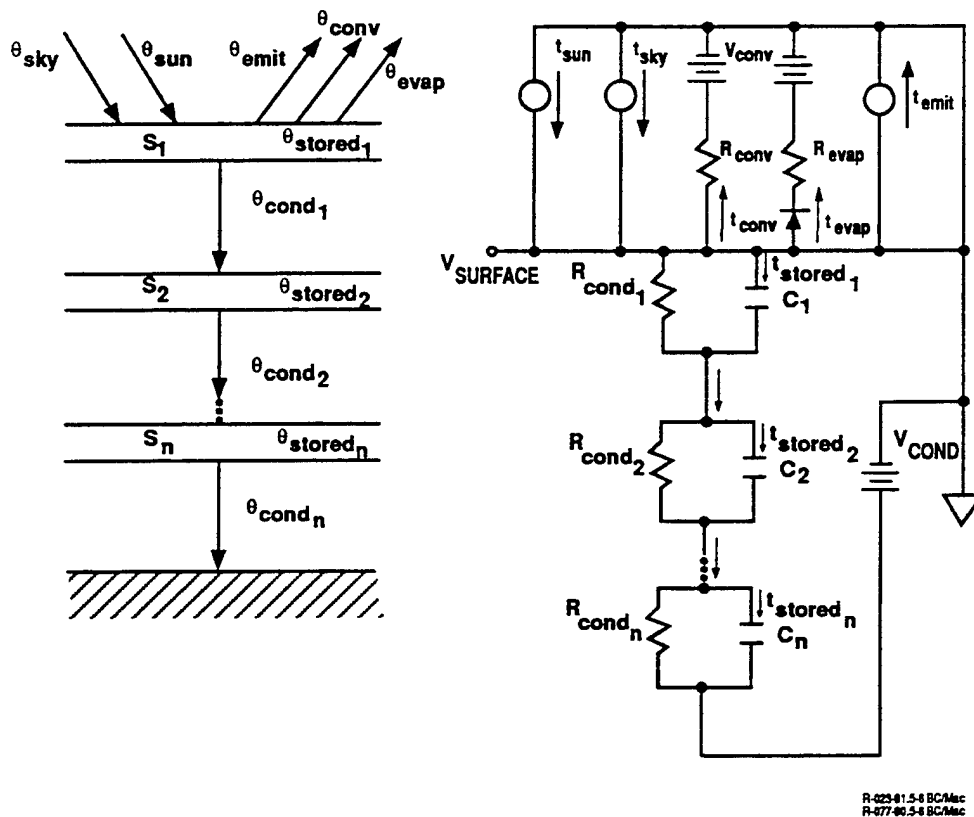
a) Physical Model b) Equivalent Electrical Circuit

FLUX DEFINITION

ϕ_{sun} = solar irradiance ϕ_{evap} = surface evaporation

ϕ_{sky} = sky irradiance ϕ_{stored} = layer stored

ϕ_{emit} = emission ϕ_{conv} = air convection

  ϕ_{cond} = substrate conduction

Figure 210. Surface Temperature Heat Balance Model.

293

The solar irradiance at the surface is given by

$$E(sun,t) = E_{\psi_o}(sun,h)*f(\psi(t))$$

where E_{ψ_o} is the zenith solar irradiance as a function of surface altitude, h, and $f(\psi(t))$ is a factor to correct for increasing atmospheric attenuation with increasing solar zenith angle ψ.

The sky irradiance flux, ϕ_{sky}, is computed in the broad based solar and terrestrial models (see Sections 5.1 and 5.2).

The free and forced convective flux to the atmosphere is computed by

$$\phi_{conv} = \left[1.7 \ |T - T_a|^{0.33} + 0.0296 \ (\rho W)^{0.8} \left(\frac{\mu}{C_L} \right)^{0.2} C_p \right] (T - T_a)$$

where

ρ is the ambient air density,
C_p is the specific heat of dry air,
W   is the wind speed (m/sec),
T   is the surface temperature,
μ is a temperature-dependent viscosity of air, and
C_L is the characteristic length, determined empirically from ground truth data.

The latent flux is computed by

$$\phi_{evap} = \phi_{conv} * \left[1 + \frac{V_s - V_a}{(T - T_a) \ P_a C_p} - e \ \frac{Q_s - Q_a}{C_p(T - T_a)} \right]$$

where

e   is the latent heat of evaporation,
V_s is the saturational vapor partial pressure,
V_a is the partial vapor pressure of the air,
Q_s is the saturation-specific humidity
Q_a is the specific humidity of air
P_a is the atmospheric pressure.

This latest flux is obtained using the Penman equation.

The emitted flux is computed by

$$\phi_{emit} = \epsilon(L)\ \sigma\ T^4$$

where $\epsilon(L)$ is the effective thermal emittance, set equal to $\alpha(L)$ by Kirchoff's Law.

The conductance flux to the substrate is computed by

$$\phi_{cond} = g\ (T - T_s)$$

where g is the conductance to the substrate, equal to ℓ_s*K where ℓ_s is the depth at which the soil is diurnally constant and K is the soil conductivity, and T_s is the substrate temperature.

The stored flux in the surface layer is computed by

$$\phi_{stored} = \ell_o C\ [T(t+\Delta t) - T(t)]/\Delta t$$

where

    ℓ_o is the layer thickness
    C is the heat capacity of the surface material, and
    Δt is the time increment

The quality ℓ_o*C*material density is called the thermal mass and is stored in the material thermal properties data base.

The solution for the surface temperature T is achieved using an iterative method wherein the surface temperature is initially chosen with an internal data base, and the heat balance equation is iteratively evaluated in time increments Δt (usually set equal to 15 or 30 minutes). This iteration is continued until successive diurnal cycles match, commonly occurring within three days.

6.0 BACKGROUND RADIANCE ALGORITHMS

The background module provides the scene statistics, (i.e., the probability density function (PDF) and power spectral density (PSD)) for the background scene selected for simulation. The approach is a statistical one where the background scenes have been reduced to a few statistical parameters from which the PDF and PSD are generated.

The statistical parameters and definitions used in the algorithms are described in Section 6.1. The PDF and PSD algorithms are discussed in Sections 6.2 and 6.3, respectively. Validation of the algorithms is presented in Section 6.4.

6.1 Parameters Used to Describe Background Scenes

The background scene consists of 22 reference scene materials. Depending on the solar elevation angle, cloud cover, and surface altitude fluctuations, the reference scene materials may be partially or totally in shadow. The shadowed and unshadowed portions of the same reference scene material are treated as separate materials. For convenience all background scene components will be referred to as materials.

Background scene material parameters include the fraction of a material present in the background scene, the mean material radiance and material radiance clutter parameters. Non-material specific parameters also used to generate the background scene PDF and PSD are the reference scene surface roughness parameters from which the scene shadowed fraction is calculated.

In all cases, the PDF of each material is assumed to be Gaussian. For the ith material

$$F_i(J) = \frac{1}{\sqrt{2\pi\sigma_i^2}} e^{-(J - \mu_i)^2/2\sigma_i^2}$$

$$(6-1)$$

where J is radiance, and μ_i and σ_i are the mean radiance and the standard deviation of the radiance for the ith material, respectively. The probability that the radiance of the ith material lies in the range $J_1 \leq J \leq J_2$ is

$$P_i\{J_1 \leq J \leq J_2\} = \int_{J_1}^{J_2} F_i(J)\,DJ \qquad (6\text{-}2)$$

provided the PDF is normalized so that

$$\int_{-\infty}^{\infty} F_i(J)\,dJ = 1 \qquad (6\text{-}3)$$

The PDF of the background scene is a linear combination of the material PDF's. PDF generation is described in Section 6.2.

The background scene PSD (discussed in Section 6.3) is constructed from a linear combination of material PSD's. Each material PSD may have one of two function forms:

$$P_i(k) = \begin{cases} A_i/\left[(k_i^2 + k^2)^{\alpha_i/2}\right] & \text{Power law} \\[2mm] A_i e^{-k^2/k^2_i} & \text{Gaussian} \end{cases} \qquad (6\text{-}4)$$

where k is the spatial frequency in radiance/meter. The PSD is normalized using the material standard deviation σ_i from the relation

$$\sigma_i^2 = \frac{1}{2\pi} \int_{-\infty}^{\infty} P_i(k)\,dk \qquad (6\text{-}5)$$

297

Inserting the expressions in Equation (6-4) into Equation (6-5) gives the relations

$$A_i = \begin{cases} 2\sqrt{\pi} \; \sigma_i^2 \; k_i^{\alpha_i - 1} \Gamma(\alpha_i/2)/\Gamma\left(\dfrac{\alpha_i - 1}{2}\right) & , \; \alpha_i > 1 \quad \text{Power law} \\ \\ 2\sqrt{\pi}\sigma_i^2 \; k_i & \text{Gaussian} \end{cases} \tag{6-6}$$

The Fourier transform of the PSD is the autocorrelation function

$$R_i(x) = \frac{1}{2\pi} \int\limits_{-\infty}^{\infty} P_i(k)e^{ikx}dk \tag{6-7}$$

Substituting Equations (6-4) and (6-6) into Equation (6-7) gives

$$R_i(x) = \begin{cases} \sigma_i^2 \; \dfrac{2}{\Gamma\left(\dfrac{\alpha_i - 1}{2}\right)} \left(\dfrac{k_i x}{2}\right)^{\frac{\alpha_i - 1}{2}} \dfrac{K\alpha_i - 1}{2} (k_k x) \; , \; \alpha_i > 1 \quad \text{Power law} \\ \\ \sigma_i^2 \; e^{-k_i x^2/4} & \text{Gaussian} \end{cases} \tag{6-8}$$

The material correlation length S_i is defined as the e^{-1} width of the autocorrelation function, i.e., $R_i(S_i) = e^{-1}\sigma_i^2$ because $R_i(0) = \sigma_i^2$. In the case of the Gaussian, the PSD scale k_i is related to the correlation length S_i by

$$k_i = 2/S_i \tag{6-9}$$

For a power law the exact form of this relation depends on the power law index α_i; however, Equation (6-9) is still approximately true. (For example, for $\alpha_i = 3$, $R_i(2/k_i) = 0.28$.

298

Calculation of the parameters, S_i and k_i and verification of the algorithm requires computation of the one-dimension PSD from digital GENESSIS reference scenes. The PSD of an M point sequence is computed using a discrete Fourier transform (DFT)

$$G_k = \sum_{n=0}^{M-1} g_n e^{-j2\pi nk/M} \tag{6-10}$$

which is evaluated using the Fast Fourier Transform (FFT) algorithm (Cooley and Tukey, 1965). For a single M point sequence the PSD estimate is

$$P_k = \frac{\Delta x}{M} |G_k|^2 \tag{6-11}$$

where Δx is the spacing between samples. For an M x M point reference scene the PSD is calculated for the M^2 rows and columns and averaged. The discrete autocorrelation function is computed from the DFT of the PSD

$$R_n = \frac{1}{M} \sum_{k=0}^{M-1} P_k e^{j2\pi nk/M} \tag{6-12}$$

The reference scene roughness PSD is analogous to the material radiance PSD although one parameter set applies to the entire reference scene. The PSD of surface altitude may be either power law or Gaussian with normalization provided by the standard deviation of altitude σ_a, an altitude correlation length S_a, and, in the case of a power law spectrum, an index α_a.

6.2 Calculating the Background Radiance Histogram

The background scene consists of N materials with mean radiance μ_i and standard deviation σ_i for material i. The material radiances consist of the sum of the thermal radiation calculated from the material temperature and emissivity, reflected skyshine and reflected solar/lunar radiation (when the sun/moon is above the horizon) all multiplied by the atmospheric transmission. To this is added the atmospheric path radiance. The material standard deviations are assumed to be proportional to the mean radiances. The constants of proportionality are derived from GENESSIS scenes.

The background scene PDF is computed by summing the N material PDF's each weighted by the material fraction f_i,

$$F(J) = \sum_{i=1}^{N} f_i \frac{e^{-(J - \mu_i)^2/2\sigma_i^2}}{\sqrt{2\pi\sigma_i^2}}$$

(6-13)

Because the material fractions sum to one, F(J) has the proper normalization,

$$\int_{-\infty}^{\infty} F(J) = 1$$

The mean radiance of the background scene is the first moment of the PDF

$$\overline{J} = \int_{-\infty}^{\infty} JF(J)dJ = \sum_{i=1}^{N} f_i\mu_i$$

(6-14)

and is the sum of the mean material radiances weighted by the material fractions as expected. The total background scene radiance variance

$$\alpha^2 = \int_{-\infty}^{\infty} (J - \overline{J})^2 F(J)dJ = \sum_{i=1}^{N} f_i\mu_i^2 - \left(\sum_{i=1}^{N} f_i\mu_i\right)^2 + \sum_{i=1}^{N} f_i\sigma_i^2$$

(6-15)

has two components; a component due to the differences in mean radiance between materials

$$\sigma_1^2 = \sum_{i=1}^{N} f_i\mu_i^2 - \left(\sum_{i=1}^{N} f_i\mu_i\right)^2$$

(6-16)

and a component due to the intrinsic material variance

$$\sigma_2^2 = \sum_{i=1}^{N} f_i\sigma_i^2$$

(6-17)

In practice the PDF is approximated by a radiance probability histogram. The minimum (maximum) radiance in the histogram J_{min} (J_{max}) is the smallest (largest)

300

material mean radiance minus (plus) twice the standard deviation for that material. The histogram bin width ΔJ is then determined by J_{min}, J_{max} and the number of bins in the histogram. If a bin is bounded by radiances J_1 and J_2 then the value of the histogram at that bin is the integral over the PDF from J_1 to J_2, which yields

$$F(J_1 \leq J \leq J_2) = \sum_{i=1}^{N} f_i \frac{\text{erf}\left(\dfrac{J_2 - \mu_i}{\sqrt{2\sigma_i^2}}\right) - \text{erf}\left(\dfrac{J_1 - \mu_i}{\sqrt{2\sigma_i^2}}\right)}{2} \qquad (6\text{-}18)$$

6.3 Algorithms for Constructing Background Power Spectral Densities

The algorithm for estimation of the background scene PSD is based on the observation that, in general, the major contribution to the background clutter in the GENESSIS scenes comes from the steps in radiance due to the difference between mean material radiances, rather than the intrinsic material radiance variances. That is, from Equations (6-16) and (6-17), $\sigma_1^2 \gg \sigma_2^2$. Therefore, if the pixels of a particular scene are set equal to the main radiances of the associated materials, the PSD calculated from this scene is approximately the same as the original. This comparison is shown in Figure 211 for four GENESSIS reference scenes with solar elevation angles near 90°. The agreement is good for three of the scenes. The fourth, Brooks Range, is mountainous. The large surface roughness results in high intrinsic material variances so that $\sigma_1^2 \ll \sigma_2^2$; however, the shape of the PSD is approximately the same in both cases. The surface roughness contribution to the PSD is largest just after dawn when a significant fraction of the scene is in shadow. However for most scenes, most of the time, the background radiance PSD is driven by the spatial character of the material distributions in the scene, rather than by structure within regions of the same material due to surface roughness. This is the starting point of the PSD algorithm.

An analytic approach to modeling the one-dimensional background radiance PSD was derived by decomposing each one-dimensional cut through the scene $J(x_n)$ into a sum over the contributions from the N materials present

$$J(x_n) = \sum_{i=1}^{N} J_i(x_n) \qquad (6\text{-}19)$$
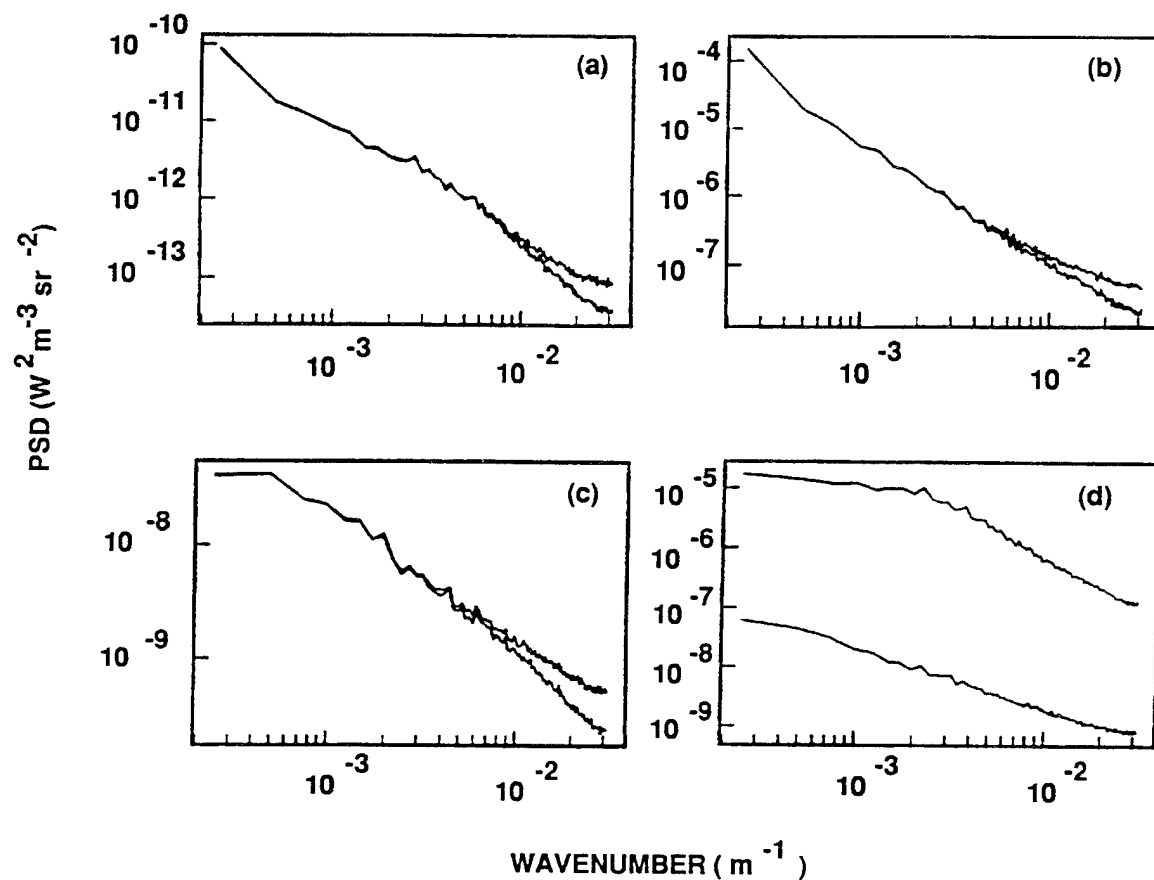
Figure 211. Comparison of PSD Computed from GENESSIS Reference Scene with PSD Computed from the Same Reference Scene with Radiances Replaced by Mean Material Radiances for a) Fulda, Germany; b) Salton Sea, California, c) Point Barrow, Alaska; and d) Brooks Range, Alaska.

302

where

$$J_i(x_n) = \begin{cases} 0 & \text{if pixel at } x_n \text{ is not material } i \\ \mu_i & \text{if pixel at } x_n \text{ is material } i \end{cases} \qquad (6\text{-}20)$$

The probability that $J_i(x_n)$ makes a transition from 0 to μ_i is

$$U_i = P\{J_i(x_{n-1}) = 0, J_i(x_n) = \mu_i\} \qquad (6\text{-}21)$$

and the probability that $J_i(x_n)$ makes a transition from μ_i to 0 is

$$D_i = P\{J_i(x_{n-1}) = \mu_i, J_i(x_n) = 0\} \qquad (6\text{-}22)$$

Therefore each $J_i(x_n)$ is a random signal which is either "on" ($J_i = \mu_i$) or "off" ($J_i = 0$). It can be shown that the PSD for one of these random signals is

$$P_i(k) = 2\mu_i^2 f_i(1 - f_i) \frac{k_i}{k_i^2 + k^2} \qquad (6\text{-}23)$$

where

$$k_i = \frac{U_i + D_i}{\Delta x} \qquad (6\text{-}24)$$

and Δx is the spacing between pixels. The relation between f_i, U_i, and D_i is

$$f_i = \frac{U_i}{U_i + D_i} \qquad (6\text{-}25)$$

For a three-material scene (N = 3), it can be shown that the PSD is (ignoring the term at k = 0),

$$P(k) = 2 \left(\mu_1^2 - \mu_1\mu_2 - \mu\mu_3 + \mu_2\mu_3 \right) f_1 (1 - f_1) \frac{k_1}{k_1^2 + k^2}$$

$$+ 2 \left(\mu_2^2 - \mu_1\mu_2 + \mu_1\mu_3 - \mu_2\mu_3 \right) f_2 (1 - f_2) \frac{k_2}{k_2^2 + k^2}$$

(6-26)

$$+ 2 \left(\mu_3^2 + \mu_1\mu_2 - \mu_1\mu_3 - \mu_2\mu_3 \right) f_3 (1 - f_3) \frac{k_3}{k_3^2 + k^2}$$

The model PSD is then a combination of components with the same scales as the individual material distributions. This statistically derived model gives good agreement with some of the GENESSIS reference scenes and poor agreement with others. The agreement is poor when the transition probabilities U_i and D_i are not constant throughout a reference scene. (For the tests the U_i and D_i were calculated from an average over the scene.)

An empirical modification of the result in Equation (6-26) was used to model the PSD. It was assumed that the scene PSD was a sum over the material components with scales derived from the material distribution as in the analytic model, but the power law indices were allowed to be values other than two. Each component is weighted by its contribution to the total scene variance, thus

$$P(k) = \sum_{i=1}^{N} \frac{A_i}{\left(k_i^2 + k^2 \right)^{\alpha_i/2}}$$

(6-27)

where from Equation (6-6)

$$A_i = \frac{f_i \left[\left(\overline{J} - \mu_i \right)^2 + \sigma_i^2 \right] k_i^{\frac{\alpha_i}{2} - 1}}{\sqrt{\pi}} \frac{\Gamma\left(\dfrac{\alpha_i}{2} \right)}{\Gamma\left(\dfrac{\alpha_i - 1}{2} \right)} , \quad \alpha_i > 1$$

(6-28)

The total scene variance

$$\sigma^2 = \sum_{i=1}^{N} f_i \left[\left(\overline{J} - \mu_i \right)^2 + \sigma_i^2 \right] \tag{6-29}$$

is equivalent to Equation (6-15). The power law indices α_i and the scales $k_i = 2/s_i$ are determined empirically. The correlation lengths S_i for the reference scene materials were calculated for the GENESSIS scenes by replacing all pixels except those representing material I to zero, calculating the autocorrelation function (Equation 6-12) and setting S_i equal to the e^{-1} width of the autocorrelation function. In most cases a value of $\alpha_i = 1.8$ gave good agreement with the computed GENESSIS scene PSD, although in some cases values as low as 1.2 were used.

Estimation of default values of k_i and α_i for the cloud layers was performed assuming the clouds in each layer were localized in one mass. That is, for any one-dimensional cut of length L through the background scene, the cloud contribution to the radiance in Equation (6-19) was equal to the mean cloud radiance for a continuous section of length equal to the cloud layer material fraction times L, and equal to zero everywhere else. The scale size was then equal to $fL(1 - e^{-1})$. The spectral shape was assumed to be a power law with index two. In the downlooking case when clouds obscure a fraction of the reference scene, the reference scene material values of S_i and α_i were assumed unchanged.

6.4 Validation of Algorithms

The background radiance algorithms were validated by comparing the PDF and PSD computed from the ten GENESSIS scenes, the open ocean scene and the sea-ice scene with those computed from the model described in Sections 6.1 through 6.3. Since the statistical parameters used in the model were derived from the same reference scenes with which they are being compared, a certain degree of agreement would not be surprising. However, these comparisons do test the validity of the functional forms used to model the PDF and PSD, and also test the universality of the material standard deviations σ_i which were derived by averaging over the GENESSIS reference scenes in two wavebands. Further validation tests are required.

The PDF and PSD comparisons for the 12 reference scenes in various bands for near noon conditions are shown in Figures 212 through 223. The top graph in each figure contains the one-dimensional model PSD for the scene (the smooth curve) overplotted by the PSD computed directly from the scene by applying an FFT to the rows and columns (Equations 6-10 and 6-11). The lower graph contains the

305

model PDF for the scene (plotted inverted) compared with the radiance histogram computed directly from the scene radiance. The agreement is adequate in all cases.

Comparison of the PSD and the PDF for a range of solar elevation angles and comparisons for scenes containing clouds should be performed in the future. The PDF algorithm should be quite robust with respect to the angle of solar illumination. The PSD algorithm should also be robust except, possibly, when there is significant shadowing. In this case the correlation lengths derived from the material distributions may not be accurate although the model will still get the correct total radiance variance.
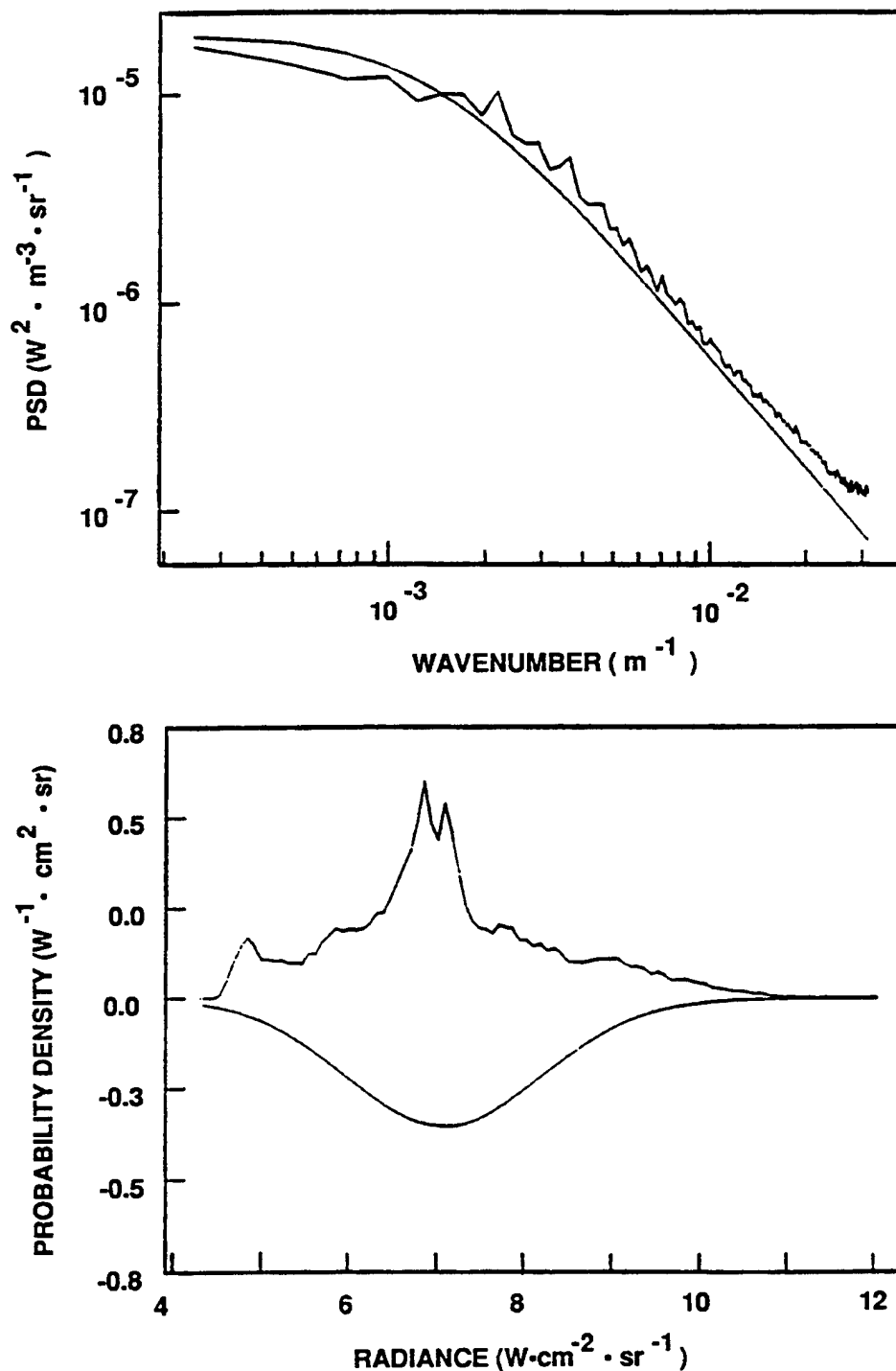
Figure 212. Model PSD (top) and PDF Compared with PSD and PDF Computed Directly from Brooks Range, Alaska GENESSIS Reference Scene for Noon Conditions in the 8.2-9.2 μm Band. The model PDF is plotted inverted with respect to the scene PDF.
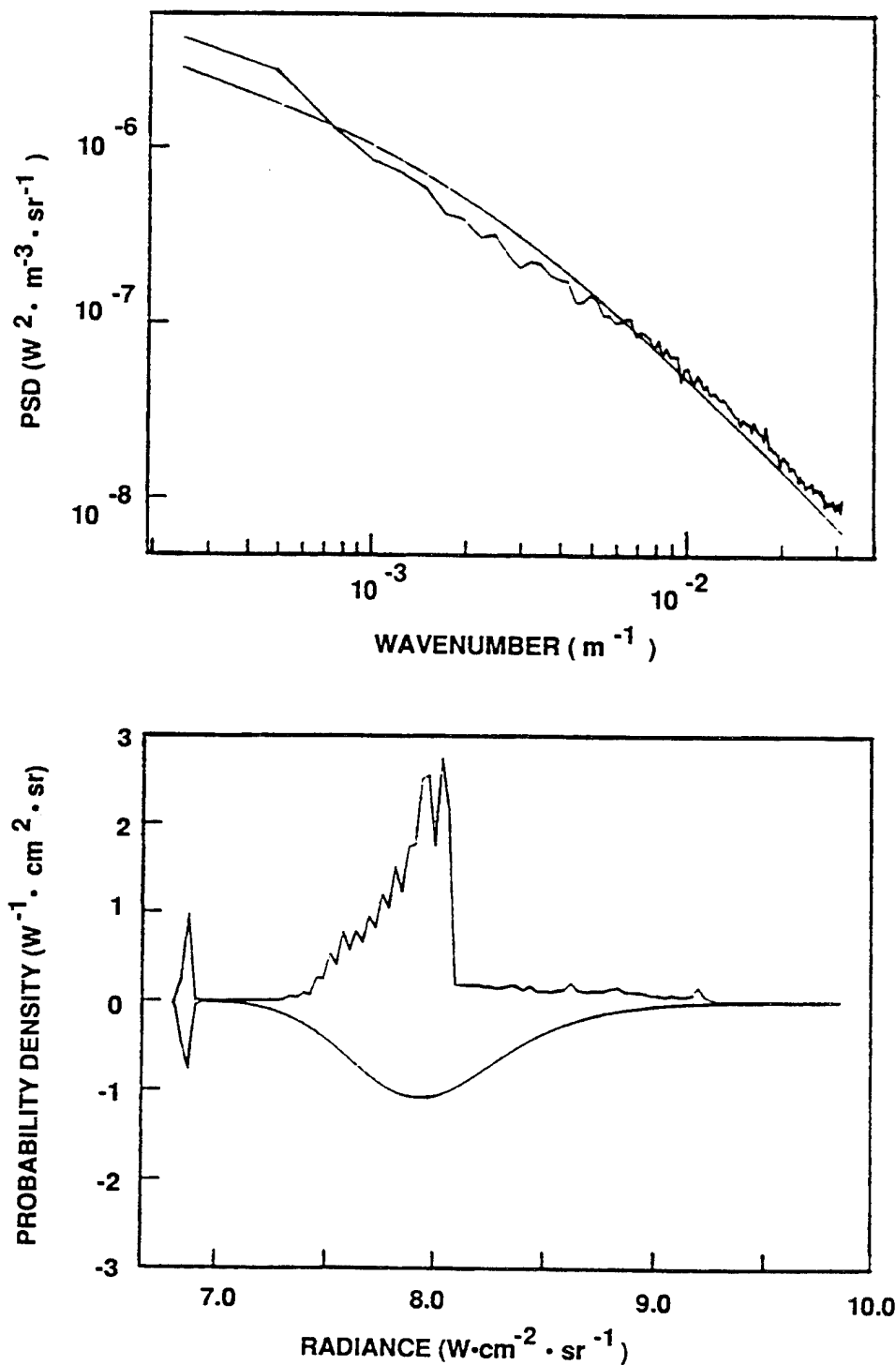
Figure 213. Model PSD (top) and PDF Compared with PSD and PDF
Computed Directly from Santa Cruz, California GENESSIS
Reference Scene for Noon Conditions in the 8.2-9.2 μm Band.
The model PDF is plotted inverted with respect to the
scene PDF.
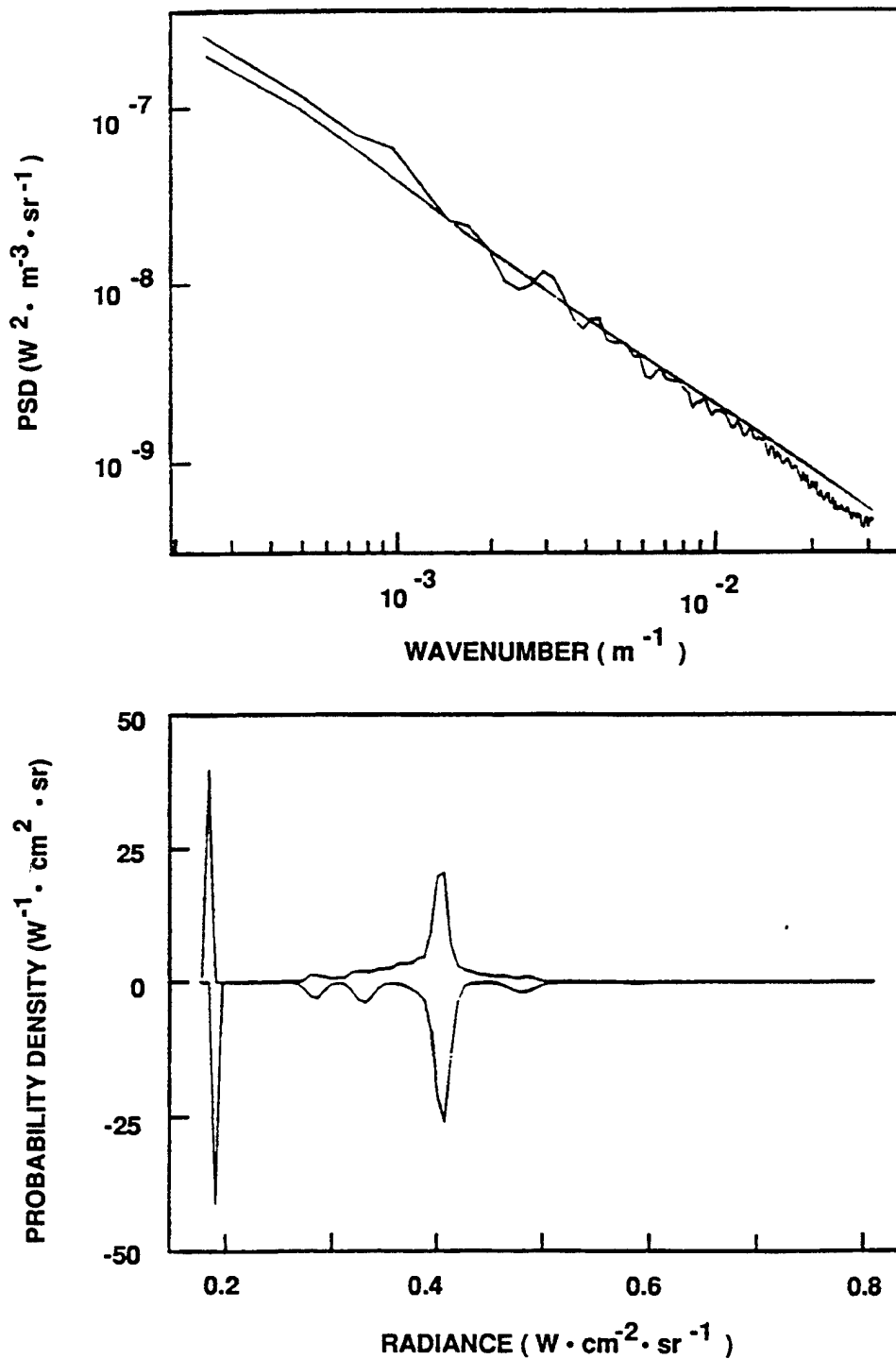
Figure 214. Model PSD (top) and PDF Compared with PSD and PDF
Computed Directly from San Diego, California GENESSIS
Reference Scene for Noon Conditions in the 3.7-4.1 μm Band.
The model PDF is plotted inverted with respect to the
scene PDF.

Figure 215. Model PSD (top) and PDF Compared with PSD and PDF
Computed Directly from Salton Sea, California GENESSIS
Reference Scene for Noon Conditions in the 8.2-9.2 μm Band.
The model PDF is plotted inverted with respect to the
scene PDF.

Figure 216. Model PSD (top) and PDF Compared with PSD and PDF
Computed Directly from Imperial Valley, California GENESSIS
Reference Scene for Noon Conditions in the 3.7-4.1 μm Band.
The model PDF is plotted inverted with respect to the
scene PDF.

311
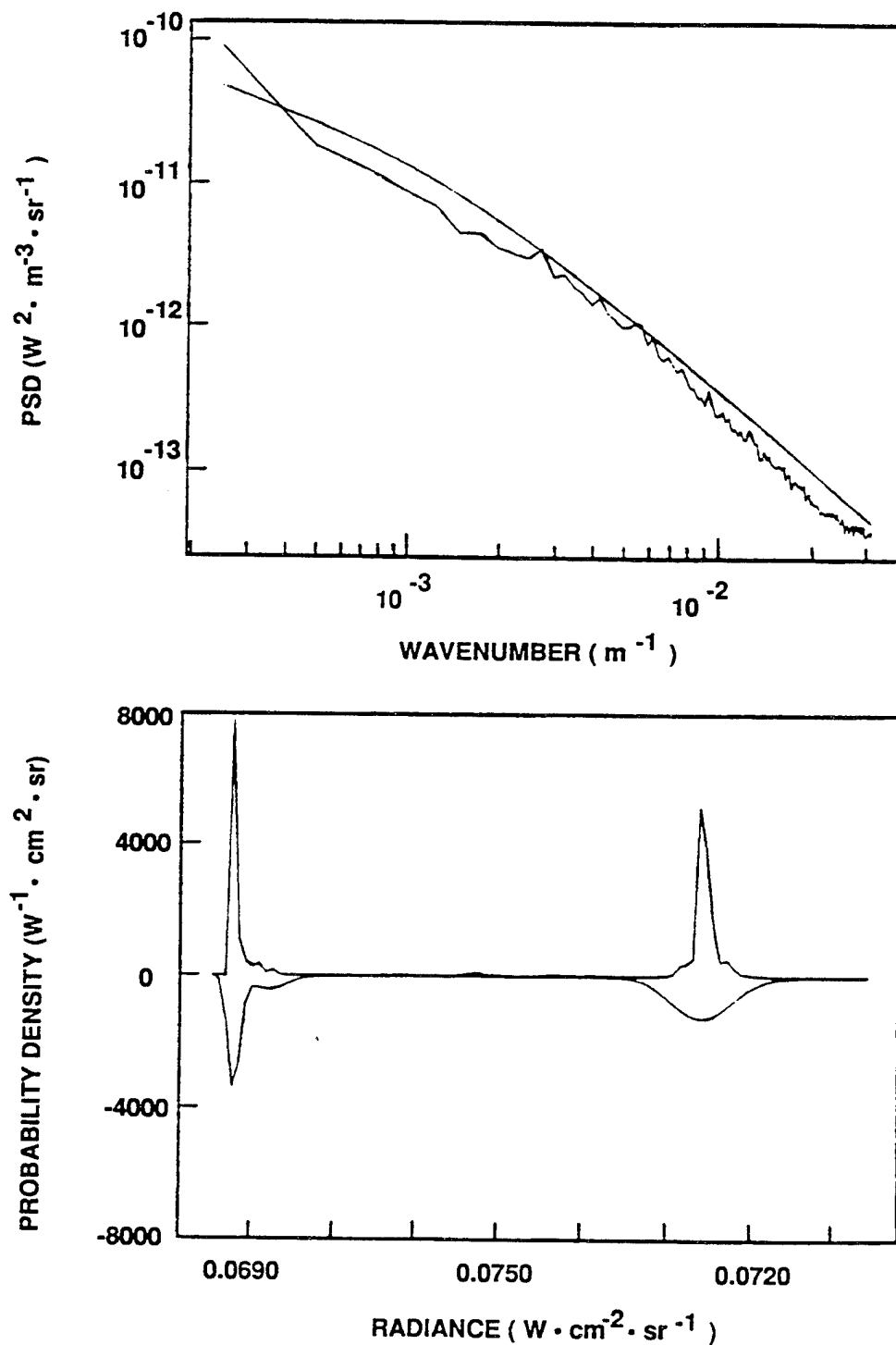
Figure 217. Model PSD (top) and PDF Compared with PSD and PDF Computed Directly from Point Barrow, Alaska GENESSIS Reference Scene for Noon Conditions in the 3.7-4.1 μm Band. The model PDF is plotted inverted with respect to scene PDF.

312
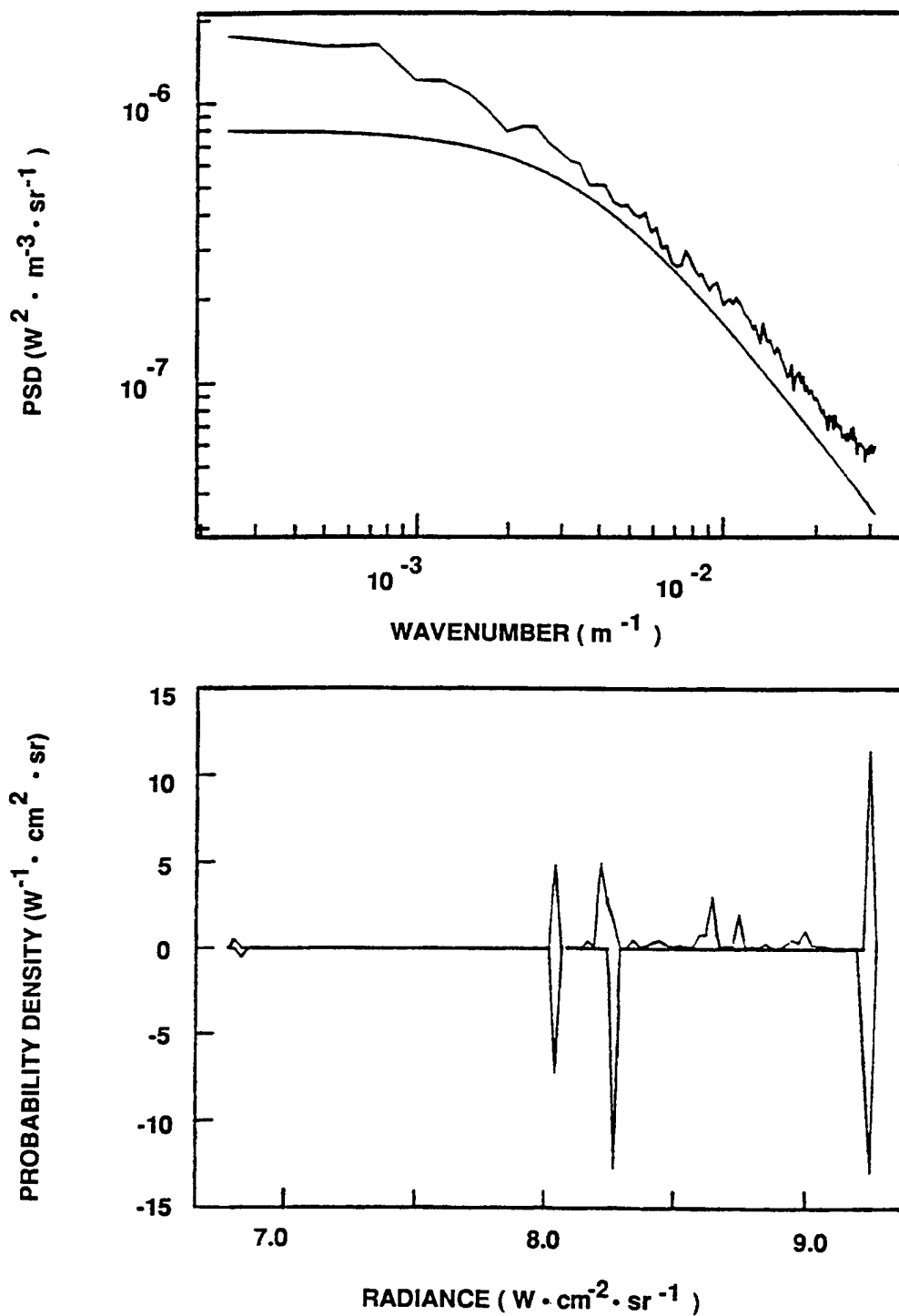
Figure 218. Model PSD (top) and PDF Compared with PSD and PDF
Computed Directly from Alberta Farms, Alberta GENESSIS
Reference Scene for Noon Conditions in the 8.2-9.2 μm Band.
The model PDF is plotted inverted with respect to the
scene PDF.

313
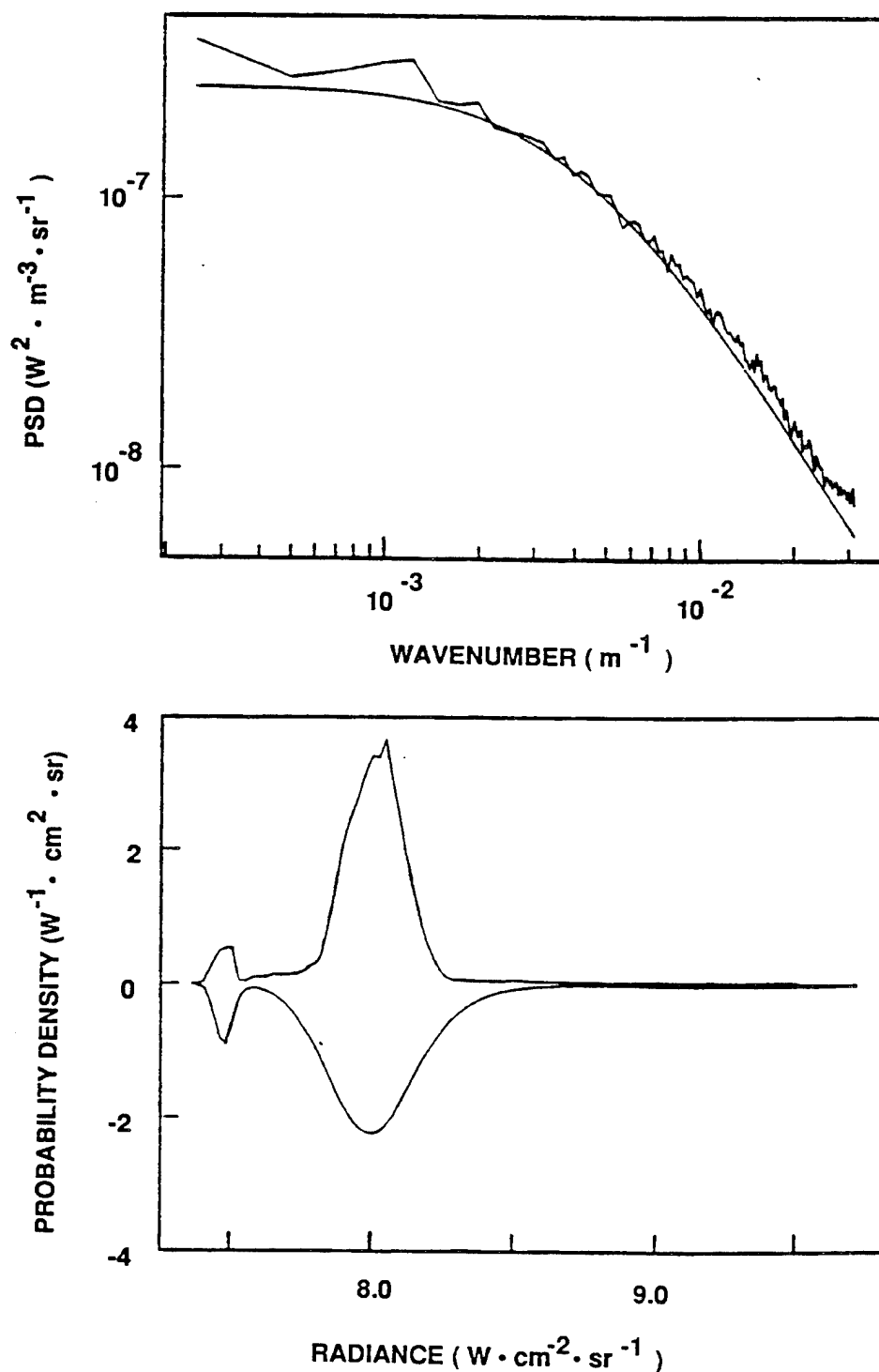
Figure 219. Model PSD (top) and PDF Compared with PSD and PDF Computed Directly from Wa Wa, Ontario GENESSIS Reference Scene for Noon Conditions in the 8.2-9.2 μm Band. The model PDF is plotted inverted with respect to the scene PDF.
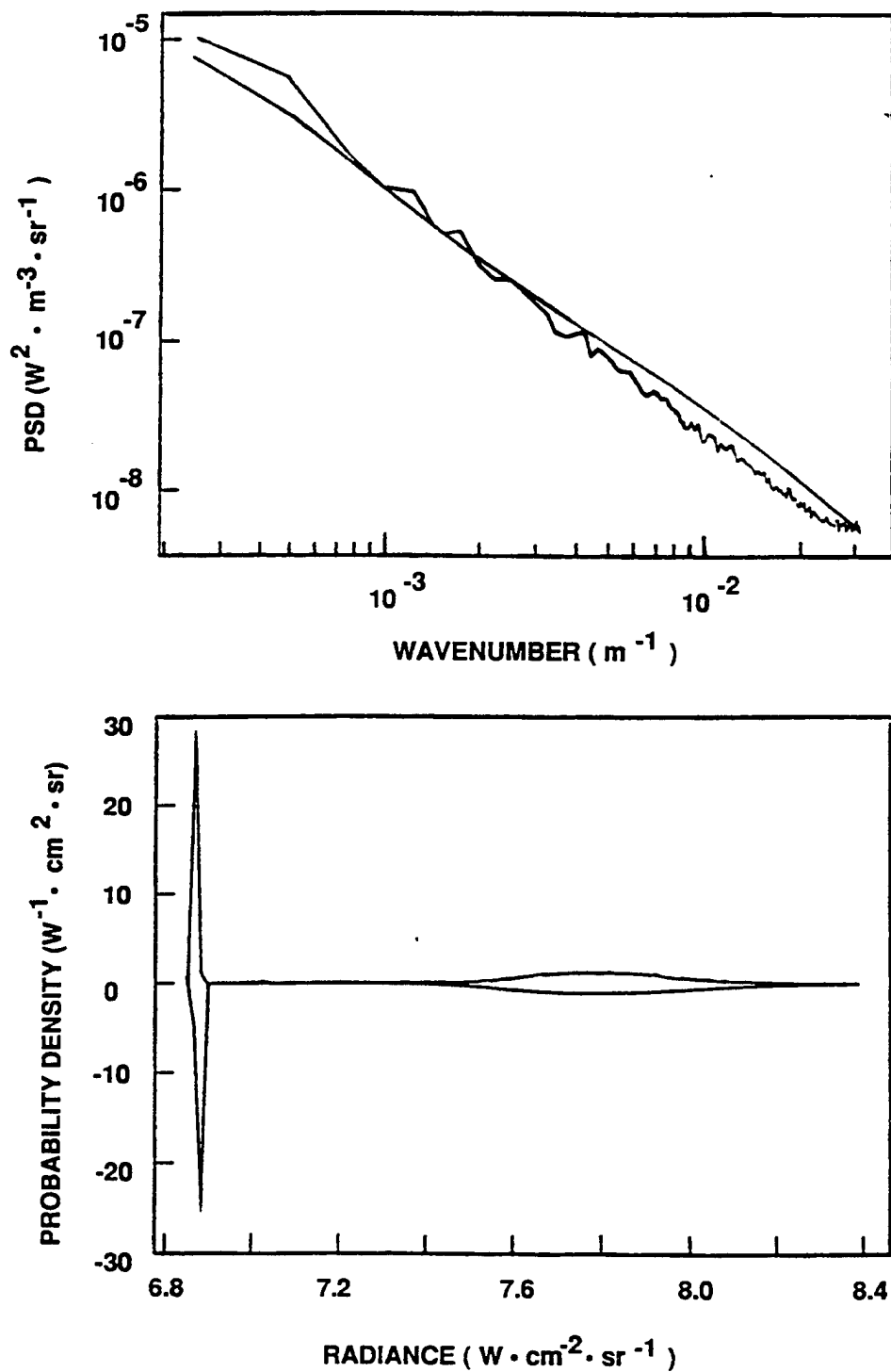
Figure 220. Model PSD (top) and PDF Compared with PSD and PDF
Computed Directly from Trondheim, Norway GENESSIS
Reference Scene for Noon Conditions in the 8.2-9.2 μm Band.
The model PDF is plotted inverted with respect to the
scene PDF.

315
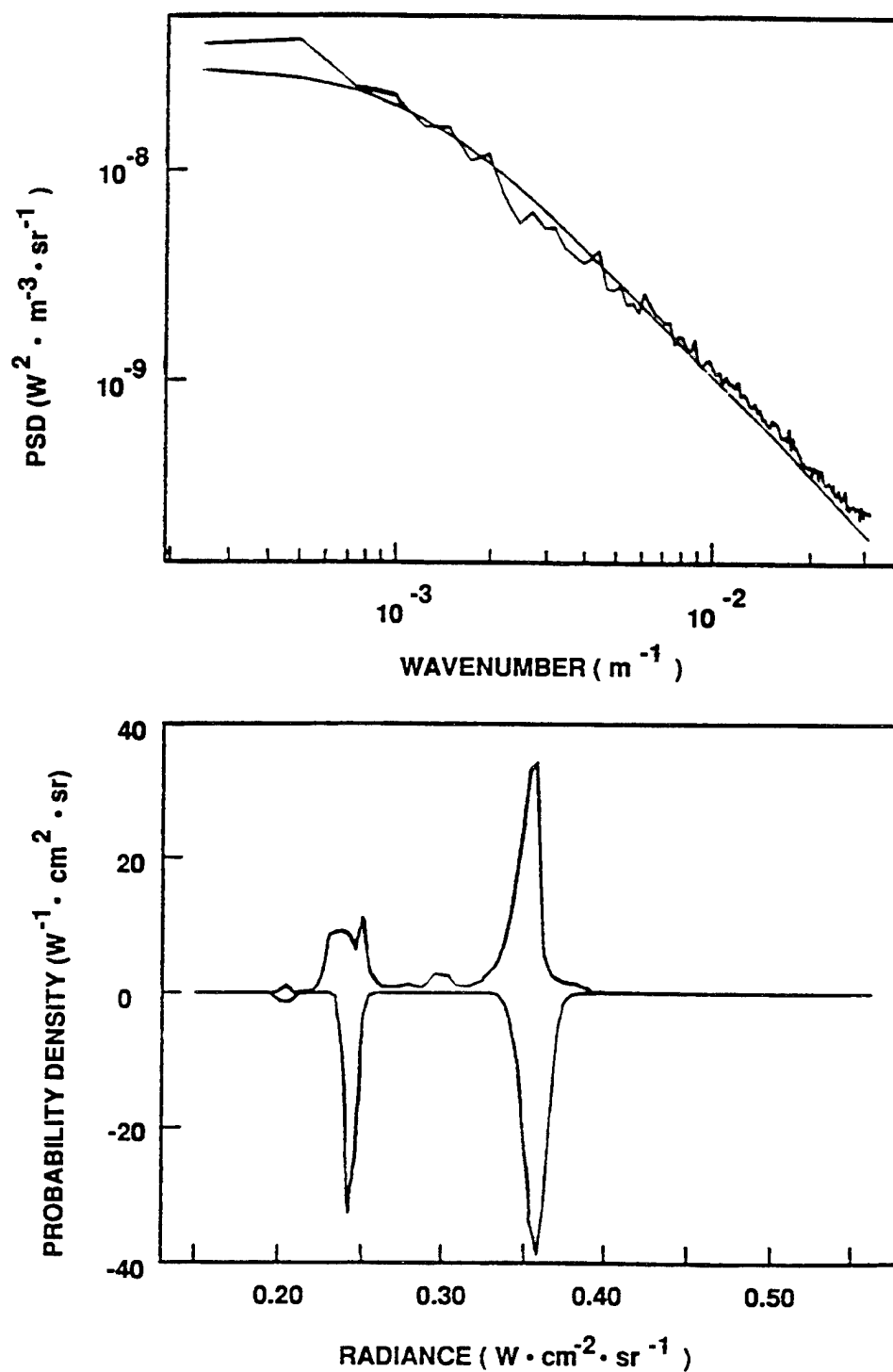
Figure 221. Model PSD (top) and PDF Compared with PSD and PDF
Computed Directly from Fulda, Germany GENESSIS Reference
Scene for Noon Conditions in the 3.7-4.1 μm Band. The
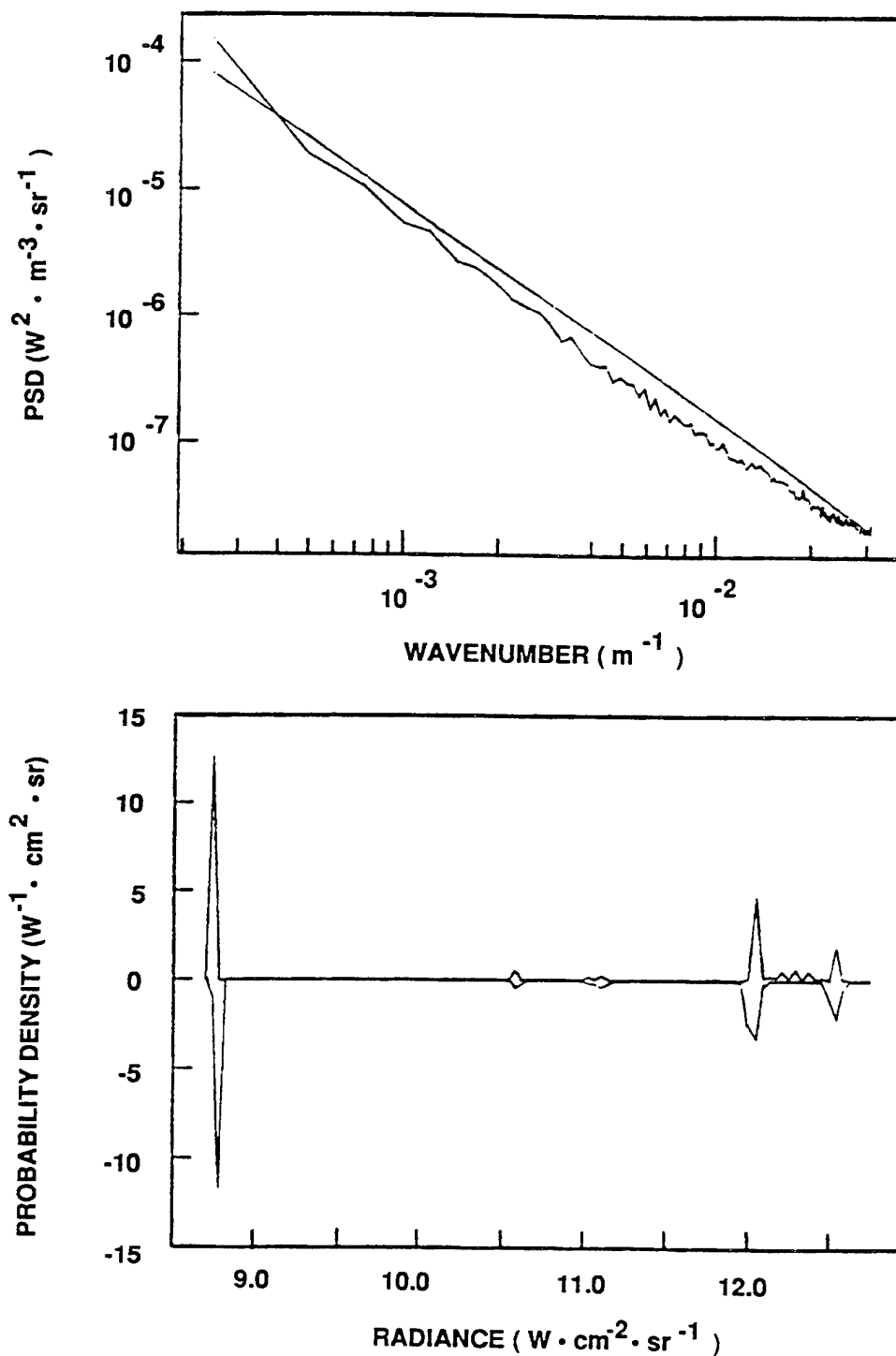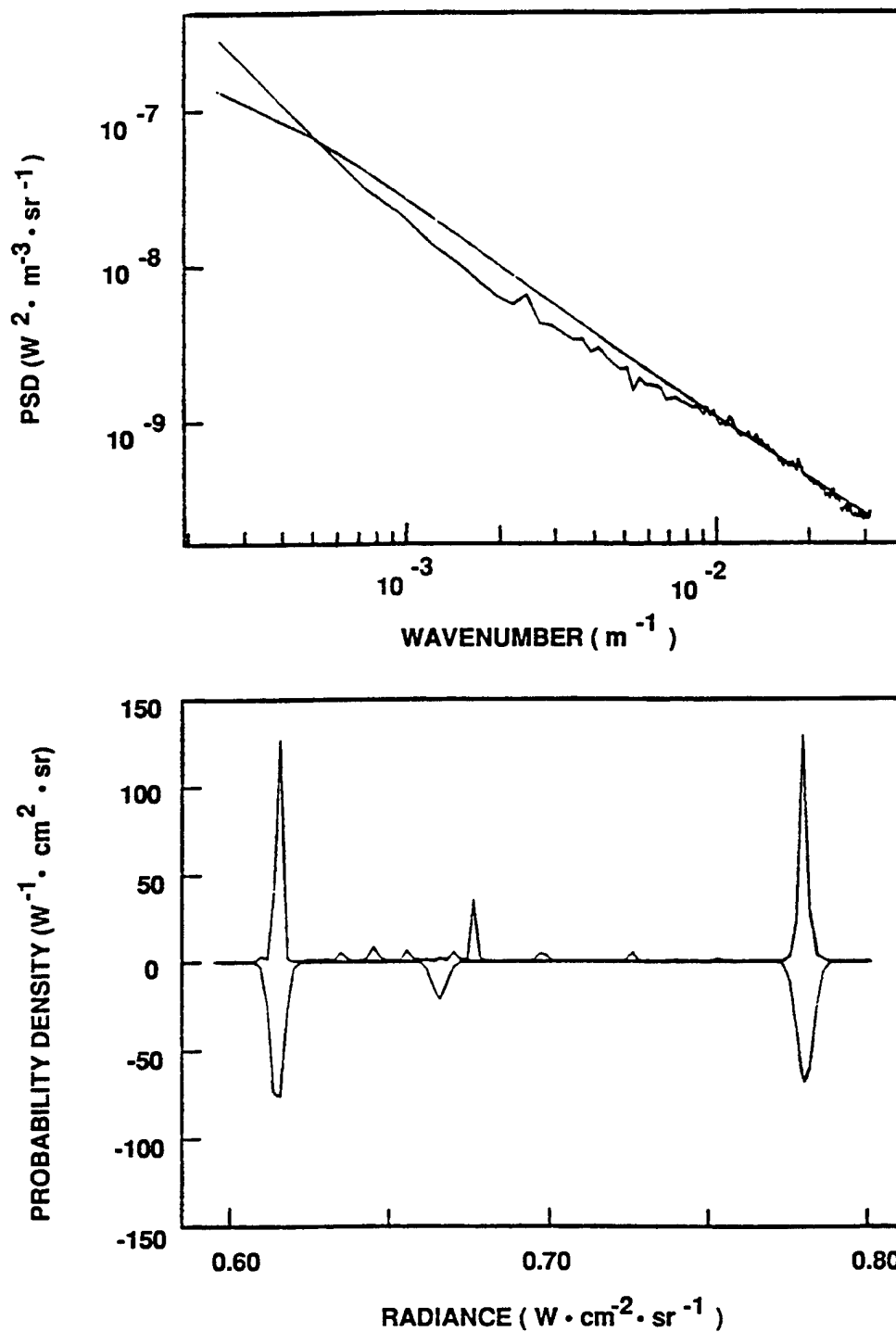model PDF is plotted inverted with respect to the scene PDF.

316
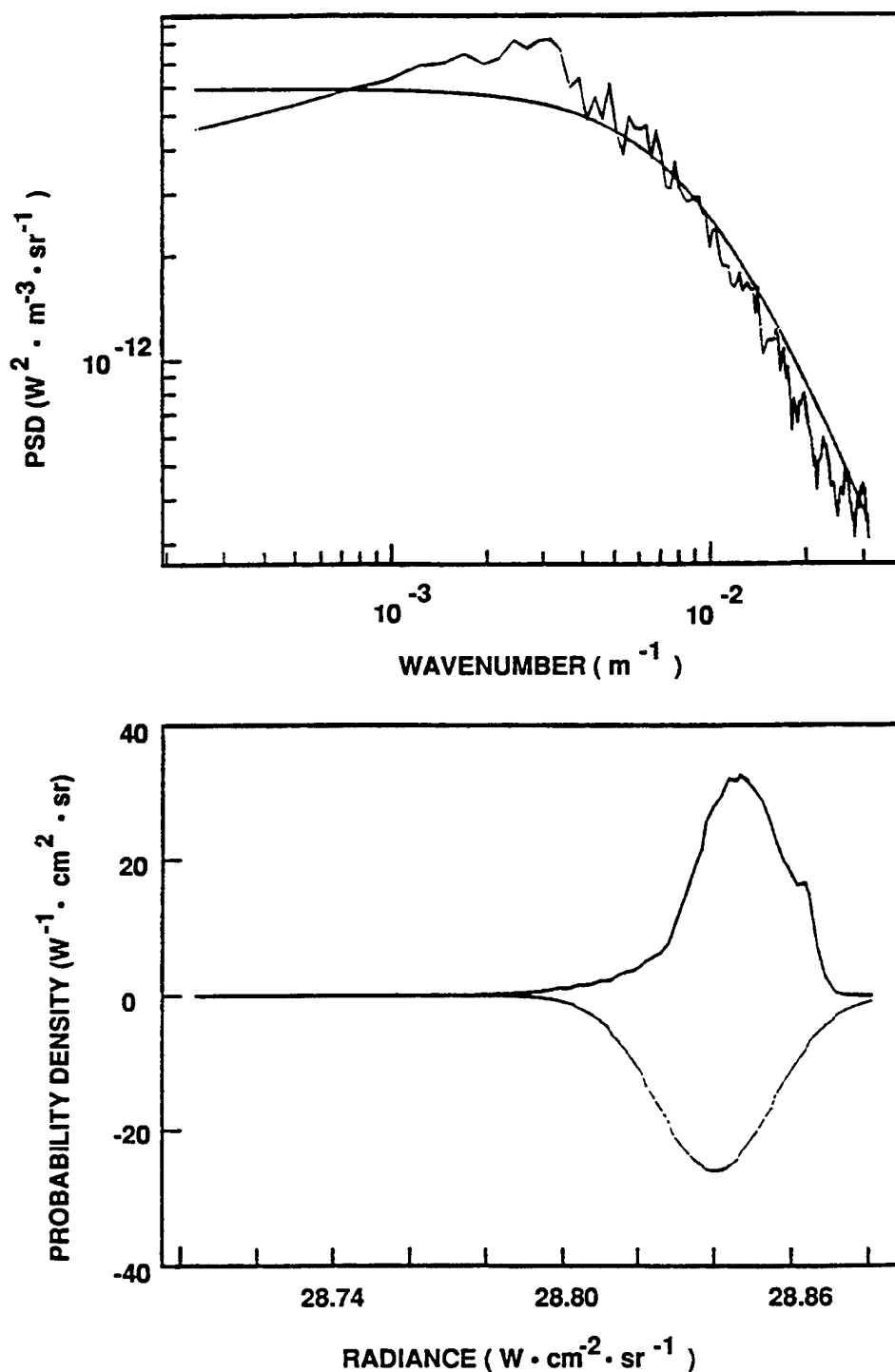
Figure 222. Model PSD (top) and PDF Compared with PSD and PDF
Computed Directly from Open Ocean Reference Scene in the
8-12 μm Band. The model PDF is plotted inverted with
respect to the scene PDF.

317
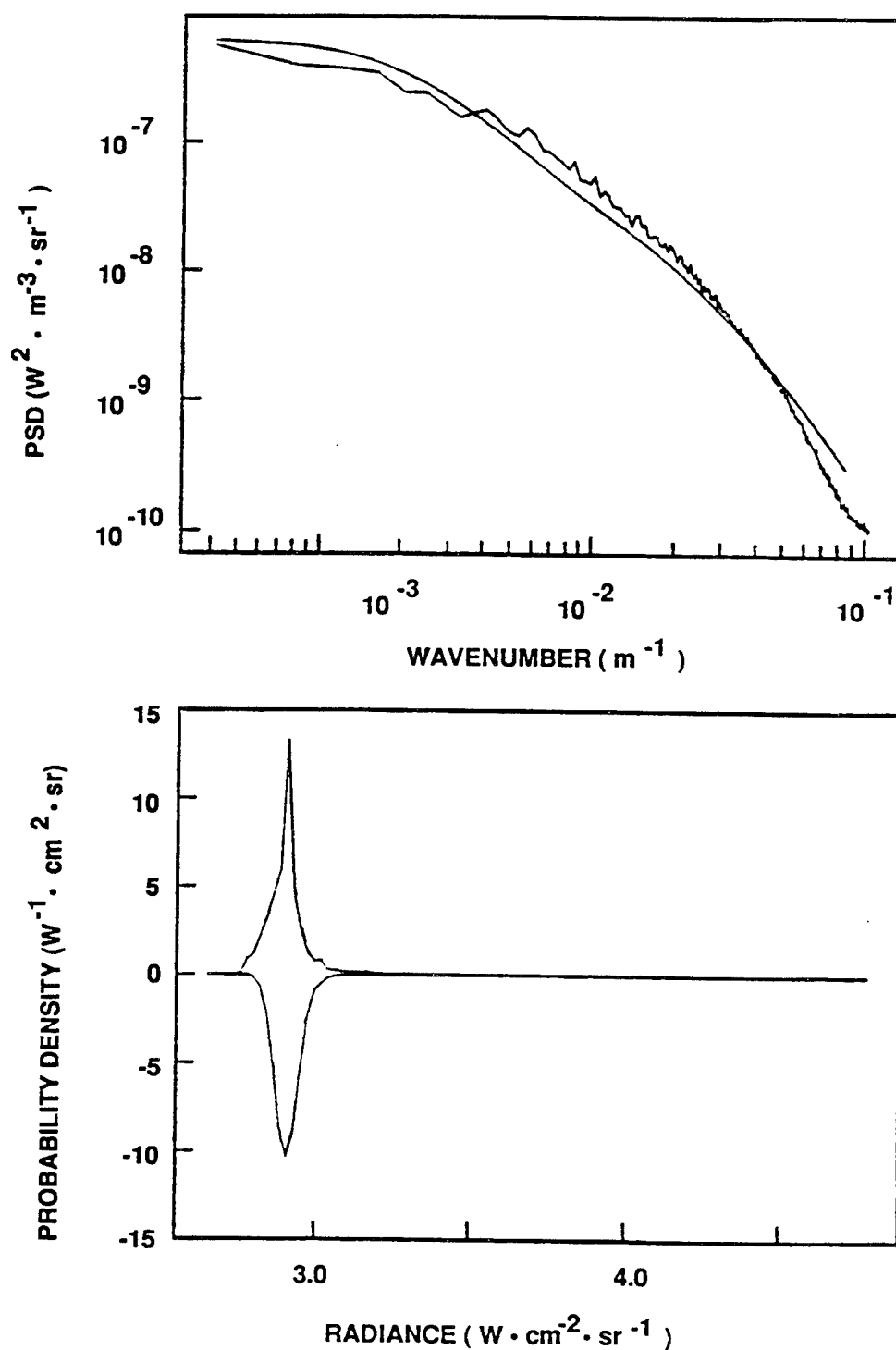
Figure 223. Model PSD (top) and PDF Compared with PSD and PDF
Computed Directly from Sea-Ice Reference Scene in the
8-13 μm Band. The model PDF is plotted inverted with
respect to the scene PDF.

7.0 REFERENCES AND BIBLIOGRAPHY

Abreu, L. W., 1988: Private communication.

Acquista, C. A., and D. C. Anding, 1986: Space Surveillance Systems Simulation. Proceedings of the 12th DARPA Strategic Systems Symposium.

Acquista, C. A., F. House, and J. C. Jafolla, 1981: N-stream Approximation to Radiative Transfer, J. Atmos. Sci., 38, 1446-1451.

American Ephemeris and Nautical Almanac, 1974: U.S. Government Printing Office, Washington, D.C.

Bean, B. R., and E. J. Dutton, 1968: Radio Meteorology. New York: Dover.

Bean, B. R., E. J. Dutton, and B. D. Warner, 1970: "Weather Effects on Radar", Radar Handbook, M. I. Skolnik (Ed.). New York: McGraw-Hill.

Bean, B. R., B. A. Cahoon, C. A. Samson, and G. D. Thayer, 1966: A World Atlas of Atmospheric Radio Refractivity. Washington: Environmental Science Services Administration, Monograph 1.

Benedict, W. S., and L. D. Kaplan, 1964: "Calculation of Line Widths in H_2O-H_2O and H_2O-O_2 Collisions." J. Quant. Spectry. Radiative Transfer 4, pp. 453-469.

Ben-Shalom, A., A. D. Devir, and S. G. Lipson, 1983: Infrared Spectral Radiance of the Sky, Optical Engineering, 22, 460-463.

Berk, A., L. S. Bernstein, and D. C. Robertson, 1989: MODTRAN: A Moderate Resolution Model for LOWTRAN 7. Air Force Geophysics Laboratory. GL-TR-89-0122, ADA214337.

Brown, E. W., 1919: Tables of Motion of the Moon (3 vols.), New Haven.

Burch, D. E., D. A. Gryunak, R. R. Patty, and C. E. Bartky, 1969: "Absorption of Infrared Radiant Energy by CO_2 and H_2O. IV. Shapes of Collision-Broadened CO_2 Lines." JOSA 59, 267.

Burge, C. J. and J. H. Lind, 1977: Line-of-Sight Handbook, Naval Weapons Center NWC-TP-5908.

Burrows, C. R., and S. S. Attwood, 1949: Radio Wave Propagation. New York: Academic Press.

Central Intelligence Agency, 1978: Polar Regions Atlas. GC-78-10040.

Chandrasekhar, S., 1960: Radiative Transfer. Dover Publications.

Cheung, A. S. -C., K. Yoshino, W. H. Parkinson, S. L. Guberman, and D. E. Freeman, 1986, "Absorption Cross Section Measurements of Oxygen in the Wavelength Region 195-241 nm of the Herzberg Continuum," Planetary and Space Science, May 1986 (to appear).

Coakley, J. A., and P. Chylek, 1975: The Two-Stream Approximation in Radiative Transfer: Including the Angle of Incident Radiation, J. Atmos. Sci., 32, 409-418.

Cooley, J. W., and J. W. Tukey, 1965: An Algorithm for Machine Calculation of Complex Fourier Series, Math Computation, 19.

Cornette, W. M., 1977a: Naval Weapons Center Version of the Atmospheric Transmittance Code LOWTRAN: User's Manual and Program Listing, Naval Weapons Center, NWC-TM-3107.

Cornette, W. M., 1977b: Infrared Sensor System Performance Model: User's Guide and Program Listing, Naval Weapons Center, TM-3112.

Cornette, W. M., 1977c: Atmospheric Refraction and the Effect Earth's Radius: Problems and Pitfalls. Naval Weapons Center, NWC TM-3028.

Cornette, W. M., A. Shlanta, W. -M. Yu, and E. T. Wu, 1978: Search and Detection Radar System Performance Simulation with Environmental Effects. Naval Weapons Center. NWC TM 3396.

Cornette, W. M., 1979a: Low Resolution Atmospheric Propagation, The Boeing Company, D180-25000-1.

Cornette, W. M., 1979b: Atmospheric Propagation and Radiation Transfer Computer Code - User's Manual, the Boeing Company, D180-25382-1.

Cornette, W. M., 1979c: A Low Resolution/High Resolution Atmospheric Propagation Computer Code, presented at the 1979 Annual Meeting of the Optical Society of America.

Cornette, W. M., 1980: Suggested Modification to the Total Volume Molecular Scattering Coefficient in LOWTRAN, Applied Optics 19, A182.

Cornette, W. M., 1983: The Effect of Band Correlation on Aircraft Skin Signatures, presented at the Annual Review Conference on Atmospheric Transmission Models.

Cornette, W. M., 1984: Suggested Numerical Modifications to LOWTRAN 6, presented at the Annual Review Conference on Atmospheric Transmission Models.

Cornette, W. M., 1985a: Comparisons between the LOWTRAN 6 Water Vapor Continuum and the 5 cm^{-1} LOWTRAN BMOD Water Vapor Tails, presented at the Annual Review Conference on Atmospheric Transmission Models.

Cornette, W. M., 1985b: The Atmospheric Propagation and Radiative Transfer (APART) Environmental Prediction Code, presented at the Annual Review Conference on Atmospheric Transmission Models.

Cornette, W. M., 1987: Impact of Multiple vs. Single Scatter in the Visible Spectral Region, PRA R-092-87.

Cornette, W. M, 1989: Development of a Global Atmosphere and Background Data Base for System Studies, presented at the AFGL Annual Review Conference on Atmospheric Transmission Models.

Cornette, W. M., 1990a: Atmospheric Propagation and Radiative Transfer (APART) Computer Code (Version 7.00). Vol. I: Installation Reference Manual. Photon Research Associates, Inc. PRA R-024-90.

Cornette, W. M., 1990b: Atmospheric Propagation and Radiative Transfer (APART) Computer Code (Version 7.00). Vol. II: User Reference Manual. Photon Research Associates, Inc. PRA R-062-90.

Cornette, W. M., 1990c: Atmospheric Propagation and Radiative Transfer (APART) Computer Code (Version 7.00). Vol. III: Technical Reference Manual. Photon Research Associates, Inc. PRA R-077-90.

Cornette, W. M., 1990d: Atmospheric Propagation and Radiative Transfer (APART) Computer Code (Version 7.00). Vol. IV: Software Reference Manual. Photon Research Associates, Inc. PRA R-075-90.

Cornette, W. M., 1990e: Atmospheric Propagation and Radiative Transfer (APART) Computer Code (Version 7.00). Vol. V: Source Code Listing. Photon Research Associates, Inc. PRA R-070-90.

Cornette, W. M., 1991a: Coupling Atmosphere and Background Effects. Presented at the 14th Annual Review Conference on Atmospheric Transmission Models.

Cornette, W. M., 1991b: Atmospheric Effects on Background Thermal Clutter. Photon Research Associates, Inc. PRA R-023-91.

Cornette, W. M., 1991c: Kwajalein Atoll Standard Atmosphere Model (KASAM). Final Report. Photon Research Associates, Inc. PRA R-110-91.

Cornette, W. M., 1992a: Robust Algorithm for Correcting the Layer Problem in LOWTRAN. AO 31, pp. 5767-5768.

Cornette, W. M., 1992b: Strategic Scene Generation Model (SSGM) Requirements for the Moderate Spectral Atmospheric Radiance and Transmittance (MOSART) Computer Code. Photon Research Associates, Inc. PRA R-102-92.

Cornette, W. M., 1992c: Millimeter Wave Scene Modeling. Photon Research Associates, Inc. PRA R-107-92.

Cornette, W. M., 1993: The MOSART Global Climatological and Terrain Data Bases for Modeling Background and Clutter. Presented at the Aerial Targeting Environment Meeting. Also Presented at the 16th Annual Review Conference on Atmospheric Transmission Models.

Cornette, W. M., and D. C. Anding, 1991: Atmospheric Models in the Strategic Scene Generation Model. Presented at the 14th Annual Review Conference on Atmospheric Transmission Models.

Cornette, W. M., and J. C. Jafolla, 1988: Update on the Atmospheric Propagation and Radiative Transfer (APART) Computer Code (Version 7.0), presented at the AFGL Annual Review Conference on Atmospheric Transmission Models.

Cornette, W. M., and J. C. Jafolla, 1989: PRA Signature and Background Codes, presented at the EO Aerial Targeting Models Users' Meeting, Wright-Patterson AFB, Ohio, 24-25 October 1989.

Cornette, W. M., and D. C. Robertson, 1992: MODTRAN and APART Code Evaluation. Photon Research Associates and Spectral Sciences, Inc. PRA B-199-91.

Cornette, W. M., and D. C. Robertson, 1993: The Moderate Spectral Atmospheric Radiance and Transmittance (MOSART) Program. Presented at the 16th Annual Review Conference on Atmospheric Transmission Models.

Cornette, W. M., D. C. Robertson, and G. P. Anderson, 1993: The Moderate Spectral Atmospheric Radiance and Transmittance (MOSART) Program. Proceedings of the Workshop on Atmospheric Correction of Landsat Imagery, P. N. Slater and L. D. Mendenhall (Eds.). pp. 70-74.

Cornette, W. M., and J. G. Shanks, 1991a: An Assessment of Cirrus Cloud Transmission Models. Photon Research Associates, Inc. PRA R-115-90.

Cornette, W. M., and J. G. Shanks, 1991b: Cirrus Cloud Transmission Modeling. Presented at the 14th Annual Review Conference on Atmospheric Transmission Models.

Cornette, W. M., and J. G. Shanks, 1992a: Physically Reasonable Analytic Expression for the Single-Scattering Phase Function. AO 31, pp. 3152-3160. Also presented at the 15th Annual Review Conference on Atmospheric Transmission Models.

Cornette, W. M., and J. G. Shanks, 1992b: Cirrus Cloud Parameters as They Pertain to the Study of the Impact of Cirrus Clouds on Determining Background Temperature. Photon Research Associates, Inc. PRA R-110-92.

Cornette, W. M., and J. G. Shanks, 1993a: Impact of Cirrus Clouds on Remote Sensing of Surface Temperatures. Passive Infrared Remote Sensing of Clouds and the Atmosphere. SPIE Proc. 1934, pp. 252-263. Photon Research Associates, Inc. PRA R-044-93.

Cornette, W. M., and J. G. Shanks, 1993b: The Impact of Thin Cirrus Clouds on Terrain Remote Sensing. Presented at the 16th Annual Review Conference on Atmospheric Transmission Models.

Cornette, W. M., J. G. Shanks, and F. C. Mertz, 1993: Visual and Subvisual Cirrus Cloud Characterization and Effects. Presented at the Aerial Targeting Environmental Meeting.

323

Edlen, B., 1953: The Dispersion of Standard Air. J. Opt. Soc. Am. 43, 339.

Edlen, B., 1966: The Refractive Index of Air. Metrologia 2, 71-80.

Elsasser, W. M., and M. F. Culbertson, 1961: Atmospheric Radiation Tables. Am. Meteor. Soc. Monograph, 4, No. 23.

Hauser, M. G., F. C. Gillett, F. J. Low, T. N. Gautier, C. A. Beichman, G. Neugebauer, H. H. Aumann, B. Bond, N. Boggess, J. P. Emerson, J. R. Houck, B. T. Soifer, and R. G. Walker, 1984: IRAS Observations of the Diffuse Infrared Background. Astrophys. J.

Hayford, J. F., 1909: The Figure of the Earth and Isostasy and Supplementary Investigation in 1909. Washington: U.S. Coast and Geodetic Survey.

Helmut, F. R., 1911: S. B. preuss Akad. Wiss., pp. 10-19.

Humlicek, J., 1979: "An Efficient Method for the Evaluation of the Complex Probability Function: The Voight Function and Its Derivations. J. Quant. Spectr. Rad. Trans., 21, pp. 309-313.

Jafolla, J. C., 1981: An Investigation of the Non-Linear Radiative Response of the Climate System, Ph.D. Thesis, Drexel Univ.

Jeffreys, Sir Harold, 1970: The Earth; Its Origins, History, and Physical Constitution, 5th ed. London: Cambridge Univ. Press.

Johnson, J. C., 1954: Physical Meteorology. MIT Press.

Johnson, R. W. and W. S. Hering, 1981: An Analysis of Natural Variations in European Sky and Terrain Radiance Measurements, University of California, San Diego, Visibility Laboratory, AFGL-TR-81-0317, ADA120487.

Kantor, A. J. and A. E. Cole, 1975: Tropical Atmospheres, 0 to 90 km, Air Force Cambridge Research Laboratories, AFCRL-TR-75-0527, ADA019940.

Kantor, A. J. and A. E. Cole, 1976: Monthly Midlatitude Atmospheres, Surface to 90 km, Air Force Geophysics Laboratory, AFGL-TR-76-0140, ADA030740.

Kantor, A. J. and A. E. Cole, 1977a: Arctic and Subarctic Atmospheres, 0 to 90 km, Air Force Geophysics Laboratory, AFGL-TR-77-0046, ADA040917.

Kantor, A. J. and A. E. Cole, 1977b: Monthly 90° N Atmospheres and High Latitude Warm and Cold Winter Stratosphere/Mesosphere, Air Force Geophysics Laboratory. AFGL-TR-77-0289, ADA051421.

Kerr, D. E. (Ed.), 1965: <u>Propagation of Short Radio Waves</u>. New York: Dover.

Kneizys, F. X., E. P. Shettle, W. O. Gallery, J. H. Chetwynd, Jr., L. W. Abreu, J. E. A. Selby, R. W. Fenn, and R. A. McClatchey, 1980: Atmospheric Transmittance/Radiance: Computer Code LOWTRAN 5, Air Force Geophysics Laboratory, AFGL-TR-80-0067, ADA088215.

Kneizys, F. X., E. P. Shettle, W. O. Gallery, J. H. Chetwynd, Jr., L. W. Abreu, J. E. A. Selby, S. A. Clough, and R. W. Fenn, 1983: Atmospheric Transmittance/Radiance: Computer Code LOWTRAN 6, Air Force Geophysics Laboratory, AFGL-TR-83-0187, ADA137786.

Kneizys, F. X., G. P. Anderson, E. P. Shettle, W. O. Gallery, L. W. Abreu, J. E. A. Selby, J. H. Chetwynd, Jr., and S. A. Clough, 1988: Users Guide to LOWTRAN 7. Air Force Geophysics Laboratory, AFGL-TR-88-0177, ADA206773.

Kornfeld, G., and W. Lawson, 1971: Visual Perception Models, <u>J. Opt. Soc. Amer.</u>, <u>61</u>, 811-820.

Lacis, A. A., and J. E. Hansen, 1974: A Parameterization for the Absorption of Solar Radiation in the Earth's Atmosphere, <u>J. Atmos. Sci.</u>, <u>31</u>, 118-133.

Liou, K.-N., and G. D. Wittman, 1979: (unknown reference, see Wittman, 1978).

Low, F. J., D. A. Beintema, T. N. Gautier, F. C. Gillett, C. A. Beichman, G. Neubauer, E. Young, H. H. Aumann, N. Boggess, J. P. Emerson, H. J. Habing, M. G. Hauser, J. R. Houck, M. Rowan-Robinson, B. T. Soifer, R. G. Walker, and P. R. Weissilius, 1984: Infrared Cirrus: New Components of the Extended IR Emission, Astrophys. J. 278, pp. 119-122.

Ludwig, C. B., 1985: Private Communication

Ludwig, C. B., A. Klier, and J. A. Myer, 1982: Long Slant Path Atmospheric Effects Investigation Based Upon Recent Stellar Observations from AMOS, Photon Research Associates, Inc., R-065-82.

Ludwig, C. B., W. Malkmus, J. E. Reardon, and J. A. L. Thomson, 1973: Handbook of Infrared Radiation from Combustion Gases. NASA SP-3080.

Malkmus, W., 1967: Random Lorentz Band Model with Exponentially-Tailed S^{-1} Line-Intensity Distribution Function. J. Opt. Soc. Am. 57, 323-329.

McClatchey, R. A., R. W. Fenn, J. E. A. Selby, F. E. Volz, and J. S. Garing, 1972: Optical Properties of the Atmosphere (Third Edition), Air Force Cambridge Research Laboratories, AFCRL-72-0497, AD753075.

Nautical Almanac, 1981: Her Majesty's Stationary Office, London.

Newcomb, S., 1895: "Tables of the Sun," Astronomical Papers prepared for the use of the American Ephemeris and Nautical Almanac 6 (part 1).

Nicholls, R. W., M. W. P. Cann, and J. B. Shin, 1986, "Realistic Numerical Synthesis of Shock-Excited Molecular Spectra," Presented at the 15th International Symposium on Shock Tubes and Waves. To Be Published by Stanford University Press.

Orr, R. K., and F. S. Hall, 1976: A Static Model for FLIR System Performance Prediction, Naval Weapons Center, TM-2827.

Owens, J. C., 1967: Optical Refractive Index of Air: Dependence on Pressure, Temperature and Composition. Applied Optics 6, 51-59.

Patterson, E. M., and J. B. Gillespie, 1989: Simplified Ultraviolet and Visible Wavelength Atmospheric Propagation Model, Applied Optics 28, 425 - 429.

Plass, G. N., 1958, Models for Spectral Band Absorption. JOSA, 48.

Pottasch, S. R., et al., 1984: IRAS Spectra of Planetary Nebula, Astrophys. J. (preprint).

Price, S. D., and J. P. Kennealy, 1989: The Infrared Celestial Background Scene Descriptor. SPIE Proc. 1110, p. 38.

Reeves, R., D. Anding, and F. Mertz, 1988: First-Principles Deterministic Simulation of IR and Visible Imagery. SPIE Proc. 933, pp. 207-230.

Robertson, D. C., L. S. Bernstein, and R. Haimes, 1980: Addition of a 5 cm^{-1} Spectral Resolution Band Model to LOWTRAN 5, Aerodyne Research Associates, Inc., ARI-RR-232.

Rothman, L. S., R. R. Gamache, A. Barbe, A. Goldman, J. R. Gillis, L. R. Brown, R. A. Toth, J. -M. Fland, and C. Camy-Peyret 1983a: AFGL Atmospheric Absorption Line Parameters Compilation: 1982 Edition, Applied Optics 22, 2247-2256.

Rothman, L. S., A. Goldman, J. R. Gillis, R. R. Gamache, H. M. Pickett, R. L. Poynter, H. Husson, and A. Chedin, 1983b: AFGL Trace Gas Compilation: 1982 Edition, Applied Optics 22, 1616-1627.

Rothman, L. S., R. R. Gamache, C. P. Rinsland, M. A. H. Smith, D. C. Benner, V. M. Devi, J. -M. Fland, C. Camy-Peyret, A. Perrin, A. Goldman, J. T. Massie, L. R. Brown, and R. A. Toth, 1992: The HITRAN Molecular Data Base: Editions of 1991 and 1992. J. Quant. Spectrosc. Radiat. Transfer, 48, pp. 469-507.

Sagan, C. and J. B. Pollack, 1967: Anisotropic Nonconservative Scattering and the Clouds of Venus. J. Geophys. Res. 72, 469-477.

Schelling, J. C., C. R. Burrows, and E. B. Ferrell, 1933: "Ultra-short-wave Propagation", Proc. IRE, Vol. 21, pp. 427-463.

Selby, J. E. A. and R. A. McClatchey, 1972: Atmospheric Transmittance from 0.25 to 28.5 Microns: Computer Code LOWTRAN 2, Air Force Cambridge Research Laboratories, AFCRL-72-0745, AD763721.

Selby, J. E. A. and R. A. McClatchey, 1975: Atmospheric Transmittance from 0.25 to 28.5 Microns: Computer Code LOWTRAN 3, Air Force Cambridge Research Laboratories, AFCRL-TR-75-0255, ADA017734.

Selby, J. E. A., E. P. Shettle, and R. A. McClatchey, 1975: Atmospheric Transmittance from 0.25 to 28.5 Microns: Supplement LOWTRAN 3B, Air Force Geophysics Laboratory, AFGL-TR-76-0258, ADA040701.

Selby, J. E. A., F. X. Kneizys, J. H. Chetwynd, Jr., and R. A. McClatchey, 1978: Atmospheric Transmittance/Radiance: Computer Code LOWTRAN 4, Air Force Geophysics Laboratory. AFGL-TR-78-0053, ADA058643.

Shanks, J. G., and W. M. Cornette, 1993: Impact of Cirrus Clouds on Remote Sensing of Surface Temperatures. Proceedings of the Workshop on Atmospheric Correction of Landsat Imagery, P. N. Slater and L. D. Mendenhall (Eds.), pp. 134-138.

Shettle, E. P., and R. W. Fenn, 1979: Models for the Aerosols of the Lower Atmosphere and the Effects of Humidity Variations on Their Optical Properties. AFGL-TR-79-0214, ADA085951.

Staley, D., and G. Jurica, 1974: Flux Emissivity Tables for Water Vapor, Carbon Dioxide, and Ozone. J. Appl. Meteor., 365-372.

Stamnes, K., S. Tsay, and M. Yeh, 1993: Inclusion of Accurate Multiple Scattering in MODTRAN. Presented at the 16th Annual Review Conference on Atmospheric Transmission Models.

Stavroudis, O. N., 1972: The Optics of Rays, Wavefronts, and Caustics. New York: Academic Press.

Stephens, G. L., 1978a: Radiation Profiles in Extended Water Clouds. I: Theory. J. Atmos. Sci., 35, 2111-2122.

Stephens, G. L., 1978b: Radiation Profiles in Extended Water Clouds. II: Parameterization Schemes, J. Atmos. Sci., 35, 2123-2132.

Stephens, G. L., G. W. Paltridge, and C. M. R. Platt, 1978: Radiation Profiles in Extended Water Clouds. III: Observations, J. Atmos. Sci., 35, 2133-2141.

Sundberg, R. L., J. W. Duff, J. H. Gruninger, L. S. Bernstein, M. W. Matthew, S. M. Adler-Golden, D. C. Robertson, R. D. Sharma, J. H. Brown, and R. J. Healey, 1995: SHARC, a Model for Calculating Atmospheric Infrared Radiation Under Non-Equilibrium Conditions. The Upper Mesosphere and Lower Thermosphere: A Review of Experiment and Theory: Geophysical Monograph 87. American Geophysical Union.

Thekaekara, M. P., 1974: Extraterrestrial Solar Spectrum, 3000-6100 A at 1A Intervals, Applied Optics 13.

Ulrich, P., 1988: (unknown title) WJSA/MA-TN-88-013, dated 22 April 1988.

U. S. Standard Atmosphere, 1976, NOAA-S/T 76-1562.

U. S. Standard Atmosphere Supplements, 1966.

Valley, G.C., 1980: Isoplanatic degradation of Tilt Correction and Short-Term Imaging Systems, AO 19 pp. 574-577.

van de Hulst, H., 1980: Multiple Light Scattering: Tables, Formulas, and Applications (2 vols.), Academic Press.

von Bochove, Ir. A. C., 1982: The Computer program "ILLUM": calculation of the positions of sun and moon and the natural illumination. Physics Laboratory TNO, Report No. PHL 1982-13 (OPAQUE D/NL-8210).

Wilson, W. H., 1980, Solar Ephemeris Algorithm, Visibility Laboratory, SIO Ref 80-13.

Wiscombe, W. J., and G. W. Grams, 1976: The Backscattering Fraction in Two-Stream Approximations, J. Atmos. Sci., 33, 2440-2451.

Wiscombe, W. J., and J. W. Evans, 1977: Exponential-Sum Fitting of Radiative Transmission Functions. J. of Comp. Physics 24, 416-444.

Wittman, G. D., 1978: Parameterization of the Solar and Infrared Properties of Clouds, M.S. Thesis, Dept. of Meteorology, Univ. of Utah.

Wolfe, W. L., and G. J. Zissis, 1978: The Infrared Handbook. Office of Naval Research.